
The crustal evolution of the Chatham Rise:

Mid-Cretaceous Hikurangi Plateau collision and breakup between Zealandia and Antarctica

A thesis submitted in partial fulfilment of the requirements
for the doctoral degree of Natural Sciences (Dr. rer. nat.)
to the Department of Geosciences, University of Bremen

March 2, 2020

by

Florian Riefstahl



ALFRED-WEGENER-INSTITUT
HELMHOLTZ-ZENTRUM FÜR POLAR-
UND MEERESFORSCHUNG



Federal Ministry
of Education
and Research



Helmholtz Graduate School for
Polar and Marine Research



Universität Bremen

Gutachter / Reviewer

PD Dr. Karsten Gohl

Alfred-Wegener-Institut Helmholtz-Zentrum für Polar- und Meeresforschung
Am Alten Hafen 26
27568 Bremerhaven

Prof. Dr. Sebastian Krastel

Universität Kiel
Institut für Geowissenschaften
Otto-Hahn-Platz 1
24118 Kiel

Versicherung an Eides Statt / *Affirmation in lieu of an oath*

gem. § 5 Abs. 5 der Promotionsordnung vom 18.06.2018 /
according to § 5 (5) of the Doctoral Degree Rules and Regulations of 18 June, 2018

Ich / I, Florian Riefstahl, Walter-Delius-Straße 79, 27574 Bremerhaven, 2135613

(Vorname / First Name, Name / Name, Anschrift / Address, ggf. Matr.-Nr. / student ID no., if applicable)

versichere an Eides Statt durch meine Unterschrift, dass ich die vorliegende Dissertation selbständig und ohne fremde Hilfe angefertigt und alle Stellen, die ich wörtlich dem Sinne nach aus Veröffentlichungen entnommen habe, als solche kenntlich gemacht habe, mich auch keiner anderen als der angegebenen Literatur oder sonstiger Hilfsmittel bedient habe und die zu Prüfungszwecken beigelegte elektronische Version (PDF) der Dissertation mit der abgegebenen gedruckten Version identisch ist. / *With my signature I affirm in lieu of an oath that I prepared the submitted dissertation independently and without illicit assistance from third parties, that I appropriately referenced any text or content from other sources, that I used only literature and resources listed in the dissertation, and that the electronic (PDF) and printed versions of the dissertation are identical.*

Ich versichere an Eides Statt, dass ich die vorgenannten Angaben nach bestem Wissen und Gewissen gemacht habe und dass die Angaben der Wahrheit entsprechen und ich nichts verschwiegen habe. / *I affirm in lieu of an oath that the information provided herein to the best of my knowledge is true and complete.*

Die Strafbarkeit einer falschen eidesstattlichen Versicherung ist mir bekannt, namentlich die Strafandrohung gemäß § 156 StGB bis zu drei Jahren Freiheitsstrafe oder Geldstrafe bei vorsätzlicher Begehung der Tat bzw. gemäß § 161 Abs. 1 StGB bis zu einem Jahr Freiheitsstrafe oder Geldstrafe bei fahrlässiger Begehung. / *I am aware that a false affidavit is a criminal offence which is punishable by law in accordance with § 156 of the German Criminal Code (StGB) with up to three years imprisonment or a fine in case of intention, or in accordance with § 161 (1) of the German Criminal Code with up to one year imprisonment or a fine in case of negligence.*

Ort / Place, Datum / Date

Unterschrift / Signature

Summary

The breakup of supercontinents is often associated with the changing polarity of tectonic forces from lithospheric convergence to lithospheric divergence. The initiation of the last supercontinent disintegration occurred simultaneously with the breakup of Gondwana. During the mid-Cretaceous, the East Gondwana margin underwent a remarkably fast transformation from a long-lived active subduction margin to a passive continental rifted margin, which led to the separation of southern Zealandia from West Antarctica. Recent studies suggest that the cessation of subduction and onset of extension in southern Zealandia was initiated by the collision and subduction of the thick oceanic Hikurangi Plateau with the East Gondwana subduction zone. However, little is known about the crustal structure of the Chatham Rise, east off New Zealand, although the Chatham Rise played a central role in change in tectonic forces. In particular, the nature of the southern Chatham Rise margin and the SE Chatham Terrace, an area of anomalously shallow seafloor hosting abundant seamounts and guyots, is poorly constrained.

To investigate the role of the Hikurangi Plateau collision and subduction on the onset of extension and rifting in southern Zealandia, geophysical data including wide-angle reflection and refraction seismic, multi-channel seismic reflection, and potential field data were acquired during RV Sonne cruise SO246 in 2016. Geophysical data were collected along four profiles across two sub-provinces of the Chatham Rise, the SE Chatham Terrace and adjacent oceanic crust. P-wave velocity and gravity modelling of the new geophysical data yield insights into the crustal structure and therefore the breakup mechanism of the southern Chatham Rise margin, constrain the extent of the Hikurangi Plateau underthrust beneath the Chatham Rise, and enhance our understanding of the driving forces behind the abrupt change from subduction to rifting along the East Gondwana margin.

Along the Chatham Rise, the P-wave velocity models highlight distinct differences in the crustal thickness between the eastern and western sub-provinces, but also reveal common characteristics in crustal composition. The crust of the western Chatham Rise is up to 25 km thick, whereas the eastern Chatham Rise is substantially thinner (14-18 km). Modelled P-wave velocities and densities suggest a similar geology for both parts. The Chatham Rise mainly consists of greywackes, meta-greywackes, and schist in the upper crust, and their high-temperature equivalents in the lower crust. This is consistent with its past position at an active continental margin. Seismic imaging and gravity data show that the 10-16 km thick Hikurangi Plateau is restricted to the lower crust of the western Chatham Rise. The geophysical data suggest that the Hikurangi Plateau does not reach as far south as previously proposed. Furthermore, southward thinning of the lower crustal layer along the westernmost profile, together with previously published data, indicates that a piece of the subducted oceanic Phoenix Plate is still present below the Chatham Rise and southern Zealandia. The crustal thickness of the SE Chatham Terrace varies between 5 and 8 km, which can be correlated to slightly thinner or thicker than Pacific oceanic crust (~6 km thickness). The velocity structure can be interpreted as similar to Pacific oceanic crust, but at the same time also shows characteristics of hyper-extended continental crust. Since graben structures are present, I interpret the SE Chatham Terrace as a broad continent-ocean transition zone, which consists of very thin continental crust modified by magmatic activity. Typical Pacific oceanic crust has been only found close to the easternmost Chatham Rise and is presumably not older than 88 Ma. The Pacific oceanic crust is separated from the Chatham Rise by a highly faulted area, which I interpret as exhumed lower continental crust.

High-velocity lower crust ($V_p > 7$ km/s) has been identified along the eastern Chatham Rise and at the easternmost Chatham Rise. These two areas of high-velocity lower crust are interpreted as

magmatic underplating and intrusions. Seaward-dipping reflector sequences typical of volcanic-rifted margins are completely absent along the southern Chatham Rise margin. Moreover, the southern Chatham Rise margin is largely fault-controlled, but the geophysical data do not support the presence of exhumed and serpentinised upper mantle, which is typical for magma-poor margins. On this basis, I interpret the southern Chatham Rise margin as a unique hybrid rifted margin, which shows features typical of both, volcanic-rifted and magma-poor margins.

Based on these observations, I developed a tectonic model that explains the multi-stage tectonic evolution of the southern Chatham Rise margin. Accordingly, the Hikurangi Plateau entered the subduction zone at ~110 Ma. Subsequently, convergence velocities slowed down until subduction ceased at ~100 Ma. The thicker crust of the western Chatham Rise is a result of the subduction and underthrusting of the Hikurangi Plateau, which most likely attenuated subsequent crustal extension along the western Chatham Rise. Slowing subduction in the sector of the Hikurangi Plateau led to development of subduction-transform edge propagator (STEP) faults on both sides of the plateau after 110 Ma. I suggest that the Hikurangi Plateau collision, together with fragmentation of the Phoenix Plate by these STEP faults, triggered and / or contributed to the previously hypothesized global-scale plate reorganisation event between 105 and 100 Ma. At the same time, rifting and crustal extension in southern Zealandia started. The rifting in southern Zealandia and the evolution of the southern Chatham Rise were likely the result of complex slab dynamics triggered by the Hikurangi Plateau subduction. First, rifting was initiated by shallowing of the subducted slab due to the higher buoyancy of the young and thick Hikurangi Plateau. Initial extension was oblique to the margin and arc, and led to the reactivation of former arc-parallel E-W thrust faults as normal faults. With prolonged extension, new generations of NE-SW normal faults started to form, and lower crust was exhumed along the easternmost tip of the Chatham Rise was initiated. Secondly, progressive eclogitisation of the land-ward Phoenix Plate slab is likely to have caused the slab to rollback after convergence ceased. This led to a prolonged episode of rifting during which extension focussed on the southern Chatham Rise margin (i.e. the SE Chatham Terrace and Bounty Trough). Finally, the style of extension changed after most of the Phoenix Plate slab became detached at around 90 Ma. The slab detachment opened a pathway for deep-seated and hot upwelling mantle, which resulted in (I) intrusions and magmatic underplating, (II) formation of the first oceanic crust along the easternmost tip of the Chatham Rise, (III) alkaline magmatism on the Chatham Island between 85 and 82 Ma and (IV) magmatic overprint of the SE Chatham Terrace leading to seamount formation. After 85 Ma, spreading segments became connected and the formation of the young Pacific-Antarctic Ridge led to the final separation of Zealandia from Antarctica.

Zusammenfassung

Das Auseinanderbrechen von Superkontinenten geht normalerweise mit einem Polaritätswechsel tektonischer Kräfte von lithosphärischer Konvergenz zu lithosphärischer Divergenz einher. Die letzte Trennung eines Großkontinents fand mit dem Auseinanderbrechen von Gondwana statt. Ostgondwana durchlebte während der mittleren Kreidezeit eine bemerkenswert schnelle Transformation von einem langlebigen, aktiven Kontinentalrand zu einem gerifteten, passiven Kontinentalrand. Dies führte zu der Trennung des südlichen Zealandia-Kontinents von der Westantarktis. In dieser Zeit kollidierte das Hikurangi-Plateau, das eine höhere Krustenmächtigkeit und mehr Auftrieb als normale Ozeankruste hat, mit der Ostgondwana-Subduktionszone. Aktuelle Studien gehen davon aus, dass diese Kollision das Ende der Subduktionsaktivität und den Beginn der Extension in dem Gebiet des südlichen Zealandia-Kontinents initiiert hat. Obwohl sich der submarine Chatham Rise östlich von Neuseeland in einer zentralen Position während dieser weitgreifenden Veränderung der tektonischen Kräfte befand, ist über dessen Krustenstruktur und die Art des Kontinentalrandes am südlichen Chatham Rise wenig bekannt. Genauso wenig ist über die SE Chatham Terrace südlich des Chatham Rise bekannt. Diese schlecht definierte Region ist flacher als der umliegende Meeresboden und mit viele Tiefseeberge und Guyots übersät.

Um den Zusammenhang der Kollision und Subduktion des Hikurangi-Plateaus mit dem Beginn von Extension und Rifting im südlichen Zealandia genauer zu untersuchen, wurden im Frühjahr 2016 während der Expedition SO246 auf dem FS Sonne neue geophysikalische Daten entlang von vier Profilen des östlichen und westlichen Chatham Rise gesammelt. Die Datenakquisition umfasste unter anderem Weitwinkelreflexions- und Refraktionsseismik, Reflexionsseismik und Potentialfelddaten entlang von vier Profilen am Chatham Rise, der SE Chatham Terrace und der sich daran anschließenden ozeanischen Kruste. Modellierungen der P-Wellengeschwindigkeiten und der Schwereanomalien auf der Basis der neuen geophysikalischen Daten liefern Hinweise auf die Krustenstruktur und Aufbruchmechanismen am südlichen Rand des Chatham Rise. Darüber hinaus können die neuen Daten Kenntnisse über das Ausmaß des unter den Chatham Rise geschobenen Hikurangi-Plateaus verbessern und das Verständnis der treibenden Kräfte hinter dem plötzlichen Polaritätswechsel der tektonischen Kräfte am ehemals aktiven Kontinentalrand Rand von Ostgondwana verbessern.

Die P-Wellengeschwindigkeitsmodelle der entlang des östlichen und westlichen Chatham Rise zeigen trotz deutlicher Unterschiede der Krustenmächtigkeiten auch Gemeinsamkeiten. Die Kruste des westlichen Chatham Rise ist bis zu 25 km mächtig, während die Kruste des östliche Chatham Rise eine deutlich geringere Krustenmächtigkeit (14-18 km) aufweist. Modellierete P-Wellengeschwindigkeiten und Gesteinsdichten weisen aber trotzdem auf eine ähnliche geologische Zusammensetzung beider Teile hin. Hauptsächlich besteht der Chatham Rise aus Grauwacken, Metagrauwacken und Schiefen in der Oberkruste und deren Hochtemperaturäquivalenten in der Unterkruste. Dies stimmt mit einer ehemaligen Lage an der aktiven Subduktionszone überein. Seismische sowie Schweredaten zeigen, dass die Krustenmächtigkeit des unterschobenen Hikurangi-Plateaus 10-16 km beträgt. Das Hikurangi-Plateau kommt nur in der Unterkruste des westlichen, nicht aber am östlichen Chatham Rise vor. Entgegen Annahmen früherer Studien weisen die neuen Daten darauf hin, dass das Hikurangi Plateau nicht so weit nach Süden unter den Chatham Rise reicht. Außerdem zeigt sich im westlichsten Profil eine südwärtige Ausdünnung der Unterkruste. Zusammen mit publizierten geophysikalischen Daten weist dies darauf hin, dass ein Teil der subduzierten Phoenix-Platte unter dem Chatham Rise und dem südlichem Zealandia zu finden ist. Die Kruste der SE Chatham Terrace hat eine variable Mächtigkeit zwischen 8 und 5 km. Verglichen mit typischer, 6 km mächtiger pazifischer Ozeankruste weist die SE Chatham Terrace

trotz ähnlicher Geschwindigkeitsstrukturen weitestgehend entweder niedrigere oder aber höhere Krustenmächtigkeiten auf. Die Struktur der SE Chatham Terrace ist aber auch mit sehr stark ausgedünnter, kontinentaler Kruste vergleichbar. Da auf der SE Chatham Terrace auch Gräben vorhanden sind, interpretiere ich sie als eine breite Kontinent-Ozean-Übergangszone, welche aus sehr dünner kontinentaler und magmatisch überprägter Kruste besteht. Typische Ozeankruste ist entlang des östlichsten Profils am Chatham Rise vorhanden und nicht älter als 88 Mio. Jahre. In diesem Bereich wird die Ozeankruste durch eine markante Störungszone vom Chatham Rise getrennt, welche ich als exhumierte kontinentale Unterkruste interpretiere.

Unterkruste mit hohen P-Wellengeschwindigkeiten ($V_p > 7$ km/s) wurde am östlichen Chatham Rise identifiziert. Diese zwei Zonen hoher P-Wellengeschwindigkeiten interpretiere ich als magmatische Anlagerungen unterhalb der kontinentalen Kruste und Intrusionen. Seewärts einfallende Reflektorsequenzen, welche typischerweise an magmatisch-gerifteten, passiven Kontinentalrändern vorkommen, sind am südlichen Chatham Rise aber nicht zu identifizieren. Andererseits zeigt sich, dass der südliche Rand des Chatham Rise weitestgehend durch Verwerfungen und Kippschollentektonik gebildet wurde. Weitere typische Anzeichen für magma-arme, passive Kontinentalränder wie exhumierter und serpentinierter Mantel sind jedoch in den geophysikalischen Daten nicht zu finden. Daraus folgend interpretiere ich den südlichen Kontinentalrand des Chatham Rise als einen einzigartigen, hybriden Kontinentalrand, der Merkmale sowohl von vulkanisch-gerifteten als auch magma-armen Kontinentalrändern zeigt.

Basierend auf diesen geophysikalischen Beobachtungen und Interpretationen habe ich ein tektonisches Modell entwickelt, um die verschiedenen Stadien der Entwicklung entlang des südlichen Chatham Rise zu erklären. Laut meines Modells kollidierte das Hikurangi-Plateau vor ca. 110 Mio. Jahren mit der Subduktionszone. Daraufhin verlangsamte sich die Konvergenzgeschwindigkeit, bis die Subduktion um ca. 100 Mio. Jahre stoppte. Ich erkläre die höhere Krustenmächtigkeit des westlichen Chatham Rise mit der Unterschiebung und Subduktion des Hikurangi-Plateaus, welche eine Krustenextension in diesem Bereich erschwerten. Die verlangsamte Subduktion führte zu der Ausbildung von Transformstörungen an den seitlichen Rändern des Hikurangi-Plateaus. Die Kollision des Hikurangi-Plateaus und die Fragmentierung der Phoenix-Platte löste wahrscheinlich die allgemein postulierte plattentektonische Neuordnung zwischen 105 und 100 Mio. Jahren aus. Zur selben Zeit begann das Rifting und die Krustenausdünnung im südlichen Zealandia. Das Rifting und die Entwicklung des Kontinentalrandes am südlichen Chatham Rise sind das Resultat komplexer Bewegungen der subduzierten Phoenix-Platte, die durch die Subduktion des Hikurangi-Plateaus ausgelöst wurden. Als Reaktion auf den stärkeren Auftrieb der jungen und mächtigeren Ozeankruste des Hikurangi-Plateaus wurde eine Abflachung der subduzierten Phoenix-Platte ausgelöst und schließlich die Krustendehnung initiiert. Die frühe Extension war schief zum Streichen des vulkanischen Bogens und des späteren passiven Kontinentalrands. Ursprüngliche Ost-West streichende Aufschiebungen parallel zum aktiven Kontinentalrand und vulkanischen Bogen wurden hierbei als Abschiebungen reaktiviert. Mit fortschreitender Extension begannen sich neue NO-SW streichende Abschiebungen auszubilden, und die Exhumierung der kontinentalen Unterkruste am östlichsten Chatham Rise wurde initiiert. Nach dem Ende der Konvergenz sorgte die fortschreitende Eklogitisierung der landwärtigen Phoenix-Platte für ein Zurückrollen der subduzierten Platte. Dies wiederum führte zu anhaltendem kontinentalem Rifting und Fokussierung der Extension im Bereich der SE Chatham Terrace und des Bounty-Trogs. Vor ca. 90 Mio. Jahren ist ein Großteil der Phoenix-Platte abgerissen, was die Art des Riftings zu mehr magmatischer Aktivität veränderte. Durch den Plattenabriss konnte heißes Mantelmaterial aus großer Tiefe aufsteigen. Dieses führte zu (I) Intrusionen und Bildung magmatischer Anlagerungen unterhalb des östlichen Chatham Rise, (II) der Entstehung der ersten Ozeankruste am östlichsten Chatham Rise, (III) alkalinem Magmatismus auf den Chatham Inseln zwischen 85 und 82 Mio. Jahren, (IV) einer magmatischen Überprägung der SE Chatham Terrace mit der Entstehung der heutigen Tiefseeberge. Nach 85 Ma verbanden sich die

vereinzelt Spreizungssegmente und die Entstehung des jungen pazifisch-antarktischen Rückens führte zu der finalen Trennung des Zealandia-Kontinents und der Antarktis.

Contents

<i>Versicherung an Eides Statt / Affirmation in lieu of an oath</i>	III
<i>Summary</i>	V
<i>Zusammenfassung</i>	VII
<i>Contents</i>	X
<i>Nomenclature</i>	XIII
<i>List of Figures</i>	XIV
<i>List of Tables</i>	XVIII
1. Introduction and Motivation	1
1.1. Subduction of oceanic plateaux	3
1.2. Formation and types of passive rifted margins	3
1.3. Geological and tectonic background	5
1.3.1. Tectonic setting and geology of the Chatham Rise and southern Zealandia	5
1.3.2. Evolution and collision of the Hikurangi Plateau with the East Gondwana margin	7
1.3.3. Onset of mid-Cretaceous rifting in southern Zealandia	8
1.3.4. Rift-drift transition along the southern Chatham Rise margin	8
1.4. Main objectives and scientific questions	8
Crustal structure and nature of the southern Chatham Rise margin	8
Extent of the Hikurangi Plateau beneath the Chatham Rise	9
Relationship between the Hikurangi Plateau collision and Zealandia rifting	9
1.5. Thesis outline	10
2. Declaration of co-author contributions	11
3. Datasets, methods and processing	13
3.1. Geophysical principles of seismic data acquisition	14
3.2. Data acquisition during the expedition SO246 and pre-existing data	15
3.2.1. Wide-angle reflection and refraction seismic data acquisition	15
3.2.2. Multi-channel seismic (MCS) data	18
3.2.3. Free-air gravity anomaly (FAA) data	19
3.2.4. Magnetic data	19
3.2.5. Bathymetric data	20
3.2.6. Pre-existing geophysical and geological datasets	20
3.3. Seismic data processing, P-wave velocity and density modelling	21
3.3.1. Onboard processing of the OBS / OBH data	21
3.3.2. MCS reflection data processing	22
3.3.3. Modelling the crustal structure from P-wave arrivals	23
3.3.4. Modelling the gravity anomaly	25
3.3.5. Plate kinematic / tectonic modelling	26
4. Manuscript I	27
Abstract	27
4.1. Introduction	28
4.2. Tectonic and geological background	29
4.2.1. Geologic history of South Zealandia and the Chatham Rise	31
4.3. Data acquisition, processing and modelling procedure	33
4.3.1. Seismic wide-angle reflection/refraction data	33
4.3.2. P-wave velocity modelling	33

4.3.3.	Multi-channel seismic (MCS) reflection data _____	33
4.3.4.	Potential field data and gravity modelling _____	34
4.3.5.	Plate-tectonic reconstruction _____	34
4.4.	Results and interpretation.....	34
4.4.1.	Model uncertainties _____	34
4.4.2.	The easternmost Chatham Rise and adjacent ocean floor _____	35
4.4.3.	The western and eastern Chatham Rise boundary and the eastern SE Chatham Terrace__	41
4.4.4.	The western Chatham Rise and central SE Chatham Terrace _____	47
4.5.	Crustal structure of the southern Chatham Rise margin	52
4.5.1.	The western and eastern Chatham Rise _____	52
4.5.2.	Geology of the western and eastern Chatham Rise _____	54
4.5.3.	Indications for crustal extension directions _____	56
4.5.4.	Extent of the Hikurangi Plateau beneath the western Chatham Rise_____	56
4.5.5.	Continent-ocean transition east of the Udintsev Fracture Zone (UFZ)_____	58
4.5.6.	The SE Chatham Terrace _____	59
4.5.7.	Implications for the onset of seafloor spreading at the southern Chatham Rise margin __	60
4.5.8.	Nature of the southern Chatham Rise margin _____	61
4.6.	Tectonic evolution of the Chatham Rise and its southern margin.....	62
4.6.1.	The collision of the Hikurangi Plateau with the East Gondwana margin _____	62
4.6.2.	The onset of continental rifting between Zealandia and West Antarctica _____	63
4.6.3.	The origin of the SE Chatham Terrace and onset of seafloor spreading_____	67
4.7.	Conclusions	68
	Acknowledgements	69
	Supplemental tables	71
	Supplemental figures	72
5.	Manuscript II	77
	Abstract.....	77
5.1.	Introduction	78
5.2.	Geological and tectonic background	79
5.3.	Methods.....	80
5.4.	Results and Interpretation	80
5.5.	Discussion.....	86
5.5.1.	Extent and thickness of the Hikurangi Plateau _____	86
5.5.2.	Extent and age of the Phoenix Plate _____	87
5.5.3.	Subduction geometry of the Phoenix Plate _____	89
5.5.4.	Plateau collision/underthrusting, slab flattening and onset of extension _____	89
5.5.5.	Development of STEP faults and slab rollback _____	91
5.5.6.	Slab detachment and focus of rifting in the Bounty Trough _____	91
5.5.7.	Plate tectonic implications _____	92
5.6.	Conclusions	93
	Acknowledgements	93
	Supplemental methods	95
	Seismic wide-angle reflection/refraction data _____	95
	Multi-channel seismic (MCS) reflection data _____	95
	Gravity data _____	95
	Supplemental tables _____	97
	Supplemental figures	98

6. Co-authorship I	99
Abstract	99
6.1. Introduction	100
6.2. Geological background	101
6.2.1. Oceanic crust east of Zealandia	101
6.2.2. Zealandia intraplate lavas	102
6.3. Samples and methods.....	102
6.4. Data	104
6.4.1. Osbourn MORB lava	104
6.4.2. Intraplate lavas: eastern Zealandia	105
6.4.3. Intraplate lavas and dikes: South Island	105
6.5. Discussion	107
6.5.1. Osbourn Trough spreading system	107
6.5.2. Oceanic crust age constraints	109
6.5.3. Zealandia syn-rift intraplate magmatism	109
6.5.4. Hikurangi Plateau-Gondwana collision	110
6.6. Tectonic model	111
6.7. Conclusions	112
Acknowledgments	113
Supplemental material	114
7. Co-authorship II	115
Abstract	115
7.1. Introduction	116
7.2. Samples and analytical methods	117
7.3. Results	118
7.4. Discussion	119
7.4.1. Formation of four intraplate volcanic provinces after Hikurangi Plateau collision	121
7.4.2. A common HIMU end member for the Late Cretaceous intraplate volcanism	124
7.4.3. A model to explain Late Cretaceous HIMU Intraplate volcanism	127
7.4.4. Origin of Cenozoic HIMU-like lavas and the “Zealandia-Antarctic” mantle domain	129
7.5. Conclusions and wider implications.....	130
Acknowledgements	131
Supplemental material	132
8. Conclusions.....	133
Crustal structure and nature of the southern Chatham Rise margin	133
Nature of the southern Chatham Rise margin	133
Extent of the Hikurangi Plateau beneath Chatham Rise	133
Tectonic evolution of the southern Chatham Rise margin	134
9. Outlook and future research.....	135
References.....	137
Danksagung	151
Appendix	153
A1. AWI-20160100.....	154
A2. AWI-20160200.....	192
A3. AWI-20160300.....	229
A4. AWI-20160400.....	252

Nomenclature

AGC	=	Automatic gain control	OJNP	=	Ontong Java Nui Plateau
Anl	=	Antipodes Island	OT	=	Osborn Trough
ANT	=	Antarctica	PAC	=	Pacific (Plate)
Aul	=	Auckland Island	PHO	=	Phoenix (Plate)
ASE	=	Amundsen Sea Embayment	RMS	=	Residual mean square
AUS	=	Australia	SDR	=	Seward-dipping reflector
AWI	=	Alfred Wegener Institute	SI	=	South Island of New Zealand
BGA	=	Bellingshausen Gravity Anomaly	STEP	=	Subduction-transform edge propagator
BI	=	Bounty Island	TFZ	=	Tharp Fracture Zone
BP	=	Bounty Platform	TI	=	Total magnetic field intensity
Cal	=	Campbell Island	TTJ	=	Tongareva Triple Junction
CB	=	Canterbury Basin	TWT	=	Two-way traveltime
Chl / CI	=	Chatham Island	UCSB	=	University of California Santa Barbara
CDP	=	Common-depth point	UFZ	=	Udintsev Fracture Zone
COB	=	Continent-ocean	VEI	=	Volcanic explosivity index
COT	=	Continent-ocean transition	WANT	=	West Antarctica
COTZ	=	Continent-ocean transition zone	WCR	=	Western Chatham Rise
CP	=	Campbell Plateau	WMBL	=	Western Marie Byrd Land
CR	=	Chatham Rise	WU	=	Western Uprising Seamount
CT	=	SE Chatham Terrace	WWR	=	West Wishbone Ridge
DAMP	=	Diffuse alkalic magmatic province			
DGGA	=	De Gerlache Gravity Anomaly			
DM	=	Depleted mantle			
DSDB	=	Deep-Sea Drilling Program			
EANT	=	East Antarctica			
ECR	=	East Chatham Rise			
EM	=	Enriched mantle			
EMBL	=	Eastern Marie Byrd Land			
EWS	=	East Wishbone Scarp			
FAA	=	Free-air gravity anomaly			
FAR	=	Farallon (Plate)			
FF	=	Forty Fours			
FZ	=	Fracture Zone			
GEBCO	=	General Bathymetric Chart of the Oceans			
GSB	=	Great South Basin			
HFZ	=	Heezen Fracture Zone			
HIMU	=	high μ = 238U/204Pb			
HP	=	Hikurangi Plateau			
HVLC	=	High-velocity lower crust			
KA	=	Kermadec Arc			
LIP	=	Large igneous province			
MCS	=	Multi-channel seismic / seismics			
MORB	=	Mid-ocean ridge basalt			
MS	=	Manihiki Scarp			
MSWD	=	Mean square weighted deviation			
N-MORB	=	Normal mid-ocean ridge basalts			
NHM	=	Northern Hikurangi Margin			
NI	=	North Island of New Zealand			
NMO	=	Normal-moveout			
NZ	=	New Zealand			
OBH	=	Ocean-bottom hydrophone			
OBS	=	Ocean-bottom seismometer			
OIB	=	Ocean-island basalt			
OJP	=	Ontong Java Plateau			

List of Figures

Fig. 1.1: The Wilson cycle	1
Fig. 1.2: General structure of the continent-ocean transitions.....	4
Fig. 1.3: Overview of the continent Zealandia	6
Fig. 1.4: Reconstruction of the former East Gondwana active margin.	7
Fig. 3.1: Cruise logo of the SO246 expedition	13
Fig. 3.2: Schematic illustration of geophysical data acquisition.....	14
Fig. 3.3: Overview of newly acquired geophysical data	16
Fig. 3.4: Photographs of the OBS/OBH instruments	17
Fig. 3.5: Photographs of the streamer and G-Gun cluster	18
Fig. 3.6: Photographs of the marine gravity meter and magnetometer	19
Fig. 3.7: Overview of pre-existing geophysical data.....	21
Fig. 3.8: Processing scheme os the OBS/OBH data	22
Fig. 3.9: Processing scheme of the MCS reflection data	23
Fig. 3.10: Processing flow for P-wave velocity and gravity modelling	24
Fig. 3.11: OBS/OBH data example.....	25
Fig. 3.12: P-wave velocity-density relationship.....	26
Fig. 4.1: Bathymetry map of Zealandia’s continental and surrounding areas	29
Fig. 4.2: Satellite free-air gravity anomaly map and detail bathymetry map.....	30
Fig. 4.3: Time-migrated MCS reflection profiles	36
Fig. 4.4: P-wave velocity model along seismic line AWI-20160300	37
Fig. 4.5: Ray coverage and hit count along seismic profile AWI-20160300	39
Fig. 4.6: Examples for OBS/OBH records along the seismic line AWI-20160300	40
Fig. 4.7: P-wave velocity model of the seismic line AWI-20160200.....	42
Fig. 4.8: Ray coverage and hit count along seismic profile AWI-20160200	43
Fig. 4.9: Examples for OBS/OBH records along the seismic line AWI-20160200	45
Fig. 4.10: Examples for the P_{HVLCP} and P_mP reflection phases from st216	46
Fig. 4.11: P-wave velocity model of the seismic line AWI-20160100.....	48
Fig. 4.12: Ray coverage and hit count along seismic profile AWI-20160100	49
Fig. 4.13: Examples for OBS/OBH records along the seismic line AWI-20160100	51
Fig. 4.14: 1D velocity-depth profiles	53
Fig. 4.15: Geological interpretation of the profiles.....	55
Fig. 4.16: Structural interpretation and proposed continen-ocean boundary.....	57
Fig. 4.17: Tectonic reconstructions for the Zealandia-West Antarctica region.....	63
Fig. S4.1: Uninterpreted time-migrated seismic reflection profiles.....	72
Fig. S4.2: Ray coverage plots along seismic refraction profile AWI-20160300	73
Fig. S4.3: Ray coverage plots along seismic refraction profile AWI-20160200	74
Fig. S4.4: Ray coverage plots along seismic refraction profile AWI-20160100	75
Fig. 5.1: Bathymetry overview map of the Chatham Rise and Hikurangi Plateau	78
Fig. 5.2: P-wave velocity-depth model along profile AWI-20160400.....	81
Fig. 5.3: MCS reflection data and interpretation along profile AWI-20160400	83
Fig. 5.4: Ray phases, resolution, and hit count plots along profile AWI-20160400	84
Fig. 5.5: Examples of OBS/OBH records along profile AWI-20160400	85
Fig. 5.6: Geological interpretation and extent of the Hikurangi Plateau	88
Fig. 5.7: Conceptual model of the Hikurangi Plateau underthrusting.....	90
Fig. S5.1: Ray coverage plots along seismic refraction profile AWI-20160400	98
Fig. 6.1: Present day map of the Zealandia continent and adjacent SW Pacific Ocean	100
Fig. 6.2: Seafloor bathymetry of the sample sites.....	103
Fig. 6.3: Composition plots of dated lavas	106

Fig. 6.4: Selected $^{40}\text{Ar}/^{39}\text{Ar}$ ages	108
Fig. 6.5: Interpretation of four main tectonic blocks in Zealandia	109
Fig. 6.6: Plot of age versus present day latitude	110
Fig. 6.7: New model for Late Cretaceous magmatic and tectonic change in Zealandia	111
Fig. 7.1 Bathymetric map of Zealandia and Hikurangi Plateau.....	117
Fig. 7.2: Major element diagrams.....	118
Fig. 7.3: Immobile and incompatible element classification diagrams	120
Fig. 7.4: Representative incompatible-element patterns.....	121
Fig. 7.5: Plots of initial isotope ratios	123
Fig. 7.6: Conceptual model of the evolution of the Zealandia continental margin	128
Fig. A1: Bathymetric map along profile AWI-20160100.....	155
Fig. A2: Ray tracing results for station st102.....	156
Fig. A3: Ray tracing results for station st104.....	157
Fig. A4: Ray tracing results for station st105.....	158
Fig. A5: Ray tracing results for station st106.....	159
Fig. A6: Ray tracing results for station st108.....	160
Fig. A7: Ray tracing results for station st109.....	161
Fig. A8: Ray tracing results for station st110.....	162
Fig. A9: Ray tracing results for station st111.....	163
Fig. A10: Ray tracing results for station st112.....	164
Fig. A11: Ray tracing results for station st113.....	165
Fig. A12: Ray tracing results for station st114.....	166
Fig. A13: Ray tracing results for station st115.....	167
Fig. A14: Ray tracing results for station st116.....	168
Fig. A15: Ray tracing results for station st117.....	169
Fig. A16: Ray tracing results for station st118.....	170
Fig. A17: Ray tracing results for station st119.....	171
Fig. A18: Ray tracing results for station st120.....	172
Fig. A19: Ray tracing results for station st121.....	173
Fig. A20: Ray tracing results for station st123.....	174
Fig. A21: Ray tracing results for station st124.....	175
Fig. A22: Ray tracing results for station st125.....	176
Fig. A23: Ray tracing results for station st126.....	177
Fig. A24: Ray tracing results for station st127.....	178
Fig. A25: Ray tracing results for station st128.....	179
Fig. A26: Ray tracing results for station st129.....	180
Fig. A27: Ray tracing results for station st130.....	181
Fig. A28: Ray tracing results for station st131.....	182
Fig. A29: Ray tracing results for station st132.....	183
Fig. A30: Ray tracing results for station st133.....	184
Fig. A31: Ray tracing results for station st134.....	185
Fig. A32: Ray tracing results for station st135.....	186
Fig. A33: Ray tracing results for station st136.....	187
Fig. A34: Ray tracing results for station st137.....	188
Fig. A35: Ray tracing results for station st138.....	189
Fig. A36: Ray tracing results for station st139.....	190
Fig. A37: Ray tracing results for station st140.....	191
Fig. A38: Bathymetric along profile AWI-20160200.....	193
Fig. A39: Ray tracing results for station st201.....	194
Fig. A40: Ray tracing results for station st202.....	195
Fig. A41: Ray tracing results for station st203.....	196

List of Figures

Fig. A42: Ray tracing results for station st204.....	197
Fig. A43: Ray tracing results for station st205.....	198
Fig. A44: Ray tracing results for station st206.....	199
Fig. A45: Ray tracing results for station st207.....	200
Fig. A46: Ray tracing results for station st208.....	201
Fig. A47: Ray tracing results for station st209.....	202
Fig. A48: Ray tracing results for station st210.....	203
Fig. A49: Ray tracing results for station st211.....	204
Fig. A50: Ray tracing results for station st212.....	205
Fig. A51: Ray tracing results for station st213.....	206
Fig. A52: Ray tracing results for station st214.....	207
Fig. A53: Ray tracing results for station st215.....	208
Fig. A54: Ray tracing results for station st216.....	209
Fig. A55: Ray tracing results for station st217.....	210
Fig. A56: Ray tracing results for station st218.....	211
Fig. A57: Ray tracing results for station st219.....	212
Fig. A58: Ray tracing results for station st220.....	213
Fig. A59: Ray tracing results for station st221.....	214
Fig. A60: Ray tracing results for station st222.....	215
Fig. A61: Ray tracing results for station st223.....	216
Fig. A62: Ray tracing results for station st224.....	217
Fig. A63: Ray tracing results for station st225.....	218
Fig. A64: Ray tracing results for station st226.....	219
Fig. A65: Ray tracing results for station st227.....	220
Fig. A66: Ray tracing results for station st228.....	221
Fig. A67: Ray tracing results for station st229.....	222
Fig. A68: Ray tracing results for station st230.....	223
Fig. A69: Ray tracing results for station st231.....	224
Fig. A70: Ray tracing results for station st232.....	225
Fig. A71: Ray tracing results for station st233.....	226
Fig. A72: Ray tracing results for station st234.....	227
Fig. A73: Ray tracing results for station st235.....	228
Fig. A74: Bathymetric along profile AWI-20160300.....	230
Fig. A75: Ray tracing results for station st301.....	231
Fig. A76: Ray tracing results for station st302.....	232
Fig. A77: Ray tracing results for station st303.....	233
Fig. A78: Ray tracing results for station st304.....	234
Fig. A79: Ray tracing results for station st305.....	235
Fig. A80: Ray tracing results for station st306.....	236
Fig. A81: Ray tracing results for station st307.....	237
Fig. A82: Ray tracing results for station st308.....	238
Fig. A83: Ray tracing results for station st309.....	239
Fig. A84: Ray tracing results for station st310.....	240
Fig. A85: Ray tracing results for station st311.....	241
Fig. A86: Ray tracing results for station st312.....	242
Fig. A87: Ray tracing results for station st313.....	243
Fig. A88: Ray tracing results for station st314.....	244
Fig. A89: Ray tracing results for station st315.....	245
Fig. A90: Ray tracing results for station st316.....	246
Fig. A91: Ray tracing results for station st317.....	247
Fig. A92: Ray tracing results for station st318.....	248
Fig. A93: Ray tracing results for station st319.....	249
Fig. A94: Ray tracing results for station st320.....	250

Fig. A95: Ray tracing results for station st321	251
Fig. A96: Bathymetric map along profile AWI-20160100	253
Fig. A97: Ray tracing results for station st401	254
Fig. A98: Ray tracing results for station st402	255
Fig. A99: Ray tracing results for station st403	256
Fig. A100: Ray tracing results for station st404	257
Fig. A101: Ray tracing results for station st405	258
Fig. A102: Ray tracing results for station st406	259
Fig. A103: Ray tracing results for station st407	260
Fig. A104: Ray tracing results for station st408	261
Fig. A105: Ray tracing results for station st409	262
Fig. A106: Ray tracing results for station st410	263
Fig. A107: Ray tracing results for station st411	264
Fig. A108: Ray tracing results for station st412	265
Fig. A109: Ray tracing results for station st413	266
Fig. A110: Ray tracing results for station st414	267
Fig. A111: Ray tracing results for station st415	268
Fig. A112: Ray tracing results for station st416	269
Fig. A113: Ray tracing results for station st417	270
Fig. A114: Ray tracing results for station st418	271
Fig. A115: Ray tracing results for station st419	272

List of Tables

Tab. 4.1: Layer parameters and according uncertainties along AWI-20160300	38
Tab. 4.2: Layer parameters and according uncertainties along AWI-20160200	44
Tab. 4.3: Layer parameters and according uncertainties along AWI-20160100	50
Tab. S4.1: Statistics of the P-wave velocity model along profile AWI-20160100.....	71
Tab. S4.2: Statistics of the P-wave velocity model along profile AWI-20160200.....	71
Tab. S4.3: Statistics of the P-wave velocity model along profile AWI-20160300.....	71
Tab. 5.1 Layer parameters and according uncertainties along AWI-20160400	82
Tab. S5.1: Inversion results for different layers along AWI-20160400	97
Tab. S5.2: Inversion results for different stations along AWI-20160400	97
Tab. 6.1: Sample location data and interpreted Ar-Ar ages.....	104
Tab. A1: Configurations and quality of the OBS / OBH stations along profile AWI-20160100	154
Tab. A2: Configurations and quality of the OBS / OBH stations along profile AWI-20160200	192
Tab. A3: Configurations and quality of the OBS / OBH stations along profile AWI-20160300	229
Tab. A4: Configurations and quality of the OBS / OBH stations along profile AWI-20160400	252

1. Introduction and Motivation

Convergence and divergence are the key forces in plate tectonics. Subduction of oceanic crust and continental collision at active margins result from lithospheric convergence. In contrast, lithospheric divergence leads to rifting in continental settings, formation of passive continental margins and formation of new oceanic crust at mid-ocean ridges. The Wilson cycle (e.g. Dewey & Burke, 1974; Wilson et al., 2019) describes the repeating supercontinent assembly and dispersal through the Earth's history in response to these tectonic forces (Fig. 1.1). The last disintegration of a supercontinent was initiated with the Mesozoic breakup of the Gondwana, which includes the continents of South America, Africa, Australia, Arabia, and the subcontinent India.

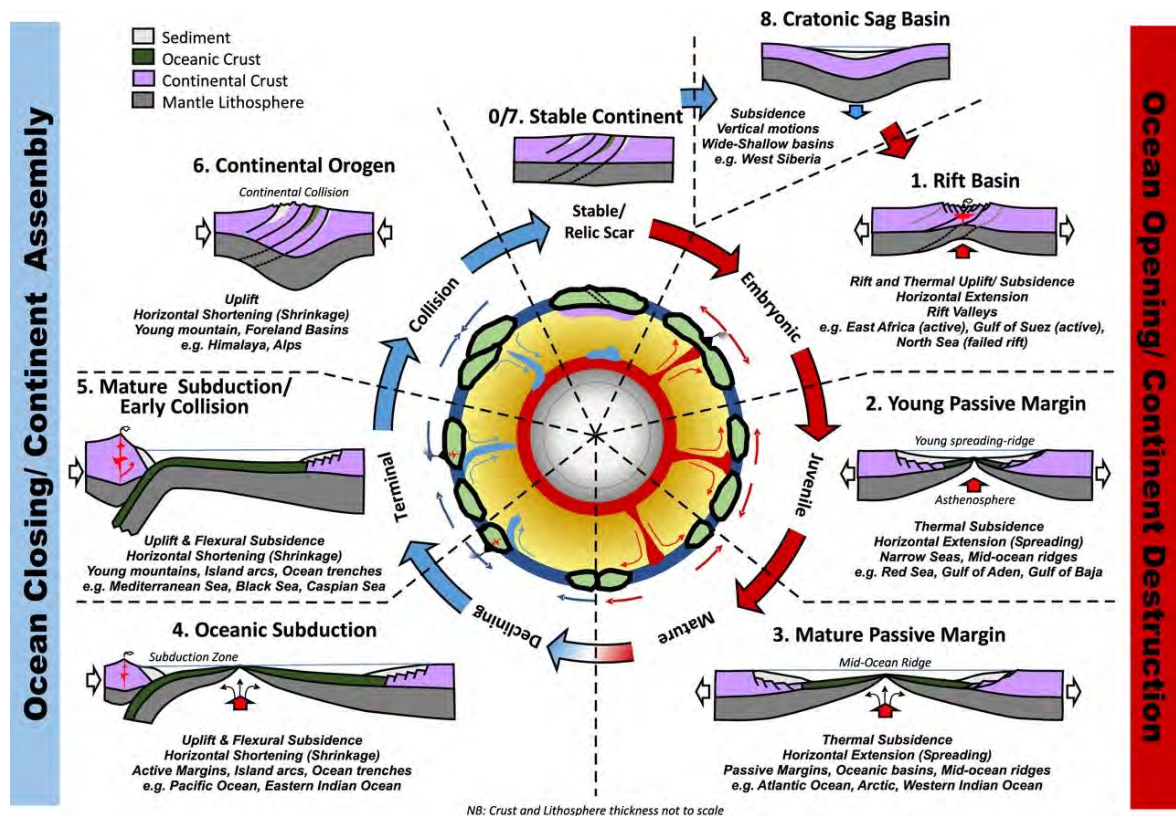


Fig. 1.1: The Wilson cycle describes the stages from ocean opening and continent disintegration to ocean closure and continent assembly (after Wilson et al., 2019).

Comprehension of the Wilson cycle also leads to a better understanding about geological risk factors and geological hazards. Many hazardous geological processes such as large volcanic eruptions or high-magnitude earthquakes commonly occur at the divergent and convergent plate boundaries. Among transform faults, earthquakes with magnitudes higher than 7.0 on the logarithmic Richter scale are mostly restricted to continent-continent collisions and subduction zones at active margins. Two prominent examples from the recent past are the Indian Ocean earthquake offshore Sumatra in 2004 (magnitude ~9.1) and Tōhoku earthquake offshore Japan in 2011 (magnitude ~9.0). Both events triggered catastrophic tsunamis up to 30 m or even more in height, which caused in total more than 240,000 casualties. Over 85% of the global magma production takes place at the divergent mid-ocean ridges ($>20 \text{ km}^3$) and convergent subduction zones ($8\text{-}9 \text{ km}^3$; e.g. Frisch et al., 2011). Accordingly, the global distribution and length of mid-ocean ridges and subduction zones at active margins has superior effects on global magma production. Magmatism in submarine environment at mid-ocean ridges is relatively non-hazardous. The most

catastrophic subaerial eruptions occur along volcanoes or even supervolcanoes at active margins. One of these events was the 26.5 ka Oruanui eruption in the Taupo Volcanic Zone onshore the North Island of New Zealand. Around 1200 km³ of volcanic material were erupted, which covered an area of ~1000 km² (e.g. Wilson, 2001). This was the youngest eruption with the highest volcanic explosivity index (VEI = 8) on the logarithmic VEI scale. Eruptions with high VEIs also occur along rift systems. The 12.9 ka Laacher See Volcano eruption (VEI = 6) along the Rhine rift system in southern Germany is an example for that. The explosion felled trees up to 4 km from the vent (Schmincke et al., 1999). The amount of huge tephra volumes led to a complete disruption of the Rhine River and the damming up of a lake ca. 140 km² (Schmincke et al., 1999).

Intracontinental rifts also play an essential role in the global carbon cycle since rifting can release immense amounts of carbon stored in the lithosphere into the atmosphere (e.g. Foley & Fischer, 2007). Carbon in form of gases (CO₂ and CH₄) can be directly released due to migration along faults in rift system. The storage and concentration of dissolved CO₂ or CH₄ within lakes like in the Lake Kivu along the East African Rift system is potentially dangerous (e.g. Nayar, 2009). The sudden gas releases (limnic eruptions) at Lake Nyoz and Lake Monoun in northwestern Cameroon in 1984 and 1986 killed in total more than 1,800 residents (Halbwachs et al., 2004; Kling et al., 1987; Sigurdsson et al., 1987). Especially, greater abundance of continental rifts during supercontinent breakups can release immense amounts carbon (142 – 170 Mt/yr) and contribute to global atmospheric CO₂ levels (Foley & Fischer, 2007). It has been shown that the global rift lengths correlate with greenhouse climate episodes during the past 200 Ma (Brune et al., 2017a). Although changes in plate motions occur on distinctly longer timescales, different stages of the Wilson cycle may have several effects on the Earth's highly dynamic system:

- (I) Changing global and regional sea-levels (e.g. Cloetingh et al., 1985; Miller et al., 2005).
- (II) Global climate changes caused by varying ocean circulations in response to the opening and closure of oceanic gateways, or by the movement of continents into high-latitudes, which promote the construction of ice-sheets (e.g. Smith & Pickering, 2003).
- (III) Regional climatic effects caused by the construction and destruction of mountain belts (e.g. Ruddiman & Kutzbach, 1989).

All the extensional and convergent stages of the Wilson cycle are found on the modern Earth (Fig. 1.1). Rifting within formerly stable continents may be actively initiated by uprising hot mantle material or, passively, by far-field stresses in the moving lithospheric plates or by dragging at the base of the lithosphere (e.g. Condie, 2016). The most prominent example of an early-stage rift system is the East African Rift, where extensional forces are compensated by crustal thinning (e.g. Brune et al., 2017b). In the Red Sea, rifting led to the formation of passive continental margins, the onset of seafloor spreading, and the birth of a young ocean in the past 5 Myr (e.g. Ligi et al., 2018). Continuous basalt production at mid-ocean ridges may eventually lead to the growth of a larger ocean basin like the South Atlantic Ocean, which started spreading in the Early Cretaceous (e.g. Brune et al., 2018) or the North Atlantic Ocean, which has developed since the Palaeocene-Eocene (Ellis & Stoker, 2014). Oceanic lithosphere can also be subducted at active margins, where it sinks down and is recycled in the mantle. Subduction initiation within the Atlantic Ocean is suggested to take place offshore Spain at present day (Duarte et al., 2013). Subduction presently takes place around the edge of most the Pacific Ocean. The Mediterranean Sea is an example of the final subduction stages before mountain ranges evolve through continental collision, such as in the Himalayas or the European Alps. At latest stage of the Wilson cycle, a stable continent is constructed, before it eventually breaks up again some tens or hundreds of million years later.

1.1. Subduction of oceanic plateaux

Another factor in the Wilson cycle are oceanic plateaux, which consist of anomalously thick oceanic crust and are the product of extensive magmatism associated with the formation of LIPs (Coffin & Eldholm, 1994). LIPs evolve from primarily basaltic magmas and their voluminous emplacement can form flood basalts in continental settings (e.g. the Dekkan Traps), on volcanic passive margins (e.g. North Atlantic margins), and/or oceanic plateau like the Ontong Java, Manihiki and Hikurangi Plateaux. The formation of oceanic plateaux and LIPs is widely thought to be related to deep-seated asthenospheric upwelling in the form of plume heads (e.g. Coffin & Eldholm, 1994; Kerr, 2003), but other mechanisms are also proposed in the literature (e.g. Ingle & Coffin, 2004). At the final stage of their life cycle, oceanic plateaux may be also subducted and recycled in the Earth's mantle similar to normal oceanic crust through the Wilson cycle. These, however, are rare events in global geodynamics. In contrast to normal-thickness oceanic crust of 6-7 km thickness, oceanic plateaux consist of basaltic crust, which can reach a thickness of up to 42 km (Furumoto et al., 1976). Numerical modelling and buoyancy calculations suggest that thick oceanic plateaux remain positively buoyant even up to 80 Myr after their formation or even longer (Cloos, 1993; van Hunen et al., 2002). Due to their positive buoyancy, oceanic plateaux can resist subduction. Accordingly, the life cycle of oceanic plateaux may include obduction onto continental crust, 'underplating' of continental crust by shallow or flat subduction, or even subduction cessation – all of which represent enigmatic and geologically rare events not captured within the Wilson cycle. Some diverse examples illustrating the consequences of oceanic plateau subduction include:

(I) The still-ongoing collision of the Ontong Java Plateau – the Earth's largest and thickest oceanic plateau – with the Melanesian arc. This collision, which began in the Miocene, led to partial subduction of the Ontong Java Plateau, crustal accretion, and subduction cessation (Mann & Taira, 2004; Taira et al., 2004). Moreover, the collision of the Ontong Java Plateau with Melanesian arc is suggested to have triggered a subduction reversal, which significantly changed the motion of the Australian Plate and resulted in rapid changes in the motions of all global plates in the mid- to late Miocene (Knesel et al., 2008; Austermann et al., 2011).

(II) The conjugate part of the Shatsky Rise subducted below North America in the Late Cretaceous. Here, the subduction itself did not have a significant impact on the plate motions and local tectonics. Progressive eclogitisation, however, led to the removal of the subducted Shatsky Rise conjugate. This, in turn, is suggested to have led to the Laramide Orogeny through regional-scale surface rebound following lithospheric removal (Liu et al., 2010).

(III) Subduction of the 'lost' Inca Plateau beneath the Nazca Ridge from Miocene to present-day. Here, flat subduction of a slab segment is thought to account for the absence of arc magmatism in the Peruvian Andes. This slab segment (the Inca Plateau) is the hypothetical conjugate to the Marquesas Plateau in the Central Pacific (Gutscher et al., 1999; Gutscher et al., 2000a; Gutscher et al., 2000b; Rosenbaum et al., 2005).

As illustrated by these examples, the effects of the collision and subduction of oceanic plateaux can impact upon both regional and global tectonics. Additionally, the cessation of arc magmatism in response to flat subduction triggered by oceanic plateaux may also affect the atmospheric gas budgets. Therefore, oceanic plateaux are an imported factor in geodynamics, but can also influence the atmosphere.

1.2. Formation and types of passive rifted margins

Rifted continental margins such as the eastern and western coasts of Greenland represent the transition between continental and oceanic lithosphere, and consist of crust that formed by

continental rifting before the onset of seafloor spreading. Different endmember models are used to classify conjugate rifted margins based on their symmetry, width, magmatic additions, or tectonic setting. One set of these models classifies rifted continental margins into magma-poor and volcanic endmembers (Fig. 1.2; Franke et al., 2013; Doré & Lundin, 2015). Although the driving forces for the initiation of rifting and continental drift are still under debate, volcanic-rifted margins are often associated with LIPs (e.g. Coffin & Eldholm, 1994). Passive margin formation is proposed to result from active rifting triggered by the upwelling of anomalously hot mantle 120-200 °C above average mantle temperatures (White & McKenzie, 1987; White & Smith, 2009). The upwelling mantle is thought to penetrate, uplift and stretch the continental crust. In contrast, the formation of magma-poor passive margins is assumed to be related to far-field extensional forces, which stretch and depress the continental crust, and later lead to passive and cold mantle upwelling (Huisman et al., 2001). The timing of magmatism (pre-rift vs. post-rift) and the amount of magma supply (poor vs. rich) have considerable effects on the crustal architecture of the continent-ocean transition (COT) zone along passive rifted margins. The COT zone may be a simple progression from normal continental to normal oceanic crust, or a complex transition with magmatic intrusions, failed rifts or separated blocks of continental crust (e.g. Pérez-Gussinye et al., 2003; Grobys et al., 2007). Decades of geophysical research on both magma-poor and volcanic-rifted continental margins have resulted in the identification of distinct characteristics for both endmembers (Fig 1.2; Franke et al., 2013; Doré & Lundin, 2015).

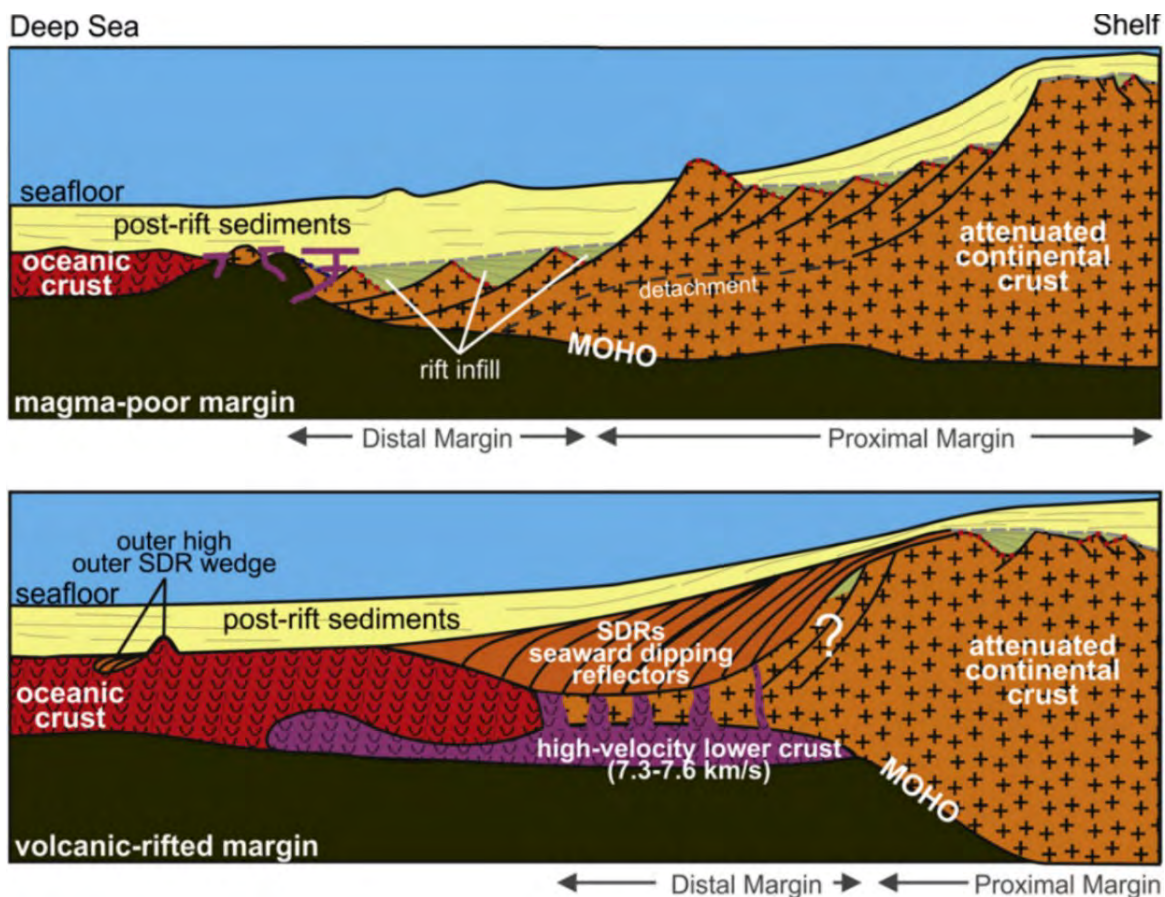


Fig. 1.2: General structure of the continent-ocean transition and typical features of the two passive margin endmembers (after Franke, 2013). Top: Magma-poor rifted margin endmember. Bottom: Volcanic-rifted margin endmember. SDRs = Seaward-dipping reflector sequences.

The presence of seaward-dipping reflector sequences – thick layers of subaerial basalt flows clearly visible in seismic reflection data (e.g. Mutter, 1985) – are typical of volcanic rifted margins. The basalts likely erupt on continental crust but can extend to the oceanic crust. Volcanic rifted margins

are also associated with mafic intrusions and underplating (e.g. Mjelde et al., 2008). These are identified based on continuous high-velocity lower crust (HVLC) with P-wave velocities exceeding 7.0 km/s, together with a clearly visible Moho in seismic refraction data (e.g. Faleide et al., 2008; White & Smith, 2008). Furthermore, volcanic-rifted margins are considered to evolve through rapid extension and subaerial breakup, and generally have a narrow necking zone at the border of thin continental crust (Fig. 1.2; Doré & Lundin, 2015).

Many magma-poor margins include a broad zone of complex polyphase faulting, in which the continental crust progressively thins with distance away from the continent (e.g. Contrucci et al., 2004). Detachment faulting between crust and mantle is thought to allow the lithospheric mantle to be exhumed at the distal magma-poor margin (e.g. Whitmarsh et al., 2001). Seismic refraction experiments indicate that the exhumed mantle is often serpentinised. P-wave velocities therefore gradually increase to normal mantle velocities of 8.0 km/s without any obvious Moho reflection (e.g. Funck et al., 2003). Mantle exhumation takes place until the final breakup and onset of seafloor spreading. Conceptual models suggest a systematic oceanward increase in magmatism through space and time (Whitmarsh et al., 2001).

1.3. Geological and tectonic background

The tectonic evolution of the active East Gondwana margin differs from the rest of the Earth's plate tectonic puzzle. In the mid-Cretaceous, the area of southern Zealandia that includes New Zealand's South Island and the submarine Chatham Rise experienced different stages of the Wilson cycle, from oceanic subduction to rifting and passive margin formation, in an unusually short time. Cessation of subduction is suggested to have been initiated by the collision of the thick, oceanic Hikurangi Plateau – a fragment of the former Ontong Java Nui “super”-large igneous province (LIP) – with the East Gondwana active margin in the area of the Chatham Rise and South Island (Davy et al., 2008; Davy, 2014). Subsequently, widespread continental rifting affected southern Zealandia. Less than 25 Myr after the collision of the Hikurangi Plateau with the East Gondwana margin, a passive continental margin was formed along the southern Chatham Rise and seafloor spreading initiated along the young Pacific-Antarctic Ridge, which still separates southern Zealandia from West Antarctica at the present day (e.g. Eagles et al., 2004a).

1.3.1. Tectonic setting and geology of the Chatham Rise and southern Zealandia

At the present day, most of the continent Zealandia is submerged. Only 6 % of the continental landmass is elevated above sea level, and New Zealand's North and South Islands, and New Caledonia make up the largest of those exposed areas (Fig. 1.3; Mortimer et al., 2017). The Alpine Fault, a prominent dextral strike-slip fault on New Zealand's South Island, subdivides Zealandia into northern and southern parts (Fig. 1.3). The submerged continental area of northern Zealandia includes Norfolk Ridge, Lord Howe Rise, and the Challenger Plateau, which are part of the Australian Plate. The submerged part of southern Zealandia includes Campbell Plateau and the Chatham Rise, both of which belong to the Pacific Plate (Fig. 1.3).

The Chatham Rise is an elongated bathymetric feature, which extends up to 1500 km east of New Zealand's South Island (Fig. 1.3). To the north, the Chatham Rise is bordered by the Hikurangi Plateau – a Cretaceous oceanic plateau that is presently subducting below the North Island (e.g. Reyners, 2013). This subduction is driven by the westward movement of the Pacific Plate relative to the Australian Plate (Fig. 1.3). East of the Hikurangi Plateau, a bathymetric step separates the Chatham Rise into shallower western (<1000 m water depth), and deeper eastern (1000 – 3000 m water depth) provinces. This step is in line extension of the West Wishbone Ridge – a mid-

Cretaceous dextral strike-slip fault zone (Barrett et al., 2018). To the southwest, the Bounty Trough – a bathymetric depression that deepens eastward – separates the Chatham Rise from the Campbell Plateau and Bounty Platform (Fig. 1.3). In the southeast, the Chatham Rise transitions to the SE Chatham Terrace (Fig 1.3). The SE Chatham terrace is a poorly constrained deep sea domain, which is distinctly shallower than the surrounding seafloor, and hosts abundant guyots and seamounts.

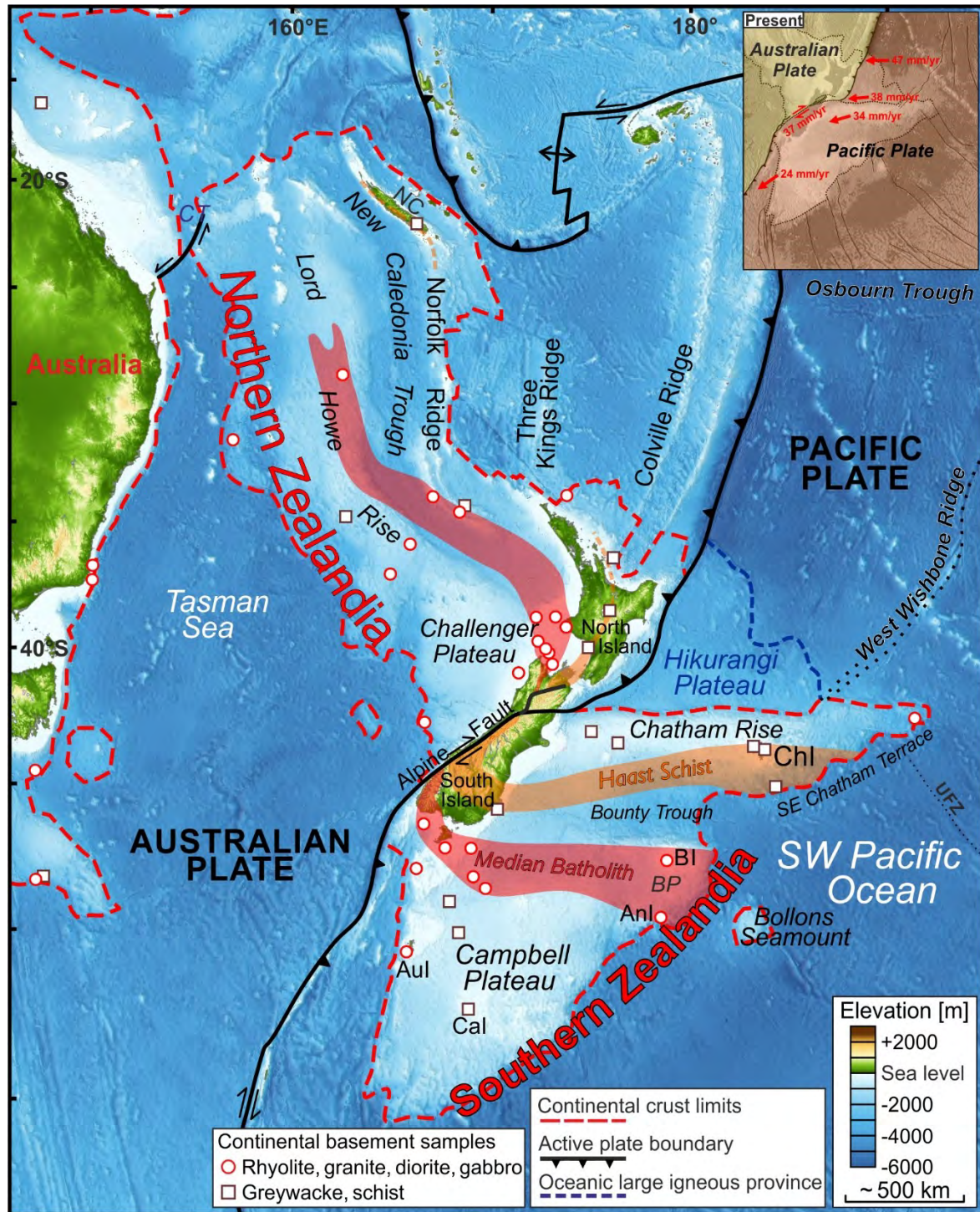


Fig. 1.3: The continental boundaries of the continent Zealandia with basement sample locations (Mortimer et al., 2017). Inlet: Present-day plate motions of the Pacific Plate relative to the Australian Plate after DeMets et al. (2010). Anl = Antipodes Island; Aul = Auckland Island; BI = Bounty Island; BP = Bounty Platform; Cal = Campbell Island; Chl = Chatham Island; UFZ = Udintsev Fracture Zone.

From the Paleozoic until the early Mesozoic, Zealandia formed a large part of the active continental margin of East Gondwana (Fig. 1.4). Subsequently, in the mid-Cretaceous, Zealandia started to rift and drift away from Australia and Antarctica (e.g. Mortimer et al., 2017). The Chatham Rise and Campbell Plateau were attached to West Antarctica near the present-day Ross Sea, Marie Byrd Land, Amundsen Sea Embayment and Thurston Island (Larter et al., 2002; Eagles et al., 2004a; Wobbe et al., 2012; Wright et al., 2016). Basement rocks across southern Zealandia are consistent with this long active margin history. These are mainly composed of Palaeozoic to Mesozoic subduction-related plutonic rocks (i.e. the Median Batholith, see Figs. 1.3 and 1.4) and, further arcward, Permian-Cretaceous allochthonous terranes, which include greywackes and regionally metamorphosed equivalents typical of accretionary wedges (e.g. Mortimer et al., 2014). The oldest known basement rocks across the Chatham Rise are exposed on northern Chatham Island and include the Middle to Late Jurassic Chatham Schist and Permo-Triassic greywackes (Campbell et al., 1993, Mortimer et al., 2019a). Similar metamorphic/isotopic characteristics and Permo-Triassic protolith ages of the Chatham Schist suggest a close relationship with the Haast Schist onshore South Island (Figs. 1.3 and 1.4; Adams et al., 2008; Mortimer et al., 2019a).

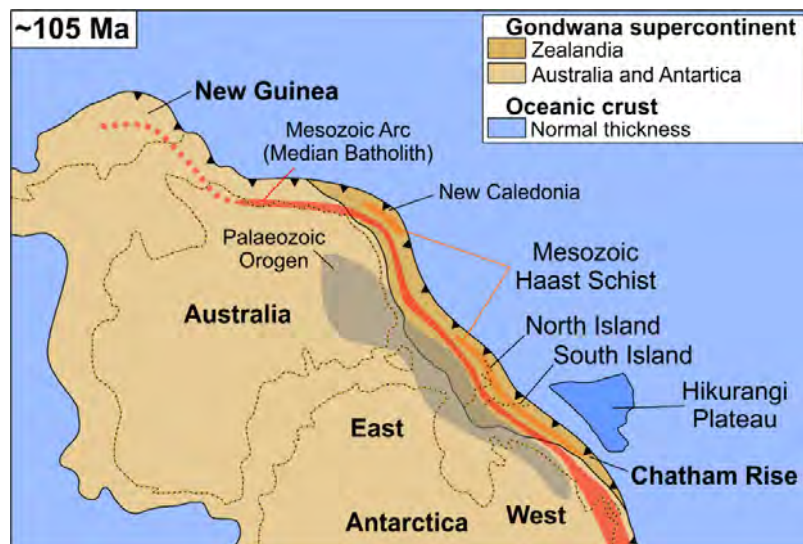


Fig. 1.4: Zealandia as part of the former East Gondwana active margin (redrawn and modified from Mortimer et al., 2017). In this reconstruction, only the present-day surface expression Hikurangi Plateau is shown (see Fig. 1.3). Passive and active seismic studies indicate that the Hikurangi Plateau was much larger (e.g. Davy et al., 2008; Reyners et al., 2011).

1.3.2. Evolution and collision of the Hikurangi Plateau with the East Gondwana margin

During the mid-Cretaceous, the Hikurangi Plateau (Figs. 1.3) formed as part of the Ontong Java Nui “super”-plateau between 125 and 120 Ma (Hoernle et al., 2010; Taylor, 2006). Shortly after its formation, Ontong Java Nui separated and the Hikurangi Plateau drifted southward to the East Gondwana margin (e.g. Hochmuth et al., 2015), where it collided with the active subduction zone in the area of the South Island at ~110 Ma (e.g. Davy, 2014). Following the initial collision, the Hikurangi Plateau partially subducted (Fig. 1.4), jammed the subduction margin, and subduction ceased at ~100 or ~96 Ma (Davy, 2014; Davy et al., 2008). The exact timing, however, is poorly constrained because seafloor spreading at the Osborn Trough north of the Hikurangi Plateau (Fig. 1.3) took place during the Cretaceous Normal Superchron (Downey et al., 2007; Larson et al., 2002). The segmentation of the Chatham Rise has been interpreted to be due to dextral strike-slip movements along the West Wishbone Ridge following the cessation of subduction of the Hikurangi Plateau (Fig. 1.3; Barrett et al., 2018).

1.3.3. Onset of mid-Cretaceous rifting in southern Zealandia

Subsequent to the cessation of subduction along the Chatham Rise and upper South Island, widespread crustal extension and intracontinental rifting initiated in southern Zealandia (Laird & Bradshaw, 2004; Mortimer et al., 2016). This is manifested by several factors, including (I) the exhumation of Median Batholith core complexes on the southwest South Island after 108 Ma, (II) the development of grabens and half-grabens, and (III) the successive deepening of fault-controlled rift basins like the Great South Basin and Canterbury Basin east of the South Island (Bache et al., 2014; Laird & Bradshaw, 2004; Schwartz et al., 2016; Strogon et al., 2017; Tulloch et al., 2009b). On the Chatham Rise, the only outcrop of terrestrial deposits is found on the Chatham Islands (Fig. 1.3; Waihere Bay Formation on Pitt Island). This formation is as old as 100 Ma (Campbell et al., 1993). In conjunction with the abrupt change in tectonic forces, subduction-related magmatism ceased between 101 to 97 Ma. This magmatism was replaced by widely-distributed, but overall low volume, A-type granite emplacement and alkali-basaltic magmatic activity across the eastern Chatham Rise, the South Island, and West Antarctica (e.g. Tulloch et al., 2019 and references therein).

1.3.4. Rift-drift transition along the southern Chatham Rise margin

Magnetic spreading anomalies suggest that the onset of seafloor spreading between southern Zealandia and West Antarctica occurred around 90 Ma, east of the present-day Udintsev Fracture Zone (UFZ, see Fig. 1.3; Eagles et al., 2004a; Larter et al., 2002; Wobbe et al., 2012). West of the UFZ, however, the timing of the onset of seafloor spreading is unclear due to a lack of knowledge about the crustal structure of the SE Chatham Terrace. Wide-spread volcanic features make the magnetic anomaly pattern quite complex (Davy, 2006), and the seafloor spreading anomalies are not always distinguishable from each other. Moreover, highly metamorphosed schist samples dredged from the Stuttgart Seamount suggest the SE Chatham Terrace has continental affinities (Mortimer et al., 2006, 2016). Davy (2006) explained the magnetic anomaly pattern between the Bounty Trough and SE Chatham Terrace using several southward ridge jumps and highly asymmetric spreading between 83 and 79 Ma, which led to the separation of the Bollons Seamount (Fig. 1.3). In contrast, Tulloch et al. (2019) suggested that the magnetic anomalies are instead part of a larger rift-related mafic complex that includes the SE Chatham Terrace, Bounty Platform and Campbell Plateau, and formed at the same time as 85-82 Ma basaltic intraplate lavas on the Chatham Islands (Panter et al., 2006). However, it is widely agreed that the Campbell Plateau and Bounty Platform separated from West Antarctica after 83 Ma, distinctly later than the Chatham Rise did (Davy, 2006; Eagles et al., 2004a, 2004b; Sutherland, 1999; Wobbe et al., 2012).

1.4. Main objectives and scientific questions

Crustal structure and nature of the southern Chatham Rise margin

Apart from studies onshore and just offshore of the South Island, the continental crust of southern Zealandia (i.e. Chatham Rise, Bounty Platform and Campbell Plateau) is only constrained by two modern seismic refraction profiles, which indicate crustal thicknesses of 22-24 km (Grobys et al., 2007, 2009). The only other knowledge of the structure of the Chatham Rise comes from sparsely distributed sonobuoy data around the Chatham Islands, which reveals information about the graben infills and the uppermost crust (Wood & Anderson, 1989; Wood et al., 1989). Bathymetry and gravity data indicate clear differences between the eastern (deeper) and western (shallower) Chatham Rise.

- How thick is the crust beneath the eastern and western Chatham Rise?

- Are there any compositional and internal structural variations within and between these two Chatham Rise segments?

Several studies indicate spreading anomaly c34n to be present on the SE Chatham Terrace, suggesting underlying oceanic crust (Davy, 2006; Larter et al., 2002; Wobbe et al., 2012). Contrastingly, continental fault blocks, such as the Stuttgart Fault Block (Mortimer et al., 2006), are present and seismic data suggest block-faulted basement interspersed with volcanics (Carter et al., 1994; Davy, 1993). The SE Chatham Terrace forms the eastern along-strike continuation of the Bounty Trough, and seismic refraction experiments there indicate very thin continental crust close to oceanic breakup (Grobys et al., 2007).

- What is the crustal nature of the SE Chatham Terrace?
- Does the SE Chatham Terrace consist of oceanic crust or thinned continental crust?
- Where was the first oceanic crust along the southern Chatham Rise margin formed?

Seismic refraction studies provide evidence for high-velocity lower crust beneath the Bounty Trough and Campbell Plateau (Grobys et al., 2007, 2009). This high-velocity lower crust was interpreted as indicative of rift-related magmatic underplating or mafic intrusions, which is a common feature of volcanic-rifted margins.

- What kind of continental margin is the southern Chatham Rise margin?
- Is the southern Chatham Rise margin a volcanic-rifted or magma-poor continental margin?
- What triggered rifting? Was rifting passive or active?

Extent of the Hikurangi Plateau beneath the Chatham Rise

A few seismic studies have provided constraints for the location of the Hikurangi Plateau beneath the Chatham Rise (Davy et al., 2008; Mochizuki et al., 2019; Scherwath et al., 2010). The N-S orientated seismic profile HKDC-1 west of the Chatham Islands shows that the Hikurangi Plateau extends at least 50-100 km beneath the Chatham Rise (Davy et al. 2008). Based on the results of Davy et al. (2008) and seismological data from the South Island, Reyners et al. (2011) proposed that the Hikurangi Plateau reaches all the way to the southern Chatham Rise margin.

- How far does the Hikurangi Plateau reach beneath the Chatham Rise?
- Is the whole Chatham Rise underlain by the Hikurangi Plateau?

Relationship between the Hikurangi Plateau collision and Zealandia rifting

The role of the Hikurangi Plateau collision in subduction cessation and the transition to rifting remain unclear. Davy (2014) and Barrett et al. (2018) proposed that dextral strike-slip movements along the West Wishbone Ridge northeast of the Chatham Rise, which were initiated in response to slowing subduction, played an important role in transferring extensional movements into East Gondwana's interior. The plate-tectonic model of Eagles et al. (2004), however, suggests that extension was transferred into East Gondwana's interior after a spreading segment of the Tongareva triple junction propagated into the area between Chatham Rise and West Antarctica.

- What is the role of the Hikurangi Plateau collision in the onset of rifting and breakup?

A global plate reorganisation event is thought to have affected all major plates between 105 and 100 Ma (Matthews et al., 2012). Reyners et al. (2017b) proposed that this event was related to the cessation of subduction along the East Gondwana active margin in response to the Hikurangi Plateau choking the East Gondwana subduction zone.

- Did the subduction of the Hikurangi Plateau trigger this plate reorganisation event?

1.5. Thesis outline

Chapter 1 introduces the current research knowledge and research questions. This incorporates the geological setting and an outline of the mid-Cretaceous evolution of the larger southern Zealandia area, including the Chatham Rise.

Chapter 2 lists the co-author contributions to the two first-author manuscripts (chapter 5 to 6) and the two co-authored manuscripts (chapter 6 to 7) in this thesis.

Chapter 3 gives a brief description of the geophysical data acquisition during expedition SO246 in 2016 and other available geophysical datasets. Furthermore, the scientific background of the applied geophysical methods, data processing and modelling approaches are explained in detail.

Chapter 4 (Riefstahl et al., 2020) presents wide-angle reflection / refraction, MCS reflection and potential field data along three profiles acquired during expedition SO246 across the Chatham Rise, SE Chatham Terrace and adjacent oceanic crust. The focus of this manuscript lies in the investigation of the crustal structure of the Chatham Rise, the extent of the continent-ocean transition along the southern Chatham Rise margin, and its nature. The main finding is that the southern Chatham Rise margin does not fit into the typical endmember models for passive margins and is, therefore, interpreted as a hybrid margin. Based on the results, I developed a model for the Cretaceous change in tectonic forces along the Chatham Rise, which links the subduction of the Hikurangi Plateau to the onset of rifting in southern Zealandia.

Chapter 5 (Riefstahl et al., submitted) presents the fourth geophysical profile from expedition SO246, which extends the HKDC-1 profile (Davy et al., 2008) further south towards the Bounty Trough to investigate the extent of the Hikurangi Plateau beneath the Chatham Rise. The presented geophysical data together with pre-existing seismic data from southern Zealandia provides useful constraints on the southern limit of the Hikurangi Plateau. Additionally, the seismic data indicate the existence of a large slice of the ancient Phoenix Plate beneath southern Zealandia.

Chapter 6 (Mortimer et al., 2019b) reports $^{40}\text{Ar}/^{39}\text{Ar}$ ages of onshore and offshore intraplate lavas sampled during expeditions SO168 and Deep Sea Drilling Program 91, together with recently collected and existing GNS Science rock samples. The ages together with the regional tectonic model refine the plate movements in the South Pacific area during the mid-Cretaceous, including Ontong Java Nui emplacement and breakup, Hikurangi Plateau collision and subduction, and breakup along the East Gondwana margin.

Chapter 7 (Hoernle et al., 2020) reports geochemical, isotopic and age data from numerous intraplate lavas across Zealandia including the South Island, Chatham Rise, seamounts on the SE Chatham Terrace and seamounts on the adjacent Hikurangi Plateau and oceanic crust, which were mainly sampled during the expeditions SO168 and SO246. Based on isotopic and age constraints, four magmatic provinces are defined and the source of alkaline magmatism after 99 Ma in southern Zealandia is discussed.

Chapter 8 provides extensive conclusions about the tectonic and tectono-magmatic evolution of the Chatham Rise and southern Chatham Rise margin.

Chapter 9 gives an outlook for further relevant research and modelling approaches based on the data, results, and models presented in this thesis.

2. Declaration of co-author contributions

This cumulative Ph.D. thesis consists of two first-authored and two co-authored manuscripts. One of the first-authored manuscripts is already published and the second one is submitted. The two co-authored manuscripts are also already published. All manuscripts were developed in close cooperation with the co-authors following considerable discussions. The following chapter lists the individual contributions of each co-author for the corresponding manuscripts.

Chapter 4: *“Cretaceous intracontinental rifting at the southern Chatham Rise margin and initialisation of seafloor spreading between Zealandia and Antarctica”*

By Florian Riefstahl, Karsten Gohl, Bryan Davy, Kaj Hoernle, Nick Mortimer, Christian Timm, Reinhard Werner, Katharina Hochmuth. **Personal contribution: 80 %.**

The geophysical datasets along the three profiles presented in this study were acquired during expedition SO246 to the Chatham Rise east of New Zealand in 2016 led by Karsten Gohl (Gohl & Werner, 2016). I was the leader of the wide-angle reflection / refraction seismic data acquisition team during this cruise. Bryan Davy recorded and processed the potential field data during SO246. Katharina Hochmuth led the MCS reflection acquisition team during SO246 and supported the development of the P-wave velocity and gravity modelling approaches. Kaj Hoernle, Christian Timm and Reinhard Werner contributed with fundamental ideas about the origin of the identified high-velocity lower crust and the contribution of an upwelling mantle plume to the evolution of the southern Chatham Rise margin. Nick Mortimer and I discussed several aspects about the early continental rifting in Zealandia, which intellectually contributed to this manuscript. I performed all seismic data processing as well as P-wave velocity, gravity and plate-tectonic modelling, which were the basis for this manuscript. I created all figures and tables, and wrote all sections of this manuscript. Karsten Gohl helped to improve this manuscript and directed its scientific output. The manuscript benefits from the intellectual contributions of, and discussions with, all co-authors who reviewed the manuscript before submission.

Status: Published in *Tectonophysics*, 2020 (accepted on the 21st of November 2019)

Chapter 5: *“Extent and cessation of the mid-Cretaceous Hikurangi Plateau underthrusting and its impact on global plate tectonics and the submarine Chatham Rise”*

By Florian Riefstahl, Karsten Gohl, Bryan Davy, Rachel Barrett. **Personal contribution: 85 %.**

The geophysical datasets along the profile west of the Chatham Islands utilised in this study were also acquired during expedition SO246 to the Chatham Rise east of New Zealand in 2016 led by Karsten Gohl (Gohl & Werner, 2016). I performed all seismic data processing as well as P-wave velocity and gravity modelling. Furthermore, I created all figures and tables, and wrote the initial draft of this manuscript. Bryan Davy recorded the gravity data during SO246 and further processed the free-air gravity data. Again, Karsten Gohl helped to direct the scientific output of this manuscript. Intense discussion with Rachel Barrett substantially influenced discussions on the development of a side-transform edge propagator fault (i.e. the West Wishbone Ridge). All three co-authors reviewed the manuscript and made essential intellectual contributions.

Status: Submitted to *Journal of Geophysical Research: Solid Earth* on the 26th of February 2020)

Chapter 6: *“Late Cretaceous oceanic plate reorganization and the breakup of Zealandia and Gondwana”*

By Nick Mortimer, Paul van den Bogaard, Kaj Hoernle, Christian Timm, Phillip Gans, Reinhard Werner, Florian Riefstahl. **Personal contribution: <10 %.**

The samples of intraplate lavas incorporated in this manuscript were sampled during SO168 (Hoernle et al., 2003) and during several field campaigns by GNS Science. Additionally, samples from hole U1365 were ordered from the Integrated Ocean Drilling Program core repository. The manuscript was written by Nick Mortimer. All figures and tables apart from the $^{40}\text{Ar}/^{39}\text{Ar}$ measurements were also created by Nick Mortimer. Paul van den Bogaard and Phillip Gans performed and interpreted the $^{40}\text{Ar}/^{39}\text{Ar}$ age dating. Kaj Hoernle, Christian Timm and Reinhard Werner were mainly involved in SO168 sampling and the geochemical analyses. During my research stay in New Zealand from August to November in 2017, I had intense discussions with Nick Mortimer (GNS Science, Dunedin, New Zealand) about the evolution of the Chatham Rise and surrounding area. I provided the proposed continent-ocean boundary based on the SO246 seismic data, which influenced the interpretation of the petrological data of this manuscript.

Status: Published in Gondwana Research in 2019 (accepted on the 25th of July 2018)

Chapter 7: *“Late Cretaceous (99-69 Ma) basaltic intraplate volcanism on and around Zealandia: Tracing upper mantle geodynamics from Hikurangi Plateau collision to Gondwana breakup and beyond”*

By Kaj Hoernle, Christian Timm, Folkmar Hauff, Vanessa Tappenden, Reinhard Werner, Ester Jolis, Nick Mortimer, Steve Weaver, Florian Riefstahl, Karsten Gohl. **Personal contribution: <10 %.**

The geochemical and isotopical datasets presented in this study were collected from samples during the SO168 (Hoernle et al., 2003) and SO246 expeditions (Gohl & Werner, 2016), and onshore sampling campaigns of GNS Science and the University of Canterbury. This manuscript was written by Kaj Hoernle. Figures and tables were compiled by Christian Timm. Folkmar Hauff and Ester Jolis performed geochemical analyses of the dredge samples from SO168 and SO246. Vanessa Tappenden, Nick Mortimer and Steve Weaver contributed with geochemical analyses and ages of samples from onshore South Island. One goal of the Chatham Rise project was the close collaboration and integration of petrological and geophysical data. This was realised by several scientific meetings with Karsten, Gohl, Kaj Hoernle, Christian Timm, Folkmar Hauff and Reinhard Werner at the GEOMAR in Kiel. The proposed model of a southern Chatham Rise hybrid margin evolved through the geophysical interpretation of the seismic data, which is my intellectual contribution, combined with the interpretation of the geochemical / isotopical data of K. Hoernle.

Status: Published in Earth and Planetary Science Letters in 2020 (accepted 24th of September 2019)

3. Datasets, methods and processing

In this PhD thesis, I mainly make use of refraction seismic data (=wide-angle reflection and refraction seismic data) to model the P-wave velocities along four (260–485 km long) profiles across the Chatham Rise, the southern Chatham Rise margin, the SE Chatham Terrace, and adjacent Pacific oceanic crust. I utilise the new information about the crustal structure of the Chatham Rise to (I) reconstruct the collision of the Hikurangi Plateau with East Gondwana active margin, (II) improve the understanding about rifting and crustal stretching in southern Zealandia and (III) infer the mechanism behind the change from divergence to extension along the East Gondwana margin between 125 to 80 Ma.

The Chatham Rise project is a cooperation between the Alfred Wegener Institute Helmholtz-Centre for Polar and Marine Research (Bremerhaven, Germany), the GEOMAR Helmholtz-Centre for Ocean Research Kiel (Kiel, Germany) and GNS Science (Lower Hutt and Dunedin, New Zealand). This project was mainly funded by the German Federal Ministry of Education and Research (grant no. 03G02246A), but additional funding was provided by GNS Science. In the framework of this project, new geophysical data and geological seamount samples were collected by the German research vessel RV Sonne during the expedition SO246 (Fig. 3.1, Gohl & Werner, 2016).

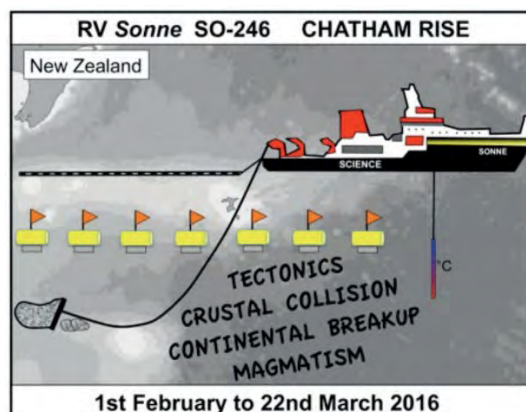


Fig. 3.1: Cruise logo of the SO246 expedition on RV Sonne from February to March 2016. The expedition included geophysical data acquisition and geological sampling of seamounts and guyots by dredging.

Geophysical data acquisition during SO246 includes refraction seismic, multi-channel seismic (MCS) reflection, potential field (gravimetry and magnetic), heat flow, bathymetry and sediment echosounder (Parasound) data. Among geophysical data acquisition, several seamounts and guyots at the southern Chatham Rise margin are sampled by dredging. This work mainly focusses on the P-wave velocity modelling of the acquired refraction data along four refraction seismic profiles acquired during SO246. I use these data for crustal-scale P-wave velocity with additional constraints from the bathymetry and the processed MCS reflection data. Additionally, I model the gravity anomalies along these profiles to support and verify the interpretations of the P-wave velocity models and gain constraints in areas of low ray coverage.

In the following section 3.1., I describe the geophysical principles of seismic data acquisition. Since all methods are all standard techniques in geophysics, I will only briefly explain the methods and their background. Furthermore, I explain the geophysical data acquisition during SO246 in section 3.2., which also includes a description on the origin of the pre-existing geophysical data. In the last section 3.3., I explain the processing and modelling procedures in more detail.

3.1. Geophysical principles of seismic data acquisition

Seismic wave velocities (e.g. P-wave velocities) are dependent on the density and elasticity of a material. In the Earth's interior and overlying sedimentary cover, P-wave velocities generally increase with depth due to changes in physical properties such as higher P-wave velocity and rock density related to changes in rock chemistry, composition, and mineralogy. The acoustic impedance is the product of P-wave velocity and density of medium. At interfaces between subsurface layers, seismic waves are refracted and eventually reflected due to acoustic impedance contrasts. This physical behaviour is made use of during active seismic surveys whereby the traveltime of the different seismic wave phases are measured. Arrivals of the seismic waves are recorded by receiver units. With increasing distance (offset) of the receiver from the active source, wave phases from deeper geologic structures of the Earth, such as the crust or the mantle (Fig. 3.2), arrive earlier due to higher P-wave velocities.

For marine seismic surveys the active source is constructed of a single airgun or an array of airguns, which is towed behind the vessel (Fig. 3.2). The airguns create a short seismic pulse by highly pressurised air. The amount of air airgun volume, air pressure, and water depth define produced frequency spectrum.

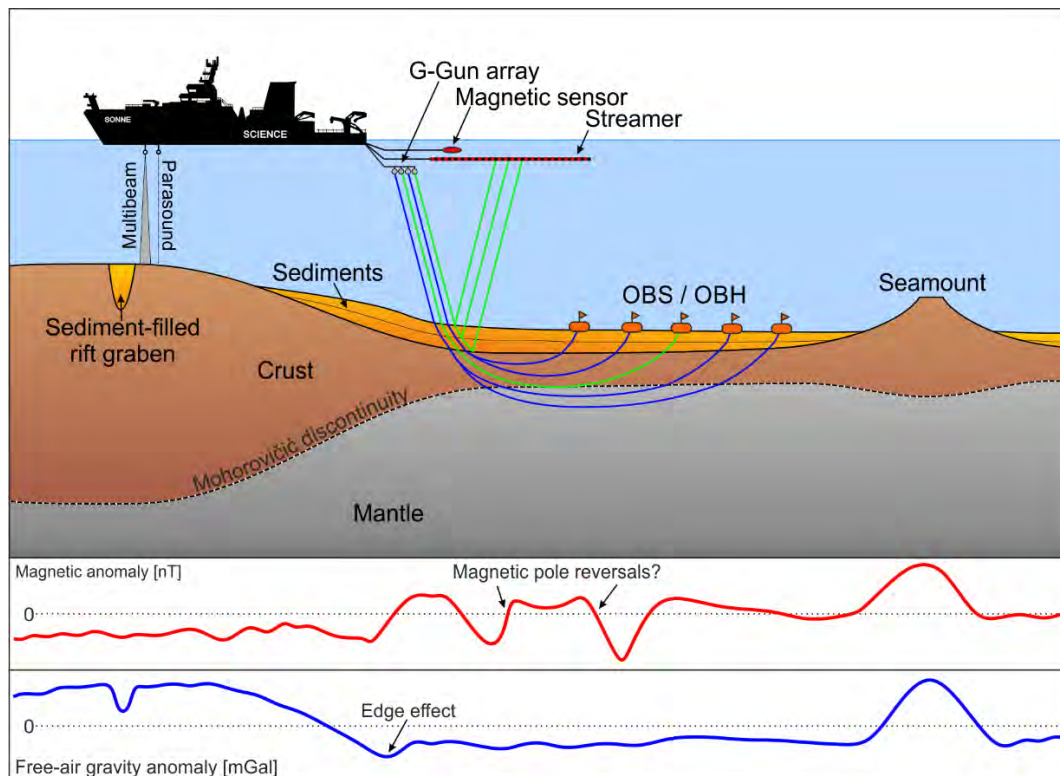


Fig. 3.2: Schematic illustration of geophysical data acquisition. This sketch is simplified and not to scale. Traveltime paths of the seismic waves recorded by the streamer or OBS / OBH instruments are shown as green (reflected waves) and blue lines (refraction waves).

Receivers for refraction seismic surveys are either ocean-bottom seismometer (OBS) or ocean-bottom hydrophone (OBH) systems (see section 3.2.1.), which are deployed along a profile on the seafloor (Fig. 3.2). During refraction seismic surveys, seismic signals are also detected at high offsets, and therefore, recorded refraction phases contain information about the P-wave velocity structure of sediments, crust, and mantle. The subsurface resolution is controlled by the spacing between the OBS/OBH instruments. OBS/OBH generally consist of (I) floats mounted on a steel frame, (II) a rope with another smaller float, (III) a data recorder unit within a pressure tube, (IV) a

hydrophone and a three-component geophone or broad-band seismometer, (V) flag, (VI) radio transmitter, (VII) flashlight unit, (VIII) releaser unit, (IX) and an anchor weight. In contrast with OBSs, OBHs only have hydrophones attached. X, Y and Z-channels from geophones and seismometers are very important to identify and distinguish different wave phases from earthquakes. However, hydrophones usually record better quality signals during refraction seismic surveys. The subsurface resolution is controlled by the spacing between the receiver units. Because of the anchor weight, which is attached to the releaser unit by a hook, the OBS/OBH sinks to the seafloor after release into the water. Signals from seismic wave arrivals at the hydrophone, geophone, or seismometer are stored by the recorder within the pressure tube. After seismic profiling, an acoustic release signal is sent by the onboard transducer and arrives at the releaser unit, the hook opens and detaches from the anchor weight so that the floats have enough buoyancy to lift the OBS/OBH instruments to the sea surface. At this point, the OBS/OBH systems can be located by a direction finder, which locates the frequency of the attached radio transmitter. Otherwise, the flag or the flashlight of the OBS/OBH can be visually located during the daytime or at night. Another possibility is to use a direction finder to find the OBS/OBH system, which locates the frequency of the attached radio transmitter. After the instrument is located, it can be picked up by the vessel.

The receivers for seismic reflection experiments are numerous equally-spaced hydrophones, which are attached to a floating cable (the “streamer”, see Fig. 3.2.). Shorter shot intervals and smaller source-receiver offsets compared to refraction seismic surveys allow a detailed visualisation of the architecture of sedimentary layers and the structure of the acoustic basement (Fig. 3.2) through the use of traveltimes within the sedimentary cover. During marine seismic reflection surveys the reflected energy from interfaces with acoustic impedance contrasts is measured along the streamer. Since the signals (traces) are recorded at all hydrophone channels along the streamer after each shot, the data quality can be increased by processing the data (e.g. stacking and migration).

3.2. Data acquisition during the expedition SO246 and pre-existing data

3.2.1. Wide-angle reflection and refraction seismic data acquisition

Four refraction seismic profiles with different numbers of stations were acquired during SO246 to resolve the crustal structure of the southern Chatham Rise margin (Tab. 3.1 and Fig. 3.3). The refraction seismic profiles comprise 116 OBS/OBS deployments and recoveries. No instrument was lost during the expedition. The following section gives a summary of the deployed OBS/OBH instruments.

Tab. 3.1: Table with information about the profiles, recorded data types (Rfr = refraction seismic data; Rfl = MCS reflection data), shot intervals, number of stations (total / successful data acquisition), station spacing, and the profile start / end points.

Profile	Type	Shot Interval	Number of stations	Station spacing	Start	End
AWI-20160100	Rfr	60s	40 / 36	11 km	175.9752°W 42.8203°S	174.2421°W 46.9913°S
AWI-20160001	Rfl	20s	-	-	175.9207°W 42.9671°S	174.2423°W 46.9904°S
AWI-20160200	Rfr	60s	35 / 35	11 km	171.4330°W 45.4819°S	174.6948°W 42.6505°S
AWI-20160003	Rfl	20s	-	-	171.4074°W 45.5025°S	174.6243°W 42.7085°S
AWI-20160300	Rfr	60s	21 / 21	15 km	166.7450°W 44.9849°S	168.5993°W 42.3516°S
AWI-20160301	Rfl	60s	-	-		
AWI-20160400	Rfr	60s	20 / 19	12 km	178.1329°W 45.4881°S	178.3637°W 43.1756°S
AWI-20160401	Rfl	60s	-	-		

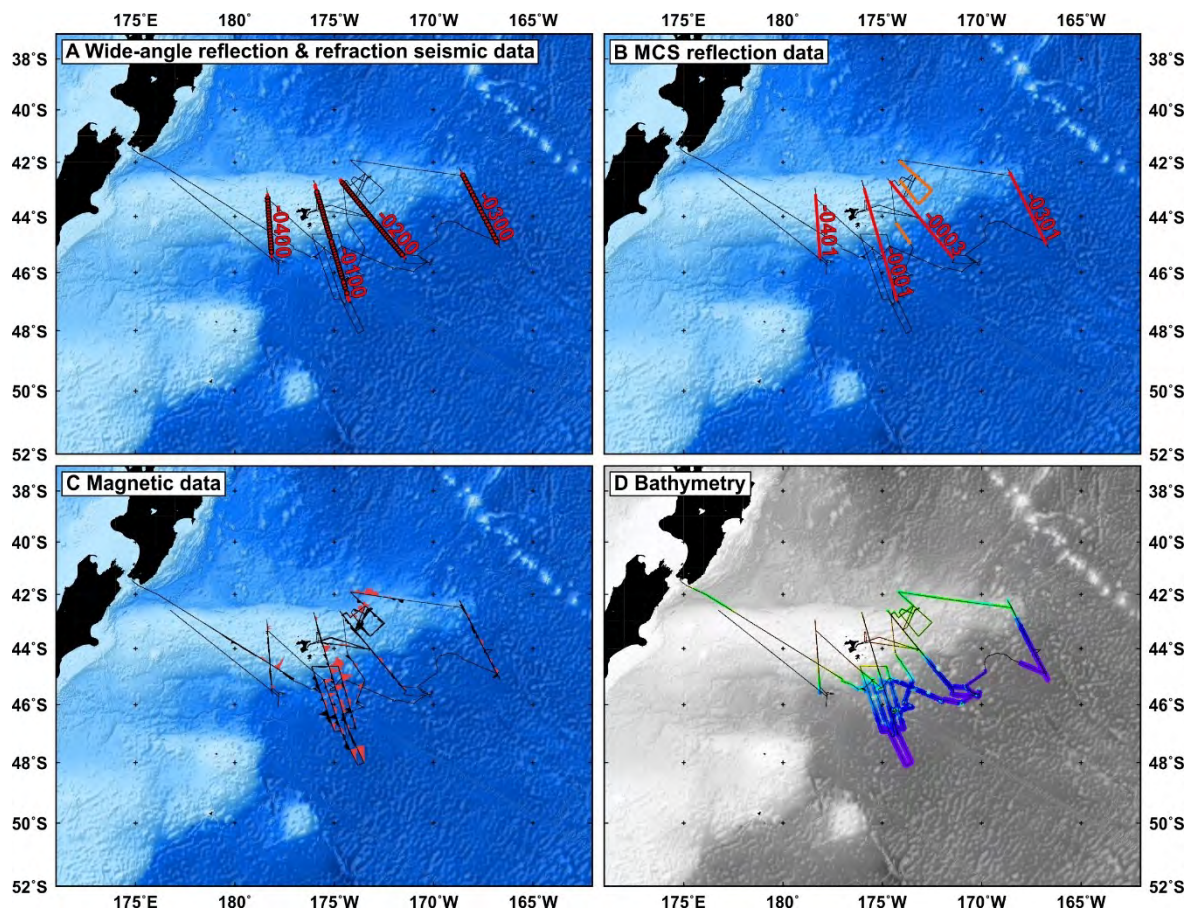


Fig. 3.3: Geophysical data recorded during expedition SO246 on RV Sonne in 2016 (track path is shown as a thin black line). (A) Wide-angle reflection and refraction profiles, (B) multi-channel seismic (MCS) reflection profiles (red = this study, orange = processed and interpreted by others), (C) magnetic data (red wiggles correspond to positive and black wiggles to negative magnetic anomalies), and (D) multibeam bathymetric data. Gravimetric data was continuously recorded throughout the cruise.

Four OBH/OBS systems with different recorders were used during acquisition of the SO246 refraction seismic profiles. For all recorders, the sampling rate was set to 250 Hz. I performed a detailed quality check for all recordings after each profile. Based on the quality control, the setup of the instruments was optimised during subsequent profiles. Although the instruments require different onboard handling, the data quality of all system is of same quality. Complete lists of the configurations within each refraction seismic profile are included in the appendix (Tab. A1 to Tab. A4), but generally the setups were as follows:

(I) AWI LOBSTER-type OBS systems (Fig. 3.4A) with KUM QUAT-type releasers. All AWI Lobsters were equipped with hydrophones and MCS recorders (SEND GmbH). One AWI/LOBSTER system incorporated a 6d6-recorder (manufactured by KUM), and three stations in each profile included three-component 3.5 kHz geophones.

(II) GEOMAR-type OBS systems (Fig. 3.4B) with KUM QUAT-type releasers. All GEOMAR-type OBS systems were armed with hydrophones, three-component 3.5 kHz geophones and MBS recorders (manufactured by SEND GmbH). After the first profile (AWI-20160100), three of these OBS system MBS recorders were replaced with GEOMAR-manufactured Geolog-type recorders with two hydrophone channels, which allow the application of different gains to the hydrophone signal.

(III) GEOMAR-type OBH systems (Fig. 3.4C) with IXSEA releasers. These vertical-framed OBH systems were equipped with hydrophones and MBS recorders.

(IV) KUM NAMMU prototype OBS (Fig. 3.4D). In contrast to the other OBS systems, the float-foam also makes up the OBS system's frame and is, therefore, only half the size of the AWI Lobsters or GEOMAR-type OBSs. NAMMU was only used in the first three profiles at different water depths (up to 5000 m.b.s.l.). These were the first and successful tests of NAMMU under deep-water conditions. This OBS system was equipped with a hydrophone, a 6d6 recorder, and a three-component seismometer (Nanometrics Trillium Compact).

The source consisted of an array of 8 G-Guns with 8.5 litres (520 in³) volume per G-Gun, which is equal to a total volume of 68 l (4160 in³). The G-Guns were towed in two clusters of four G-Guns (Fig. 3.5) on both starboard and portside at a water depth of 10 m. The G-Gun arrays were triggered every full minute by a Meinberg GPS clock and fired at 205 bar. These full minute shots were also recorded by the MCS streamer (see section 3.1.4.). As a result of an unplanned exchange of a member of the whale observer team, profile AWI-20160200 was split into two parts. In the first part of this profile, one G-Gun was shut down due to a malfunction but this had no significant effects on the data quality. Several whale sightings during surveying required a complete shutdown of the G-Guns. However, gaps in the recorded data due to these shutdowns were not longer than 30 minutes, which is approximately 5 km at a constant speed of 5 knots.

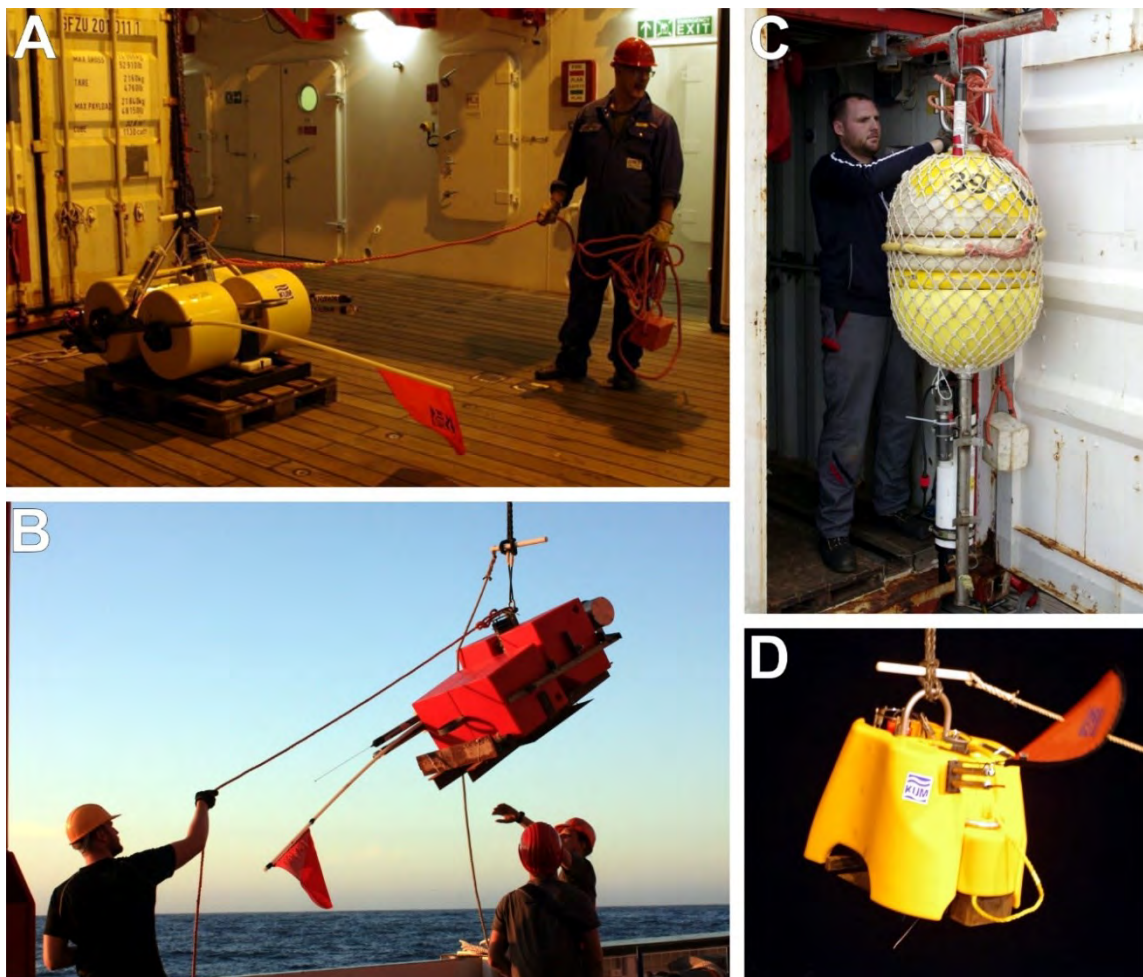


Fig. 3.4: Images of the OBS/OBH instruments used in this study. (A) AWI Lobster OBS, (B) GEOMAR OBS, (C) GEOMAR OBH, and (D) KUM NAMMU prototype OBS. All photos were taken by Till Niels Gades.

Overall, the data quality was good to excellent, although reverberations and echoes from the shots mask some primary signals in shallow waters (< 400 m water depth) with rough subsurface topography. The hydrophone channel yielded the best quality and signal-to-noise ratios along all

profiles, and were consequently used for data interpretation and wave-phase picking (see section 3.3.). The Z-channel of the geophone was used at station st234 along profile AWI-20160200 as the hydrophone malfunctioned or was disconnected from the recorder. On profile AWI-20160100, data recordings failed at the stations st101, st103, st107, and st122 as the batteries were empty before RV Sonne passed the station while profiling. No data was recorded at station st420 on profile AWI-20160400 because the power cable for the recorder was cut while closing the pressure cylinder.

The recorders were synchronised with a GPS antenna to account for the drift (skew) of the internal recorder clocks both before deployment and after collection of the OBS/OBH stations. The synchronisation of the internal clocks was successful at most stations. However, at some stations the GPS-clock synchronisation failed. The skew could not be determined as the recorder hard disk drive had frozen, which probably occurred due to shocks during recovery of the instruments. The time accuracy for these stations was validated by comparing the water depth measured from the bathymetry and water depth calculated from the arrivals of the direct wave. Both, water depth and water depth calculated from the water depth were reliable. Accordingly, the seismic records were further processed without clock drift correction.

3.2.2. Multi-channel seismic (MCS) data

For MCS reflection data acquisition during SO246, the AWI-owned 240-channel digital solid streamer (Sercel Sentinel™, see Fig. 3.5) with an active length of 3000 m was used, whereby eight hydrophones were grouped in 12.5 m intervals. Analogue hydrophone signals were digitally converted, decimated, filtered and compressed before the signals arrived at the onboard recording system (Sercel SEAL™ installed on a Sun Blade 2500 computer), which stored the seismic data on hard disk drives in SEG-D format (see Gohl & Werner, 2016).



Fig. 3.5: Photographs of the (A) AWI Sercel Sentinel™ Streamer and the portside 2x2 G-Gun cluster during maintenance work onboard RV Sonne. The photographs were taken by Andreas Brotzer (A) and Katharina Hochmuth (B).

MCS reflection data were acquired along all refraction profiles with the same G-Gun setup for the refraction profiles (2x4 G-Gun in 10 m depth with 60 s shot interval fired at 205 bar; see section 3.1.2. for further information). In addition, high-resolution MCS reflection data were recorded along profiles AWI-20160001 (along seismic refraction profile AWI-20160100) and AWI-20160003 (along seismic refraction profile AWI20160200), and are processed and analysed in this work to reveal the crustal structure of the southern Chatham Rise margin (Tab. 3.1). Beside this work, the same four SO246 profiles were processed and interpreted together with pre-existing MCS reflection data to

reconstruct Late Cretaceous to Cenozoic ocean-bottom currents along the Chatham Rise (Steinbrink, 2017; Steinbrink et al., 2020). Furthermore, several of the MCS reflection profiles that were recorded during the SO246 expedition were processed and interpreted by others (see Fig. 3.3; Flenner, 2016; Barrett, 2017; Barrett et al., 2018). Pure MCS reflection profiles were acquired with 2x3 G-Guns (51 l / 3120 in³) towed in 6 m water depth, and fired at 200 bar every 20 s. Due to a failure of the pressure hoses of the portside G-Gun array profile AWI-20160002 was acquired with only 4 G-Guns (34 l / 2080 in³) towed in 6 m water depth (Gohl & Werner, 2016).

3.2.3. Free-air gravity anomaly (FAA) data

The gravimetry measurements during SO246 were performed with a LaCoste & Romberg S-80/Ultrasys gravity meter that was fixed in the gravity meter room of RV Sonne (Fig. 3.6), the most stable position of RV Sonne. The S-80 is a dynamic marine/airborne gravity meter attached in a gyro-stabilised platform, which is constantly moving and monitored. The gravity meter continuously operated during the cruise with a sampling rate of 1 Hz but was turned off and fixed during two heavy storm events. Reference base readings were performed by GNS scientists before and after the cruise, and tied to the regional onshore gravity network. After the cruise, B. Davy (GNS Science) calculated the FAA from the acquired data and provided me with the final gravity data. I used the FAA for gravity modelling along the four refraction seismic profiles to gain additional constraints about the density distribution along the profiles.

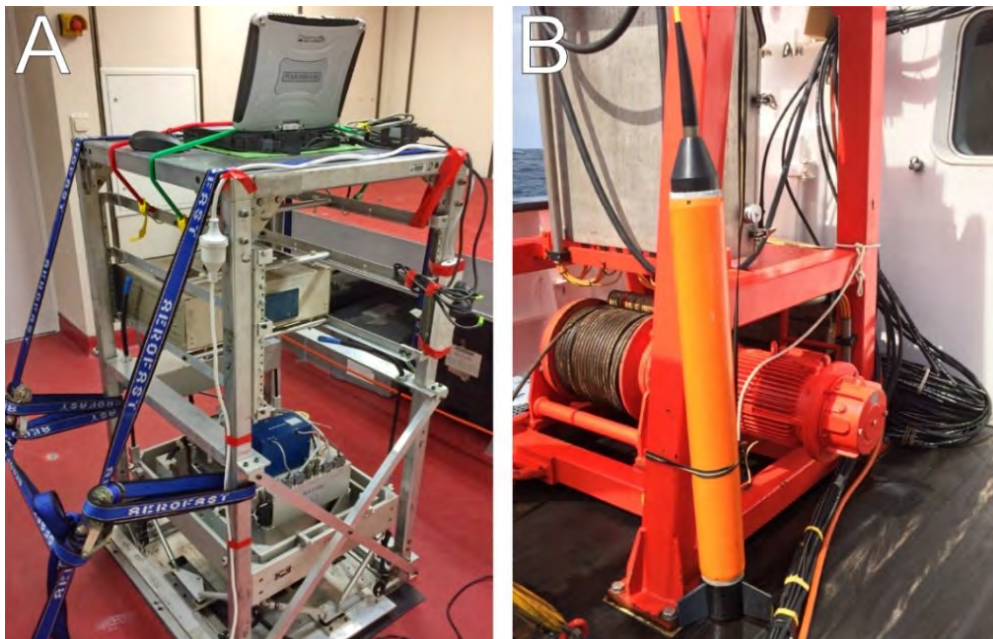


Fig. 3.6: Images of the (A) LaCoste & Romberg S80/Ultrasys marine gravity meter and (B) Seaspy magnetometer. Both instruments are owned by GNS Science. The images are from Gohl & Werner (2016).

3.2.4. Magnetic data

Magnetic measurements during SO246 were performed with a marine Seaspy magnetometer (Fig. 3.6), which uses the Overhauser effect to derive stable and high precision magnetic data. The magnetometer was deployed with the portside crane and towed 350 m behind the stern of RV Sonne. Magnetic measurements were made along the four refraction seismic profiles and along several other lines at different locations crossing the Chatham Rise, SE Chatham Terrace and West Wishbone Ridge (Fig. 3.3C). Magnetic data (including navigation and time information) were recorded in 0.5 s intervals. Magnetic anomaly calculation was undertaken by subtracting the latest version of the International Geomagnetic Reference Field (Thébaud et al., 2015) at reduced data

resolution (10 s). At the end of the expedition, I received the processed magnetic data from B. Davy (GNS Science).

3.2.5. Bathymetric data

During the SO246 expedition, bathymetric surveys were conducted with the multibeam echosounder MBES Kongsberg Simrad EM122. Data were processed in real time, with combined motion, position and time data from a Kongsberg Seapath System compensating for ship movements. More technical information about the bathymetric acquisition and processing is available in Gohl & Werner (2016).

Bathymetry data were recorded throughout the cruise with the exception of one heavy storm event, transit through the Territorial Seas of New Zealand close to Wellington and the Chatham Islands, and for the recovery of the OBS/OBH instruments because of interferences with the acoustic release signals and since the data was already recorded during seismic profiling. The data was continuously processed and cleaned by the bathymetry team using Caris HIPS, and traveltimes of the acoustic signals were corrected using eleven sound velocity profiles that were collected during the cruise (Gohl & Werner, 2016). After the last refraction seismic profile, S. Dreutter (AWI) produced an up-to-date gridded bathymetry dataset (Fig. 3.3D), which I used for plotting maps and extracting the depth of the seafloor along all profiles.

3.2.6. Pre-existing geophysical and geological datasets

In addition to the geophysical and geological datasets acquired during SO246, I also had access to reflection seismic data, bathymetry, and potential field data, which were acquired during numerous cruises over the past ~50 years by GNS Science (and previous institutes and organisations that were merged with GNS Science in 1992), contractors (e.g. Hunt International) and cooperation partners (e.g. AWI and GEOMAR). The geophysical data was provided by B. Davy (GNS Science) during the SO246 expedition included:

(I) Single-channel reflection data (Fig. 3.7A): (I) two contractor profiles from Hunt International across the Bounty Trough (e.g. Davy, 1993), and (II) profiles from the BT8202 and BT8203 cruises around the Chatham Islands (e.g. Wood & Anderson, 1989) and across the Bounty Trough collected by the Department of Scientific and Industrial Research. The original data are printouts that were later scanned and digitized as SEG-Y files by GNS Science. During my research stay at GNS Science from August to November 2017, I additionally had access to scans of a dense single-channel reflection survey around the Chatham Islands. This was a contractor survey operated by Tasman Petroleum Co Ltd between 1969 and 1971.

(II) MCS reflection data (Fig. 3.7A) from AWI-led expedition SO169 from the Bounty Trough and Great South Basin (Grobys et al., 2007; 2009); and MCS reflection data from Hikurangi Plateau, Chatham Rise and the SE Chatham Terrace, which were mostly acquired within the framework of New Zealand's UNCLOS (United Nations Convention on the Law of the Sea) and EEZ (Exclusive Economic Zones) programs (e.g. Davy et al., 2008; Barrett et al., 2017).

(III) Magnetic data (Fig. 3.7B) from 70 cruises along the Chatham Rise and surrounding area, including the projects named above.

(IV) Multibeam bathymetry data from the Chatham Rise and Hikurangi Plateau (Fig. 3.7C), including the bathymetric datasets from the GEOMAR-led SO168 and AWI-led SO169 expeditions.

For further local and regional interpretations on the free-air gravity anomaly (Fig. 3.7D), I have used the latest version (v2.3) of the globally compiled and gridded gravity data from Sandwell et al. (2014), which includes satellite-derived gravimetric data and gravity data recorded by GNS Science and contractors in the area around Chatham Rise.

For displaying the regional bathymetry (Figs. 3.3 and 3.7A-C) I used the GEBCO2014 dataset (Weatherall et al., 2014) with a resolution of 500 m. An up-to-date bathymetric dataset with higher resolution (250 m) compiled from single-beam and multi-beam bathymetry data is available by New Zealand's National Institute of Water and Atmospheric Research for the area around New Zealand including Chatham Rise (<https://niwa.co.nz/our-science/oceans/bathymetry>). Unfortunately, the western border of this gridded bathymetry dataset is at 167°W, and therefore, does include all our data except the southwestern half of profile AWI-20160300.

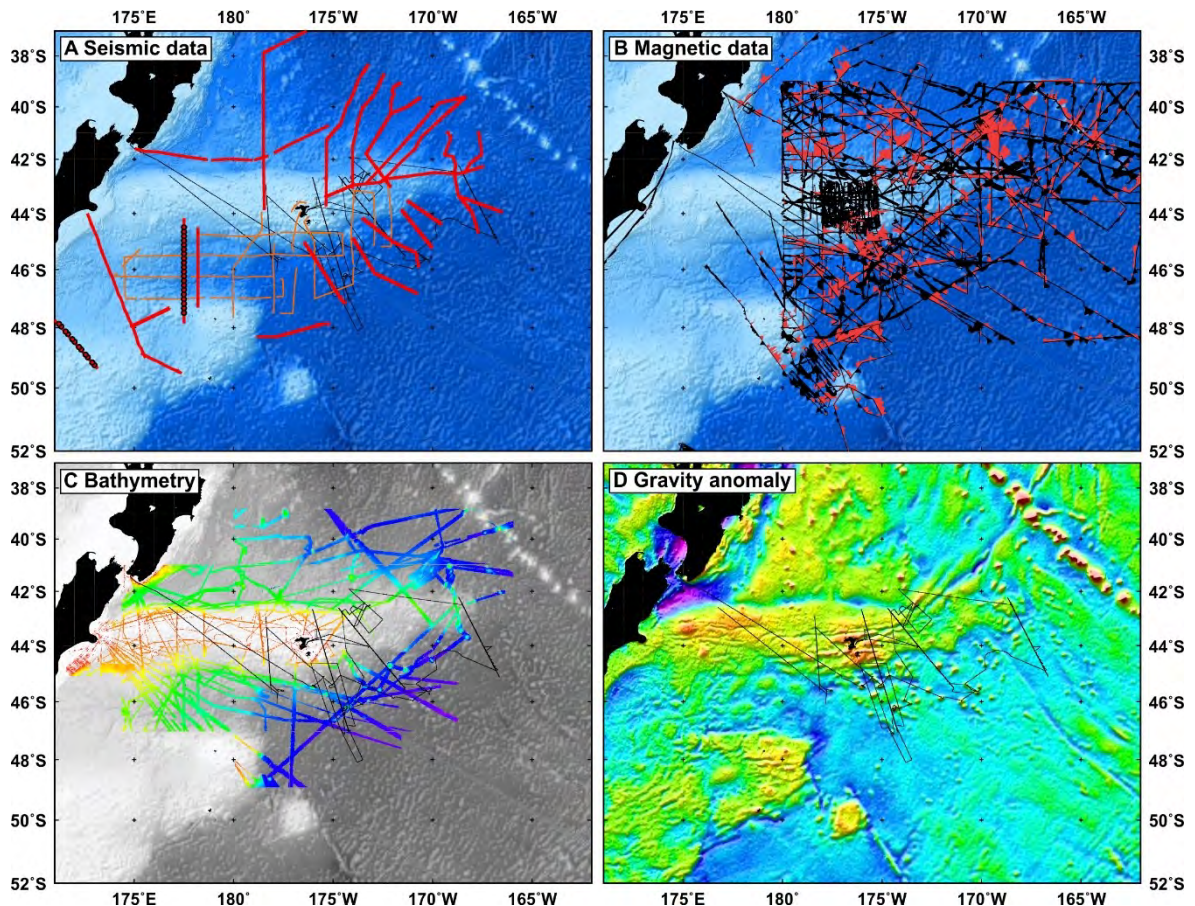


Fig. 3.7: Maps showing the pre-existing geophysical data in the area of the Chatham Rise. (A) Wide-angle reflection and refraction (red circles), MCS (red lines), and single-channel seismic reflection data, (B) magnetic data (red wiggles correspond to positive and black wiggles to negative magnetic anomalies), (C) free-air gravity anomaly data (Sandwell et al., 2014), (D) multibeam bathymetric data. The SO246 cruise track (thin black line) is shown as reference in all maps.

3.3. Seismic data processing, P-wave velocity and density modelling

In the next sections, I explain the different processing flows for the OBS / OBH and MCS reflection data. Furthermore, I describe the used modelling techniques, which I have used for the P-wave velocity and gravity modelling. All used processing and modelling techniques are widely used, and therefore, I only provide a condensed overview.

3.3.1. Onboard processing of the OBS / OBH data

During expedition SO246, refraction data were processed onboard in order to perform initial first quality control after each profile. After the internal clocks of the recorders were synchronised and the recording process was stopped, the data was downloaded from the data storage units of the recorders. Raw data from the MBS, MCS and 6D6 recorders were reformatted to s2x-format (Fig. 3.8) using the corresponding programs (i.e. MBSREAD, MCSREAD, and 6D6READ). In the next

step, the navigational data, shot timing and deployment position were reformatted to match the format requirement for the program SEG-YWRITE (SEND GmbH). This program converts the data from the s2x-format to the SEG-Y-format with 15000 samples per trace (= 60 s per trace). After that, the navigational data and shot positions were recalculated to include offsets for each station (source-receiver distances), and were written into the SEG-Y headers (Fig. 3.8).

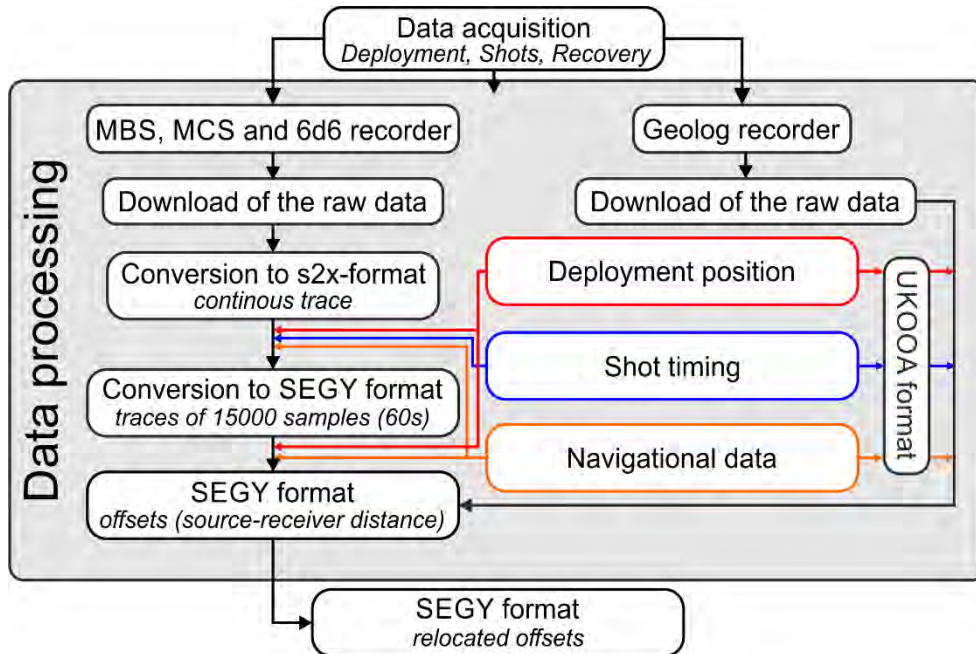


Fig. 3.8: Processing steps for the OBS/OBH data recorded with the four different recorders used during the SO246 expedition. See text for further information.

In contrast, the raw data of the Geolog recorders were demultiplexed using the corresponding Geolog software to create a pseudo-SEG-Y format for each channel. Navigational data, shot timing and deployment positions were all included in a single UKOOA-formatted file (Fig. 3.8). This UKOOA-file was merged with the pseudo-SEG-Y using programs and shell-scripts shared by F. Petersen (GEOMAR) to create the same SEG-Y-format as those for the other recorder types (Fig. 3.8).

Theoretically, the centre of the water wave (= the least travelttime) for each station should be at 0 m offset after including the offset of the station position. Practically though, the exact position of the OBS/OBH instruments is unknown as the instruments drift away from the deployment position while sinking down due to water currents. Therefore, the offsets were manually relocated by positive or negative shifting, and were updated in the SEG-Y headers.

3.3.2. MCS reflection data processing

The target of MCS reflection data processing is to improve the data quality of the seismic subsurface image. This can be done by filtering, stacking and migration. First, seismic raw data needs to be demultiplexed from SEG-D-format (Fig. 3.9) and binned in common-depth points (CDPs), taking the geometry of the source and receivers into account. These processing steps were done as part of the initial quality control by K. Gohl onboard RV Sonne. Shot intervals were 20 s for pure MCS reflection profiles and 60 s for MCS reflection data recorded along refraction seismic profiles. Therefore, the applied bin-spacings are either 25 m for 20 s shot interval or 50 m 60 s for shot interval. Resulting CDP-folds are ~115 and ~80, respectively.

My goal when processing was to time-migrated seismic images of the subsurface in order to enable interpretation of the acoustic basement along the profile. Furthermore, significant sedimentary

reflectors and the acoustic basement (depth-converted) were then utilised as additional constraints for P-wave velocity modelling. With these targets, I performed the following seismic processing flow at the Alfred Wegener Institute (Fig. 3.9) using the seismic processing software Paradigm Echos. In the first step, I applied an exponential gain and a spherical divergence correction to the CDP-sorted data (Fig. 3.9) to compensate for attenuation losses of the signal, and to account for the decreasing wave strength with distance resulting from geometric spreading. I performed a velocity analysis every 50 or 100 CDPs on average, depending on the applied bin-spacing and subsurface topography. Afterwards, I utilise the velocity analysis of each profile to apply the normal-moveout correction, which accounts for the difference in the reflection arrival times for increasing source-receiver offsets. A stretch mute of 30 % was applied to reduce or eliminate frequency distortions, which occur in shallow reflection events at larger receiver offsets. After that, traces within each CDP were combined using a mean stack. I applied a post-stack time-migration to calculate the true subsurface geometry of diffraction hyperbolas. Finally, the sections were filtered using a trapezoidal (Ormsby) bandpass filter with 5-15 Hz low-pass and 150-200 Hz high-pass frequencies. These time-migrated and filtered sections were then used for further analysis and interpretation. To pick and integrate seismic reflectors such as the acoustic basement into the P-wave velocity models, I converted the section to depth by using the same velocity analyses as previously used for NMO correction and time-migration.

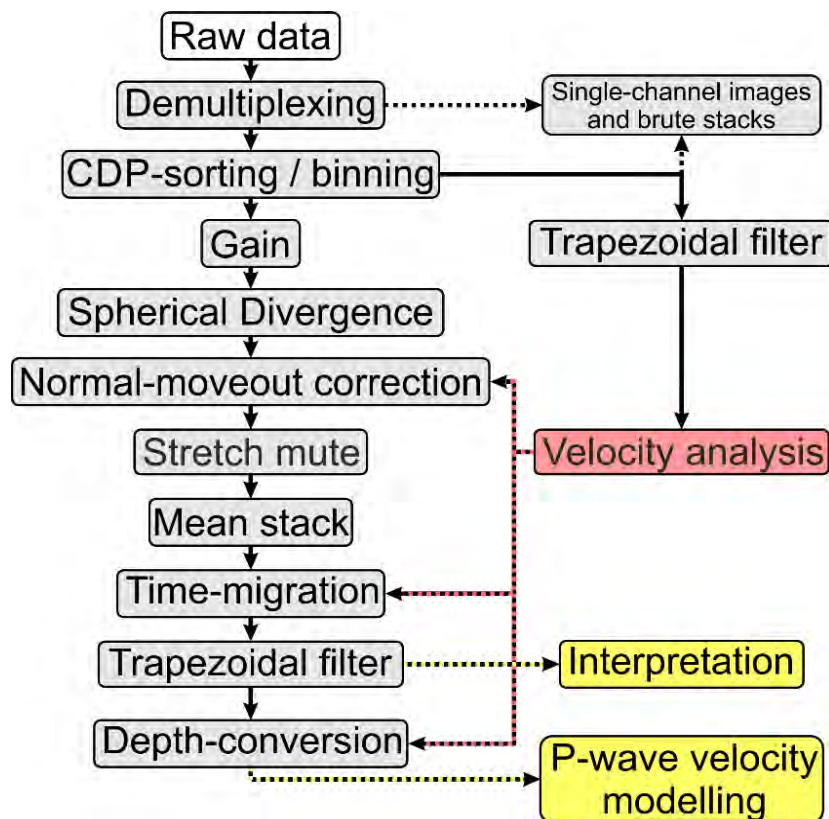


Fig. 3.9: MCS reflection data handling and processing flow for the four profiles. Demultiplexing and binning were already performed onboard. Final time-migrated and depth-converted seismic sections were used for interpretation of the basement structure and P-wave velocity modelling (see Fig. 3.10).

3.3.3. Modelling the crustal structure from P-wave arrivals

Arrivals of different wave phases were identified and picked using the “ZP” software (Zelt, 2004; see Fig. 3.10). During the wave phase identification process, the relocated refraction seismic data from all stations were displayed, bandpass filtered (low-pass = 6 Hz and high-pass = 14 Hz), and an automatic gain control (1000 ms) to amplify weak and late-arriving events. ZP calculates the signal-

to-noise ratio automatically, providing independent uncertainty windows. The resulting uncertainties typically range between 50 and 100 ms, but reach up to 250 ms at far offsets and for weak signals. The hydrophone seismograms usually have better quality and were used to pick the different wave phases. If available, other recorded channels (X-, Y-, and Z-channels) were also considered for interpretation of the first arrivals of different wave phases. Within the OBS/OBH seismograms, refracted wave phases appear as straight lines or slightly bent, while reflected waves present as hyperbolas (Fig. 3.11). Seafloor and subsurface topography, however, also have considerable effects on the pattern of the wave phases in the seismograms (Fig. 3.11). The traveltimes of the different wave phases from sedimentary and crustal layers, as well as from the mantle, were picked and saved. The output also includes the corresponding uncertainties and key identifiers for each model layer.

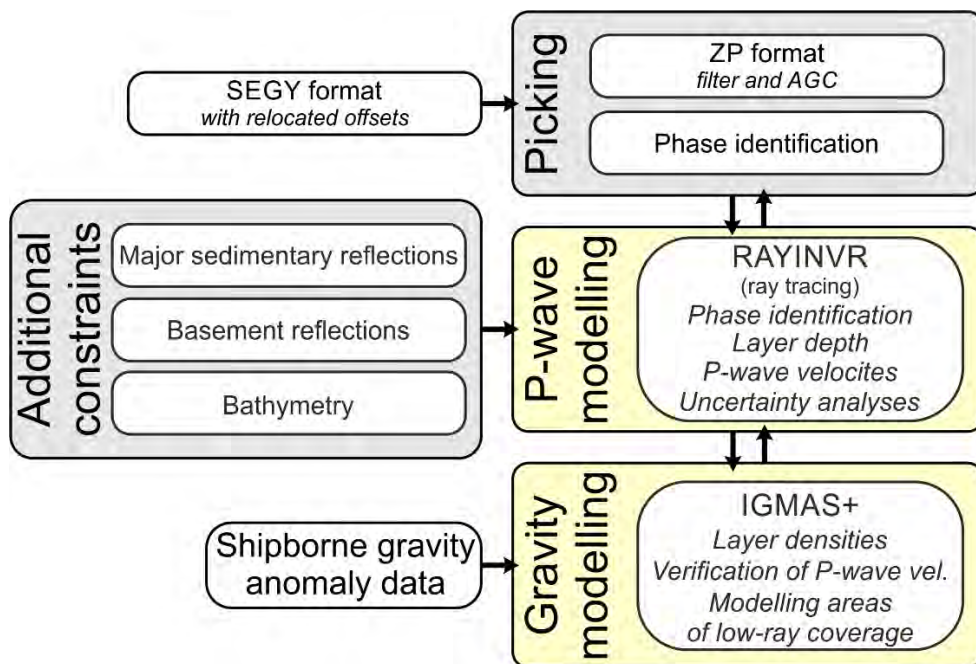


Fig. 3.10: Data input and processing flow for P-wave velocity and gravity modelling after the OBH/OBS (see section 3.3.1.) and MCS reflection data (see section 3.3.2.) were prepared.

I performed P-wave velocity modelling using the RAYINVR software package (Zelt and Smith, 1992), which uses an integrated standard ray tracing technique (Fig. 3.10). I accessed RAYINVR through the graphical user interface P-Ray (Fromm, 2015). OBS/OBH positions, bathymetry, sedimentary and basement reflections obtained from the depth-converted seismic reflection data (see section 3.3.2.) were integrated during the setup of the initial P-wave velocity models (Fig. 3.10). P-wave velocities obtained from the sedimentary layers were compared and are in good agreement with the velocity analysis of the MCS reflection data. The initial P-wave velocities for the crustal layers and the mantle were estimated using the apparent velocities (the slope of a wave phase in the seismograms) of the wave phases and were then manually assigned to the layers.

Modelling strategy followed a top-down approach. The depth of the layer boundaries and P-wave velocities in each layer were iteratively adjusted in order to fit the modelled reflected and refracted wave phase arrivals within the calculated uncertainties (Fig. 3.11). RAYINVR inversion methods also delivered statistics on the resolution, ray coverage and variability of the model. If any layer fit well within the uncertainties of the modelled arrivals, I repeated the modelling procedure for the underlying layers until the lowermost layer (i.e. the upper mantle) was reached. Finally, I performed a detailed uncertainty analysis for every model using the approach of Schlindwein & Jokat (1999). Accordingly, P-wave velocities and layer boundaries were separately and systematically perturbed

until the calculated traveltimes exceeded the uncertainty range of the observed traveltimes. The P-wave velocity model uncertainty analyses was repeated for every layer and model. Estimated uncertainties were within the same range of other refraction seismic studies using the same approach (e.g. Mueller et al., 2016) and are shown as tables for each profile in chapter 4 and 5.

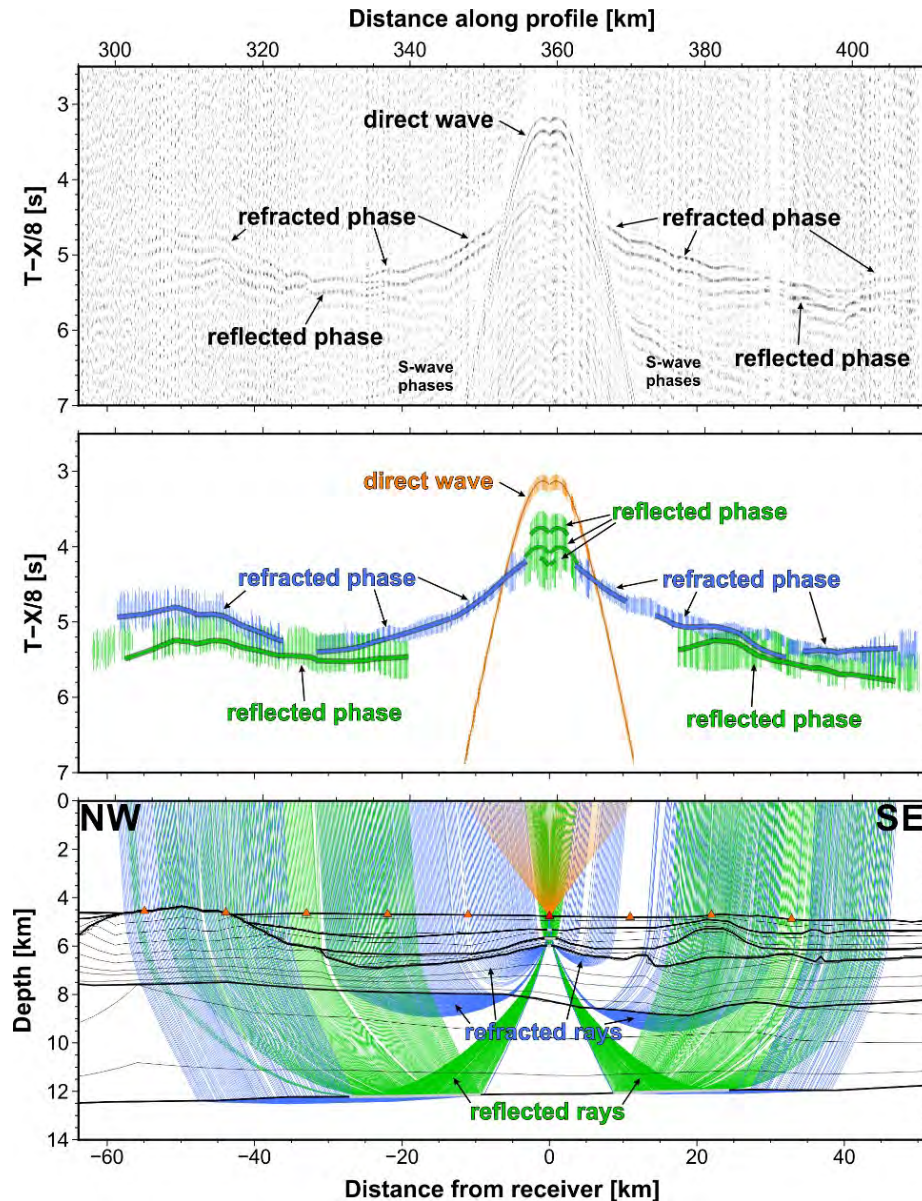


Fig. 3.11: Data and modelling example along profile AWI-20160200. Top: Seismogram (hydrophone channel) of station st232. Middle: Picked reflected (green), refracted (blue), direct (orange) wave phases and their modelled arrival times corresponding to the P-wave velocity model (bottom). Bottom: Section of the P-wave velocity model along profile AWI-20160200 with direct, refracted and reflected ray path.

3.3.4. Modelling the gravity anomaly

Rock densities, together with P-wave velocities, provide valuable information about crustal composition and geologic structures along the profiles (see example in Fig. 3.12). A 2.5D gravity modelling approach was performed to determine densities by using the shipborne FAA along the profiles. This was in particular very useful for verifying the P-wave velocity-depth distribution and constraining areas along the P-wave velocity models that were characterised by low ray coverage. I performed gravity modelling using the IGMAS+ software package (Götze, 2007; Götze and Lahmeyer, 1988; Schmidt et al., 2007). For the setup of the gravity models, I extracted the geometry

and layer boundaries from the P-wave velocity models. To account for significant lateral P-wave velocity variations, several layers were vertically subdivided within the gravity models. Densities for the initial gravity model were based on published P-wave velocity-density relationships (see Fig. 3.12; Barton, 1986; Christensen & Mooney, 1995). Densities were iteratively adjusted to fit the modelled FAA and the observed gravity anomaly data within a 5 mGal uncertainty range. During modelling, I ensured that the densities correlated with modelled P-wave velocities within the uncertainties given for the P-wave velocity-density relationships.

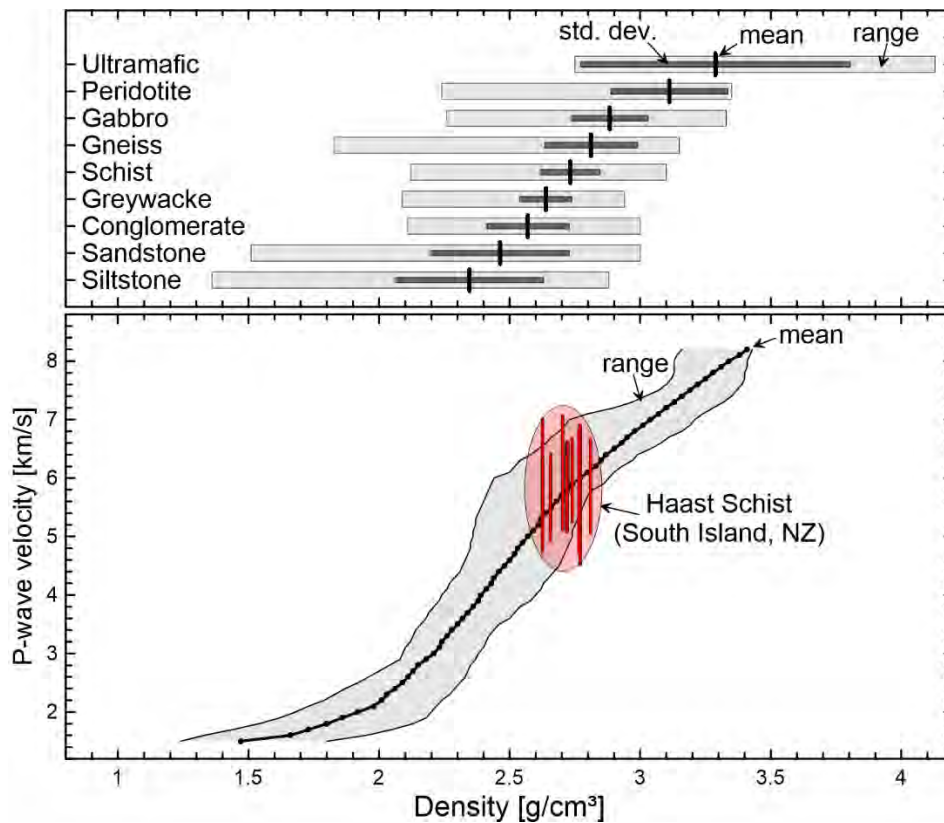


Fig. 3.12: Bottom: P-wave velocity-density relationship (Barton, 1986) with geophysical parameters of the Haast Schist (Godfrey et al., 2000). Top: Densities, standard deviations and density range for different rock types from onshore North and South Island of New Zealand (Tenzer et al., 2011).

3.3.5. Plate kinematic / tectonic modelling

In order to illustrate the results about the evolution of the southern Chatham Rise margin within a broader plate-tectonic context (southern Zealandia, South Pacific and West Antarctica; see section 4.6), I prepared a plate-kinematic model for using the latest version of the open-source software GPlates (Müller et al., 2018). GPlates makes use of an absolute reference frame and rotation parameters combined with age and timing of the motion of different tectonic plates. Significant changes in rotation poles were not modelled. I used coastlines, static polygons of the continents, and rotational parameters published with the latest GPlates version (Mueller et al., 2018). From this dataset, I subdivided several polygons in the southern Zealandia area based on the refractions seismic results using geographic information systems (ArcGIS 9.3). The positions of the Chatham Rise, New Zealand's South Island, Campbell Plateau and Bollons Seamount with respect to West Antarctica at 90 Ma are based on rotational parameters of Eagles et al. (2004a), Larter et al. (2002) and Grobys et al. (2008). Movements between Australia, East Antarctica, and the continental fragments of northern Zealandia were integrated using parameters compiled from several published sources (Cande and Stock, 2004; Croon et al., 2008; Gaina et al., 1998; Granot et al., 2013; Whittaker et al., 2013).

4. Manuscript I

Cretaceous intracontinental rifting at the southern Chatham Rise margin and initialisation of seafloor spreading between Zealandia and Antarctica

Florian Riefstahl^{1,6}, Karsten Gohl¹, Bryan Davy², Kaj Hoernle³, Nick Mortimer⁴, Christian Timm^{2,3}, Reinhard Werner³, Katharina Hochmuth^{1,5}

¹Alfred Wegener Institute Helmholtz-Centre for Polar and Marine Research, Bremerhaven, Germany

²GNS Science, Avalon, Lower Hutt, New Zealand

³GEOMAR Helmholtz-Centre for Ocean Research, Kiel, Germany

⁴GNS Science, Dunedin, New Zealand

⁵Now at: School of Geography, Geology and the Environment, University of Leicester, Leicester, United Kingdom

⁶Now at: Christian-Albrechts-Universität zu Kiel, Institute of Geosciences, Kiel, Germany

Abstract

Passive continental margins are commonly classified as magma-poor and magma-rich types. Related breakup processes are often associated with far-field tectonic stresses or upwelling mantle plumes. The Chatham Rise east off New Zealand records a sequence of Late Cretaceous tectonic events, which include subduction and collision of the oceanic Hikurangi Plateau to subsequent continental rifting and breakup. The mechanisms triggering the change in tectonic forces are poorly understood but address open questions regarding the formation of passive margins. We acquired wide-angle seismic reflection/refraction, multi-channel seismic and potential field data along three profiles crossing the southern Chatham Rise margin and SE Chatham Terrace to the oceanic crust in order to image and understand the crustal structure and breakup mechanisms. Variations in crustal thickness along the highly faulted Chatham Rise are most likely related to the collision with the Hikurangi Plateau. Our data indicate that the SE Chatham Terrace represents a broad continent-ocean transition zone (COTZ), which we interpret to consist of very thin continental crust affected by magmatic activity. Along the southern Chatham Rise margin, features of both, magma-poor and magma-rich rifted margins are present. We suggest that passive rifting initiated at 105-100 Ma related to slab dynamics after the Hikurangi Plateau collision. We revise the onset of seafloor spreading south of the eastern Chatham Rise to ~88 Ma from the extent of our inferred COTZ. Geographically extensive, but low-volume intraplate magmatism affected the margin at 85-79 Ma. We suggest that this magmatism and the onset of seafloor spreading are a response to upwelling mantle through a slab window after 90 Ma. After 85 Ma, spreading segments became connected leading to the final separation of Zealandia from Antarctica. We interpret the southern Chatham Rise margin as a unique hybrid margin whose tectonic history was influenced by passive continental rifting and mantle upwelling.

4.1. Introduction

The breakup of supercontinents such as Gondwana is often associated with a change from lithospheric convergence (i.e. subduction activity and orogeny) to lithospheric divergence (i.e. crustal thinning prior to seafloor spreading). The mechanisms controlling the polarity of tectonic forces play a key role in the Wilson cycle (Dewey and Burke, 1974), but are poorly understood. Options include triggering by mantle dynamics leading to rising plumes and result in active and ‘hot’ rifting or, alternatively, by tectonic forces through far-field processes with significantly less or without any magmatic activity, which lead to passive and ‘cold’ rifting.

The Cretaceous collision of the Hikurangi Plateau with Zealandia (Fig. 4.1A) is interpreted to have initiated the end of subduction activity and compression at the East Gondwana margin (e.g. Davy, 2014; Davy et al., 2008). At approximately the same time intracontinental rifting was initiated, which led to the separation of Zealandia and Antarctica (e.g. Mortimer et al., 2016; Tulloch et al., 2009b). While the Late Cretaceous to Cenozoic seafloor spreading history between Zealandia and Antarctica is relatively well studied (e.g. Eagles et al., 2004a; Wobbe et al., 2012; Wright et al., 2016), the early rifting history between both conjugate margins, in particular those of Chatham Rise and Amundsen Sea / eastern Marie Byrd Land sector (Fig. 4.1B), remains poorly understood. The temporal overlap of the Hikurangi Plateau collision, subduction cessation and onset of rifting raises the following questions: Did the former Hikurangi Plateau subduction influence or initiate the early rifting? Or were collision and crustal extension two independent causal processes in the highly complex continental area of the Chatham Rise?

Knowledge about the nature and crustal structure is essential for any sound reconstruction of the margin evolution and the role of subduction cessation and breakup at the former East Gondwana subduction zone. Is the southern Chatham Rise margin a volcanic-rifted type margin with seaward dipping reflectors indicating excessive emplacement of magma triggered by an upwelling plume (Storey et al., 1999; Weaver et al., 1994)? Or was the breakup at the southern Chatham Rise margin non-volcanically driven by tectonic forces like transtensional movements along the West Wishbone Ridge (Fig. 4.2A; Barrett et al., 2018; Davy, 2014)? Contrasting palaeotectonic scenarios are possible depending on whether oceanic, stretched continental crust and/or exhumed mantle is assumed to underlie the SE Chatham Terrace (Figs. 4.1A and 4.2A), an area of seafloor south of the Chatham Rise, where water depth is shallower than the abyssal oceanic crust and hosts abundant seamounts and guyots. For a fundamental understanding of the driving forces of the breakup it is also essential to know details on the exact timing for the first formation of oceanic crust and the amount of volcanism related to the breakup.

In this study we attempt to answer these questions for the particular situation of the Chatham Rise east of the Chatham Islands and SE Chatham Terrace. We acquired three 330-485 km long seismic wide-angle reflection and refraction profiles during the RV Sonne cruise SO246 in 2016 (Gohl and Werner, 2016). Additionally, multi-channel seismic (MCS) reflection and potential field (gravity, magnetic) data were collected along these profiles. Here, we present the results of P-wave velocity and density forward modelling together with an interpretation of the MCS reflection data. Subsequently, we define crustal thicknesses and specify the nature of the southern Chatham Rise margin. Our study explores potential processes governing the cessation of subduction along the East Gondwana active margin and the earliest East Gondwana breakup along the southern Chatham Rise margin, i.e. the transformation of a formerly active subduction margin to a passive rifted margin. Our findings also have implications for the geological and tectonic evolution of other, once nearby, continental areas like the Bounty Trough and rift basins east of the South Island as well as the conjugate Marie Byrd Land margin of West Antarctica.

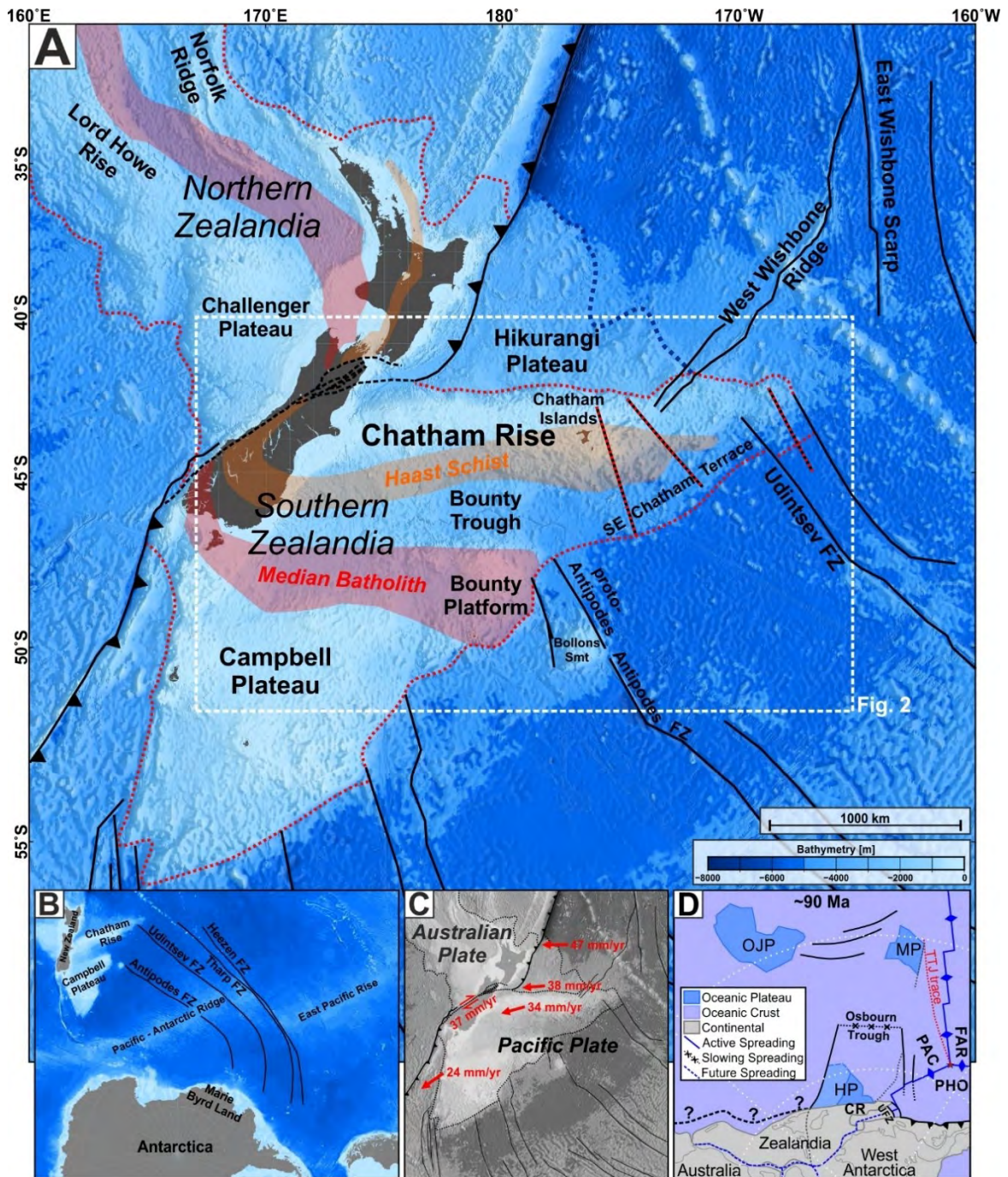


Fig. 4.1: (A) Bathymetry overview map of Zealandia's continental areas, Hikurangi Plateau, and South Pacific adjacent to Zealandia (GEBCO, Weatherall et al., 2015). The three profiles are indicated by the red-black dotted lines. The red dotted lines represent the extent of Zealandia's continental areas modified after Barret et al. (2018), Mortimer et al. (2017), and Tulloch et al. (2019). Offshore continuation of New Zealand's onshore geology (Haast Schist in orange and Median Batholith in red) are redrawn from Mortimer et al. (2017). (B) Overview map of the South Pacific and Marie Byrd Land conjugate margin of the Chatham Rise and Campbell Plateau. (C) Present-day plate velocities of the Pacific Plate relative to the Australian Plate (DeMets et al., 2010). (D) Tectonic model at ~90 Ma simplified after Mortimer et al. (2019) showing the trace of the Tongareva Triple Junction (TTJ) separating the Pacific (PAC), Phoenix (PHO) and Farallon (FAR) plates after the spreading along the Osborn Trough slowed down or even ceased in response to the Hikurangi Plateau (HP) collision. CR = Chatham Rise, MP = Manihiki Plateau, OJP = Ontong Java Plateau.

4.2. Tectonic and geological background

The North and South Islands of New Zealand represent a small fraction of the Zealandia Continent, which are elevated above the sea level (Fig. 4.1A; Mortimer et al., 2017). The larger submerged part

of Zealandia is formed by thinned continental crust and includes Challenger Plateau, Lord Howe Rise and Norfolk Ridge (Fig. 4.1A; among New Caledonia further in the north) as parts of North Zealandia and Campbell Plateau, Bounty Platform and the Chatham Rise as parts of South Zealandia (Fig. 4.1A; e.g. Mortimer et al., 2017; Timm et al., 2010).

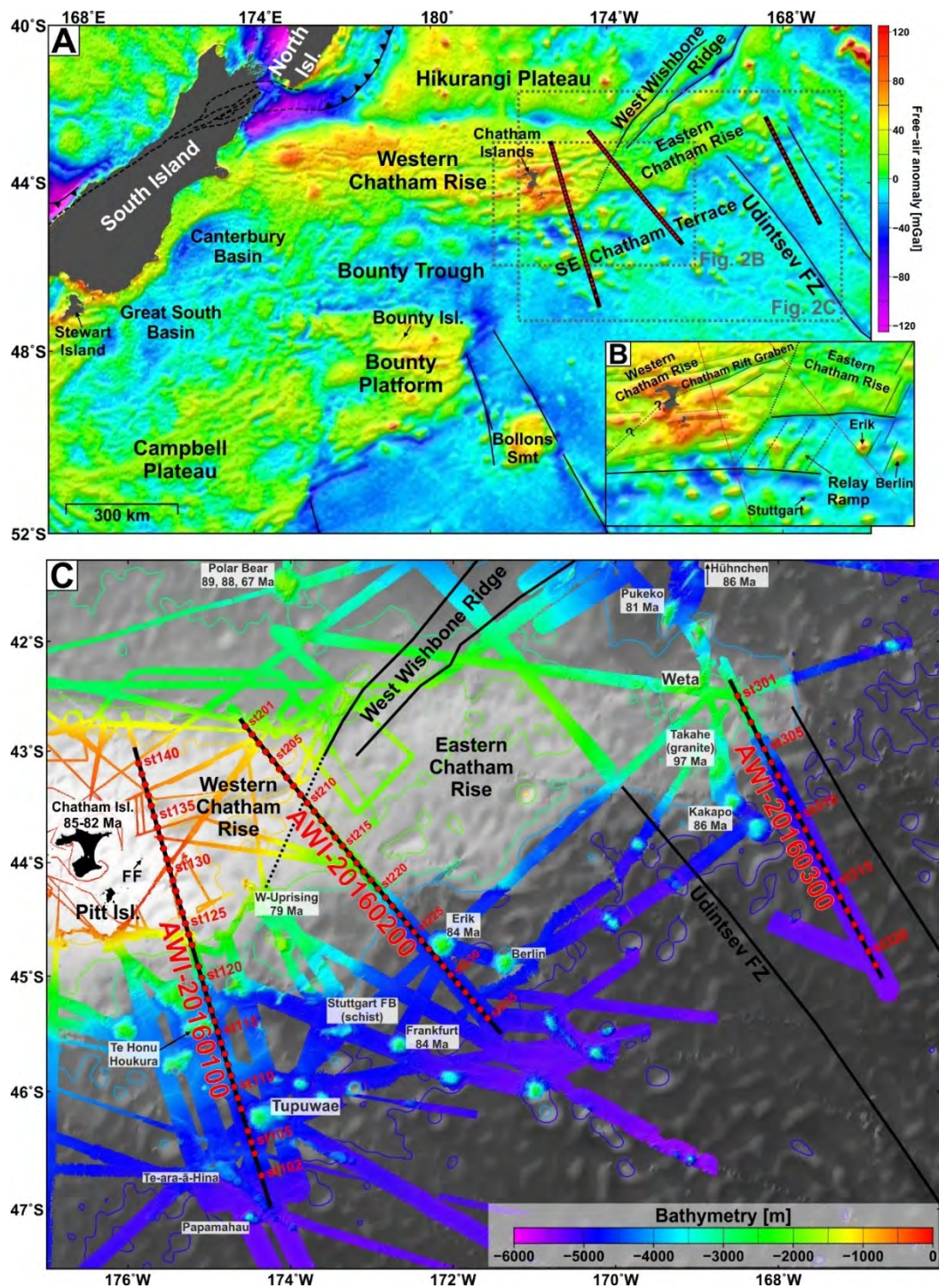


Fig. 4.2: (A) Satellite free-air gravity anomaly (Satgrav23, Sandwell et al., 2014) overview map of the Chatham Rise and surrounding areas. (B) Zoom of Fig. 2A with half graben structures interpreted from the gravity lineations. The area between the profiles AWI-21060100 and AWI-20160200 represents a relay ramp (series of accommodating faults) indicating oblique rifting. (C) Swath bathymetry overview maps of the seismic profiles (black lines) and OBS / OBH stations (red circles). Swath bathymetry apart from the expedition SO246 cruise was collected over the past decades from previous cruises to the Chatham Rise and were provided by GNS Science. Greyscale GEBCO bathymetry is in the background (Weatherall et al., 2015). Names of seamounts and guyots on this map refer to working names excogitated during SO168 and SO246 cruise (Gohl and Werner, 2016; Hoernle et al., 2003). Ages from the seamounts are published in Mortimer et al. (2006), Hoernle et al. (2010), and Mortimer et al. (2019). FF = Forty Fours.

The E-W oriented submarine Chatham Rise (Fig. 4.2A) extends up to 1500 km to the east of the South Island. The Hikurangi Plateau – a Cretaceous large igneous province – borders the Chatham Rise to the north. At present day the Hikurangi Plateau subducts below the North Island (e.g. Reyners et al., 2011, Reyners, 2013) driven by the W to SW directed movement of the Pacific Plate relative to the Australian Plate (Fig. 4.1C). The Chatham Islands (Fig. 4.2C) are the only subaerial exposed part of the Chatham Rise. East of them a bathymetric (and gravimetric) step across the extension of the West Wishbone Ridge (Figs. 4.2A and 4.2C) separates the shallower western Chatham Rise crest (< 1000 m water depth) from the deepening slope of the eastern Chatham Rise crest (1000-3000 m water depth). To the south the Chatham Rise transitions into a bathymetric depression deepening from west to east, the Bounty Trough, and into the SE Chatham Terrace (Fig. 4.1A). The SE Chatham Terrace is a poorly constrained deep-sea domain at the southeastern Chatham Rise margin. It is shallower than the surrounding seafloor and comprises abundant guyots, seamounts and ridges (Fig. 4.2C). Bathymetry, seismic and geological data from the SE Chatham Terrace indicate that at least some of the free-air gravity anomaly highs (Fig. 4.2A) correspond to block-faulted basement and volcanics (Carter et al., 1994; Davy, 1993; Mortimer et al., 2006).

4.2.1. Geologic history of South Zealandia and the Chatham Rise

During the Paleozoic to early Mesozoic, South Zealandia was part of the active continental margin of East Gondwana (e.g. Mortimer et al., 2017), subsequently rifted from West Antarctica, uplifted and finally subsided throughout the Mesozoic (Campbell et al., 1993; Wood et al., 1989). The geologic history is obtained from the basement rocks of South Zealandia, which mainly consists of (i) a Paleozoic-Mesozoic magmatic arc, i.e. the Median Batholiths (Fig. 4.1A), (ii) Permian-Cretaceous allochthonous terranes, including typical accretionary wedge greywackes and metamorphic equivalents (e.g. Mortimer et al., 2014). The oldest basement rock known from the Chatham Rise and the Chatham Islands (Figs. 4.2A and 4.2C) is the Chatham Schist, which comprises Permo-Triassic low pressure and temperature schists and greywackes (e.g. Adams et al., 2008; Adams and Robinson, 1977; Allan, 1928; Campbell et al., 1993; Mortimer et al., 2019a). Similarities in metamorphic grade / texture, age and isotopic composition suggest that the Chatham Schist is similar to schists found onshore the South Island (Adams et al., 2008, Mortimer et al., 2019a), which demonstrate the close relation between the Chatham Rise and South Island's geological and tectonic history. In the following text we avoid usage of regional names for the Zealandia schists and refer all as Haast Schist (Fig. 4.1A) according to Mortimer et al. (2014).

In the mid-Cretaceous at ~110 Ma, the then-young oceanic Hikurangi Plateau (Fig. 4.1A) is interpreted to have collided with South Zealandia of Gondwana. Subsequently, it was partially subducted and jammed the subduction margin (e.g. Barrett et al., 2018; Davy, 2014; Davy et al., 2008; Reyners et al., 2017b). Cessation of the Hikurangi Plateau subduction was estimated to be at ~100 Ma or ~96 Ma (Barrett et al., 2018; Davy, 2014; Davy et al., 2008), which is in agreement with the latest stage of subduction related magmatism at 96 Ma known from eastern Marie Byrd Land, West Antarctica (Fig. 4.1A; Kipf et al., 2012) and Mt. Somers on the South Island of New Zealand (van der Meer et al., 2016).

Since seafloor spreading north of the Hikurangi Plateau took place during the Cretaceous Normal Superchron, the exact timing of end of the collision and subduction activity is poorly constrained (e.g. Downey et al., 2007; Larson et al., 2002). Lack of dating of seismic reflectors also limits our knowledge of the timing of these events. According to Davy (2014) interpreted that the Gondwana margin along the Chatham Rise was segmented, offset from the South Island and rotated counter-clockwise relative to the Hikurangi Plateau in response to the collision and initial subduction jamming onshore New Zealand. Furthermore, the Hikurangi Plateau collision is interpreted to have

caused the segmentation into eastern and western Chatham Rise and offset of the northern Chatham Rise margin (Fig. 4.2C; Barrett et al., 2018). After cessation of the Hikurangi Plateau subduction at around 100 Ma, subduction of oceanic crust continued at the eastern Chatham Rise and dextral strike-slip movements became active along the West Wishbone Ridge (Fig. 4.2C; Barrett et al., 2018; Davy, 2014).

Spatially very limited extension along the Gondwana margin started at ~112.5 Ma onshore South Island as manifested in non-marine graben deposits located within the Haast Schist (Fig. 4.1A; Mitchell et al., 2009; Tulloch et al., 2009b). However, wide-spread extension and intracontinental rifting were initiated later as expressed by the exhumation of metamorphic core complexes of the Median Batholith on the southwestern South Island between 108 and 106 Ma (Fig. 4.1A; Schwartz et al., 2016). At least since 105 Ma, graben formation became significant and several sedimentary basins such as the Great South Basin and Canterbury Basin offshore east coast South Island (Fig. 4.2A) started to form and successively deepen in Zealandia (Bache et al., 2014; Strogon et al., 2017). Exposed terrestrial graben deposits on Pitt Island (Fig. 4.2C), located SE of Chatham Island are as old as 100 Ma (Campbell et al., 1993). The extension and subsequent crustal thinning also triggered a change from subduction-related magmatism in the Median Batholith to more widespread low-volume and distributed A-type granite emplacement and alkali-basaltic magmatic activity between 101 and 97 Ma, which affected Marie Byrd Land, the Hikurangi Plateau, the South Island of New Zealand and the eastern Chatham Rise (Hoernle et al., 2010; Homrighausen et al., 2018; Mortimer et al., 2019b, 2016, 2006; Schwartz et al., 2016; Tulloch et al., 2009a, 2009b, van der Meer et al., 2018, 2016; Weaver et al., 1994).

From identification of magnetic spreading anomalies, the onset of seafloor spreading between Zealandia and West Antarctica is inferred to be around 90 Ma east of the present-day Udintsev Fracture Zone (UFZ; Figs. 4.1A and 4.1D; Eagles et al., 2004a; Larter et al., 2002; Wobbe et al., 2012). After 117 Ma, the Tongareva Triple Junction (TTJ), separating the Pacific, Phoenix and Farallon plates, migrated into a direction towards the East Gondwana active margin (Fig. 4.1D; Larson et al., 2002). Its western spreading segment (Pacific-Phoenix plate boundary) migrated between the Chatham Rise and Marie Byrd Land at around 90 Ma (e.g. Larter et al., 2002; Eagles et al., 2004a).

The onset of seafloor spreading west of the UFZ in the area of the SE Chatham Terrace is unclear due to the unknown crustal structure of the SE Chatham Terrace. Barrett et al. (2018) suggested that seafloor spreading started at the same time as that east of the UFZ based on available magnetic spreading anomaly c34n picks (Larter et al., 2002; Wobbe et al., 2012). However, magnetic anomaly pattern on the SE Chatham Terrace is quite complex due to widespread volcanic features (Davy, 2006) and does not show clear indications that it is related to seafloor spreading. Published geochemical and $^{40}\text{Ar}/^{39}\text{Ar}$ age data confirm an intraplate origin and emplacement age of around 85 Ma of the SE Chatham Terrace seamounts similar to that of the oldest lavas from the Chatham Islands (Fig. 4.2C; Mortimer et al., 2019b; Panter et al., 2006). Another dredge sample from the Stuttgart Seamount, southeast of the Chatham Islands (Fig. 4.2C), contains high-grade metamorphic schists comparable to those found on the Chatham Islands (Mortimer et al., 2016, 2006). East of the SE Chatham Terrace, Davy (2006) interpreted well-lineated NE-SW striking magnetic anomalies - oblique to the E-W elongated Chatham Rise - to be spreading anomalies c34n to c33r close to the mouth of the Bounty Trough and estimated the onset of seafloor spreading at 85 Ma east of the SE Chatham Terrace. Southward ridge jumps and highly asymmetric spreading between 83 and 79 Ma are inferred to explain the magnetic anomaly at the southern Chatham Rise margin and the separation of the Bollons Seamount, which was initially part of the Antarctic Plate and then transferred to the Pacific Plate (Davy, 2006; Eagles et al., 2004a, 2004b; Sutherland, 1999; Wobbe et al., 2012). In contrast, Tulloch et al. (2019) questioned that the origin of magnetic anomalies

close to the mouth of the Bounty Trough is related to seafloor spreading, but suggested that these are part of a larger rift-related mafic complex that includes Chatham Islands, SE Chatham Terrace, Bounty Platform and Campbell Plateau (Figs. 4.1A and 4.2A). There is, however, a broad agreement that the separation of Campbell Plateau and Bounty Platform from Antarctica postdates the onset of seafloor spreading at the southern Chatham Rise margin (Davy, 2006; Eagles et al., 2004a, 2004b; Sutherland, 1999; Wobbe et al., 2012).

4.3. Data acquisition, processing and modelling procedure

4.3.1. Seismic wide-angle reflection/refraction data

Seismic wide-angle reflection/refraction data were collected along three deep-crustal profiles across the southern Chatham Rise margin (Figs. 4.2A and 4.2C) using ocean-bottom seismometers (OBSs), each equipped with a three-component seismometer and a hydrophone, and ocean-bottom hydrophone (OBH) systems with hydrophones only. Along profiles AWI-20160100 and AWI-20160200, 40 and 35 OBS/OBH instruments were deployed at ~11 km spacing. 21 OBS/OBH instruments were deployed with ~15 km spacing along profile AWI-20160300. The sampling rate was set to 250 Hz for all recorder types. 8 G-Guns arranged in 2x4 G-Gun clusters with a total volume of 68 l (4150 in³) were fired at 205 bar every 60 s while towed 10 m below sea level.

All OBS/OBHs were recovered, but four instruments along AWI-20160100 (st101, st103, st107, st122) recorded no data due to malfunction. In general, the data quality is good to excellent, and the hydrophone channel provided the best data quality throughout. Along profile AWI-20160200, the hydrophone channels of two instruments (st213 and st234) did not record any data, but the vertical-component channels yield usable data.

We relocated OBS/OBH positions using the direct-wave arrivals, converted the data into SEGY format, and applied a 4-14 Hz bandpass filter as well as a 1000 m length automatic gain control.

4.3.2. P-wave velocity modelling

We selected all refracted and reflected seismic phases with the software ZP (Zelt, 2004), which calculates the individual picking uncertainty of each pick by taking the signal-to-noise ratio into account. Applied picking uncertainties range between 50 and 250 ms. P-wave velocity modelling was performed with the program Rayinvr (Zelt and Smith, 1992) and its graphical user interface PRay (Fromm, 2016). If observed, we picked wide-angle reflection phases to help determine the depth of layer boundaries. Initial P-wave velocities for each layer were determined primarily from the refracted phases and iteratively refined to match all picks within their uncertainty range. The number of model layers was kept as small as possible to avoid unconstrained structural complexities. Statistics corresponding to the presented models are listed in Tabs. S1-S3.

We estimated uncertainties for the layer boundary depths and P-wave velocities by using the same approach as Schlindwein and Jokat (1999). Accordingly, P-wave velocities and layer boundaries were systematically perturbed (layer-wise and separately) until the calculated traveltimes exceeded the uncertainty range of the observed traveltimes. The estimated uncertainties are presented for each profile in Tabs. 4.1-4.3.

4.3.3. Multi-channel seismic (MCS) reflection data

We produced high-resolution MCS data along the three profiles to resolve the sedimentary architecture and acoustic basement. MCS reflection data were recorded using a 3000 m long digital

solid streamer of 240 channels (Sercel Sentinel™). For acquisition of MCS reflection profiles AWI-20160001 and AWI-20160003 (MCS data along refraction profiles AWI-20160100 and AWI-20160200), we used 6 G-Guns arranged in 2x3 G-Gun clusters with a total volume of 51 l (3120 in³), which were fired at 200 bar every 20 s at 6 m below water depth. Along MCS profile AWI-20160301 (MCS data along refraction profile AWI-20160300), we used the G-Gun setup of the seismic refraction data acquisition (section 4.3.1).

Processing steps included common depth point (CDP) sorting, velocity analyses every 1.25-2.5 km (every 50th to 100th CDP on average dependent on the G-Gun setup), normal moveout corrections, stacking, and time migration. A 5/15-150/200 Hz trapezoidal bandpass filter was applied for displaying the time-migrated sections. Acoustic basement reflection and sedimentary reflectors with high velocity contrasts were converted from time to depth and integrated into the P-wave velocity models.

4.3.4. Potential field data and gravity modelling

Gravity modelling was used to verify the consistency of our P-wave velocity models and free-air gravity anomaly (FAA). Shipborne gravity data were recorded by a LaCoste & Romberg S80/Ultrasy marine gravity meter along all profiles. To test the modelled P-wave velocity-depth distribution and constrain areas along the crustal models that suffer from low ray coverage, we performed 2.5D density modelling using the IGMAS+ software package (Götze, 2007; Götze and Lahmeyer, 1988; Schmidt et al., 2007). The geometry and layer boundaries were extracted from the P-wave models. Layers were subdivided in case lateral P-wave velocity variations were present. For the initial gravity model, average P-wave velocities for the resulting polygons were converted into densities using the P-wave velocity-density relationships of Barton (1986) and Christensen & Mooney (1995). We tried to fit the modelled FAA and the observed gravity data within a 5 mGal uncertainty range. During iterative adjustment of the densities, we took care that the densities correlated with modelled velocities within the uncertainties given for the P-wave velocity-density relationships of Barton (1986) and Christensen & Mooney (1995).

Additionally, magnetic field data were acquired along the seismic profiles and other tracks by using a SeaSpy magnetometer which was towed 350 m behind the vessel. Magnetic anomalies were calculated relative to the latest International Geomagnetic Reference Field version (Thébault et al., 2015).

4.3.5. Plate-tectonic reconstruction

We used GPlates (Müller et al., 2018) to illustrate our results in a plate-tectonic context. For the positions of Chatham Rise, New Zealand's South Island, Campbell Plateau and Bollons Seamount with respect to West Antarctica at 90 Ma, we used the rotation parameters of Eagles et al. (2004a), Larter et al. (2002) and Grobys et al. (2008). Rotation poles between Australia, East Antarctica, and the continental fragments of Northern Zealandia are based on several sources (Cande and Stock, 2004; Croon et al., 2008; Gaina et al., 1998; Granot et al., 2013; Whittaker et al., 2013).

4.4. Results and interpretation

4.4.1. Model uncertainties

Generally, we find that the estimated layer boundary depth and velocity uncertainties in our three P-wave velocity models increase with depth (Tabs. 4.1-4.3) and decreasing ray coverage. Velocity uncertainties are less than ± 0.2 km/s for the sedimentary layers, ± 0.1 to ± 0.15 km/s for the upper

crustal layers and reach up to ± 0.4 km/s in a few zones of the lower crustal layers where refracted phases are sparse. Since several large-offset mantle refractions have been observed, mantle velocity uncertainties remain less than ± 0.25 km/s throughout the profiles. Boundary depth uncertainties are between ± 0.1 and ± 0.15 km for the sedimentary layers, up to ± 0.2 km for the upper crustal layers, and ± 0.2 to ± 0.5 km for the top of the lower crustal layers. The estimated Moho depth uncertainty is between ± 0.3 km and ± 0.5 km in zones of thin crust (< 10 km), but up to ± 0.8 km where the crust is thicker than 10 km. Our velocity and boundary uncertainties lie in the same range as those of other recent crustal seismic refraction studies which used the same approach for uncertainty estimation (e.g. Hochmuth et al., 2019; Mueller et al., 2016).

4.4.2. *The easternmost Chatham Rise and adjacent ocean floor*

Profile AWI-20160300 extends from the eastern end of the Chatham Rise east of the UFZ (Fig. 4.2C) southward into deeper water, where the oldest seafloor adjacent to the Chatham Rise is expected (e.g. Larter et al., 2002). The top of the easternmost Chatham Rise along this profile is relatively smooth (Fig. 4.3A) with water depth between 2200 to 3500 m at the southern edge of the Chatham Rise. Close to the profile, several larger seamounts and fault blocks rise from the Chatham Rise seafloor (Fig. 4.2C; Hoernle et al., 2003; Mortimer et al., 2006). Smaller seamounts are also present at the northernmost part of our profiles (Fig. 4.3A, profile km 0-25).

Sedimentary strata with generally low P-wave velocities reach up to 1.5 km thickness (profile km 20-60, Fig. 4.3A, layer sed1 in Fig. 4.4A) on top of the Chatham Rise and are bounded by a fault-controlled acoustic basement high, which represents the southern flank of the eastern Chatham Rise along seismic line AWI-20160300. Clearly visible acoustic basement reflections below the sediments indicate southward normal faulting (profile km 35-55, Fig. 4.3A). Low P-wave velocities of the acoustic basement (~ 2.8 km/s at the top of layer sed2, Fig. 4.4A) argue that this layer represents crystalline crustal basement. More likely, this layer represents up to 3 km thick variably metamorphosed sedimentary strata of pre-rift origin (i.e. metasediments), which extend onto the SE Chatham Terrace until profile km 100 (Fig. 4.4A). The seafloor of the SE Chatham Terrace along profile AWI-20160300 is distinctly shallower (4200-5500 m) than seafloor further to the south (> 5500 m). Discontinuous acoustic basement reflections in the seismic data at the foot of the Chatham Rise mostly indicate oceanward down-to-the south normal faulting with increasing displacements of > 300 m (Fig. 4.3A, profile km 70-120), whereby seaward-dipping reflectors are completely absent. The top of the acoustic basement and P-wave velocities are well-resolved along the Chatham Rise and SE Chatham Terrace by the P_{sed2} refraction (Fig. 4.5A) and $P_{\text{sed2}}P$ reflection phases (Figs. 4.5B and 4.6A). Uncertainties range from ± 0.05 - 0.15 km for the top of layer sed2 and ± 0.1 - 0.2 km/s for P-wave velocities in layer sed2 (Tab. 4.1).

Two crustal phases representing refractions of the upper and lower crust (layer uc and lc, Fig. 4.4A) are observed along the easternmost Chatham Rise and SE Chatham Terrace. The top of both crustal layers is slightly reflective as observed from the $P_{\text{uc}}P$ and $P_{\text{lc}}P$ phases (Figs. 4.5B and 4.6A). Layer uc is a maximum 5 km thick and extends up to profile km 100 (Fig. 4.4A). P-wave velocities range from 5.2-6.2 km/s (profile km 0-60) along the Chatham Rise are slightly lower along the SE Chatham Terrace (profile km 60-100). Here, the intense normal faulting indicated by the MCS reflection profile (Fig. 4.3A, profile km 60-120) might be responsible for lower P-wave velocities. P-wave velocities and thicknesses of layer lc, which is present until profile km 135 (Fig. 4.4A), are quite variable. Along the Chatham Rise, layer lc is characterised by relatively uniform velocities between 6.2 to 6.8 km/s and a maximum thickness of 8 km (profile km 0-60, Fig. 4.4A). The total crustal thickness along the easternmost Chatham Rise ranges from only 10.5 to 13.5 km. The velocities and

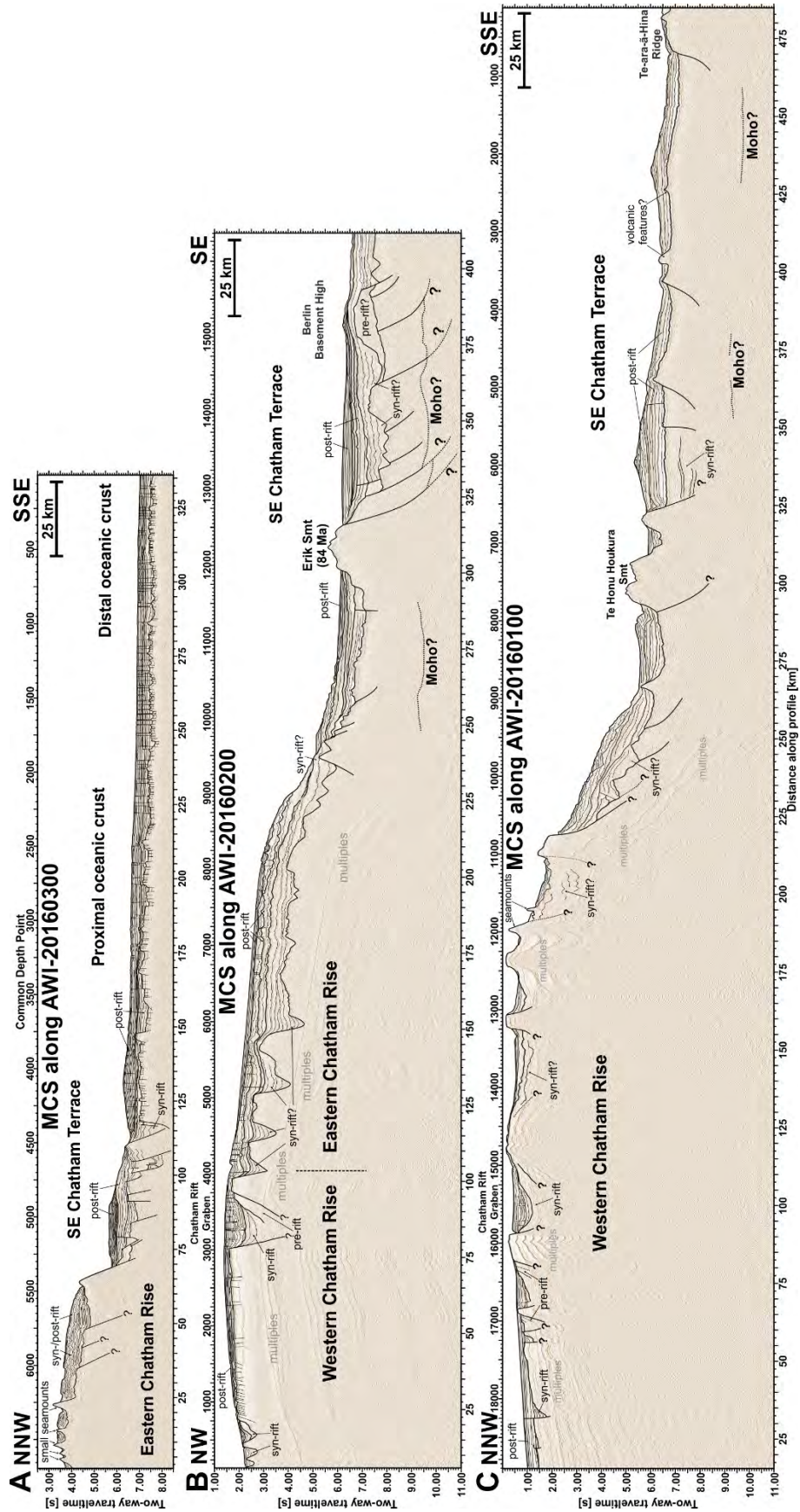


Fig. 4.3: Time-migrated MCS reflection profiles along (A) AWI-20160300, (B) AWI-20160200, and (C) AWI-20160100 with interpreted horizons and faults. Y-axis limits differ but the vertical exaggeration is the same in all three profiles. A high-resolution uninterpreted version of the profiles is available online in Fig. S4.1. Age for Erik Seamount from Mortimer et al. (2019).

thicknesses of the crustal layers are well-resolved by refractions (P_{uc} and P_{lc} phases, Figs. 4.5A and 4.6A) and Moho reflections (P_{mP} phase, Figs. 4.5B and 4.6A). Nevertheless, deep diving wave phases in the northern part of the profile are mostly absent, which results in higher uncertainties of ± 0.8 km for the Moho boundary along the Chatham Rise (Tab. 4.1).

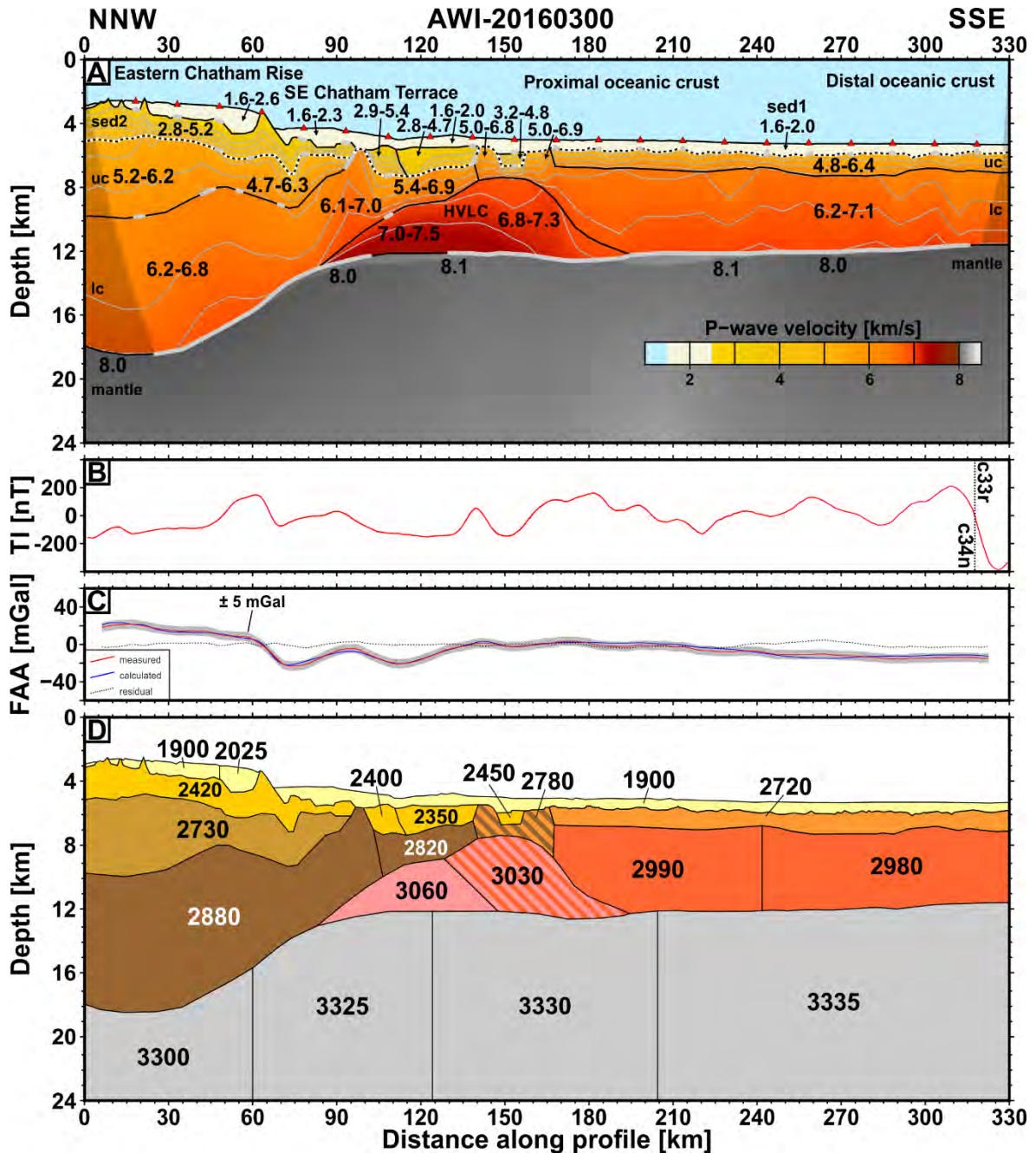


Fig. 4.4: (A) P-wave velocity model along seismic line AWI-20160300 derived from ray tracing. The position of the OBS/OBH stations along the profile are indicated by red triangles. Velocities labels for the different layers are given in km/s. The crystalline basement boundary is indicated by the white dotted line. Reflections at layer boundaries are indicated by thick grey lines. The model is based on 19934 arrival picks, total RMS misfit is 0.069 s and corresponding χ^2 is 0.72 (see Tab. S4.1 for detailed model statistics). (B) Total magnetic field intensity (TI) along the profile. Magnetic anomalies c34n and c33n are interpolated from Larter et al. (2002). (C) Free-air gravity anomaly (FAA) and anomaly calculated from density model in D. (D) Density model along AWI-20160300. Density values are given as kg/m³.

Lower crustal layer lc observed along the Chatham Rise climbs onto the SE Chatham Terrace (profile km 75-105, Fig. 4.4A). Here, the layer has a constant thickness between 4.5 to 5 km. P-wave velocities of 6.1-7.0 km/s are slightly elevated compared to those found along the Chatham Rise

(Fig. 4.4A). Two distinct peaks in the total magnetic field intensity are present along the southern Chatham Rise margin (Fig. 4.4B), most likely suggesting magmatic activity along or close to the profiles AWI-20160300. This is further supported by the occurrence of several seamounts close to the seismic line (e.g. Kakapo Seamount, Fig. 4.2C). Accordingly, we explain the elevated lower crustal P-wave velocities by magmatic activity along this part of the southern Chatham Rise margin. Layer lc continues further south until profile km 140, where it is only 1.5 ± 0.2 km thick and characterised by a high velocity gradient (Fig. 4.4A). Here, layer lc is overlain by two thin layers of low P-wave velocities (Fig. 4.4A), which we infer by late first arrivals of the crustal refraction phases and clearly delay in the P_mP Moho reflection and P_n mantle refraction phases passing through this area (Fig. 4.6B). Sparse observed reflections (Fig. 4.5B) from the top and base of the low-velocity layers support their presence. Similar observations imply another, but smaller low-velocity layer further to the south. It is surrounded by layer uc with higher P-wave velocities, which represents the upper crust in this area (profile km 135-170, Fig. 4.4A). Moreover, we would expect higher P-

Tab. 4.1: Layer parameters and according uncertainties along AWI-20160300. P-wave velocities vary within one respective layer due to different geological setting and burial.

Layer	Type	P-wave velocity range	Upper boundary uncertainty	Velocity uncertainty
		[km/s]	[km]	[km/s]
Water layer	Water	1.5	0.0	± 0.01
Sediment 1 (sed 1)				
<i>Eastern Chatham Rise</i>	Sediments	1.6 - 2.6	± 0.1	± 0.1
<i>SE Chatham Terrace</i>	Sediments	1.6 - 2.3	± 0.1	± 0.1
<i>Proximal & Distal</i>	Sediments	1.6 - 2.0	± 0.1	± 0.1
Sediment 2 (sed 2)				
<i>Eastern Chatham Rise</i>	Metasediments	2.8 - 5.2	$\pm 0.05 - \pm 0.15^*$	± 0.1
<i>SE Chatham Terrace</i>	Metasediments	2.8 - 5.4	± 0.15	± 0.2
<i>Proximal & Distal</i>	not present	-	-	-
Upper crust (uc)				
<i>Eastern Chatham Rise</i>	Continental	5.2 - 6.2	± 0.2	± 0.1
<i>SE Chatham Terrace</i>	Continental	4.7 - 6.3	± 0.1	± 0.1
<i>Proximal & Distal</i>	Oceanic layer 2	4.8 - 6.4	± 0.1	± 0.1
Lower crust (lc)				
<i>Eastern Chatham Rise</i>	Continental	6.2 - 7.0	± 0.4	± 0.1
<i>SE Chatham Terrace</i>	Continental	5.4 - 7.0	± 0.2	± 0.1
<i>Proximal & Distal</i>	Oceanic layer 3	6.1 - 7.2	± 0.2	± 0.1
HVLC	Intrus. / Underp.	6.8 - 7.5	± 0.3	± 0.2
Mantle				
<i>Eastern Chatham Rise</i>		8.0	± 0.8	± 0.2
<i>SE Chatham Terrace</i>		8.0 - 8.1	± 0.3	± 0.2
<i>Proximal & Distal</i>		8.0 - 8.1	± 0.3	± 0.2

*dependent on the presence / thickness of the overlying layer sed1

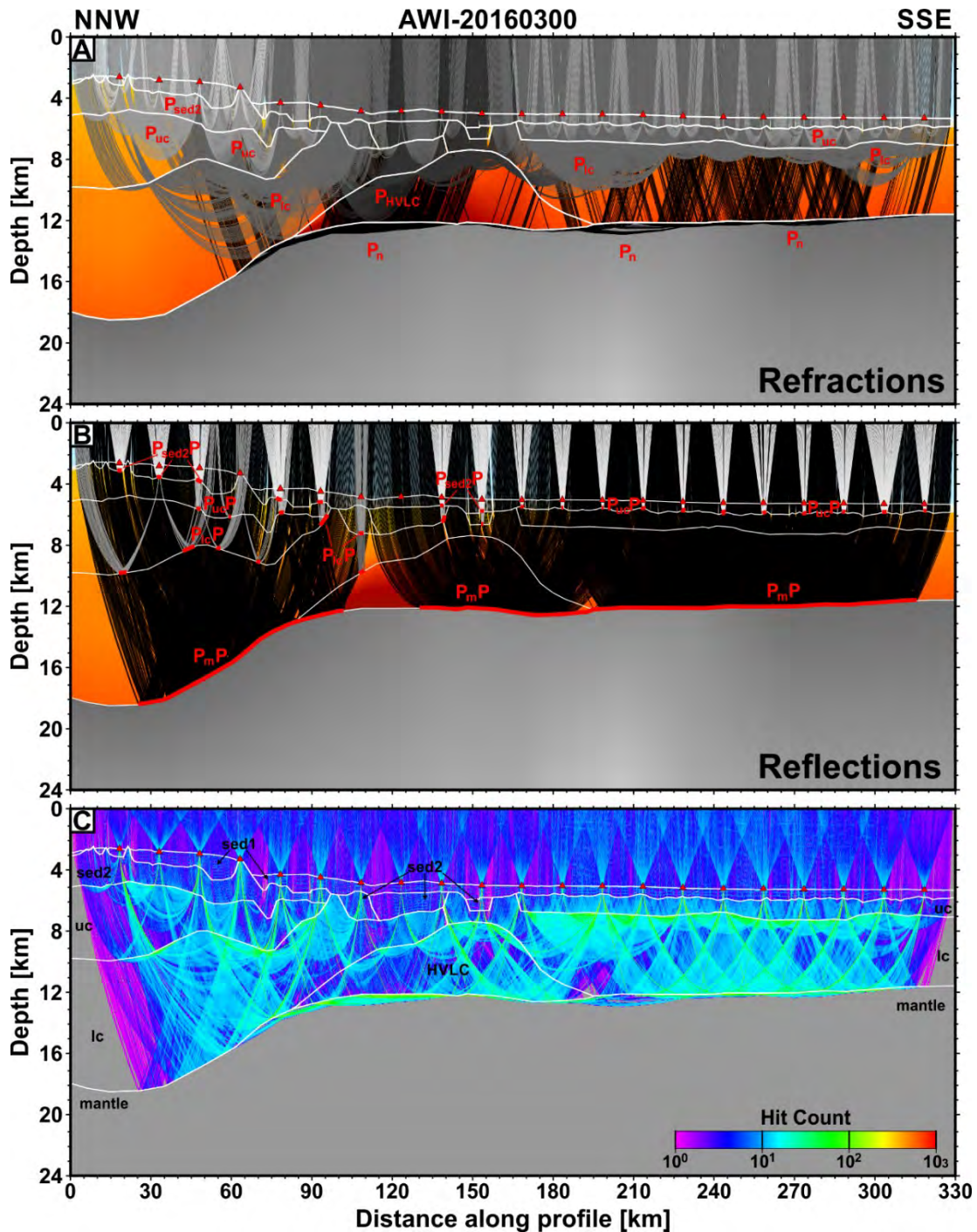


Fig. 4.5: (A) Refracted ray coverage, (B) reflected ray coverage, and (C) hit count for all rays along seismic refraction profile AWI-20160100. Different ray groups in (A) and (B) are shown in different grayscales. See Fig. S4.2 for a detailed image of the coverage of each ray group.

wave velocities for crystalline basement than present in the low-velocity layers. We interpret the low-velocity layers as to consist of metasedimentary strata comparable or similar to layer sed2 along the Chatham Rise. Another up to 5 km thick layer is forming the lowermost crust between profile km 80 to 195. P-wave velocities in the lowermost crust (layer HVLC) reach up to 7.5 km/s between profile km 80 to 120 and are slightly lower further in the south (6.8-7.3 km/s, Fig. 4.4A). The high velocities are well-constrained by several refractions through this layer (P_{HVLC} , Figs. 4.5A and 4.6B). We interpret the clearly visible high-amplitude reflection (Fig. 4.6A and 4.6B) from the base of this high-velocity lower crust (HVLC) as the Moho reflection (P_mP phase, see Fig. 4.5B). The total crustal thickness is only 5.0-5.5 km (profile km 80-195, Fig. 4.4A).

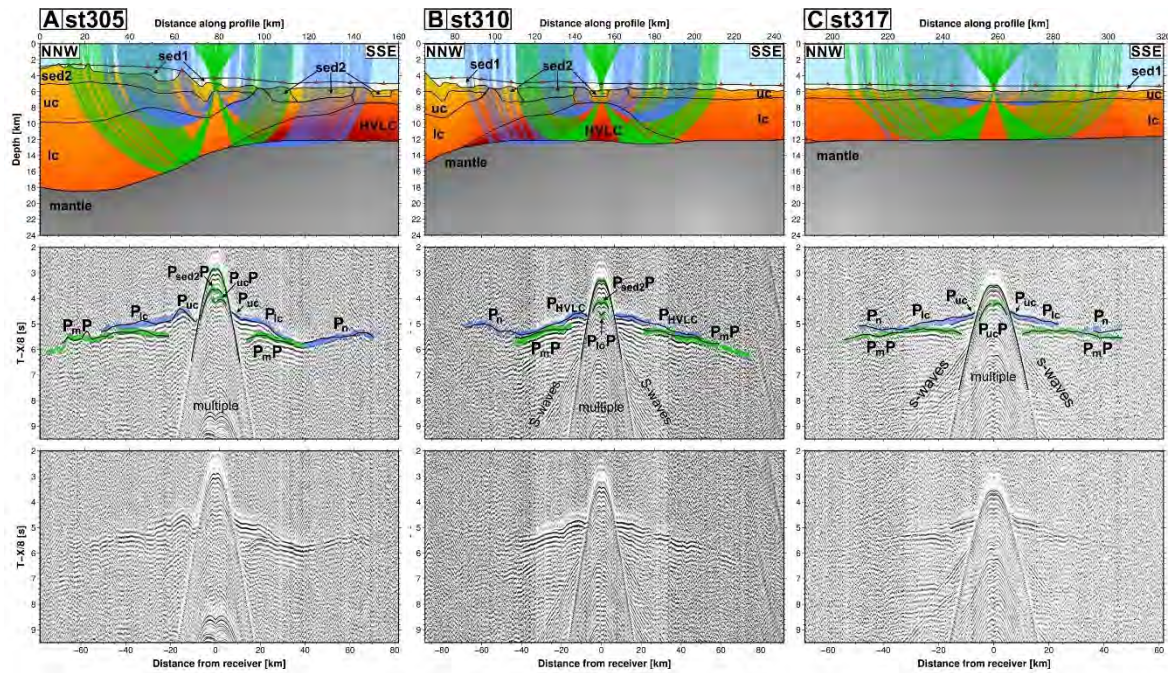


Fig. 4.6: Examples for OBS/OBH records (hydrophone channels) reduced by 8.0 km/s, picked arrivals, and traced ray paths for stations (A) st305, (B) st310, and (C) st317 along the seismic refraction line AWI-20160300. Picked refractions and ray paths are shown in blue colours whereas picked reflections and ray paths are shown as green lines. Black lines indicate the modelled arrival times for each ray group. See Fig. 2C for the station locations.

The crustal structure further south of the SE Chatham Terrace with the HVLC and low-velocity layers is very homogeneous (profile km 120-330, Fig. 4.4A). The acoustic basement reflections are also continuously visible in the areas proximal and distal from the Chatham Rise but are rougher on a smaller scale (4-10 km) compared to the SE Chatham Terrace (Fig. 4.3A). The basement is overlain by up to 800 m of well-layered sediments (Fig. 4.3A). We recognised clear reflections from the basement ($P_{uc}P$, Fig. 4.6C), refraction phases from the upper and lower crust (P_{uc} and P_{lc}) and Moho reflections (P_mP) at all stations (Figs. 4.5A and 4.5B). P-wave velocity of the thin (0.75-1.5 km) upper crustal layer increase and range between 4.7 to 6.4 km/s corresponding to a high velocity gradient (Fig. 4.4A). The thickness of the lower crustal layer range between 4.5 and 5.5 km and P-wave velocities increase gradually from 6.2 to 7.1 km/s, representing a lower velocity gradient. The total crustal thickness in the distal deep is constant between 5.8 to 6.8 km without any observed larger variations. Although, the coverage with ray phases is very good between profile km 120 to 330 (Fig. 4.5C), the P_{lc} refraction phase only cover the upper 1 km of layer lc . Therefore, uncertainties of ± 0.3 km for depth of the Moho boundary and ± 0.2 for the P-wave velocities in layer lc are slightly higher than in the overlying layers (Tab. 4.1).

Mantle refractions (P_n phase) that correspond to P-wave velocities around 8.0 ± 0.2 km/s have been identified at most of the station along AWI-20160300 (Figs. 4.5A and 4.6A-C). The transition from the SE Chatham Terrace into the deep sea (profile km 120-240, Fig. 4.4A) is the only part of profile AWI-20160300 where we observed slightly higher mantle P-wave velocities of 8.1 ± 0.2 km/s.

The densities converted from P-wave velocities resemble the amplitudes of the shipborne FAA well (Fig. 4.4C). Subdivisions were made for (i) the sedimentary layer sed1 on top of the Chatham Rise where higher P-wave velocities were observed in the sedimentary basin, (ii) all lower crustal layers, and (iii) for the mantle (Fig. 4.4D) to improve the fit of measured and calculated FAA within 5 mGal uncertainty (Fig. 4.4C). All densities lie within the uncertainty range given by the P-wave velocity-density relationships (e.g. 1620-2180 kg/m³ and 2610-3040 kg/m³ for P-wave velocities of 1.9 and 6.5 km/s; Barton, 1986).

4.4.3. *The western and eastern Chatham Rise boundary and the eastern SE Chatham Terrace*

Profile AWI-20160200 crosses the boundary between western and eastern Chatham Rise and continues onto the SE Chatham Terrace further south of Erik Seamount from which 84 Ma lavas have been dredged (Fig. 4.2C, Mortimer et al., 2019b). North of our profiles the West Wishbone Ridge separates the Hikurangi Plateau from the eastern Chatham Rise further in the north as recently identified by Barret et al. (2018). MCS data along profile AWI-20160300 (Fig. 4.3B) shows that the basements of the western Chatham Rise (profile km 0-100) and eastern Chatham Rise (profile km 100-245) are completely covered by sedimentary strata forming a very smooth seafloor, which dips gently northward and southward the shallowest area around profile km 80. The basement structures of eastern and western Chatham Rise are distinctly different. The western Chatham Rise consists of a large continuous basement block with some small intra-basement faults (Fig. 4.3B, profile km 30-70). A large half-graben, the Chatham Rift Graben (profile km 80-90 km, Fig. 4.3B), separates the large block from another near-surface basement block, which we also consider as part of the western Chatham Rise. The Chatham Rift Graben does not correspond to the boundary of eastern and western Chatham Rise, moreover, it is a NEE-SWW striking structure – sub-parallel to the West Wishbone Ridge – extending from or close to the boundary onto Chatham Island (Fig. 4.2B), where it probably continues through Chatham Island (Wood and Anderson, 1989). The southern flank of the second basement block (profile km 100-105, Fig. 4.3B) lies above the interpreted boundary of eastern and western Chatham Rise. The basement of the eastern Chatham Rise consists of three southward deepening horst structures separated by half grabens (profile km 105-155). But further in the southeast the acoustic basement reflections are flatter indicating less developed or even absence of normal faulting (profile km 155-235). Another near-seafloor basement high (profile km 235-250), normal faulted on its southern flank represents the transition to the SE Chatham Terrace (Fig. 4.3B).

P-wave velocity modelling of profile AWI-20160200 suggests two layers (sed1 and sed2) for the sedimentary cover (Fig. 4.7A). P-wave velocities in layer sed1 are up to 4.4 ± 0.1 km/s (Tab. 4.2), which are well-resolved by the P_{sed2} refracted phase (Fig. 4.8A). The boundary between both was continuously identified by the $P_{\text{sed2}}P$ reflection (Fig. 4.8B) with uncertainties of ± 0.1 km (Tab. 4.2). We identified two upper crustal layers along eastern and western Chatham Rise (uc1 and uc2, Fig. 4.7A), well-defined by P_{uc1} and P_{uc2} refraction phases (Figs. 4.8A, 4.9A, and 4.9B). We found that the upper crustal velocities and thicknesses significantly differ along western (Fig. 4.7A, 4.7-6.2 km/s and up to 10 km thickness) and eastern Chatham Rise (Fig. 4.7A, 5.2-6.4 km/s and up to 7 km thickness).

The lower crustal layer lc of eastern and western Chatham Rise also differ in terms of thickness and P-wave velocities (Fig. 4.7A). We observed a clear and continuous $P_{\text{lc}}P$ reflection phase (Figs. 4.8B and 4.9A) from the boundary of upper (layer uc2) and lower crust (layer lc) along the western Chatham Rise. Nevertheless, we determined higher uncertainties of ± 0.5 km for this boundary since P_{uc2} refractions only cover the uppermost part of layer uc2 (Fig. 4.8A, profile km 0-60) and P_{lc} refractions are sparse along the western Chatham Rise (Fig. 4.8A). Layer lc is more certain along the eastern Chatham Rise (Tab. 2) and the lower crustal P-wave velocities are significantly lower (6.3-6.9 km/s, Fig. 4.7A) compared to the western Chatham Rise (6.6-6.9 km/s). $P_{\text{m}}P$ reflection phases (Figs. 4.8B and 4.9A) are continuously present and indicate 15 ± 0.8 km thickness for layer lc along

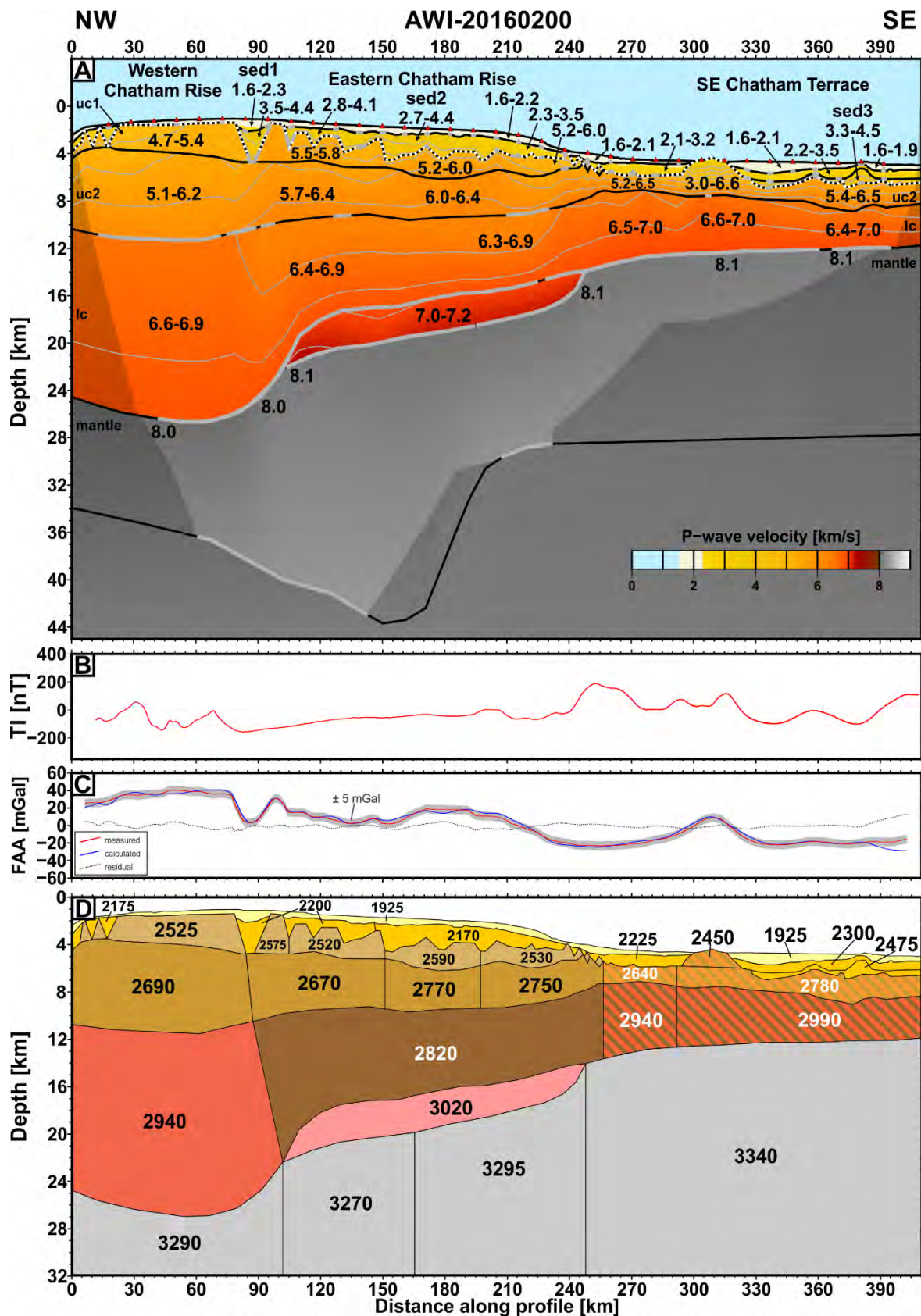


Fig. 4.7: (A) P-wave velocity model of the seismic line AWI-20160200 derived by ray tracing. The position of the OBS/OBH stations along the profile are indicated by red triangles. Velocities labels for the different layers are given in km/s. The crystalline basement boundary is indicated by the white dotted line. Reflections at layer boundaries are indicated by thick grey lines. The model is based on 43171 arrival picks, total RMS misfit is 0.153 s and corresponding χ^2 is 0.928 (see Tab. S4.2 for detailed model statistics). (B) Total magnetic field intensity (TI) along the profile. (C) Free-air gravity anomaly (FAA) and anomaly calculated from density model in D. (D) Density model along AWI-20160200. Density values are given as kg/m³.

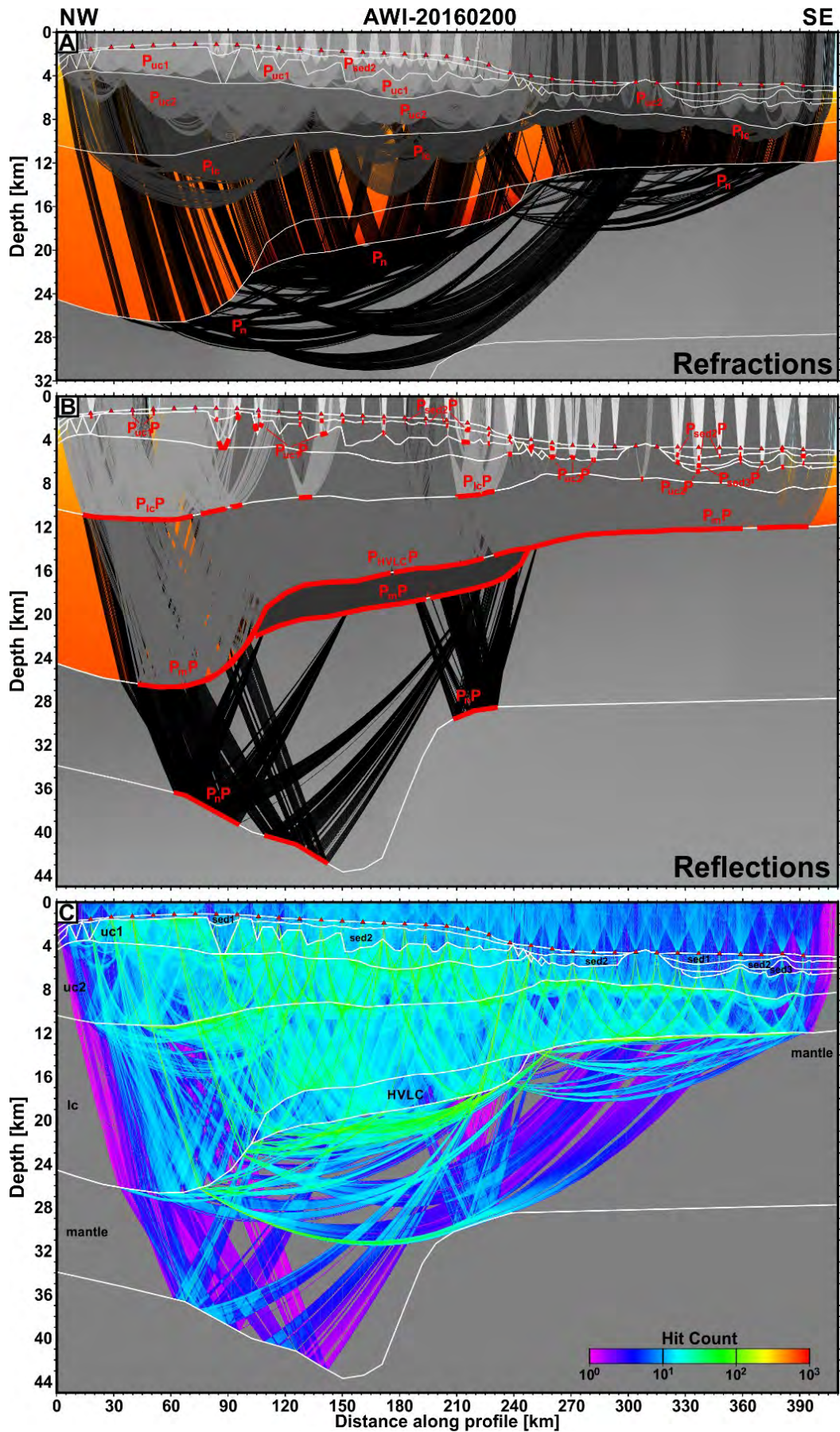


Fig. 4.8: (A) Refracted ray coverage, (B) reflected ray coverage, and (C) hit count for all rays along seismic refraction profile AWI-20160200. Different ray groups in (A) and (B) are shown in different grayshades. See Fig. S4.3 for a detailed image of the coverage of each ray group. The colormaps of the P-wave velocity models in (A) and (B) are the same as in Fig. 4.7A.

Tab. 4.2: Layer parameters and according uncertainties along AWI-20160200. P-wave velocities vary within one respective layer due to different geological setting and burial.

Layer	Type	P-wave velocity range	Upper boundary uncertainty	Velocity uncertainty
		[km/s]	[km]	[km/s]
Water Layer	Water	1.5	0.0	± 0.01
Sediment 1 (sed1)				
<i>Western Chatham Rise</i>	Sediments	1.6 - 2.3	± 0.1	± 0.1
<i>Eastern Chatham Rise</i>	Sediments	1.6 - 2.2	± 0.1	± 0.1
<i>SE Chatham Terrace</i>	Sediments	1.6 - 2.1	± 0.1	± 0.1
Sediment 2 (sed2)				
<i>Western Chatham Rise</i>	Sediments	3.5 - 4.4	± 0.1	± 0.1
<i>Eastern Chatham Rise</i>	Sediments	2.3 - 4.4	± 0.1	± 0.15
<i>SE Chatham Terrace</i>	Sediments	2.1 - 3.5	± 0.15	± 0.1
Sediment 3 (sed3)				
<i>Western Chatham Rise</i>	not present	-	-	-
<i>Eastern Chatham Rise</i>	not present	-	-	-
<i>SE Chatham Terrace</i>	Metasediments	3.3 - 4.5	± 0.2	± 0.15
Upper crust 1 (uc1)				
<i>Western Chatham Rise</i>	Continental	4.7 - 5.4	± 0.1 - ± 0.2**	± 0.1
<i>Eastern Chatham Rise</i>	Continental	5.2 - 6.0	± 0.15	± 0.1
<i>SE Chatham Terrace</i>	not present	-	-	-
Upper crust 2 (uc2)				
<i>Western Chatham Rise</i>	Continental	5.1 - 6.2	± 0.15	± 0.15
<i>Eastern Chatham Rise</i>	Continental	5.7 - 6.4	± 0.2	± 0.15
<i>SE Chatham Terrace</i>	Transitional	5.2 - 6.6*	± 0.15	± 0.15
Lower crust (lc)				
<i>Western Chatham Rise</i>	Continental	6.6 - 6.9	± 0.5	± 0.3
<i>Eastern Chatham Rise</i>	Continental	6.3 - 6.9	± 0.4	± 0.2
<i>SE Chatham Terrace</i>	Transitional	6.4 - 7.0	± 0.25	± 0.2
HVLC	Underplating	7.0 - 7.2	± 0.4	± 0.2
Mantle				
<i>Western Chatham Rise</i>		8.0	± 0.8	± 0.25
<i>Eastern Chatham Rise</i>		8.1	± 0.8	± 0.2
<i>SE Chatham Terrace</i>		8.1	± 0.5	± 0.2

*P-wave velocity is 3.0-6.6 close to Erik Seamount. **dependent on the presence / thickness of overlying sediment layers.

western Chatham Rise (Fig. 4.7A). Reflections from the base of layer lc along the eastern Chatham Rise suggest a thickness of 10 ± 0.8 km close to the western Chatham Rise (profile km 95), but only 6 ± 0.5 km at the transition to the SE Chatham Terrace (profile km 230). We identified another reflection phase with distinctly higher amplitudes and later arrivals, which we interpret as the P_mP

reflection phase from the crust-mantle boundary along the eastern Chatham Rise (Fig. 4.10). We infer the first reflection with generally lower amplitude to result from the top of a HVLC layer (P_{HVLC} phase). Since we could not observe any refraction from the HVLC, we measured the normal-moveout velocities of both reflections to estimate the corresponding average crustal velocities. They are in the range between 5.4 to 5.8 km/s for the P_{HVLC} reflections. Average crustal velocities estimated from the P_mP reflections are higher (5.7-6.1 km/s). The higher estimated crustal velocities are in good agreement with P-wave velocities around 7.0-7.2 km/s for the HVLC layer and a thickness in the range between 2 to 3 km. The total crustal thicknesses for western and eastern Chatham Rise are up to 24 km and 14-19 km, respectively.

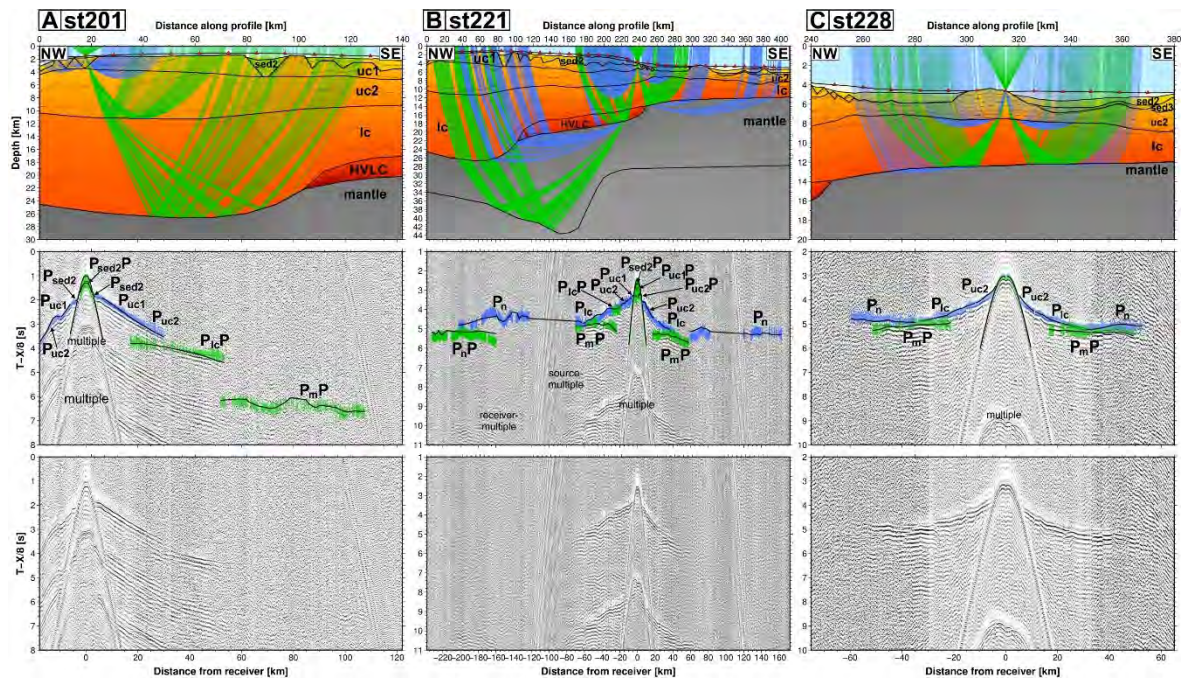


Fig. 4.9: Examples for OBS/OBH records (hydrophone channels) reduced by 8.0 km/s, picked arrivals, and traced ray paths for stations (A) st228, (B) st221, and (C) st201 along the seismic line AWI-20160200. Picked refractions and ray paths are shown in blue colours whereas picked reflections and ray paths are shown as green lines. Black lines indicate the modelled arrival times for each ray group. The colormap of the P-wave velocity model is the same as in Fig. 4.7A. See Fig. 4.2C for the station locations.

The SE Chatham Terrace is located south of the normal-faulted basement high at the margin of the Chatham Rise (profile km 235-250, Fig. 4.3B). The seafloor is very flat except for the edge of Erik Seamount and a smaller elevation further to the south (profile km 375-390). Several sedimentary units cover the acoustic basement on both sides of Erik Seamount (Fig. 4.3B). Similar to the SE Chatham Terrace east of the UFZ, MCS data along AWI 20160200 does not indicate any seaward-dipping reflectors close to the Chatham Rise. We used two and three sedimentary layers north and south of Erik Seamount in the P-wave velocity model, which are evident from several reflected wave phases ($P_{sed2}P$, $P_{sed3}P$, Fig. 4.8B). The top of the acoustic basement north of Erik Seamount is flat and gently southward dipping (profile km 265-285, Fig. 4.3B). Acoustic basement pattern is rougher south of Erik Seamount and indicate two basement highs (profile km 350-400). The southern Berlin basement high (profile km 375-400, Fig. 4.3B) is a NE-SW lineated feature and extends from the Berlin Seamount in the northeast onto our profile as evident from the free-air gravity anomaly (Fig. 4.2B). Here, non-crystalline P-wave velocities between 3.3 and 4.5 km/s (Fig. 4.7A) likely indicate the presence of older sedimentary strata (pre-rift metasediments). Several steep sub-basement reflections most likely indicate intense south-directed normal faulting between Erik Seamount and Berlin Basement High (Fig. 4.3B). The crust of the Chatham Rise is laterally homogeneous consisting of two layers (layer uc2 and lc, Fig. 4.7A). P-wave velocities in layer uc2

are between 5.2 to 6.5 km/s on both sides of Erik Seamount. Lower P-wave velocities of 3.3 ± 0.15 km/s are present beneath the seamount but are slightly higher (6.6 ± 0.2 km/s) at the base of the upper crust (Fig. 4.7A, Tab. 4.2). In the lower crustal layer Ic P-wave velocity variations are only small (6.4-7.0 km/s). The crustal P-wave velocity are well-resolved by P_{uc} and P_{lc} phases (Fig. 4.8A). P_{lc} lower crustal refractions only cover the uppermost 2 km of layer Ic, which results in higher uncertainty of ± 0.2 km/s for the P-wave velocities at the base of the crust (Tab. 4.2). We observed a clear P_mP reflection all over the eastern SE Chatham Terrace (Figs. 4.8B and 4.9C) which is also partially visible in the MCS profile along AWI-20160200 (Fig. 4.3B). The total crustal thickness is between 6.8 to 7.3 km north and only 5.3-6.2 km south of Erik Seamount.

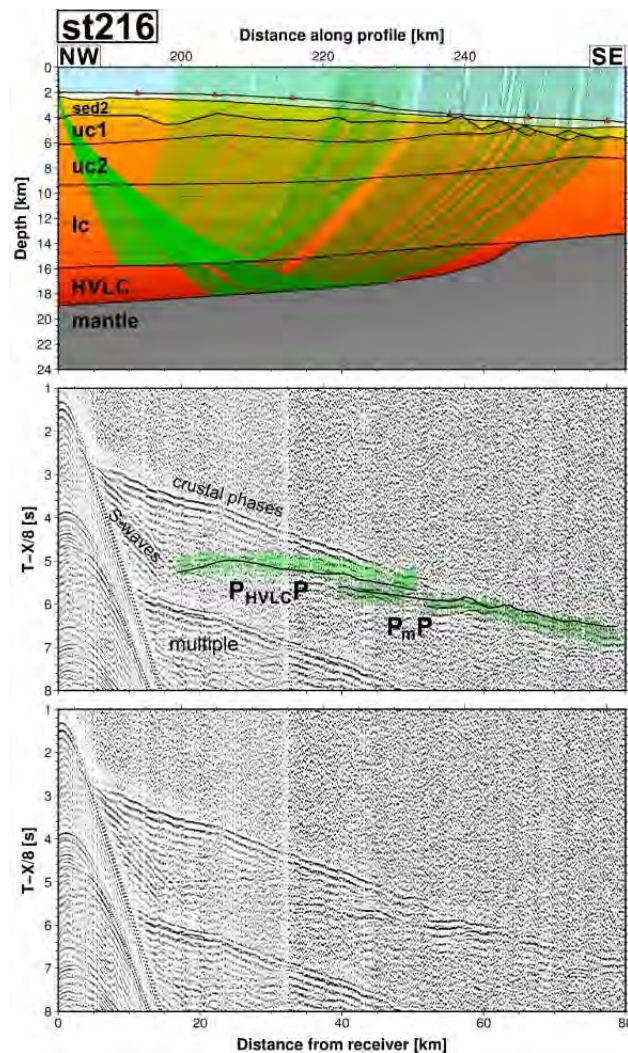


Fig. 4.10: Examples for the $P_{HVLC}P$ and P_mP reflection phase from st216 from top and base of the HVLC along seismic reflection line AWI-20160200. Picked reflections and corresponding ray paths are shown as green lines. Black lines indicate the modelled arrival times for each reflection. The colormap of the P-wave velocity model is the same as in Fig. 4.7A. See Fig. 4.2C for the station locations.

Mantle velocities are estimated to increase from 8.0 km/s beneath the western Chatham Rise (profile km 30-90, Fig. 4.7A) to 8.1 km/s beneath eastern Chatham Rise and Chatham Terrace (profile km 90-410). At several stations along the Chatham Rise we observed the P_n mantle refraction at a source-receiver distance of up to 200 km (Fig. 4.9B) and especially along the SE Chatham Terrace, the P_n phase shows an excellent signal (Fig. 4.9C). Furthermore, we observed several reflections within the mantle in depth between 30 to 43 km (P_nP phase, Fig. 4.8B). The arrivals are distinctly later and in larger source-receiver distances than the P_n phase (Fig. 4.9B). Since

these reflections origin from different depths and locations along the profile (Figs. 4.7A and 4.8B), they possibly represent different mantle features.

For the gravity model along line AWI-20160200 (Fig. 4.7D), we vertically divided several layers based on the P-wave velocity variations to enhance the fit between calculated and measured FAA (Fig. 4.7C). Overall, the gravity model is in good agreement with the modelled P-wave velocity variations in the lower crust of western and eastern Chatham Rise and velocity variations in the upper crustal layer along the eastern Chatham Rise (Fig. 4.7A and 7D). Only upper crustal densities of the western Chatham Rise are slightly higher than expected from P-wave velocities compared to the eastern Chatham Rise (layer uc2, Fig. 4.7D), but still within the uncertainties of the density conversion (e.g. 2380-2770 kg/m³ for 5.4 km/s; Barton, 1986). Although P-wave velocities do not change laterally along the SE Chatham Terrace, a subdivision of the upper and lower crustal layers was required to fit the gravity low between Chatham Rise and Erik Seamount, which suggests lower densities in this narrow area (profile km 260-290, Fig. 4.7D) compared to the SE Chatham Terrace south of Erik Seamount. Here, the lower densities are also still within the uncertainties of the velocity-depth conversion (e.g. 2440-2880 kg/m³ for P-wave velocities of 6.0 km/s; Barton, 1986). The residual gravity anomaly at the southeastern termination of profile AWI-20160200 exceeds the 5 mGal misfit range (profile km 380-410, Fig. 4.7D) in an area where the P-wave velocity model is constrained with less rays and shots are recorded only from one side. Since all gravity models exceed both ends of the P-wave velocity profiles by 100 km to avoid edge effects of the gravity calculation, the higher misfit can be explained by the presence of thinner crust or higher mantle densities at the end of the profile or further to the south.

4.4.4. *The western Chatham Rise and central SE Chatham Terrace*

Profile AWI-20160100 crosses the western Chatham Rise east of the Chatham Islands where the water depth on top of the Chatham Rise is only 1000-100 m (Fig 4.2C). The FAA around the Chatham Islands is significantly higher than elsewhere of the Chatham Rise (Fig. 4.2A). The profiles continue to the south onto the central SE Chatham Terrace where abundant guyots, seamounts and ridge-like volcanic features are hosted (Gohl and Werner, 2016), approximately 100 km west of the continental Stuttgart Fault Block (Fig. 4.2C; Mortimer et al., 2006).

MCS data along AWI-20160100 indicate graben and half graben structures, which separate several basement highs at several locations (Fig. 4.3C, profile km 0-220). Basement highs show up as distinct positive anomalies (Fig. 4.2A) and crop out to the seafloor (Fig. 4.3C), which is different from the sediment-covered Chatham Rise along the profiles AWI-20160300 and AWI-20160200 further to the east (Figs. 4.3A and 4.3B). The top of the acoustic basement in the northernmost section of AWI-20160100 is nearly continuous and only separated by some 10-25 km broad half grabens (profile km 0-80, Fig. 4.3C). Only few post-rift sediments cover the top of the Chatham Rise (Fig. 4.3C). The graben and half graben structures are mainly filled with syn-rift and less prevalent pre-rift sediments (Fig. 4.3C, profile km 80). Acoustic basement reflections at the southern flank of the Chatham Rise also suggest a normal-fault controlled transition to the SE Chatham Terrace (profile km 215-265). At the transition the vertical displacement is distinctly higher but also over a broader lateral distance (~50 km) compared to AWI-20160200 (Figs. 4.3B and 4.3C). In the P-wave velocity model along AWI-20160100 (Fig. 4.11A), we identified two sedimentary layers (sed1 and sed2). The lowermost sediments in the up to 4 km deep grabens reach P-wave velocities of up to 4.5 ± 0.2 km/s (P_{sed2} , Fig. 4.12A) similar to those observed along AWI-20160200 (Fig. 4.7A).

No arrivals of basement reflections ($P_{\text{uc1}}P$) were observed at shallow water depth because early arrivals of the multiples and reverberations from the tilted basement along the graben structures mask the primary signals. Again, we found two upper crustal layers (uc1 and uc2) along profile AWI-

20160100 (Fig. 4.11A). Here, the transition between both upper crustal layers is slightly reflective as indicated by the $P_{uc2}P$ reflections observed at several stations (Fig. 4.12B). Upper crustal P-wave velocities along the western Chatham Rise are slightly lower in the south (profile km 150-260, 4.9-6.2 km/s, Fig. 4.11A) than in the north (profile km 0-90, 4.9-6.0 km/s), but distinctly higher in the large basement block (profile km 90-150, 5.1-6.5 km/s). This basement block is different since both flanks are gently dipping to the north and south (Figs. 4.3C and 4.11A). The free-air gravity anomaly (Fig. 4.2A) suggests that the northern half graben is the continuation of the large NEE-SWW striking

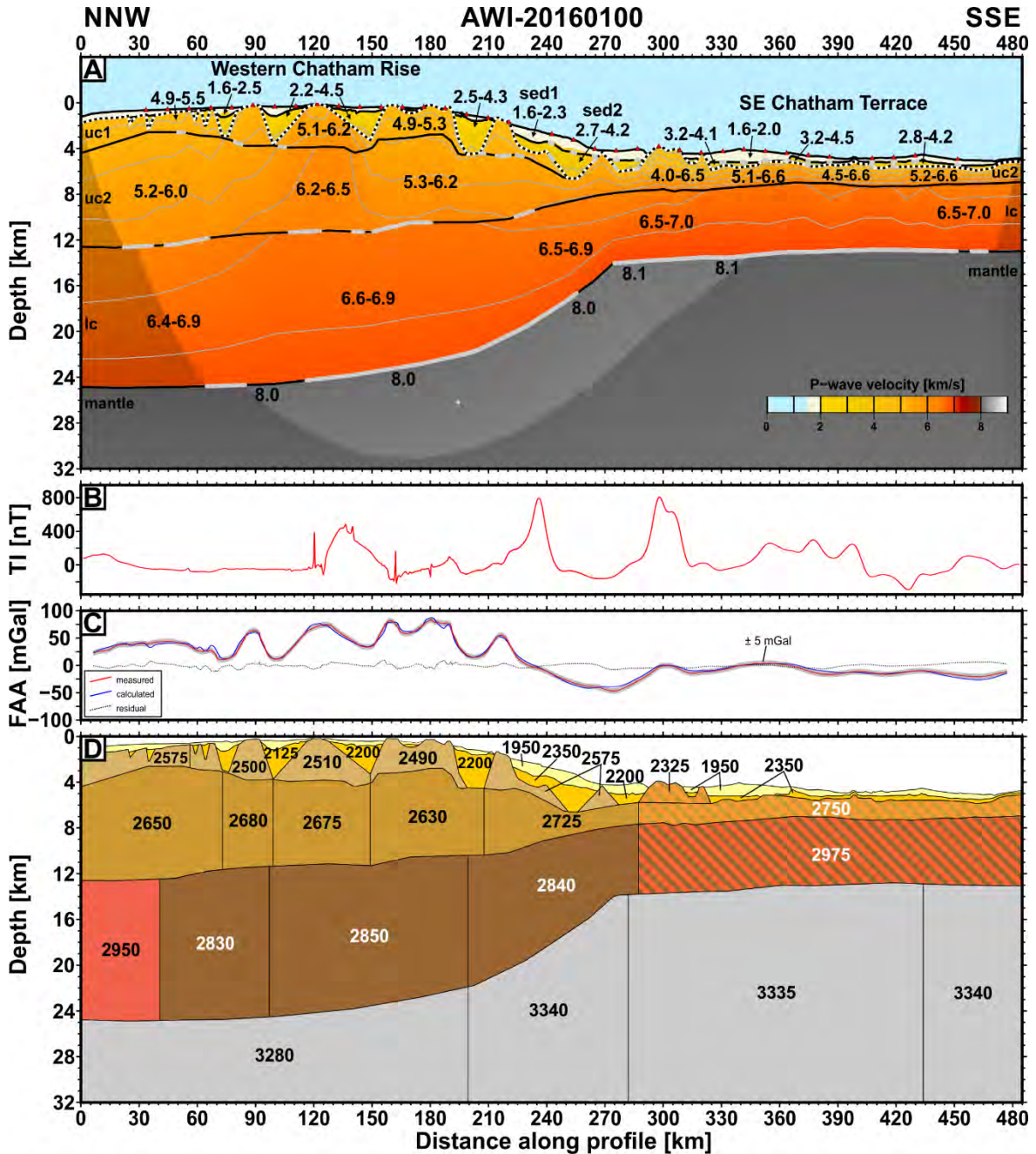


Fig. 4.11: (A) P-wave velocity model of the seismic line AWI-20160100 derived from ray tracing. The position of the OBS/OBH stations along the profile are indicated by red triangles. Velocities labels for the different layers are given in km/s. The crystalline basement boundary is indicated by the white dotted line. Reflections at layer boundaries are indicated by grey black lines. The model is based on 32509 arrival picks, total RMS misfit is 0.142 s and corresponding χ^2 is 0.885 (see Tab. S4.3 for detailed model statistics). (B) Total magnetic field intensity (TI) along the profile. (C) Free-air gravity anomaly (FAA) and anomaly calculated from density model in D. (D) Density model along AWI-20160100. Density values are given as kg/m³.

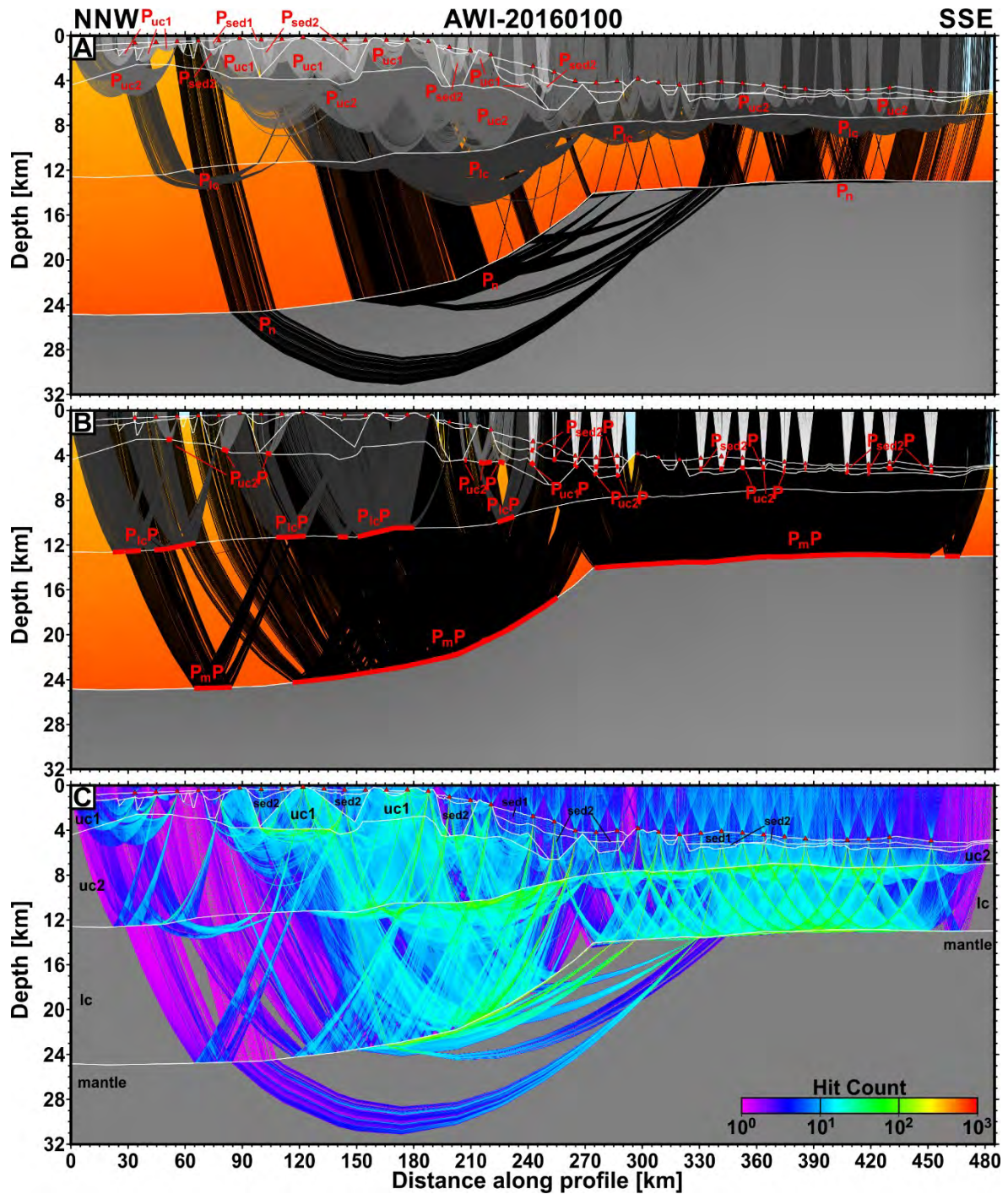


Fig. 4.12: (A) Refracted ray coverage, (B) reflected ray coverage, and (C) hit count for all rays along seismic refraction profile AWI-20160100. Different ray groups in (A) and (B) are shown in different grayscales. See Fig. S4.4 for a detailed image of the coverage of each ray group.

Chatham Rift Graben observed along profile AWI-20160200 (Figs. 4.3B and 4.7A) whereas the southern one is a strictly E-W striking half graben. The top of the lower crustal layer is partially reflective as demonstrated by the $P_{lc}P$ reflection phase observed in at several stations (Figs. 4.12B and 4.13A). Variations of the P-wave velocities in the lower crust are low and range from 6.4-6.9 km/s with an uncertainty of ± 0.4 km/s (Tab. 4.3). Although within the P-wave velocity uncertainties, we recognise slightly higher velocities in the lower crustal layer lc in the central part of the Chatham Rise (profile km 90-150, Fig. 4.11A) than in the surrounding lower crust. The coverage of refracted rays in layers $uc1$ and $uc2$ (P_{uc1} and P_{uc2} refractions, Fig. 4.12A) as well as for southern part of the

Tab. 4.3: Layer parameters and according uncertainties along AWI-20160100. P-wave velocities vary within one respective layer due to different geological setting and burial.

Layer	Type	P-wave velocity range	Upper boundary uncertainty	P-wave velocity uncertainty
		[km/s]	[km]	[km/s]
Water layer	Water	1.5	0.0	± 0.01
Sediment 1 (sed1)				
Western Chatham Rise	Sediments	1.6 - 2.6	± 0.1	± 0.1
SE Chatham Terrace	Sediments	1.6 - 2.0	± 0.1	± 0.1
Sediment 2 (sed2)				
Western Chatham Rise	Sediments	3.5 - 4.4	± 0.1	± 0.1
SE Chatham Terrace	Sediments	2.8 - 4.5	± 0.15	± 0.2
Upper crust 1 (uc1)				
Western Chatham Rise	Continental	4.9 - 6.2	± 0.1 - ± 0.2**	± 0.1
SE Chatham Terrace	not present	-	-	-
Upper crust 2 (uc2)				
Western Chatham Rise	Continental	5.2 - 6.5	± 0.15	± 0.15
SE Chatham Terrace	Transitional	4.5 - 6.5*	± 0.15	± 0.15
Lower crust (lc)				
Western Chatham Rise	Continental	6.4 - 6.9	± 0.5	± 0.4
SE Chatham Terrace	Transitional	6.5 - 7.0	± 0.3	± 0.25
Mantle				
Western Chatham Rise		8.0	± 0.8	± 0.25
SE Chatham Terrace		8.1	± 0.6	± 0.2

*P-wave velocity is 4.0-6.6 close to Te Honu Huakara Seamount.

**dependent on the presence / thickness of overlying sediment layers.

lower crustal layer lc (P_{lc} refraction, Figs. 4.12A and 4.13A). In the northern part of the Chatham Rise, however, we only observed few the P_{uc2} and P_{lc} refractions. Nevertheless, we still consider the modelled P-wave velocities still as meaningful. Along the western Chatham Rise, we did not observe any reflections indicating the presence of a HVLC. The crust-mantle boundary is well-resolved by the P_mP reflection between profile km 60 to 250 (Fig. 4.12B). The total crustal thickness (22-24.5 km) of the western Chatham Rise along AWI-20160100 is in the same range as along AWI-20160200.

Less than 1 km of sediments cover the SE Chatham Terrace along AWI-20160100 (Figs. 4.3C and 4.11A). At the foot of the Chatham Rise (profile km 260-295) and between Te Honu Houkara Seamount and Te-ara-ā-Hina Ridge the top of acoustic basement is generally smooth and largely unfaulted, only showing some smaller basement highs (profile km 325-485, Fig. 4.3C). Some reflections observed south of Te Honu Houkara Seamount most likely indicate the presence of older sedimentary strata (probably syn-rift sediments) on the SE Chatham Terrace in a graben-like structure (profile km 330-350). We found two thin sedimentary layers (sed1 and sed2, Fig. 4.11A) indicated by the presence of a $P_{sed2}P$ phase among the basement reflection $P_{uc2}P$ on the SE Chatham Terrace (Figs. 4.12 and 4.13B). Several steeply dipping reflections below the top of acoustic basement probably indicate normal faulting (Fig. 4.3C), but they are less common compared to AWI-20160200 (Fig. 4.3B). The crust of the SE Chatham Terrace consists of two layers (uc2 and lc,

Fig. 4.11A). P-wave velocities in the upper crustal layer uc2 are variable (5.1-6.6 km/s). Only at the Te Honu Houkara Seamount basement P-wave velocities are significantly lower (Fig. 4.11A, profile km 375-410). P-wave velocities in the $\sim 6 \pm 0.6$ km thick lower crustal layer range from 6.5 to 7.0 km/s without any significant variations. The upper and lower crustal layers are well-resolved by $P_{uc2}P$ reflections and P_{lc} refractions (Figs. 4.12A, 4.12B and 4.13B), but the P_{lc} refractions only cover the uppermost 2 km of the layer lc (Fig. 4.12A), therefore resulting in larger uncertainties of the deep crustal P-wave velocities of ± 0.25 (Tab. 4.3). We have identified the P_mP reflections from most of the SE Chatham Terrace indicating that the crust-mantle boundary is at the same depth (Fig. 4.11A). The total crustal thickness of the western SE Chatham Terrace along AWI-20160100 ranges between 7.5 to 8.0 km.

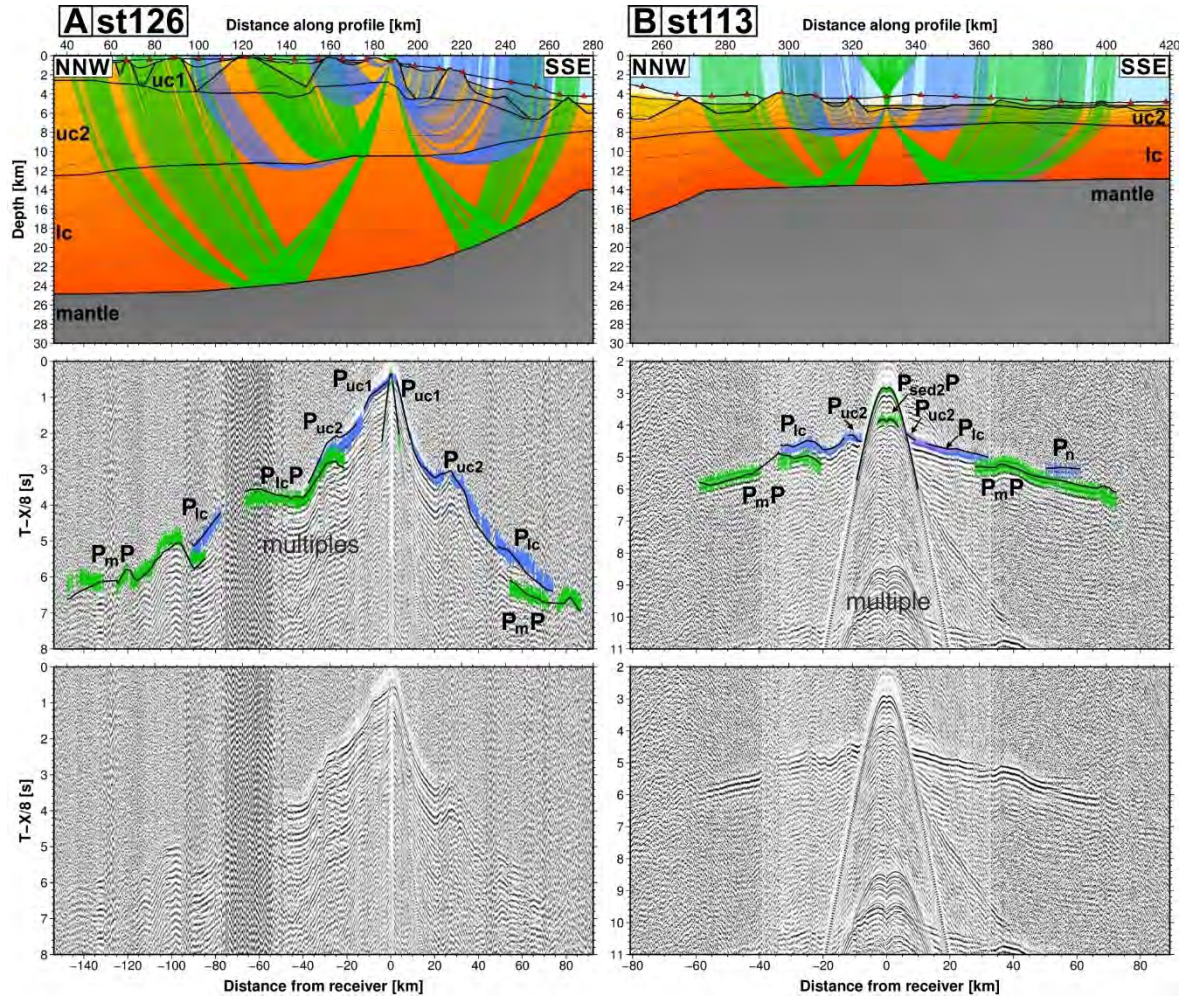


Fig. 4.13: Examples for OBS/OBH records (hydrophone channels) reduced by 8.0 km/s, picked arrivals, and traced ray paths for stations (A) st126 and (B) st113 along the seismic refraction line AWI-20160100. Picked refractions and ray paths are shown in blue colours whereas picked reflections and ray paths are shown as green lines. Black lines indicate the modelled arrival times for each ray group. See Fig. 4.2C for the station locations.

At several stations along profile AWI-20160100 we observe a P_n mantle refraction phase (Figs. 4.12A and 4.13B) suggesting P-wave velocities of 8.0 ± 0.2 km/s below the Chatham Rise, increasing slightly to 8.1 ± 0.2 km/s below the SE Chatham Terrace.

Gravity modelling along AWI-20160100 required subdivisions of upper and lower crustal layers along the Chatham Rise (Fig. 4.11D) to fit calculated and measured FAA within the 5 mGal uncertainty (Fig. 4.11C). Determined crustal densities in the centre of the Chatham Rise are lower than expected from P-wave velocity model. In contrast, densities at the southern flank of the Chatham Rise are slightly higher than expected (Fig. 4.11D), but all lie within the limits of the P-

wave-velocity-to-density conversions (e.g. 2410-2800 kg/m³ for 5.7 km/s; Barton, 1986). Since the half grabens along our profiles strike in different directions (Fig. 4.2A), significant 3D side-effects on the FAA cannot be ruled out. The modelled densities along AWI-20160100 (Fig. 4.11D) are in a similar range of densities along AWI-20160200 (Fig. 4.7D), and, therefore, we consider them as meaningful. The lower crust has largely similar densities but requires higher densities in the north (profile km 0-30, Fig. 4.11D) where our P-wave velocity model has no ray coverage (Fig. 4.12C). The SE Chatham Terrace does not require any further subdivisions along AWI-20160100 (Fig. 4.11D). Here, the derived densities are in good agreement with those calculated for the SE Chatham Terrace along AWI-20160200 (compare Figs. 4.7D and 4.10D). Density variations in the mantle are low and largely consistent with those of the modelled P-wave velocities.

4.5. Crustal structure of the southern Chatham Rise margin

Both the P-wave velocity-depth profiles and the density models from gravity data reveal a detailed structure of the various regions of the Chatham Rise, the SE Chatham Terrace, and adjacent ocean crust. We extracted 1D velocity-depth profiles in 5-10 km steps along all regions covered by the three P-wave velocity models and compared them to published data to compare and classify crustal types (Fig. 4.14). The three profiles indicate distinct variations of crustal thicknesses and occurrence of the HVLCs between the eastern and western Chatham Rise, but comparable P-wave velocities and densities also suggest similarities between both regions.

4.5.1. The western and eastern Chatham Rise

The crustal structure of the western Chatham Rise is revealed by the profiles AWI-20160200 (Fig. 4.7, profile km 0-80) and AWI-20160100 (Fig. 4.11, profile km 0-240). Our P-wave velocity models show that the crust of western Chatham Rise is 22-25 km thick. We compared the extracted 1D velocities depth profiles of the western Chatham Rise (Figs. 4.14B and 4.14C) to the global compilation of extended continental crust by Christensen and Mooney (1995), thin continental crust of North Zealandia (Fairway Ridge and Lord Howe Rise, Klingelhoefer et al., 2007). Additionally, we compared our data to continental crust along the Galicia margin, which might be a type location for non-volcanic rifting (Pérez-Gussinyé et al., 2003). At the Galicia margin, the continental Galicia Interior Basin, an abandoned continental Mesozoic rift basin separates thin continental crust of Galicia Bank and Shelf. This is potentially a comparable tectonic situation to the Bounty Trough further west of our profiles (Figs. 4.1A and 4.2A), which is also interpreted to represent a failed rift (Grobys et al., 2007). The comparison shows that the crustal thickness, velocity gradients and structure of along both parts of the western Chatham Rise are within the range extended continental crust (Figs. 4.14B and 4.14C). Although the lower crustal velocities along the western Chatham Rise are slightly lower and maximum crustal thicknesses are slightly higher (~25 km) compared to those observed from North Zealandia (21-23 km) and the Galicia Shelf (~22 km), we find that velocity structures generally resemble (Figs. 4.14B and 4.14C). Areas along AWI-20160100 where the crust thins towards the SE Chatham Terrace are comparable to the thinner Galicia Bank (Fig. 4.14C).

The crust of eastern Chatham Rise is covered by our profiles AWI-20160300 (Fig. 4.4, profile km 0-80) and AWI-20160200 (Fig. 4.7, profile km 100-250). We determined a crustal thickness of only 11-14 km at the eastern Chatham Rise (Fig. 4.14A) and 14-19 km close to the boundary of western Chatham Rise (Fig. 4.14B). We compared 1D velocity-depth profiles to the same data as for

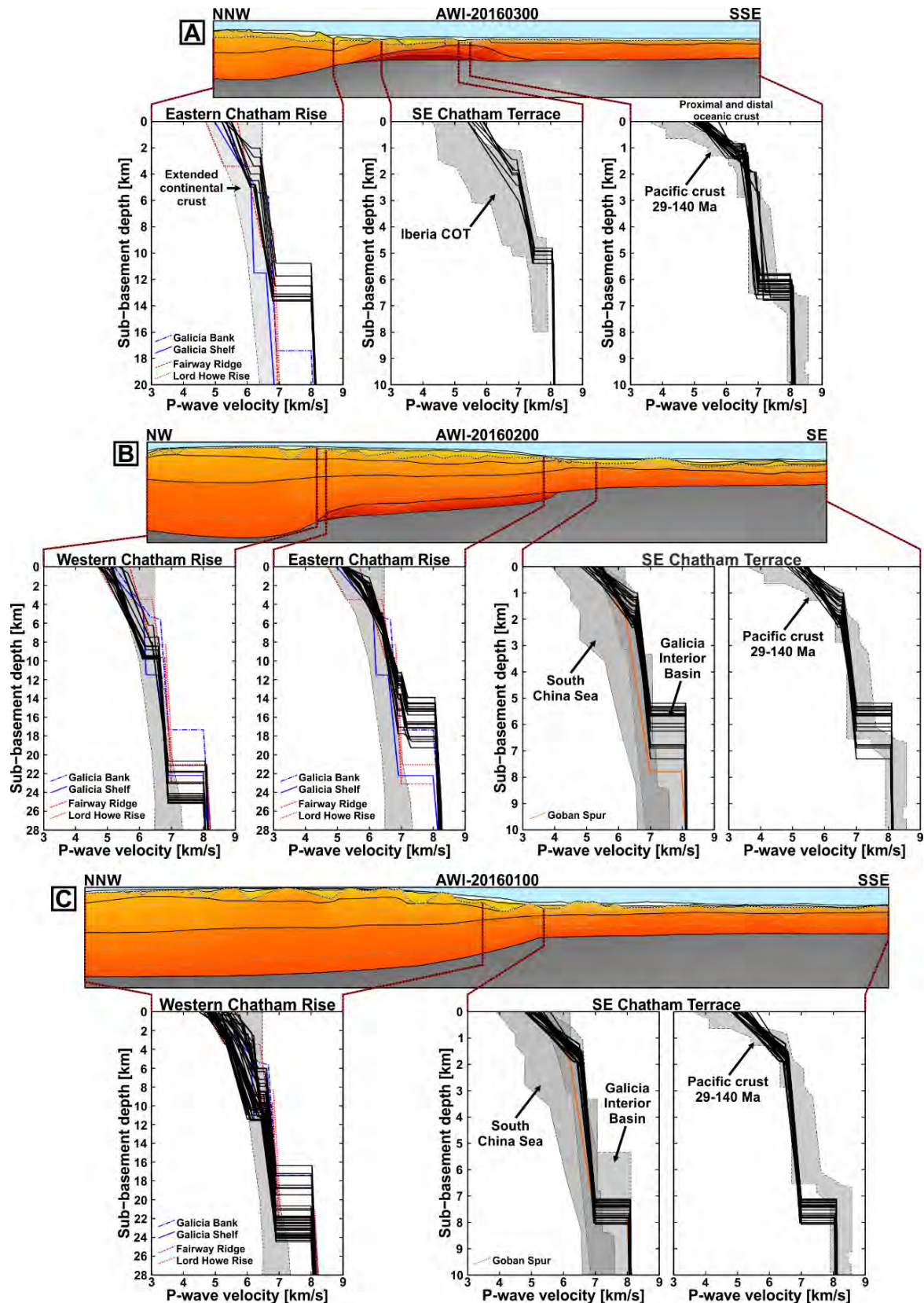


Fig. 4.14: 1D velocity-depth profiles extracted from the P-wave velocity models along the seismic refraction lines (A) AWI-20160300 (Fig. 4.4), (B) AWI-20160200 (Fig. 4.7), and (C) AWI-20160100 (Fig. 4.11). The different domains are compared to extended continental crust (Christensen and Mooney, 1995), submarine continental crust of Northern Zealandia (Fairway Ridge and Lord Howe Rise; Klingelhofer et al., 2007), the Galicia margin (Pérez-Gussinyé et al., 2003), thinned continental crust of the South China Sea (compilation of Liu et al., 2018), the Iberia COT (compilation of Minshall, 2009), the Goban Spur consisting of very thin continental crust (Horsefield et al., 1994), and typical 29-140 Ma Pacific crust (White et al., 1992).

the western Chatham Rise (Figs. 4.14). The eastern Chatham Rise is still in agreement with extended continental crust (Christensen and Mooney, 1995). Although velocity gradients in the lower crust along both areas slightly exceed those of extended continental crust, they are in good agreement with those from the thin continental Lord Howe Rise and Fairway Ridge of North Zealandia (Figs. 4.14A and 4.14B). Disregarding the very thin crust along AWI-20160300 (Fig. 4.14A), the crustal structure of the eastern Chatham Rise is in good agreement with the Galicia Bank (Figs. 4.14A and 4.14B).

Overall the crustal thickness differs along and between eastern and western Chatham Rise, upper and lower crustal P-wave velocities are largely in good agreement. We find that the Chatham Rise is distinctly thinner than the 30 km thick extended continental crust of Christensen and Mooney, but its thickness lies within the range of other continental fragments of North Zealandia. Accordingly, we consider the eastern and western Chatham Rise to consist of thin continental crust with up to 25 km thickness (Figs. 4.15 and 4.16).

4.5.2. Geology of the western and eastern Chatham Rise

From surface geology, the Chatham Rise is expected to represent the accretionary prism of the former East Gondwana subduction zone prior to the subduction and jamming of the Hikurangi Plateau (e.g. Tulloch et al., 2019). Sampled basement rocks from the Chatham Islands and smaller Forty Fours Islets further to the east (Fig. 4.2C) are composed of Permian-Jurassic lower greenschist facies schists and low-grade metagreywackes typically found in accretionary prisms (Adams et al., 2008; Adams and Robinson, 1977; Andrews et al., 1978; Campbell et al., 1993; Mortimer et al., 2019a). Geological correlations of exposed schists and greywackes from the Chatham Islands with onshore South Island suggest low-metamorphic greywackes and the Haast Schist (Fig. 4.1A) continue eastwards offshore along the Chatham Rise (Adams et al., 2008; Mortimer et al., 2019a; Tulloch et al., 2019). Densities of meta-greywackes and schists onshore New Zealand equivalent to the Chatham Islands are $2639 \pm 115 \text{ kg/m}^3$ for greywackes and $2732 \pm 115 \text{ kg/m}^3$ for schists (Tenzer et al., 2011) or even in a narrower range between 2630 and 2770 kg/m^3 for schists of different metamorphic grades (Godfrey et al., 2001). These densities are in good agreement with our determined densities of 2490-2590 kg/m^3 and 2630-2770 kg/m^3 for the upper crustal layers along our three profiles. Therefore, we consider the upper crustal layers of the Chatham Rise to mainly consist of greywackes and schists of different metamorphic grades.

The presence of schists can also explain the variations in P-wave velocities since schists are highly anisotropic media (Christensen and Mooney, 1995; Godfrey et al., 2000). Since our profiles AWI-20160100 and AWI-20160200 are not quite parallel to each other and cross several horst structures and rotated fault blocks with strike in different directions (Fig. 4.2A), we explain the variations of P-wave velocities at approximately constant densities by presence of anisotropic schists.

Along AWI-20160200 and AWI-20160100 we observed a trend towards higher P-wave velocities and densities in the upper crustal layers in direction of the SE Chatham Terrace (Figs. 4.7A+D and 4.8A+D). Schists with higher metamorphic grade (upper greenschist-amphibolite facies) than those from the Chatham Islands were recovered from the Stuttgart Fault Block located on the SE Chatham Terrace (Figs. 4.2C and 4.16, Mortimer et al., 2006, Mortimer et al., 2019a). We explain this trend towards higher P-wave velocities and densities from north to south to reflect a metamorphic gradient related the Cretaceous regional metamorphism north of the volcanic arc (Median Batholith, Fig. 4.1A). Thus, schists in the north have reached temperatures of lower-greenschist facies (Fig. 4.15), whereas schists at the southern Chatham Rise margin have higher metamorphic grades closer to the Median Batholith (Mortimer et al., 2019a; upper greenschist facies or even higher).

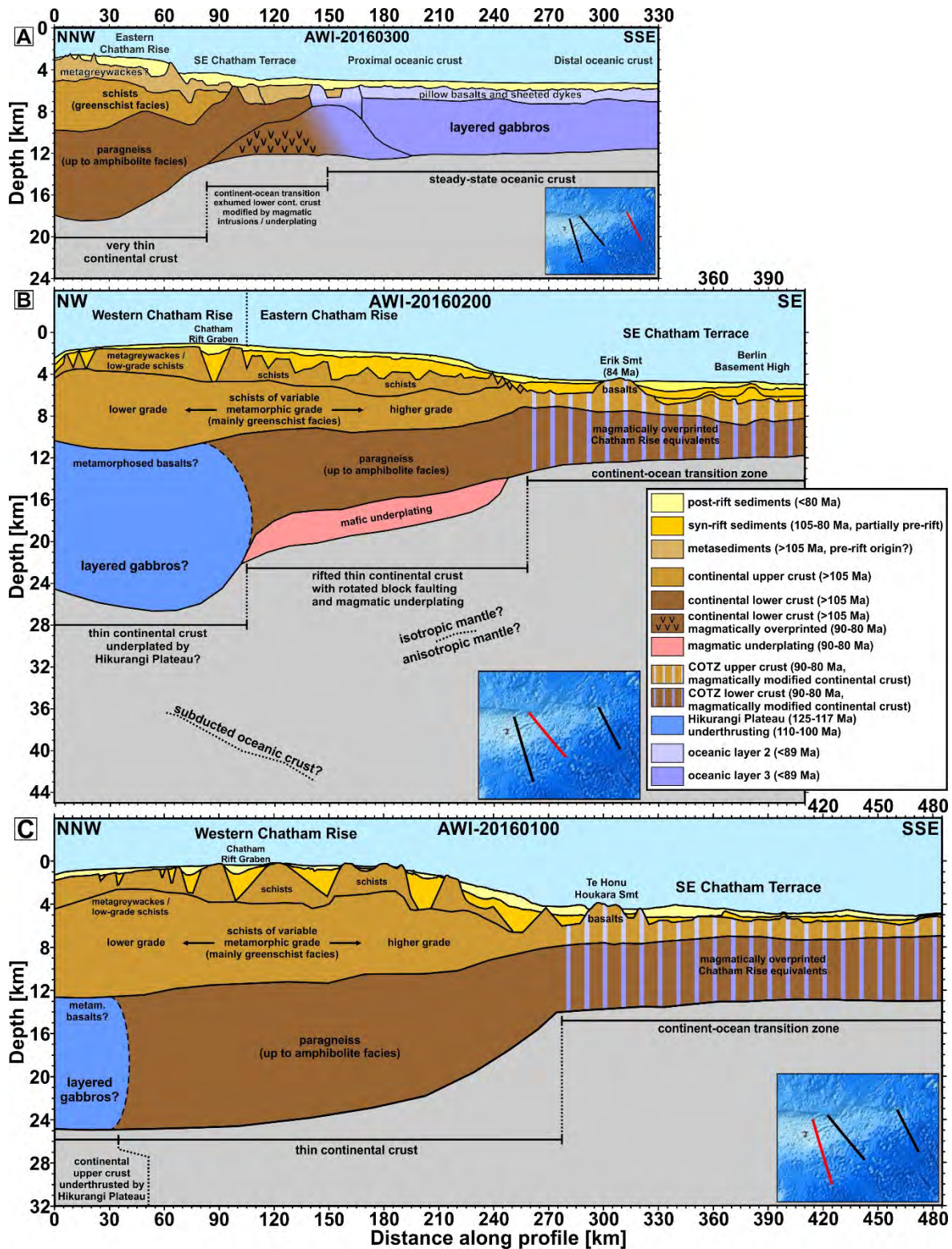


Fig. 4.15: Geological interpretation of the profiles (A) AWI-20160300, (B) AWI-20160200, and (C) AWI-20160100 along the southern Chatham Rise margin.

Densities of 2820-2880 kg/m³ are modelled for most parts of our lower crustal layers along all three profiles (Figs. 4.4D, 4.7D, and 11D). According to our interpretation of the upper crustal layers, we interpret the lower crustal layers with densities of 2820-2880 kg/m³ of eastern and western Chatham Rise to consist of higher metamorphic rocks of up to amphibolite facies, thus, most likely paragneiss (Fig. 4.15).

4.5.3. Indications for crustal extension directions

The western Chatham Rise comprises abundant E-W gravity lineations (Fig. 4.2A), which correspond to half graben structures interpreted to be filled with Cretaceous terrestrial strata (Campbell et al., 1993; Davy, 2014; Wood et al., 1989). These E-W structures are approximately parallel to the sharp southern Chatham Rise margin, which is segmented to the north along the eastern Chatham Rise (Fig. 4.16). The pattern of gravity lineations is more complex between the Chatham Islands and the eastern Chatham Rise. The Chatham Rift Graben (Figs. 4.2B, 4.3B, and 4.3C) strikes in NEE-SWW direction distinctly different from the E-W lineations. Moreover, gravity lineations in the area between AWI-20160100 and AWI-20160200 north of the Stuttgart Seamount strike in NE-SW direction approximately parallel to the boundary between eastern and western Chatham Rise and the graben structure between Erik and Berlin Seamounts (Fig. 4.2B). The bathymetry from this area shows water depth between 2500 m in the west close to the eastern / western Chatham Rise boundary gradually deepening to 4500 m close to the SE Chatham Terrace (Fig. 4.2C). Consistent with the gravity lineations, the bathymetry also suggests some NE-SW elongated horst-like structures. We interpret this structure as a relay ramp (a series of accommodation faults) between two zones of inherent weaknesses, i.e. the sharp southern Chatham Rise margin, which may have been similar features as the E-W striking lineations before rifting became focussed on along the southern Chatham Rise. These E-W lineations are probably former thrust faults in the Chatham accretionary prism, which were reactivated as normal faults by extension. If this interpretation is correct, the inferred relay ramps indicate oblique NNW-SEE extension sub-parallel to extension directions suggested for southern Zealandia (Tulloch et al., 2019). A similar pattern of fault accommodation were created in laboratory analogue experiments and numerical models with an oblique extension angle between 15° and 45° along pre-defined zones of weakness (Corti, 2009; Zwaan et al., 2016), which are known from modern oblique rifts world-wide (e.g. Brune et al., 2017b).

4.5.4. Extent of the Hikurangi Plateau beneath the western Chatham Rise

Several wide-angle reflections from the top of the lower crust ($P_{lc}P$ phase) are observed at the eastern and western Chatham Rise along profiles AWI-21060200 and AWI-20160100 (Figs. 4.8B, and 4.12B). Most of these reflections are spatially restricted to a narrow area, but in the northern part of the western Chatham Rise the observed high-amplitude $P_{lc}P$ phase is continuously observed (Fig. 9A). It abruptly disappears southwest of the boundary of the eastern and western Chatham Rise (Fig. 4.9A). Here, gravity modelling suggests highest densities (Fig. 4.7D) and highest P-wave velocities in the lower crust along AWI-20160200 (Fig. 4.7A). From seismic tomography along the South Island, plate tectonic reconstructions, and gravity anomalies, it is inferred that the thick oceanic Hikurangi Plateau subducted below the area of South Island and the Chatham accretionary prism in mid-Cretaceous (Davy, 2014; Davy et al., 2008; Reyners et al., 2017b, 2011). The underthrust Hikurangi Plateau interface has been imaged along several reflection seismic lines underneath northern Chatham Rise margin (Bland et al., 2017; Davy et al., 2008). Around 200 km west of the Chatham Islands, the imaged extent of an intracrustal reflection interpreted as the Hikurangi Plateau interface is around 100 km southward from the northern boundary Chatham Rise and was limited to the extent of the seismic line (Davy et al., 2008). Although 1D P-wave velocity-depth profiles from that area are within the range of extended continental crust (Fig. 4.14A), we interpret this lower crust of higher density as the Hikurangi Plateau underthrust below the western Chatham Rise. Although we do not observe any internal structure, it probably consists of metamorphosed basalts close to its top and layered gabbros below. Moreover, the profile AWI-20160200 shows that the underthrust Hikurangi Plateau is restricted to the western Chatham Rise but is not present below the eastern Chatham Rise. The sharp eastern boundary of the Hikurangi

4.5.5. Continent-ocean transition east of the Udintsev Fracture Zone (UFZ)

East of the UFZ, the profile AWI-20160300 reveals insights into the continent-ocean crust transition at the easternmost Chatham Rise (Fig. 4.4). We find the continental lower crustal layer rises to shallower depth in southern direction along the SE Chatham Terrace (profile km 65-100) with part of it reaching the top of acoustic basement at around profile km 100. Southward this crustal layer remains thin until profile km 140 (Fig. 4.4). The lower continental crust is (i) overlain by a thin layer of upper continental crust and metasediments north of profile km 95 (Fig. 4.15A), (ii) heavily faulted as evident from the seismic reflection data (Fig. 4.3A, profile km 70-120), and (iii) exhumed to the top of basement in a narrow corridor (Fig. 4.4A, profile km 95-100). North of profile km 100, the upper crustal layer is absent and the lower crust is only overlain by metasediments until km 140 (Fig. 4.15A). In this area, a HVLC is present within the lower continental crust (Fig. 4.4A, profile km 80-140). In exhumed mantle domains, which are typical features along magma-poor passive continental margins (e.g. Doré and Lundin, 2015; Franke, 2013), P-wave velocities exceed 7.0 km/s and increase gradually up to normal mantle velocities of around 8.0 km/s without any Moho reflections (e.g. Funck, 2003). Therefore, we compared 1D P-wave velocity-depth profiles from profile AWI-20160300 between profile km 80 to 140 with those of the continent-ocean transition close to the Iberian Peninsula where continental mantle is exhumed (Fig. 4.14A, Minshull, 2009). Our P-wave velocities in the shallow crust (1-2 km) exceed those of the Iberia continent-ocean transition, and the P-wave velocity gradient in the lower crust is lower. Although no Moho reflection (P_mP phase) was observed in a narrow corridor (profile km 90-110, Fig. 4.5B), a typical Moho reflection was recorded along most of the base of the HVLC. Deep-diving refractions in the HVLC (P_{HVLC}) and a clear P_n mantle refraction (Fig. 4.5A) indicate P-wave velocities of less than 7.5 km/s (Fig. 4.4A). Accordingly, exhumed mantle does not seem to be present. We interpret this HVLC as magmatic underplating below thin lower continental crust and/or continental lower crust strongly modified by intrusive magmatic activity (Fig. 4.15A). Magmatic underplating and intrusions can significantly increase the P-wave velocities in the lower continental crust to higher than 7.0 km/s without any clear reflection on top of the intrusives (e.g. Sibuet et al., 2016). Similar HVLCs have been also inferred for the Bounty Trough and Great South Basin (Fig. 4.2A; Grobys et al., 2009, 2007). Moreover, the presence of several nearby large igneous Kakapo and Takahe Seamounts (Fig. 4.2C) and the slightly elevated P-wave velocities compared to surrounding lower crustal layer (Fig. 4.4A, profile km 90-95) suggests a relationship between extrusive magmatic activity and the magmatic underplating.

South of the region of inferred magmatic underplating, the P-wave velocities are still slightly higher than 7.0 km/s (Fig. 4.4A, profile km 140-170) but decrease towards the south to \sim 7.0 km/s (profile km 170-330). We compared 1D velocity-depth profiles from the distal oceanic crust (profile km 150-330) with typical 29-140 Ma old Pacific oceanic crust (Fig. 4.14A, White et al., 1992). The P-wave velocity structure south of the SE Chatham Terrace resemble the structure of the Pacific crust older than 29 Ma. Moreover, the crustal thickness is also in the same range as the Pacific crust. Accordingly, we conclude that the southeastern part of our profile east of the UFZ consists of oceanic crust (Figs. 4.15A and 4.16) with a typical thin oceanic layer 2 (up to 1.5 km massive basalts and sheeted dykes) and a thick oceanic layer 3 ($<$ 5.5 km dikes and gabbros). We recognised a small zone of low P-wave velocities (profile km 150-160, Fig. 4.4A). Here and nearby, the total magnetic field anomaly indicates high magnetic susceptibility contrasts (Fig. 4.4B). Accordingly, another narrow piece of SE Chatham Terrace crust is most likely present on this profile.

Larter et al. (2002) identified magnetic spreading anomalies c34n(y) (\sim 83 Ma) east of the UFZ (Fig. 4.16), which we projected onto our profile AWI-20160300 (Fig. 4.4B). Here, this reversal is obvious at around profile km 320. Since the half-spreading rates during the Cretaceous Normal

Superchron (pre-83 Ma) are unknown, Larter et al. (2002) used the post c33r(o) anomaly half-spreading rates of 32 mm/yr to estimate the onset of seafloor spreading at around 90 Ma close to the eastern Chatham Rise. However, our P-wave velocity model indicates only up to 180 km of pre-83 Ma oceanic crust east of the UFZ and a broader continent-ocean transition zone (Figs. 4.16). If the extrapolated half-spreading rates of 32 mm/yr are correct, the onset of seafloor spreading must be revised to be at 89-88 Ma.

4.5.6. *The SE Chatham Terrace*

The crustal thickness and structure central and eastern part of the SE Chatham Terrace are notably different from the Pacific oceanic crust along profile AWI-20160300. Along AWI-20160200 the crust is only up to 7.0 km thick close to the eastern Chatham Rise and gradually thins in a southeastern direction to 5.5 km close to the end of profile (Fig. 4.7A). In contrast, the crust of the western part of the SE Chatham Terrace along profile AWI-20160100 has a more constant thickness of 7.5-8.0 km (Fig. 4.11A). Modelled P-wave velocities and densities only slightly differ between both profiles and are largely consistent (Figs. 4.7A+D and 4.11A+D). Thus, we suggest a similar composition and structure of the SE Chatham Terrace along both profiles.

We compared the velocity structure of the SE Chatham Terrace along both lines with typical 29-140 Ma old Pacific-type oceanic crust (Figs. 4.14B and 4.14C). Generally, the P-wave velocity structures of the SE Chatham Terrace along both profiles (high velocity gradient in the upper crust and low velocity gradient in the lower crust) are still in agreement with Pacific-type crust. However, the continent-ward part of the eastern SE Chatham Terrace along AWI-20160200 is slightly thicker, whereas the ocean-ward part is distinctly thinner than Pacific crust (Figs. 4.7A and 4.14B). Moreover, the crustal thickness of the SE Chatham Terrace along AWI-20160100 is, on average, around 1 km thicker than typical Pacific oceanic crust (Fig. 4.14C).

The basement structure also differs strongly along our profiles. MCS reflection data along AWI-20160100 shows a very smooth basement for the SE Chatham Terrace (Fig. 4.3C), but also evidence for a graben structure close to Te Honu Houkara Seamount (Fig. 4.3C, profile km 325-350). Moreover, we found another large graben structure with strong normal faulting between Erik Seamount and the basement highs further to the southwest along AWI-20160200 (Fig. 4.3B, profile km 315-410), where normal faults are abundant. The basement structure along the SE Chatham Terrace distinctly differs from the typical oceanic crust like roughness east of the UFZ (Fig. 4.3A). Comparable flat acoustic basement different from oceanic crust has been observed for the 7-km thick Middleton Basin in Northern Zealandia (Boston et al., 2019; Gallais et al., 2019). Therefore, we also compare 1D velocity-depth profiles from the SE Chatham Terrace with very thin and hyper-extended continental crust of the Galicia Interior Basin separating the thicker continental Galicia Bank and Galicia Bank, offshore Iberia Peninsula (Pérez-Gussinyé et al., 2003), with the Goban Spur consisting of very thin continental crust, offshore Ireland (Horsefield et al., 1994), and with ~10 km thin continental crust of the South China Sea (Liu et al., 2018). The comparison demonstrates that the P-wave velocity structures of the SE Chatham Terrace are within the range of the Galicia Interior Basin and South China Sea (Figs. 4.14B and 4.14C). Although P-wave velocities at the upper-lower crustal boundary are slightly higher along the SE Chatham Terrace, the general velocity structure is similar to that of the Goban Spur. Moreover, the crustal thickness of the SE Chatham Terrace along AWI-20160100 is close to the Goban Spur (Fig. 4.14C) and at both parts the thickness is clearly within the range of the Galicia Interior Basin. On the basis of the schists from the Stuttgart Fault Block in the area between our profiles (Fig. 4.2C, Mortimer et al., 2006), bathymetric evidence for other continental fault blocks (Gohl and Werner, 2016; Hoernle et al., 2003), and graben-like structures we infer that the SE Chatham Terrace has largely continental affinities most likely with

composition equivalent to the Chatham Rise (Figs. 4.15B and 4.15C). Since P-wave velocities higher than 7.0 km/s are not observed along the SE Chatham Terrace, we suggest that no larger magmatic underplating affected the SE Chatham Terrace. Moreover, we infer a magmatic overprint of the SE Chatham Terrace, which only slightly increased the P-wave velocities along the SE Chatham Terrace compared to Goban Spur (Fig. 4.14D). During the seamount formation along the SE Chatham Terrace magma probably used pre-existing normal faults while ascending during the continental crust, which is well known from parts of the Tyrrhenian Sea (Prada et al., 2015). We do not entirely exclude the possibility that some minor segments of oceanic crust exist along the SE Chatham Terrace. Although P-wave velocities appear very homogenous along AWI-20160100 and AWI-20160200, the SE Chatham Terrace most probably consists of a hybrid crust, which we interpret as very thin (<8 km) continental crust modified by magmatic addition forming a ~200 km broad continent-ocean transition zone (Figs. 4.15A, 4.15B and 4.16). Our observations and interpretation are consistent with earlier studies inferring that the SE Chatham Terrace is mostly of continental origin (Carter et al., 1994). Moreover, we show that the SE Chatham Terrace extends more southward than previously suggested (Davy, 2006).

4.5.7. Implications for the onset of seafloor spreading at the southern Chatham Rise margin

Plate tectonic reconstructions of the early Zealandia-Antarctica separation are based on only few interpreted c34n(y) magnetic spreading anomaly picks close to the SE Chatham Rise margin (Davy, 2006; Eagles et al., 2009; Larter et al., 2002; Wobbe et al., 2012). In the area between the UFZ and east of 176°W (Fig. 4.16), the magnetic anomaly signature is highly variable since distinct positive and negative medium- to high-amplitude magnetic anomalies are present on the SE Chatham Terrace (Davy, 2006). Wobbe et al. (2012) identified several c34n(y) spreading anomalies on the SE Chatham Terrace close to our profiles AWI-20160100 and s AWI-20160200. However, almost all of these c34n(y) spreading anomaly picks were obtained close to the seamounts and ridges located on the SE Chatham Terrace. Moreover, corresponding c34n(y) magnetic anomalies on the anomalously shallow seafloor around the Marie Byrd Seamounts close to the conjugate West Antarctic margin are missing. Only few identified c34n(y) spreading anomalies along the southern Chatham Rise margin with counterparts on the conjugate margin are observed close to the UFZ (Fig. 4.16; Larter et al., 2002; Wobbe et al., 2012). These c34n anomalies demonstrate that seafloor spreading west of the UFZ was initiated at around 85 Ma, shortly after, but distinctly later than east of the UFZ, which we estimated to 89-88 Ma (section 4.5.4).

Isolated, but well lineated c34n(y) have been recognised in the mouth of the Bounty Trough between 176°W and 179°W east of the SE Chatham Terrace (Davy, 2006; Wobbe et al., 2012). Compared to the SE Chatham Terrace, the seafloor of the mouth of the Bounty Trough is slightly deeper Terrace and seamounts or ridges are absent. Davy (2006) explained the isolated c34n(y) magnetic anomalies by a southward ridge jump shortly after anomaly c34n. However, based on an improved version of Sutherland's (1999) regional magnetic map, Tulloch et al. (2019) have shown that the magnetic anomalies in the mouth of the Bounty Trough are along strike with magnetic anomalies south of the Chatham Islands and large Campbell Magnetic Anomaly System on the Campbell Plateau. This probably indicates that the magnetic anomalies in the mouth of the Bounty Trough are of continental origin (i.e. rifting anomalies; Tulloch et al., 2019). It is very unlikely that a small and isolated piece of oceanic crust would be located between the very thin continental SE Chatham Terrace (section 4.5.5) and the heavily rifted thin continental crust of the Bounty Trough (Grobys et al., 2007). Therefore, we show the mouth of the Bounty Trough and the SE Chatham Terrace as parts of the same continent-ocean transition zone. Regarding the bathymetry and gravimetry, the crust of the mouth of the Bounty Trough is probably thinner (<8 km, Fig. 4.16). Since

seamounts are absent in the mouth of the Bounty Trough, its crust is likely less affected by magmatic activity compared to the of SE Chatham Terrace.

4.5.8. Nature of the southern Chatham Rise margin

Although we consider seismic array was powerful enough to sufficiently map the basement and overlying strata along the southern Chatham Rise margin, we found no evidence for seaward-dipping reflector sequences, which are typical indicators for magma-rich passive continental margins (e.g. Franke, 2013). The onset of rifting in Zealandia was between 110 and 100 Ma. Magmatic activity was widespread in Late Cretaceous and Cenozoic (Laird and Bradshaw, 2004; Timm et al., 2010). All igneous rocks on the Chatham Islands are less than 100 Ma in age and are of intraplate rather than subduction character (Campbell et al., 1993; Panter et al., 2006). The same applies for igneous rocks on the eastern Chatham Rise close to our profile AWI-20160300 (Mortimer et al., 2006), the northernmost seamounts on the SE Chatham Terrace (Mortimer et al., 2019b), onshore New Zealand (Mortimer et al., 2019b; Tulloch et al., 2009b; van der Meer et al., 2018, 2017, 2016), and northern Zealandia (Mortimer, 2004; Mortimer et al., 2018; Tulloch et al., 2009b). Seamounts located on the Hikurangi Plateau north of the Chatham Rise are also of Cretaceous age (Fig. 4.2C; Hoernle et al., 2010). The present understanding of igneous rocks demonstrably related to the Zealandia rift phase between 105 and 80 Ma, although spatially widespread, was overall of low volume. More recently, on the basis of continental magnetic anomalies, Tulloch et al. (2019) postulated the existence of a spatially extensive intraplate igneous field on the Campbell Plateau (Campbell Mafic Igneous Complex), probably related to the Southern Volcanic on the Chatham Islands. However, it is not clear that Zealandia's intraplate magmatism can be compared to the emplacement of large igneous provinces that pre-date continental breakup along magma-rich passive continental margins like the North or South Atlantic (e.g. Clerc et al., 2018; Franke, 2013).

We found HVLC regions along our profiles AWI-20160200 (Fig. 4.7A) and AWI-20160300 (Fig. 4.4A) which commonly occur at volcanic-rifted margins such as those in the North Atlantic (e.g. Faleide et al., 2008; Franke, 2013). Both HVLCs are in an atypical position compared to volcanic-rifted margins. Although located below continental crust, we would expect the position and extent of the HVLC along AWI-20160300 to be closer to the continent to refer it as normal (Fig. 4.15A). In contrast, the HVLC along AWI-20160200 is entirely located below the thin continental crust of eastern Chatham Rise in an area, which is heavily affected by block rotation and normal faulting. Here, we would consider the HVLC as normal if it extended below the thin SE Chatham Terrace where it is not present (Fig. 4.15B). However, exhumation of lower continental crust (Fig. 4.15A) is atypical for volcanic-rifted margins. On the basis of the crustal structure along AWI-20160300 (Fig. 4.4A), we suggest that the onset of rifting and lower crustal exhumation most likely pre-dates the formation of the HVLC. Furthermore, we infer a similar age for the HVLC along AWI-20160200. More speculative, it is possible that both HVLCs formed in the time interval between 85 and 82 Ma together with the Campbell Mafic Igneous Complex (Tulloch et al., 2019), Southern Volcanics on the Chatham Islands (Panter et al., 2006), and Erik Seamount on the SE Chatham Terrace close to profile AWI-20160200 (Mortimer et al., 2019b). Accordingly, the southern Chatham Rise margin most likely underwent a two-stage evolution: (i) A prolonged phase of rifting with few or no magmatic activity (magma-poor) and (ii) another magmatic event, which was initiated after the onset of rifting.

Overall the southern Chatham Rise margin along all three profiles is heavily affected by oceanward-directed normal faulting (Fig. 4.3), which is typical for many magma-poor continental margins (e.g. Clerc et al., 2018; Franke, 2013). Fault-controlled rifted margins without any clear evidence for large-scale magmatic activity are also present in Northern Zealandia (Boston et al., 2019; Gallais et

al., 2019; Klingelhoefer et al., 2007). Although HVLCs are present in two of our profiles (Fig. 4.15) and further to the west in the Bounty Trough and Great South Basin (Fig. 4.2A; Grobys et al., 2009, 2007), we interpret the southern Chatham Rise margin as a magma-poor passive margin with localised magmatic additions during a second event.

4.6. Tectonic evolution of the Chatham Rise and its southern margin

4.6.1. The collision of the Hikurangi Plateau with the East Gondwana margin

Along two of our seismic refraction profiles, we observe an Hikurangi Plateau that is underthrust beneath the thicker Chatham Rise (Fig. 4.15B and 15C) east of the Chatham Islands (Fig. 4.15B and 15C). Collision and underthrusting of the Hikurangi Plateau with the East Gondwana margin in the area of the South Island is inferred to have taken place at 110 Ma (Fig. 4.17A; Davy, 2014), pre-dating the collision along the Chatham Rise west of the Chatham Islands (Fig. 4.17B) in the area of the two profiles. The young and thick oceanic crust of the Hikurangi Plateau was likely too buoyant, and therefore, geodynamically unfavourable for subduction as indicated by buoyancy analysis (Cloos, 1993), analogue, and numerical models (Espurt et al., 2008; van Hunen et al., 2002). If the subducting slab south of the Hikurangi Plateau was already shallow or even flat as suggested by Jacob et al. (2017), the subduction of the young buoyant Hikurangi Plateau may have promoted or initiated shallow subduction, which may lead to forearc extension similar to the present-day Andes (e.g. Espurt et al., 2008; van Hunen et al., 2002).

Another factor for facilitating extension along the Chatham Rise is the proposed rotation of the East Gondwana margin in response to the Hikurangi Plateau collision (Davy, 2014). Indentation of buoyant features, such as the Hikurangi Plateau into a subduction zone may trigger forearc extension (Wallace et al., 2009). However, the effects of the margin rotation may be only spatially limited to the area of the Chatham Rise, but extension also affected the arc and back-arc areas (Tulloch et al., 2019). As a response to the margin rotation and collision, seafloor spreading directions of the Osborn Trough (Fig. 4.1D) changed from NE-SW to N-S (Davy, 2014).

Assuming that the present-day reference frame is correct, then the convergence direction of the Hikurangi Plateau towards the Gondwana margin probably also changed to more N-S (Fig. 4.17B) and spreading and subduction rates slowed down until 100 Ma (Barrett et al., 2018; Davy, 2014; Downey et al., 2007). In our reconstruction we agree with Barrett et al. (2018) who interpreted the offset of the northern boundary between eastern and western Chatham Rise (Fig. 4.16) as a result of the ongoing collision with the Hikurangi Plateau between 105 and 100 Ma (Fig. 4.17B). We explain the differences in crustal thickness as being due to the collision and underthrusting of the Hikurangi Plateau along the western Chatham Rise west of the Wishbone Ridge intersection in contrast to oceanic crust subduction along the eastern Chatham Rise. This led to ongoing compression and uplift of the outer accretionary prism along the western Chatham Rise and, therefore, thickening and uplift at least in the northern part of the western Chatham Rise compared to the eastern Chatham Rise (Fig. 4.17B). A second factor explaining the differences in crustal thicknesses along the different parts of the Chatham Rise may be that the Hikurangi Plateau slowed down the velocity of the overriding plate (i.e. the western Chatham Rise). Accordingly, crustal extension in the forearc region was probably favoured and more intense along the eastern Chatham Rise where normal thickness oceanic crust has been subducted.

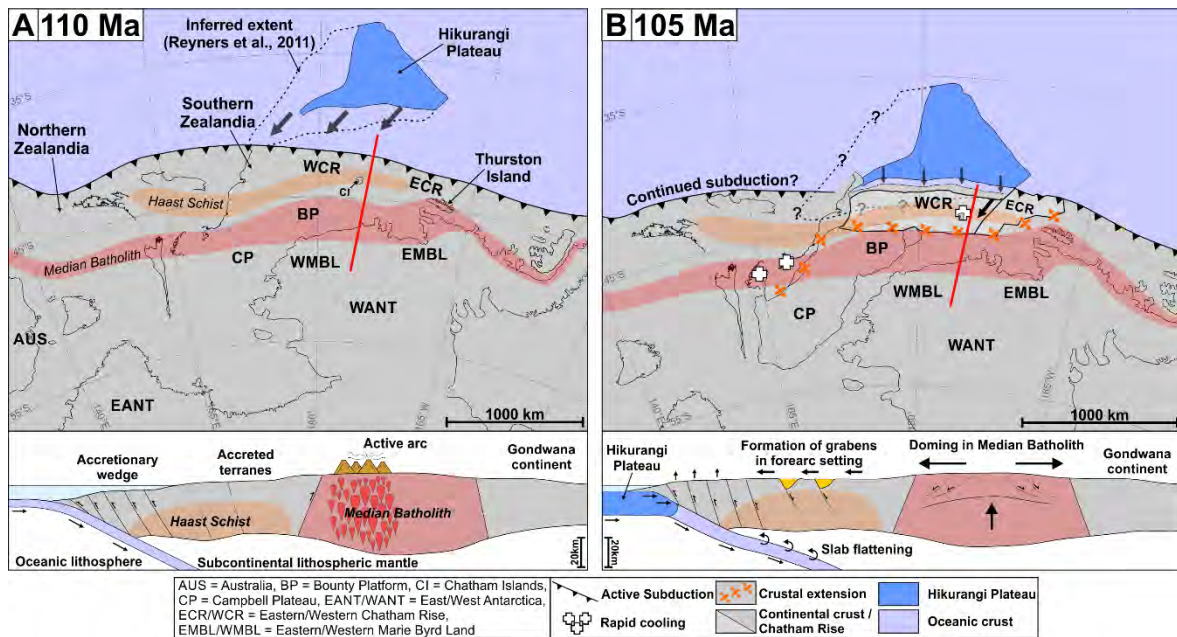


Fig. 4.17: Tectonic reconstructions for the Zealandia-West Antarctica region and schematic cross sections through different areas along the Gondwana margin from 110 to 78 Ma. Orthographic projections with the western Chatham Rise kept fixed. In each reconstruction slide, we show magmatic activities (Hoernle et al., 2010; Kipf et al., 2012; Mortimer et al., 2019b, 2006; Tulloch et al., 2009b; Weaver et al., 1994), metamorphic doming and rapid cooling events (Klepeis et al., 2016; Kula et al., 2009, 2007; Lindow et al., 2016; McFadden et al., 2015, 2010; Mortimer et al., 2016; Ring et al., 2015; Schwartz et al., 2016; Siddoway et al., 2004b, 2004a; Spiegel et al., 2016; Zundel et al., 2019), and offshore tectonic features (Barrett et al., 2018; Cunningham et al., 2002; Davy, 2014; Eagles et al., 2004a; Mortimer et al., 2019b; Reyners et al., 2011). The Hikurangi Plateau is shown with its speculative extent after Reyners et al. (2011) modified with our observed extent. The cross section through the 'Cordillera Zealandia' in (A) and (B) are simplified and modified after Mortimer et al. (2014) and Schwartz et al. (2017). The cross sections X and Y in (C) to (F) illustrate the tectonic evolution along the profiles AWI-20160300 and AWI-20160200. (A) Reconstruction at 110 Ma (section 6.1): along the long-lived Gondwana subduction zone when the Hikurangi Plateau started to subduct in SW direction. (B) Reconstruction at 105 Ma (section 6.1 and 6.2): Southward underthrusting of the Hikurangi Plateau below the Chatham Rise. As a response the slab flattened and resulted in extension in the forearc of the Median Batholith where crustal extension initiation is manifested by metamorphic doming in Fiordland. (C) Reconstruction between 100 to 92 Ma (section 6.2): The Hikurangi subduction ceased along the western Chatham Rise. A rollback of the slab led to continued crustal extension and heating of the lithosphere which resulted in felsic magmatism (i.e. Takahe granite) and HT-UHT metamorphism on the South Island. Oblique NW-SE directed rifting started to affect southern Zealandia and Marie Byrd Land. (D) Reconstruction between 92 and 88 Ma (section 6.2 and 6.3): Subduction ceased at the eastern Chatham Rise, a large slab window opened beneath the western and eastern Chatham Rise, and upwelling mantle material migrated into shallower mantle levels and initiating seafloor spreading at the easternmost Chatham Rise. (E) Reconstruction between 88 to 82 Ma (section 6.3): Upwelling mantle resulted in the formation of the HVLCs along the eastern Chatham Rise, magmatic overprint of the Chatham Terrace, formation of the Chatham Terrace Seamounts and magmatism on the Chatham Islands. South of the SE Chatham Terrace seafloor spreading migrated southwestward. (F) Reconstruction between 82 and 78 Ma (section 6.3): Continuing southwestward propagation of the proto-Pacific-Antarctic ridge driven by mantle upwelling broke to Bollons Seamount apart from Bounty Platform. After the 79 Ma the breakup between southern Zealandia and Marie Byrd Land is completed and Southern Zealandia became tectonically stable for the rest of Cretaceous.

4.6.2. The onset of continental rifting between Zealandia and West Antarctica

The northern parts of the Chatham Rise were thickened in response to the collision and underthrusting of the Hikurangi Plateau. In contrast, the southern parts of the Chatham Rise were affected by rifting and crustal extension as evident from (i) the E-W large graben structures (Fig. 4.2A), (ii) the NEE-SWW striking Chatham Rift Graben (Figs. 4.2B, 4.3B and 4.3C) and (iii) intense ocean-ward normal faulting along our three profiles (Fig. 4.3). The timing of extension along the Chatham Rise is poorly constrained. Thermochronological data from onshore New Zealand indicate a major change from typical arc-building to extensional processes between 105 and 100 Ma close in age Hikurangi Plateau collision (Figs. 4.17A and 4.17B). High-temperature thermo-

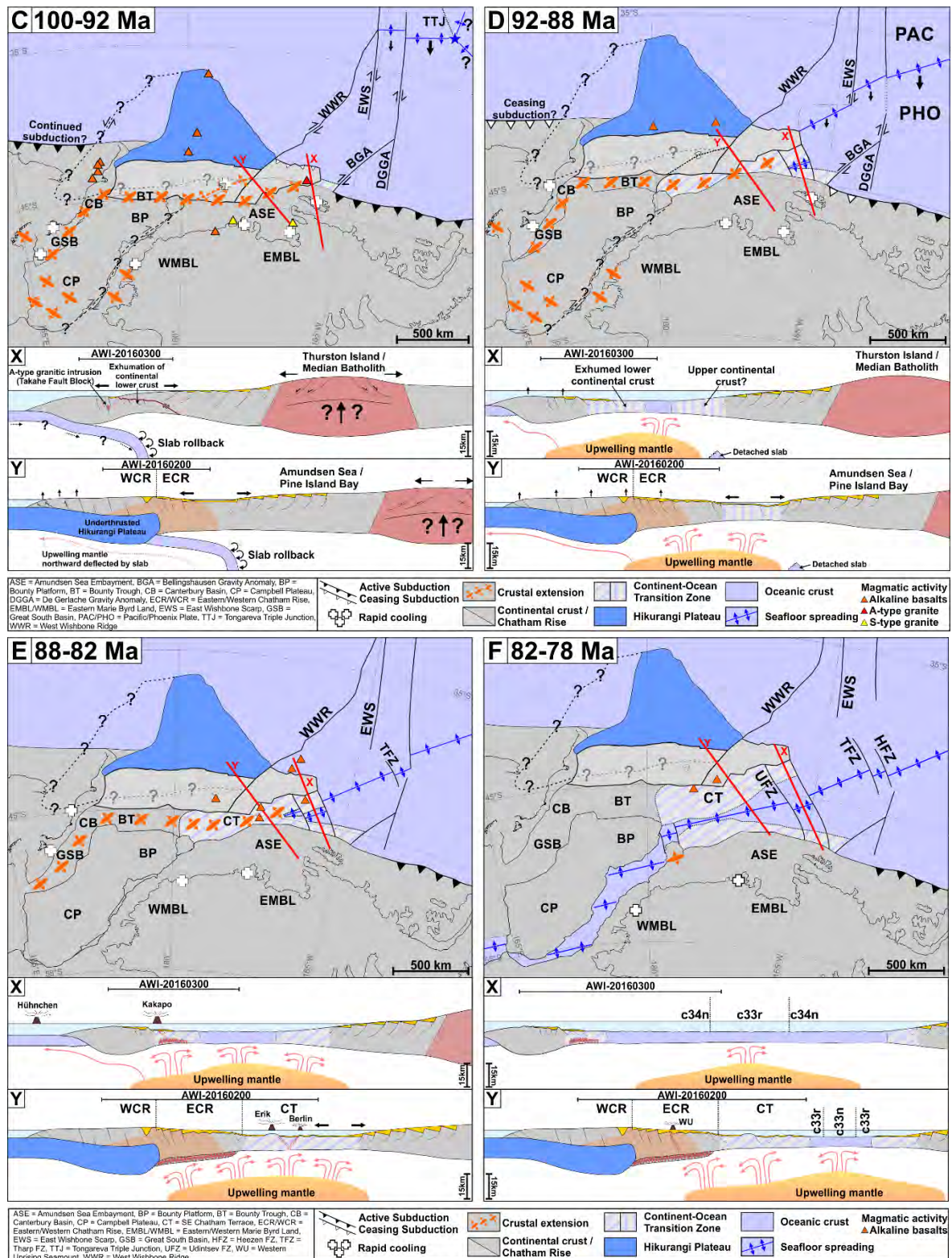


Fig. 4.17: (continued)

chronological data from the Median Batholith on the southwestern South Island, reveal that arc magmatism and contractional deformation dominated the so-called 'Zealandia Cordillera' prior to 108-106 Ma (Fig. 4.17A; Klepeis et al., 2016; Schwartz et al., 2017, 2016). One set of models interpret the onset of regional extension as being caused by metamorphic doming and orogenic collapse of the overthickened volcanic arc (Figs. 4.17B and 4.17C). This is based on thermochronological data from several shear zones in Fiordland, South Island between 106 to 97

Ma and 96 to 89 Ma (Klepeis et al., 2016). Hereby, the lower crust was thinned, and horizontal flow of lower crustal material oblique to the arc and trench has been proposed. As recognised by Tulloch et al. (2009b) the early rift-related magmatism across Zealandia was restricted to grabens, which mainly strike 30° oblique to the remnant Cretaceous trench and arc. Moreover, sedimentary basins of Northern Zealandia, the Great South Basin and Canterbury Basin (Fig. 4.17C) also started to progressively deepen after ~105 Ma (Fig. 4.17C; Bache et al., 2014; Strogon et al., 2017). Zundel et al. (2019) interpreted from low-temperature thermochronological ages that the onset of widespread extension-related crustal cooling progressed from western Marie Byrd Land (105-100 Ma), along eastern Marie Byrd Land (~100 Ma) to Thurston Island in the east (~95 Ma). Accordingly, extension along the eastern and western Chatham Rise may have been at least initiated between 100 and 95 Ma (Fig. 4.17C) and formed the E-W striking graben structures we observe along two of our profiles (Figs. 4.15B and 4.15C). These lineations likely represent former thrust faults in the Chatham accretionary complex, reactivated as normal faults leading to the formation of the first half grabens on the Chatham Rise (Figs. 4.17A and 4.17B). With ongoing extension, a younger generation of NE-SW to NEE-SWW striking normal faults like the Chatham Rift Graben (Figs. 4.2B, 4.3B, and 4.3C) started to form approximately orthogonal to the extension direction and was progressively filled with terrestrial material. This can explain the complex gravity anomaly pattern around the Chatham Islands (Fig. 4.2A) and would be in agreement with structural interpretations of the acoustic basement observed from the dense seismic network in the Canterbury Basin (Fig. 4.17C). This acoustic basement also shows E-W striking reactivated structures which pre-date NE-SW directed normal faults (Barrier et al., 2017). Moreover, we speculate that earliest extensional movements also affected the southern Chatham Rise margin before 100 Ma, contemporaneous or shortly after onshore extension on the South Island (Fig. 4.17B). This would be in agreement with low-temperature thermochronological ages of the Haast Schist on northern Chatham Island (Mortimer et al., 2016).

In contrast to the SE Chatham Terrace consisting of slightly overprinted continental crust west of the UFZ (Figs. 4.15B and 4.15C), exhumed and intruded lower continental crust is present west of the UFZ (Fig. 4.15A). Since this part of the southern Chatham Rise margin was in the vicinity of the areas, which were affected by the Hikurangi Plateau collision, it probably underwent a different tectonic evolution. The cessation of the Hikurangi Plateau subduction and underthrusting is inferred to around 100 Ma along the East Gondwana margin (Fig. 4.17C; Davy, 2014), but south of the eastern Chatham Rise 96 Ma old subduction-related granitoids were emplaced in the Amundsen Sea Embayment, Antarctica (Fig. 4.17C; Kipf et al., 2012). When dextral strike-slip movements became active along the West Wishbone Ridge after ~105 Ma (Barrett et al., 2018; Davy, 2014), subduction of normal oceanic crust most likely continued at least until 96 Ma along the eastern Chatham Rise (Fig. 4.17C). Although dextral strike slip movements have been also inferred between the Campbell Plateau and Western Marie Byrd Land (Siddoway et al., 2004a), it is kinematically not ultimately required that strike-slip movements in this area and along the West Wishbone Ridge were related. Both strike-slip movements could have been compensated by prolonged subduction along the eastern Chatham Rise and crustal extension south of the Chatham Islands, i.e. the future Bounty Trough and SE Chatham Terrace. Jacob et al. (2017) described granulites evolved from ultra-high temperature at ~92 Ma in the area of eastern South Island. Lower crustal heating was probably induced by a slab rollback after cessation of the Hikurangi Plateau subduction (Jacob et al., 2017). Shortly before that, the 97 Ma old Takahe granite dredged at the eastern Chatham Rise close to our AWI-20160300 shows an A-type granitic composition rather typical subduction-related composition (Fig. 4.17C; Mortimer et al., 2006; Tulloch et al., 2019). We speculate that the melts for the Takahe granite are also related to crustal heating in response to a slab rollback when subduction along the eastern Chatham Rise was still ongoing in this area. Moreover, we suggest that the slab rollback

focussed extension along the southern Chatham Rise margin and initiated the decoupling of upper and lower crust north of Thurston Island, which led to exhumation of lower continental crust along our profile AWI-20160300 (Fig. 4.17C).

Marie Byrd Land was also affected by crustal extension as evident from rapid cooling events between 100 and 88 Ma (Figs. 4.17C and 4.17D; Lindow et al., 2016; McFadden et al., 2010; Siddoway et al., 2005; Spiegel et al., 2016; Zundel et al., 2019). NE-SW striking magnetic anomalies are also present on the shelf of the Amundsen Sea Embayment and are probably also related to the same period of crustal extension affecting the Chatham Rise (Figs. 4.17C and 4.17D; Gohl et al., 2013).

Changes in the extensional regime affected southern Zealandia in response to slab detachment (e.g. Davy et al., 2008). Identified reflections within the mantle along profile AWI-20160200 indicate a possible piece of oceanic crust attached to the Hikurangi Plateau (Fig. 4.15B), but we found no evidence for oceanic crust still attached southward to the Hikurangi Plateau along our profile AWI-20160100 (Fig. 4.15C). We suggest that the slab detachment partially took place along both (i) the transition of the Hikurangi Plateau to oceanic crust and (ii) within oceanic crust as proposed by Reyners et al. (2017a). Since larger pieces of old oceanic crust are interpreted to underlay the western Bounty Trough and Canterbury Basin (Davy, 2014; Van Avendonk et al., 2004), the slab detachment along the eastern of western Chatham Rise occurred closer or directly at the transition between Hikurangi Plateau and adjacent oceanic crust (Fig. 4.17D). The timing of the slab detachment is so far unclear. Davy et al. (2008) proposed a slab detachment at around 96 Ma, but Reyners et al. (2017a) suggested a later slab detachment at around 85 Ma. However, the style of rifting changed in Southern Zealandia between 92 and 88 Ma as suggested from thermochronological data and varying extension directions on the Campbell Plateau and South Island (Tulloch et al., 2019).

Our reconstruction shows that the southern margins of the eastern and western Chatham Rise including the interpreted relay ramp between the profiles AWI-20160100 and AWI-20160200 still overlapped with the Amundsen Sea Embayment, Antarctica, Campbell Plateau and Bounty Platform until around 92 Ma (Fig. 4.17C). Eagles et al. (2004a) inferred a 90 Ma onset of an echelon rifting in Bounty Trough and the area further in the west. This 90 Ma age corresponds to the inception of fast cooling during tectonic exhumation of the foot wall of the Sisters Shear Zone offshore Stewart Island (Fig. 4.2A) west of the Great South Basin (Figs. 4.17C and 4.17D; Kula et al., 2007), while rapid cooling was already ongoing in the hanging wall of the Sisters Shear Zone (Mortimer et al., 2016). We suggest that the downgoing slab south of the Hikurangi Plateau became detached between 92 and 88 Ma, approximately 10 Ma after subduction cessation. Timings of slab detachments are controlled by the age of the oceanic crust (van Hunen and Allen, 2011). Therefore, an early slab detachment after 10 Ma would be in good agreement with young oceanic crust expected south of the Hikurangi Plateau (e.g. Hochmuth et al., 2015). As a consequence, the Chatham Rise was most likely topographically uplifted after the loss of negative buoyancy from the detached downgoing slab (Fig. 4.17D; Davy et al., 2008; Gerya et al., 2004; Gvirtzman and Nur, 1999; Reyners et al., 2017a). After that, the style of crustal extension and rifting likely switched from a wide-rift mode affecting Southern Zealandia and West Antarctica to more narrow and intensified rifting affecting the SE Chatham Terrace, Bounty Trough, Canterbury Basin as well as Great South Basin expressed as significant topographic deepening and crustal thinning in these areas.

4.6.3. *The origin of the SE Chatham Terrace and onset of seafloor spreading between Zealandia and Antarctica*

East of the UFZ, seafloor spreading started at 89-88 Ma (Fig. 4.17D) as extrapolated from the inferred continent-ocean boundary east of the UFZ to the identified c34n(y) magnetic anomalies (Fig. 4.16; Larter et al., 2002). Here, the onset of seafloor spreading took place shortly after the slab detachment and likely took place along pre-existing extensional structures, which were dynamically favourable, i.e. the formerly thinned and exhumed lower continental crust along profile AWI-20160300 (Fig. 4.15A). Plate tectonic reconstructions and abyssal hill trends show that the TTJ migrated to the southeast towards the East Gondwana margin (Fig. 4.17C, Hochmuth et al., 2015; Larson et al., 2002). This southeast directed migration of the TTJ was probably a response to the slowdown or end of spreading along the Osbourn Trough north of the Hikurangi Plateau (Fig. 4.1D) and cessation of the Hikurangi Plateau subduction (Davy, 2014). With ongoing southeast-ward migration of the TTJ, its western spreading segment (Pacific-Phoenix plate boundary) came close to the eastern margin of the Chatham Rise shortly before 90 Ma (Fig. 4.17D). N-S to NNW-SSE directed spreading propagated in SWW direction of the spreading Pacific-Phoenix spreading segment south of the eastern Chatham Rise may explain the onset of seafloor spreading (Barrett et al., 2018; Davy, 2014; Davy et al., 2008; Eagles et al., 2004a; Larter et al., 2002), but would require an around 200-km-long-offset transform at the eastern Chatham Rise margin (Fig. 4.17D). However, short time later at around 85 Ma seafloor spreading have been also initiated west of the UFZ where c34n(y) have been identified south the SE Chatham Terrace and profile AWI-20160200 (Figs. 4.16 and 17E; Larter et al., 2002; Wobbe et al., 2012), but we suggest that continental rifting and crustal extension were still ongoing along the SE Chatham Terrace at that time. The formation of grabens on the SE Chatham Terrace along AWI-20160100 and AWI-20160200 may be an evidence for that but rifting and block faulting leading the formation of the Stuttgart Seamount may have also occurred before 90 Ma. However, the onset of seafloor spreading probably also led to enhanced extension in the Bounty Trough and Great South Basin, where rapid cooling at the Sisters Shear Zone lasted until 82 Ma (Fig. 4.17E; Kula et al., 2009, 2007; Mortimer et al., 2016).

We interpret HVLCs below the eastern Chatham Rise as magmatic underplating (Fig. 4.15B) and magmatically modified lower continental crust (Fig. 4.15A). The SE Chatham Terrace west of the UFZ is interpreted as a broad continent-ocean transition zone (hybrid crust), which consists of highly thinned continental crust slightly modified by magmatic activity during the evolution of the seamounts. $^{40}\text{Ar}/^{39}\text{Ar}$ age data from alkaline basalts of the SE Chatham Terrace's guyots and seamount are in the range of 86-84 Ma (Fig. 4.2C; Mortimer et al., 2019b) and contemporaneous alkaline magmatism affected Pitt Island (85-82 Ma; Panter et al., 2006) and seamounts located on oceanic crust north of the eastern Chatham Rise (86-81 Ma; Homrighausen et al., 2018; Mortimer et al., 2019b). At the time of magmatism of Erik and Frankfurt Seamounts (Fig. 4.2C), the SE Chatham Terrace already was at water depths of 2000 to 2500 m, which can be estimated from the difference between the base and top of these guyots. The ages are in good agreement with the 88 Ma onset of seafloor spreading south of the SE Chatham Terrace. However, a relationship seafloor spreading cannot explain the magmatic activity far away from the vicinity of the SE Chatham Terrace (i.e. Chatham Islands and north of the eastern Chatham Rise). Furthermore, the magmatism around the Chatham Rise has intraplate setting and its alkaline character strongly suggests a fertile source unrelated to seafloor spreading (Mortimer et al., 2019b; Panter et al., 2006). We explain the origin of the SE Chatham Terrace guyots by mantle upwelling through a slab window after the subducted slab became detached at around 90 Ma (Fig. 4.17D). Slab window formation is capable to trigger upwelling mantle flow and increasing mantle temperatures by carrying deeper and hotter material so shallower mantle levels (e.g. Thorkelson, 1996). Accordingly, we suggest that the inferred magmatic underplating along AWI-20160300 and AWI-20160200 (Figs. 4.15A and 4.15B) is

also related to mantle upwelling through a slab window (Fig. 4.17E). Upwelling mantle probably underplated the eastern Chatham Rise along our profile AWI-20160200 (Fig. 4.15E), modified the previously exhumed lower continental crust along AWI-20160300 (Fig. 4.15E), caused magmatism of the Southern Volcanics on Pitt Island, formed the first seamounts on the SE Chatham Terrace and slightly modified the SE Chatham Terrace by magmatic activity (Fig. 4.17E). The HVLCs recognised in the Bounty Trough (Grobys et al., 2007) and the inferred mafic complex on the Campbell Plateau (Tulloch et al., 2019) might be also related to the slab window formation. On Pitt Island and the SE Chatham Terrace, the magma probably ascended through pre-existing extension-related fault systems in already rifted and thinned continental crust. This can explain the geometrical arrangement and elongated geometry of the seamounts (Figs. 4.2A and 4.2C). Eventually, the slab window formation may have also initiated seafloor spreading by shallower melting east and west of the UFZ before 83 Ma. Hoernle et al. (2019) found isotopic evidence for an HIMU endmember, which is common in the volcanic provinces onshore New Zealand, on Chatham Rise, SE Chatham Terrace and Hikurangi Plateau between 99 and 69 Ma. This indicates that the upwelling mantle was most likely caused by a deep and long-lived mantle plume, already active before the slab detachment at the Chatham Rise. Another evidence for plume involvement may be the unique composition of the Pacific-Antarctic ridge basalts, which indicates a different mantle domain for the ridge segments between southern Zealandia and West Antarctica (Park et al., 2019).

After 82 Ma, the seafloor spreading between southern Zealandia and West Antarctica became most likely continuous and more NNW-SSE directed as indicated by the NEE-SWW directed c33r anomaly (~79 Ma) south of the SE Chatham Terrace (Figs. 4.16 and 4.17F). The 79 Ma Western Uprising Seamount may be the latest seamount formed in response to the slab window formation (Fig. 4.17F). No chronological data is available for the time of crustal extension in the Bounty Trough, where the crust is thin and inferred to be close to initiation of seafloor spreading (Grobys et al., 2007). The only zircon and apatite thermochronological data are from the Bounty Islands (Fig. 4.2A) indicate that accelerated cooling probably lasted until 80 Ma, similar to what was found on the Chatham Islands (Mortimer et al., 2016). Extension-related displacement along normal faults in the Haast Schist, onshore South Island, were also active at least in the time interval between 93 and 85 Ma (Mortimer et al., 2015), in agreement with thermochronological data from the Sisters Shear Zone, which indicate decreasing cooling rates at 82 Ma (Kula et al., 2007). Seafloor spreading also became active south of the Bounty Platform and rapidly propagated westward, separating the Campbell Plateau from the western Marie Byrd Land margin (Fig. 4.17F; Eagles et al., 2004a; Larter et al., 2002; Sutherland, 1999; Wobbe et al., 2012). A ridge jump between 80 and 79 Ma from north to south of the Bollons Seamount transferred it to its present situation as part of Zealandia and the Pacific Plate (Davy, 2006). After that, the symmetric pattern of seafloor spreading between southern Zealandia and West Antarctica evolved (Sutherland, 1999). Accordingly, the Chatham Rise as well as large areas of southern Zealandia have been tectonically stable within the Pacific Plate to the present day.

4.7. Conclusions

In this study, we present three newly acquired seismic reflection, seismic refraction/wide-angle reflection and potential field data from the southern Chatham Rise margin, including SE Chatham Terrace, and adjacent oceanic crust. P-wave velocity modelling reveals the crustal structure of these areas and provide new insights into the changeover from a convergent tectonic regime with subduction and collision of the Hikurangi Plateau with the East Gondwana subduction zone to a divergent regime with supercontinent rifting and breakup between Zealandia and West Antarctica.

P-wave velocity models indicate significant differences in crustal thickness between the continental western and eastern Chatham Rise, which we explain by the Hikurangi Plateau collision with the East Gondwana subduction margin between 110 and 100 Ma. Gravity modelling and wide-angle seismic reflection data indicate that the extent of the Hikurangi Plateau subduction and underthrusting did not progress very far southward beneath the Chatham Rise as previously suspected. It is plausible that the subduction caused thickening and uplift of the outer Chatham accretionary prism before cessation of the Hikurangi Plateau subduction.

Among the abundant E-W striking gravity lineaments, several NE-SW to NEE-SWW striking lineations and half-grabens indicate NW-SE extension along the southern Chatham Rise margin. We infer that the onset of NW-SE crustal extension led to reactivation of former E-W striking thrust faults within the Chatham accretionary prism as normal faults after 105 Ma. Subsequently, younger NE-SW to NEE-SWW striking normal faults started to evolve. Crustal extension was probably triggered by shallowing of the slab due to the Hikurangi Plateau collision and/or a rollback of the subducting slab.

The P-wave velocity models indicate oceanic crust south of an area where lower continental crust is exhumed at the easternmost Chatham Rise margin east of the UFZ. This piece of lower continental crust was likely exhumed during prolonged rifting since ~100 Ma. The formation of the oceanic crust was initiated at ~88 Ma east of the UFZ where the continental crust was already thin and weak.

As indicated by the seismic refraction data, the SE Chatham Terrace west of the UFZ represents a broad continent-ocean transition zone consisting of hybrid crust, a very thin continental crust modified by magmatic activity. After initiation of seafloor spreading east of the UFZ, rifting became intensified in the area of SE Chatham Terrace and further to the west. When the slab of oceanic crust south of the thicker Hikurangi Plateau crust was detached, a slab window opened, leading a pathway for upwelling mantle. In response, alkaline basaltic magmas extruded on the Chatham Islands, formed the SE Chatham Terrace seamounts, magmatically modified the hyper-extended continental crust of the SE Chatham Terrace and underplated the eastern Chatham Rise as evident from the HVLCs identified along the eastern Chatham Rise at ~85 Ma. Between 83 and 79 Ma, seafloor spreading west of the UFZ became stable and continuous, leading to the final separation of Zealandia from Antarctica.

Typical features of both magma-poor and magma-rich margins are present (HVLCs, normal faulting and block rotation) or absent (seaward-dipping reflectors and exhumed mantle) along the southern Chatham Rise margin. Accordingly, we interpret the southern Chatham Rise margin as a unique hybrid rifted margin whose tectonic evolution is influenced by passive rifting, subduction dynamics and upwelling mantle.

Acknowledgements

We thank Captain Oliver Meyer and his crew for their support and assistance during the RV Sonne cruise SO246. We are grateful to the two anonymous reviewers for their constructive comments and suggestions. This project was funded through grant no. 03G0246A of the German Federal Ministry of Education and Research (BMBF) and by AWI internal funding through the AWI Research Program PACES-II and its work package 3.2 "Earth systems on geological timescales: From greenhouse to icehouse world". The involvement of GNS staff was made possible by a grant to GNS from the New Zealand Ministry of Business and Innovation and Employment's Strategic Science Investment Fund and the GNS Science EEZ programme. C.T. has been funded from grants made by the New Zealand Ministry of Business, Innovation and Education to GNS Science and the European

Union's Horizon 2020 research and innovation programme under the Marie Skłodowska-Curie grant agreement #79308. Additional thanks go to the POLMAR Graduate School at AWI which funded a three-month research visit of F.R. at GNS Science in New Zealand.

Maps and figures for this manuscript were created with Generic Mapping Tools (Wessel and Smith, 1998). The authors would also like to thank Emerson E&P Software, Emerson Automation Solutions, for providing licenses for the seismic software Paradigm in the scope of the Emerson Academic Program.

Supplemental tables

Tab. S4.1: Number of picks (n), RMS Misfit, and χ^2 for different layers of the P-wave velocity model along profile AWI-20160100.

Velocity layer	Phases	n	RMS Misfit (s)	χ^2
1, rfl	waterwave	2807	0.045	0.439
2, rfl	$P_{sed2}P$, $P_{uc}P_{(oceanic)}$	948	0.045	0.202
3, rfr	P_{sed2} , $P_{uc(oceanic)}$	560	0.033	0.313
3, rfl	$P_{uc}P_{(continental)}$	98	0.045	0.187
4, rfr	$P_{ic(oceanic)}$	4033	0.07	0.9
4, rfl	$P_{ic}P_{(continental)}$, $P_mP_{(oceanic)}$	3576	0.066	0.499
5, rfr	$P_{ic(continental)}$	1691	0.086	1.243
5, rfl	$P_mP_{(continental)}$	1558	0.106	1.388
6, rfr	P_{HVLZ}	1102	0.055	0.532
6, rfl	$P_mP_{(HVLZ)}$	1472	0.07	0.518
7, rfr	P_n	2089	0.073	0.819
All layers	All phases	19934	0.069	0.72

Tab. S4.2: Number of picks (n), RMS Misfit, and χ^2 for different layers of the P-wave velocity model along profile AWI-20160200.

Velocity layer	Phases	n	RMS Misfit (s)	χ^2
1, rfl	waterwave	3858	0.070	0.188
2, rfr	P_{sed1}	23	0.039	0.148
2, rfl	$P_{sed2}P$, $P_{uc1}P$	740	0.108	0.212
3, rfr	P_{sed2}	368	0.048	0.390
3, rfl	$P_{sed2}P$, $P_{uc1}P$	592	0.124	0.606
4, rfr	P_{uc1}	3425	0.075	0.310
4, rfl	$P_{uc2}P$	125	0.090	0.289
5, rfr	P_{uc2}	5614	0.105	0.514
5, rfl	$P_{ic}P$	1601	0.136	0.657
6, rfr	P_{ic}	6137	0.125	0.735
6, rfl	P_mP , $P_{HVLZ}P$	9200	0.169	1.146
7, rfl	$P_mP_{(HVLZ)}$	4668	0.214	1.733
8, rfr	P_n	5425	0.212	1.646
8, rfl	P_nP	1395	0.174	1.144
All layers	All phases	43171	0.153	0.928

Tab. S4.3: Number of picks (n), RMS Misfit, and χ^2 for different layers of the P-wave velocity model along profile AWI-20160300.

Velocity layer	Phases	n	RMS Misfit (s)	χ^2
1, rfl	waterwave	2866	0.064	0.202
2, rfr	P_{sed1}	46	0.051	0.335
2, rfl	$P_{sed2}P$, $P_{uc1}P$	615	0.069	0.122
3, rfr	P_{sed2}	177	0.07	0.788
3, rfl	$P_{sed2}P$, $P_{uc1}P$, $P_{uc2}P$	181	0.09	0.157
4, rfr	P_{uc1}	2160	0.107	0.637
4, rfl	$P_{uc2}P$	255	0.1	0.628
5, rfr	P_{uc2}	5039	0.139	0.97
5, rfl	$P_{ic}P$	1476	0.167	1.208
6, rfr	P_{ic}	6597	0.129	0.778
6, rfl	P_mP	10572	0.165	1.094
7, rfr	P_n	2525	0.172	1.203
All layers	All phases	32509	0.142	0.885

Supplemental figures

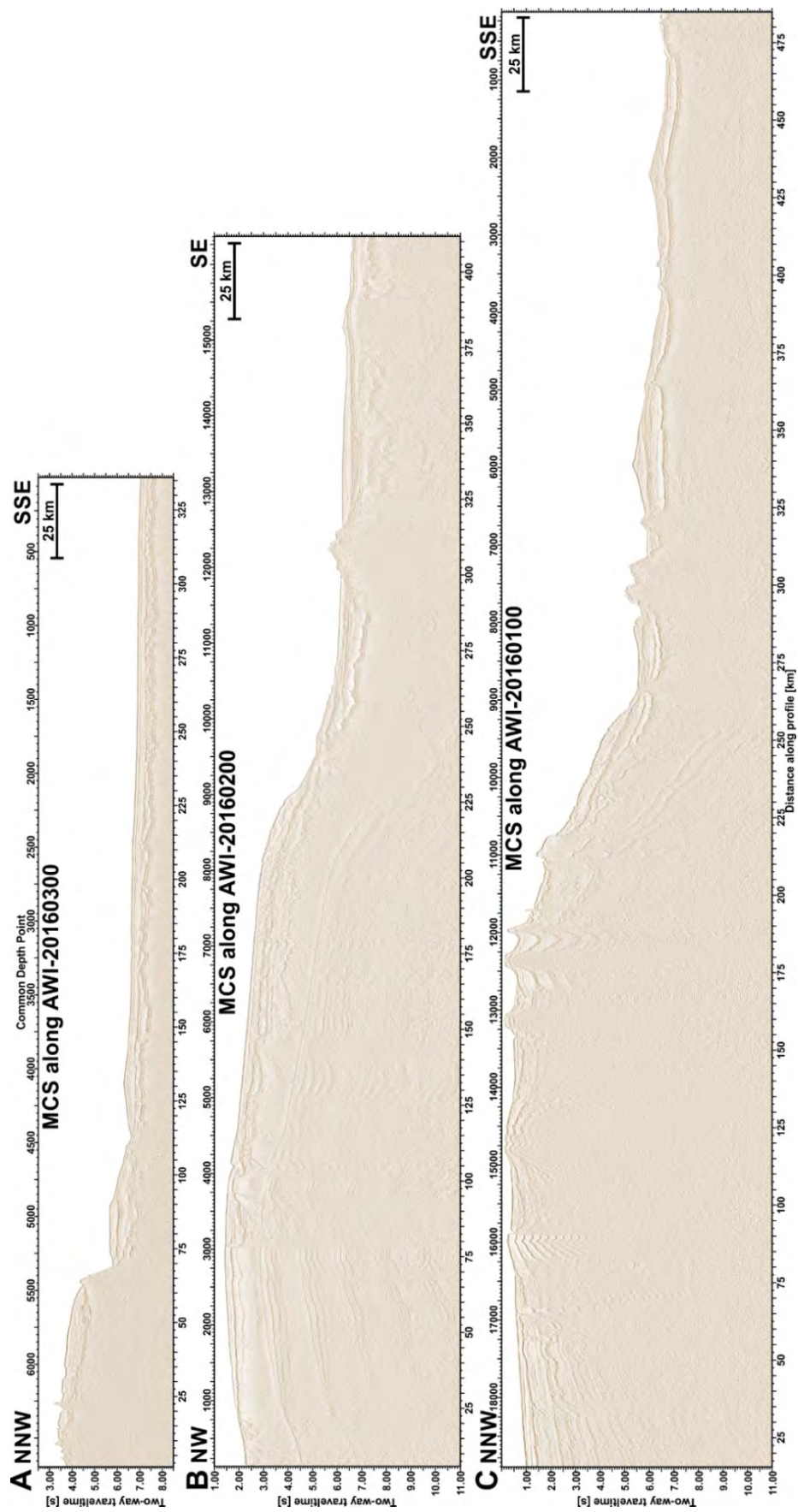


Fig. S4.1: Uninterpreted time-migrated seismic reflection profiles (A) AWI-20160301, (B) AWI-20160002, and (C) AWI-20160001. Y-axis limits differ but the vertical exaggeration is the same in all three profiles.

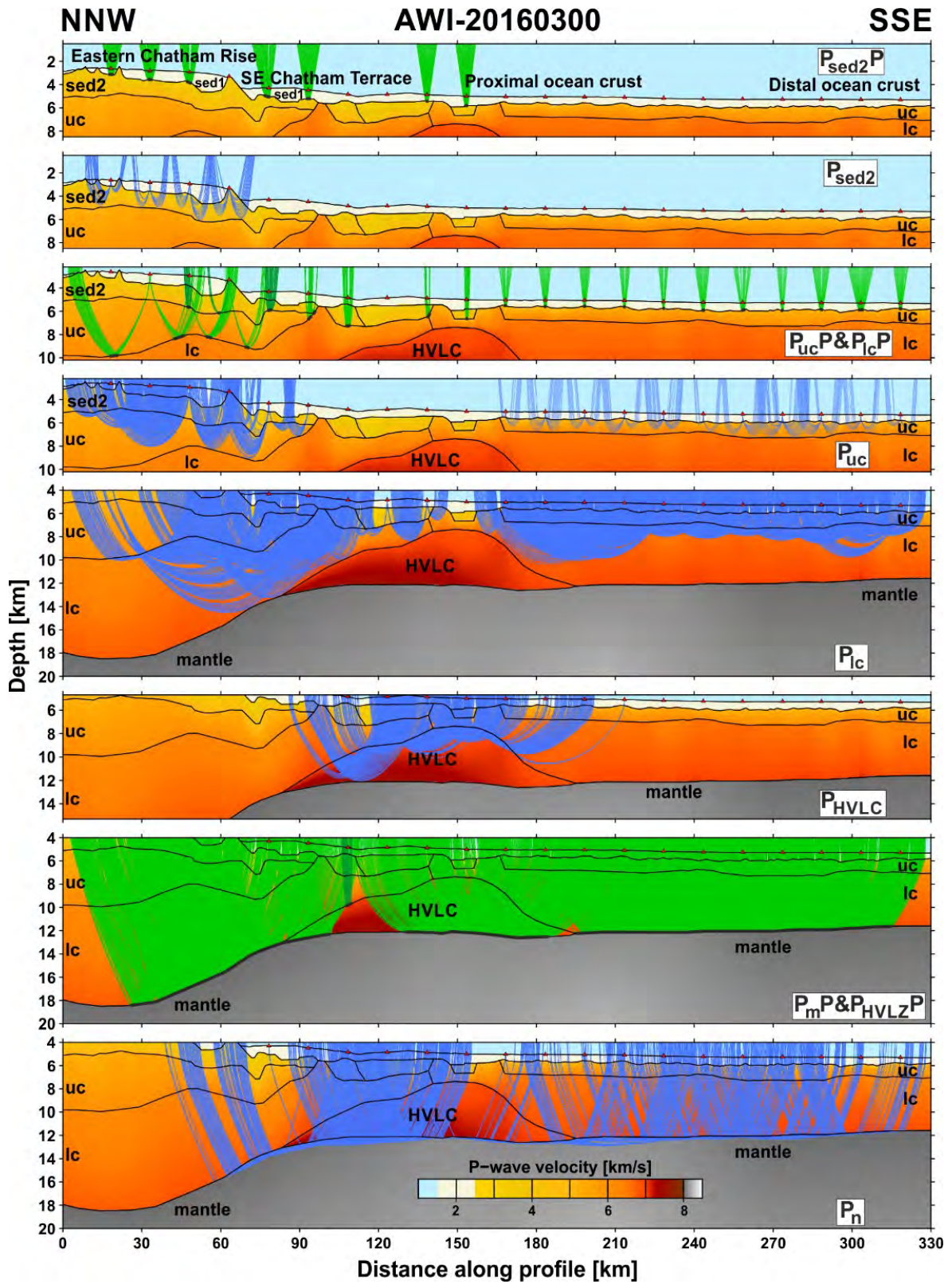


Fig. S4.2: Ray coverage plots for the different identified reflected (green colours) and refracted (blue colours) wave phases along seismic refraction profile AWI-20160300.

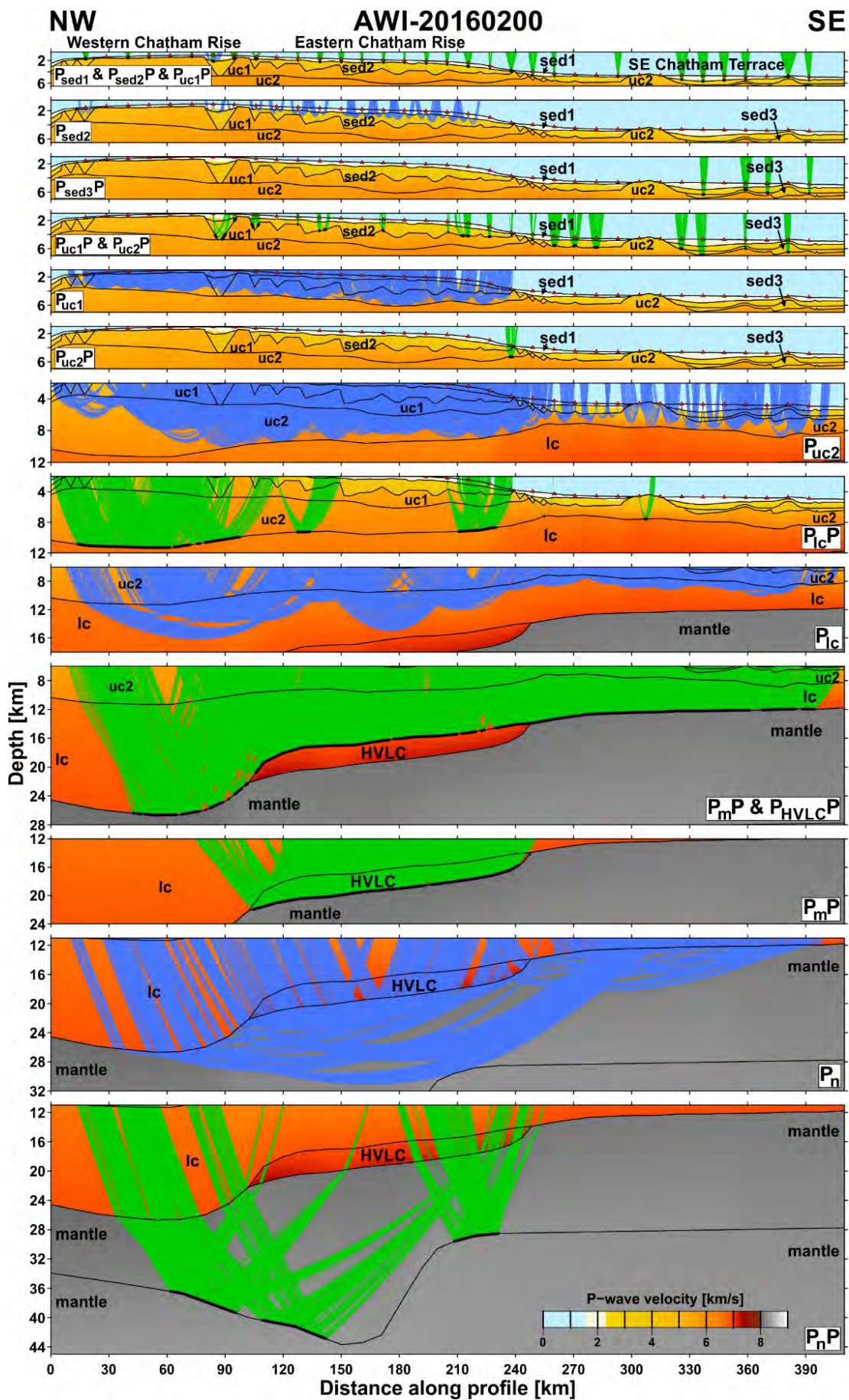


Fig. S4.3: Ray coverage plots for the different identified reflected (green colours) and refracted (blue colours) wave phases along seismic refraction profile AWI-20160200.

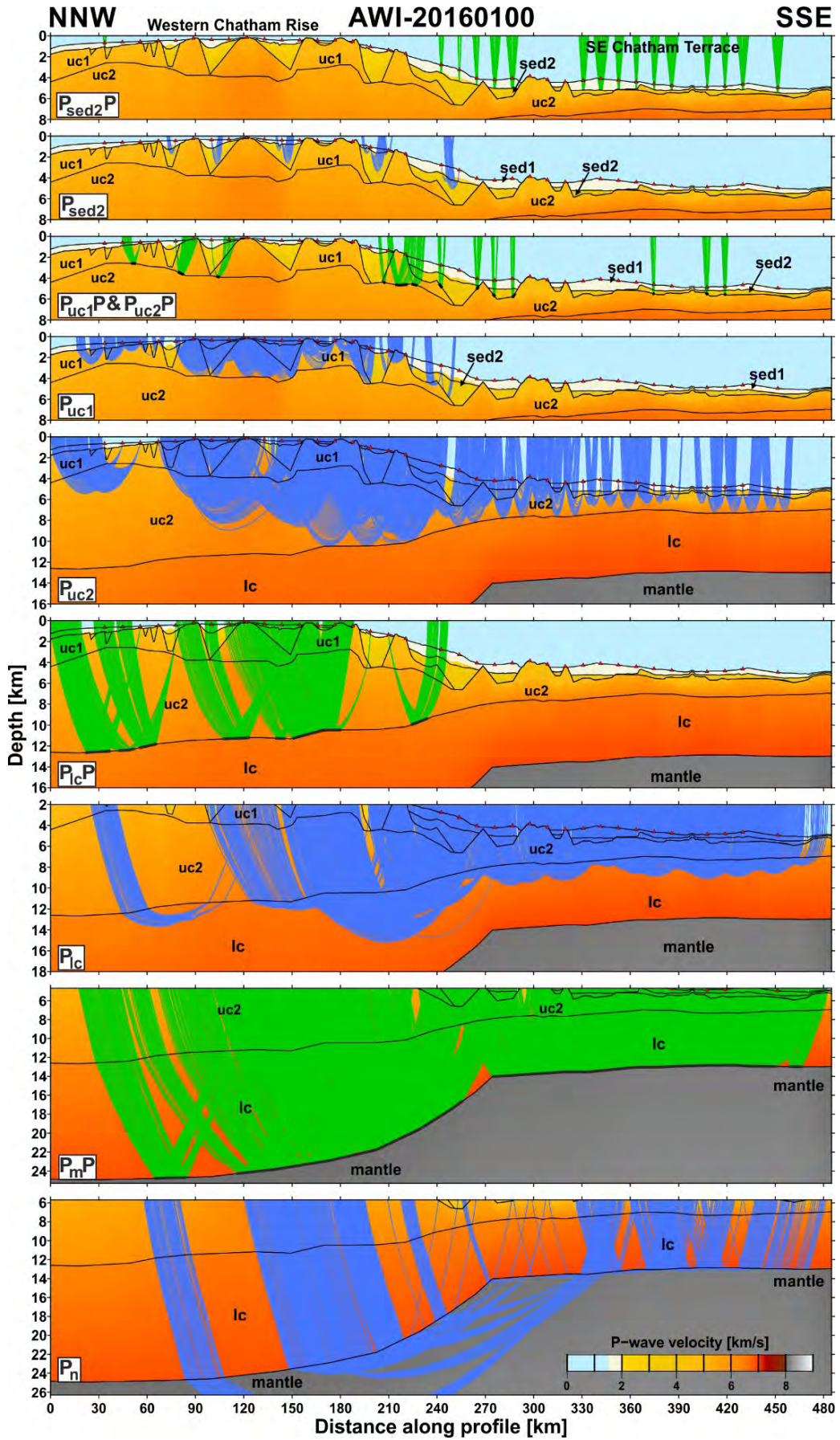


Fig. S4.4: Ray coverage plots for the different identified reflected (green colours) and refracted (blue colours) wave phases along seismic refraction profile AWI-20160100.

5. Manuscript II

Extent and cessation of the mid-Cretaceous Hikurangi Plateau underthrusting: Impact on global plate tectonics and the sub-marine Chatham Rise

By F. Riefstahl¹, K. Gohl¹, B. Davy², R. Barrett³

¹Alfred Wegener Institute Helmholtz-Centre for Polar and Marine Research, Bremerhaven, Germany

²GNS Science, Avalon, Lower Hutt, New Zealand

³Christian-Albrechts-Universität zu Kiel, Institut für Geowissenschaften, Kiel, Germany

Abstract

Subduction of oceanic plateaux are events that have occurred infrequently in Earth's history but are thought to considerably influence regional tectonics and global plate motions. The mid-Cretaceous collision of the Hikurangi Plateau with the then-active East Gondwana margin falls into the same period as a global plate reorganisation event and a sudden change from subduction to extension in the continent of Zealandia. Using recently acquired seismic refraction and gravity data, we demonstrate that the extent of the Hikurangi Plateau beneath the submarine Chatham Rise is less than previously suggested and locate parts of the subducted Phoenix Plate south of the plateau. Flattening, rollback and detachment of the southern Phoenix slab played an important role in the regional change in tectonic forces across Zealandia. We suggest that fragmentation of the Gondwana subduction zone in response to subduction cessation along the Hikurangi Plateau segment potentially triggered the regional mid-Cretaceous plate reorganisation event.

5.1. Introduction

The formation of oceanic plateaux – extraordinarily thick oceanic crust resulting from primarily basaltic magmatism – is considered as the most extreme volcanic events on Earth. The life cycle of oceanic plateaux may include obduction and enlargement of landmasses, underplating through shallow flat-subduction or subduction and recycling back into the Earth’s mantle, both of which represent rare events in global geodynamics. Their influence on global plate tectonics and its significance within the Wilson’s Cycle (Dewey & Burke, 1974) remain, however, enigmatic. Two well-studied, but contradictory, examples of the influence of oceanic plateaux on regional and global tectonics include (I) the still-ongoing collision of the Ontong Java Plateau with the Melanesian arc, which led to partial subduction and crustal accretion (Mann & Taira, 2004; Taira et al., 2004), and (II) the Late Cretaceous lithospheric removal of the subducted Shatsky Rise conjugate, which led to regional-scale surface rebound and, thereby, initiated the Laramide Orogeny in North America (Liu et al., 2010). Both examples were accompanied by complex collisional tectonics but, while subduction of the Shatsky Rise conjugate resulted in spatially-limited uplift, the collision of the Ontong Java Plateau triggered subduction cessation and reversal, which influenced the motion of the Australian Plate in the mid-Miocene (Knesel et al., 2008) and induced rapid changes in plate motions in the late Miocene (Austermann et al., 2011). Accordingly, oceanic plateau collision and subduction are capable of triggering both far-field and local tectonic effects.

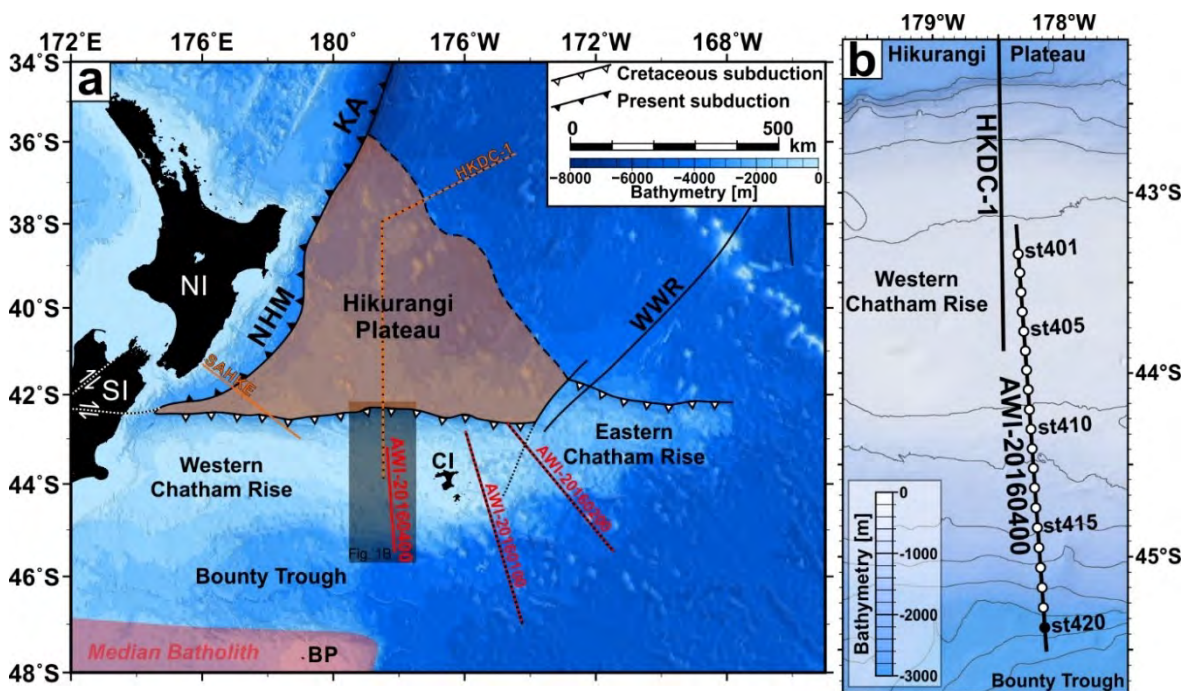


Fig. 5.1: (a) Bathymetry map of the Chatham Rise and Hikurangi Plateau with seismic refraction profiles (red) and seismic reflection profiles (orange). BP = Bounty Platform, CI = Chatham Islands, KA = Kermadec Arc, NHM = Northern Hikurangi Margin, NI = North Island, SI = South Island, WWR = West Wishbone Ridge. (b) Detailed map view of seismic refraction profile AWI-20160400 that is a southward extension of the previously collected seismic reflection profile HKDC-1. White dots mark locations of ocean-bottom seismometers (OBS). The black dot marks a failed OBS record (st420).

Another unique example for the subduction of oceanic plateaux is the Hikurangi Plateau (Fig. 5.1a), which has undergone a two-fold subduction history. The southward-directed collision of the Hikurangi Plateau with the long-lived East Gondwana active margin during the mid-Cretaceous is believed to have initiated the end of subduction activity in the area of New Zealand’s South Island and Chatham Rise (Davy et al., 2008; Fig. 5.1a). Subsequently, extensional processes, including the formation of rift grabens and intraplate volcanic activity, started to affect the micro-continent ‘Zealandia’. The collision of the Hikurangi Plateau with the East Gondwana margin, the end of

compressional tectonics, and the initiation of extension all fell within the time range of a global-scale plate-reorganisation event that affected all major tectonic plates (Matthews et al., 2012). The second stage of subduction of the Hikurangi Plateau, this time directed westward at the Australian-Pacific plate boundary beneath the North Island of New Zealand, began at least in the Miocene and is still ongoing (Reyners, 2013; Timm et al., 2014).

In this study, we present seismic reflection and wide-angle reflection/refraction data along a profile across the southwestern Chatham Rise margin, where the Hikurangi Plateau is thought to have underthrust the former East Gondwana active margin. We combine our newly acquired data with published seismic reflection and wide-angle reflection/refraction data to map the extent of the underthrust Hikurangi Plateau and oceanic crust of the former Phoenix Plate beneath the Chatham Rise. The aim of this is to shed light on the processes of oceanic plateau subduction, resulting regional effects, and global consequences on plate tectonics.

5.2. Geological and tectonic background

The Hikurangi Plateau (Fig. 5.1a) formed between 125 and 120 Ma as part of the Ontong Java Nui superplateau, the Earth's largest oceanic plateau (Hoernle et al., 2010; Taylor, 2006). Shortly after its formation, Ontong Java Nui rifted and drifted apart into three major pieces – the Ontong Java, Manihiki and Hikurangi plateaux (Hochmuth et al., 2015; Hochmuth & Gohl, 2017). The Hikurangi Plateau drifted southward before underthrusting, partially subducting beneath, and jamming a ~1500 km-wide section of the East Gondwana subduction zone at ~100 Ma (Davy et al., 2008; Davy, 2014).

Present knowledge of the extent and thickness of the subducted and underthrust Hikurangi Plateau beneath southern Zealandia, especially along the active Cretaceous margin (Fig. 5.1a), is based on only a few data. The Hikurangi Plateau's eastern extent is coincident with a prominent mid-Cretaceous dextral strike-slip fault zone – the West Wishbone Ridge (WWR, Fig. 5.1a), which evolved in response to plateau collision (Barrett et al., 2018). The top of the subducted Hikurangi Plateau has been imaged with seismic reflection profiles beneath several areas of the present-day submarine Chatham Rise and up to 100 km south of it (Fig. 5.1a; Bland et al., 2015; Davy et al., 2008). Gravity models suggest a thickness of 12-17 km for the Hikurangi Plateau north of Chatham Rise (Barrett et al., 2018; Davy et al., 2008). In the north, where the Hikurangi Plateau is currently subducting westwards beneath the North Island, seismic refraction profiles indicate that the plateau is significantly thinner, reaching a thickness of only 10 km (Mochizuki et al., 2019; Scherwath et al., 2010). Further north along the southern Kermadec arc (Fig. 5.1a), geochemical variations of arc basalts-andesites provide evidence that a much larger proportion of the Hikurangi Plateau has been subducted within the past 10 Myr (Timm et al., 2014, 2016). V_p and V_s/V_p models based on seismological data suggest a thickness of 30-35 km for the Hikurangi Plateau in the area beneath the lower North Island and South Island, where it is already deeply subducted to depths of 65-100 km (Reyners et al., 2011; Reyners, et al., 2017b). On the basis of these models, Reyners et al. (2011) inferred that the entire Chatham Rise is 'underplated' by the Hikurangi Plateau. Detailed analyses of gravity gradient fabrics led Davy (2014) to extend the limit of the Plateau southward, beneath the inner Bounty Trough. However, the full southern extent of the Hikurangi Plateau remains poorly constrained. Seismic refraction and deep-crustal seismic reflection studies indicate the presence of old oceanic crust of normal thickness beneath the sedimentary basins and stretched continental crust off the east coast of the South Island (Van Avendonk et al., 2004; Godfrey et al., 2001; Mortimer et al., 2002; Scherwath et al., 2003), highlighting the absence of the plateau in this region.

Shortly after subduction cessation and jamming of the Hikurangi Plateau, the East Gondwana margin was affected by widespread extension and rifting during the 'Zealandia Rift Phase'. Evidence for this even is provided by a major Albian unconformity that has been radiometrically dated at ~100 Ma with the youngest associated zircon population (Laird & Bradshaw, 2004). This rapid transition between tectonic regimes is also made evident by a switch from arc-constructive processes and subduction-related magmatism in the Median Batholith (Fig. 5.1a), to arc-destructive processes such as detachment faulting and metamorphic doming (Schwartz et al., 2016). Long-lasting arc magmatism was replaced by alkaline intraplate magmatism, which was spatially widespread but overall of low volume (Hoernle et al., 2020; van der Meer et al., 2016; 2017; McCoy-West et al., 2010; Mortimer et al., 2016; Panter et al., 2006; Tulloch et al., 2019). Crustal extension in the form of half-graben formation was substantial, and affected the forearc and back-arc of the Median Batholith (Tulloch et al., 2019), as well as terrestrial sediments that had accumulated in several fault-controlled basins around the present North and South Islands in the mid-Cretaceous (e.g. Strogen et al., 2017). Opening of the Bounty Trough (Fig. 5.1a) presumably also occurred during the 'Zealandia Rift Phase' before seafloor spreading was initiated shortly after 90 Ma and the then-young Pacific-Antarctic Ridge separated Zealandia from Antarctica at ~80 Ma (Riefstahl et al., 2020).

5.3. Methods

We collected deep-crustal seismic wide-angle reflection and refraction, multi-channel seismic (MCS), and gravity data along the N-S oriented profile AWI-20160400 (Fig. 5.1b). The geophysical data were acquired during the SO246 expedition on RV Sonne in 2016 (Gohl & Werner, 2016). 20 ocean-bottom seismometer (OBS) and hydrophone (OBH) systems were deployed at ~15 km spacings along the profile (Fig. 5.1b), which extends across the southern Chatham Rise and the marginal area of the Bounty Trough. Our profile extends the MCS profile HKDC-1 southwards, where the top of the under-thrust Hikurangi Plateau has been imaged up to 100 km south of the Chatham Rise (Davy et al., 2008). Our seismic source was made up of 8 G-Guns in 2x4 G-Gun clusters with a total volume of 68 l (4150 in³), and was fired at 205 bar every 60 s while towed 10 m below sea level. Subsequently, the seismic refraction data and MCS data were processed with standard methods (Riefstahl et al., 2020), and a P-wave velocity-depth distribution model was derived using traveltimes modelling/inversion with the Rayinvr software (Zelt & Smith, 1992). Shipborne gravity data were used to model the density-depth distribution, which particularly helped to model zones that are sparsely resolved by seismic refracted and reflected phases. Detailed information about the setup and modelling procedure is provided in the supplement.

5.4. Results and Interpretation

Free-air gravity anomalies across the Chatham Rise have been correlated with half-graben structures, which are mostly E-W orientated (Davy, 2014). In contrast with the area around the Chatham Islands (Riefstahl et al., 2020), the Chatham Rise along AWI-20160400 is completely covered with sedimentary strata. Here, we find a series of 10-15 km broad half-grabens that are separated by several near-seafloor basement highs between 0 to 130 km along the profile (Fig. 5.2a and 6.3). These half-grabens likely represent thrust faults in the Chatham Rise accretionary wedge that were reactivated as normal faults during the Zealandia Rift Phase after 105 Ma (Riefstahl et al., 2020; Tulloch et al., 2019). The two largest and deepest graben structures are separated by two distinct basement highs at the southern slope of the Chatham Rise, where the seafloor deepens from ~400 to 3500 m.b.s.l. (Fig. 5.2). These large grabens are most likely related to rifting along the southern Chatham Rise margin and in the Bounty Trough (Riefstahl et al., 2020). Further south of

the basement high at ~200 km along profile, the upper surface of the basement is comparatively smooth, but some smaller graben structures are evident from the OBS and MCS data (Figs. 5.2 and 5.3).

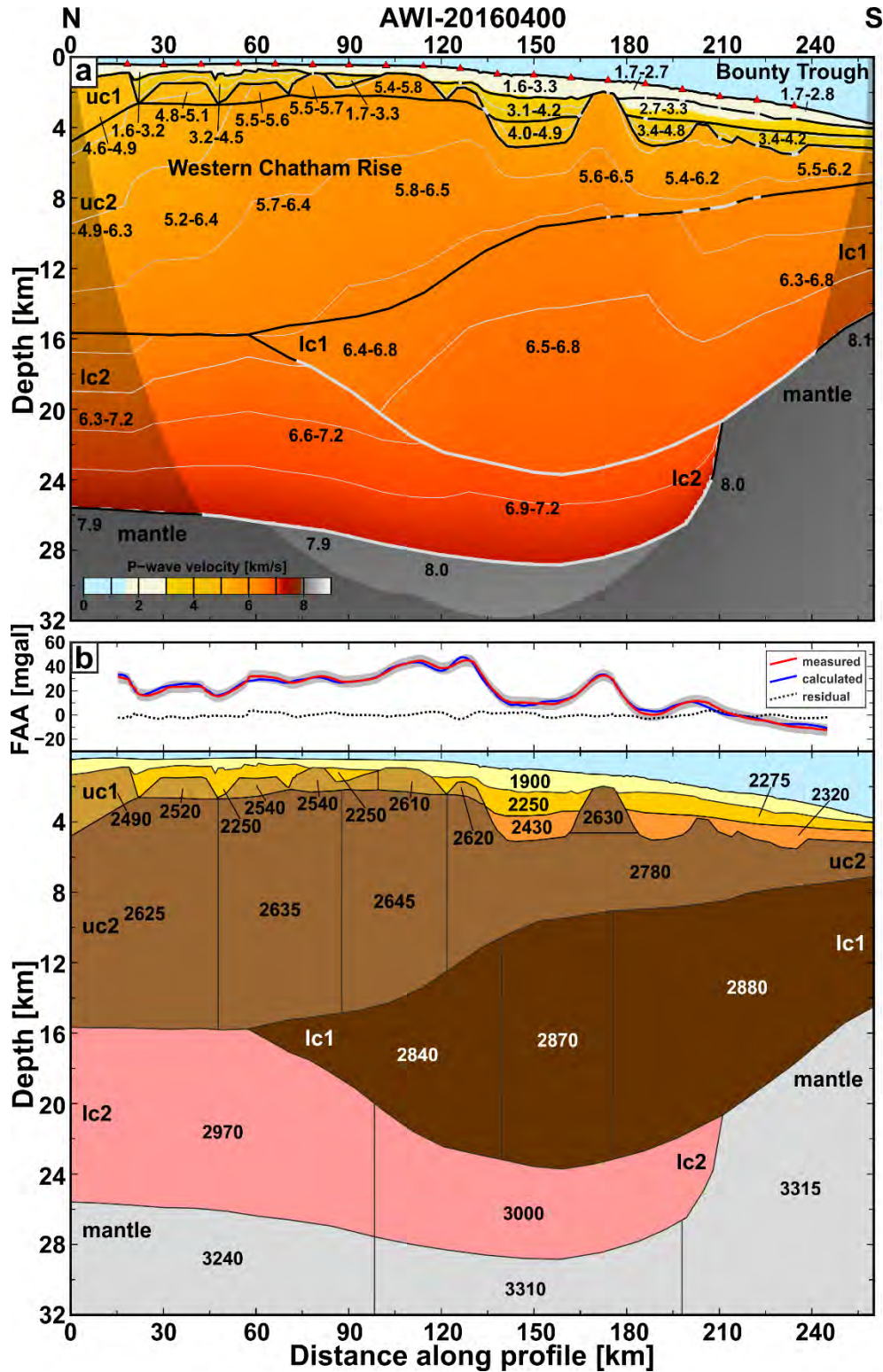


Fig. 5.2: (a) P-wave velocity-depth model along profile AWI-20160400. The presented model is based on 20530 picked arrivals. RMS traveltimes is 0.130 s with a corresponding χ^2 of 0.706. Detailed statistics on the P-wave velocity-depth model are shown in Tabs. S5.1 and S5.2. (b) Density-depth model from measured and modelled free-air gravity anomaly (FAA). Densities are given in kg/m^3 .

Based on MCS data (Fig. 5.3) and recorded reflection/refraction phases (Fig. 5.4a and b), we subdivide the sedimentary strata into: i) uppermost, well-layered sediments (layer sed1) that represent a post-rift deposit covering the Chatham Rise basement and underlying strata; and ii) syn-rift units (layers sed2 and sed3) that fill and cover the graben structures. Layers sed2 and sed3 merge into a single layer along the top of the Chatham Rise. The total sedimentary cover reaches a maximum thickness of 3.5 km within the largest graben at the southern slope of the Chatham Rise (between 130 to 170 km profile distance). The oldest sediments within this graben may have an age of up to 100 Ma, similar to those from the Chatham Islands (Campbell et al., 1993). Within the syn-rift sedimentary layers sed2 and sed3, P-wave velocities mostly increase gradually up to 4.9 km/s. Distinct reflections ($P_{\text{sed2}}P$ phase, Figs. 5.4a and S5.1), however, indicate a stepwise increase of P-wave velocities between layers sed1 and sed2. Estimated uncertainties range between ± 0.10 to ± 0.20 km for sedimentary layer depths, and ± 0.10 to ± 0.20 km/s for the P-wave velocities within the layers (Tab. 5.1). Overall the ray coverage is relatively low for the sedimentary layers (Fig. 5.4a-b and S5.1) but, as the MCS and wide-angle reflection / refraction data are in good agreement, we consider that the architecture of the sedimentary strata is well-resolved.

Tab. 5.1 Layer parameters and corresponding uncertainties along AWI-20160400. P-wave velocities vary within one respective layer due to different geological settings and burial depths.

Layer	Type	P-wave velocity range [km/s]	Velocity uncertainty [km/s]	Upper boundary uncertainty [km]	Densities / Density range [kg/m ³]
Water Layer					
0 - 260 km	Water	1.5	± 0.01	0.00	1020
Sediment 1 (sed1)					
0 - 170 km	Post-rift sed.	1.6 - 3.3	± 0.10	± 0.10	1900
170 - 260 km	Post-rift sed.	1.7 - 2.8	± 0.10	± 0.10	1900
Sediment 2 (sed2)					
0 - 170 km	Syn-rift sed.	3.1 - 4.2	± 0.10	± 0.10	2250
170 - 260 km	Post- or syn-rift sed.	2.7 - 3.3	± 0.15	± 0.15	2250 - 2275
Sediment 3 (sed3)					
130 - 170 km	Syn-rift sed.	4.0 - 4.9	± 0.20	± 0.20	2430
170 - 260 km	Syn-rift sed.	3.4 - 4.8	± 0.20	± 0.20	2320
Upper crust 1 (uc1)					
0 - 135 km	Continental	4.6 - 5.8	± 0.10	$\pm 0.10 - \pm 0.20$	2490 - 2620
Upper crust 2 (uc2)					
0 - 120 km	Continental	4.9 - 6.5	± 0.15	± 0.15	2625 - 2645
120 - 260 km	Continental	5.4 - 6.5	± 0.2	± 0.20	2780
Lower crust 1 (lc1)					
55 - 260 km	Continental	6.3 - 6.8	± 0.20	± 0.30	2840 - 2885*
Lower crust 2 (lc2)					
0 - 100 km	Oceanic plateau	6.3 - 7.2	± 0.25	± 0.30	2970
100 - 215 km	Oceanic crust	6.9 - 7.2	± 0.25	± 0.40	3000
Mantle					
0 - 100 km	Mantle	7.9 - 8.0	± 0.30	± 0.40	3240
100 - 260 km	Mantle	8.0 - 8.1	± 0.30	± 0.40	3310 - 3315

*Density is 2650 kg/m³ at the basement high between 165-180 km profile distance

The basement of the Chatham Rise and the southern slope can be divided into two upper crustal layers (Fig. 5.2 and Tab. 5.1, layers uc1 and uc2). Both layers are well-resolved by P_{uc1} and P_{uc2} refraction phases (Fig. 5.4b and 5.5). Layer uc1 is only present along the crest of the Chatham Rise, where the total thickness of the upper crustal layers is up to 14.5 ± 0.2 km, between 0-135 km along profile (Fig. 5.2). The thickness of layer uc2 continuously decreases across the Chatham Rise slope, reaching 2 ± 0.1 km at the border of the Bounty Trough. The absence of any reflection at the base of layer uc1 indicates that the P-wave velocities gradually increase from layer uc1 to uc2. Moreover, across the Chatham Rise, we find P-wave velocities and densities within these two upper crustal layers gradually increase southwards towards the large graben at 135 km along profile (Fig. 5.2). A similar north to south lateral gradient has also been recognised along two wide-angle reflection/refraction profiles across the eastern Chatham Rise (Riefstahl et al., 2020). We suggest that these lateral P-wave velocity and density gradients are a result of regional metamorphism that affected the forearc of the Mesozoic arc. Such regional metamorphism would be consistent with geological observations from the Chatham Islands (Mortimer et al., 2019a). Accordingly, rock assemblages consistent with the modelled P-wave velocities and densities range from sub- or lower greenschist facies (i.e. meta-greywackes to schists) in the north, to upper greenschist facies (mainly schist) in the southern part of profile AWI-20160400 (Fig. 5.6a).

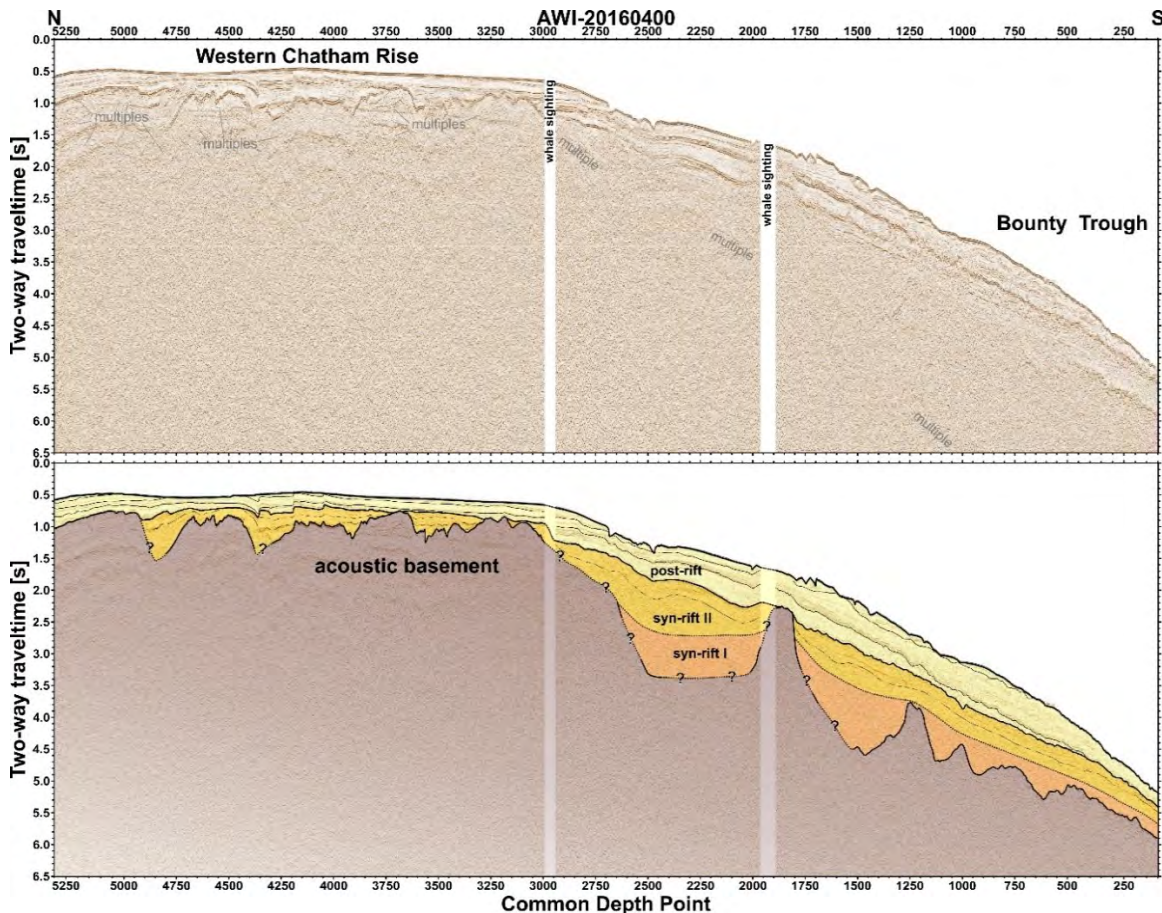


Fig. 5.3: MCS reflection data and interpretation along seismic refraction profile AWI-20160400.

We divided the lower crust of the Chatham Rise into two layers (Fig. 5.2 and Tab. 5.1, layers lc1 and lc2). Layer lc1 is present between ~ 60 and 260 km along profile (Fig. 5.2a). Observed reflections ($P_{lc1}P$) indicate an abrupt increase of P-wave velocities along the upper boundary of layer lc1 (separating it from uc2) between 160 and 220 km along profile. Layer lc1 reaches its maximum thickness (~ 14 km) between 150 and 180 km along profile. In this area, we modelled the highest P-wave velocities ($6.5 - 6.8 \pm 0.2$ km/s) that were moderately resolved by the P_{lc1} refraction phase

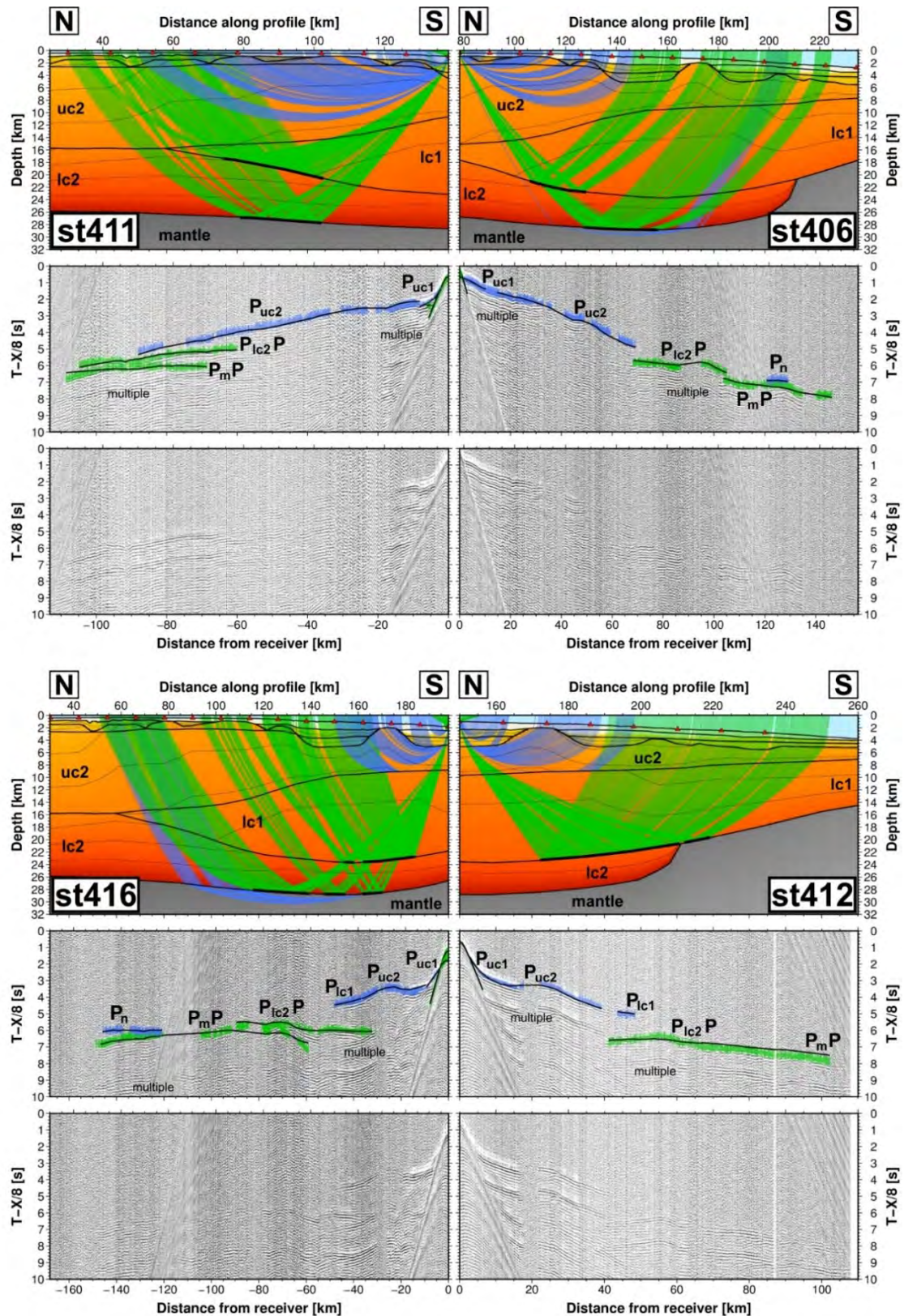


Fig. 5.5: Examples of OBS/OBH records from several stations along profile AWI-20160400 indicating the presence of deep-crustal reflections.

interpret this part of layer lc2 as the underthrust Hikurangi Plateau beneath the Chatham Rise accretionary wedge. A thickness of 10 km for the Hikurangi Plateau is in good agreement with that estimated by Davy et al. (2008) using gravity models along HKDC-1 (10-12 km), as well as with the

~10-km-thickness indicated by P-wave velocity models along the deep crustal seismic SAHKE profile west of our profile AWI-20160400 (Fig. 5.1a; Henrys et al., 2013; Mochizuki et al., 2019; Tozer et al., 2017). Moreover, we find that the layer lc_2 thins to less than 6 km thickness between 60 and 120 km along profile before disappearing ~210 km along profile, features which are well-resolved by continuously recorded $P_{lc_2}P$ and P_mP phases (Figs. 5.4b and 5.5). We interpret the thinning of layer lc_2 between 60 and 120 km along profile as the transition from the thick oceanic Hikurangi Plateau to normal, ~6 km thick oceanic crust: the ancient Phoenix Plate (Fig. 5.6a). The presence of oceanic crust older than and south of the Hikurangi Plateau has previously been inferred to be present below or close to the Chatham Rise (Davy, 2014; Reyners et al., 2017a; Reyners et al., 2017b), but this is the first evidence along a seismic refraction profile for that oceanic crust.

We observe several P_n mantle refractions below the Chatham Rise and underthrust Phoenix Plate (Fig. 5.4b), and note a slight increase in their velocity from 7.9 km/s in the north to 8.1 km/s at the southern slope (Fig. 5.2a). Mochizuki et al. (2019) modelled higher mantle velocities (~8.3 km/s) along the SAHKE profile and interpreted these as indicative of highly depleted upper mantle. Accordingly, the upper mantle below our profile AWI-20160400, with velocities of up to 8.1 km/s, likely consists of less depleted material.

5.5. Discussion

5.5.1. Extent and thickness of the Hikurangi Plateau

We compare the results of our P-wave velocity-depth and gravity models with other observations of the extent of the Hikurangi Plateau and adjacent oceanic crust beneath the Chatham Rise and southern Zealandia region (Fig. 5.6). The 10 km thickness of the Hikurangi Plateau underlying the Chatham Rise implied by our P-wave velocity-depth model along profile AWI-20160400 is in very good agreement with thicknesses derived from (i) gravity models along HKDC-1 line (Fig. 5.6d; Davy et al., 2008); (ii) the AWI-20160100 seismic refraction profile east of the Chatham Islands (Fig. 5.6c; Riefstahl et al., 2020); and (iii) seismic refraction profiles from the northern Hikurangi margin east of the North Island (Fig. 5.6d; Mochizuki et al., 2019; Scherwath et al., 2010; Tozer et al., 2017). The available data from the Hikurangi Plateau do not suggest large variations in thickness along the Chatham Rise between 175°E to 176°W. Contrastingly, at the eastern margin of the Plateau, seismic reflection data and gravity models close to the WWR (Fig. 5.6d; Barrett et al., 2018), as well as seismic refraction profile AWI-20160200 at the southward extension of the WWR on the Chatham Rise (Fig. 5.6b; Riefstahl et al., 2020), indicate a thickness of 12-16 km for the Hikurangi Plateau. This thickening of the Hikurangi Plateau along its eastern margin is likely due to either complex dextral strike-slip movements along the WWR, where compressional and extensional features are in close proximity to each other (Barrett et al., 2018), massive volcanic activity during stretching and rifting from the conjugate Manihiki Plateau (Hochmuth et al., 2015), or reflect normal variations in the crustal thickness of oceanic plateaux (e.g. Hochmuth et al., 2019). The extent of the subducted Hikurangi Plateau beneath the North Island and South Island was previously illustrated using seismological V_p and V_s/V_p models (Reyners et al., 2011; Reyners et al., 2017b). Beneath the eastern South Island, the Hikurangi Plateau has been inferred to dip steeply westwards to a depth of 65-100 km, where it eventually collides with the eastward down-dipping slab of the Australian Plate along the southwest side of the South Island (Reyners et al., 2017b). Here, the Hikurangi Plateau is interpreted to be 30-35 km thick (Fig. 5.6a-c; Reyners, 2013; Reyners et al., 2017b). However, it is important how the base of the Hikurangi Plateau is defined. Reyners et al. (2017b) considered P-wave velocities around 8.5 km/s (= eclogitisation) observed from a seismological network as a proxy for the subducted Hikurangi Plateau. This approach is based on observation

from seismic refraction studies, which noticed similar high or even higher P-wave velocities observed below the 40 km thick Ontong Java Plateau (Furumoto et al., 1976). In this study, we define P-wave velocities higher than 7.9-8.0 km/s as the mantle, which is clearly separated from the Hikurangi Plateau, Phoenix Plate and Chatham Rise crust by a distinct P_{mP} (Moho) reflection similar to the area of the easternmost Chatham Rise where only the Phoenix Plate and not Hikurangi Plateau was not subducted (Riefstahl et al., 2020). If similar high-velocity mantle features exist in the mantle beneath the subducted Hikurangi Plateau, its estimated thickness of 35 km below North and South Island could be an overestimation. We do not rule out that the Hikurangi Plateau is thicker below the North and South Island than below the Chatham Rise since the western part of the Hikurangi Plateau was closer to the Ontong Java Nui eruption centre (Hochmuth et al., 2015), where the Ontong Java Plateau is the Earth's distinctively thickest known oceanic plateau crust (Furumoto et al., 1976). In contrast, the Manihiki Plateau distant from the Ontong Java Nui eruption centre does not show any thicknesses higher than 20 km (Hochmuth et al., 2019). Moreover, large parts of the western Manihiki Plateau are between 17 to 9 km thick (Hochmuth et al., 2019), which is in the same range of the thickness of the Hikurangi Plateau beneath the Chatham Rise (this study; Mochizuki et al., 2019; Riefstahl et al., 2019). Accordingly, we consider our modelled thickness of 10 km for the Hikurangi Plateau below the Chatham Rise as meaningful.

5.5.2. Extent and age of the Phoenix Plate

Based on seismological studies of the South Island, Reyners et al. (2011) suggested that the whole Chatham Rise is underlain by the Hikurangi Plateau. However, the results of modelling along our combined MCS, gravity, and wide-angle seismic reflection/refraction profile AWI-20160400 (Figs. 5.2 and 5.3a) – together with interpreted MCS and wide-angle seismic reflection/refraction profiles east of the Chatham Islands (Riefstahl et al., 2020) (Fig. 5.5b and 5.6c) – show that the underthrust Hikurangi Plateau reaches only approximately half the full N-S lateral extent of the Chatham Rise. Moreover, we find evidence along AWI-20160400 that the oceanic crust of the leading Phoenix Plate is still attached to the Hikurangi Plateau beneath the central Chatham Rise (Fig. 5.6a); however, is detached further east (Figs. 5.5b and 5.6c; Riefstahl et al., 2020). Seismological studies of the southeastern South Island highlight the presence of westward-dipping oceanic crust in the mantle (Reyners et al., 2017b). We suggest that this oceanic crust beneath the South Island (Fig. 5.6d) is the continuation of the Phoenix Plate oceanic crust that we observe beneath the Chatham Rise (Fig. 5.6a). Oceanic crust has also been identified beneath the highly extended continental crust underlying the Cretaceous sedimentary basins east of the South Island and west of our profile AWI-20160400 (Fig. 5.6d; SIGHT-I/II/III; Godfrey et al., 2001; Scherwath et al., 2003; Van Avendonk et al., 2004). East of these basins, gravity anomalies within the inner Bounty Trough have been interpreted to reflect the southern extent of the Hikurangi Plateau and/or oceanic crust (Davy, 2014). Our model derived from the combined refraction seismic and gravity data along profile AWI-20160400 does not directly indicate the presence of oceanic crust in the inner Bounty Trough. Between our profile and the inner Bounty Trough, neither subducted oceanic crust nor remnants of Hikurangi Plateau have been recognised below the 21-km-thick Chatham Rise by the only seismic refraction line crossing the Bounty Trough (Fig. 5.6d; Grobys et al., 2007). However, the northern termination of seismic line AWI-20030002 has very limited ray coverage at the southern Chatham Rise margin (Grobys et al., 2007). Accordingly, the presence of oceanic crust at the northern limit of the Bounty Trough west of our profile AWI-20160400 cannot be ruled out. If oceanic crust is present in that area, it implies that a piece of the ancient Phoenix Plate extending ~1200 km from east to west is still attached to the southern edge of the Hikurangi Plateau (Fig. 5.6d).

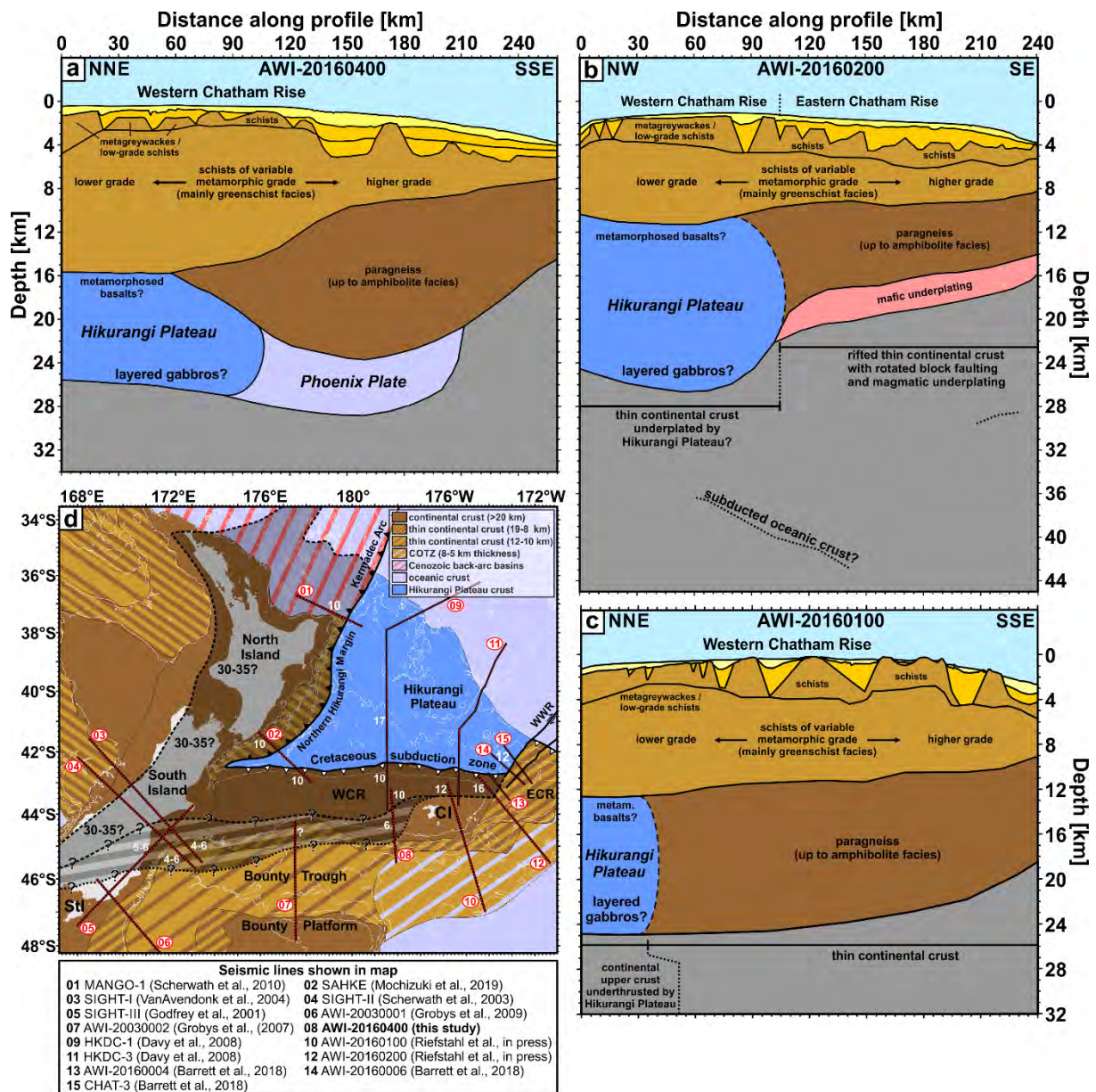


Fig. 5.6: Geological interpretation along seismic refraction profile (a) AWI-20160400 as well as the northern parts of profiles (b) AWI-20160200 and (c) AWI-20160100 indicating the extent of the Hikurangi Plateau under-thrust beneath the western Chatham Rise. The locations of these profiles are shown in Fig. 5.1. (d) Structural map showing crustal types with estimated thicknesses (in km) of the Hikurangi Plateau and oceanic crust. The proposed extent of the under-thrust Hikurangi Plateau and adjacent Phoenix Plate oceanic crust beneath New Zealand and the Chatham Rise are shown as greyish and hatched greyish transparent overlay, respectively. CI = Chatham Islands, ECR = Eastern Chatham Rise, StI = Stewart Island, WCR = Western Chatham Rise, WWR = West Wishbone Ridge.

As for beneath the Chatham Rise, determining the southward extent of the Phoenix Plate beneath southern Zealandia is challenging. V_p and V_s/V_p models of the South Island (Reyners et al., 2017b), as well as the seismic refraction line SIGHT-III that runs east of and parallel to the South Island (Godfrey et al., 2001), indicate an absence of oceanic crust beneath the Median Batholith – the ancient volcanic arc of the former East Gondwana subduction zone that is located beneath the southernmost South Island and Stewart Island (Fig. 5.6d). This provides a possible southern limit to the extent of the Phoenix Plate oceanic crust in the vicinity of the South Island, and explains why oceanic crust has not been observed along the seismic refraction line AWI-20030001, located southeast of the South Island (Fig. 5.6d; Groby et al., 2009). As the widely-rifted continental Bounty Trough is apparently not underlain by oceanic crust (Groby et al., 2007), we suggest that the

southern limit of the Phoenix Plate corresponds with the southern margin of the Chatham Rise, as inferred by Davy (2014) from variations in gravity gradient fabrics in the inner Bounty Trough. With this constraint, we find that the N-S extent of the Phoenix Plate attached to the Hikurangi Plateau varies between 100 and 200 km, but probably does not exceed more than 200 km south of the under-thrusted Hikurangi Plateau.

Because most of its oceanic crust was subsequently subducted during the mid-Cretaceous, the age and much of the spreading history of the Phoenix Plate are unknown (Seton et al., 2012). It is thought that the Ontong Java Plateau, northwest of the Hikurangi Plateau, was emplaced on or beside oceanic crust that formed between M29 (~156 Ma) and M0 (~120 Ma) along the Pacific-Phoenix spreading ridge (e.g. Hochmuth et al., 2015; Seton et al., 2012). Accordingly, the piece of subducted Phoenix Plate that we have identified below the Chatham Rise is most likely older than the emplacement of Ontong Java Nui at 125-120 Ma (Hoernle et al., 2010; Taylor et al., 2006). Considering recent plate tectonic reconstructions and spreading anomalies (Hochmuth et al., 2015; Hochmuth & Gohl, 2017; Matthews et al., 2012; Seton et al., 2012), the piece of the Phoenix Plate south of the Hikurangi Plateau is likely not, or not much, older than the M29 spreading anomaly (~156 Ma).

5.5.3. Subduction geometry of the Phoenix Plate

A dramatic change of tectonic forces affected Zealandia during the mid-Cretaceous, with the previous compressional regime being replaced by widespread extension (Bradshaw, 1989; Laird & Bradshaw, 2004). The end of long-lived subduction along the East Gondwana margin was initiated when the Hikurangi Plateau entered the subduction zone between 110 and 100 Ma (Davy, 2014; Davy et al., 2008). No direct data are available regarding the timing of the inferred Hikurangi Plateau subduction, or the slab geometry before, during and after Hikurangi Plateau subduction. In our conceptual model (Fig. 5.7), we envisage the subducting oceanic Phoenix Plate as a shallow slab in the pre-collisional setting before 105 Ma, since changing geochemical/isotopic compositions of subduction-related granitoids within the Median Batholith onshore South Island indicate shallow mantle wedge melting, and thermochronological data suggest a continent-ward migration of the arc after 125 Ma (Tulloch & Kimbrough, 2003). This may be related to younger oceanic slab entering the trench (van Hunen et al., 2002) and would be in agreement with a young age of the Phoenix Plate during the evolution of the OJP (Hochmuth et al., 2015) that was then subducted along the East Gondwana margin. In modern subduction zones, the distance between arc and trench (width of the accretionary wedge and forearc area) most likely exceeds distances of 100-300 km (Dickinson, 1973). This is consistent with geological observations from the South Island (e.g. Jacob et al., 2017).

5.5.4. Plateau collision/underthrusting, slab flattening and onset of extension

Our conceptual model is consistent with earlier tectonic models inferring that the Hikurangi Plateau started to collide and subduct from the NNW beneath the South Island and western Chatham Rise at 110 Ma, and beneath the eastern Chatham Rise at 105-100 Ma (Fig. 5.7b; Davy, 2014; Reyners et al., 2017b). The part of the Hikurangi Plateau that first entered the trench was most likely the part that is now located in the mantle beneath the southernmost South Island, and inferred to be 30-35 km thick (Reyners et al., 2017b). In contrast with normal oceanic crust, over-thickened volcanic oceanic plateaux like the Hikurangi Plateau have insufficient negative buoyancy to be subducted without consequences for margin deformation and convergence rate (Cloos, 1993; Espurt et al., 2008; van Hunen et al., 2002). An oceanic plateau of even 12 km thick remains positively buoyant until an age of around 80 Myr, and thicker plateaux are positively buoyant for even longer (van Hunen et al., 2002). In response to the onset of subduction of the thicker part of

the Hikurangi Plateau in the area of the South Island at 110 Ma, the convergence rate in this region slowed down. Further east, beneath the Chatham Rise, subduction of the oceanic Phoenix Plate continued at least until 105 Ma and the convergence rate in this region was, therefore, higher. This asymmetry likely led to the proposed clockwise rotation of the East Gondwana margin in the Chatham Rise region (Davy, 2014; Reyners et al., 2017b). In response, the direction of seafloor spreading north of the Hikurangi Plateau rotated from NNW-SSE to approximately N-S (Davy, 2014; Davy et al., 2008; Downey et al., 2007). Initial subduction of the eastern, thinner (~10-km thick) part of the Hikurangi Plateau led to progressive southward uplift of the accretionary prism, i.e. the northern Chatham Rise margin (Fig. 5.7b). We suggest that the positive buoyancy of the thicker Hikurangi Plateau initiated further flattening of the Phoenix Plate slab after the onset of subduction and underthrusting of the Hikurangi Plateau. Both the slab flattening and decreasing convergence velocity may explain the abrupt cessation of arc construction processes, and the onset of metamorphic doming and extensional collapse between 108 and 106 Ma (Fig. 5.7b; Schwartz et al., 2016). Crustal extension in the forearc area of the East Gondwana margin – the ‘Zealandia Rift Phase’ – then began after ca. 105 Ma, as evidenced by the evolution of mid-Cretaceous graben-controlled rift basins around New Zealand (Strogen et al., 2017). Slab flattening has been suggested as a plausible mechanism of producing extension and eventually uplift in forearc areas (Espurt et al., 2008). Consequently, we postulate that the initiation of forearc extension along the present-day Chatham Rise was largely triggered by flattening of the subducted Phoenix Plate slab (Fig. 5.7b). Additionally, transfer of dextral motions along the WWR and divergence of these dextral motions through smaller fault system may have also played a role in facilitating extension along the eastern part of the Chatham Rise.

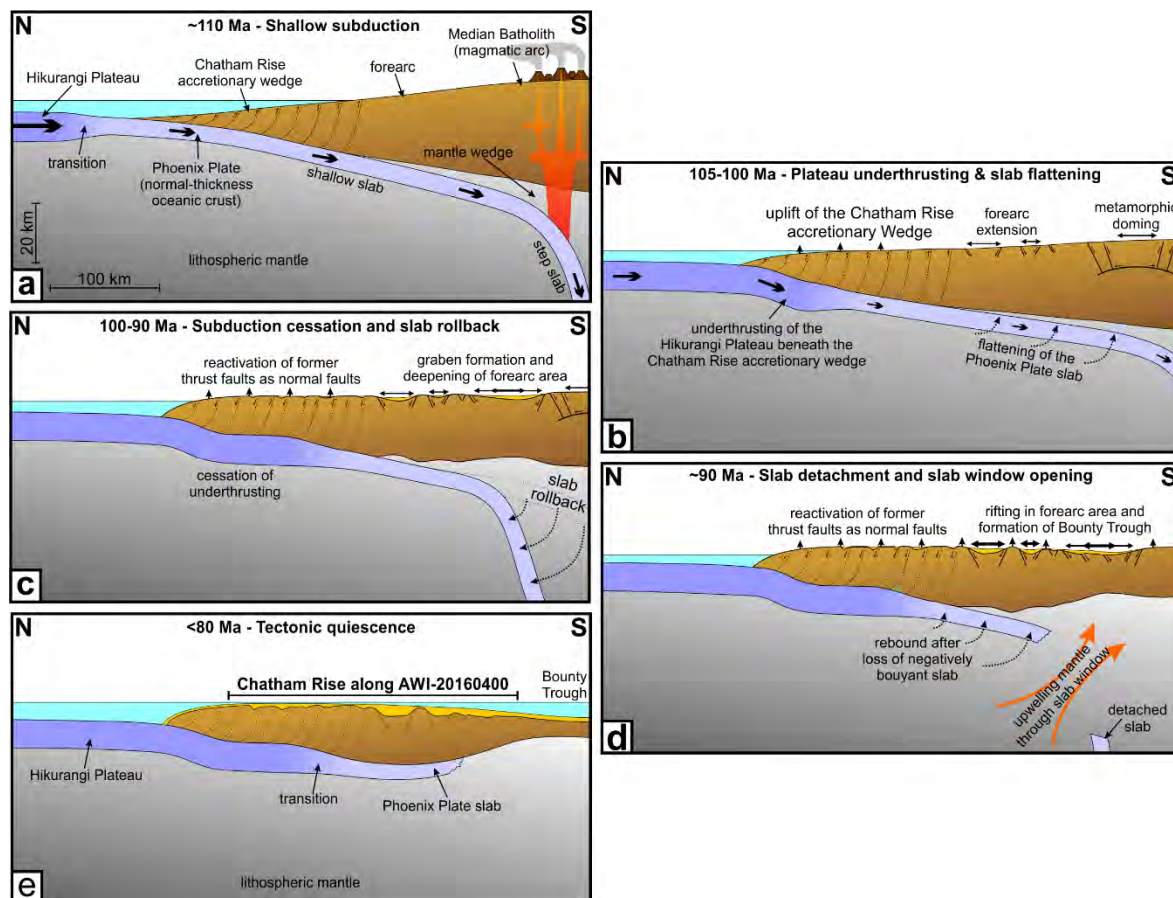


Fig. 5.7: Conceptual model of the Hikurangi Plateau underthrusting and subsequent slab processes along the Chatham Rise between the initial Hikurangi Plateau collision and subduction at ~110 Ma and the final separation of southern Zealandia and West Antarctica at ~80 Ma. See text for further explanations.

5.5.5. *Development of STEP faults and slab rollback*

Subduction presumably continued both east and west of the Hikurangi Plateau (Mortimer et al., 2019b), leading to the development of Subduction-Transform Edge Propagator (STEP) faults (Govers & Wortel, 2005). The last remnants of oceanic crust west of the Hikurangi Plateau were completely subducted at the Australian-Pacific plate boundary in the Eocene (Reyners, 2013). However, the presence of alkaline intraplate magmatism in Marlborough and Westland onshore of the South Island shortly after 100 Ma implies that a slab window or tear opened along the sinistral STEP fault at the western edge of the Hikurangi Plateau (Hoernle et al., 2020; van der Meer et al., 2016, van der Meer et al., 2017). East of the Hikurangi Plateau, subduction continued and was compensated by another STEP fault that has remained as the prominent dextral WWR (Figs. 5.1a and 5.6d; Barrett et al., 2018; Davy, 2014; Davy et al., 2008; Riefstahl et al., 2020), which is inferred to have first become active after 105 Ma (Barrett et al., 2018). Along the northeastern Chatham Rise margin east of the WWR, oceanic crust of the Phoenix Plate continued to subduct until at least 100 Ma (Riefstahl et al., 2020). We suggest that the slab of the Phoenix Plate south of the Hikurangi Plateau became decoupled from the Phoenix Plate slabs to the east and to the west after both STEP faults became active. Although subduction slowed and finally ceased due to blockage by the buoyant Hikurangi Plateau, eclogitisation and associated densification of the steeper, arc-ward Phoenix Plate slab is likely to have continued (Duesterhoeft et al., 2014; Huangfu et al., 2016; Li et al., 2013). The additional negative buoyancy of progressive eclogitisation will have continued to pull down the Phoenix Plate slab and led to slab roll-back along the Hikurangi Plateau segment of the Phoenix Plate. This would have triggered further rifting and focused extension, which is expressed by graben formation and successive deepening of the forearc in the area that later formed the Bounty Trough (Fig. 5.7c). Moreover, this enabled the lower lithosphere to heat up to granulite facies conditions, as evidenced by granulite xenoliths with peak metamorphic ages of 91.7 ± 2.0 Ma that were collected in Otago in the South Island (Jacob et al., 2017). We suggest that a ca. 97 Ma A-type granite from the Chatham Rise (Mortimer et al., 2006) is also related to this event. Synchronously with the cessation of subduction at the Chatham Rise, seafloor spreading north of the Hikurangi Plateau either ceased (Davy, 2014), or continued at a slower rate until 79 Ma (Mortimer et al., 2019b).

5.5.6. *Slab detachment and focus of rifting in the Bounty Trough*

Geological studies of southern Zealandia's basement indicate that the direction of extension rotated by $\sim 60^\circ$ from NE-SW (orthogonal to the then-active East Gondwana margin) to NNW-SSE (approximately orthogonal to the Pacific-Antarctic ridge active after ~ 85 Ma) at around 90 Ma (Tulloch et al., 2019). This is consistent with the timing of onset of rifting in the Bounty Trough (Fig. 5.6d) inferred by most plate tectonic reconstructions (Eagles et al., 2004; Larter et al., 2002; Wobbe et al., 2012). This second stage of the 'Zealandia Rift Phase' resulted in the formation of oceanic crust between the eastern Chatham Rise and eastern Marie Byrd Land of West Antarctica (Eagles et al., 2004; Larter et al., 2002; Wobbe et al., 2012; Riefstahl et al., 2020). We postulate that the observed change in the direction of extension was triggered by detachment of the subducted Phoenix Plate slab at ~ 90 Ma, approximately 15-20 Myr after the initial collision and onset of underthrusting of the Hikurangi Plateau beneath the Chatham Rise. The delay time between the initial collision and subsequent slab detachment depends mostly on the strength of the previously-subducted oceanic plate. 3D numerical models indicate that typical delay times range from more than 20 Myr for old and strong slabs, to 10 Myr for young and weak slabs (van Hunen & Allen, 2011). Correspondingly, slab detachment 15-20 Myr after the collision of the Hikurangi Plateau with the Chatham Rise is not unreasonable.

Numerical models suggest that significant asymmetry in a collisional setting leads to slab detachment that preferentially begins near one edge of the slab (van Hunen & Allen, 2011). We suggest that slab tearing beneath the Chatham Rise began at the southwestern leading edge of the Hikurangi Plateau close to the already evolved western STEP fault, which is linked to alkaline intraplate magmatism that affected parts of the northern and western South Island shortly after 100 Ma (Fig. 5.6d; Hoernle et al., 2020). Here, the transition between the thicker, more buoyant crust of the Hikurangi Plateau and the thinner oceanic crust of the Phoenix Plate would mechanically favour slab necking and detachment (Baumann et al., 2010). Low convergence rates after the Hikurangi Plateau collision would have led to a shallower depth (<100 km) for the slab detachment (Huangfu et al., 2016). The slab tear presumably migrated eastwards into the interior of the Phoenix Plate where we infer the Phoenix Plate segment to be present on profile AWI-20160400 (Fig. 5.6a). As for the delay time between collision and slab detachment, propagation of slab tears also depends on the strength and age of the oceanic crust (van Hunen & Allen, 2011). Assuming an age of ~60 Ma for this part of the Phoenix Plate, the tear propagation speed would be ~300 km/Myr (van Hunen & Allen, 2011). This implies that the Phoenix Plate slab south of the Hikurangi Plateau was fully detached within 5 Myr of the onset of slab tearing. The loss of the deeper, steeply dipping, and presumably largely eclogitized slab of the Phoenix Plate – and the corresponding loss of negative buoyancy – would have caused the shallower Phoenix Plate slab and the buoyant Hikurangi Plateau crust to rebound (Duretz et al., 2011; Edwards et al., 2015; Gerya et al., 2004) and ‘under-plate’ the thin Chatham Rise continental accretionary wedge and forearc crust (Fig. 5.7d). Moreover, the loss of a large segment of the oceanic Phoenix Plate by slab detachment, together with rebound of the remaining slab, will have triggered a regional dynamic topographic response along the East Gondwana margin (Duretz et al., 2011; Wortel & Spakman, 2000). The margin uplifted and extension focussed in the forearc area, which most likely intensified rifting and led to the formation of the Bounty Trough by ca. 80 Ma, when westward-propagating seafloor spreading finally separated southern Zealandia from West Antarctica (Fig. 5.7d; Riefstahl et al., 2020).

Slab tearing created a pathway for mantle upwelling, which affected the evolving southern Zealandia rifted margin around 85 Ma (Hoernle et al., 2020; Riefstahl et al., 2020; Tulloch et al., 2019). Alkaline magmatism occurred on the Chatham Islands between 86 and 79 Ma (Panter et al., 2006) and at several seamounts further to the south and west of the Chatham Islands (Hoernle et al., 2020; Homrighausen et al., 2018; Mortimer et al., 2019b). Isotopic constraints of this intraplate volcanic event indicate a common HIMU end-member across multiple volcanic provinces in southern Zealandia (Hoernle et al., 2020), and suggest that the same deep-mantle source was involved in the evolution of the alkaline volcanic provinces located on the South Islands Marlborough (98-69 Ma; McCoy-West et al., 2010; Mortimer et al., 2019b; van der Meer et al., 2016; van der Meer et al., 2017) and seamounts on the Hikurangi Plateau (99-86 Ma; Hoernle et al., 2010). If the mantle was already upwelling beneath the Hikurangi Plateau and the Phoenix Plate at or before 100 Ma, this could have also contributed to shallow subduction and flattening of the Phoenix Plate slab before 100 Ma (Fig. 5.7b). This is comparable with the central Andes, where a plume is suggested to have resulted in shallow and flat subduction (Gianni et al., 2017). Although alkaline volcanism in southern Zealandia was apparently spatially limited and of low volume, magnetic anomalies in the region suggest that it affected larger areas (Tulloch et al., 2019).

5.5.7. Plate tectonic implications

A global-scale plate reorganisation, presumably triggered by the cessation of subduction along the East Gondwana margin in response to jamming by the Hikurangi Plateau (Davy, 2014; Reyners et al., 2017b), is inferred to have occurred between 105 and 100 Ma (Matthews et al., 2012). In this

time interval this event is inferred to be the cause for fracture zone bendings and terminations in all ocean basins and the trigger for changes in the tectonic regime like thrusting initiation, transpression and basin inversions (Matthews et al., 2012). Geodynamic modelling suggests that the slab width has significant first-order effects on plate kinematic processes (Schellart et al., 2007). Cessation of subduction in response to under-thrusting of the Hikurangi Plateau would have split the ultra-wide subduction zone – which, at that time, extended across New Guinea, Australia, Zealandia, West Antarctica, and South America (Matthews et al., 2016) – into two narrower subduction zones east and west of the Hikurangi Plateau. We suggest that this fragmentation of the East Gondwana subduction zone – the major consequence of the cessation of subduction of the Hikurangi Plateau – led to the global plate reorganization event between 105 and 100 Ma. Our study highlights that oceanic plateau subduction, underthrusting and subduction zone jamming can result in various local, regional, and global effects with massive consequences.

5.6. Conclusions

In this study, we present newly acquired seismic refraction/wide-angle reflection, MCS reflection and potential field data along a profile across the submarine Chatham Rise. Our P-wave velocity and gravity modelling reveal the crustal structure of the Chatham Rise west of the Chatham Islands. The models provide new insights into the former East Gondwana subduction zone, which was blocked by subduction and underthrusting of the Hikurangi Plateau in the mid-Cretaceous.

P-wave velocities for the continental part of the Chatham Rise accretionary wedge suggest a composition similar to that observed elsewhere on the Chatham Rise: mainly meta-greywackes, schist and high-metamorphic equivalents. Our P-wave velocity and density models indicate that the southernmost extent of the underthrusted Hikurangi Plateau is less than 200 km from the northern border of the Chatham Rise. Moreover, a piece of the ancient Phoenix Plate is still attached south of the Hikurangi Plateau. Linking our observations with published geophysical data, we suggest that this piece of oceanic crust extends from east of the Chatham Islands to the South Island of New Zealand (up to 1000x250 km).

On the basis of our observations, we propose a multi-stage evolution of the East Gondwana subduction zone prior to the onset of seafloor spreading between southern Zealandia and West Antarctica, as follows: The 110-100 Ma subduction of the buoyant Hikurangi Plateau decreased convergence velocities and triggered flattening of the Phoenix Plate slab, which led to initial extension along the East Gondwana margin. Synchronously, STEP faults became active east and west of the Hikurangi Plateau became active. After cessation of subduction activity, slab rollback intensified extension in the Bounty Trough area. At 90 Ma, detachment of large proportions of the Phoenix Plate slab led a pathway for upwelling mantle.

A global-scale plate reorganisation event is suggested to have affected all major plates between 105 to 100 Ma. We propose that cessation of subduction and fragmentation of the Phoenix Plate in response to the Hikurangi Plateau subduction significantly contributed to or triggered this event. This study underlines the effects that the subduction of an oceanic plateau can have on global plate tectonics.

Acknowledgements

We thank Captain Oliver Meyer and his crew for their support and assistance during the RV Sonne cruise SO246. This project was funded through grant no. 03G0246A of the German Federal Ministry of Education and Research (BMBF) and by AWI internal funding through the AWI Research Program

PACES-II and its work package 3.2 “Earth systems on geological timescales: From greenhouse to icehouse world”. The involvement of B.D. was made possible by a grant to GNS from the New Zealand Ministry of Business and Innovation and Employment’s Strategic Science Investment Fund and the GNS Science Zealandia program. R.B. acknowledges funding from the European Union's Horizon 2020 research and innovation programme under the Marie Skłodowska-Curie Actions grant agreement No. 721403. Additional thanks go to the POLMAR Graduate School at AWI which funded a three-month research visit of F.R. at GNS Science in New Zealand. The new wide-angle seismic refraction and MSC reflection data used for this publication are available upon request at Alfred Wegener Institute Helmholtz Centre for Polar and Marine Research in Bremerhaven, Germany. Maps and figures for this manuscript were created with Generic Mapping Tools (Wessel & Smith, 1998). The authors would also like to thank Emerson E&P Software, Emerson Automation Solutions, for providing licenses for the seismic software Paradigm in the scope of the Emerson Academic Program. The MCS reflection and refraction seismic data will be made available in the PANGAEA database hosted by the Alfred Wegener Institute, Helmholtz Centre for Polar and Marine Research in Bremerhaven.

Supplemental methods

Geophysical data were recorded during RV Sonne expedition SO246 (Gohl & Werner, 2016) during February-March 2016 to resolve the crustal architecture of the Chatham Rise.

Seismic wide-angle reflection/refraction data

We deployed 20 ocean-bottom seismometer/hydrophones (OBS/OBH) along profile AWI-20160400 with a sampling rate of 250 Hz. All instruments were recovered, but no data were recorded by the instrument at the southernmost station st420 due to malfunction (Fig. 5.1B of the manuscript). The data quality is good to excellent, and the hydrophone channel provided the best data quality throughout. We relocated the OBS/OBH positions using the direct-wave arrivals, converted the data into SEG-Y format and applied a 4-14 Hz bandpass filter and a 1000 ms length automatic gain control.

We selected all refracted and reflected seismic phases with the software ZP (Zelt, 2004) and calculated individual picking uncertainties between 50 to 250 ms for each pick by taking the signal-to-noise ratio into account. P-wave velocity modelling was performed with the program Rayinvr (Zelt & Smith, 1992) and the graphical user interface P-Ray (Fromm, 2016) by using a top-to-down approach. As a priori information the multibeam bathymetry data along the profile were used to define the depth of the seafloor. Interpretation of sedimentary layers and the basement structure of the Chatham Rise were incorporated from the interpretation of the MSC reflection profile AWI-20160401. We picked wide-angle reflection phases to help to determine the layer boundaries of the model. P-wave velocities for each layer were determined primarily from the refracted phases and subsequently refined to match all picks within their uncertainty range.

We estimated depth and velocity uncertainties according to Schlindwein and Jokat (1999). Model velocity and boundary knots were systematically perturbed until the calculated traveltimes were out of range of the assigned uncertainties of the observed data. These perturbations were applied layer-wise and separately for velocities and depths. The estimated uncertainty values are listed in Tab. 5.1 of the manuscript. The inversion results corresponding to the presented P-wave velocity model (Fig. 5.2A of the manuscript) are listed in Tabs. S5.1 and S5.2. Ray coverage and resolution plots are shown in Figs. 5.4 and S5.1.

Multi-channel seismic (MCS) reflection data

Multi-channel seismic (MCS) reflection data were recorded using a 3000 m long digital solid streamer with 240 channels (Sercel Sentinel™). The MCS seismic data along profile AWI-20160401 were recorded by using the same shots of the wide-angle reflection/refraction profile AWI-20160400 (8x G-Guns in 2x4 G-Gun clusters fired at 205 bar every 60 s at 10 m below sea level). Processing steps included common depth point (CDP) sorting, velocity-time profile analyses every 2.5 km (every 50th CDP on average), normal moveout corrections, stacking, and time migration. A 5/15-150/200 Hz trapezoidal bandpass filter was applied for displaying the time-migrated section.

Gravity data

Gravity data were recorded by a LaCoste & Romberg S80/Ultrasys marine gravity meter along profile AWI-20160400. To test the modelled P-wave velocity-depth distribution and constrain areas along the crustal models that suffer from low ray coverage, we performed 2.5D density modelling using the IGMAS+ software package (Schmidt et al., 2007). The geometry and layer boundaries were extracted from the P-wave velocity model. Layers were subdivided in case of distinct lateral P-wave velocity variations. For the initial model, average P-wave velocities for the resulting polygons were converted into densities using the P-wave velocity-density relationships of Barton (1986) and

Christensen & Mooney (1992). We tried to fit the modelled free-air anomaly and the observed gravity data within a 5 mGal uncertainty range. During adjustment of the densities, we took care that the densities were not out of the uncertainties given for the P-wave velocity-density relationships of Barton (1986) and Christensen & Mooney (1992).

Supplemental tables

Tab. S5.1: Inversion results (Number of picks (n), RMS traveltimes misfit and χ^2) for different layers of the P-wave velocity model along AWI-20160400.

Velocity Layer	Phase	n	RMS traveltimes [s]	χ^2
1, rfl	Waterwave	1078	0.046	0.170
2, rfr	P _{sed1}	117	0.070	0.554
2, rfl	P _{sed2} P, P _{uc1} P	204	0.097	0.164
3, rfr	P _{sed2}	416	0.042	0.256
3, rfl	P _{sed3} P, P _{uc2}	38	0.051	0.171
4, rfr	P _{sed3} , P _{uc1}	1032	0.059	0.193
4, rfl	P _{uc2}	45	0.074	0.127
5, rfr	P _{uc2}	6801	0.104	0.498
5, rfl	P _{lc1} P	317	0.129	0.589
6, rfr	P _{lc1}	947	0.106	0.504
6, rfl	P _{lc2} P, P _m P	5091	0.168	1.131
7, rfl	P _m P	3456	0.161	0.997
8, rfr	P _n	988	0.129	0.663
All Layers	All Phases	20530	0.130	0.706

Tab. S5.2: Inversion results (Number of picks (n), RMS traveltimes misfit and χ^2) for different stations of the P-wave velocity model along AWI-20160400.

Station	Direction	n	RMS Traveltime [s]	χ^2
st401	N	102	0.034	0.139
st401	S	200	0.097	0.393
st402	N	165	0.083	0.292
st402	S	932	0.091	0.306
st403	N	252	0.060	0.098
st403	S	549	0.162	1.202
st404	N	219	0.078	0.280
st404	S	408	0.093	0.366
st405	N	249	0.057	0.115
st405	S	153	0.087	0.258
st406	N	604	0.225	1.967
st406	S	874	0.100	0.401
st407	N	567	0.103	0.400
st407	S	585	0.160	0.975
st408	N	569	0.143	0.667
st408	S	407	0.102	0.410
st409	N	50	0.063	0.245
st409	S	128	0.047	0.135
st410	N	781	0.152	0.872
st410	S	376	0.138	0.735
st411	N	1118	0.113	0.577
st411	S	406	0.058	0.235
st412	N	1035	0.122	0.652
st412	S	720	0.175	1.283
st413	N	792	0.119	0.650
st413	S	626	0.241	2.289
st414	N	28	0.042	0.047
st414	S	40	0.046	0.097
st415	N	880	0.133	0.773
st415	S	399	0.124	0.981
st416	N	1202	0.104	0.487
st416	S	495	0.076	0.284
st417	N	1475	0.170	1.177
st417	S	415	0.070	0.335
st418	N	1265	0.113	0.519
st418	S	296	0.078	0.393
st419	N	985	0.109	0.508
st419	S	183	0.049	0.164

Supplemental figures

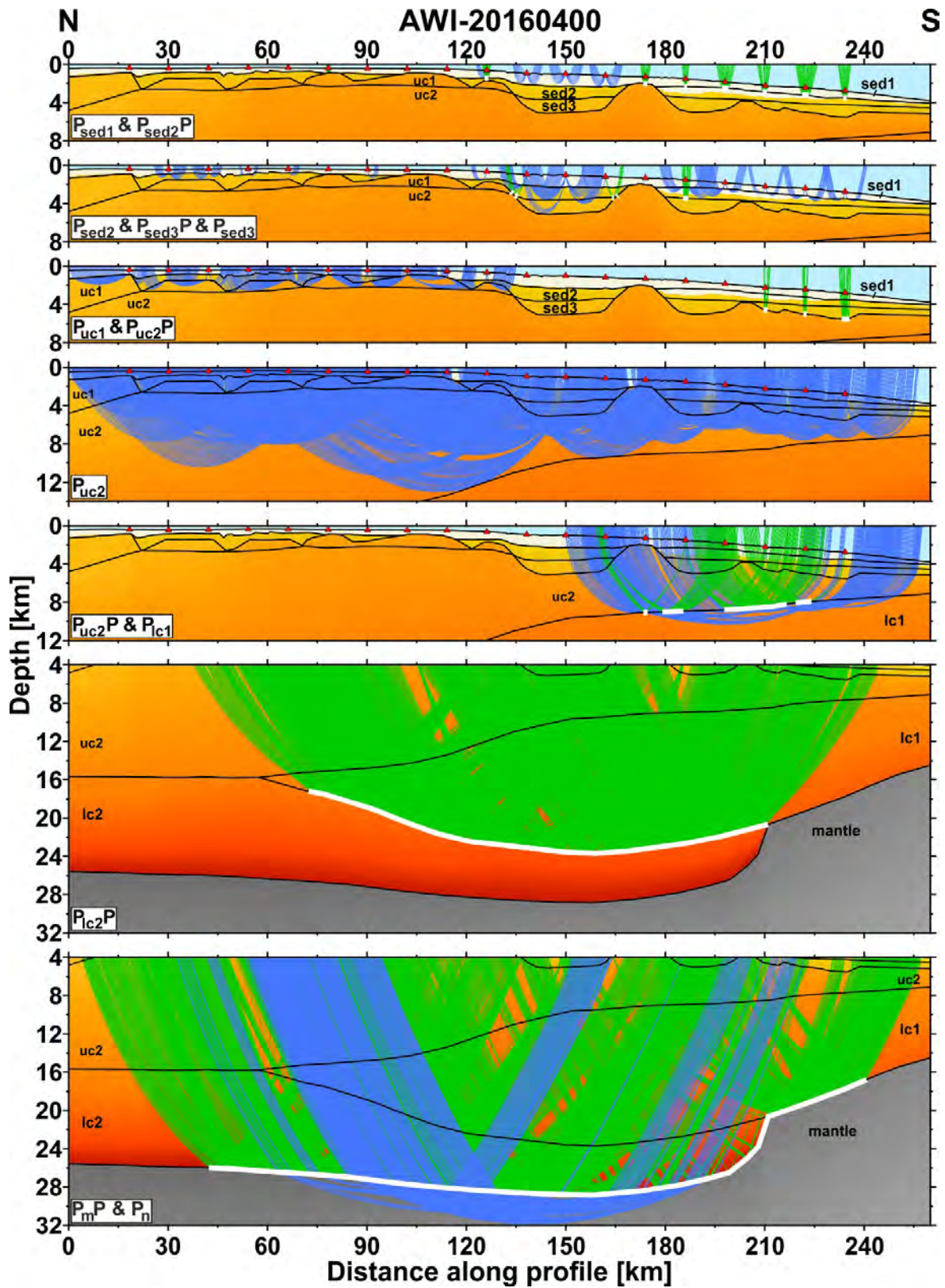


Fig. S5.1: Ray group coverage plots of the P-wave velocity-depth model along profile AWI-20160400.

6. Co-authorship I

Late Cretaceous oceanic plate reorganization and the breakup of Zealandia and Gondwana

By N. Mortimer¹, P. van den Bogaard², K. Hoernle^{2,3}, C. Timm⁴, P.B. Gans⁵, R. Werner², and F. Riefstahl⁶

¹GNS Science, Dunedin 9054, New Zealand

²GEOMAR Helmholtz Centre for Ocean Research Kiel, Kiel, Germany

³Christian-Albrechts University of Kiel, Kiel, Germany

⁴GNS Science, Lower Hutt New Zealand

⁵University of California, Santa Barbara, USA

⁶AWI Helmholtz Centre for Polar and Marine Research, Bremerhaven, Germany

Abstract

New ⁴⁰Ar/³⁹Ar ages of igneous rocks clarify the nature, timing and rates of movement of the oceanic Pacific, Phoenix, Farallon and Hikurangi plates against Gondwana and Zealandia in the Late Cretaceous. With some qualifications, cessation of spreading at the Osbourn Trough is dated c. 79 Ma, i.e. 30–20 m.y. later than 110–100 Ma Hikurangi Plateau-Gondwana collision. Oceanic crust of pre-84 Ma is confirmed to be present at the eastern end of the Chatham Rise, and a 99–78 Ma intraplate lava province erupted across juxtaposed Zealandia, Hikurangi Plateau and oceanic crust. We propose a new regional tectonic model in which a mechanically jammed Hikurangi Plateau resulted in the dynamic propagation of small, kinematically misaligned short-length 110–84 Ma spreading centres and long-offset fracture zones. It is only from c. 84 Ma that geometrically stable spreading became localized at what is now the Pacific-Antarctic Ridge, as Zealandia started to split from Gondwana.

6.1. Introduction

The SW Pacific region (Fig. 6.1) underwent major tectonic and geological change in the Cretaceous Period (145–66 Ma). For much of the Mesozoic, the continent-ocean margin between SE Gondwana and the crust of the paleo-Pacific was convergent and characterised by the development of Cordilleran batholiths and accretionary complexes (Mortimer et al., 2014). Sometime between 110 and 85 Ma this tectonic regime was interrupted and/or replaced by a passive margin and widespread intracontinental rifting and volcanism (Bradshaw, 1989; Luyendyk, 1995; Tulloch et al., 2009). This intracontinental rifting culminated in the breakup of Gondwana, such that by 83 Ma

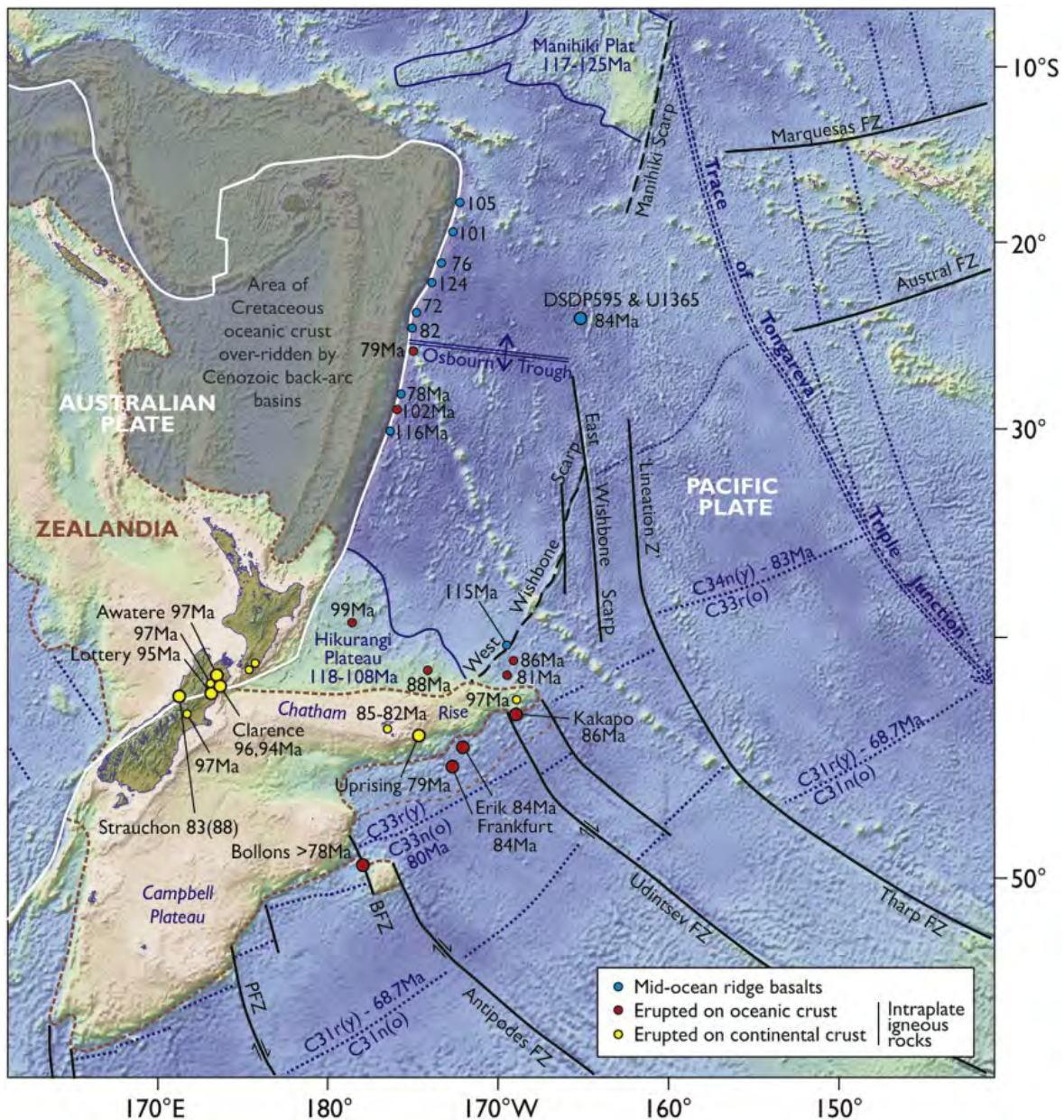


Fig. 6.1: Present day map of the Zealandia continent and adjacent SW Pacific Ocean crust showing major tectonic features and sample sites referred to in the text. The Ontong Java Plateau lies NW of the area of the figure. White lines and labels = Cenozoic features, black and blue lines and labels = Cretaceous features. Numbers are ages of lavas (in Ma) from Thomas (2002), Tappenden (2003), Mortimer et al. (2006), Panter et al. (2006), Hoernle et al. (2010), and Homrighausen et al. (2018). Sample sites from this study are shown as in larger symbols with names. Lineation Z is from Eagles et al. (2004). PFZ=Pahemo Fracture Zone, BFZ=Bollons Fracture Zone.

(anomaly 34n(y); Seton et al., 2014) new oceanic crust had started to form between the continents of Australia, Antarctica and Zealandia (Stock and Cande, 2002; Wright et al., 2016; Mortimer et al., 2017). Meanwhile, in the ocean basins the eruption of 125–115 Ma large igneous provinces (LIPs) such as Ontong Java, Manihiki and Hikurangi Plateaus took place, likely as a single superplateau (Taylor, 2006; Davy et al., 2008; Hoernle et al., 2010; Timm et al., 2011; Chandler et al., 2012; Hochmuth et al., 2015). There has been much speculation on the cause and effect between rapid Cretaceous spreading, LIP eruption, LIP collision, and the change in continental tectonic regime (Luyendyk, 1995; Mortimer et al., 2006; Downey et al., 2007; Davy et al., 2008; Tulloch et al., 2009; Davy, 2014; Hochmuth and Gohl, 2017). Satellite gravity maps (Sandwell and Smith, 1997) have provided extremely useful insights into kinematic aspects of oceanic crust tectonics. But the dearth of sampled rocks, particularly from the widespread oceanic crust of Cretaceous Normal Superchron (121–83 Ma) age (Fig. 6.1), has hindered our ability to date the age of events, and hence define spreading rates and tectonic events.

This paper increases our knowledge of SW Pacific tectonics by providing new $^{40}\text{Ar}/^{39}\text{Ar}$ ages of igneous rocks, particularly in the parts of the large and difficult-to-access oceanic crust northeast and east of Zealandia (Fig. 6.1). The direct dating provides a critical check on oceanic crust ages inferred from magnetic reversals. This paper is relevant to, and develops, themes of Ontong Java Nui Large Igneous Province (LIP) breakup and collision (Larson et al., 2002; Taylor, 2006; Davy et al., 2008; Hoernle et al., 2010; Chandler et al., 2012; Hochmuth and Gohl, 2017; Barrett et al., 2018), SW Pacific volcanism (Mortimer et al., 2006, 2018; Tulloch et al., 2009; Timm et al., 2010; van der Meer et al., 2016), and SW Pacific-Zealandia-Antarctica Cretaceous tectonics (Luyendyk, 1995; Sutherland and Hollis, 2000; Larter et al., 2002; Eagles et al., 2004; Wright et al., 2016). Our data clarify the age and rate of breakup of the Hikurangi Plateau part of the Ontong Java Nui LIP and our tectonic model emphasises the role of LIP collision in controlling subsequent continental and oceanic magmatic and tectonic events. This is a companion paper to Homrighausen et al. (2018) in which trace element and isotopic data for some of the dated samples are described and discussed.

6.2. Geological background

6.2.1. Oceanic crust east of Zealandia

Lying east of the Kermadec Trench, the Osborn Trough is an east west trending fossil spreading ridge that split the once contiguous Hikurangi and Manihiki Plateau LIPs (Fig. 6.1; Billen and Stock, 2000; Taylor, 2006, Downey et al., 2007). Rocks dredged from the Osborn Trough axial valley and drilled at International Ocean Discovery Program (IODP) Site U1365 are altered lavas of normal mid-ocean ridge basalt (N-MORB) composition (Worthington et al., 2006; Zhang et al., 2012). All or most of the oceanic crust between the two LIPs is believed to have formed c. 118–83 Ma during the Cretaceous Normal Superchron (e.g. Seton et al., 2014, Fig. 6.1), but the exact time of inception, rates of spreading and time of cessation of spreading at the Osborn Trough have been the subject of debate. Geophysical estimates of the age of cessation of spreading at the Osborn Trough range between 105 and 71 Ma, and are based on magnetic anomaly interpretations, abyssal hill fabrics and/or regional tectonic considerations (Billen and Stock, 2000; Worthington et al., 2006; Downey et al., 2007; Davy et al., 2008). There are no published dates of rocks directly dredged from the Osborn Trough. However, rocks at DSDP site 595 and the adjacent IODP site U1365, both c. 250 km north of the Osborn Trough (Fig. 6.1) have been dated and potentially offer an important age constraint on the spreading history of the Osborn system. Montgomery and Johnson (1987) reported $^{40}\text{Ar}/^{39}\text{Ar}$ whole rock total fusion ages of 96.8 ± 0.6 and 101.5 ± 0.6 Ma (DSDP 595B, 4-2, 13-16), which they regarded as minimum eruptive ages. In contrast, Sutherland and Hollis (2000)

reported radiolarians of late Berriasian-Valanginian age (144–132 Ma) from near the base of the sedimentary section in DSDP 595 and of Cenomanian age (99–94 Ma) in nearby DSDP 596. More recently, Zhang and Li (2016) reported a 103.7 ± 2.3 Ma Re-Os isochron age for basalts in U1365. Previous estimates of the geological age of basement at DSDP 595/U1365 therefore range from c. 132 to c. 104 Ma. The oldest ocean floor marine magnetic anomaly that is recognized along the entire length of the southern Zealandia margin and through to the Tasman Sea is 33r(y) (74 Ma; Stock and Cande, 2002). Northeast of Bollons Seamount (Fig. 6.1), there is general agreement that anomaly 34n(y) (83 Ma) is present (Stock and Cande, 2002; Larter et al., 2002; Davy, 2006; Wright et al., 2016) and that, to the east, it connects with the trace of the Tongareva Triple Junction (TTJ) (Larson et al., 2002). A large triangular area between the TTJ, Manihiki Scarp and Bollons Seamount is poorly surveyed and its age and spreading patterns are undemonstrated.

6.2.2. Zealandia intraplate lavas

The Zealandia continent has a geological record of scattered, low volume intraplate volcanism over the last c. 100 Ma that is not related to subduction or to hotspot tracks (e.g. Weaver and Smith, 1989; Panter et al., 2006; Hoernle et al., 2006; Tulloch et al., 2009; Timm et al., 2010; Mortimer et al., 2018; van der Meer et al., 2017). This intraplate volcanism - the Horomaka Supersuite (Mortimer et al., 2014) - shares some common ages and compositions with intraplate volcanism in formerly adjacent West Antarctica and Australia (Finn et al., 2005). The initial eruption of intraplate (mainly alkaline) lavas, and intrusion of associated plutons has long been recognised to be associated with the syn-rift (c. 105–85 Ma) phase of South Gondwana breakup (e.g. Bradshaw, 1989; Tulloch et al., 2009, and references therein).

6.3. Samples and methods

Samples were obtained from several sources including Sonne 168 dredges, the International Ocean Discovery Programme core repository, newly collected onland samples and existing samples in the GNS Petrology Collection (Tab. 6.1; Fig. 6.2). All samples prefixed “P” refer to the GNS Science Petrology Collection. Sample data are lodged in the PETLAB database (<http://pet.gns.cri.nz>; Strong et al., 2016). Dating of most samples was done at GEOMAR, Kiel using step heating and single crystal laser fusion $^{40}\text{Ar}/^{39}\text{Ar}$ methods, as described in supplementary files of Hoernle et al. (2010) and Timm et al. (2011). Plagioclase separates were acid-leached with 5% HF prior to dating; matrix separates were ultrasonically washed in distilled H_2O . The neutron flux was monitored using Taylor Creek sanidine with an age of 27.92 Ma. K/Ca ratios, percent of atmospheric ^{40}Ar and calculated $^{36}\text{Ar}/^{37}\text{Ar}$ alteration index (AI) values (Baksi, 2007) were used to determine the degree of alteration of the laser step-heating or total fusion analyses. Inverse isochron ages were calculated to confirm both the plateau and total fusion ages and identify if the samples preserved initial atmospheric $^{40}\text{Ar}/^{36}\text{Ar}$ ratios, without the presence of extraneous ^{40}Ar components (i.e. an atmospheric $^{40}\text{Ar}/^{36}\text{Ar}$ ratio of 295.5). Statistically valid weighted mean plateau ages have a well-defined age spectrum plateau created by three or more continuous and concordant steps overlapping at the 2 σ confidence level, with >50% of the cumulative ^{39}Ar , a mean square of weighted deviations (MSWD) ≤ 2 , and probability (P) of fit is ≥ 0.05 . For three samples (P63810, P63853 and P63854), $^{40}\text{Ar}/^{39}\text{Ar}$ dating was done at the University of California Santa Barbara (UCSB) using step heating methods described by Gans (1997). Major elements and Cr, Ni, Zr, Sr of whole-rock samples were determined by X-ray fluorescence methods as described in Timm et al. (2010). Raw data and plots are given in Supplementary Files. All errors in $^{40}\text{Ar}/^{39}\text{Ar}$ ages are reported at two sigma level and include errors in the J value (reactor neutron flux).

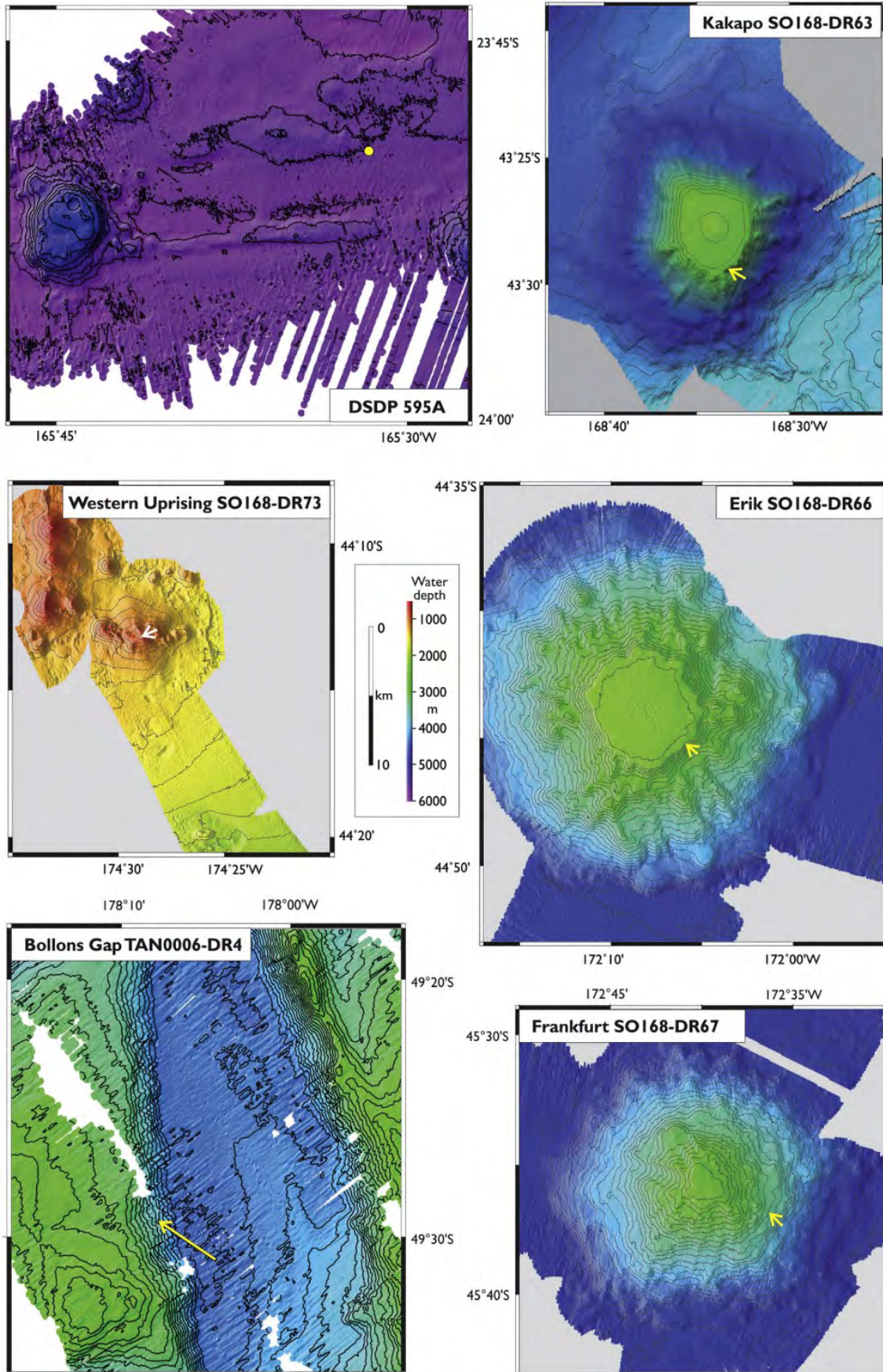


Fig. 6.2: Seafloor bathymetry of the sample sites at the same scale. Inferred dredge on bottom tracks shown by arrows, DSDP 595 drill site shown by yellow dot. Isobath interval 100 m; the bathymetry scale is the same for all panels.

Tab. 6.1: Sample location data and interpreted Ar-Ar ages and two-sigma errors. Abbreviations smt, seamount; Hwy, Highway; Fmn, Formation; Trachybas, trachybasalt; xtal, crystal; Plag, Plagioclase; Kspar, K-feldspar; Prob, probability.

Sample number	Location	Rock	Lat (°S)	Long (°) (west-ve)	Depth (m)	Lab number	Method	Material	Age (Ma)	MSWD	Prob	% ³⁹ Ar or xtals
MORB: Osborn Trough area												
P63853	Drill core 595A, 10,1,101-109	Basalt	23.8223	-165.5271	70.81 bsf	Kiel 30 63852fss	Step heat	Plag	84.4 ± 3.5	1.5	0.11	82
P63853	Drill core 595A, 10,1,101-109	Basalt	23.8223	-165.5271	70.81 bsf	UCSB 57-03	Step heat	Matrix	>c. 82	–	–	75
P63854	Drill core 595A, 11,2,116-124	Basalt	23.8223	-165.5271	82.06 bsf	UCSB 57-04	Step heat	Matrix	>c. 86	–	–	74
Intraplate: Eastern Zealandia region												
P67444	SO168-DR63-1. Kakapo smt	Basanite	43.4923	-168.5473	2830–3220	Kiel 26 63-1fs	Single xtal	Plag	85.5 ± 2.6	1.1	0.36	6/12
P67448	SO168-DR66-1. Erik smt	Trachyte	44.757	-172.0952	2530–2950	Kiel 26 66-1fs	Single xtal	Kspar	83.9 ± 0.1	1.7	0.08	10/12
P67450	SO168-DR67-1. Frankfurt smt	Basalt	45.6912	-172.5988	3560–4030	Kiel 26 67-1fs	Single xtal	Plag	84.5 ± 5.2	1.2	0.32	9/10
P67467	SO168-DR73-1. W Uprising smt	Trachyte	44.2175	-174.4759	870–960	Kiel 26 73-1fs	Single xtal	Plag	79.3 ± 0.4	1.1	0.42	14/14
P63810	TAN006-D4-1B. Bollons Gap	Trachybas.	44.2175	-174.4759	870–960	UCSB 36-38	Step heat	Kspar	>77.6 ± 0.3	–	–	96
Intraplate: South Island New Zealand												
MSI 31	Lottery River, North Canterbury	Basalt float	42.5301	173.0557	na	Kiel 28 MSI31mxs	Step heat	Matrix	94.8 ± 1.6	1.7	0.11	56
MSI 46A	Clarence River at State Hwy 1	Basalt float	42.1609	173.9094	na	Kiel 28 MS46Afs	Step heat	Plag	94.4 ± 0.6	1.6	0.1	81
MSI 47M	Clarence River at Waiautoa Road	Basalt float	42.1106	173.8413	na	Kiel 28 MS47Mbt2	Step heat	Biotite	96.5 ± 0.3	1.2	0.3	63
MSI 54A	Awatere River, Lookout Fmn	Basalt	41.9617	173.4571	na	Kiel 28 MS54Amx2	Step heat	Matrix	97.5 ± 0.5	1.4	0.22	64
NZS1	Hohonu Dike, Strauchon Creek	Basalt float	42.6425	171.4736	na	Kiel 30 NZS1hbs	Step heat	Amph	82.8 ± 0.3	1.2	0.27	96
P45280	Hohonu Dike, Strauchon Creek	Basalt float	42.6432	171.4695	na	Kiel 28 45280hbs	Step heat	Amph	82.7 ± 0.3	1.4	0.23	77

At latitudes 40°S and higher, there is the risk of dredging iceberg-rafted dropstones of Antarctic origin rather than in situ material (e.g. Mortimer et al., 2016). Dredges of dropstones tend to be unweathered, thinly manganese-coated and include very different rock types that are rounded or faceted in shape. The dredged samples reported in this paper showed some weathering rinds, often had thick Mn encrustations, and were single rock types that were angular in shape and/or had broken faces, all consistent with an in situ origin.

6.4. Data

6.4.1. Osborn MORB lava

Whole rock chemical analysis of DSDP 595A sample P63853 confirms a Pacific N-MORB composition that matches other samples from the plate between the Osborn Trough and Manihiki Plateau (Fig. 6.1; Saunders, 1987; Thomas, 2002; Worthington et al., 2006; Castillo et al., 2009; Zhang et al., 2012). This is especially evident in Fig. 6.3 where the basalt is seen to be subalkaline and with the moderate Ti/V of MORBs. Our dated DSDP595 samples P63853 and 63854 are from basalt unit 2 (Saunders, 1987). This underlies unit 1 and is thus not the youngest recognised unit in the borehole. Step heating ⁴⁰Ar/³⁹Ar dating of plagioclase from P63853 at Kiel revealed a gas release spectrum in which 92% of the gas gave a statistically valid weighted mean plateau age of 84.4 ± 3.5 Ma (Fig. 6.4A). Alteration indices (Baksi, 2007) for most of these steps are acceptably low (<0.001, see supplementary files). However, many of the steps in the plateau have high percentages of atmospheric argon, and we cannot entirely rule out the effects of seawater alteration. Step heating ⁴⁰Ar/³⁹Ar dating of hard, grey matrix from the same sample, P63853 at UCSB (Tab. 6.1) gave a gas release spectrum that was humpshaped with flattish middle parts at c. 80–86 Ma (figure in Supplementary Files). K/Ca values were low (0.01–0.05). Clearly this is not a fresh basalt, as

indicated by the c. 1.6 wt% loss on ignition of the whole rock (see Supplementary Data). The young apparent ages in hump-shaped spectra like this usually reflect a combination of argon loss from minerals or glass at the low temperature steps and reactor-induced recoil in the higher temperature steps. But it is impossible to evaluate how much argon loss there has been so we regard c. 82 Ma as a minimum age for the lava as established from the weighted mean of the oldest three steps. This is within error of the plagioclase age of P63853 dated at Kiel. Matrix from a lava 12 m deeper in DSDP595A (P63854) was also dated at UCSB. It has slightly higher K/Ca (0.01–0.25) than matrix from P63853. It also gave a similar gas release spectrum except that the steps at the top of the hump ranged from c. 79 to 87 Ma. We regard c. 86 Ma as a minimum age for this sample, again based on the age of the oldest three steps. All things considered, we tentatively regard the plagioclase stepheating age of 84.4 ± 3.5 Ma as possibly approximating the age of crystallisation of the unit 2 lava flow in DSDP 595A, an age supported by the minimum ages of matrix in two samples. A comparison of this age with other Osbourn Trough lava ages is given in the Discussion below.

6.4.2. *Intraplate lavas: eastern Zealandia*

We dated lava samples from four seamounts and one fault scarp near the eastern Zealandia margin (Tab. 6.1; Fig. 6.2). Three analysed samples are basaltic-basanitic and two are trachytes (Fig. 6.3). In simple petrotextonic terminology, they are intraplate lavas. Like Cenozoic intraplate lavas from Zealandia (Hoernle et al., 2006; Timm et al., 2009, 2010) the basalts show a range of silica saturation. Feldspars from Kakapo, Erik, Frankfurt and Western Uprising lavas were dated by single crystal laser fusion $^{40}\text{Ar}/^{39}\text{Ar}$ methods at Kiel. Some single crystal fusion ages were excluded from weighted mean calculations because of their high $^{36}\text{Ar}/^{37}\text{Ar}$ based alteration indices (Baksi, 2007). Relatively high percentages of atmospheric ^{40}Ar in some samples, particularly 63-1fs and 67-1fs may also be indicative of seawater alteration (Baksi, 2007) but we provisionally interpret weighted mean single crystal ages as unreset eruptive ages (selected examples are shown in Fig. 6.4). The $^{40}\text{Ar}/^{39}\text{Ar}$ ages from the seamounts range from 85 to 79 Ma (Tab. 6.1; Supplementary Files). In the Bollons Gap lava P63810, adularia (replacing plagioclase) was dated by furnace step-heating at UCSB. The spectrum is flat with single step ages ranging from 77.9 to 78.2 Ma (Fig. 6.4E) with very high K/Ca (30–60) and high radiogenic yields (95–96%) throughout. All of the steps define a high precision inverse isochron with an age of 77.65 ± 0.26 Ma (2σ), a trapped Ar component with a $^{40}\text{Ar}/^{36}\text{Ar}$ ratio of 337 ± 7 . We interpret this age as the age of K-feldspar formation in the basalt. Because the adularia is a metasomatic mineral, this is a minimum age for the basalt eruption rather than dating the cooling of the lava flow.

6.4.3. *Intraplate lavas and dikes: South Island*

We dated material from six lavas and dikes in the northern South Island (Fig. 6.1), that potentially were related to the lavas described in section 6.4.2. Step heating methods at Kiel were employed. Chemically, the lavas are basanites, basalts and trachybasalts, and Ti/V ratios indicate an intraplate setting of eruption or intrusion (Fig. 6.3). Matrix from Lottery River basanite MSI 31 gives a plateau age of 94.8 ± 1.6 Ma which we interpret as approximating the age of crystallization of the basalt. The immediately surrounding rocks are Cookson Volcanic Group basalts, well dated as Oligocene (Rattenbury et al., 2006; Timm et al., 2010, $^{40}\text{Ar}/^{39}\text{Ar}$ ages = 31.2 ± 0.6 , 26.6 ± 0.3 and 25.8 ± 0.5 Ma). Because our dated sample is a stream cobble (not in situ) and Cretaceous, it probably is derived from a dike cutting greywacke basement upstream in the Seaward Kaikoura Ranges (Rattenbury et al., 2006 map no volcanic rocks in the catchment). Basaltic float samples MSI 47 M (coarse-grained) and MSI 46A (porphyritic) were collected from the lower Clarence River. The Clarence River drains a large area of the Seaward and Inland Kaikoura Ranges, and the samples could have come from Wallow Group lavas, numerous dikes that intrude greywacke basement or, more likely for the

6.5. Discussion

6.5.1. Osbourn Trough spreading system

DSDP 595 is in a sparsely surveyed region (Fig. 6.1). Available nearby multibeam bathymetry, single channel seismic reflection lines and satellite gravity maps indicate tectonic continuity, and no identifiable fracture zones, between the DSDP 595 site and the Osbourn Trough. DSDP 595 is c. 200 km off-axis from the main Osbourn Trough and knowledge of the age of the DSDP 595 basalts provide a date on the later spreading history of the ridge system. A 78.8 ± 1.3 Ma age from Osbourn Seamount at the northwestern end of the Louisville Seamount Chain (Koppers et al., 2004) provides a minimum age for Osbourn Trough spreading. Previous direct age interpretations of 144–132 Ma have been made on microfossils from DSDP 595 (Sutherland and Hollis, 2000): this is by far the oldest claimed age, and was used by Sutherland and Hollis as the basis for their Moa Plate, an extra Early Cretaceous oceanic microplate next to the Gondwana margin. The age is puzzling as it predates the formation of the Ontong Java Nui superplateau (Taylor, 2006; Hoernle et al., 2010; Timm et al., 2011; Chandler et al., 2012; Hochmuth et al., 2015) whereas DSDP 595 is located in the breakup region between the Hikurangi and Manihiki plateaus (Fig. 6.1). Following Downey et al. (2007) we explain the Early Cretaceous microfossils as being reworked, and not necessarily representative of the true stratigraphic age of DSDP 595. Speculatively, the microfossils could be derived from Early Cretaceous accretionary complexes along the Gondwana-Zealandia margin or from abyssal ooze on or near one of the LIPs. More recently, Zhang and Li (2016) have reported a 12 point Re-Os whole rock isochron age of 103.7 ± 2.3 Ma (MSWD 3.2) for basalts in IODP-U1365, 15 km west of DSDP 595A (so co-located at the scale of Fig. 6.1). Despite the care taken by Zhang and Li (2016), dating basalts by the Re-Os isochron method is not without potential problems. We note that the MSWD of 3.2 for the Re-Os isochron of Zhang and Li (2016) is slightly high for acceptable isochrons, and there is a correlation between Re content and loss on ignition, suggesting that alteration may play a role in forming the correlation between $^{187}\text{Re}/^{188}\text{Os}$ and $^{187}\text{Os}/^{188}\text{Os}$ interpreted as an isochron. Furthermore, the large range of initial Os, Nd, Hf and Pb isotope ratios for U1365 basalts is not consistent with all samples having been derived from a homogeneous source and thus the criteria for original isotopic homogeneity and closed system behavior (necessary for a positive correlation between $^{187}\text{Re}/^{188}\text{Os}$ and $^{187}\text{Os}/^{188}\text{Os}$ to have age significance and thus be a meaningful isochron) are not met. Anomalously old isochron ages in basalts resulting from binary mixing without complete isotopic equilibrium have been reported by Li et al. (2015). Other potential issues include 1) ultra-low concentrations of Os, resulting in the melts being particularly sensitive to crustal contamination, 2) a peridotite-pyroxenite issue that can skew the $^{187}\text{Os}/^{188}\text{Os}$ ratio, 3) possible correlated errors between $^{187}\text{Re}/^{188}\text{Os}$ and $^{187}\text{Os}/^{188}\text{Os}$, and 4) lack of common Os corrections of blanks (Zimmerman et al., 2014). As noted by Zhang and Li (2016), the initial $^{187}\text{Os}/^{188}\text{Os}$ ratio of the U1365 basalts (0.196 ± 0.080) is much higher than found in fresh modern Pacific N-MORB (~ 0.127 ; e.g. Snow and Reisberg, 1995). Thus, we do not regard Zhang and Li's (2016) c. 104 Ma age of U1365 basalts as an eruptive age. Instead the $^{187}\text{Re}/^{188}\text{Os}$ and $^{187}\text{Os}/^{188}\text{Os}$ correlation is likely to reflect a mixing line between a MORB source mantle component and a radiogenic crustal component assimilated by the magmas during ascent (cf. Tejada et al., 2013). Our c. 84 Ma $^{40}\text{Ar}/^{39}\text{Ar}$ plagioclase age from DSDP 595 could also be criticised as not being an eruptive age as plagioclase is regarded as being somewhat vulnerable to resetting during post-eruption alteration. However, the UCSB minimum ages are consistent with the GEOMAR age, the Baksi alteration indices are acceptably low (Supplementary Files), and there is no evidence of tectonism, reheating or later dikes at DSDP 595 (Fig. 6.2; Saunders, 1987). The rest of this paper is written on the basis that an 84 Ma age rather than a 104 Ma age for DSDP595/U1365 volcanism is correct. However, since lavas with MORB chemistry can erupt tens of millions of years after

spreading cessation (e.g. O'Connor et al., 2015), and seawater alteration can lead to spuriously young ages, we acknowledge that further sampling and dating from this region is desirable. The assumed c. 84 Ma age for DSDP 595 basalt in this paper should be used with caution. Taking an age of inception of Osborn spreading as 115 Ma (Mortimer et al., 2006), an 84 Ma age for DSDP 595 and a DSDP 595-Manihiki plateau separation distance of 1200 km gives an average half spreading rate on the Osborn system of c. 40 mm/a. This is slower than the >70 mm/a half spreading rate interpreted by Zhang et al. (2012) based on basalt compositions and c. 110 mm/a using a 104 Ma age (Fig. 6.6). All these spreading rate calculations are approximate as all three inputs are still poorly known: the exact timing of rifting of the Hikurangi and Manihiki plateaus, choice of distance between plateaus and Osborn Trough, and error limits on the DSDP 595 age. The K/Ar and $^{40}\text{Ar}/^{39}\text{Ar}$ ages of oceanic crust immediately east of the Tonga Trench reported in Thomas (2002) are very scattered and do not show any clear age-latitude co-variation (Figs. 6.1, 6.6); however, they do support the general Late Cretaceous age of sea floor spreading. As previously noted, DSDP 595 is not located at the Osborn Trough, but lies north of it. At a 40 mm/a half spreading rate, the age difference between basalts at DSDP 595 and those at the trough axis would be c. 5 m.y., so the implication is that spreading would have ceased at the Osborn trough at c. 79 Ma. The 79 Ma age for inferred spreading cessation is younger than the age of Cretaceous Magnetic Superchron. Billen and Stock (2000) interpreted anomalies 33 and 32 to be present in the vicinity of the Osborn Trough and thus our 84 Ma age at DSDP 595 is in agreement with their interpretation.

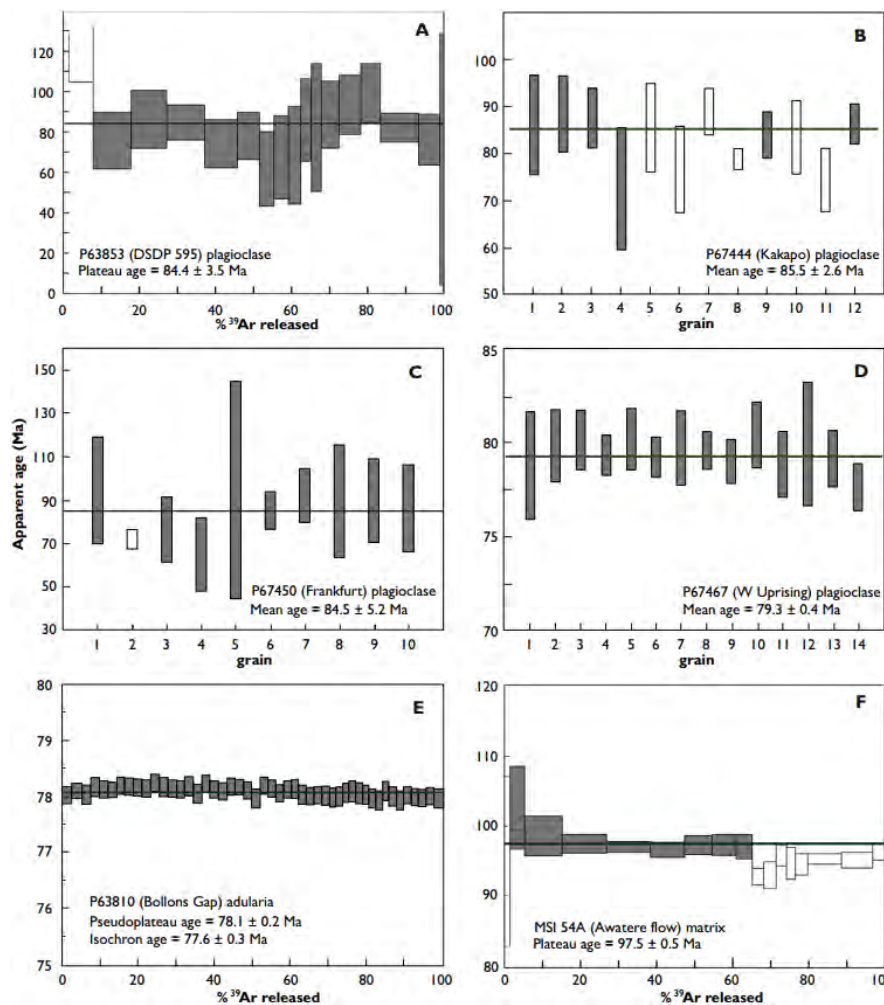


Fig. 6.4: Selected $^{40}\text{Ar}/^{39}\text{Ar}$ ages (A) DSDP 595, (B) Kakapo seamount, (C) Frankfurt seamount, (D) Western Uprising seamount, (E) Bollons Gap, (F) Awatere Valley. Shaded bars used in age calculations, white ones not used because of high alteration indices. Complete data and plots for all dated samples are given in Supplementary Files.

6.5.2. Oceanic crust age constraints

Two seamounts, Hühnchen and Pukeko lie north of the tip of Zealandia on oceanic crust. These have been dated by Homrighausen et al. (2018) as 85.5 ± 3.3 Ma and 81.2 ± 0.5 Ma respectively. The ages of these seamounts are important in that they provide minimum ages for the underlying oceanic crust and independently confirm the presence of Cretaceous Normal Superchron, pre-86 Ma, oceanic crust immediately southeast of the West Wishbone Scarp. About 1000 km further southwest along the Zealandia continent margin is Bollons Seamount (Fig. 6.1), and our dated intraplate lavas from Bollons Gap. According to Davy (2006) Bollons Seamount lies close to magnetic anomaly c34n(y). If the adularia in the Bollons Gap lava either grew soon after eruption and/or is related to movement on the Bollons Fracture Zone, its 78 Ma age dates the timing of separation of Bollons Seamount from Zealandia. As such it corroborates the models of Sutherland (1999) and Davy (2006) in which Bollons Seamount (Fig. 6.1) is interpreted to have been stranded in its position off Zealandia by a ridge jump near the end of chron 33r to just after the start of chron 33n i.e. 78–80 Ma.

6.5.3. Zealandia syn-rift intraplate magmatism

The pre-breakup phase of Gondwana margin rifting is generally thought to have taken place in the interval 105–85 Ma (Bradshaw, 1989; Luyendyk, 1995; Mortimer et al., 2014 and references therein). Tulloch et al. (2009) identified silicic magmatic pulses throughout Zealandia at c. 101, c. 97 and 88–82 Ma. For the most part, our new ages data on igneous rocks from the South Island and from the eastern continent-ocean margin region, match and reinforce the two younger intraplate magmatic pulses (Figs. 6.1, 6.5). This was manifested as extensive c. 85–82 Ma tholeiitic volcanism on the Chatham Islands (Panter et al., 2006), c. 99–67 Ma seamount volcanism on the Hikurangi Plateau (Hoernle et al., 2010), 86–79 Ma volcanism around the tip of easternmost Zealandia (Homrighausen et al., 2018; this study), and 98–83 Ma ages in the South Island (e.g. van der Meer et al., 2013; this study).

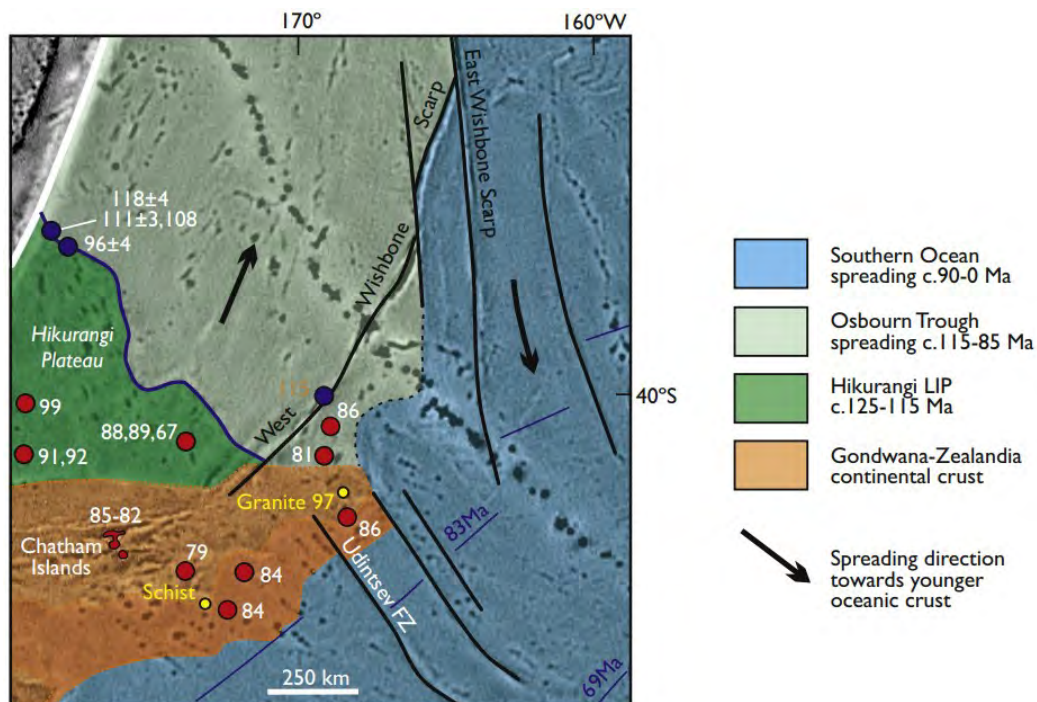


Fig. 6.5: Interpretation of four main tectonic blocks in and near present day eastern Zealandia along with dated lavas and magnetic lineations. Background is gravity gradient map from Sandwell et al. (2014). The prominent NW-SE trending line of black dots is the Louisville Seamount Chain, a Late Cretaceous to Cenozoic hotspot track superimposed on the Cretaceous crust of the region.

6.5.4. Hikurangi Plateau-Gondwana collision

The collision or docking of the Hikurangi Plateau LIP against the Chatham Rise part of Zealandian Gondwana has been cited as a primary cause of numerous Cretaceous geological events including cessation of local subduction of oceanic crust beneath Gondwana, cessation of spreading at the Osbourn Trough, Alpine Schist metamorphism, exhumation of the schist basement of the Chatham Rise and localization of the position of the Cenozoic Alpine Fault Pacific-Australia plate boundary (Vry et al., 2004; Davy et al., 2008; Reyners, 2013; Cooper and Ireland, 2013; Davy, 2014; Mortimer et al., 2016; Mortimer, 2018). Although the Late Cretaceous plate interface is clearly imaged in seismic reflection profiles (Davy et al., 2008; Bland et al., 2015; Barrett et al., 2018), drilling and dating of critical horizons needed to directly establish the age of plateau collision against the Chatham Rise has not yet been done. The best indirect estimate for the time of collision of the Hikurangi Plateau with Gondwana, based on relatively near-field effects, is 108 ± 11 Ma based on the rapid exhumation of a partial He retention zone in zircons of the schist basement of the Chatham Islands (Mortimer et al., 2016). This is in accord with the cessation of subduction-related magmatism and accretion in the Zealandia part of Gondwana at 110–100 Ma (Bradshaw, 1989; Mortimer et al., 2014) and widespread inception of post-subduction intraplate magmatism across Zealandia by c. 100 Ma (see section 6.5.3 above). It has been implicit or stated in some earlier models that the cessation of Osbourn Trough spreading occurred simultaneously with Hikurangi Plateau-Chatham Rise collision (e.g. Worthington et al., 2006; Downey et al., 2007; Davy et al., 2008; Davy, 2014). In other words, there was an implied effect of collision causing spreading to cease almost simultaneously. If our new c. 79 Ma inferred age for the cessation of Osbourn Trough spreading is accepted (section 6.5.1, Fig. 6.6), instead suggests that sea floor spreading continued for another 20–30 m.y. after LIP-Gondwana collision.

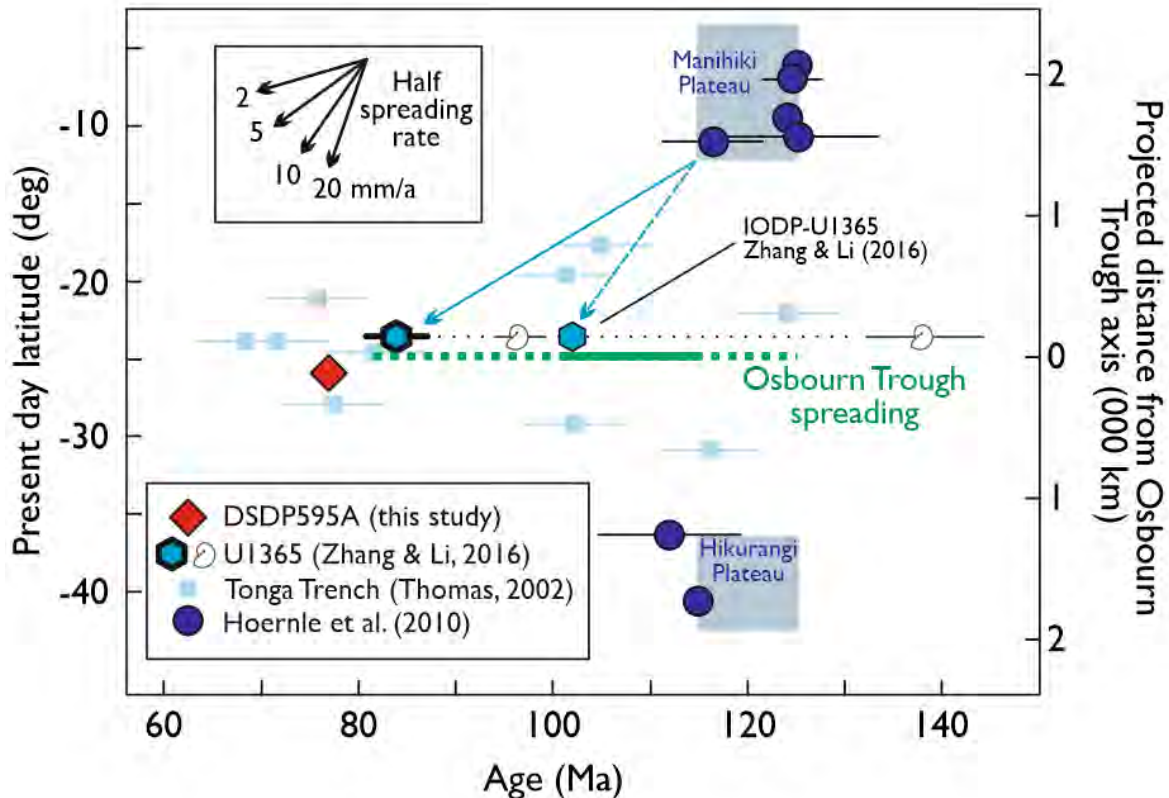


Fig. 6.6: Plot of age versus present day latitude for lavas related to Osbourn Trough spreading system. Outer Tonga Trench ages (tholeiites only) from Thomas (2002), Manihiki and Hikurangi plateau ages from Hoernle et al. (2010) and Timm et al. (2011), DSDP595 microfossil ages from Sutherland and Hollis (2000).

6.6. Tectonic model

Our new age data require changes to previous tectonic models of the region (e.g. Bradshaw, 1989; Weaver et al., 1994; Luyendyk, 1995; Sutherland and Hollis, 2000; Larter et al., 2002; Eagles et al., 2004). Key new points in Fig. 6.7 are a potentially relatively young (c. 79 Ma) cessation of spreading at the Osborn Trough and demonstration of an area of pre-83 Ma oceanic crust between the West Wishbone Scarp and magnetic anomaly c34n(y). The Ontong Java Nui superplateau formed in the Pacific Ocean basin between 125 and 117 Ma and breakup of the superplateau commenced from 117 to 115 Ma (Larson et al., 2002; Mortimer et al., 2006; Taylor, 2006; Davy et al., 2008; Chandler et al., 2012). At that time, the oceanic crustal plate or plates of the paleo-Pacific Basin were

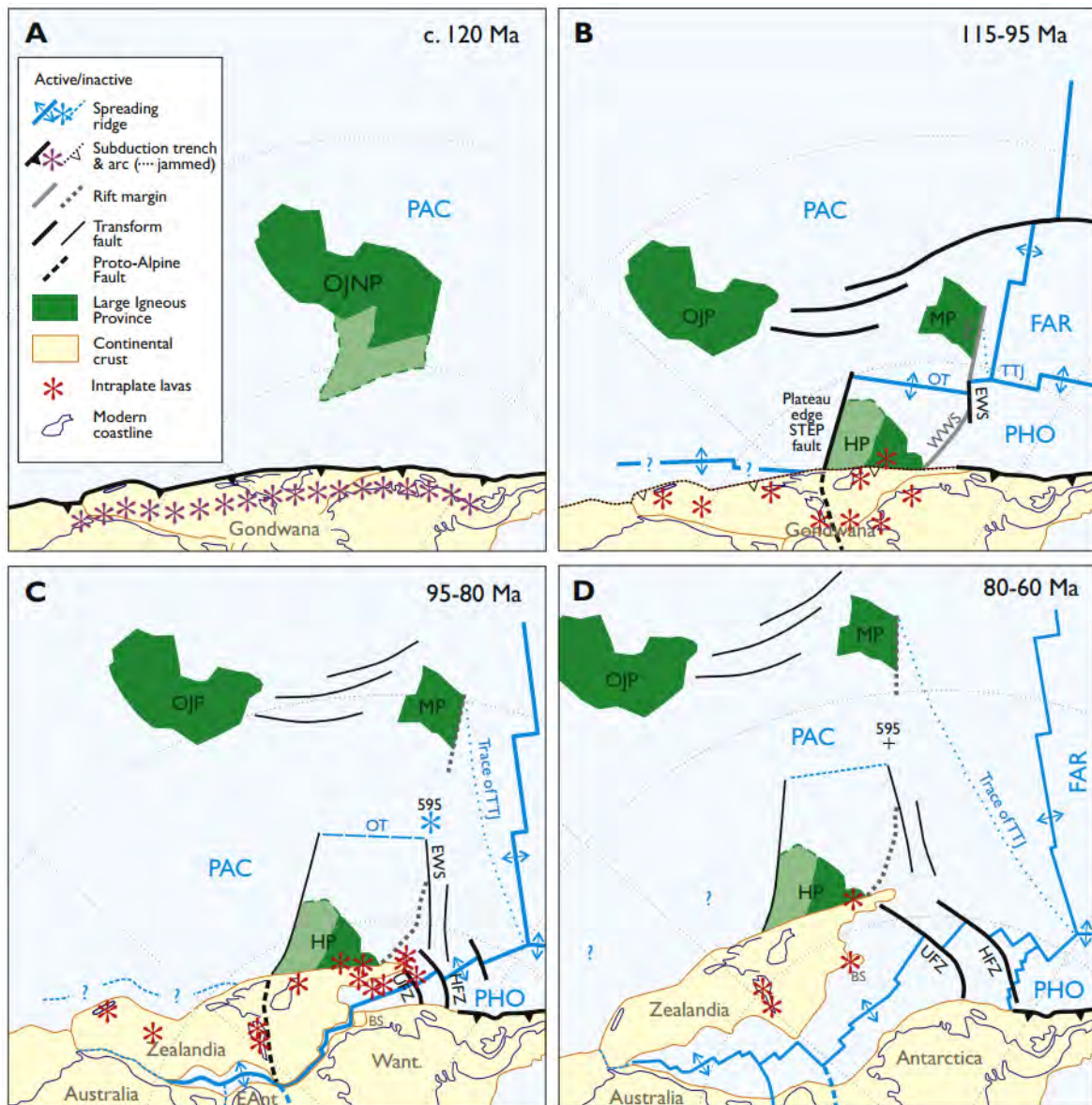


Fig. 6.7: New model for Late Cretaceous magmatic and tectonic change in and near the Zealandia continent-ocean margin: (A) Early Cretaceous subduction phase; (B) superplateau breakup, collision of Hikurangi Plateau with Gondwana and subduction cessation; (C) spreading ceases at Osborn Trough but continues east of Hikurangi Plateau; (D) establishment of kinematically stable spreading in Southern Ocean. EAnt = East Antarctica, WAnt = West Antarctica, PAC = Pacific Plate, FAR = Farallon Plate, HIK = Hikurangi Plate, PHO = Phoenix plate, OJNP = Ontong-Java Nui Plateau, OJP = Ontong Java plateau, MP = Manihiki Plateau, HP = Hikurangi Plateau, TTJ = Tongareva Triple Junction, OT = Osborn Trough, MS = Manihiki Scarp, EWS = East Wishbone Scarp, WWS = West Wishbone Scarp, UFZ = Udintsev Fracture Zone, HFZ = Heezen Fracture Zone. The time span of panels C and D is too broad to show the short-lived Bellingshausen Plate near West Antarctica (Eagles et al., 2004). Elements of model based on Larson et al. (2002), Larter et al. (2002), Mortimer et al. (2006) and Reyners et al. (2011).

converging on Gondwana generating the Median Batholith and Torlesse accretionary wedge (Fig. 6.7A; Mortimer et al., 2014). We agree with Sutherland and Hollis (2000), Davy et al. (2008) and Davy (2014) that collision of the Hikurangi Plateau was indeed the prime cause of 110–100 Ma subduction cessation at the Zealandia part of the then Gondwana margin (Fig. 6.7B). However, spreading at the Osbourn Trough did not necessarily cease then but could have continued for up to another 20–30 m.y. The persistence or resumption of spreading around the jammed Hikurangi Plateau took place to the east of the plateaus (present day geographic coordinates). The Manihiki Scarp is a rift edge feature with oceanic crust to the SE and dates from c. 119 Ma (Larson et al., 2002). Mortimer et al. (2006) proposed that, from 115 Ma, the West Wishbone Scarp was, likewise, a SE-facing intra-oceanic rift edge and was obliquely cut by the East Wishbone Ridge and a parallel, un-named fault (Fig. 6.1). Eagles et al. (2004) were the first to suggest that the West Wishbone Scarp was formerly co-linear and conjoined with the Manihiki Scarp, a proposition with which we agree. By c. 105 Ma the West Wishbone and Manihiki scarps had started to move apart on the East Wishbone Scarp which transferred motion from the Osbourn Trough and of the Tongareva Triple Junction (Fig. 6.7B). The 86–81 Ma ages of intraoceanic seamounts around the eastern tip of the Chatham Rise allow assignment of minimum ages to the Cretaceous Normal Superchron crust SE of the West Wishbone Scarp. From 95 to 80 Ma, progressive mechanical misalignment of the SE-migrating spreading system along the long-offset Wishbone Scarp eventually led to abandonment of the Osbourn Centre spreading and all Pacific-West Antarctica plate motion was taken up on the more southerly spreading system that broke Zealandia off Gondwana (Fig. 6.7C). The best constraint on the age of new seafloor between the eastern Chatham Rise and West Antarctica is the K-feldspar age of 83.9 ± 0.1 Ma from trachyte DR66-1 from Erik Seamount, representing a minimum age for the inception of seafloor spreading in this region. In the interval 80–60 Ma, Bollons Seamount was initially attached to West Antarctica but a ridge jump stranded it in its present position as, with time, spreading propagated to the SW further splitting Zealandia from West Antarctica and establishing the spreading system that persists today (Fig. 6.7D). The tectonic events to the west of the Hikurangi Plateau are necessarily more speculative because that crust has since subducted beneath the Kermadec Arc (Fig. 6.1). The full and original size of the Hikurangi Plateau is inferred to be about double its present day exposed area (Hoernle et al., 2010; Reyners et al., 2011; Timm et al., 2014). The Osbourn Trough likely continued west (present day coordinates) and it is possible that the west side of the Hikurangi Plateau was the site of a major transform, possibly a subduction-transform edge propagator (STEP) fault (Govers and Wortel, 2005). Conceivably, the spreading systems to the west of the Hikurangi Plateau were as complex as those to the east.

6.7. Conclusions

New geochronological data from Late Cretaceous igneous rocks in the SW Pacific-New Zealand region highlight regional changes in tectono-magmatic regime from subduction to a rift and intraplate setting to stable seafloor spreading. Cessation of long-lived subduction at the SE Gondwana margin is reasonably attributed to collision of the Hikurangi Plateau at 110–100 Ma. Widespread but low-volume intraplate volcanic rocks erupted in the interval 99–78 Ma across Gondwana/Zealandia continental lithosphere, oceanic crust and Hikurangi Plateau. Based on new dating of DSDP 595 basalts, we propose that Osbourn Trough spreading could have ceased at c. 79 Ma rather than earlier as proposed by previous workers. However, more material and more dating will be needed before this result can be used with confidence. Following collision, a regime of dynamically changing ridge and transform spreading patterns was arrayed around the east edge of the collided Hikurangi Plateau. From c. 84 Ma the spreading pattern became simplified and focussed on the Pacific-Antarctic ridge that split Zealandia away from Gondwana.

Acknowledgments

We thank the Captain and crew of F/S Sonne 168 “Zealandia” cruise for dredged rocks and the IODP/DSDP core repository for providing the DSDP 595 samples. The New Zealand Ministry of Foreign Affairs and Trade gave permission to use the data obtained from Bollons Gap. We also thank John Simes, Belinda Smith Lyttle and Jenny Black for technical assistance, and Karsten Gohl, Bryan Davy and Hamish Campbell for discussions. An earlier version of the manuscript was improved by comments from Quinten van der Meer and an anonymous referee. The German Ministry of Education and Research (BMBF; grant SO168 Zealandia), the DFG (grants HO18/ 12-1 and 2), GEOMAR Helmholtz Centre for Ocean Research and the New Zealand Government (core grant to GNS Science), are gratefully acknowledged for providing funding for this project.

Supplemental material

Supplemental materials for this manuscript are available online and include (A) table data and graphical presentations of the $^{40}\text{Ar}/^{39}\text{Ar}$ measurements and (B) table data of the whole-rock geochemistry of all new samples presented in study. Supplements can be accessed by the following link: <https://doi.org/10.1016/j.gr.2018.07.010>

7. Co-authorship II

Late Cretaceous (99-69 Ma) basaltic intraplate volcanism on and around Zealandia: Tracing upper mantle geodynamics from Hikurangi Plateau collision to Gondwana breakup and beyond

By K. Hoernle^{1,2}, C. Timm^{1,3}, F. Hauff¹, V. Tappenden⁴, R. Werner¹, E.M. Jolis¹, N. Mortimer⁵, S. Weaver⁴, F. Riefstahl^{2,6}, and K. Gohl⁶

¹GEOMAR Helmholtz Centre for Ocean Research Kiel, Kiel, Germany

²Kiel University, Institute of Geosciences, Kiel, Germany

³GNS Science, Lower Hutt, New Zealand

⁴University of Canterbury, Christchurch, New Zealand

⁵GNS Science, Dunedin New Zealand

⁶Alfred Wegener Institute Helmholtz Centre for Polar and Marine Research, Bremerhaven, Germany

Abstract

Margins resulting from continental breakup are generally classified as volcanic (related to flood basalt volcanism from a starting plume head) or non-volcanic (caused by tectonic processes), but many margins (breakups) may actually be hybrids caused by a combination of volcanic and tectonic processes. It has been postulated that the collision of the Hikurangi Plateau with the Gondwana margin ~110 Ma ago caused subduction to cease, followed by large-scale extension and ultimately breakoff of the Zealandia micro-continent from West Antarctica through seafloor spreading which started at ~85 Ma. Here we report new geochemical (major and trace element and Sr-Nd-Pb-Hf isotope) data for Late Cretaceous (99-69 Ma) volcanism from Zealandia, which include the calc-alkalic, subduction-related Mount Somers (99-96 Ma) and four intraplate igneous provinces: 1) Hikurangi Seamount Province (99-88 Ma), 2) Marlborough Igneous Province (98-94 Ma), 3) Westland Igneous Province (92-69 Ma), and 4) Eastern Chatham Igneous Province (86-79 Ma). Each of the intraplate provinces forms mixing arrays on incompatible-element and isotope ratio plots between HIMU (requiring long-term high $\mu = {}^{238}\text{U}/{}^{204}\text{Pb}$) and either a depleted (MORB-source) upper mantle (DM) component or enriched continental (EM) type component (located in the crust and/or upper mantle) or a mixture of both. St. Helena end member HIMU could be the common component in all four provinces. Considering the uniformity in composition of the HIMU end member despite the type of lithosphere (continental, oceanic, oceanic plateau) beneath the igneous provinces, we attribute this component to a sub-lithospheric source, located beneath all volcanic provinces, and thus most likely a mantle plume. We propose that the plume material rose beneath the active Gondwana margin and flowed along the subducting lithosphere beneath the Hikurangi Plateau and neighbouring seafloor and through slab tears/windows beneath the Gondwana (later to become Zealandia) continental lithosphere. We conclude that both plateau collision, resulting in subduction cessation, and the opening of slab tears/windows, allowing hot asthenosphere and/or plume material to upwell to shallow depths, were important in causing the breakup of Zealandia from West Antarctica. Combined tectonic-volcanic processes are also likely to be responsible for causing breakup and the formation of other hybrid type margins.

7.1. Introduction

A fundamental question in the Earth Sciences is what triggers continental breakup (e.g. Sleep, 1971; Condie, 2016). Many rifted margins are characterized by up to 15 km of underplated mafic crust and submarine seaward-dipping reflectors, which reflect subaerially-erupted basaltic volcanism tilted during subsidence (e.g. Condie, 2016). They are generally associated with flood basalt events formed during the initial (plume head) stage of mantle plumes (Richards et al., 1989). It is proposed that large plume heads (≤ 2000 km in diameter) impinge on the base of the lithosphere, causing lithospheric thinning, uplift, extension, rifting and eventually seafloor spreading. Far-field extensional plate tectonic forces are believed to govern the formation of non-volcanic margins (Geoffroy, 2005). At some stage in their development, supercontinents are surrounded by subduction zones. Rollback of the subducting slab along much of this subduction network can lead to internal extension, resulting in continental breakup. Progressive extension of cool continental lithosphere far from a mantle plume, for example the Iberian margin, has been proposed as a mechanism for generating nonvolcanic margins (Reston, 2007). Alternatively, it has also been proposed that subduction of a spreading centre or other change in plate boundary forces can lead to continental breakup (e.g. Bradshaw, 1989). Here we investigate one of the late breakup phases of the Gondwana supercontinent: One of the most enigmatic continental breakup events in recent Earth history. This breakup event resulted in the separation of pieces of the present Zealandia micro-continent from Marie Byrd Land, West Antarctica. Proposed models to explain the breakup of Zealandia from Antarctica include: 1) collision of the Pacific-Phoenix spreading centre with the Gondwana active margin (Bradshaw, 1989; Luyendyk, 1995; Storey et al., 1999), 2) impingement of a mantle plume head at the base of the Gondwana margin lithosphere at what is now Marie Byrd Land, Antarctica (Weaver et al., 1994; Storey et al., 1999), 3) collision of the Hikurangi Plateau with the Gondwana active margin (now the Chatham Rise) clogging the subduction system (e.g. Sutherland and Hollis, 2001; Davy et al., 2008; Hoernle et al., 2010; Reyners et al., 2011; Mortimer et al., 2019). In most recent models, the collision of the Hikurangi Plateau, one of the three major fragments of the Ontong Java-Manihiki-Hikurangi superplateau (e.g. Taylor, 2006; Davy et al., 2008; Hochmuth et al., 2015), with the Gondwana active margin is invoked as the initial trigger of this breakup. Since the proposed models include both tectonic and volcanic processes, this is a key place to investigate hybrid mechanisms for causing continental breakup and the formation of hybrid margins. Here we will evaluate these questions using age and geochemical data from four different intraplate magmatic provinces (Fig. 7.1, 7.2): Hikurangi Igneous Seamount Province (99-88 Ma; Hoernle et al., 2010) - consisting of alkalic seamounts on the Hikurangi Plateau, formed after collision of Hikurangi Plateau with the Gondwana margin, 2) Marlborough Igneous Province (98-94 Ma; Tappenden, 2003; McCoy-West et al., 2010; Mortimer et al., 2019) - alkalic volcanism on the northern South Island east of the South Alpine Fault, including Lookout, Gridiron, Mandamus and Tapuaenuku Igneous complexes, 3) Westland Igneous Province (92-69 Ma; van der Meer et al., 2016; van der Meer et al., 2017; Mortimer et al., 2019) - tholeiitic to lamprophyric Westland and Hohonu dikes on the northern South Island west of the Alpine Fault, and 4) East Chatham Volcanic Province (86-79 Ma; Panter et al., 2006; Homrighausen et al., 2018; Mortimer et al., 2019) - transitional to alkalic lavas on Chatham Island and seamounts on the East Chatham Rise and the surrounding seafloor. We use the temporal and spatial evolution of these four intraplate volcanic provinces to reconstruct processes occurring within the subducted lithosphere and within the mantle beneath the former Zealandia active margin until breakup, including the early history of seafloor spreading between Zealandia and West Antarctica.

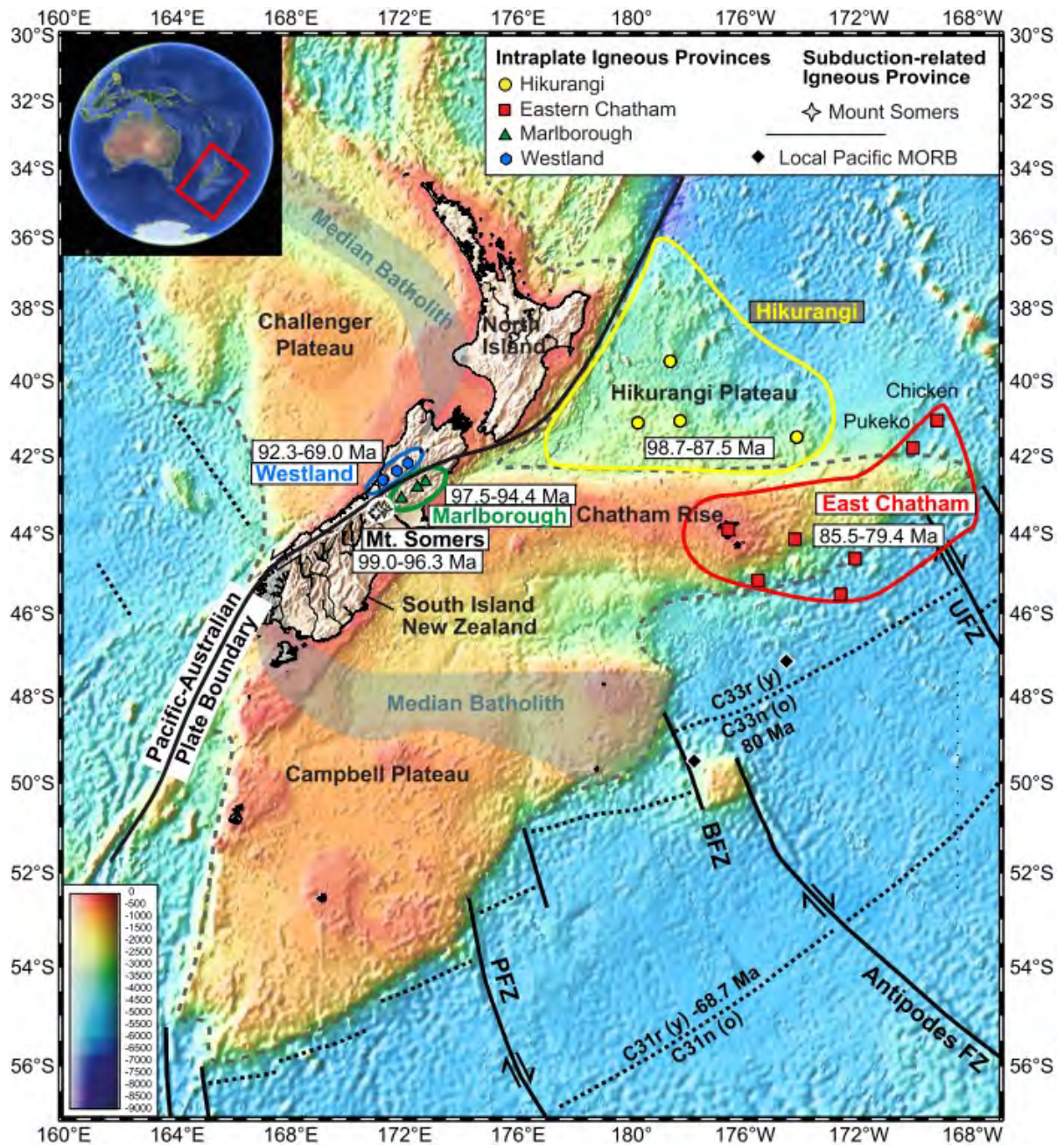


Fig. 7.1 Bathymetric map (after Smith and Sandwell, 1997), showing Zealandia and the Hikurangi Plateau, with inset map from Google Earth (2018), showing the location of the bathymetric map. Also shown are the four Cretaceous (99-69 Ma) intraplate igneous provinces (Hikurangi in yellow, Marlborough in green, Westland in blue and East Chatham in red), including sample locations within them, and the location of the Mt. Somers subduction-related volcanism (~99-96 Ma). The black line marks the plate boundary between the Pacific and Indo-Australian Plates. UFZ = Udintsev Fracture Zone; BFZ = Bollons Fracture Zone; PFZ = Pahemo Fracture Zone.

7.2. Samples and analytical methods

Volcanic rock samples come from DSDP Site 595, five seamounts on the eastern Chatham Rise collected by dredging on the R/V SONNE SO168 and SO246 expeditions, 30 locations from the Marlborough Province (Mandamus Igneous complex, Lookout and Gridiron volcanics), 10 locations from the Westland Province (Hohonu Dikes), and 28 locations from the Mount Somers volcanic group (including two sites from Torlesse metasediments) (Fig. 7.1). For the dredged rocks, their angular shape, freshly broken surfaces and the homogeneity of rock types indicate an in-situ (not

ice-rafted) origin. Sampling localities are summarized in Supplementary Table 1. Analytical methods are reported in Supplementary File 1.

7.3. Results

We present new geochemical (major and trace element and Sr-Nd-Hf-Pb isotope) data in Supplementary Tables 1 and 2. $^{40}\text{Ar}/^{39}\text{Ar}$ ages, major element data for dated samples, and additional background information are reported in Mortimer et al. (2019) and Homrighausen et al. (2018). We combine our new results with those from published studies (Hoernle et al., 2006; Mortimer et al., 2006; Panter et al., 2006; McCoy-West et al., 2010; Timm et al., 2010; Homrighausen et al., 2018; van der Meer et al., 2016, 2017) to reconstruct the evolution of intraplate volcanism on and around Zealandia from ~100-70 Ma. Major element (oxide) variations are consistent with fractional

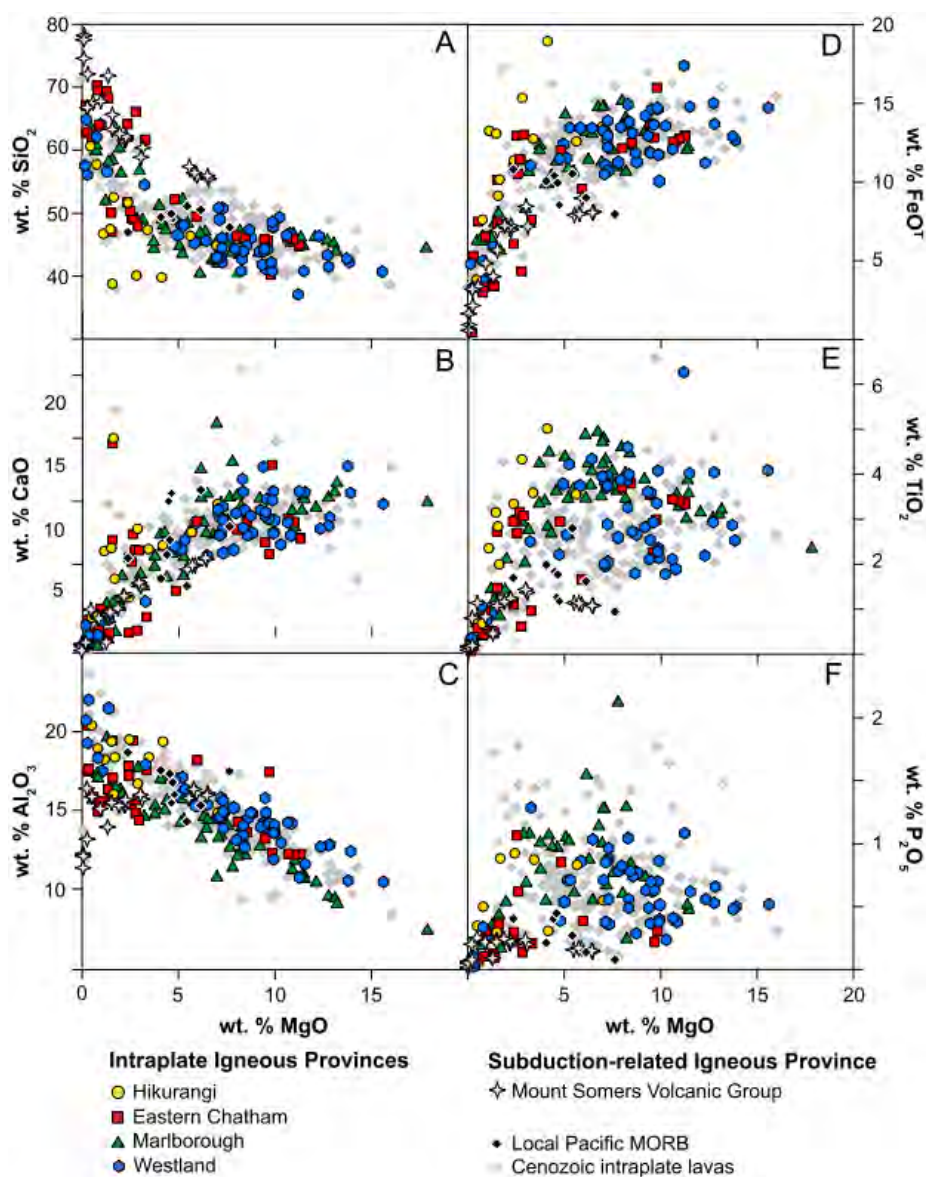


Fig. 7.2: Major element diagrams of MgO vs. A) SiO_2 , B) CaO , C) Al_2O_3 , D) FeO_t = total iron as FeO , E) TiO_2 and F) P_2O_5 . Data sources: Eastern Chatham Rise = this study, Mortimer et al. (2019), Homrighausen et al. (2018); Chatham Island Southern Volcanic rocks = Panter et al. (2006); Hikurangi Seamounts = Hoernle et al. (2010); Osborn Trough = Worthington et al. (2006); DSDP Site 595 = Mortimer et al. (2019); Marlborough = this study, McCoy-West et al. (2010); Mount Somers volcanic group = this study; Westland Province = this study, van der Meer et al. (2016), van der Meer et al. (2017); Cenozoic intraplate lavas = Hoernle et al. (2006), Timm et al. (2009) and Timm et al. (2010).

crystallization (Fig. 7.2). With decreasing MgO, both SiO₂ and Al₂O₃ (until ~5 wt.% MgO for East Chatham and Mt. Somers samples) roughly increase, whereas CaO (until ~7 wt.% MgO) and FeO_t (total iron until ~5 wt.% MgO) remain roughly constant and then decrease. TiO₂ and P₂O₅ increase initially and decrease below MgO ~5 wt.% (except Westland samples). The observed trends are consistent with fractionation of the observed major phenocryst phases in the samples in the sequence olivine, clinopyroxene, Fe-Ti oxides, ± plagioclase and apatite, although assimilation processes may also have affected oxide contents (Tappenden, 2003; Panter et al., 2006; McCoy-West et al., 2010; van der Meer et al., 2016, 2017). Alteration has affected the chemistry of some samples, considering the Late Cretaceous age and submarine history of some samples. Therefore, we use the Nb/Y vs. Zr/Ti plot (Pearce, 1996) to classify the rocks (Fig. 7.3A), which relies on ratios of immobile incompatible elements. The intraplate samples range from transitional tholeiites (Southern Volcanics, Chatham Island) to alkali basalts (most samples) through alkali rhyolites to foidites through phonolites, whereas the Mt. Somers rocks range from andesite to rhyolite and trachyte. On the Nb/Yb vs. Th/Yb and TiO₂/Yb diagrams (Fig. 7.3B,C; after Pearce, 2008), most of the intraplate igneous rocks have alkalic ocean-island basalt (OIB) affinities. The Hikurangi, Marlborough, Westland and East Chatham igneous rocks form arrays that extend from OIB-type compositions to lower Nb/Yb ratios, with some samples plotting within the mantle array in the direction of mid-ocean-ridge basalts (MORBs) and other samples plotting above the mantle array in the volcanic arc and crustal field. The Mt. Somers volcanic rocks with subduction and/or continental geochemical affinities (Tappenden, 2003) plot well above the mantle array clustering around typical Torlesse metasediments from the Canterbury region. On multi-element diagrams, we show incompatible elements normalized to primitive mantle for samples with LOI < 3.5 wt.% (except MSI_47A with 4.6 wt.%) and with low SiO₂ (43-49 wt.% for alkalic and 55-58 wt.% for calc-alkalic lavas) to minimize the effects of alteration and differentiation (Fig. 7.4). On primitive-mantle-normalized diagrams, the Hikurangi, Marlborough, Westland and Eastern Chatham volcanic rocks display positive Nb, Ta anomalies and negative K, Pb anomalies characteristic of OIBs, in particular HIMU (high time integrated $\mu = {}^{238}\text{U}/{}^{204}\text{Pb}$) type OIBs. When normalizing to average MORB instead of primitive mantle, however, these anomalies largely disappear. The Mt. Somers rocks display clear negative Nb, Ta and positive K, Pb anomalies characteristic of subduction-related volcanic and crustal rocks on both primitive-mantle and MORB normalized diagrams. Isotope correlation diagrams can be used to evaluate the sources from which igneous rocks are derived (Fig. 7.5). On the ${}^{206}\text{Pb}/{}^{204}\text{Pb}_{90\text{Ma}}$ vs ${}^{207}\text{Pb}/{}^{204}\text{Pb}_{90\text{Ma}}$ (Fig. 7.5A), ${}^{87}\text{Sr}/{}^{86}\text{Sr}_{90\text{Ma}}$, ${}^{143}\text{Nd}/{}^{144}\text{Nd}_{90\text{Ma}}$ (Fig. 7.5B,C) and ${}^{176}\text{Hf}/{}^{177}\text{Hf}_{90\text{Ma}}$ isotope diagrams (with isotope ratios calculated at 90 Ma), the four intraplate provinces form largely binary arrays that converge on the St. Helena HIMU field at radiogenic Pb isotope ratios. At unradiogenic Pb isotope ratios, the Hikurangi Seamount samples extend towards the enriched mantle (EM) type Hikurangi Plateau basement (older rocks forming the plateau beneath the Hikurangi seamounts), Westland samples towards MORB, Marlborough samples towards EM-type Mt. Somers samples and East Chatham samples towards MORB or Mt. Somers samples.

7.4. Discussion

During much of the Mesozoic, present-day Zealandia formed part of the southern Gondwana active continental margin, located adjacent to what is presently Marie Byrd Land, West Antarctica. At ~120-125 Ma ago, the Ontong Java Nui, the largest known Phanerozoic volcanic event on Earth, formed in the western Pacific, covering more than 1% of Earth's surface (Taylor, 2006; Davy et al., 2008; Hoernle et al., 2010; Timm et al., 2011; Hochmuth et al., 2015). Shortly after its formation, this superplateau broke apart into at least three major plateau fragments: 1) Ontong Java, 2) Manihiki and 3) Hikurangi. The Hikurangi and Manihiki Plateaus rifted apart between 115-120

Ma along the Osborn Trough spreading system (Worthington et al., 2006; Mortimer et al., 2006; Hochmuth et al., 2015). Thereafter the Hikurangi Plateau drifted southwards until it collided with the Gondwana active margin at ~110-105 Ma (e.g. Bradshaw, 1989; Mortimer et al., 2006; Davy et al., 2008). The buoyant (~15-20 Ma old) Hikurangi Plateau clogged the Gondwana subduction zone, causing cessation of subduction along the northern edge of what is now the Chatham Rise (e.g. Sutherland and Hollis, 2001; Davy et al., 2008; Reyners et al., 2011; Mortimer et al., 2019).

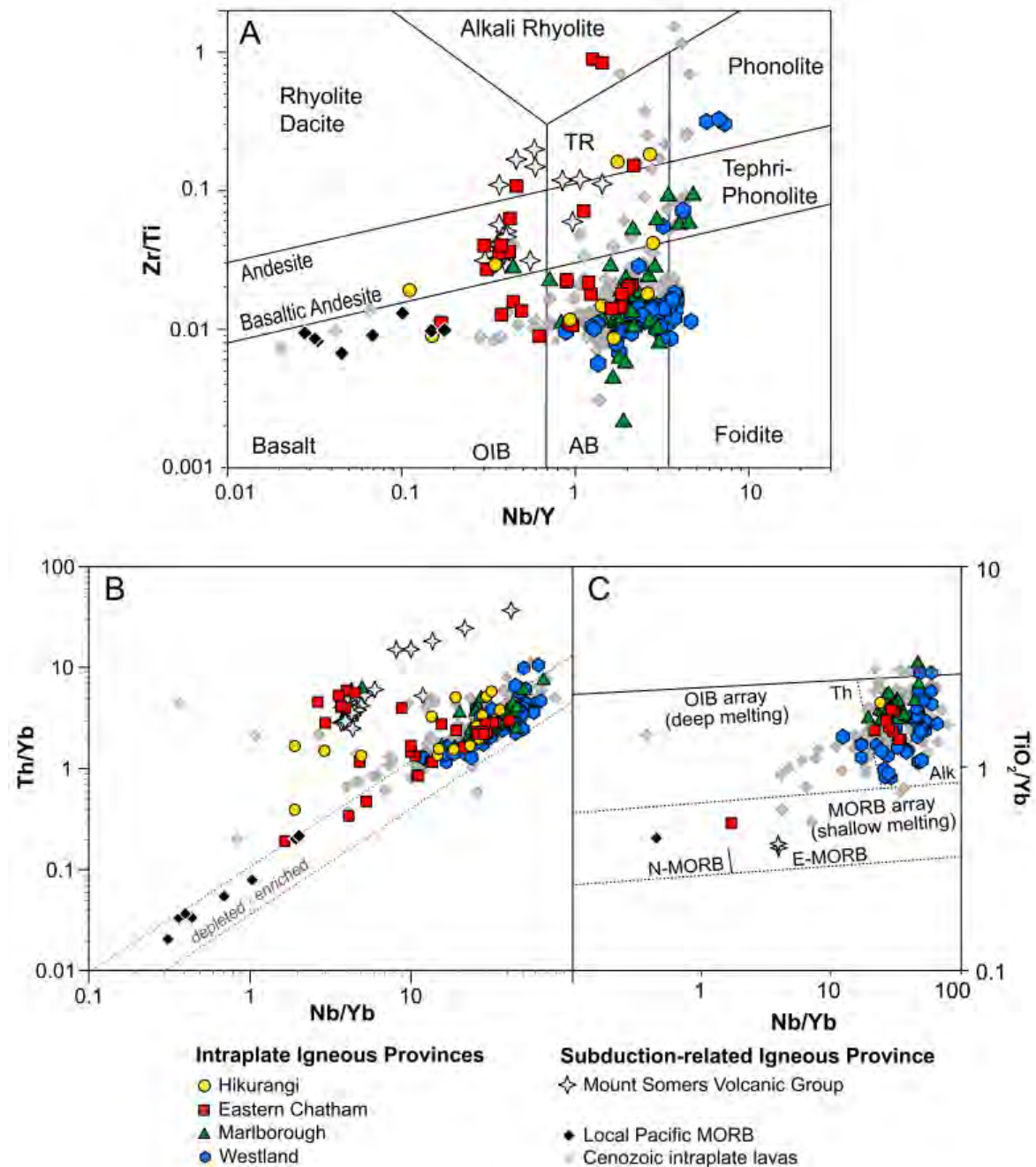


Fig. 7.3: Immobility, incompatible element classification diagrams: A) Nb/Y versus Zr/Ti after Pearce (1996), B) Nb/Yb versus Th/Yb, and C) Nb/Yb versus TiO₂/Yb after Pearce (2008). Only samples with MgO > 6 wt.% are shown in C) to minimize the effect of magnetite-ilmenite fractionation. Data sources are as follows: Hikurangi Seamount Province = yellow circles (Hoernle et al., 2010); Marlborough Igneous Province = green triangles: Lookout Volcanics (this study; McCoy-West et al., 2010), Gridiron Volcanics (this study), Mandamus Igneous Complex (this study); Eastern Chatham Igneous Province = red squares: Seamounts (this study; Homrighausen et al., 2018); Chatham Islands Southern Volcanic rocks (Panter et al., 2006); Westland Igneous Province = blue hexagons (this study; van der Meer et al., 2016; van der Meer et al., 2017). Black diamonds represent nearby Late Cretaceous MORB from DSDP Site 595, the Osborn Trough and the Bollons Fracture Zone (this study; Worthington et al., 2006; Mortimer et al., 2019). Grey diamonds represent published data from Cenozoic Volcanic centres (age of <60 Ma) (sources as in Fig. 7.2).

7.4.1. Formation of four intraplate volcanic provinces after Hikurangi Plateau collision

Four different mafic intraplate volcanic provinces (~99-69 Ma) formed on Gondwana continental crust (now Zealandia), the Hikurangi Plateau and the surrounding seafloor shortly after the Hikurangi Plateau collided with the Gondwana margin. Samples from the four intraplate volcanic provinces form distinct arrays on some incompatible element and isotope diagrams (Fig. 7.5) that converge on a common composition. Below we will first discuss the different arrays formed by each volcanic province, and then the common component involved in all four of the provinces. The seamounts on the Hikurangi Plateau record ages of 99-88 Ma (Hoernle et al., 2010). The seamounts have a distinct geochemical composition from the underlying Hikurangi Plateau basement. The

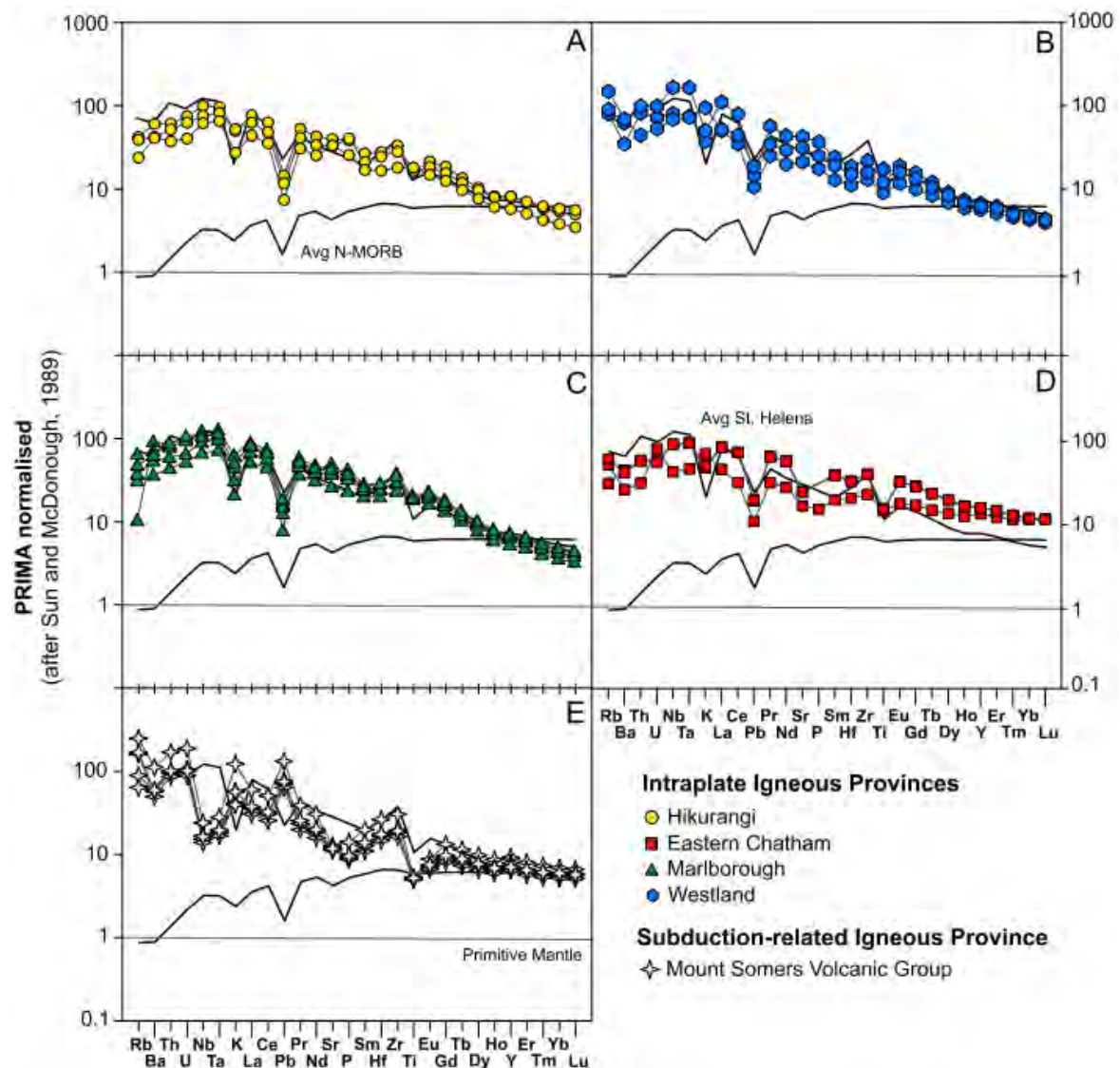


Fig. 7.4: Representative incompatible-element patterns (normalized to primitive mantle) that show HIMU-type signatures for low-SiO₂ (43-49 wt.%) lavas from A) Hikurangi Seamount Province (Hoernle et al., 2010), B) Westland Volcanic Province, C) Marlborough Volcanic Province, and D) Eastern Chatham Province; and subduction-zone signatures for high-SiO₂ (55-58 wt.%) lavas from E) Mt. Somers. Neither minor differentiation (MgO = 3-9 wt.%) nor alteration (LOI < 3.5 wt.%, except sample MSI_47A with LOI = 4.6 wt.%) appear to have caused significant changes in the incompatible-element patterns. We note that sharp changes in geochemistry of submarine rocks, even K, generally don't occur until LOI > 5 wt.% (e.g. Golowin et al., 2018). Data sources are as listed in Fig. 7.2 captions. The flatter HREE patterns of the Eastern Chatham samples are consistent with decompression melting extending into the spinel stability field, due to extension and thinning of the lithosphere in this region. Primitive mantle and average N-MORB compositions are from Sun and McDonough (1989) and average St. Helena pattern from data in Chaffey et al. (1989) and Hanyu et al. (2011).

basement has relatively flat incompatible-element patterns on multi-element diagrams and Sr-Nd-Pb isotopic composition similar to the main plateau-building stage on Ontong Java formed by the Kwaimbaita / Kroenke lavas (Hoernle et al., 2010). The Hikurangi seamounts, however, have more enriched incompatible element abundances and fractionated heavy rare earth element (HREE) contents, i.e. patterns with a negative slope of multi-element diagrams. The seamounts form an array, extending from St. Helena HIMU to the EM-type plateau basement field on incompatible-element and isotope-ratio diagrams (Fig. 7.3, 7.5), which can be explained by mixing of HIMU melts with EM-type melts from the Hikurangi Plateau basement or underlying lithosphere, overprinted with a similar composition during emplacement of the plateau.

Although a HIMU-type component has been found in the ~125 Ma Manihiki basement (Timm et al., 2011; Golowin et al., 2017), no evidence for this component has been found within the Hikurangi Plateau basement. The most radiogenic Manihiki basement lavas only have $^{206}\text{Pb}/^{204}\text{Pb}$ of ~19.7 and both $^{207}\text{Pb}/^{204}\text{Pb}$ and $^{208}\text{Pb}/^{204}\text{Pb}$ are lower at a given $^{206}\text{Pb}/^{204}\text{Pb}$ than in the Hikurangi Seamount lavas, indicating that the Hikurangi Seamount St. Helena HIMU component is distinct from the Manihiki basement HIMU-like component. Since the Hikurangi Plateau formed on young ocean crust near a spreading centre (Hochmuth et al., 2015), the pre-existing lithosphere is also an unlikely source for the HIMU component. The large size and HIMU- rather than EM1-type composition of the Hikurangi guyots (and thus former ocean island volcanoes) is not consistent with them being petit spots related to plate flexure just before subduction (e.g. Machida et al., 2009). Therefore, we favour an asthenospheric source for the HIMU component in the Hikurangi seamount lavas, as proposed by Hoernle et al. (2010). The intraplate Marlborough Igneous Province (98-94 Ma; Tappenden, 2003; McCoy-West et al., 2010; Mortimer et al., 2019) on the northern South Island and the calc-alkalic Mt. Somers volcanic rocks, located in the central South Island, were both located in the forearc of the Gondwana subduction zone, trenchwards of the 232-105 Ma Median Batholith (e.g. Tappenden, 2003; van der Meer et al., 2018). On incompatible-element and isotope ratio diagrams (Fig. 7.3, 7.5), the Marlborough intraplate rocks form an array from the St. Helena HIMU towards an enriched composition, which has lower (Ce, Nd)/Pb ratios and more radiogenic Sr and less radiogenic Nd, Hf and Pb isotope ratios than the HIMU end member. The Sr-Nd-Pb-Hf isotopic variations in the Marlborough igneous rocks can be explained by assimilation of up to ~25%, but generally <10%, crustal rocks from the Early Cretaceous Pahau terrane (Tappenden, 2003; McCoy-West et al., 2010). We however do not see any clear correlations between indices of differentiation (e.g. SiO_2 or MgO) with Sr-Nd-Pb isotope ratios in our data. Therefore, if these trends are caused by crustal assimilation, they are not coupled to differentiation, i.e. assimilation during fractional crystallization (AFC). More importantly, crustal assimilation has not been substantial enough in the low-silica rocks to change their HIMU signatures significantly (Fig. 7.4). The calc-alkalic Mt. Somers rocks (99-96 Ma) also have enriched isotopic compositions, as well as low (Ce, Nd, Sr)/Pb ratios, and thus could also serve as the enriched end member for the Marlborough Province intraplate rocks. They display typical incompatible-element characteristics of subduction zone volcanism, such as relative depletion in Nb, Ta and relative enrichment in K, Pb on diagrams with concentrations normalized to primitive mantle (Fig. 7.4) and average MORB. Their chemistry could reflect the composition of the mantle wedge of the Gondwana subduction zone (i.e. a mixture of depleted MORB-source upper mantle and subducted marine sediments) and/or contamination of depleted upper mantle melts by Pahau terrane crustal rocks. The Anita Peridotite, a block of sub-arc wedge exhumed from the Gondwana subduction zone in Fiordland, has enriched isotopic compositions (e.g. amphiboles have $^{87}\text{Sr}/^{86}\text{Sr}$ up to 0.706, $^{143}\text{Nd}/^{144}\text{Nd}$ as low as 0.5127 and $^{206}\text{Pb}/^{204}\text{Pb}$ similar to Mt. Somers rocks; Czertowicz et al., 2016), indicating that the subcontinental-

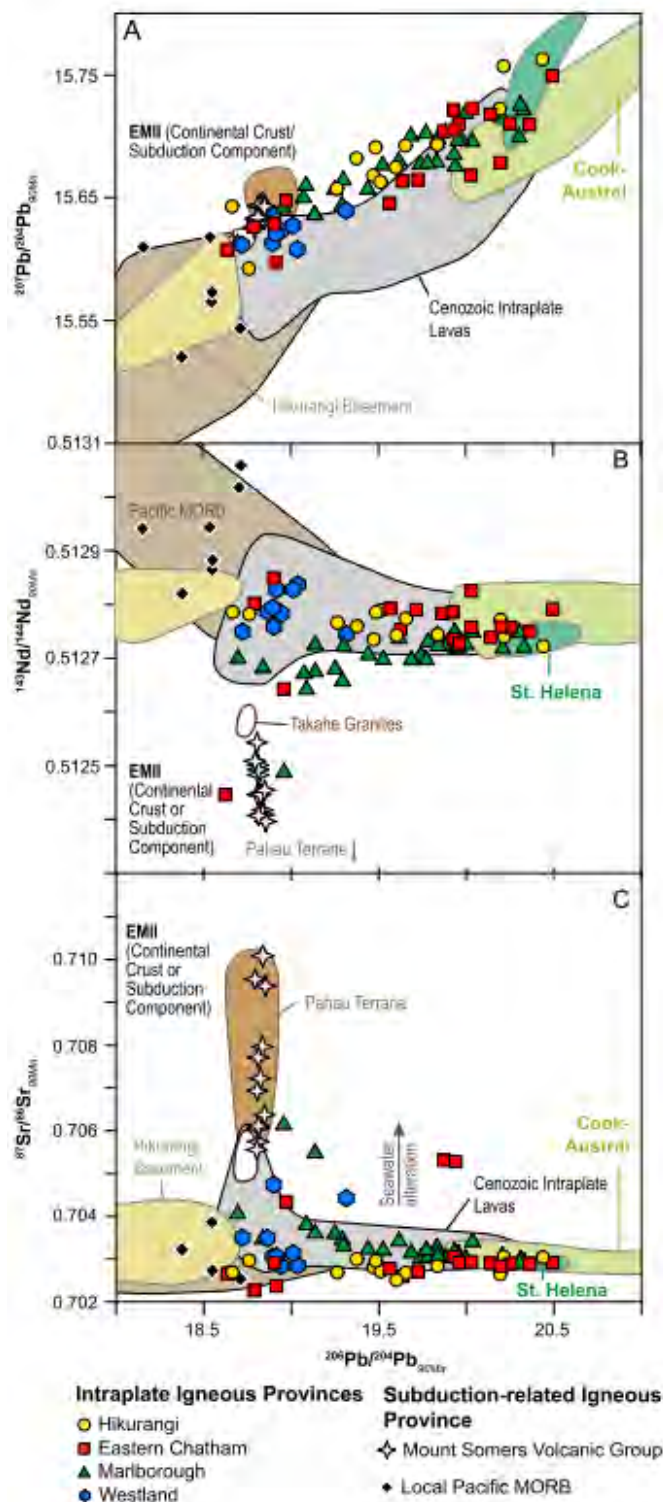


Fig. 7.5: Plots of initial A) $^{206}\text{Pb}/^{204}\text{Pb}$ vs $^{207}\text{Pb}/^{204}\text{Pb}$, B) $^{206}\text{Pb}/^{204}\text{Pb}$ vs $^{143}\text{Nd}/^{144}\text{Nd}$ and C) $^{206}\text{Pb}/^{204}\text{Pb}$ vs $^{87}\text{Sr}/^{86}\text{Sr}$ isotope ratios for samples from this study and published data (see below), assuming an average age of 90 Ma for all Late Cretaceous samples. The St. Helena HIMU (Chaffey et al., 1989; Kawabata et al., 2011), Cook Austral HIMU (Kawabata et al., 2011; Hanyu et al., 2011) and Cenozoic Zealandia and Pacific MORB fields have been projected to 90 Ma, using the same parent/daughter ratios as employed by Homrighausen et al. (2018 and references therein). $Sm = 6.5$ ppm and $Nd = 20$ ppm were assumed for the DSDP Site 595 $^{143}\text{Nd}/^{144}\text{Nd}$ age correction. Mantle end members are from Zindler and Hart (1986). Data sources are: this study; McCoy-West et al. (2010), McCoy-West et al. (2016), Hoernle et al. (2010), Panter et al. (2006), Homrighausen et al. (2018), Mortimer et al. (2006), van der Meer et al. (2016), Hoernle et al. (2006), Timm et al. (2009) and Timm et al. (2010). Late Cretaceous ocean crust, sampled at Bollons Gap (~77–85 Ma; Mortimer et al., 2019), DSDP Site 595 (~84 Ma; Mortimer et al., 2019) and the Osborn Trough (Late Cretaceous; Worthington et al., 2006), has a depleted composition, pointing to a primarily depleted composition for the upper mantle in this area in the Late Cretaceous.

lithospheric mantle (SCLM) can have an EM-like composition similar to the least enriched Mt. Somers lavas. The Marlborough Province mixing array could be explained by interaction of HIMU mantle melts with enriched Pahau terrane crustal rocks, enriched SCLM similar to the Anita Peridotite, and/or enriched (Mt. Somers-type) mantle wedge (asthenosphere and/or lithospheric mantle), contaminated with subducted Pahau terrane crustal rocks. After cessation of Marlborough volcanism at ~94 Ma, volcanism moved to the Westland Igneous Province (92-69 Ma; van der Meer et al., 2016; van der Meer et al., 2017; Mortimer et al., 2019), located ~500 km SW of the Marlborough Province and south of the Median Batholith and thus in the backarc region. The basement beneath this province consists of Cambrian to Ordovician volcanic arc, passive margin and forearc turbidite assemblages, which were intruded by Mesozoic granites (van der Meer et al., 2018). The mafic volcanic rocks were erupted in two distinct phases becoming younger to the south: 1) northern Westland and Hohonu dikes (~92-83 Ma), 2) central Westland dikes (~72-69 Ma) (van der Meer et al., 2016). This confirms a southern progression in intraplate volcanism on the overriding plate after cessation of subduction at ~100 Ma from the Marlborough Province to northern Westland/Hohonu to central and southern Westland. These volcanic rocks have OIB-type incompatible element abundances (Fig. 7.3, 7.4), displaying relative Nb enrichment and relative K and Pb depletions on primitive-mantle-normalized incompatible element diagrams (van der Meer et al., 2016; van der Meer et al., 2017). They form a crude array on isotope diagrams between a HIMU-like component and a depleted upper mantle MORB source (Fig. 7.5B). The overall lower $^{206}\text{Pb}/^{204}\text{Pb}_{90\text{Ma}}$ (≤ 19.4) isotope ratios for the Westland samples could reflect greater dilution of HIMU-type mantle melts with depleted upper mantle. The elevated $^{87}\text{Sr}/^{86}\text{Sr}$ ratio (>0.704) in two more evolved samples is consistent crustal contamination in these Westland rocks. Contemporaneous with the Westland / Hohonu magmatism, the Eastern Chatham Province, including the Chatham Islands and seamounts on the eastern Chatham Rise and surrounding ocean crust, were active from ~86-79 Ma (Panter et al., 2006; Mortimer et al., 2006; Homrighausen et al., 2018; Mortimer et al., 2019). Two intraplate seamounts north of the easternmost Chatham Rise, located on the mid Cretaceous (98-92 Ma; Mortimer et al., 2019) Pacific Ocean crust, have similar ages of 86 Ma (Chicken or Hühnchen Seamount) and 81 Ma (Pukeko Seamount) to the East Chatham Rise volcanism (Panter et al., 2006; Homrighausen et al., 2018; Mortimer et al., 2019). The East Chatham rocks have incompatible element characteristics that extend from the OIB field to EMORB-type and to subduction-related or crustal compositions (Fig. 7.3B). Chicken Seamount and southern Chatham Island volcanic rocks have St. Helena HIMU-type isotopic composition (Panter et al., 2006; Homrighausen et al., 2018), overlapping with the Hikurangi and Marlborough rocks with the most radiogenic Pb on the isotopic diagrams (Fig. 7.5). The East Chatham isotope data can be explained by mixing HIMU mantle melts with both enriched mantle wedge (asthenospheric and/or SCLM) and/or crustal Takahe granite (Mortimer et al., 2006) and/or normal MORB type compositions. The elevated Sr isotope ratios (>0.705) in two samples with radiogenic Pb are likely to be the result of seawater alteration. In conclusion, the components with low $^{206}\text{Pb}/^{204}\text{Pb}$ ratios, observed in each volcanic province, are most likely located in the shallow (asthenospheric or lithospheric) mantle or crust.

7.4.2. A common HIMU end member for the Late Cretaceous intraplate volcanism

Four different mafic intraplate volcanic provinces (99-69 Ma), emplaced on contiguous Gondwana continental crust (now Zealandia), the Hikurangi Plateau and the surrounding seafloor shortly after the Hikurangi Plateau collided with the Gondwana margin, form distinct arrays on incompatible-element and isotope diagrams (Fig. 7.3B, 7.5). As discussed above, the end of the mixing arrays with low $^{206}\text{Pb}/^{204}\text{Pb}$ ratios can be explained through interaction of HIMU asthenospheric melts with different types of overlying lithosphere (crust and mantle) and shallow depleted or subduction-modified asthenosphere. The Hikurangi seamounts formed on the oceanic Hikurangi Plateau after

it was transported nearly 3000 km southwards from where it formed together with the Manihiki Plateau at ~120 Ma on Late Jurassic or Early Cretaceous oceanic crust (Davy et al., 2008; Hoernle et al., 2010; Timm et al., 2011; Hochmuth et al., 2015). The Westland, Marlborough and East Chatham volcanic provinces formed largely on different age and types of Gondwana continental lithosphere (backarc and forearc lithosphere respectively). Finally, several seamounts of the East Chatham Province (e.g. Chicken and Pukeko seamounts) are located on Cretaceous (~98-92 Ma; Mortimer et al., 2019) Pacific Ocean crust. Despite the variation in the age and nature of the overlying lithosphere (ranging from mid-ocean ridge to oceanic plateau to continental type), incompatible-element and isotope ratios from each volcanic province form arrays that converge on a common end member (e.g. Fig. 7.3B, 7.5). The common end member of the Late Cretaceous intraplate lavas has radiogenic Pb, relatively radiogenic Nd and Hf, and unradiogenic Sr isotope ratios, falling within the range of end member HIMU compositions from St. Helena Island, which has a similar isotopic composition to the Austral Island HIMU, but with higher $^{207}\text{Pb}/^{204}\text{Pb}$ at a given $^{206}\text{Pb}/^{204}\text{Pb}$ isotope ratio (e.g. Chaffey et al., 1989; Hanyu et al., 2011; Nebel et al., 2013). The common end member is also characterized by enrichment of highly and moderately incompatible elements, and displays relative enrichment in Nb and Ta and relative depletion of K and Pb compared to elements with similar incompatibility on primitive mantle-normalized diagrams (Fig. 7.4). Although the relative depletion in K and Pb have been used to argue for amphibole in the source of the Late Cretaceous New Zealand lavas and thus for a SCLM source (Panter et al., 2006; McCoy-West et al., 2016; van der Meer et al., 2017), we note that the classic end member HIMU localities (St. Helena and Austral Islands) with these trace element and isotopic characteristics were erupted on oceanic lithosphere and thus cannot be derived directly from SCLM. Furthermore, these negative K and Pb anomalies are largely absent on MORB-normalized diagrams and thus appear to be an artifact of normalizing to primitive mantle - a composition pre-dating continent extraction from the mantle. Although Archean and Early Proterozoic SCLM can have HIMU-type compositions, intraplate lavas not located on continental crust of this age and on oceanic crust could be derived from ocean crust or SCLM recycled through the lower mantle via subduction and mantle plumes (e.g. Hofmann and White, 1982; Weiss et al., 2017; Homrighausen et al., 2018). One of the most compelling arguments that the HIMU end member is derived from mantle plumes is that at both type localities (St. Helena and Austral Islands) mantle plumes have been imaged from the base of the lithosphere to the base of the lower mantle (Montelli et al., 2006; French and Romanowicz, 2015). A popular model for the formation of the HIMU component in Zealandia lavas invokes derivation from relatively young (no more than a few hundred million years old) metasomatized lithospheric mantle, possibly by subduction related fluids/melts (e.g. Panter et al., 2006; McCoy-West et al., 2016; van der Meer et al., 2017; Scott et al., 2016). This model, however, is unrealistic for the common HIMU end member observed in the Late Cretaceous Zealandia/Hikurangi volcanic provinces, because 1.0-3.2 Ga are needed to form end member HIMU from St. Helena and the Austral Islands based on Pb isotope model ages (e.g. Hofmann, 1997; Hanyu et al., 2011; Nebel et al., 2013; Homrighausen et al., 2018). Numerical simulations of the source evolution, however, suggest a minimum formation age for HIMU of 2.0-2.5 Ga (Kimura et al., 2016) and negative 33S isotope ratios in olivine from Austral HIMU samples point to an age of ≥ 2.45 Ga (Cabral et al., 2013). Although high $^{206}\text{Pb}/^{204}\text{Pb}$ isotope ratios of end member HIMU can be produced by very high $^{238}\text{U}/^{204}\text{Pb}$ ratios on the scale of a few hundred million years, high $^{207}\text{Pb}/^{204}\text{Pb}$ cannot be generated in such a short time span in the present Earth from recycled normal MORB type ocean crust or in the depleted upper mantle, because most of the ^{235}U (half-life ~0.7 Ga) has decayed since Earth formation (~4.5 Ga) in contrast to ^{238}U (half-life ~4.5 Ga), with the present $^{238}\text{U}/^{235}\text{U}$ being ~138. Furthermore, the oldest crustal ages for the Late Cretaceous intraplate provinces are ~0.5 Ga, whereas the oldest Re-depletion ages for mantle xenoliths from Marlborough and Westland Provinces are also ~0.5 Ga and from Chatham Island and Marie Byrd Land are ~1.0 Ga (McCoy-

West et al., 2013). Therefore, the lithosphere beneath the intraplate volcanic provinces is most likely too young to have generated end-member St. Helena-type HIMU. Finally, although peridotite mantle xenoliths from Zealandia have HIMU-like compositions, they have lower $^{207}\text{Pb}/^{204}\text{Pb}$ at a given $^{206}\text{Pb}/^{204}\text{Pb}$ than end-member St. Helena HIMU (McCoy-West et al., 2016; Scott et al., 2016). Other problems also exist with the proposition that subduction-related melts metasomatized the overlying SCLM to form the HIMU type compositions. There is, for example, no evidence that subduction ever occurred beneath the oceanic Hikurangi lithosphere, either before or after formation of the plateau, and beneath the oceanic lithosphere on which the Chicken and Pukeko seamounts are located. Furthermore, metasomatism generally creates very heterogeneous sources, which is inconsistent with the convergence of the Cretaceous intraplate volcanism on a fairly narrow isotopic compositional range similar to that of St. Helena lavas. Instead, the uniform composition of the common HIMU component must be derived from a well-mixed sub-lithospheric source that could generate melts beneath diverse oceanic and continental lithosphere. In conclusion, we favour derivation of the HIMU end member from a relatively homogeneous, deep reservoir and that the different igneous provinces were fed by (a) mantle upwelling(s) or plume(s) from such a reservoir. Based on studies of dikes from Marie Byrd Land, Antarctica with $^{40}\text{Ar}/^{39}\text{Ar}$ ages of 107 ± 5 Ma, it has been proposed that emplacement of a HIMU-type plume head beneath Marie Byrd Land may have served as the trigger for the final phase of Gondwana breakup (Weaver et al., 1994; Storey et al., 1999). We note, however, that none of the dikes has classic HIMU incompatible element (lacking pronounced relative Nb, Ta enrichments and K, Pb depletions on primitive-mantle-normalized diagrams; Weaver et al., 1994; Storey et al., 1999) or radiogenic Pb isotopic compositions (e.g. $^{206}\text{Pb}/^{204}\text{Pb} > 20.5$, as is the case for St. Helena, Tubuaii and Mangaia end-member HIMU islands and the Late Cretaceous Zealandia, Hikurangi and nearby seafloor volcanism). The incompatible-element characteristics and Pb isotope ratios of the dikes ($^{206}\text{Pb}/^{204}\text{Pb} = 18.74\text{-}19.02$, $^{207}\text{Pb}/^{204}\text{Pb} = 15.61\text{-}15.63$ and $^{208}\text{Pb}/^{204}\text{Pb} = 38.53\text{-}38.78$) are instead typical of Antarctic Peninsula crust (Fig. 7 in Storey et al., 1999), either reflecting extensive crustal assimilation or source contamination by subducted sediments with a similar composition to the Antarctic Peninsula crust. In addition, it was assumed that the Hikurangi Plateau was formed at the same time as the Antarctica dikes and that it had a HIMU composition (Storey et al., 1999). We now know that the Hikurangi Plateau formed contemporaneous with the Ontong Java and Manihiki Plateaus, ~ 3000 km to the north of the Gondwana margin and that the basement has an EM (rather than HIMU) type composition similar to the Kwaimbaita/Kroenke lavas from Ontong Java (Davy et al., 2008; Hoernle et al., 2010). Finally, the SE margin of Zealandia (i.e. Campbell Plateau) and conjugate margin in Marie Byrd Land, Antarctica aren't volcanic margins (Tulloch et al., 2019). Thus, there is no direct evidence for the emplacement of a HIMU-type plume head beneath Marie Byrd Land at ~ 107 Ma; in contrast to the evidence for a HIMU plume(s) ascending beneath Zealandia and the Hikurangi Plateau between 99-69 Ma. Some evidence exists for a deep reservoir that could have fed mantle plumes beneath the Gondwana margin upon subduction cessation (Montelli et al., 2006; Timm et al., 2010). Anomalous basement topography (0.5-1.2 km) centred beneath the West Antarctic margin and anomalously high Paleogene subsidence rates (0.5-0.9 km) of the Campbell Plateau point to a long-lived (>80 Ma), several thousand kilometers in size, low-density anomaly in the mid-mantle with possible excess temperature of 150-200 K (Sutherland et al., 2010). Subduction may have previously dragged this mantle downwards, preventing it from rising. Alternatively slab detachment and/or change of subduction angle may have allowed the slab to intersect and thus destabilize the low-velocity anomaly. Therefore, subduction cessation and slab detachment may have triggered the rise of hotter material from this broad low-velocity anomaly from 700-1500 km to its present depth of 400-1000 km. Although Sutherland et al. (2010) speculated that this anomaly resulted from metasomatism of the mid-mantle by subducting slabs over the last 400 Ma, we note that this is not enough time to derive the high $^{207}\text{Pb}/^{204}\text{Pb}$ isotopic signatures of the HIMU end

member from a MORB source, requiring 1.0-3.2 Ga, but probably >2.0-2.5 Ga, as discussed above. Therefore, this anomaly may ultimately tap a source in the lower mantle containing substantially older recycled ocean crust and/or SCLM. In summary, this large-scale, low-density anomaly (possibly a stalled plume head or dome-like upwelling) may be the source of the Late Cretaceous HIMU end member and collision of the Hikurangi Plateau with the Gondwana margin at ~110-105 Ma may have triggered its further upwelling, including generation of a secondary plume(s) (Sutherland et al., 2010).

7.4.3. A model to explain Late Cretaceous HIMU Intraplate volcanism

We now present a model (Fig. 7.6) to explain the interaction of upwelling HIMU mantle with the Gondwana subduction zone, jammed by the Hikurangi Plateau collision. Upwelling HIMU mantle beneath the Gondwana margin would be deflected upwards along the base of the slab until it arrived beneath the Hikurangi Plateau (Fig. 7.6a). Although it was no doubt difficult for magmas to ascend through the thickened plateau lithosphere, explaining why many show contamination by enriched (EM-type) Hikurangi plateau lithosphere, deep lithospheric fractures and faults formed during the collision of the plateau with the Gondwana margin at ~110-105 Ma (e.g. Davy et al., 2008) could have facilitated the rise of the plume-derived magmas between 99-88 Ma (Fig. 7.6b). An important question is why extensive intraplate volcanism took place in Marlborough between 98-94 Ma, because the plume material would have likely been blocked from upwelling to shallow depths by the lithosphere subducting beneath the Torlesse accretionary wedge. The Marlborough Igneous Province was located close to the subducted western margin of the Hikurangi Plateau, which presumably was bounded by a major transform fault/fracture zone (Mortimer et al., 2019). A sharp transition in thickness in the subducting crust along a tectonic lineament, such as a fracture zone, is a likely place for a slab tear to form, allowing HIMU plume mantle to flow into the mantle wedge beneath the Marlborough area (Fig. 7.6b). This plume mantle could have interacted with a mantle wedge enriched by subduction processes, as well as forearc crust. In the Late Cretaceous, the Westland igneous province was located SW of the Marlborough igneous province (e.g. van der Meer et al., 2018; Mortimer et al., 2019). The slab tear could have propagated down dip of the western Hikurangi Plateau edge. The geochemical characteristics of the Westland igneous rocks are consistent with increased dilution of the HIMU end member as the plume material flowed through a progressively deeper slab tear below the arc/backarc region, resulting in greater contamination of the melts with enriched (E-MORB type) Gondwana mantle wedge. In addition, the hot plume mantle, streaming through the elongate slab tear (window), could have thermally weakened the overlying lithosphere. Interestingly, the progression of intraplate volcanism to the south (or backarc region) appears to have occurred along what in the future (at ~45 Ma) would become the Pacific-Australia plate boundary, suggesting that the Alpine Fault's location may have initially been influenced or even controlled by the slab tear at the western margin of the subducted portion of the Hikurangi Plateau in the Cretaceous (e.g. Reyners et al., 2011; van der Meer et al., 2016). Considering the similarity in isotopic composition, the East Chatham HIMU end member is likely to be derived from the same source (plume) that feed the Hikurangi, Marlborough and Westland volcanism. A SW propagating detachment of the subducting slab, possibly along an extension of the NE-SW-trending Western Wishbone Ridge, which has been interpreted to be a fracture zone or a major dextral strike-slip fault system (e.g. Mortimer et al., 2006), or along the eastern boundary of the thick Hikurangi Plateau, could explain the opening of a slab window beneath the SE Chatham Rise margin (Fig. 7.6c). The opening of a slab window would have facilitated the upwelling of hotter, deeper asthenosphere, including hot plume mantle, to shallow depths, interacting with the Gondwana mantle wedge, thermally eroding and weakening the overlying lithosphere, and possibly

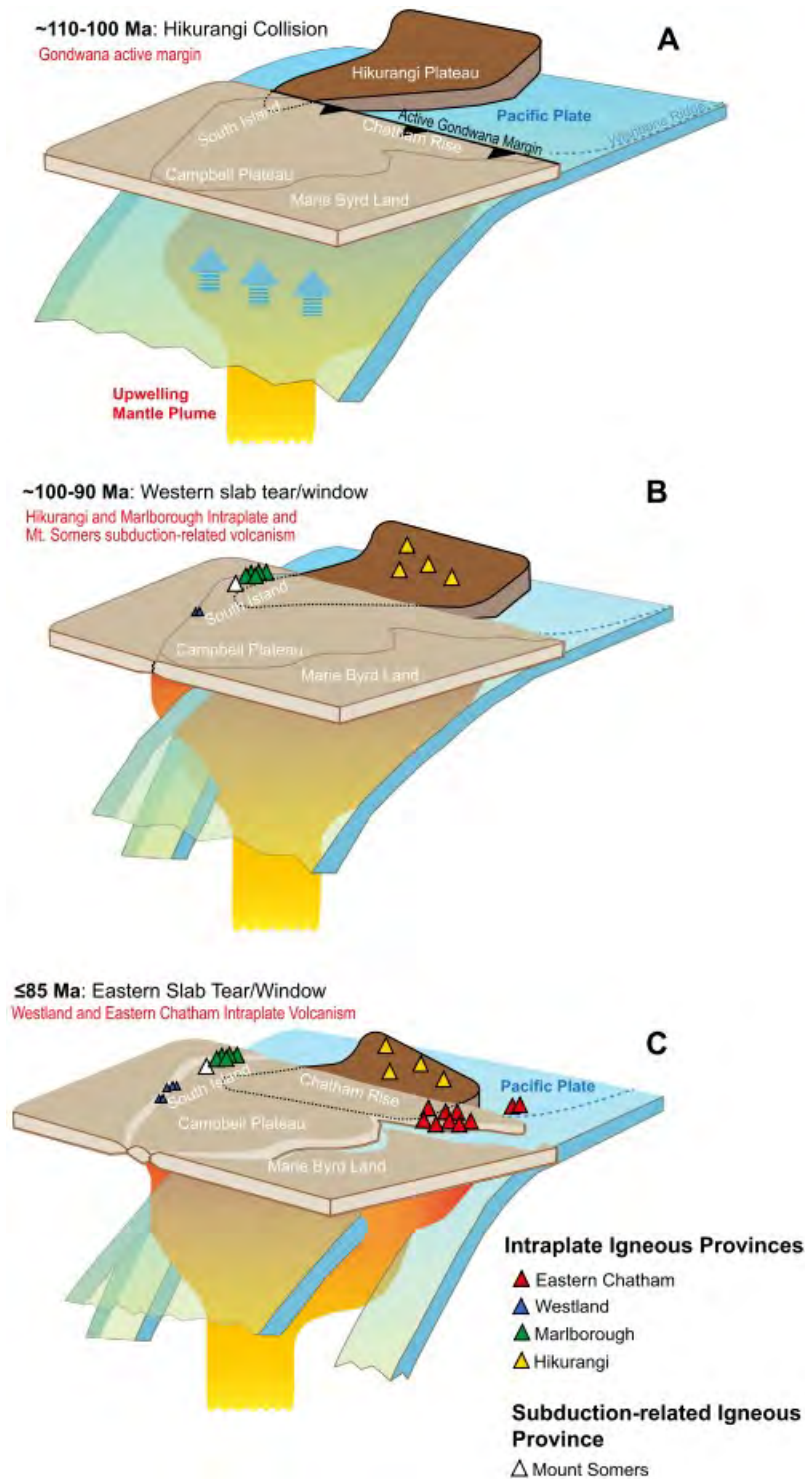


Fig. 7.6: Conceptual model showing the evolution of the Zealandia continental margin during three different time periods (A = ~110-100 Ma; B = ~100-90 Ma and C ≤ 85 Ma). (A) At ~110 Ma, the Hikurangi Plateau collided with the Gondwana margin triggering rise of HIMU plume mantle to the base of the subducting Pacific Plate. (B) At ~100 Ma, upwelling plume material flows along the base of the subducting slab until it reaches the base of the Hikurangi Plateau, melting by decompression to form the Hikurangi Seamounts (yellow triangles). Mt. Somers volcanism (white triangle) takes place in the Gondwana forearc at ~99-96 Ma. A slab tear/window opened along the western, presumably fracture zone boundary, of the subducted portion of the Hikurangi Plateau. This tear allowed plume material to upwell to the base of the Gondwana lithosphere, partially melting by decompression to form the Marlborough Igneous Province at 98-94 Ma and begin forming the Westland mafic igneous rocks (small blue triangles) beginning at ~92 Ma. (C) At ~85 Ma, a slab tear began at the eastern boundary of the Hikurangi Plateau (possibly at the Wishbone Fracture Zone) and propagated to the SW opening a slab window and eventually resulting in slab detachment. The slab window allowed HIMU plume material to flood into the former Gondwana margin mantle wedge, triggering extension to form the Bounty Trough (≤90 Ma), seafloor spreading (≤85 Ma) and formation of the Eastern Chatham Volcanic Province (86-79 Ma).

triggering extension and rifting along the southern margin of the Chatham Rise, thus forming the Bounty Trough (~90 Ma; Eagles et al., 2004). Once significant thinning of the Gondwana continental lithosphere had occurred, plume material could have melted by decompression to form the large intraplate seamounts (many being guyots, i.e. former ocean island volcanoes eroded to sea level) and the extensive Cretaceous southern Chatham Island volcanism. The volcanism shortly preceded and was concurrent with seafloor spreading that initiated at ≥ 83 Ma in the mouth of the Bounty Trough (Davy, 2006).

7.4.4. Origin of Cenozoic HIMU-like Zealandia lavas and the newly recognized “Zealandia-Antarctic” mantle domain

In contrast to the Late Cretaceous Volcanic Provinces, Cenozoic intraplate volcanism on Zealandia and West Antarctica requires an end member with radiogenic $^{206}\text{Pb}/^{204}\text{Pb}$ but with lower $^{207}\text{Pb}/^{204}\text{Pb}$ than generally found in St. Helena HIMU (Fig. 7.5; Timm et al., 2010). The former Gondwana mantle wedge (asthenospheric and lithospheric portions) is likely to have consisted of depleted upper mantle (DM) that was partially metasomatized by subduction-zone fluids/melts containing a subducted sediment component (and thus EM-type composition), as seen in the Anita Peridotite (Czertowicz et al., 2016). Ascending Cretaceous HIMU melts would have mixed with the former Gondwana mantle wedge material, generating mixing arrays between St. Helena HIMU and low- μ (DM- and EM-type) components in the shallow asthenospheric and lithospheric mantle. Many mantle xenoliths from the South Island of New Zealand fall on such an array on the uraniumogenic Pb isotope diagram, although others have isotopic compositions shifted to the right of this mixing array, i.e. to more radiogenic $^{206}\text{Pb}/^{204}\text{Pb}$ but with lower $^{207}\text{Pb}/^{204}\text{Pb}$ than HIMU (e.g. Fig. 7.4c in McCoy-West et al., 2016). The shift to the right of the HIMU - low- μ (DM and/or EM) mixing arrays can be explained by short-term (99-69 Ma) radiogenic ingrowth of mantle with elevated μ ratios, since little ^{235}U (which decays to ^{207}Pb) remains on Earth. Such an ingrowth model could explain the lower $^{207}\text{Pb}/^{204}\text{Pb}$ at elevated $^{206}\text{Pb}/^{204}\text{Pb}$ of the xenoliths and many of the Cenozoic lavas from Zealandia and West Antarctica (Hart et al., 1997; Panter et al., 2000) compared to the Cretaceous HIMU lavas. A Cenozoic diffuse alkalic magmatic province (DAMP) with HIMU geochemical affinities was recognized extending from eastern Australia, through Zealandia, to West Antarctica (Finn et al., 2005). Plate tectonic reconstructions at 100 Ma show that most of the volcanism in DAMP with the highest $^{206}\text{Pb}/^{204}\text{Pb}$ isotope ratios (>20.5) was located in a restricted area on the Gondwana margin from which Zealandia was derived, leading to the conclusion that the HIMU signature was related to subduction. As we have discussed above, however, the HIMU signature cannot be derived from Gondwana subduction but rather from a Late Cretaceous plume event at this location. Recently a distinct “Zealandia-Antarctic” geochemical domain was recognized in MORBs from the Antarctic-Pacific spreading ridge, which is located between the Pacific and Indian Ocean mantle domains (Park et al., 2019). The proposed new geochemical domain largely coincides with the region containing Cenozoic DAMP volcanism. The Late Cretaceous St. Helena-type HIMU volcanism on Zealandia and the Hikurangi Plateau serves as an end member for the geochemical composition of this domain. Therefore, the Late Cretaceous HIMU event could have not only contributed to the breakup of Gondwana but also have polluted large portions of the upper mantle (lithosphere and asthenosphere) beneath the Zealandia part of the Gondwana margin (Timm et al., 2010), generating a new upper mantle domain (Park et al., 2019). The HIMU signature from the Late Cretaceous plume event was in part carried northward away from West Antarctica within the Zealandia and eastern Australia lithosphere. Contaminated upper asthenospheric mantle, in part through detachment of lithospheric mantle from Zealandia (Hoernle et al., 2006) and Australia, must also have spread out in the region beneath and between Zealandia, eastern Australia and Antarctica, in order to be sampled by volcanism along the Australian-Antarctic Ridge.

7.5. Conclusions and wider implications

Determining the sources of volcanism associated with continental breakup is crucial for evaluating the origin of the breakup. Four Late Cretaceous intraplate igneous provinces (Hikurangi, Marlborough, Westland and East Chatham) located on diverse oceanic and continental crust form crude mixing arrays between a common St. Helena-type HIMU component and depleted and/or enriched components located in the former Gondwana mantle wedge and the overlying lithosphere. In contrast to most continental breakup events involving volcanism, there are no flood basalts associated with the final phase of Gondwana breakup separating Zealandia from Antarctica, as expected from a starting plume head (Richards et al., 1989), and no evidence for seaward-dipping reflectors at the rifted Chatham Rise margin (Tulloch et al., 2019). A possible source for the HIMU component was the large-scale, low-density anomaly in the mid mantle. Upwelling of this HIMU mantle may have been triggered by the Hikurangi Plateau collision and subduction cessation. Upwelling HIMU material from the mid mantle could have begun to feed intraplate volcanism at ~100 Ma north and south of the Gondwana margin, lasting for ~30 Ma. Rise of this plume material beneath the Gondwana continental margin was facilitated by the formation of a slab tear on the western side of the partially subducted Hikurangi Plateau (between ~98-88 Ma), followed by the opening of a slab window as a result of slab breakoff on the SE side of the subducted plateau (beginning at ~86 Ma). We propose that upwelling of hotter, deeper asthenosphere and hotter HIMU mantle from mid mantle or greater depths through slab tears/windows played a fundamental role in thermally weakening and extending the overlying lithosphere, first causing rifting in the Bounty Trough and Chatham Rise-Amundsen Sea sector (100-90 Ma) and then breakup and seafloor spreading along the SE margin of the Chatham Rise at ≤85 Ma, which propagated southwards to split the Campbell Plateau from West Antarctica. At ~65 Ma, there was a slight shift in the flavour of the HIMU end member composition towards less radiogenic $^{207}\text{Pb}/^{204}\text{Pb}$, as is the case for the HIMU end member in the Cenozoic Zealandia lavas and mantle xenoliths from Zealandia. The Cenozoic HIMU-type compositions could be generated by a two-step process: 1) mixing of Late Cretaceous plume-derived HIMU with the depleted upper mantle (both lithospheric and asthenospheric), partly enriched by Gondwana subduction, and 2) short-term (100-70 Ma) radiogenic ingrowth. Some of the Cenozoic volcanism could also be fed by younger HIMU-like plumes, e.g. Balleny and Ross Island plumes (Park et al., 2019). In summary, both tectonic (Hikurangi Plateau collision and slab tearing/detachment) and volcanic (decompression melting of upper mantle and HIMU plume mantle) mechanisms were essential in causing the separation of Zealandia from Gondwana and in forming a new “Zealandia-Antarctic” upper mantle geochemical domain. In conclusion, neither the non-volcanic nor volcanic margin models adequately explain the final breakup stage of Gondwana separating Zealandia from West Antarctica. The absence of evidence for seaward-dipping seismic reflectors and flood basalts associated with the Zealandia and conjugate Marie Byrd Land margins are not consistent with this being a classic volcanic margin related to the emplacement of a plume head. There is, however, evidence for the interplay between magmatic and tectonic processes in the form of slab tears/windows and slab detachment allowing deeper and hotter asthenosphere and HIMU plume mantle to upwell to the base of the Gondwana margin causing extension, rifting and ultimately seafloor spreading. Thus, the SE Zealandia passive margin represents a hybrid (volcanic-tectonic) type margin in-between the two classic end members, indicating that continental breakup can occur in a variety of forms and that subduction cessation can trigger breakup. Hybrid types of breakup mechanisms may have occurred in other areas, for example they could help explain the separation of India from Gondwana (Kent et al., 1997) and of India from Madagascar (Storey et al., 1997), where breakup-related volcanism has been recognized but cannot be explained by the classic plume head model. Hybrid breakup

mechanisms are also likely to have played a role in the more ancient geological record and may play an important role in continental breakup that has not been previously recognized.

Acknowledgements

We thank the captains, crews and scientific parties of R/V SONNE cruises SO168 and SO246 for their excellent support. S. Hauff, K. Junge, and J. Sticklus (GEOMAR) and U. Westernströer (Kiel University) are acknowledged for analytical support. J. Pearce and K. Panter are thanked for constructive reviews that improved this manuscript. The German Ministry of Education and Research (BMBF; grants 03G0246 and 03G0168A), the German Research Foundation (DFG; grants HO1833/12-1,2), GNS Science, Canterbury University, GEOMAR Helmholtz Centre for Ocean Research Kiel and Alfred Wegener Institute Helmholtz-Centre for Polar and Marine Research (AWI) are thanked for providing funding. CT received funding from the European Union's Horizon 2020 research and innovation program (Marie Skłodowska-Curie grant #79308) and VT from the German Academic Exchange Service (DAAD).

Supplemental material

Supplemental materials for this manuscript are available online and include (A) descriptions of the analytical methods for whole-rock and trace elemental and isotope measurements and (B) table data of analytical results presented in this study (geochemistry and isotope analyses). Supplements can be accessed by the following link: <https://doi.org/10.1016/j.epsl.2019.115864>

8. Conclusions

This thesis provides new geophysical insights into the crustal structure of the Chatham Rise, SE Chatham Terrace, and adjacent oceanic crust using newly acquired seismic and potential field data. The gathered results are interpreted, discussed and incorporated within the geodynamic framework of subduction cessation and breakup along the East Gondwana margin in the area of southern Zealandia. In this chapter, I return to the scientific questions posed in section 1.4., and summarise the main findings related to them.

Crustal structure and nature of the southern Chatham Rise margin

P-wave velocity modelling based on wide-angle reflection / refraction seismic data, together with gravity modelling reveal the crustal structure of the two provinces of the Chatham Rise. These two provinces (eastern and western) have significantly different crustal thicknesses, but largely similar P-wave velocities and densities. The two profiles that cross the eastern (deeper) part of the Chatham Rise indicate a crustal thickness of only 14-18 km, while the three profiles that cross the western (shallower) province of the Chatham Rise indicate a crustal thickness up to 25 km. In both provinces, P-wave velocities and densities are consistent with a continental origin close to the East Gondwana active margin (i.e. in the accretionary wedge), and are indicative of greywackes, metagreywackes and schist in the upper crust, and higher-metamorphic equivalents in the lower crust. I suggest that the different crustal thicknesses are related to the subduction and underthrusting of the thick Hikurangi Plateau, which caused thickening and uplift of the outer Chatham accretionary prism before subduction ceased.

East of the Udintsev Fracture Zone (UFZ), the P-wave velocity models and seismic reflection data indicate the presence of normal-thickness (~6 km) Pacific oceanic crust. Additionally, the data suggest the presence of a highly faulted continent-ocean transition (COT), which I interpret as exhumed lower continental crust. Based on the new information about the extent of the COT, I suggest that seafloor spreading east of the UFZ was not active before 88 Ma. West of the UFZ, the SE Chatham Terrace has abundant seamounts, varying crustal thickness (~5 km or ~8 km thick), and distinct continental graben structures evident in MCS reflection data. P-wave velocities for the SE Chatham Terrace also fall within the range of globally recognised very thin to hyperextended continental crust. Accordingly, I interpret the SE Chatham Terrace as a COT consisting of hybrid crust – a very thin continental crust modified by magmatic activity during seamount formation.

Nature of the southern Chatham Rise margin

Seismic refraction data indicate the presence of high-velocity lower crust (HVLC) along the eastern Chatham Rise and in the area of exhumed lower continental crust east of the UFZ. Despite the presence of HVLC, other features like seaward-dipping reflector sequences that are typical for volcanic-rifted margins are absent. Moreover, MCS reflection data show that the southern Chatham Rise margin is fault-controlled (typical for magma-poor margins), but continuously observed Moho reflections argue against the presence of exhumed mantle along the margin. Accordingly, I interpret the southern Chatham Rise margin as a unique hybrid rifted margin. The evolution of the margin was most likely influenced by an initial phase of passive rifting followed by active mantle upwelling.

Extent of the Hikurangi Plateau beneath Chatham Rise

The presence of strong wide-angle reflections and gravity modelling reveal the extent of the Hikurangi Plateau beneath the Chatham Rise. We find that the Hikurangi Plateau does not extend

as far south as previously suggested, reaching less than 200 km from the northern border of the Chatham Rise east of 179°W. Moreover, the new geophysical data suggests that southern limit of the Hikurangi Plateau is located north of Chatham Islands. West of 179°W, the lower crustal layer, which I interpret to be underthrust Hikurangi Plateau, is 10 km thick. This thickness is consistent with other refraction seismic studies east of the North Island where the Hikurangi Plateau subducts at the present-day. South of the central Chatham Rise, the lower crustal layer thins to 6 km. I interpret this thinning of the lower crustal layer as the transition to the normal-thickness oceanic crust of the ancient Phoenix Plate. Combining the data presented in this study with previously published refraction seismic data, I suggest that a large piece of the Phoenix Plate is located beneath the thinned crust of southern Zealandia, still attached to the southern edge of the Hikurangi Plateau.

Tectonic evolution of the southern Chatham Rise margin

Based on the features identified from P-wave velocity and gravity modelling, together with published geological and geophysical data, I propose a multi-stage evolution of the Chatham Rise. This model explains the rapid transition from subduction to extension, as well as passive margin development.

Between 110 and 100 Ma, west to east progressive subduction and underthrusting of the buoyant Hikurangi Plateau gradually decreased convergence velocities until subduction ceased. The additional buoyancy of the Hikurangi Plateau is likely to have initiated flattening of the Phoenix Plate slab, which led to the onset of crustal extension and rifting along the East Gondwanan margin. I suggest that extension was oblique to the arc, leading to NW-SE directed reactivation of former arc-parallel thrust faults within the Chatham accretionary prism as normal faults. This fault reactivation led to the formation of half grabens, which are expressed as E-W striking gravity lineaments, after 105 Ma. Subsequently, new generations of NE-SW to NEE-SWW striking normal faults started to evolve with prolonged extension.

As subduction velocities decreased in response to the collision of the Hikurangi Plateau with the East Gondwanan active margin, subduction-transform edge propagator (STEP) faults became active along both the eastern and western margins of the Hikurangi Plateau. This led to fragmentation of the Phoenix Plate. I propose that this fragmentation and the subduction cessation triggered, or contributed to, the global-scale plate reorganisation event that occurred between 105 and 100 Ma. After development of the STEP faults and subduction cessation, rollback of the Phoenix Plate slab likely intensified rifting and crustal extension in the area of Bounty Trough and SE Chatham Terrace. This, in turn, led to exhumation of the lower continental crust along the easternmost southern margin of the Chatham Rise.

Large proportions of the Phoenix Plate slab became detached at ~90 Ma. The resulting slab window opened a pathway for hot and upwelling sub-lithospheric mantle. In response, the eastern Chatham Rise was affected by mafic underplating and intrusions and alkaline lavas extruded on the Chatham Islands. I suggest that this event led to the formation of seamounts on the SE Chatham Terrace and magmatically modified the hyper-extended continental crust of the SE Chatham Terrace. Furthermore, the HVLC observed along the eastern Chatham Rise indicates that this event led to underplating of, and intrusions along, the eastern Chatham Rise at ~85 Ma. Later, between 83 and 79 Ma, seafloor spreading west of the UFZ became stable and continuous, leading to the final separation of Zealandia from Antarctica.

Accordingly, the southern Chatham Rise margin is a unique hybrid rifted margin. Passive rifting initiated by complex subduction dynamics was substituted for mantle upwelling and active rifting after the cessation of subduction and slab detachment.

9. Outlook and future research

This thesis answered several research questions concerning the tectonic setting, evolution and nature of the southern Chatham Rise margin. Modelling of the presented data resulted in increased knowledge of the breakup between southern Zealandia and West Antarctica. However, several hypotheses developed during this work still need to be tested:

(I) The SE Chatham Terrace has been interpreted as very thin to hyper-extended continental crust (section 4.5.6.) based on the crustal thicknesses estimated from wide-angle reflection / refraction data and P-wave velocity modelling. While thin, these crustal thicknesses are not compatible with Pacific oceanic crust. Additionally, the acoustic basement structure indicates graben structures and basement highs that are unusual for oceanic crust. MCS data along profile AWI-20160200 suggest the presence of pre-rift strata on the Berlin Basement High (Fig 4.3), southwest of a NE-SW striking graben structure between Berlin and Erik Seamounts (Fig. 4.2). Since the strata, interpreted to be pre-rift, overlying the Berlin Basement High outcrops at the surface, it would be suitable target for scientific drilling. The geology of the SE Chatham Terrace can be directly inferred from core samples and prove if the SE Chatham Terrace is of largely continental origin. Furthermore, additional near-surface targets are also present along profiles AWI-20160100 and AWI-20160300 (Fig. 4.3). A proposal for drilling can be submitted to the International Ocean Discovery Program via an ancillary project letter to extend an already scheduled drilling expedition in that area.

(II) Tulloch et al. (2019) included a magnetic anomaly map based on the map of Sutherland (1999) and magnetic data held by GNS Science. Magnetic anomalies proximal to the Bounty Trough and on the SE Chatham Terrace have been interpreted as continental rifting anomalies and intrusions (Tulloch et al., 2019), or seafloor spreading anomalies (Davy, 2006). However, the new magnetic data from SO246 and other recent cruises have not yet been integrated in these maps. These new and pre-existing magnetic data need to be levelled and integrated into a new magnetic grid for the southern Chatham Rise margin. Additionally, denser and systematic lines of airborne magnetic data help to reveal more information about the complex magnetic anomaly pattern of the SE Chatham Terrace. This can address the question if the magnetic anomalies are of continental origin or if these are spreading anomalies. In either case, the knowledge of their origin improves plate tectonic models. The airport on the Chatham Islands lies within suitable range for aeromagnetic surveying.

(III) The shipborne gravity data were a very helpful constraint to support the modelling of the crustal structure of the Chatham Rise using P-wave velocity modelling. Particularly at the transition between the eastern and western Chatham Rise (profile AWI-20160200), free-air gravity and gravity modelling helped to better identify the Hikurangi Plateau. Below the South Island, Reyners et al. (2017b) found unusual high P-wave velocities (>8.5 km/s) at the base of the 30 km thick Hikurangi Plateau. They interpreted these high P-wave velocities as indicative of eclogitisation typical for the base of the plateau, or mantle below thick oceanic plateaux. However, our results as well as other refraction studies (Mochizuki et al., 2019; Scherwath et al., 2010) suggest a plateau thickness of only 10-16 km, and no evidence for eclogitisation. If eclogitisation occurred at the base of the Hikurangi Plateau beneath the Chatham Rise, this can be accessed with 3D gravity modelling. The most recent regional gravity anomaly grid (Sandwell et al., 2014) and the acquired SO246 gravity anomaly data with higher resolution show a good correlation. Integration of the new SO246 gravity data into the gravity anomaly grid increase the precision and resolution. 3D gravity models, that extend across the margins of the Chatham Rise, cover the different mantle domains below the Hikurangi Plateau, the former forearc (i.e. mantle wedge), and Pacific oceanic crust. The P-wave velocity data from this study, together with other geophysical data like MCS reflection data, provide

important constraints along the Chatham Rise and adjacent areas for large-scale modelling approaches.

(IV) This study and many other studies around Zealandia (e.g. Strogen et al., 2016; Tulloch et al., 2019) suggest that regional extension began between 105 and 100 Ma. Tulloch et al. (2019) proposed different extension directions before and after ~90 Ma. Regional plate kinematic models in the South Pacific are mainly based on the assumption that rifting in southern Zealandia's offshore basins, the Bounty Trough, and along the southern Chatham Rise margin started at or after 90 Ma (e.g. Eagles et al., 2004; Wobbe et al., 2012; Wright et al., 2016). Global plate tectonic reconstructions (e.g. Seton et al., 2012; Matthews et al., 2016) do not include movements within the area of southern Zealandia. For any thorough reconstruction of the South Pacific, and to find how the Chatham Rise is related to West Antarctica, it is critical that independent movements of the South Island, Chatham Rise and Campbell Plateau are included in modelling.

(V) The crustal structure along the profiles can be integrated into thermo-mechanic models in order to access geophysical parameters like crustal rheology. Recent thermomechanic modelling shows that the crustal rheology plays an important role in the evolution of passive continental margins evolution (e.g. Brune et al., 2016; Andrés-Martínez et al., 2019). Other factors that are identified to influence passive margin evolution and normal faulting pattern along rifted margins are erosion and sedimentation during normal faulting (Andrés-Martínez et al., 2019). For any thermomechanic and kinematic modelling approach, detailed information about the symmetry of the margin is required. Using gravity data, Wobbe et al. (2012) identified that the conjugate margin of the Chatham Rise (Marie Byrd Land margin, West Antarctica) also includes a broad continent-ocean transition, which also hosts seamounts – the Marie Byrd Seamounts, and probably consists of stretched continental crust. However, detailed MCS reflection and refraction seismic data is required from the Marie Byrd Land margin to access the margins symmetry for further modelling approaches.

References

- Adams, C.J.D, Campbell, H.J. & Griffin, W.J. (2008). Age and provenance of basement rocks of the Chatham Islands : An outpost of Zealandia. *New Zealand Journal of Geology and Geophysics* 51, 245–259. <https://doi.org/10.1080/00288300809509863>
- Adams, C.J.D. & Robinson, P. (1977). Potassium-argon ages of schists from Chatham Island, New Zealand Plateau, southwest Pacific. *New Zealand Journal of Geology and Geophysics* 20, 287–301. <https://doi.org/10.1080/00288306.1977.10420708>
- Allan, R.S. (1928). Chatham Islands - The Physical Features and Structure. *Transactions and Proceedings of the Royal Society of New Zealand*.
- Andrés-Martínez, M., Pérez-Gussinyé, M., Armitage, J. & Morgan, J. P. (2019). Thermomechanical Implications of Sediment Transport for the Architecture and Evolution of Continental Rifts and Margins. *Tectonics* 38(2), 641–665. <https://doi.org/10.1029/2018TC005346>
- Andrews, P.B., Campbell, H.J. & Watters, W.A. (1978). The Forty Fours: The most easterly outcrop of Mesozoic basement in the New Zealand region. *New Zealand Journal of Geology and Geophysics* 21, 649–652. <https://doi.org/10.1080/00288306.1978.10424092>
- Austermann, J., Ben-Avraham, Z., Bird, P., Heidbach, O., Schubert, G. & Stock, J.M. (2011). Quantifying the forces needed for the rapid change of Pacific plate motion at 6 Ma. *Earth and Planetary Science Letters*, 307(3–4), 289–297. <https://doi.org/10.1016/j.epsl.2011.04.043>
- Bache, F., Mortimer, N., Sutherland, R., Collot, J., Rouillard, P., Stagpoole, V. & Nicol, A. (2014). Seismic stratigraphic record of transition from Mesozoic subduction to continental breakup in the Zealandia sector of eastern Gondwana. *Gondwana Research* 26, 1060–1078. <https://doi.org/10.1016/j.gr.2013.08.012>
- Baksi, A.K. (2007). A quantitative tool for detecting alteration in undisturbed rocks and minerals - I: water, chemical weathering, and atmospheric argon. *Geological Society of America Special Papers* 430, 285–303. [https://doi.org/10.1130/2007.2430\(15\)](https://doi.org/10.1130/2007.2430(15))
- Barrett, R.S., Davy, B., Stern, T. & Gohl, K. (2018). The Strike-Slip West Wishbone Ridge and the Eastern Margin of the Hikurangi Plateau. *Geochemistry, Geophysics, Geosystems*, 1–18. <https://doi.org/10.1002/2017GC007372>
- Barrier, A., Nicol, A., Bassett, K., Browne, G. & Sahoo, T. (2017). Late Cretaceous Rifting of the Canterbury Basin during Zealandia intra-continental extension. *Geological Society of New Zealand*, poster presentation.
- Barton, P.J. (1986). The relationship between seismic velocity and density in the continental crust - a useful constraint? *Geophysical Journal International* 87, 195–208. <https://doi.org/10.1111/j.1365-246X.1986.tb04553.x>
- Baumann, C., Gerya, T. V. & Connolly, J. A. D. (2010). Numerical modelling of spontaneous slab breakoff dynamics during continental collision. *Geological Society Special Publication*, 332(1), 99–114. <https://doi.org/10.1144/SP332.7>
- Billen, M.I. & Stock, J. (2000). Morphology and origin of the Osborn Trough. *Journal of Geophysical Research* 105, 13481–13489. <https://doi.org/10.1029/2000JB900035>
- Bland, K.J., Uruski, C.I. & Isaac, M.J. (2015). Pegasus Basin, eastern New Zealand: A stratigraphic record of subsidence and subduction, ancient and modern. *New Zealand Journal of Geology and Geophysics* 58, 319–343. <https://doi.org/10.1080/00288306.2015.1076862>
- Boston, B., Nakamura, Y., Gallais, F., Hackney, R. & Fujie, G. (2019). Delayed Subsidence After Rifting and a Record of Breakup for Northwestern Zealandia. *Journal of Geophysical Research: Solid Earth*, 3057–3072. <https://doi.org/10.1029/2018JB016799>
- Bradshaw, J.D. (1989). Cretaceous geotectonic patterns in the New Zealand region. *Tectonics* 8, 803–820. <https://doi.org/10.1029/TC008i004p00803>
- Brune, S., Corti, G. & Ranalli, G. (2017b). Controls of inherited lithospheric heterogeneity on rift linkage: Numerical and analog models of interaction between the Kenyan and Ethiopian rifts across the Turkana depression. *Tectonics* 36, 1767–1786. <https://doi.org/10.1002/2017TC004739>
- Brune, S., Williams, S. E. & Müller, R. D. (2017a). Potential links between continental rifting, CO₂ degassing and climate change through time. *Nature Geoscience* 10(12), 941–946. <https://doi.org/10.1038/s41561-017-0003-6>
- Brune, S. (2018). Forces within continental and oceanic rifts: Numerical modeling elucidates the impact of asthenospheric flow on surface stress. *Geology* 46(2), 191–192. <https://doi.org/10.1130/focus022018.1>

References

- Cabral, R.A., Jackson, M.G., Rose-Koga, E.F., Koga, K.T., Whitehouse, M.J., Antonelli, M.A., Farquhar, J., Day, J.M.D. & Hauri, E.H. (2013). Anomalous sulphur isotopes in plume lavas reveal deep mantle storage of Archaean crust. *Nature* 496, 490–493. <https://doi.org/10.1038/nature12020>
- Campbell, H.J., Andrews, P.B., Beu, A.G., Maxwell, P.A., Edwards, A.R., Laird, M.G., Hornibrook, N. de B., Mildenhall, D.C., Watters, W.A., Buckeridge, J.S., Lee, D.E., Strong, C.P., Wilson, G.J. & Hayward, B.W. (1993). Cretaceous–Cenozoic geology and biostratigraphy of the Chatham Islands, New Zealand. *Institute of Geological & Nuclear Sciences Monograph 2*, Lower Hutt, Institute of Geological & Nuclear Sciences,.
- Cande, S.C. & Stock, J.M. (2004). Cenozoic reconstructions of the Australia–New Zealand–South Pacific Sector of Antarctica. *Geophysical Monograph Series* 151, 5–17. <https://doi.org/10.1029/151GM02>
- Castillo, P.R., Lonsdale, P.F., Moran, C.L. & Hawkins, J.W. (2009). Geochemistry of mid-Cretaceous Pacific crust being subducted along the Tonga–Kermadec Trench: implications for the generation of arc lavas. *Lithos* 112, 87–102. <https://doi.org/10.1016/j.lithos.2009.03.041>
- Carter, R.M., Carter, L. & Davy, B. (1994). Seismic stratigraphy of the Bounty Trough, south-west Pacific Ocean. *Marine Petroleum Geology* 11, 79–93. [https://doi.org/10.1016/0264-8172\(94\)90011-6](https://doi.org/10.1016/0264-8172(94)90011-6)
- Chaffey, D.J., Cliff, R.A. & Wilson, B.M. (1989). Characterization of the St Helena magma source. *Geological Society London Special Publication* 42, 257–276. <https://doi.org/10.1144/GSL.SP.1989.042.01.16>
- Chandler, M.T., Wessel, P., Taylor, B., Seton, M., Kim, S.-S. & Hyeong, K. (2012). Reconstructing Ontong Java Nui: implications for Pacific absolute plate motion, hotspot drift and true polar wander. *Earth and Planetary Science Letters* 331–332, 140–151. <https://doi.org/10.1016/j.epsl.2012.03.017>
- Christensen, N.I. & Mooney, W.D. (1995). Seismic velocity structure and composition of the continental crust: A global view. *Journal of Geophysical Research: Solid Earth* 100, 9761–9788. <https://doi.org/10.1029/95JB00259>
- Clerc, C., Ringenbach, J.C., Jolivet, L. & Ballard, J.F. (2018). Rifted margins: Ductile deformation, boudinage, continentward-dipping normal faults and the role of the weak lower crust. *Gondwana Research* 53, 20–40. <https://doi.org/10.1016/j.gr.2017.04.030>
- Cloetingh, S., McQueen, H. & Lambeck, K. (1985). On a tectonic mechanism for regional sealevel variations. *Earth and Planetary Science Letters* 75(2–3), 157–166. [https://doi.org/10.1016/0012-821X\(85\)90098-6](https://doi.org/10.1016/0012-821X(85)90098-6)
- Cloos, M. (1993). Lithospheric buoyancy and collisional orogenesis: Subduction of oceanic plateaus, continental margins, island arcs, spreading ridges, and seamounts. *Geological Society of America Bulletin* 105, 715. [https://doi.org/10.1130/0016-7606\(1993\)105<0715:LBACOS>2.3.CO;2](https://doi.org/10.1130/0016-7606(1993)105<0715:LBACOS>2.3.CO;2)
- Coffin, M. F. & Eldholm, O. (1994). Large igneous provinces: crustal structure, dimensions, and external consequences. *Reviews in Geophysics.*, 32(1), 1–36. <https://doi.org/10.1029/93RG02508>
- Cooper, A.F. & Ireland, T.R. (2013). Cretaceous sedimentation and metamorphism of the western Alpine Schist protoliths associated with the Pounamu Ultramafic Belt, Westland, New Zealand. *New Zealand Journal of Geology and Geophysics* 56, 188–199. <https://doi.org/10.1080/00288306.2013.809776>
- Condie, K.C. (2016). Tectonic settings. In: Condie, K.C. (Ed.), *Earth as an Evolving Planetary System*, 3rd edition. Academic Press, Cambridge, MA, pp. 43–88. <https://doi.org/10.1016/C2015-0-00179-4>
- Corti, G. (2009). Continental rift evolution: From rift initiation to incipient break-up in the Main Ethiopian Rift, East Africa. *Earth-Science Reviews* 96, 1–53. <https://doi.org/10.1016/j.earscirev.2009.06.005>
- Contrucci, I., Matias, L., Moulin, M., Géli, L., Klingelhofer, F., Nouzé, H., Aslanian, D., Olivet, J.L., Réhault, J.P. & Sibuet, J.C. (2004). Deep structure of the West African continental margin (Congo, Zaïre, Angola), between 5°S and 8°S, from reflection/refraction seismics and gravity data. *Geophysical Journal International* 158(2), 529–553. <https://doi.org/10.1111/j.1365-246X.2004.02303.x>
- Croon, M.B., Cande, S.C. & Stock, J.M. (2008). Revised Pacific–Antarctic plate motions and geophysics of the Menard Fracture Zone. *Geochemistry, Geophys. Geosystems* 9, 1–20. <https://doi.org/10.1029/2008GC002019>
- Cunningham, A.P., Larter, R.D., Barker, P.F., Gohl, K. & Nitsche, F.O. (2002). Tectonic evolution of the Pacific margin of Antarctica 2. Structure of Late Cretaceous–early Tertiary plate boundaries in the Bellingshausen Sea from seismic reflection and gravity data. *Journal of Geophysical Research: Solid Earth* 107, EPM 6-1 - EPM 6-20. <https://doi.org/10.1029/2002JB001897>
- Czertowicz, T.A., Scott, J.M., Waight, T.E., Palin, J.M., Van der Meer, Q.H.Z., Le Roux, P., Müncker, C. & Piazzolo, S. (2016). The Anita Peridotite, New Zealand: ultra-depletion and subtle enrichment in sub-arc mantle. *Journal of Petrology* 57 (4), 717–750. <https://doi.org/10.1093/petrology/egw001>
- Davy, B. (2006). Bollons seamount and early New Zealand–Antarctic seafloor spreading. *Geochemistry, Geophysics, Geosystems* 7. <https://doi.org/10.1029/2005GC001191>

- Davy, B. (2014). Rotation and offset of the Gondwana convergent margin in the New Zealand region following Cretaceous jamming of Hikurangi Plateau large igneous province subduction. *Tectonics* 33, 1577–1595. <https://doi.org/10.1002/2014TC003629>
- Davy, B., Hoernle, K. & Werner, R. (2008). Hikurangi Plateau: Crustal structure, rifted formation, and Gondwana subduction history. *Geochemistry, Geophysics, Geosystems* 9. <https://doi.org/10.1029/2007GC001855>
- Davy, B. (1993). The Bounty Trough - Basement structure influences on sedimentary basement evolution. In: Ballance, P.F. (Ed.), *Sedimentary Basins of the World, Vol. 2, South Pacific Sedimentary Basins*. Elsevier, New York, pp. 69–92.
- DeMets, C., Gordon, R.G. & Argus, D.F. (2010). Geologically current plate motions. *Geophysical Journal International* 181, 1–80. <https://doi.org/10.1111/j.1365-246X.2009.04491.x>
- Dewey, J.F. & Burke, K. (1974). Hot spots and continental break-up: Implications for collisional orogeny. *Geology* 2, 57–60. [https://doi.org/10.1130/0091-7613\(1974\)2<57:HSACBI>2.0.CO;2](https://doi.org/10.1130/0091-7613(1974)2<57:HSACBI>2.0.CO;2)
- Dickinson, W.R. (1973). Widths of modern arc-trench gaps proportional to past duration of igneous activity in associated magmatic arcs. *Journal of Geophysical Research*, 78(17), 3376–3389. <https://doi.org/10.1029/jb078i017p03376>
- Doré, T. & Lundin, E. (2015). Hyperextended continental margins — Knowns and unknowns. *Geology* 43(1), 95–96. <https://doi.org/10.1016/0040>
- Downey, N.J., Stock, J.M., Clayton, R.W. & Cande, S.C. (2007). History of the Cretaceous Osborn spreading center. *Journal of Geophysical Research: Solid Earth* 112, 1–18. <https://doi.org/10.1029/2006JB004550>
- Duarte, J. C., Rosas, F. M., Terrinha, P., Schellart, W. P., Boutelier, D., Gutscher, M. A. & Ribeiro, A. (2013). Are subduction zones invading the atlantic? Evidence from the southwest iberia margin. *Geology* 41(8), 839–842. <https://doi.org/10.1130/G34100.1>
- Dueterhoeft, E., Quinteros, J., Oberhänsli, R., Bousquet, R. & de Capitani, C. (2014). Relative impact of mantle densification and eclogitization of slabs on subduction dynamics: A numerical thermodynamic/thermokinematic investigation of metamorphic density evolution. *Tectonophysics*, 637, 20–29. <https://doi.org/10.1016/j.tecto.2014.09.009>
- Duret, T., Gerya, T.V. & May, D.A. (2011). Numerical modelling of spontaneous slab breakoff and subsequent topographic response. *Tectonophysics*, 502(1–2), 244–256. <https://doi.org/10.1016/j.tecto.2010.05.024>
- Eagles, G., Gohl, K. & Larter, R.D. (2009). Animated tectonic reconstruction of the Southern Pacific and alkaline volcanism at its convergent margins since Eocene times. *Tectonophysics* 464, 21–29. <https://doi.org/10.1016/j.tecto.2007.10.005>
- Eagles, G., Gohl, K. & Larter, R.D. (2004a). High-resolution animated tectonic reconstruction of the South Pacific and West Antarctic Margin. *Geochemistry, Geophysics, Geosystems* 5. <https://doi.org/10.1029/2003GC000657>
- Eagles, G., Gohl, K. & Larter, R.D. (2004b). Life of the Bellingshausen plate. *Geophysical Research Letters* 31, 1–5. <https://doi.org/10.1029/2003GL019127>
- Edwards, S. J., Schellart, W. P. & Duarte, J. C. (2015). Geodynamic models of continental subduction and obduction of overriding plate forearc oceanic lithosphere on top of continental crust. *Tectonics*, 34(7), 1494–1515. <https://doi.org/10.1002/2015TC003884>
- Ellis, D. & Stoker, M. S. (2014). The Faroe-Shetland Basin: A regional perspective from the Paleocene to the present day and its relationship to the opening of the North Atlantic Ocean. *Geological Society Special Publication*, 397(1), 11–31. <https://doi.org/10.1144/SP397.1>
- Espurt, N., Funicello, F., Martinod, J., Guillaume, B., Regard, V. & Faccenna, C. (2008). Flat subduction dynamics and deformation of the South American plate : Insights from analog modeling 27, 1–19. <https://doi.org/10.1029/2007TC002175>
- Faleide, J.I., Tsikalas, F., Breivik, J.A., Mjelde, R., Ritzmann, O., Engen, Ø., Wilson, J. & Eldholm, O. (2008). Structure and evolution of the continental margin off Norway and the Barents Sea. *Episodes* 33, 82–91. <https://doi.org/10.18814/epiiugs/2008/v31i1/012>
- Finn, C.A., Mueller, R.D. & Panter, K.S. (2005). A Cenozoic diffuse alkaline magmatic province (DAMP) in the southwest Pacific without rift or plume origin. *Geochemistry, Geophysics, Geosystems* 6, Q02005. <https://doi.org/10.1029/2004GC000723>
- Flenner, D. (2016). Seismische Analyse einer Sedimentdrift im Bereich des Chatham Rise (Neuseeland). *B.Sc. thesis*, Department 5 Geosciences, University of Bremen, Bremen, Germany, 69pp.
- Foley, S. F. & Fischer, T. P. (2017). An essential role for continental rifts and lithosphere in the deep carbon cycle. *Nature*

References

- Geoscience* 10(12), 897–902. <https://doi.org/10.1038/s41561-017-0002-7>
- Franke, D. (2013). Rifting, lithosphere breakup and volcanism: Comparison of magma-poor and volcanic rifted margins. *Marine Petroleum Geology* 43, 63–87. <https://doi.org/10.1016/j.marpetgeo.2012.11.003>
- French, S.W. & Romanowicz, B. (2015). Broad plumes rooted at the base of the Earth's mantle beneath major hotspots. *Nature* 525 (7567), 95–99. <https://doi.org/10.1038/nature14876>
- Frisch, W., Meschede, M., & Blakey, R. C. (2011). *Plate Tectonics*. Springer, Heidelberg/Dordrecht/London/New York, 212 pp. <https://doi.org/10.1007/978-3-540-76504-2>
- Fromm, T. (2016). PRay - A graphical user interface for interactive visualization and modification of rayinvr models. *Journal of Applied Geophysics* 124, 1–3. <https://doi.org/10.1016/j.jappgeo.2015.11.004>
- Funck, T. (2003). Crustal structure of the ocean-continent transition at Flemish Cap: Seismic refraction results. *Journal of Geophysical Research* 108(B11), 2531. <https://doi.org/10.1029/2003JB002434>
- Furumoto, A. S., Webb, J. P., Odegard, M. E. & Hussong, D. M. (1976). Seismic studies on the Ontong Java Plateau, 1970. *Tectonophysics*, 34(1–2), 71–90. [https://doi.org/10.1016/0040-1951\(76\)90177-3](https://doi.org/10.1016/0040-1951(76)90177-3)
- Gans, P.B. (1997). Large-magnitude Oligo-Miocene extension in southern Sonora: implications for the tectonic evolution of northwest Mexico. *Tectonics* 16, 388–408. <https://doi.org/10.1029/97TC00496>
- Gallais, F., Fujie, G., Boston, B. & Hackney, R. (2019). Crustal Structure Across the Lord Howe Rise, Northern Zealandia, and Rifting of the Eastern Gondwana Margin. *Journal of Geophysical Research : Solid Earth* 124, 3036–3056. <https://doi.org/10.1029/2018JB016798>
- Gaina, C., Müller, D.R., Royer, J.-Y., Stock, J., Hardebeck, J. & Symonds, P. (1998). The tectonic history of the Tasman Sea: A puzzle with 13 pieces. *Journal of Geophysical Research: Solid Earth* 103, 12413–12433. <https://doi.org/10.1029/98JB00386>
- Geoffroy, L. (2005). Volcanic passive margins. *Comptes Rendus Geoscience* 337, 1395–1408. <https://doi.org/10.1016/j.crte.2005.10.006>
- Gerya, T. V., Yuen, D.A. & Maresch, W.V. (2004). Thermomechanical modelling of slab detachment. *Earth and Planetary Science Letters* 226, 101–116. <https://doi.org/10.1016/j.epsl.2004.07.022>
- Gianni, G. M., García, H. P. A., Lupari, M., Pesce, A. & Folguera, A. (2017). Plume overriding triggers shallow subduction and orogeny in the southern Central Andes. *Gondwana Research*, 49, 387–395. <https://doi.org/10.1016/j.gr.2017.06.011>
- Godfrey, N.J., Christensen, N.I. & Okaya, D.A. (2000). Anisotropy of schists: Contribution of crustal anisotropy to active source seismic experiments and shear wave splitting observations. *Journal of Geophysical Research* 105, 27991–28007. <https://doi.org/10.1029/2000JB900286>
- Godfrey, N.J., Davey, F., Stern, T.A. & Okaya, D. (2001). Crustal structure and thermal anomalies of the Dunedin Region, South Island, New Zealand. *Journal of Geophysical Research* 106, 30835–30835. <https://doi.org/10.1029/2000JB000006>
- Gohl, K., Denk, A., Eagles, G. & Wobbe, F. (2013). Deciphering tectonic phases of the Amundsen Sea Embayment shelf, West Antarctica, From a magnetic anomaly grid. *Tectonophysics* 585, 113–123. <https://doi.org/10.1016/j.tecto.2012.06.036>
- Gohl, K. & Werner, R. (2016). The Expedition SO246 of the Research Vessel SONNE to the Chatham Rise in 2016. *Berichte zur Polar- und Meeresforschung = Reports on polar and marine research*. Alfred Wegener Institute for Polar and Marine Research, Bremerhaven, Germany. https://doi.org/10.2312/BzPM_0698_2016
- Golowin, R., Portnyagin, M., Hoernle, K., Hauff, F., Gurenko, A., Garbe-Schönberg, D., Werner, R. & Turner, S. (2017). Boninite-like intraplate magmas from Manihiki Plateau require ultra-depleted and enriched source components. *Nature Communications*. 8, 14322. <https://doi.org/10.1038/ncomms14322>
- Golowin, R., Portnyagin, M., Hoernle, K., Hauff, F., Werner, R. & Garbe-Schönberg, D. (2018). Geochemistry of deep Manihiki Plateau crust: implications for compositional diversity of large igneous provinces in the Western Pacific and their genetic link. *Chemical Geology* 493, 553–566. <https://doi.org/10.1016/j.chemgeo.2018.07.016>
- Govers, R. & Wortel, M.J.R. (2005). Lithosphere tearing at STEP faults: response to edges of subduction zones. *Earth and Planetary Science Letters* 236, 505–523. <https://doi.org/10.1016/j.epsl.2005.03.022>
- Götze, H.-J. (2007). IGMAS+, Interactive Geophysical Modelling Assistant, v1.1.1892.1. Transinsight GmbH, Dresden.
- Götze, H.-J. & Lahmeyer, B. (1988). Application of three-dimensional interactive modeling in gravity and magnetics. *Geophysics* 53, 1096–1108. <https://doi.org/10.1190/1.1442546>
- Granot, R., Cande, S.C., Stock, J.M. & Damaske, D. (2013). Revised Eocene–Oligocene kinematics for the West Antarctic rift system. *Geophysical Research Letters* 40, 279–284. <https://doi.org/10.1029/2012GL054181>

- Grobys, J.W.G., Gohl, K., Davy, B., Uenzelmann-Neben, G., Deen, T. & Barker, D. (2007). Is the Bounty Trough off eastern New Zealand an aborted rift? *Journal of Geophysical Research: Solid Earth* 112, 1–21. <https://doi.org/10.1029/2005JB004229>
- Grobys, J.W.G., Gohl, K. & Eagles, G. (2008). Quantitative tectonic reconstructions of Zealandia based on crustal thickness estimates. *Geochemistry, Geophysics, Geosystems* 9. <https://doi.org/10.1029/2007GC001691>
- Grobys, J.W.G., Gohl, K., Uenzelmann-Neben, G., Davy, B. & Barker, D. (2009). Extensional and magmatic nature of the Campbell Plateau and Great South Basin from deep crustal studies. *Tectonophysics* 472, 213–225. <https://doi.org/10.1016/j.tecto.2008.05.003>
- Gutscher, M. A., Olivet, J. L., Aslanian, D., Eissen, J. P. & Maury, R. (1999). The “lost Inca Plateau”: cause of flat subduction beneath Peru? *Earth and Planetary Science Letters* 171(3), 335–341. [https://doi.org/https://doi.org/10.1016/S0012-821X\(99\)00153-3](https://doi.org/https://doi.org/10.1016/S0012-821X(99)00153-3)
- Gutscher, M. A., Maury, F., Eissen, J. P. & Bourdon, E. (2000a). Can slab melting be caused by flat subduction? *Geology*, 28(6), 535–538. [https://doi.org/10.1130/0091-7613\(2000\)28<535:csmcb>2.0.co;2](https://doi.org/10.1130/0091-7613(2000)28<535:csmcb>2.0.co;2)
- Gutscher, M. A., Spakman, W., Bijwaard, H. & Engdahl, E. R. (2000b). Geodynamics of flat subduction: Seismicity and tomographic constraints from the Andean margin. *Tectonics* 19(5), 814–833. <https://doi.org/10.1029/1999TC001152>
- Gvirtzman, Z. & Nur, A. (1999). Plate detachment, asthenosphere upwelling, and topography across subduction zones. *Geology* 27, 563–566. [https://doi.org/10.1130/0091-7613\(1999\)027<0563:PDAUAT>2.3.CO;2](https://doi.org/10.1130/0091-7613(1999)027<0563:PDAUAT>2.3.CO;2)
- Halbwachs, M., Sabroux, J.-C., Grangeon, J., Kayser, G., Tochon-Danguy, J.-C., Felix, A., Béard, J.-C., Villeveille, A., Vitter, G., Richon, R., Wüest, A. & Hell, J. (2004). Degassing the “Killer Lakes” Nyos and Monoun, Cameroon. *Eos, Transactions American Geophysical Union*, 85(30), 281. <https://doi.org/10.1029/2004EO300001>
- Hanyu, T., Tatsumi, Y., Senda, R., Miyazaki, T., Chang, Q., Hirahara, Y., Takahashi, T., Kawabata, H., Suzuki, K. & Kimura, J.-I. (2011). Geochemical characteristics and origin of the HIMU reservoir: a possible mantle plume source in the lower mantle. *Geochemistry, Geophysics, Geosystems* 12, Q0AC09. <https://doi.org/10.1029/2010GC003252>
- Hart, S.R., Blusztajn, J., LeMasurier, W.E. & Rex, D.C. (1997). Hobbs Coast Cenozoic volcanism: implications for the West Antarctic rift system. *Chemical Geology* 139, 223–248. [https://doi.org/10.1016/S0009-2541\(97\)00037-5](https://doi.org/10.1016/S0009-2541(97)00037-5)
- Henrys, S., Wech, A., Sutherland, R., Stern, T., Savage, M., Sato, H., Mochizuki, K., Iwasaki, T., Okaya, D., Seward, A., Tozer, B., Townend, J., Kurashimo, E., Iidaka & T., Ishiyama, T. (2013). SAHKE geophysical transect reveals crustal and subduction zone structure at the southern Hikurangi margin, New Zealand. *Geochemistry, Geophysics, Geosystems*, 14(7), 2063–2083. <https://doi.org/10.1002/ggge.20136>
- Hochmuth, K. & Gohl, K. (2017). Collision of Manihiki Plateau fragments to accretional margins of northern Andes and Antarctic Peninsula. *Tectonics* 36, 229–240. <https://doi.org/10.1002/2016TC004333>
- Hochmuth, K., Gohl, K. & Uenzelmann-Neben, G. (2015). Playing jigsaw with Large Igneous Provinces—A plate tectonic reconstruction of Ontong Java Nui, West Pacific. *Geochemistry, Geophysics, Geosystems* 16, 3789–3807. <https://doi.org/10.1002/2015GC006036>
- Hochmuth, K., Gohl, K., Uenzelmann-Neben, G. & Werner, R. (2019). Multiphase magmatic and tectonic evolution of a large igneous province - Evidence from the crustal structure of the Manihiki Plateau, western Pacific. *Tectonophysics* 750, 434–457. <https://doi.org/10.1016/j.tecto.2018.11.014>
- Hoernle, K., Hauff, F., van den Bogaard, P., Werner, R., Mortimer, N., Geldmacher, J., Garbe-Schönberg, D. & Davy, B. (2010). Age and geochemistry of volcanic rocks from the Hikurangi and Manihiki oceanic Plateaus. *Geochimica et Cosmochimica Acta* 74, 7196–7219. <https://doi.org/10.1016/j.gca.2010.09.030>
- Hoernle, K., Mortimer, N., Werner, R. & Hauff, F. (2003). Cruise Report SO168. *GEOMAR Repository* 113, 127. https://doi.org/10.3289/GEOMAR_REP_NS_7_2013
- Hoernle, K., Timm, C., Hauff, F., Tappenden, V., Werner, R., Jolis, E.M., Mortimer, N., Weaver, S., Riefstahl, F. & Gohl, K. (2020). Late Cretaceous (99–69 Ma) basaltic intraplate volcanism on and around Zealandia: Tracing upper mantle geodynamics from Hikurangi Plateau collision to Gondwana breakup and beyond. *Earth and Planetary Science Letters* 529, 115864. <https://doi.org/10.1016/j.epsl.2019.115864>
- Hoernle, K., White, J.D.L., van den Bogaard, P., Hauff, F., Coombs, D.S., Werner, R., Timm, C., Garbe-Schoenberg, D., Reay, A. & Cooper, A. (2006). Cenozoic intraplate volcanism on New Zealand: upwelling induced by lithospheric removal. *Earth and Planetary Science Letters* 248, 335–352. <https://doi.org/10.1016/j.epsl.2006.06.001>
- Hofmann, A.W. (1997). Mantle geochemistry: the message from oceanic volcanism. *Nature* 385 (6613), 219–229. <https://doi.org/10.1038/385219a0>
- Hofmann, A.W. & White, W.M. (1982). Mantle plumes from ancient oceanic crust. *Earth Planetary Science Letters* 57

References

- (2), 421–436. [https://doi.org/10.1016/0012-821X\(82\)90161-3](https://doi.org/10.1016/0012-821X(82)90161-3)
- Homrighausen, S., Hoernle, K., Hauff, F., Geldmacher, J., Wartho, J.-A.A., van den Bogaard, P. & Garbe-Schönberg, D. (2018). Global distribution of the HIMU end member: Formation through Archean plume-lid tectonics. *Earth-Science Reviews* 182, 85–101. <https://doi.org/https://doi.org/10.1016/j.earscirev.2018.04.009>
- Horsefield, S.J., Whitmarsh, R.B., White, R.S. & Sibuet, J.C. (1994). Crustal Structure of the Goban Spur Rifted Continental-Margin, Ne Atlantic. *Geophysical Journal International* 119, 1–19. <https://doi.org/10.1111/j.1365-246X.1994.tb00909.x>
- Huangfu, P., Wang, Y., Li, Z., Fan, W. & Zhang, Y. (2016). Effects of crustal eclogitization on plate subduction/collision dynamics: Implications for India-Asia collision. *Journal of Earth Science*, 27(5), 727–739. <https://doi.org/10.1007/s12583-016-0701-9>
- Huisman, R. S., Podladchikov, Y. Y. & Cloetingh, S. (2001). Dynamic modeling of the transition from passive to active rifting, application to the Pannonian Basin. *Tectonics* 20(6), 1021–1039. <https://doi.org/10.1029/2001TC900010>
- Ingle, S. & Coffin, M. F. (2004). Impact origin for the greater Ontong Java Plateau? *Earth and Planetary Science Letters*, 218(1–2), 123–134. [https://doi.org/10.1016/S0012-821X\(03\)00629-0](https://doi.org/10.1016/S0012-821X(03)00629-0)
- Jacob, J.-B., Scott, J.M., Turnbull, R.E., Tarling, M.S. & Sagar, M.W. (2017). High- to ultrahigh-temperature metamorphism in the lower crust: An example resulting from Hikurangi Plateau collision and slab rollback in New Zealand. *Journal of Metamorphic Geology* 35, 831–853. <https://doi.org/10.1111/jmg.12257>
- Kawabata, H., Hanyu, T., Chang, Q., Kimura, J.-I., Nichols, A.R.L. & Tatsumi, Y. (2011). The petrology and geochemistry of St. Helena alkali basalts: evaluation of the oceanic crust-recycling model for HIMU OIB. *Journal of Petrology* 52, 791–838. <https://doi.org/10.1093/petrology/egr003>
- Kerr, A.C. (2014). Oceanic Plateaus. In: Holland, H.D. & Turekian, K.K. (Eds.), *Treatise on Geochemistry (Second Edition)*, Vol. 4, 631–667. Elsevier. <https://doi.org/https://doi.org/10.1016/B978-0-08-095975-7.00320-X>
- Kent, W., Saunders, A.D., Kempton, P.D. & Ghose, N.C. (1997). Rajmahal Basalts, Eastern India: mantle sources and melt distribution at a volcanic rifted margin. In: Mahoney, J.J., Coffin, M.F. (Eds.), *Large Igneous Provinces: Continental, Oceanic, and Planetary Flood Volcanism. AGU Geophysical Monograph*, Vol. 100, pp. 145–182.
- Kimura, J.-I., Gill, J.B., Skora, S., van Keken, P.E. & Kawabata, H. (2016). Origin of geochemical mantle components: role of subduction filter. *Geochemistry, Geophysics, Geosystems* 17 (8), 3289–3325. <https://doi.org/10.1002/2016GC006343>
- Kipf, A., Mortimer, N., Werner, R., Gohl, K., Van Den Bogaard, P., Hauff, F. & Hoernle, K. (2012). Granitoids and dykes of the Pine Island Bay region, West Antarctica. *Antarctic Science* 24, 473–484. <https://doi.org/10.1017/S0954102012000259>
- Klepeis, K.A., Schwartz, J., Stowell, H. & Tulloch, A. (2016). Gneiss domes, vertical and horizontal mass transfer, and the initiation of extension in the hot lower-crustal root of a continental arc, Fiordland, New Zealand. *Lithosphere* 8, 116–140. <https://doi.org/10.1130/L490.1>
- Kling, G. W., Clark, M. A., Compton, H. R., Devine, J. D., Evans, W. C., Humphrey, A. M., Koenigsberg, E. J., Lockwood, J. P., Tuttle, M. L. & Wagner, G. N. (1987). The 1986 Lake Nyos Gas Disaster in Cameroon, West Africa. *Science*, 236(4798), 169–175. <https://doi.org/10.1126/science.236.4798.169>
- Klingelhoefer, F., Lafoy, Y., Collot, J., Cosquer, E., Géli, L., Nouzé, H. & Vially, R. (2007). Crustal structure of the basin and ridge system west of New Caledonia (southwest Pacific) from wide-angle and reflection seismic data. *Journal of Geophysical Research: Solid Earth* 112, 1–18. <https://doi.org/10.1029/2007JB005093>
- Knesel, K.M., Cohen, B.E., Vasconcelos, P.M. & Thiede, D.S. (2008). Rapid change in drift of the Australian plate records collision with Ontong Java plateau. *Nature*, 454(7205), 754–757. <https://doi.org/10.1038/nature07138>
- Koppers, A.A.P., Duncan, R.A. & Steinberger, B. (2004). Implications of a nonlinear $^{40}\text{Ar}/^{39}\text{Ar}$ age progression along the Louisville seamount trail for models of fixed and moving hot spots. *Geochemistry, Geophysics, Geosystems* 5, Q06L02. <https://doi.org/10.1029/2003GC000671>
- Kula, J., Tulloch, A., Speli, T.L. & Wells, M.L. (2007). Two-stage rifting of Zealandia-Australia-Antarctica: Evidence from $^{40}\text{Ar}/^{39}\text{Ar}$ thermochronometry of the Sisters shear zone Stewart Island, New Zealand. *Geology* 35, 411–414. <https://doi.org/10.1130/G23432A.1>
- Kula, J., Tulloch, A.J., Spell, T.L., Wells, M.L. & Zanetti, K. A. (2009). Thermal evolution of the Sisters shear zone, southern New Zealand; Formation of the Great South Basin and onset of Pacific-Antarctic spreading. *Tectonics* 28, 1–22. <https://doi.org/10.1029/2008TC002368>
- Laird, M.G. & Bradshaw, J.D. (2004). The Break-up of a Long-term Relationship: the Cretaceous Separation of New Zealand from Gondwana. *Gondwana Research* 7, 273–286. [https://doi.org/10.1016/S1342-937X\(05\)70325-7](https://doi.org/10.1016/S1342-937X(05)70325-7)

- Larson, R.L., Pockalny, R.A., Viso, R.F., Erba, E., Abrams, L.J., Luyendyk, B.P., Stock, J.M. & Clayton, R.W. (2002). Mid-Cretaceous tectonic evolution of the Tongareva triple junction in the southwestern Pacific Basin. *Geology* 30, 67–70. [https://doi.org/10.1130/0091-7613\(2002\)030<0067:MCTEOT>2.0.CO;2](https://doi.org/10.1130/0091-7613(2002)030<0067:MCTEOT>2.0.CO;2)
- Larter, R.D., Cunningham, A.P., Barker, P.F., Gohl, K. & Nitsche, O. (2002). Tectonic evolution of the Pacific margin of Antarctica 1. Late Cretaceous tectonic reconstructions. *Journal of Geophysical Research* 107, 2345. <https://doi.org/10.1029/2000JB000052>
- Le Maitre, R.W., Bateman, P., Dudek, A., Keller, J., Lameyre, J., Le Bas, M.J., Sabine, P.A., Schmid, R., Sorensen, H. & Streckeisen, A. (1989). A classification of igneous rocks and glossary of terms. Recommendations of the IUGS Subcommittee on the Systematics of Igneous rocks. Blackwell Science Publishers, Oxford, London.
- Li, Z. H., Xu, Z., Gerya, T. & Burg, J. P. (2013). Collision of continental corner from 3-D numerical modeling. *Earth and Planetary Science Letters* 380, 98–111. <https://doi.org/10.1016/j.epsl.2013.08.034>
- Li, J., Wang, X.-C., Xu, J.-F., Xu, Y.-G., Tang, G.-J. & Wang, Q. (2015). Disequilibrium-induced initial Os isotopic heterogeneity in gram aliquots of single basaltic rock powders: implications for dating and source tracing. *Chemical Geology* 406, 10–17. <https://doi.org/10.1016/j.chemgeo.2015.04.010>
- Ligi, M., Bonatti, E., Bosworth, W., Cai, Y., Cipriani, A., Palmiotto, C., Ronca, S. & Seyler, M. (2018). Birth of an ocean in the Red Sea: Oceanic-type basaltic melt intrusions precede continental rupture. *Gondwana Research*, 54(November 2017), 150–160. <https://doi.org/10.1016/j.gr.2017.11.002>
- Liu, L., Gurnis, M., Seton, M., Saleeby, J., Müller, R. D. & Jackson, J. M. (2010). The role of oceanic plateau subduction in the Laramide orogeny. *Nature Geoscience*, 3(5), 353–357. <https://doi.org/10.1038/ngeo829>
- Lindow, J., Kamp, P.J.J., Mukasa, S.B., Kleber, M., Lisker, F., Gohl, K., Kuhn, G. & Spiegel, C. (2016). Exhumation history along the eastern Amundsen Sea coast, West Antarctica, revealed by low-temperature thermochronology. *Tectonics* 35, 2239–2257. <https://doi.org/10.1002/2016TC004236>
- Liu, S., Zhao, M., Sibuet, J.C., Qiu, X., Wu, J., Zhang, J., Chen, C., Xu, Y. & Sun, L. (2018). Geophysical constraints on the lithospheric structure in the northeastern South China Sea and its implications for the South China Sea geodynamics. *Tectonophysics* 742–743, 101–119. <https://doi.org/10.1016/j.tecto.2018.06.002>
- Luyendyk, B.R. (1995). Hypothesis for Cretaceous rifting of east Gondwana caused by subduction slab capture. *Geology* 23 (4), 373–376. [https://doi.org/10.1130/0091-7613\(1995\)023%3C0373:HFCROE%3E2.3.CO;2](https://doi.org/10.1130/0091-7613(1995)023%3C0373:HFCROE%3E2.3.CO;2)
- Machida, S., Hirano, N. & Kimura, J.-I. (2009). Evidence for recycled plate material in Pacific upper mantle unrelated to plumes. *Science* 313, 1426–1428. <https://doi.org/10.1016/j.gca.2009.01.026>
- Mann, P. & Taira, A. (2004). Global tectonic significance of the Solomon Islands and Ontong Java Plateau convergent zone. *Tectonophysics* 389, 137–190. <https://doi.org/10.1016/j.tecto.2003.10.024>
- Matthews, K.J., Seton, M. & Müller, R.D. (2012). A global-scale plate reorganization event at 105–100 Ma. *Earth and Planetary Science Letters* 355–356, 283–298. <https://doi.org/10.1016/j.epsl.2012.08.023>
- Matthews, K.J., Maloney, K.T., Zahirovic, S., Williams, S.E., Seton, M. & Müller, R.D. (2016). Global plate boundary evolution and kinematics since the late Paleozoic. *Global and Planetary Change* 146, 226–250. <https://doi.org/10.1016/j.gloplacha.2016.10.002>
- McCoy-West, A., Baker, J., Faure, K. & Wysoczanski, R. (2010). Petrogenesis and origins of Mid-Cretaceous continental intraplate volcanism in Marlborough, New Zealand: implications for the long-lived HIMU magmatic mega-province of the SW Pacific. *Journal of Petrology* 51(10), 2003–2045. <https://doi.org/10.1093/petrology/egg046>
- McCoy-West, A., Bennet, V.C. & Amelin, Y. (2016). Rapid Cenozoic ingrowth of isotopic signatures simulating “HIMU” in ancient lithospheric mantle: distinguishing source from process. *Geochimica Cosmochimica Acta* 187, 79–101. <https://doi.org/10.1016/j.gca.2016.05.013>
- McCoy-West, A.J., Bennet, V.C., Puchtel, I.S. & Walker, R.J. (2013). Extreme persistence of cratonic lithosphere in the southwest Pacific: Paleoproterozoic Os isotopic signatures in Zealandia. *Geology* 41, 231–234. <https://doi.org/10.1130/G33626.1>
- McFadden, R.R., Teyssier, C., Siddoway, C.S., Cosca, M.A. & Fanning, C.M. (2015). Mid-Cretaceous oblique rifting of West Antarctica: Emplacement and rapid cooling of the Fosdick Mountains migmatite-cored gneiss dome. *Lithos* 232, 306–318. <https://doi.org/10.1016/j.lithos.2015.07.005>
- McFadden, R.R., Teyssier, C., Siddoway, C.S., Whitney, D.L. & Fanning, C.M. (2010). Oblique dilation, melt transfer, and gneiss dome emplacement. *Geology* 38, 375–378. <https://doi.org/10.1130/G30493.1>
- Miller, K. G., Kominz, M. A., Browning, J. V., Wright, J. D., Mountain, G. S., Katz, M. E., Sugarman, P. J., Cramer B. S., Christie-Blick, N. & Pekar, S. F. (2005). The Phanerozoic record of global sea-level change. *Science* 310(5752), 1293–1298. <https://doi.org/10.1126/science.1116412>

References

- Minshull, T.A. (2009). Geophysical characterisation of the ocean-continent transition at magma-poor rifted margins. *Comptes Rendus Geoscience* 341, 382–393. <https://doi.org/10.1016/j.crte.2008.09.003>
- Mitchell, M., Craw, D., Landis, C.A. & Frew, R. (2009). Stratigraphy, provenance, and diagenesis of the Cretaceous Horse Range Formation, east Otago, New Zealand. *New Zealand Journal of Geology and Geophysics* 52, 171–183. <https://doi.org/10.1080/00288300909509884>
- Mjelde, R., Raum, T., Breivik, A. J. & Faleide, J. I. (2008). Crustal transect across the North Atlantic. *Marine Geophysical Research* 29(2), 73–87. <https://doi.org/10.1007/s11001-008-9046-9>
- Mochizuki, K., Sutherland, R., Henrys, S., Bassett, D., Van Avendonk, H., Arai, R., Kodaira, S., Fujie, G., Yamamoto, Y., Bangs, N. & Barker, D. (2019). Recycling of depleted continental mantle by subduction and plumes at the Hikurangi Plateau large igneous province, southwestern Pacific Ocean. *Geology*, 47(8), 795–798. <https://doi.org/10.1130/G46250.1>
- Montelli, R., Nolet, G., Dahlen, R.A. & Masters, G. (2006). A catalogue of deep mantle plumes: new results from finite frequency tomography. *Geochemistry, Geophysics, Geosystems* 7(11), Q11007. <https://doi.org/10.1029/2006GC001248>
- Montgomery, A.F. & Johnson, H.P. (1987). Paleomagnetic studies of Leg 91 basalts and sediments. *Initial Reports of the Deep Sea Drilling Project* 91, 475–482. <https://doi.org/10.2973/dsdp.proc.91.114.1987>
- Mortimer, N. (2004). Basement gabbro from the Lord Howe Rise. *New Zealand Journal of Geology and Geophysics* 47, 501–507. <https://doi.org/10.1080/00288306.2004.9515072>
- Mortimer, N. (2018). Evidence for a pre-Eocene proto-Alpine Fault through Zealandia. *New Zealand Journal of Geology and Geophysics* 61, 251–259. <https://doi.org/10.1080/00288306.2018.1434211>
- Mortimer, N., Campbell, H.J. & Moerhuis, N. (2019a). Chatham Schist. *New Zealand Journal of Geology and Geophysics*. <https://doi.org/10.1080/00288306.2019.1662817>
- Mortimer, N., Campbell, H.J., Tulloch, A.J., King, P.R., Stagpoole, V.M., Wood, R.A., Rattenbury, M.S., Sutherland, R., Adams, C.J., Collot, J. & Seton, M. (2017). Zealandia: Earth's hidden Continent. *GSA Today* 27, 27–35. <https://doi.org/10.1130/GSATG321A.1>
- Mortimer, N., Davey, F.J., Melhuish, A., Yu, J. & Godfrey, N.J. (2002). Geological interpretation of a deep seismic reflection profile across the Eastern Province and Median Batholith, New Zealand: Crustal architecture of an extended Phanerozoic convergent orogen. *New Zealand Journal of Geology and Geophysics*, 45(3), 349–363. <https://doi.org/10.1080/00288306.2002.9514978>
- Mortimer, N., Gans, P.B., Meffre, S., Martin, C.E., Seton, M., Williams, S., Turnbull, R.E., Quilty, P.G., Micklethwaite, S., Timm, C., Sutherland, R., Bache, F., Collot, J., Maurizot, P., Rouillard, P. & Rollet, N. (2018). Regional volcanism of northern Zealandia: post-Gondwana break-up magmatism on an extended, submerged continent. *Geological Society London Special Publications* 463, 199–226. <https://doi.org/10.1144/SP463.9>
- Mortimer, N., Hoernle, K., Hauff, F., Palin, J.M., Dunlap, W.J., Werner, R. & Faure, K. (2006). New constraints on the age and evolution of the Wishbone Ridge, southwest Pacific Cretaceous microplates, and Zealandia - West Antarctica breakup. *Geology* 34, 185–188. <https://doi.org/10.1130/G22168.1>
- Mortimer, N., Kohn, B., Seward, D., Spell, T. & Tulloch, A. (2016). Reconnaissance thermochronology of southern Zealandia. *Journal of the Geological Society London* 173, 370–383. <https://doi.org/10.1144/jgs2015-021>
- Mortimer, N., Lee, J. & Stockli, D. (2015). Double dating of zircon gives new information of timing of Otago Schist deposition, metamorphism and exhumation. *Geoscience Society of New Zealand Miscellaneous Publication* 143A: 98.
- Mortimer, N., Rattenbury, M.S., King, P.R., Bland, K.J., Barrell, D.J.A., Bache, F., Begg, J.G., Campbell, H.J., Cox, S.C., Crampton, J.S., Edbrooke, S.W., Forsyth, P.J., Johnston, M.R., Jongens, R., Lee, J.M., Leonard, G.S., Raine, J.I., Skinner, D.N.B., Timm, C., Townsend, D.B., Tulloch, A.J., Turnbull, I.M. & Turnbull, R.E. (2014). High-level stratigraphic scheme for New Zealand rocks. *New Zealand Journal of Geology and Geophysics* 57, 402–419. <https://doi.org/10.1080/00288306.2014.946062>
- Mortimer, N., van den Bogaard, P., Hoernle, K., Timm, C., Gans, P.B., Werner, R. & Riefstahl, F. (2019b). Late Cretaceous oceanic plate reorganization and the breakup of Zealandia and Gondwana. *Gondwana Research* 65, 31–42. <https://doi.org/10.1016/j.gr.2018.07.010>
- Mueller, C.O., Jokat, W. & Schreckenberger, B. (2016). The crustal structure of Beira High, central Mozambique— Combined investigation of wide-angle seismic and potential field data. *Tectonophysics* 683, 233–254. <https://doi.org/10.1016/j.tecto.2016.06.028>
- Müller, R. D., Cannon, J., Qin, X., Watson, R. J., Gurnis, M., Williams, S., Pfaffelmoser, T., Seton, M., Russell, S.H.J. &

- Zahirovic, S. (2018). GPlates: Building a virtual Earth through deep time. *Geochemistry, Geophysics, Geosystems* 19, 2243–2261. <https://doi.org/10.1029/2018GC007584>
- Mutter, J. C. (1985). Seaward dipping reflectors and the continent-ocean boundary at passive continental margins. *Tectonophysics* 114(1–4), 117–131. [https://doi.org/10.1016/0040-1951\(85\)90009-5](https://doi.org/10.1016/0040-1951(85)90009-5)
- Nayar, A. (2009). Earth science: A lakeful of trouble. *Nature* 460(7253), 321–323. <https://doi.org/10.1038/460321a>
- Nebel, O., Arculus, R.J., van Westrenen, W., Woodhead, J.D., Jenner, F.E., Nebel-Jacobsen, Y.J., Wille, M. & Eggins, S.M. (2013). Coupled Hf–Nd–Pb isotope covariations of HIMU oceanic island basalts from Mangaia, Cook-Austral islands, suggest an Archean source component in the mantle transition zone. *Geochimica et Cosmochimica Acta* 112, 87–101. <https://doi.org/10.1016/j.gca.2013.03.005>
- Panter, K.S., Hart, R.S., Kyle, P.R., Blusztajn, J. & Wilch, T. (2000). Geochemistry of Late Cenozoic basalts from the Cray Mountains: characterization of mantle sources in Marie Byrd Land, Antarctica. *Chemical Geology* 165, 215–241. [https://doi.org/10.1016/S0009-2541\(99\)00171-0](https://doi.org/10.1016/S0009-2541(99)00171-0)
- Panter, K.S., Blusztajn, J., Hart, S.R., Kyle, P.R., Esser, R. & McIntosh, W.C. (2006). The origin of HIMU in the SW Pacific: Evidence from intraplate volcanism in Southern New Zealand and Subantarctic Islands. *Journal of Petrology* 47, 1673–1704. <https://doi.org/10.1093/petrology/egl024>
- Park, S., Langmuir, C.H., Sims, K.W.W., Blichert-Toft, J., Kim, S., Scott, S.R., Lin, J., Choi, H., Yang, Y. & Michael, P.J. (2019). An isotopically distinct Zealandia–Antarctic mantle domain in the Southern Ocean. *Nature Geoscience* 12, 206–214. <https://doi.org/10.1038/s41561-018-0292-4>
- Pearce, J.A. (1996). A user's guide to basalt discrimination diagrams. In: Wyman, D.A. (Ed.), Trace Element Geochemistry of Volcanic Rocks: Applications for Massive Sulphide Exploration. In: Short Course Notes, Vol. 12. Geological Association of Canada, pp. 79–113.
- Pearce, J.A. (2008). Geochemical fingerprinting of oceanic basalts with applications to ophiolite classification and the search of Archean oceanic crust. *Lithos* 100, 14–48. <https://doi.org/10.1016/j.lithos.2007.06.016>
- Pérez-Gussinyé, M., Ranero, C.R., Reston, T.J. & Sawyer, D. (2003). Mechanisms of extension at nonvolcanic margins: Evidence from the Galicia interior basin, west of Iberia. *Journal of Geophysical Research: Solid Earth* 108, 1–19. <https://doi.org/10.1029/2001JB000901>
- Prada, M., Sallares, V., Ranero, C.R., Vendrell, M.G., Grevemeyer, I., Zitellini, N. & de Franco, R. (2015). The complex 3-D transition from continental crust to backarc magmatism and exhumed mantle in the Central Tyrrhenian basin. *Geophysical Journal International* 203, 63–78. <https://doi.org/10.1093/gji/ggv271>
- O'Connor, J.M., Hoernle, K., Müller, R.D., Morgan, J.P., Butterworth, N.P., Hauff, F., Sandwell, D.T., Jokat, W., Wijbrans, J.R. & Stoffers, P. (2015). Deformation-related volcanism in the Pacific Ocean linked to the Hawaiian-Emperor bend. *Nature Geoscience* 8, 393–397. <https://doi.org/10.1038/NGEO2416>
- Rattenbury, M.S., Townsend, D.B. & Johnston, M.R. (2006). Geology of the Kaikoura area, scale 1:250,000. Institute of Geological and Nuclear Sciences 1:250,000 Geological Map 13.
- Reston, T.J. (2007). The formation of non-volcanic rifted margins by the progressive extension of the lithosphere: the example of the West Iberian margin. In: Karner, G.D., Manatschal, G. & Pinheiro, L.M. (Eds.), Imaging, Mapping and Modelling Continental Lithosphere Extension and Breakup. In: *Geological Society London Special Publications*, Vol. 282, pp. 77–110.
- Reyners, M. (2013). The central role of the Hikurangi Plateau in the Cenozoic tectonics of New Zealand and the Southwest Pacific. *Earth and Planetary Science Letters* 361, 460–468. <https://doi.org/10.1016/j.epsl.2012.11.010>
- Reyners, M., Eberhart-Phillips, D. & Bannister, S. (2011). Tracking repeated subduction of the Hikurangi Plateau beneath New Zealand. *Earth and Planetary Science Letters* 311, 165–171. <https://doi.org/10.1016/j.epsl.2011.09.011>
- Reyners, M., Eberhart-Phillips, D. & Bannister, S. (2017a). Subducting an old subduction zone sideways provides insights into what controls plate coupling. *Earth and Planetary Science Letters* 466, 53–61. <https://doi.org/10.1016/j.epsl.2017.03.004>
- Reyners, M., Eberhart-Phillips, D., Upton, P. & Gubbins, D. (2017b). Three-dimensional imaging of impact of a large igneous province with a subduction zone. *Earth and Planetary Science Letters* 460, 143–151. <https://doi.org/10.1016/j.epsl.2016.12.025>
- Richards, M.A., Duncan, R.A. & Courtillot, V.E. (1989). Flood basalts and hot-spot tracks: plume heads and tails. *Science* 246, 103–107. <https://doi.org/10.1126/science.246.4926.103>
- Riefstahl, F., Gohl, K., Davy, B., Mortimer, N., Hoernle, K., Timm, C., Werner, R. & Hochmuth, K. (2020). Cretaceous intracontinental rifting at the southern Chatham Rise margin and initialisation of seafloor spreading between Zealandia and Antarctica. *Tectonophysics* 776, 228298. <https://doi.org/10.1016/j.tecto.2019.228298>

References

- Ring, U., Bernet, M. & Tulloch, A. (2015). Kinematic, finite strain and vorticity analysis of the Sisters Shear Zone, Stewart Island, New Zealand. *Journal of Structural Geology* 73, 114–129. <https://doi.org/10.1016/j.jsg.2015.02.004>
- Rosenbaum, G., Giles, D., Saxon, M., Betts, P. G., Weinberg, R. F. & Duboz, C. (2005). Subduction of the Nazca Ridge and the Inca Plateau: Insights into the formation of ore deposits in Peru. *Earth and Planetary Science Letters* 239(1–2), 18–32. <https://doi.org/10.1016/j.epsl.2005.08.003>
- Ruddiman, W. F. & Kutzbach, J. E. (1989). Forcing of late Cenozoic Northern Hemisphere climate by plateau uplift in southern Asia and the American west. *Journal of Geophysical Research* 94(D15). <https://doi.org/10.1029/jd094id15p18409>
- Sandwell, D.T., Müller, R.D., Smith, W.H.F., Garcia, E. & Francis, R. (2014). New global marine gravity model from CryoSat-2 and Jason-1 reveals buried tectonic structure. *Science* 346(6205), 65–67. <https://doi.org/10.1126/science.1258213>
- Sandwell, D.T., Smith, W.H.F. (1997). Marine gravity anomaly from Geosat and ERS I satellite altimetry. *Journal of Geophysical Research* 102, 10039–10054. <https://doi.org/10.1029/96JB03223>
- Saunders, A.D. (1987). Geochemistry of basalts from Mesozoic Pacific Ocean crust; Deep Sea Drilling Project Leg 91. *Initial Reports of the Deep Sea Drilling Project* 91, 483–494. <https://doi.org/10.2973/dsdp.proc.91.115.1987>
- Schellart, W. P., Freeman, J., Stegman, D. R., Moresi, L. & May, D. (2007). Evolution and diversity of subduction zones controlled by slab width. *Nature* 446(7133), 308–311. <https://doi.org/10.1038/nature05615>
- Scherwath, M., Kopp, H., Flueh, E. R., Henrys, S. A., Sutherland, R., Staggpoole, V. M., Barker, D. H. N., Reyners, M. E., Bassett, D. G., Planert, L. & Dannowski, A. (2010). Fore-arc deformation and underplating at the northern Hikurangi margin, New Zealand. *Journal of Geophysical Research: Solid Earth* 115(6), 1–23. <https://doi.org/10.1029/2009JB006645>
- Scherwath, Martin, Stern, T., Davey, F., Okaya, D., Holbrook, W. S., Davies, R. & Kleffmann, S. (2003). Lithospheric structure across oblique continental collision in New Zealand from wide-angle P wave modeling. *Journal of Geophysical Research*, 108(B12), 2566. <https://doi.org/10.1029/2002JB002286>
- Schindwein, V. & Jokat, W. (1999). Structure and evolution of the continental crust of northern east Greenland from integrated geophysical studies. *Journal of Geophysical Research* 104, 15227–15245. <https://doi.org/10.1029/1999JB900101>
- Schmidt, S., Götze, H., Fichler, C., Ebbing, J. & Alvers, M.R. (2007). 3D Gravity, FTG and magnetic modeling: the new IGMAS+ software. In: EGM 2007 International Workshop. European Association of Geoscientists and Engineers, Capri. pp. 1–4.
- Schmincke, H. U., Park, C. & Harms, E. (1999). Evolution and environmental impacts of the eruption of Laacher See Volcano (Germany) 12,900 a BP. *Quaternary International* 61(1), 61–72. [https://doi.org/10.1016/S1040-6182\(99\)00017-8](https://doi.org/10.1016/S1040-6182(99)00017-8)
- Schwartz, J.J., Klepeis, K.A., Sadorski, J.F., Stowell, H.H., Tulloch, A.J. & Coble, M.A. (2017). The tempo of continental arc construction in the Mesozoic Median Batholith, Fiordland, New Zealand. *Lithosphere* 9(3), 343–365. <https://doi.org/10.1130/L610.1>
- Schwartz, J.J., Stowell, H.H., Klepeis, K.A., Tulloch, A.J., Kylander-Clark, A.R.C., Hacker, B.R. & Coble, M.A. (2016). Thermochronology of extensional orogenic collapse in the deep crust of Zealandia. *Geosphere* 12, 647–677. <https://doi.org/10.1130/GES01232.1>
- Scott, J.M., Brenna, M., Crase, J.A., Waight, T.E., van der Meer, Q.H.A., Cooper, A.F., Palin, J.M., Le Roux, P. & Münker, C. (2016). Peridotitic lithosphere metasomatized by volatile-bearing melts, and its association with intraplate alkaline HIMU-like magmatism. *Journal of Petrology* 57 (10), 2053–2078.
- Seton, M., Whittaker, J.M., Wessel, P., Muller, R.D., DeMets, C., Merkouriev, S., Cande, S., Gaina, C., Eagles, G., Granot, R., Stock, J., Wright, N. & Williams, S.E. (2014). Community infrastructure and repository for marine magnetic identifications. *Geochemistry, Geophysics, Geosystems* 15, 1629–1641. <https://doi.org/10.1002/2013GC005176>
- Sleep, N.H. (1971). Thermal effects of the formation of Atlantic continental margins by continental breakup. *Geophysical Journal International* 24(4), 325–350. <https://doi.org/10.1111/j.1365-246X.1971.tb02182.x>
- Shervais, J. (1982). Ti-V plots and the petrogenesis of modern ophiolitic lavas. *Earth and Planetary Science Letters* 59, 101–118. [https://doi.org/10.1016/0012-821X\(82\)90120-0](https://doi.org/10.1016/0012-821X(82)90120-0)
- Sibuet, J.C., Klingelhoefer, F., Huang, Y.P., Yeh, Y.C., Rangin, C., Lee, C.S. & Hsu, S.K. (2016). Thinned continental crust intruded by volcanics beneath the northern Bay of Bengal. *Marine Petroleum Geology* 77, 471–486. <https://doi.org/10.1016/j.marpetgeo.2016.07.006>
- Siddoway, C.S., Baldwin, S.L., Fitzgerald, P.G., Fanning, C.M. & Luyendyk, B.P. (2004a). Ross sea mylonites and the timing

- of intracontinental extension within the West Antarctic rift system. *Geology* 32, 57–60. <https://doi.org/10.1130/G20005.1>
- Siddoway, C.S., Richard, S.M., Fanning, C.M. & Luyendyk, B.P. (2004b). Origin and emplacement of a middle Cretaceous gneiss dome, Fosdick Mountains, West Antarctica. *GSA Special Papers* 380, 267–294. <https://doi.org/10.1130/0-8137-2380-9.267>
- Siddoway, C.S., Sass, L.C. & Esser, R.P. (2005). Kinematic history of western Marie Byrd Land, West Antarctica: Direct evidence from Cretaceous mafic dykes. *Geological Society London Special Publications* 246, 417–438. <https://doi.org/10.1144/GSL.SP.2005.246.01.17>
- Sigurdsson, H., Devine, J. D., Tchua, F. M., Presser, F. M., Pringle, M. K. W., & Evans, W. C. (1987). Origin of the lethal gas burst from Lake Monoun, Cameroun. *Journal of Volcanology and Geothermal Research* 31(1–2), 1–16. [https://doi.org/10.1016/0377-0273\(87\)90002-3](https://doi.org/10.1016/0377-0273(87)90002-3)
- Smith, A. G. & Pickering, K. T. (2003). Oceanic gateways as a critical factor to initiate icehouse Earth. *Journal of the Geological Society* 160(3), 337–340. <https://doi.org/10.1144/0016-764902-115>
- Smith, W.H.F. & Sandwell, D.T. (1997). Global sea floor topography from satellite altimetry and ship depth soundings. *Science* 277, 1956–1962. <https://doi.org/10.1126/science.277.5334.1956>
- Snow, J.E. & Reisberg, L. (1995). Erratum of “Os isotopic systematics of the MORB mantle: results from altered abyssal peridotites” [Earth Planet. Sci. Lett. 133 (1995) 411–421]. *Earth and Planetary Science Letters* 136, 723–733. [https://doi.org/10.1016/0012-821X\(95\)00165-9](https://doi.org/10.1016/0012-821X(95)00165-9)
- Spiegel, C., Lindow, J., Kamp, P.J.J., Meisel, O., Mukasa, S., Lisker, F., Kuhn, G. & Gohl, K. (2016). Tectonomorphic evolution of Marie Byrd Land – Implications for Cenozoic rifting activity and onset of West Antarctic glaciation. *Global Planetary Change* 145, 98–115. <https://doi.org/10.1016/j.gloplacha.2016.08.013>
- Stock, J.M. & Cande, S.C. (2002). Tectonic history of Antarctic seafloor in the Australia-NewZealand-South Pacific sector: implications for Antarctic continental tectonics. *Royal Society of New Zealand Bulletin* 35, 251–259.
- Steinbrink, L. (2017). Seismic investigation of sediment structures to reconstruct ocean bottom currents east of New Zealand. *M.Sc. thesis*, Department 5 Geosciences, University of Bremen, Bremen, Germany, 120 pp.
- Steinbrink, L., Gohl, K., Riefstahl, F., Davy, B. & Carter, L. (2020). Late Cretaceous to recent ocean-bottom currents in the SW Pacific Gateway, southeastern Chatham Rise, New Zealand. *Palaeogeography, Palaeoclimatology, Palaeoecology* 546, 109633. <https://doi.org/10.1016/j.palaeo.2020.109633>
- Storey, M., Mahoney, J.J. & Saunders, A.D. (1997). Cretaceous basalts in Madagascar and the transition between plume and continental lithosphere mantle sources. In: Mahoney, J.J. & Coffin, M.F. (Eds.), Large Igneous Provinces: Continental, Oceanic, and Planetary Flood Volcanism. In: *AGU Geophysical Monograph*, Vol. 100, pp. 95–122.
- Storey, B.C., Leat, P.T., Weaver, S.D., Pankhurst, R.J., Bradshaw, J.D. & Kelley, S. (1999). Mantle plumes and Antarctica–New Zealand rifting: evidence from mid-Cretaceous mafic dykes. *Journal of the Geological Society London* 156, 659–671. <https://doi.org/10.1144/gsjgs.156.4.0659>
- Strogen, D.P., Seebeck, H., Nicol, A., King, P.R. & Cret, E. (2017). Two-phase Cretaceous – Paleocene rifting in the Taranaki Basin region, New Zealand: Implications for Gondwana break-up. *Journal of the Geological Society London* 174, 929–946. <https://doi.org/10.1144/jgs2016-160>
- Strong, D.T., Turnbull, R.E., Haubrock, S. & Mortimer, N. (2016). Petlab: New Zealand's national rock catalogue and geoanalytical database. *New Zealand Journal of Geology and Geophysics* 59, 475–481. <https://doi.org/10.1080/00288306.2016.1157086>
- Sun, S.-S. & McDonough, W.F. (1989). Chemical and isotopic systematics of oceanic basalts: implications for mantle composition and processes. In: Saunders, A.D. & Norry, M.J. (Eds.), Magmatism in the Ocean Basins. In: *Geological Society London Special Publications*, Vol. 42, pp. 313–345.
- Sutherland, R. (1999). Basement geology and tectonic development of the greater New Zealand region: An interpretation from regional magnetic data. *Tectonophysics* 308, 341–362. [https://doi.org/10.1016/S0040-1951\(99\)00108-0](https://doi.org/10.1016/S0040-1951(99)00108-0)
- Sutherland, R. & Hollis, C. (2001). Cretaceous demise of the Moa Plate and strike-slip motion at the Gondwana margin. *Geology* 29 (3), 279–282. [https://doi.org/10.1130/0091-7613\(2001\)029%3C0279:CDOTMP%3E2.0.CO;2](https://doi.org/10.1130/0091-7613(2001)029%3C0279:CDOTMP%3E2.0.CO;2)
- Sutherland, R., Spasojevic, S. & Gurnis, M. (2010). Mantle upwelling after Gondwana subduction death explains anomalous topography and subsidence histories of eastern New Zealand and West Antarctica. *Geology* 38, 155–158. <https://doi.org/10.1130/G30613.1>
- Taira, A., Mann, P. & Rahardiawan, R. (2004). Incipient subduction of the Ontong Java Plateau along the North Solomon trench. *Tectonophysics* 389(3–4), 247–266. <https://doi.org/10.1016/j.tecto.2004.07.052>

References

- Tappenden, V. (2003). Magmatic Response to the Evolving New Zealand Margin of Gondwana During the Mid-Late Cretaceous. *Ph.D. thesis*, Department of Geological Sciences Christchurch, University of Canterbury, 250 pp.
- Taylor, B., 2006. The single largest oceanic plateau: Ontong Java–Manihiki–Hikurangi. *Earth and Planetary Science Letters* 241 (3–4), 372–380. <https://doi.org/10.1016/j.epsl.2005.11.049>
- Tejada, M.L.G., Suzuki, K., Hanyu, T., Mahoney, J.J., Ishikawa, A., Tatsumi, Y., Chang, Q. & Nakai, S. (2013). Cryptic lower crustal signature in the source of the Ontong Java Plateau revealed by Os and Hf isotopes. *Earth and Planetary Science Letters* 377–378, 84–96. <https://doi.org/10.1016/j.epsl.2013.07.022>
- Tenzer, R., Sirguey, P., Rattenbury, M. & Nicolson, J. (2011). A digital rock density map of New Zealand. *Computers and Geoscience* 37, 1181–1191. <https://doi.org/10.1016/j.cageo.2010.07.010>
- Thébault, E., Finlay, C.C., Beggan, C.D., Alken, P., Aubert, J., Barrois, O., Bertrand, F., Bondar, T., Boness, A., Brocco, L., Canet, E., Chambodut, A., Chulliat, A., Coïsson, P., Civet, F., Du, A., Fournier, A., Fratter, I., Gillet, N., Hamilton, B., Hamoudi, M., Hulot, G., Jager, T., Korte, M., Kuang, W., Lalanne, X., Langlais, B., Léger, J.M., Lesur, V., Lowes, F.J., Macmillan, S., Manda, M., Manoj, C., Maus, S., Olsen, N., Petrov, V., Ridley, V., Rother, M., Sabaka, T.J., Saturnino, D., Schachtschneider, R., Sirol, O., Tangborn, A., Thomson, A., Tøffner-Clausen, L., Vigneron, P., Wardinski, I. & Zvereva, T. (2015). International geomagnetic reference field: The 12th generation international geomagnetic reference field - The 12th generation. *Earth, Planets and Space* 67. <https://doi.org/10.1186/s40623-015-0228-9>
- Thomas, C.L. (2002). Geochemistry of the Pacific Lithosphere Being Subducted Along the Tonga-Kermadec Trench. *M.Sc. thesis*, University of California, San Diego, 63 pp.
- Thorkelson, D.J. (1996). Subduction of diverging plates and the principles of slab window formation. *Tectonophysics* 255, 47–63. [https://doi.org/10.1016/0040-1951\(95\)00106-9](https://doi.org/10.1016/0040-1951(95)00106-9)
- Timm, C., Davy, B., Haase, K., Hoernle, K.A., Graham, I.J., de Ronde, C.E.J., Woodhead, J., Bassett, D., Hauff, F., Mortimer, N., Seebeck, H.C., Wysoczanski, R.J., Caratori-Tontini, F. & Gamble, J.A. (2014). Subduction of the oceanic Hikurangi Plateau and its impact on the Kermadec arc. *Nature Communications* 5, 4923. <https://doi.org/10.1038/ncomms5923>
- Timm, C., Hoernle, K., van den Bogaard, P., Bindeman, I. & Weaver, S. (2009). Geochemical evolution of intraplate volcanism at Banks Peninsula, New Zealand: interaction between asthenospheric and lithospheric melts. *Journal of Petrology* 50, 1–35. <https://doi.org/10.1093/petrology/egp029>
- Timm, C., Hoernle, K., Werner, R., Hauff, F., den Bogaard, P. van, White, J., Mortimer, N. & Garbe-Schönberg, D. (2010). Temporal and geochemical evolution of the Cenozoic intraplate volcanism of Zealandia. *Earth-Science Reviews* 98, 38–64. <https://doi.org/10.1016/j.earscirev.2009.10.002>
- Timm, C., Hoernle, K., Werner, R., Hauff, F., van den Bogaard, P., Michael, P., Coffin, M.F. & Koppers, A. (2011). Age and geochemistry of the oceanic Manihiki Plateau, SW Pacific: New evidence for a plume origin. *Earth and Planetary Science Letters* 304, 135–146. <https://doi.org/10.1016/j.epsl.2011.01.025>
- Timm, C., Leybourne, M. I., Hoernle, K., Wysoczanski, R. J., Hauff, F., Handler, M., Caratori Tontini, F. & de Ronde, C.R.J. (2016). Trench-perpendicular Geochemical Variation Between two Adjacent Kermadec Arc Volcanoes Rumble II East and West: the Role of the Subducted Hikurangi Plateau in Element Recycling in Arc Magmas. *Journal of Petrology* 57(7), 1335–1360. <https://doi.org/10.1093/petrology/egw042>
- Tozer, B., Stern, T. A., Lamb, S. L. & Henrys, S. A. (2017). Crust and upper-mantle structure of Wanganui Basin and southern Hikurangi margin, North Island, New Zealand as revealed by active source seismic data. *Geophysical Journal International* 211(2), 718–740. <https://doi.org/10.1093/gji/ggx303>
- Tulloch, A. J. & Kimbrough, D. L. (2003). Paired plutonic belts in convergent margins and the development of high Sr/Y magmatism: Peninsular Ranges batholith of Baja-California and Median batholith of New Zealand. *Special Paper of the Geological Society of America* 374(303), 275–295. <https://doi.org/10.1130/0-8137-2374-4.275>
- Tulloch, A.J., Mortimer, N., Ireland, T.R., Waight, T.E., Maas, R., Palin, M., Sahoo, T., Seebeck, H., Sagar, M., Barrier, A. & Turnbull, R. (2019). Reconnaissance basement geology and tectonics of South Zealandia. *Tectonics* 38, 516–551. <https://doi.org/10.1029/2018TC005116>
- Tulloch, A.J., Ramezani, J., Kimbrough, D.L., Faure, K. & Allibone, A.H. (2009a). U-Pb geochronology of mid-Paleozoic plutonism in western New Zealand: Implications for S-type granite generation and growth of the east Gondwana margin. *Geological Society of America Bulletin* 121, 1236–1261. <https://doi.org/10.1130/B26272.1>
- Tulloch, A.J., Ramezani, J., Mortimer, N., Mortensen, J., van den Bogaard, P. & Maas, R. (2009b). Cretaceous felsic volcanism in New Zealand and Lord Howe Rise (Zealandia) as a precursor to final Gondwana break-up. *Geological Society London Special Publications* 321, 89–118. <https://doi.org/10.1144/SP321.5>

- Van Avendonk, H.J.A., Holbrook, W.S., Okaya, D., Austin, J.K., Davey, F. & Stern, T. (2004). Continental crust under compression: A seismic refraction study of South Island Geophysical Transect I, South Island, New Zealand. *Journal of Geophysical Research: Solid Earth* 109, 1–17. <https://doi.org/10.1029/2003JB002790>
- van der Meer, Q.H.A., Storey, M., Scott, J.M., Waight, T.E., Van den Meer, Q.H.A., Storey, M., Scott, J.M., Tod, E., van der Meer, Q.H.A., Storey, M., Scott, J.M. & Waight, T.E. (2016). Abrupt spatial and geochemical changes in lamprophyre magmatism related to Gondwana fragmentation prior, during and after opening of the Tasman Sea. *Gondwana Research* 36, 129–143. <https://doi.org/10.1016/j.gr.2016.04.004>
- van der Meer, Q.H.A., Waight, T.E., Tulloch, A.J., Whitehouse, M.J. & Andersen, T. (2018). Magmatic evolution during the cretaceous transition from subduction to continental break-up of the Eastern Gondwana margin (New Zealand) documented by in-situ zircon O-Hf isotopes and bulk-rock Sr-Nd isotopes. *Journal of Petrology* 59, 849–880. <https://doi.org/10.1093/PETROLOGY/EGY047>
- van der Meer, Q.H.A., Waight, T.E., Whitehouse, M.J. & Andersen, T. (2017). Age and petrogenetic constraints on the lower glassy ignimbrite of the Mount Somers Volcanic Group, New Zealand. *New Zealand Journal of Geology and Geophysics* 60, 209–219. <https://doi.org/10.1080/00288306.2017.1307232>
- van Hunen, J. & Allen, M.B. (2011). Continental collision and slab break-off : A comparison of 3-D numerical models with observations. *Earth and Planetary Science Letters* 302, 27–37. <https://doi.org/10.1016/j.epsl.2010.11.035>
- van Hunen, J., van den Berg, A.P. & Vlaar, N.J. (2002). On the role of subducting oceanic plateaus in the development of shallow flat subduction. *Tectonophysics* 352, 317–333. [https://doi.org/10.1016/S0040-1951\(02\)00263-9](https://doi.org/10.1016/S0040-1951(02)00263-9)
- Vry, J.K., Baker, J., Maas, R., Little, T.A., Grapes, R. & Dixon, M. (2004). Zoned (Cretaceous and Cenozoic) garnet and the timing of high grade metamorphism, Southern Alps, New Zealand. *Journal of Metamorphic Geology* 22, 137–157. <https://doi.org/10.1111/j.1525-1314.2004.00504.x>
- Wallace, L.M., Ellis, S. & Mann, P. (2009). Collisional model for rapid fore-arc block rotations, arc curvature, and episodic back-arc rifting in subduction settings. *Geochemistry, Geophysics, Geosystems* 10(5), Q05001. <https://doi.org/10.1029/2008GC002220>
- Weatherall, P., Marks, K.M., Jakobsson, M., Schmitt, T., Tani, S., Arndt, J.E., Rovere, M., Chayes, D., Ferrini, V. & Wigley, R. (2015). A new digital bathymetric model of the world's oceans. *Earth and Space Science* 2, 331–345. <https://doi.org/10.1002/2015EA000107>
- Weaver, S.D. & Smith, I.E.M. (1989). New Zealand intraplate volcanism. In: Johnson, R.W. & Knutson, J., Taylor, S.R. (Eds.), *Intraplate Volcanism in Eastern Australia and New Zealand*. Cambridge University Press, pp. 157–188.
- Weaver, S.D., Storey, B.C., Pankhurst, R.J., Mukasa, S.B., DiVenere, V.J. & Bradshaw, J.D. (1994). Antarctica-New Zealand rifting and Marie Byrd Land lithospheric magmatism linked to ridge subduction and mantle plume activity. *Geology* 22, 811–814. [https://doi.org/10.1130/0091-7613\(1994\)022%3C0811:ANZRAM%3E2.3.CO;2](https://doi.org/10.1130/0091-7613(1994)022%3C0811:ANZRAM%3E2.3.CO;2)
- Weiss, Y., Class, C., Goldstein, S.L. & Hanyu, T. (2017). Key new pieces of the HIMU puzzle from olivines and diamond inclusions. *Nature* 537, 666–670. <https://doi.org/10.1038/nature19113>
- Wessel, P. & Smith, W.H.F. (1998). New, improved version of generic mapping tools released. *Eos, Transactions, American Geophysical Union* 79, 579–579. <https://doi.org/10.1029/98EO00426>
- White, R. & McKenzie, D. (1989). Magmatism at rift zones: The generation of volcanic continental margins and flood basalts. *Journal of Geophysical Research* 94(B6), 7685. <https://doi.org/10.1029/JB094iB06p07685>
- White, R.S., McKenzie, D. & O’Nions, R.K. (1992). Oceanic Crustal Thickness From Seismic Measurements and Rare Earth Element Inversions. *Journal of Geophysical Research* 97, 19683–19715. <https://doi.org/10.1029/92JB01749>
- White, R. S. & Smith, L. K. (2009). Crustal structure of the Hatton and the conjugate east Greenland rifted volcanic continental margins, NE Atlantic. *Journal of Geophysical Research* 114(B2), B02305. <https://doi.org/10.1029/2008JB005856>
- Whitmarsh, R. B., Manatschal, G. & Minshull, T. a. (2001). Evolution of magma-poor continental margins from rifting to seafloor spreading. *Nature* 413(6852), 150–154. <https://doi.org/10.1038/35093085>
- Whittaker, J.M., Williams, S.E. & Müller, R.D. (2013). Revised tectonic evolution of the Eastern Indian Ocean. *Geochemistry, Geophysics, Geosystems* 14, 1891–1909. <https://doi.org/10.1002/ggge.20120>
- Wilson, C. J. N. (2001). The 26.5 ka Oruanui eruption, New Zealand: An introduction and overview. *Journal of Volcanology and Geothermal Research*, 112(1–4), 133–174. [https://doi.org/10.1016/S0377-0273\(01\)00239-6](https://doi.org/10.1016/S0377-0273(01)00239-6)
- Wilson, R. W., Houseman, G. A., Buitert, S. J. H., McCaffrey, K. J. W. & Doré, A. G. (2019). Fifty years of the Wilson cycle concept in plate tectonics: An overview. *Geological Society Special Publication* 470(1), 1–17. <https://doi.org/10.1144/SP470-2019-58>
- Wobbe, F., Gohl, K., Chambord, A. & Sutherland, R. (2012). Structure and breakup history of the rifted margin of West

References

- Antarctica in relation to Cretaceous separation from Zealandia and Bellingshausen plate motion. *Geochemistry, Geophysics, Geosystems* 13, 1–19. <https://doi.org/10.1029/2011GC003742>
- Wood, R. & Davy, B. (1994). The Hikurangi Plateau. *Marine Geology* 118, 153–173. [https://doi.org/10.1016/0025-3227\(94\)90118-X](https://doi.org/10.1016/0025-3227(94)90118-X)
- Wood, R.A. & Anderson, H.J. (1989). Basement structure at the Chatham Islands. *Journal of the Royal Society of New Zealand* 19, 269–282. <https://doi.org/10.1080/03036758.1989.10427182>
- Wood, R.A., Andrews, P.B. & Herzer, R.H. (1989). Cretaceous and Cenozoic Geology of the Chatham Rise Region, South Island, New Zealand. *New Zealand Geological Survey basin studies* 3, New Zealand Geological Survey, Lower Hutt, New Zealand, 75pp.
- Wortel, M.J.R. & Spakman, W. (2000). Subduction and slab detachment in the Mediterranean-Carpathian region. *Science* 290(5498), 1910–1917. <https://doi.org/10.1126/science.290.5498.1910>
- Worthington, T., Hekinian, R., Stoffers, P., Kuhn, T. & Hauff, F. (2006). Osbourne Trough: structure, geochemistry and implications of a mid-Cretaceous paleosubducting ridge in the South Pacific. *Earth and Planetary Science Letters* 245, 685–701. <https://doi.org/10.1016/j.epsl.2006.03.018>
- Wright, N.M., Seton, M., Williams, S.E. & Müller, R.D. (2016). The Late Cretaceous to recent tectonic history of the Pacific Ocean basin. *Earth-Science Reviews* 154, 138–173. <https://doi.org/10.1016/j.earscirev.2015.11.015>
- Zelt, B.C. (2004). ZP—Software for Plotting & Picking Seismic Refraction Data in SEG Y Format.
- Zelt, C.A. & Smith, R.B. (1992). Seismic travelt ime inversion for 2-D crustal velocity structure. *Geophysical Journal International* 108, 16–34. <https://doi.org/10.1111/j.1365-246X.1992.tb00836.x>
- Zhang, G. & Li, C. (2016). Interactions of the greater Ontong Java mantle plume component with the Osbourne Trough. *Scientific Reports* 6, 37561. <https://doi.org/10.1038/srep37561>
- Zhang, G., Smith-Duque, C., Tang, S., Li, H., Zirikian, C., D'Hondt, S., Inagaki, F. & IODP Expedition 329 scientists (2012). Geochemistry of basalts from IODP site U1365: Implications for magmatism and mantle source signatures of the mid-Cretaceous Osbourne Trough. *Lithos* 144–145, 73–87. <https://doi.org/10.1016/j.lithos.2012.04.014>
- Zimmerman, A., Stein, H.J., Morgan, J.W., Markey, R.J. & Watanabe, Y. (2014). Re–Os geochronology of the El Salvador porphyry Cu–Mo deposit, Chile: tracking analytical improvements in accuracy and precision over the past decade. *Geochimica et Cosmochimica Acta* 131, 13–32. <https://doi.org/10.1016/j.gca.2014.01.016>
- Zindler, A. & Hart, S.R. (1986). Chemical geodynamics. *Annual Reviews of Earth and Planetary Science* 14, 493–571. <https://doi.org/10.1146/annurev.ea.14.050186.002425>
- Zundel, M., Spiegel, C., Mehling, A., Lisker, F., Hillenbrand, C.-D., Monien, P. & Klügel, A. (2019). Thurston Island (West Antarctica) between Gondwana subduction and continental separation: A multi-stage evolution revealed by apatite thermochronology. *Tectonics* 38, 878–897, <https://doi.org/10.1029/2018TC005150>
- Zwaan, F., Schreurs, G., Naliboff, J. & Buitter, S.J.H. (2016). Insights into the effects of oblique extension on continental rift interaction from 3D analogue and numerical models. *Tectonophysics* 693, 239–260. <https://doi.org/10.1016/j.tecto.2016.02.036>

Danksagung

Eine Doktorarbeit bedeutet viel Arbeit. Auch wenn am Anfang dieser Dissertation mein Name steht, hätte ich dies nicht ohne tatkräftige Hilfe von vielen anderen Menschen bewältigen können.

Zuallererst möchte ich meinem Betreuer und Doktorvater Karsten Gohl herzlichst danken. Vielen Dank, dass ich mit den vielen Fragen zu dir kommen konnte und du immer Geduld mit mir hattest. Auch dafür, dass du mir immer den Rücken gestärkt hast, gerade wenn meine Interpretationsansätze nicht jedem zugesagt haben.

An dieser Stelle möchte ich mich auch bei Sebastian Krastel bedanken, der sich bereitwillig als Zweitgutachter für diese Arbeit zur Verfügung gestellt hat.

Der nächste Dank geht an Katharina Hochmuth. Vielen Dank, dass ich mich immer auf deine Hilfe beim Modellieren und deine Unterstützung, auch in schwierigsten Zeiten, verlassen konnte. Rachel Barrett noch einen zusätzlichen Dank für die vielen hilfreichen Kommentare und Korrekturen ausrichten. Ein großer Dank für die Unterstützung beim Modellieren geht aber natürlich auch an Tabea Altenbernd, Tanja Fromm and Christian Mueller. Hier geht auch noch ein Dank an Estella Weigelt, die mich immer wieder mit ihrer Expertise in der Reflexionsseismik unterstützt hat.

Ich möchte mich auch herzlich bei Wilfried Jokat bedanken. Es war immer schönes Gefühl, wenn man gedacht hat, dass ein Modell fertiggestellt ist. Zu diesem Zeitpunkt bist du dann meistens durch die Tür gekommen und hast überprüft, ob das Modell auch genug mit Daten belegt ist. Auch wenn das Gefühl, dass es sich um ein fertiges Modell handelt, dann schnell verflogen war, haben Wilfrieds Anmerkungen die Modelle maßgeblich bereichert.

Ich möchte mich herzlich bei Bryan Davy für seinen Beitrag mit den Potentialfelddaten bedanken, aber auch für die herzliche neuseeländische Willkommenskultur, die ich während meines Auslandsaufenthaltes in Neuseeland kennengelernt habe. An dieser Stelle möchte ich auch Nick Mortimer, der mich in dieser Zeit nach Dunedin eingeladen hat und mir im Feld viel Wissen und Erkenntnisse über die Geologie von Neuseeland und Zealandia vermittelt hat.

Ich möchte der POLMAR Graduiertenschule des Alfred-Wegener-Instituts, die mich finanziell bei dem Aufenthalt in Neuseeland, bei der Teilnahme eines Kurses in Oslo und bei der SEISMIX2018-Konferenz finanziell unterstützt hat. Dieser Dank bezieht sich aber viel mehr auch auf die tolle Unterstützung, die insbesondere Claudia Hanfland und Claudia Sprengel den Doktoranden während ihrer Zeit am Alfred-Wegener-Institut geben.

Ferner möchte ich noch einen Dank Cornelia Spiegel, Frank Lisker und Max Zundel, sowie dem Rest der Arbeitsgruppe "Geodynamik der Polargebiete" der Universität Bremen, für die vielen produktiven Diskussionen zur Entwicklung des Ostgondwanarandes und der Westantarktis danken. Ein Dank geht auch noch an Simon Dreutter, Laura Jensen and Jan-Erik Arndt für die Unterstützung mit der Bathymetrie und die Beantwortung von den vielen ArcGIS- und Fledermaus-Fragen.

Vielen Dank an die Offiziere und Mannschaft der FS Sonne der SO246 Expedition, die Gerätschaften auch bei widrigsten Bedingungen wieder an Bord zu holen. Ich möchte einen großen Dank an das Refraktionsseismik-Team (B. Kimmel, H. Eisermann, F. Petersen, M. Moser, T. N. Gades, L. Joeressen, R. Steinmann, K. Hagemann) und natürlich auch dem Reflexionsseismik-Team der SO246 Expedition (K. Hochmuth, R. Dziadek, E. Labahn, A. Brotzer, N. Stoll, T. Eggers, R. Barrett) einen großen Dank ausrichten. Ohne die Mitwirkung von euch allen, hätten wir nicht so wertvolle Daten eingefahren.

Bei Rachel Barrett und Felix Gross möchte ich mich auch noch kurz für die großartige Zeit in Kiel bedanken.

Danksagung

Bei Marielle Roucheray möchte ich mich vom ganzen Herzen für die Unterstützung und Bestätigung während der letzten 2 Jahre bedanken.

Zuletzt möchte ich meinen Eltern Horst († 25. August 2014) und Helga († 21. November 2019), sowie meiner Schwester Mirja danken, die mich nicht nur während der Doktorandenzeit, sondern über all die Jahre, wesentlich unterstützt haben.

Appendix

A1. AWI-20160100

Tab. A1: Table with information about the configurations and data quality (1 = excellent, 2 = medium, 3 = low, 4 = no data, - = channel not used) of the OBS / OBH stations along profile AWI-20160100. See Gohl & Werner (2016) for more information.

Station	Water Depth [m]	Type	Recorder Type	Sensors	Quality			
					C 1	C 2	C 3	C 4
					H	X	Y	Z
st101	5037	OBS (GEOMAR)	MBS	H,X,Y,Z	4	4	4	4
st102	4951	OBH (GEOMAR)	MBS	H	1	-	-	-
st103	4728	OBS (GEOMAR)	MBS	H,X,Y,Z	4	4	4	4
st104	4637	OBS (AWI)	MCS	H	1	-	-	-
st105	4813	OBS (GEOMAR)	MBS	H,X,Y,Z	1	2-3	3	2-3
st106	4878	OBH (GEOMAR)	MBS	H	1	-	-	-
st107	4840	OBS (GEOMAR)	MBS	H,X,Y,Z	4	4	4	4
st108	4761	OBS (AWI)	6D6	H,X,Y,Z	1	1-2	2	1-2
st109	4598	OBS (GEOMAR)	MBS	H,X,Y,Z	1	3	3	3
st110	4409	OBH (GEOMAR)	MBS	H	1	-	-	-
st111	4246	OBS (GEOMAR)	MBS	H,X,Y,Z	1-2	3	3	3
st112	4099	OBS (AWI)	MCS	H	1	-	-	-
st113	4271	OBS (GEOMAR)	MBS	H,X,Y,Z	1	2	2	2
st114	4391	OBS (AWI)	MCS	H	2	-	-	-
st115	4183	OBS (GEOMAR)	MBS	H,X,Y,Z	1	2	2	2
st116	3844	OBH (GEOMAR)	MBS	H	1	-	-	-
st117	4056	OBS (GEOMAR)	MBS	H,X,Y,Z	1-2	2-3	2-3	2-3
st118	4210	OBS (AWI)	MCS	H	2-3	-	-	-
st119	4054	OBS (GEOMAR)	MBS	H,X,Y,Z	2	3	3	3
st120	4057	OBS (AWI)	MCS	H,X,Y,Z	1	2-3	2	2-3
st121	2765	OBH (GEOMAR)	MBS	H	1-2	-	-	-
st122	2340	OBS (GEOMAR)	MBS	H,X,Y,Z	4	4	4	4
st123	1715	OBS (AWI)	MCS	H	1	-	-	-
st124	1336	OBS (GEOMAR)	MBS	H,X,Y,Z	1-2	2-3	2-3	2-3
st125	1044	OBS (AWI)	MCS	H	1-2	-	-	-
st126	525	OBS (GEOMAR)	MBS	H,X,Y,Z	1	2-3	2-3	2-3
st127	397	OBS (KUM NAMMU)	6D6	H,X,Y,Z	1	2	2-3	2
st128	412	OBS (GEOMAR)	MBS	H,X,Y,Z	2-3	3	3	3
st129	405	OBH (GEOMAR)	MBS	H	2-3	-	-	-
st130	391	OBS (GEOMAR)	MBS	H,X,Y,Z	1	2	2-3	2-3
st131	315	OBS (AWI)	MCS	H,X,Y,Z	2	2-3	2-3	2-3
st132	144	OBS (GEOMAR)	MBS	H,X,Y,Z	2	3	3	3
st133	327	OBH (GEOMAR)	MBS	H	2-3	-	-	-
st134	356	OBS (GEOMAR)	MBS	H,X,Y,Z	2	2-3	2-3	3
st135	235	OBS (AWI)	MCS	H	3	-	-	-
st136	443	OBS (GEOMAR)	MBS	H,X,Y,Z	2	3	3	3
st137	461	OBS (AWI)	MCS	H	3	-	-	-
st138	536	OBS (GEOMAR)	MBS	H,X,Y,Z	2	3	3	3
st139	598	OBH (GEOMAR)	MBS	H	2-3	-	-	-
st140	660	OBS (GEOMAR)	MBS	H,X,Y,Z	2-3	3	2-3	3

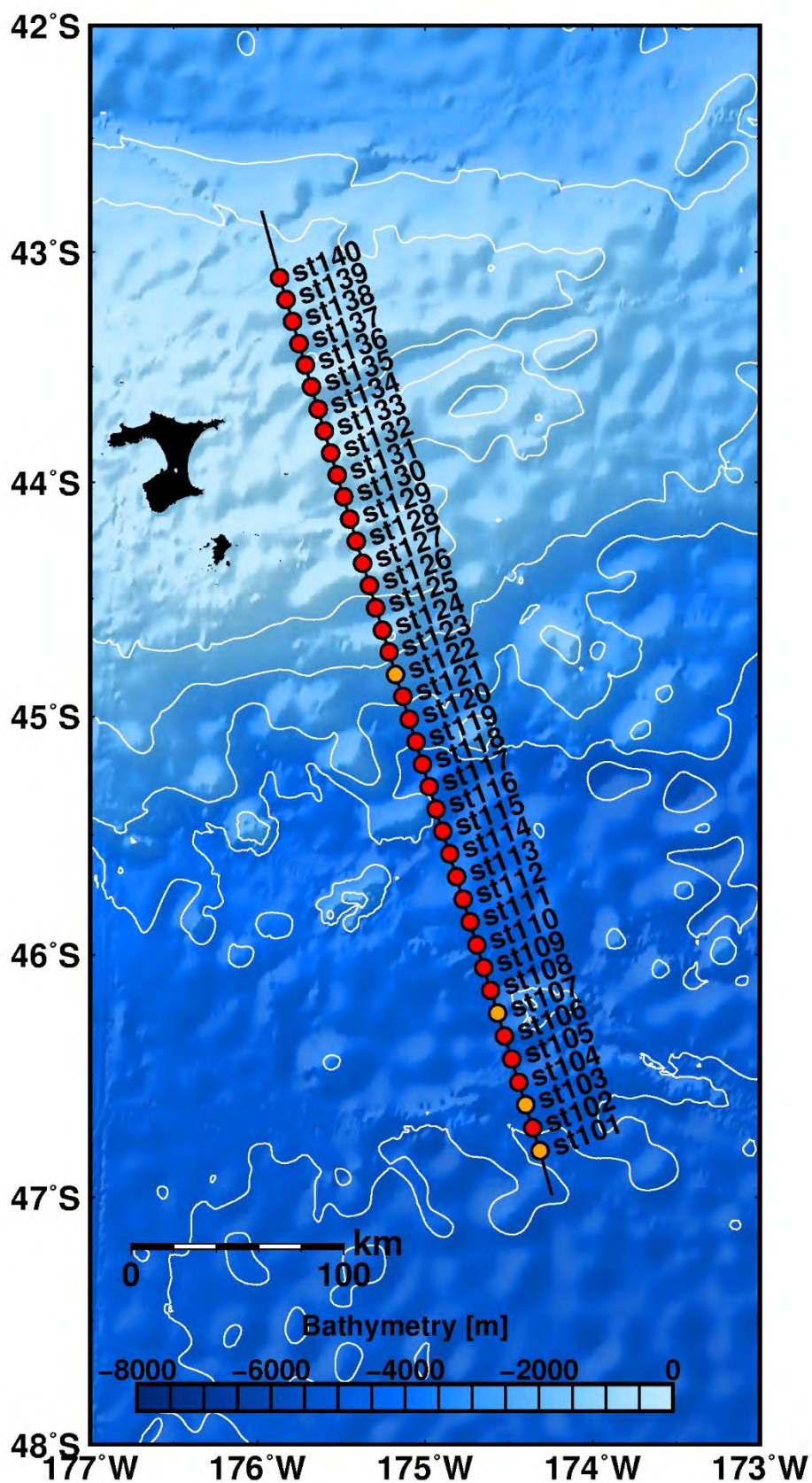


Fig. A1: Bathymetric map of the southern Chatham Rise margin and deployed OBS / OBH stations (red circles) along profile AWI-20160100. OBS / OBH without data are marked as orange circles.

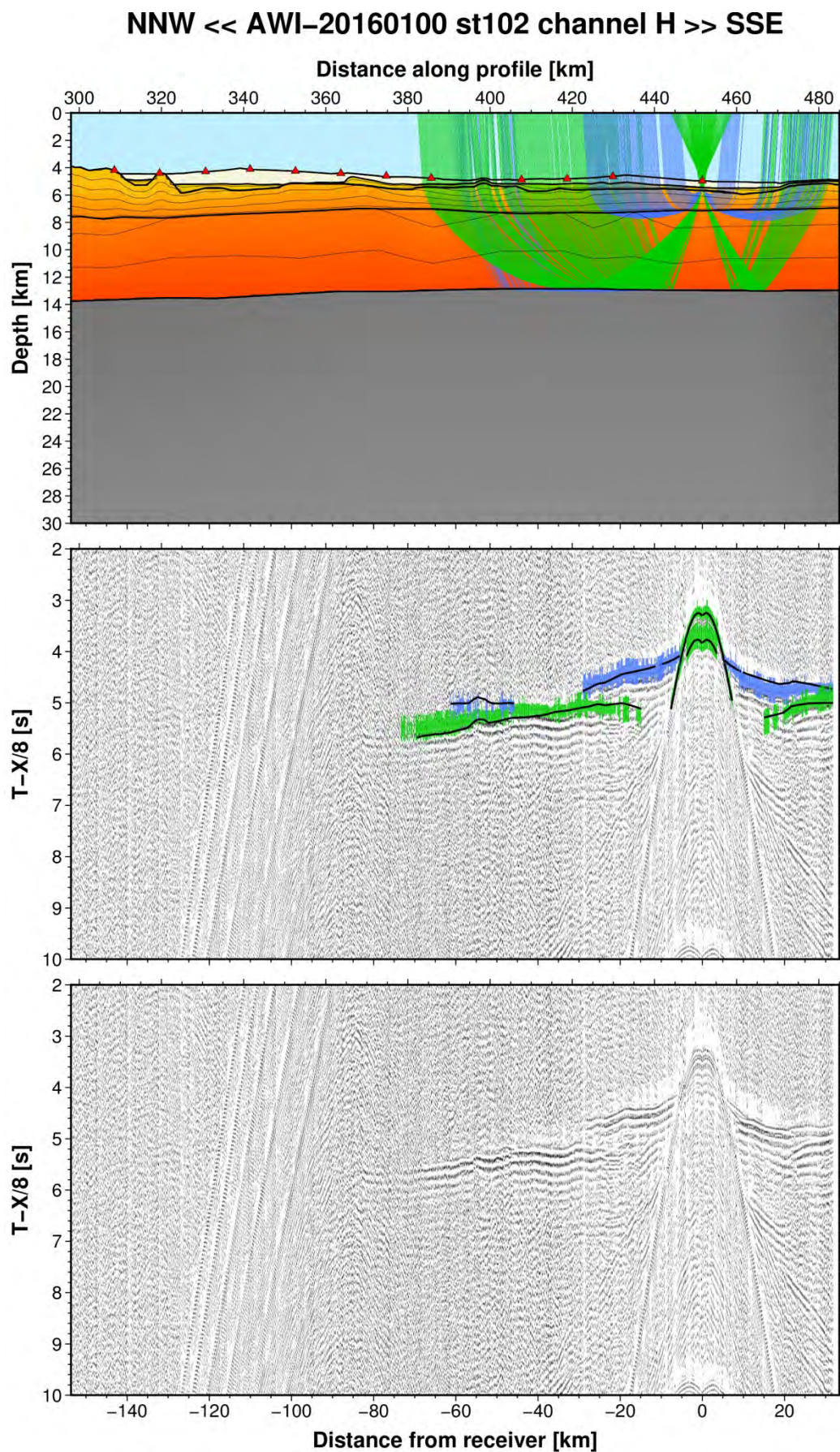


Fig. A2: Ray tracing results for station st102 along profile AWI-20160100. Lower panel: Seismic record; Middle panel: Picked and modelled arrival times; Upper panel: Section of the resulting P-wave velocity model; Green colours = reflections, blue colours = refractions.

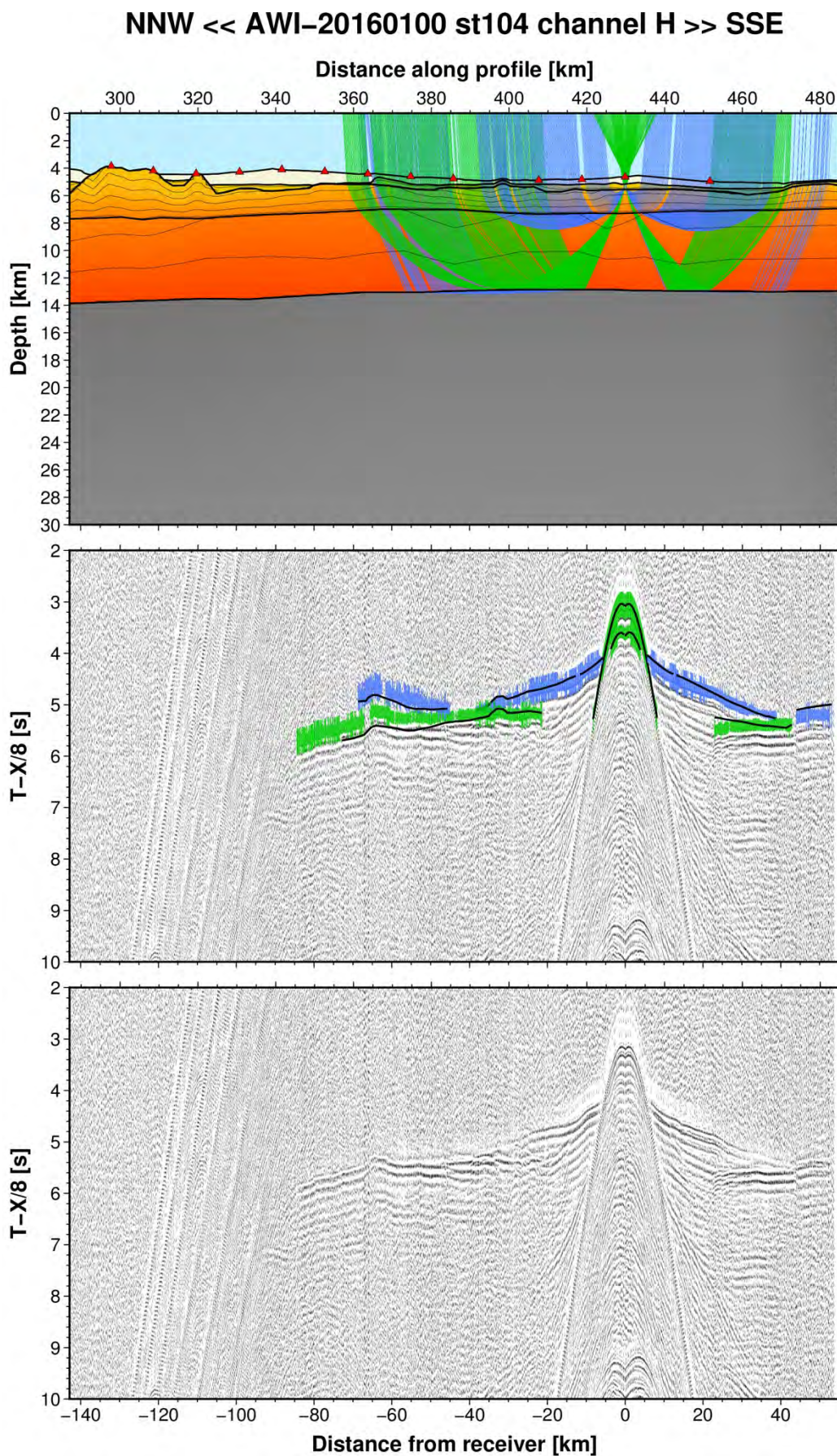


Fig. A3: Ray tracing results for station st104 along profile AWI-20160100. Lower panel: Seismic record; Middle panel: Picked and modelled arrival times; Upper panel: Section of the resulting P-wave velocity model; Green colours = reflections, blue colours = refractions.

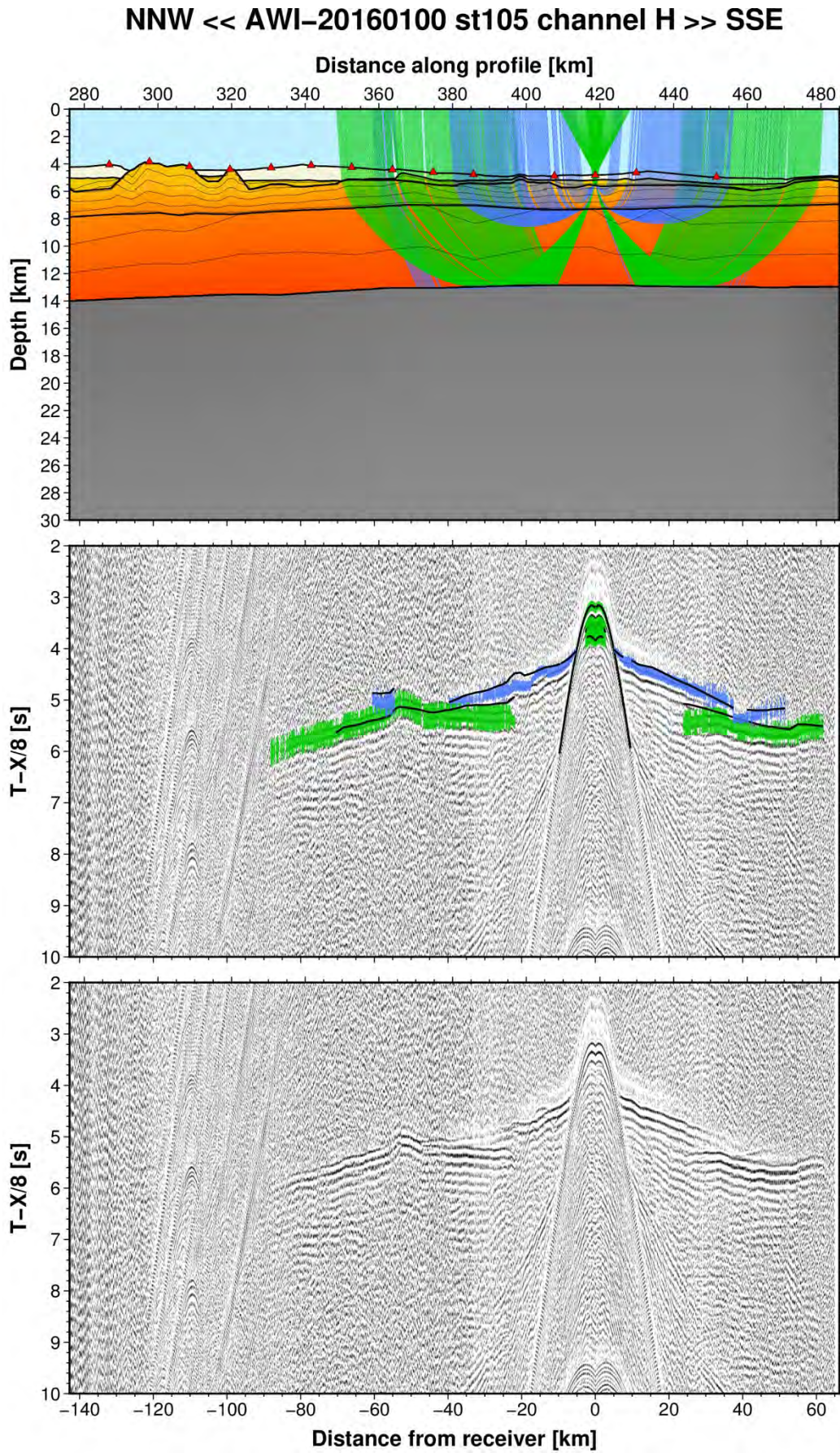


Fig. A4: Ray tracing results for station st105 along profile AWI-20160100. Lower panel: Seismic record; Middle panel: Picked and modelled arrival times; Upper panel: Section of the resulting P-wave velocity model; Green colours = reflections, blue colours = refractions.

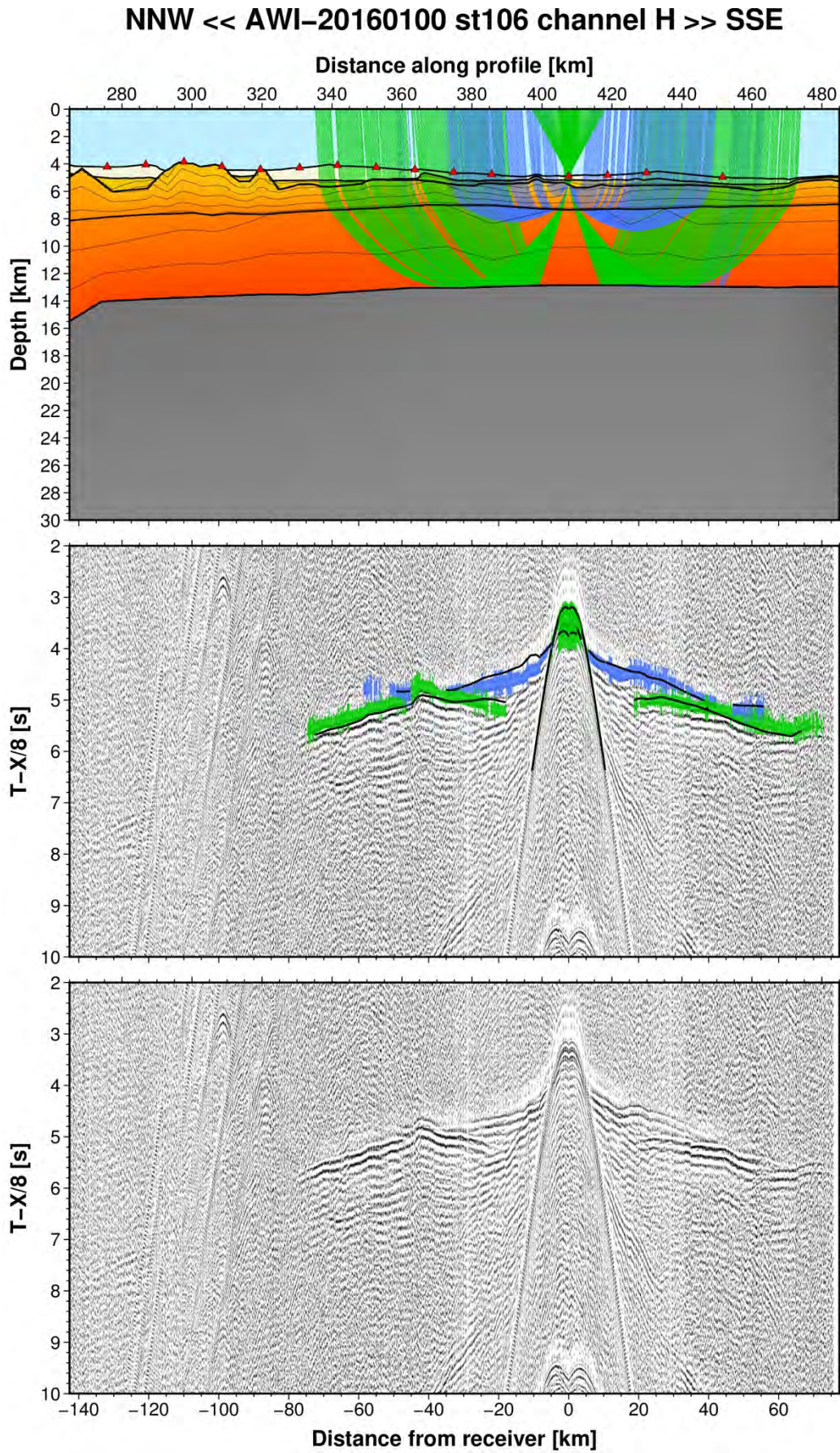


Fig. A5: Ray tracing results for station st106 along profile AWI-20160100. Lower panel: Seismic record; Middle panel: Picked and modelled arrival times; Upper panel: Section of the resulting P-wave velocity model; Green colours = reflections, blue colours = refractions.

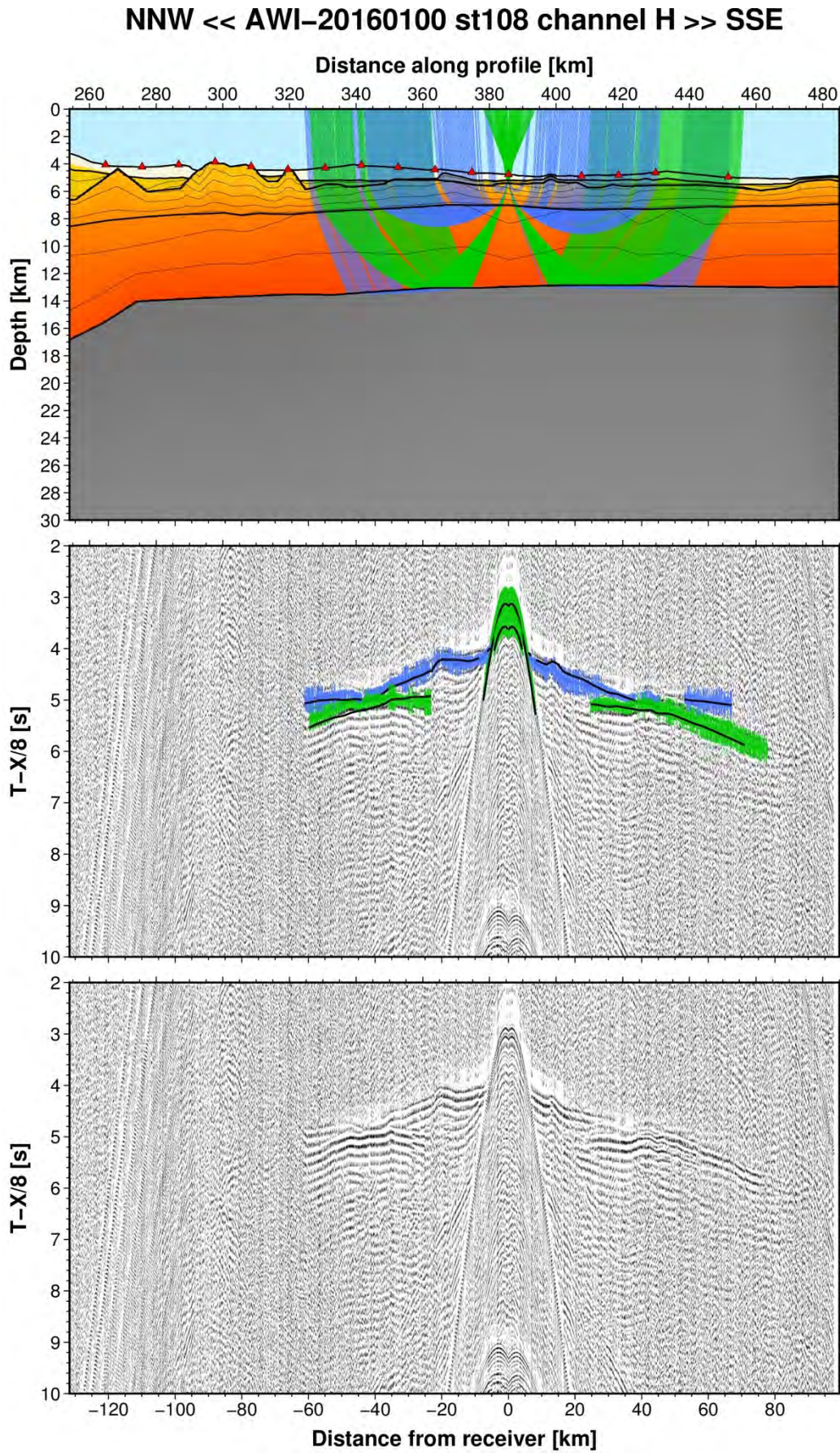


Fig. A6: Ray tracing results for station st108 along profile AWI-20160100. Lower panel: Seismic record; Middle panel: Picked and modelled arrival times; Upper panel: Section of the resulting P-wave velocity model; Green colours = reflections, blue colours = refractions.

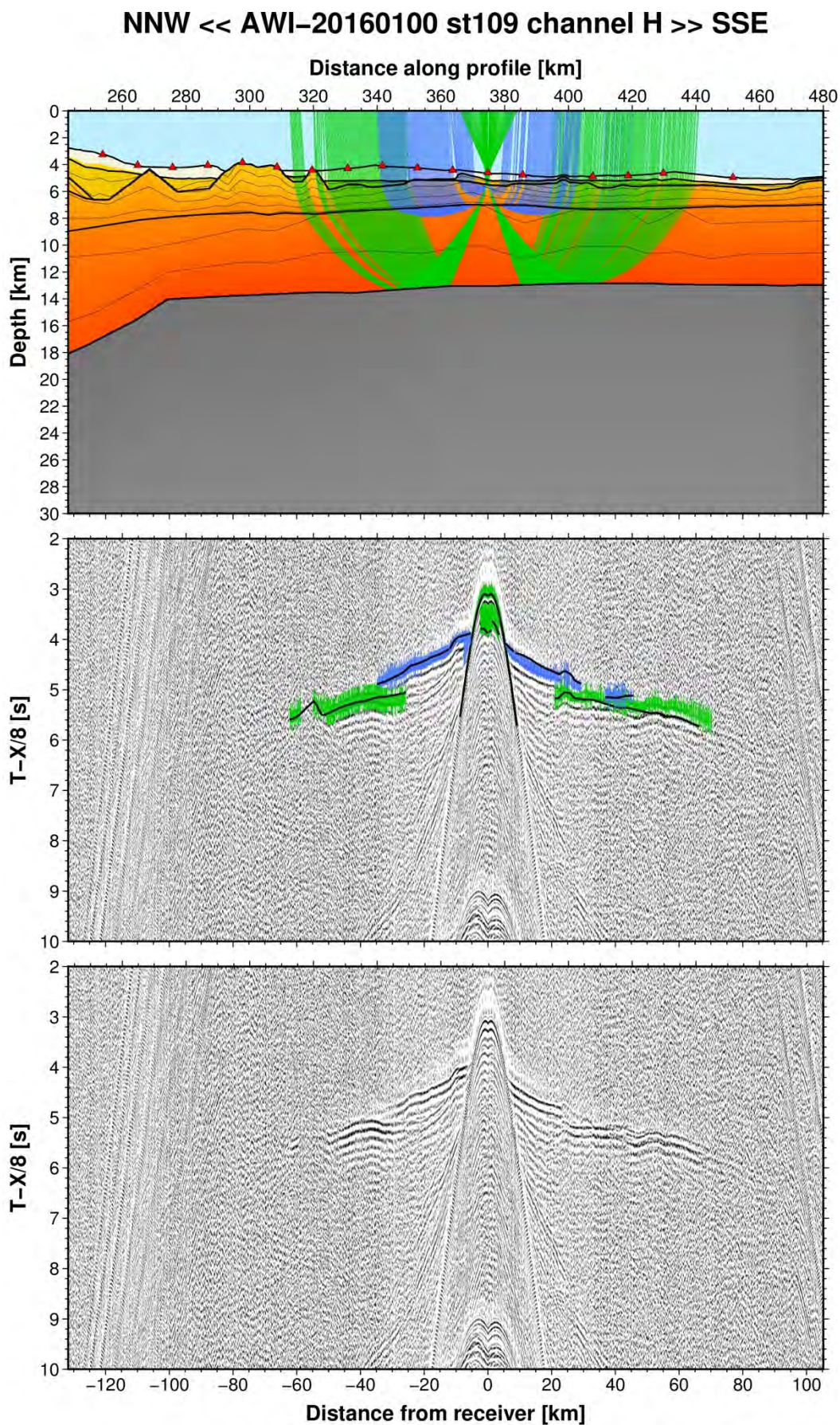


Fig. A7: Ray tracing results for station st109 along profile AWI-20160100. Lower panel: Seismic record; Middle panel: Picked and modelled arrival times; Upper panel: Section of the resulting P-wave velocity model; Green colours = reflections, blue colours = refractions.

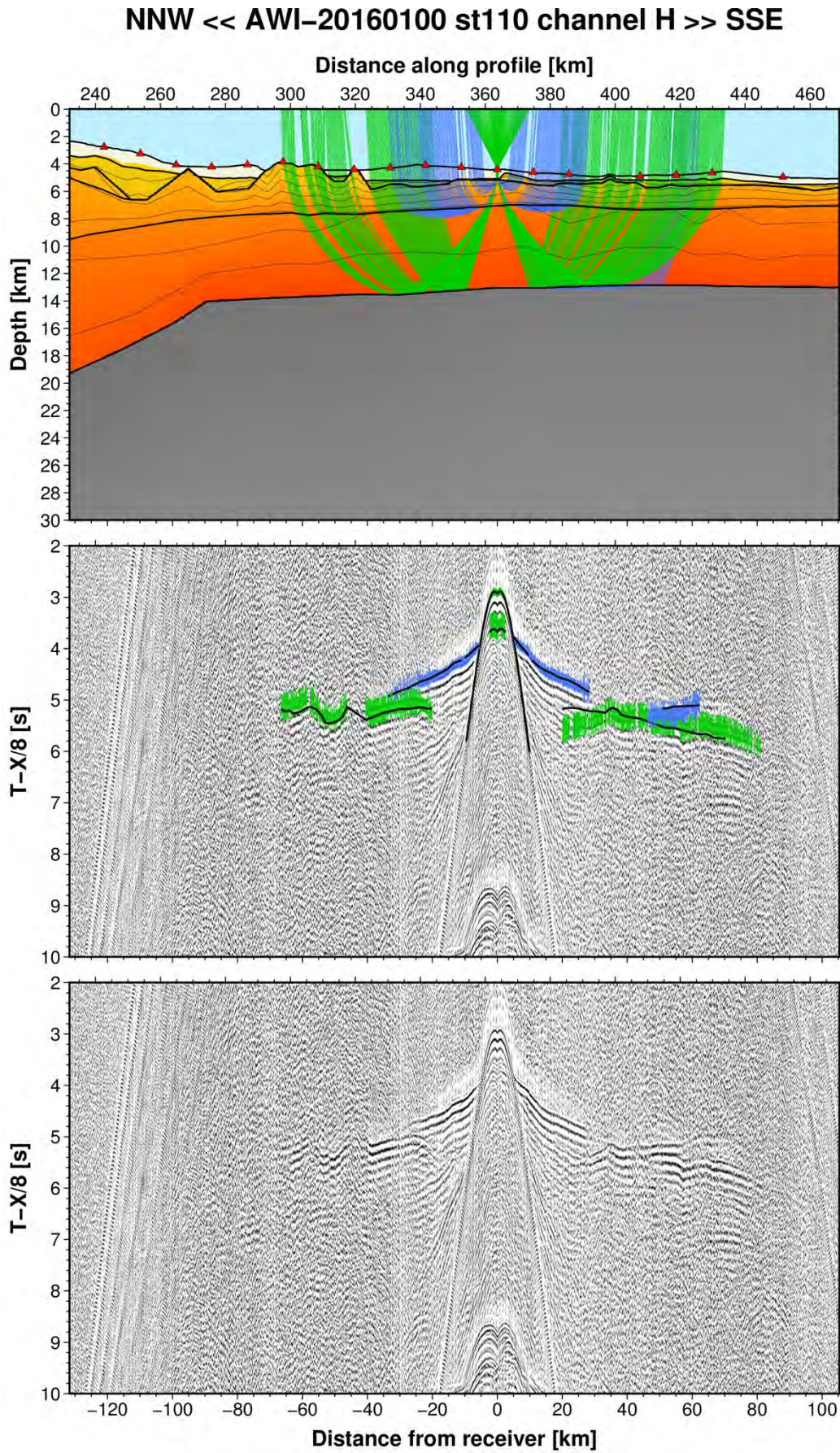


Fig. A8: Ray tracing results for station st110 along profile AWI-20160100. Lower panel: Seismic record; Middle panel: Picked and modelled arrival times; Upper panel: Section of the resulting P-wave velocity model; Green colours = reflections, blue colours = refractions.

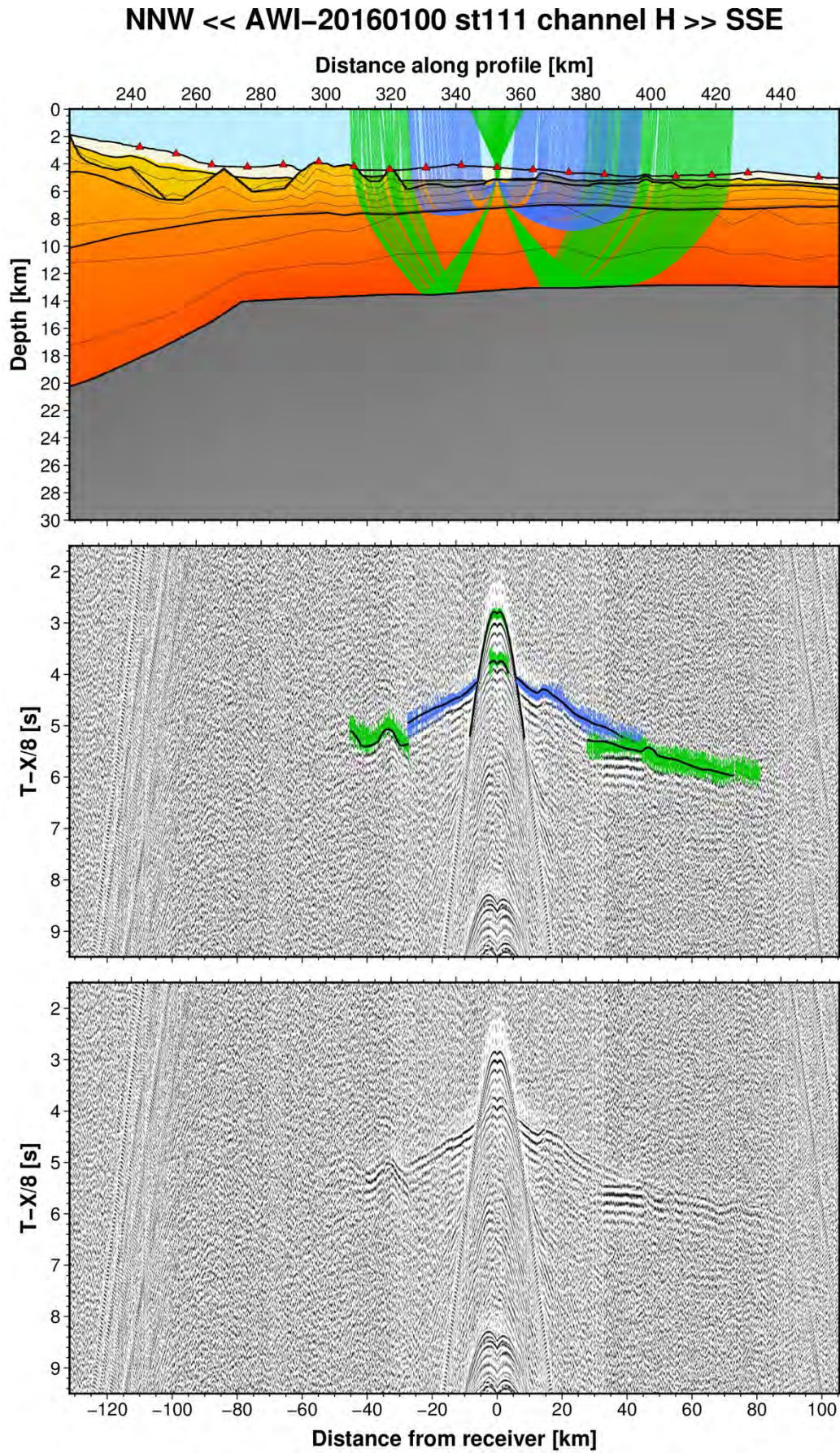


Fig. A9: Ray tracing results for station st111 along profile AWI-20160100. Lower panel: Seismic record; Middle panel: Picked and modelled arrival times; Upper panel: Section of the resulting P-wave velocity model; Green colours = reflections, blue colours = refractions.

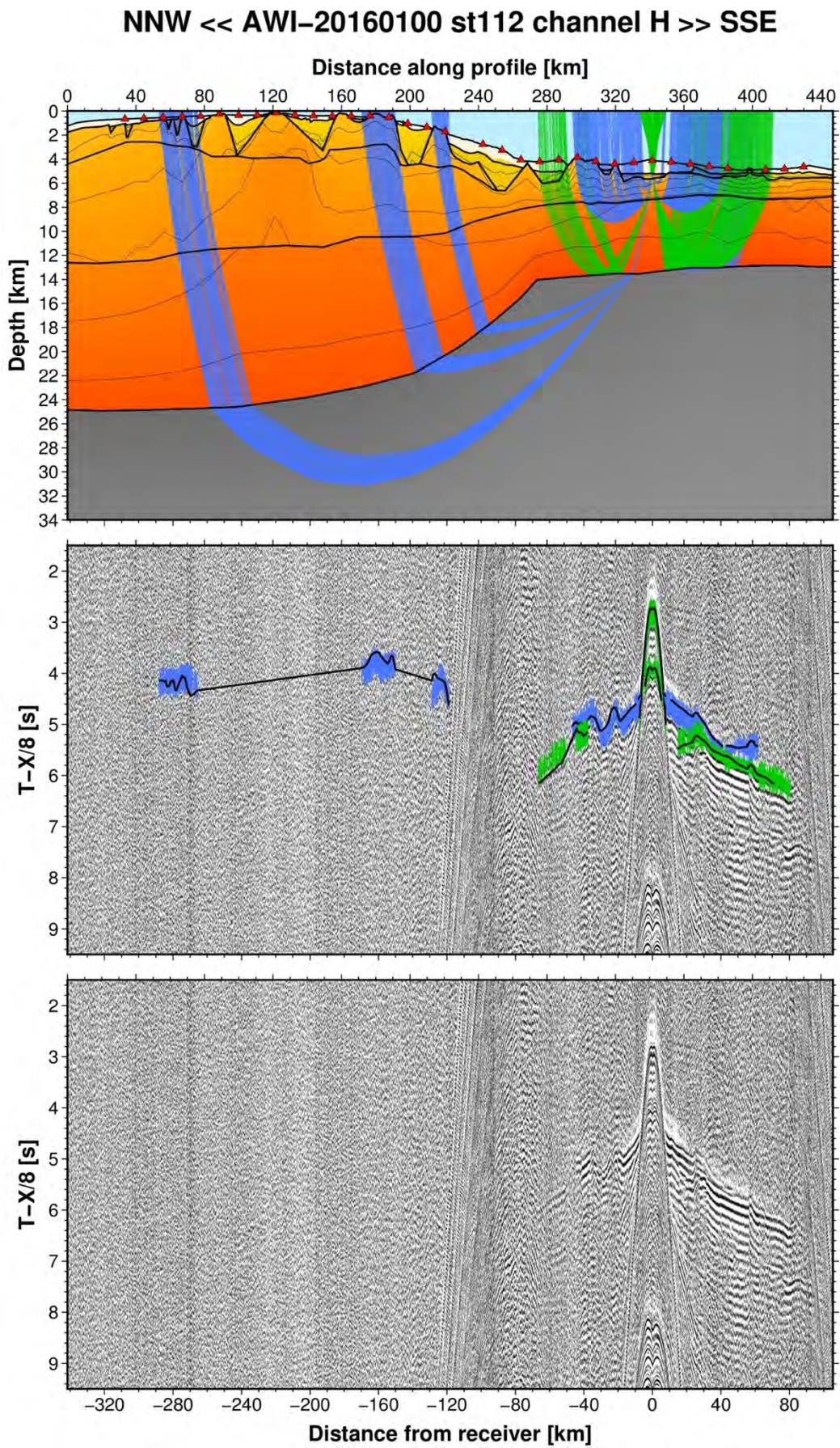


Fig. A10: Ray tracing results for station st112 along profile AWI-20160100. Lower panel: Seismic record; Middle panel: Picked and modelled arrival times; Upper panel: Section of the resulting P-wave velocity model; Green colours = reflections, blue colours = refractions.

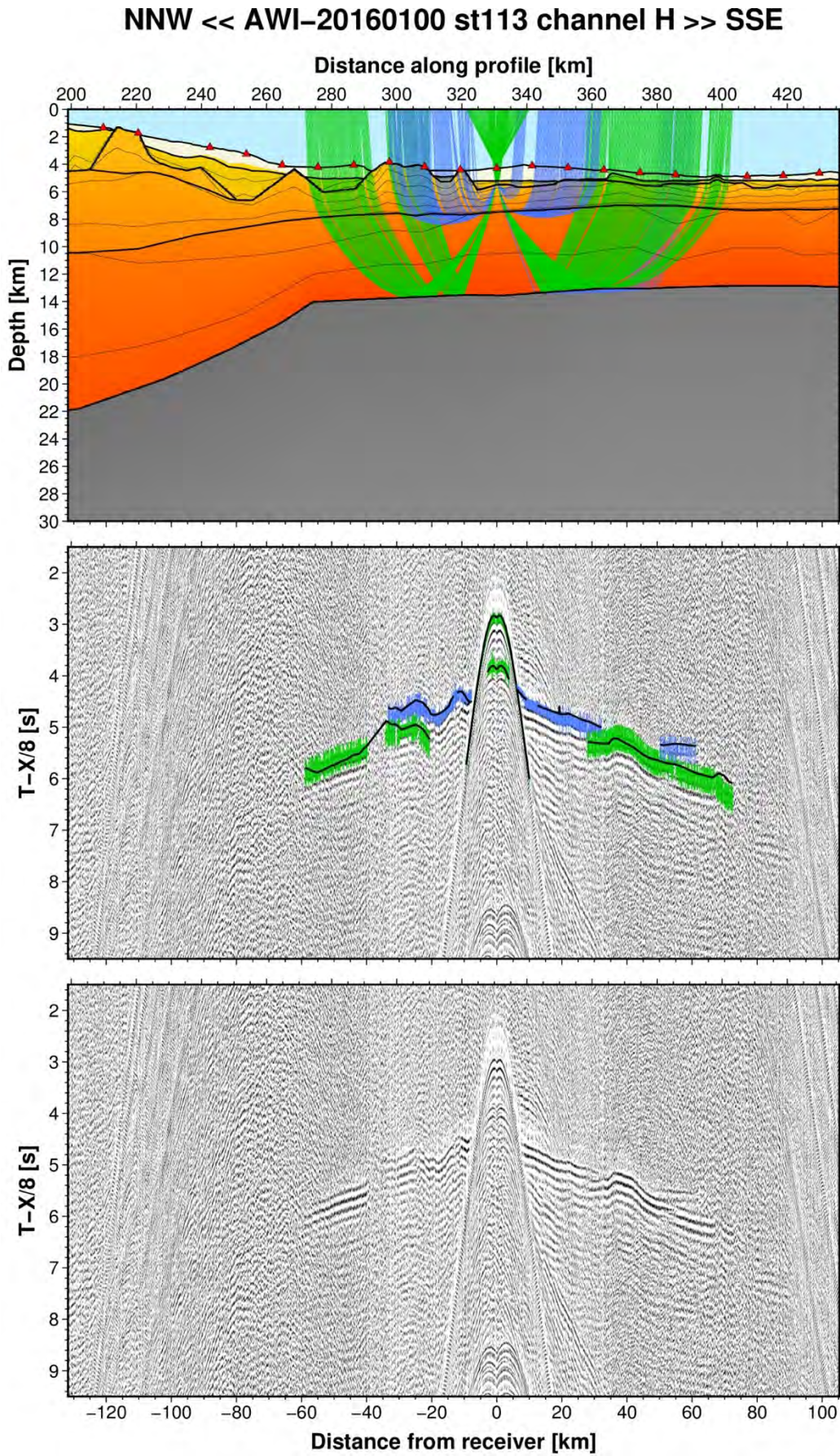


Fig. A11: Ray tracing results for station st113 along profile AWI-20160100. Lower panel: Seismic record; Middle panel: Picked and modelled arrival times; Upper panel: Section of the resulting P-wave velocity model; Green colours = reflections, blue colours = refractions.

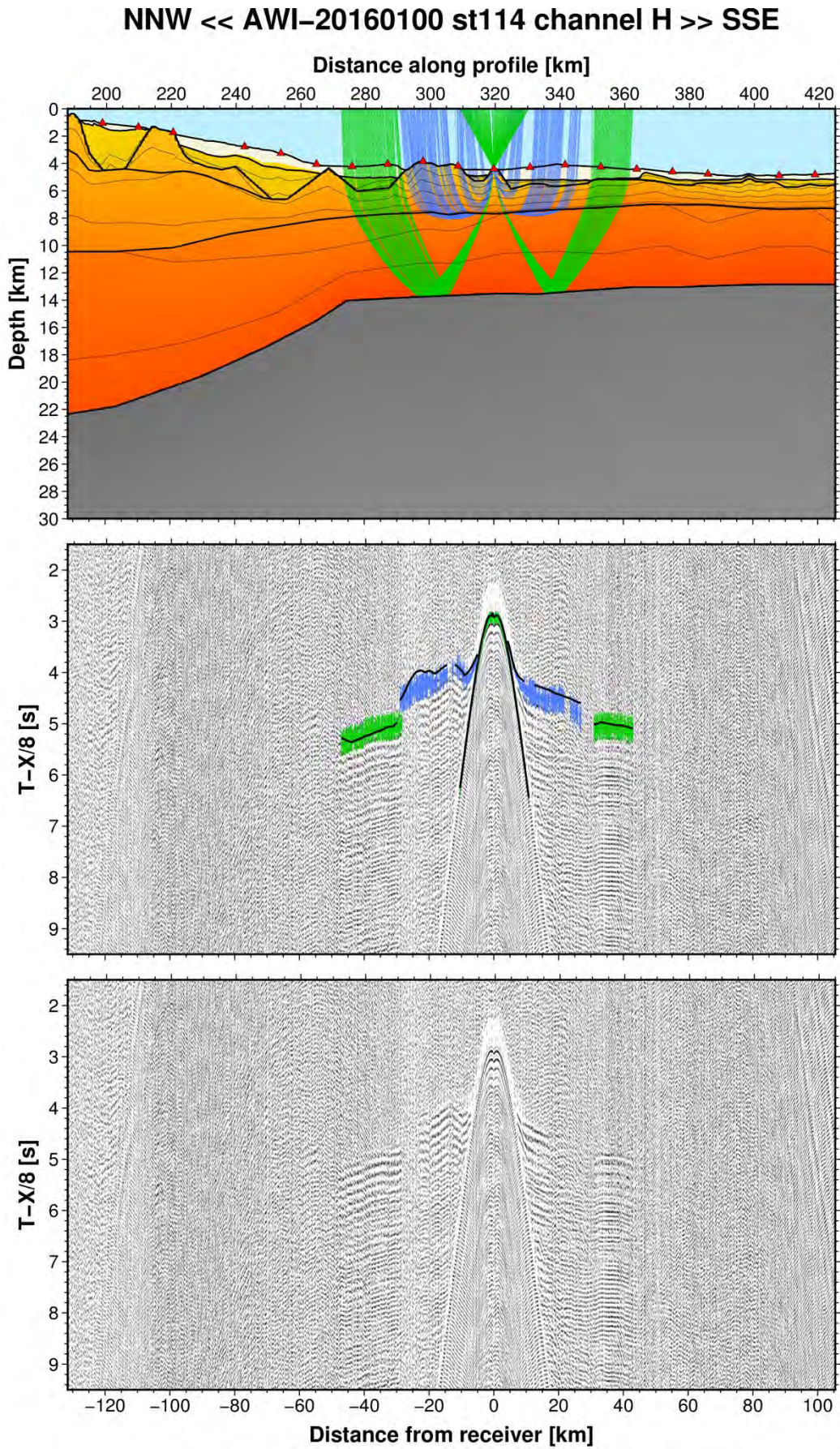


Fig. A12: Ray tracing results for station st114 along profile AWI-20160100. Lower panel: Seismic record; Middle panel: Picked and modelled arrival times; Upper panel: Section of the resulting P-wave velocity model; Green colours = reflections, blue colours = refractions.

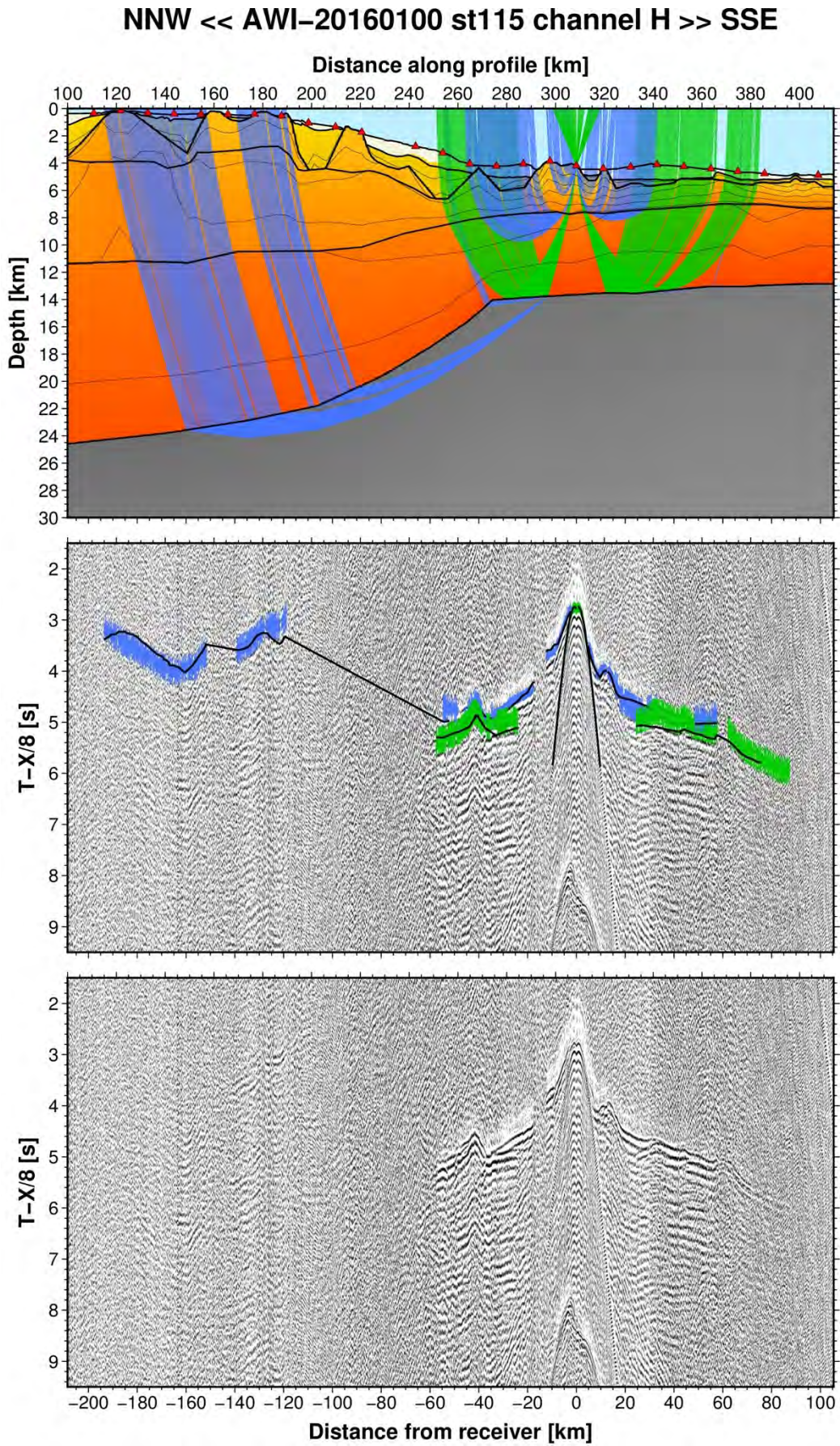


Fig. A13: Ray tracing results for station st115 along profile AWI-20160100. Lower panel: Seismic record; Middle panel: Picked and modelled arrival times; Upper panel: Section of the resulting P-wave velocity model; Green colours = reflections, blue colours = refractions.

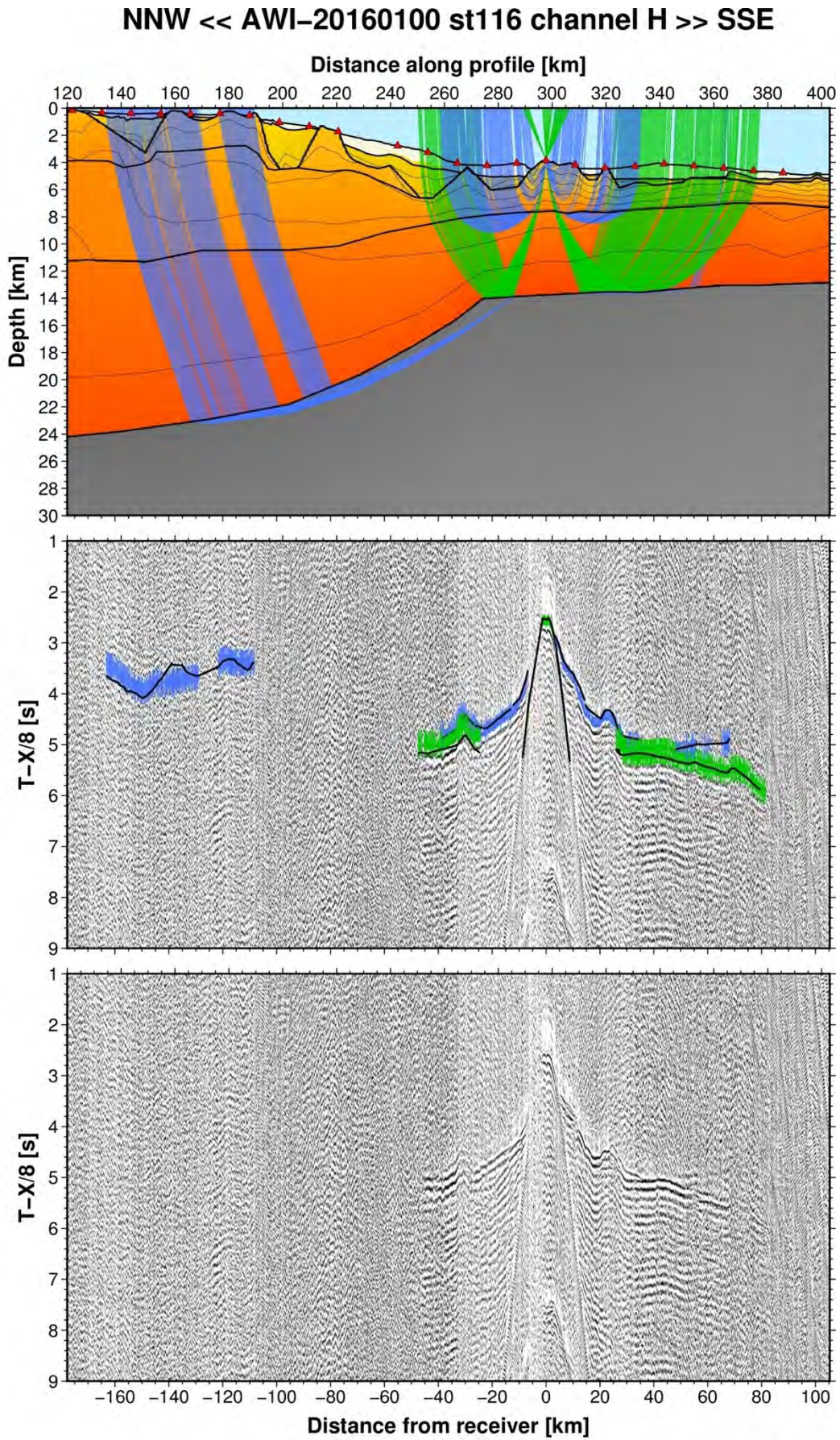


Fig. A14: Ray tracing results for station st116 along profile AWI-20160100. Lower panel: Seismic record; Middle panel: Picked and modelled arrival times; Upper panel: Section of the resulting P-wave velocity model; Green colours = reflections, blue colours = refractions.

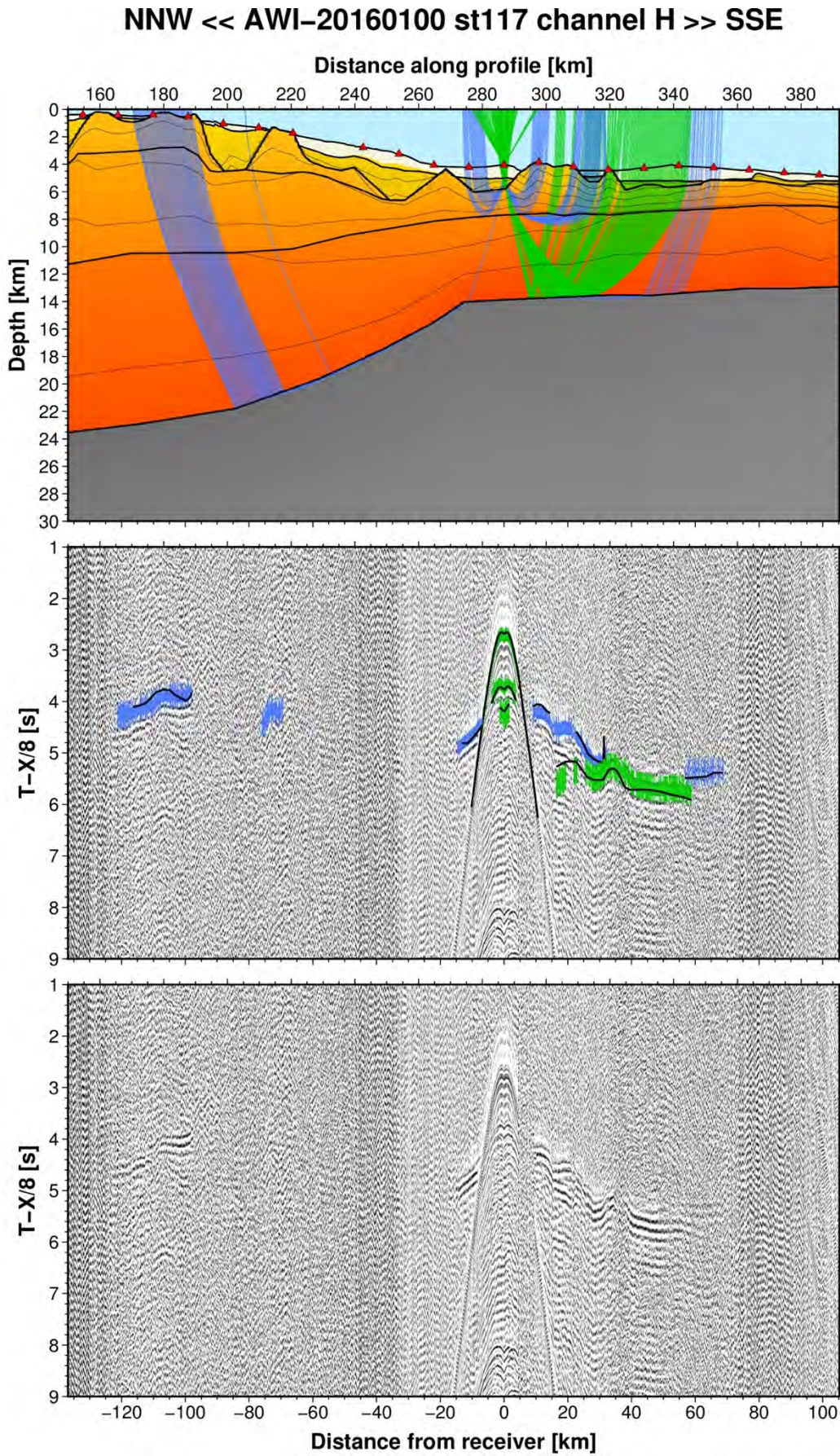


Fig. A15: Ray tracing results for station st117 along profile AWI-20160100. Lower panel: Seismic record; Middle panel: Picked and modelled arrival times; Upper panel: Section of the resulting P-wave velocity model; Green colours = reflections, blue colours = refractions.

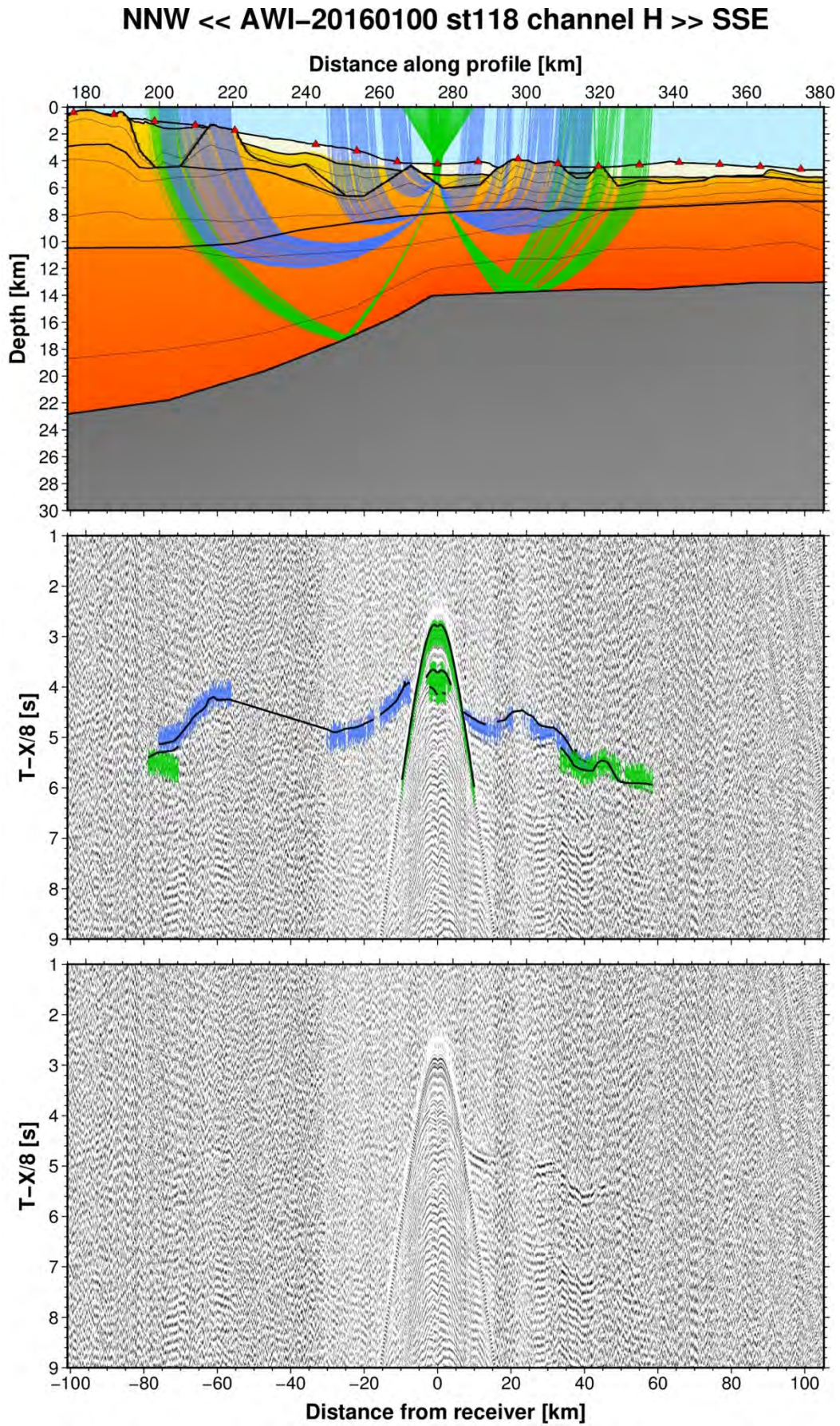


Fig. A16: Ray tracing results for station st118 along profile AWI-20160100. Lower panel: Seismic record; Middle panel: Picked and modelled arrival times; Upper panel: Section of the resulting P-wave velocity model; Green colours = reflections, blue colours = refractions.

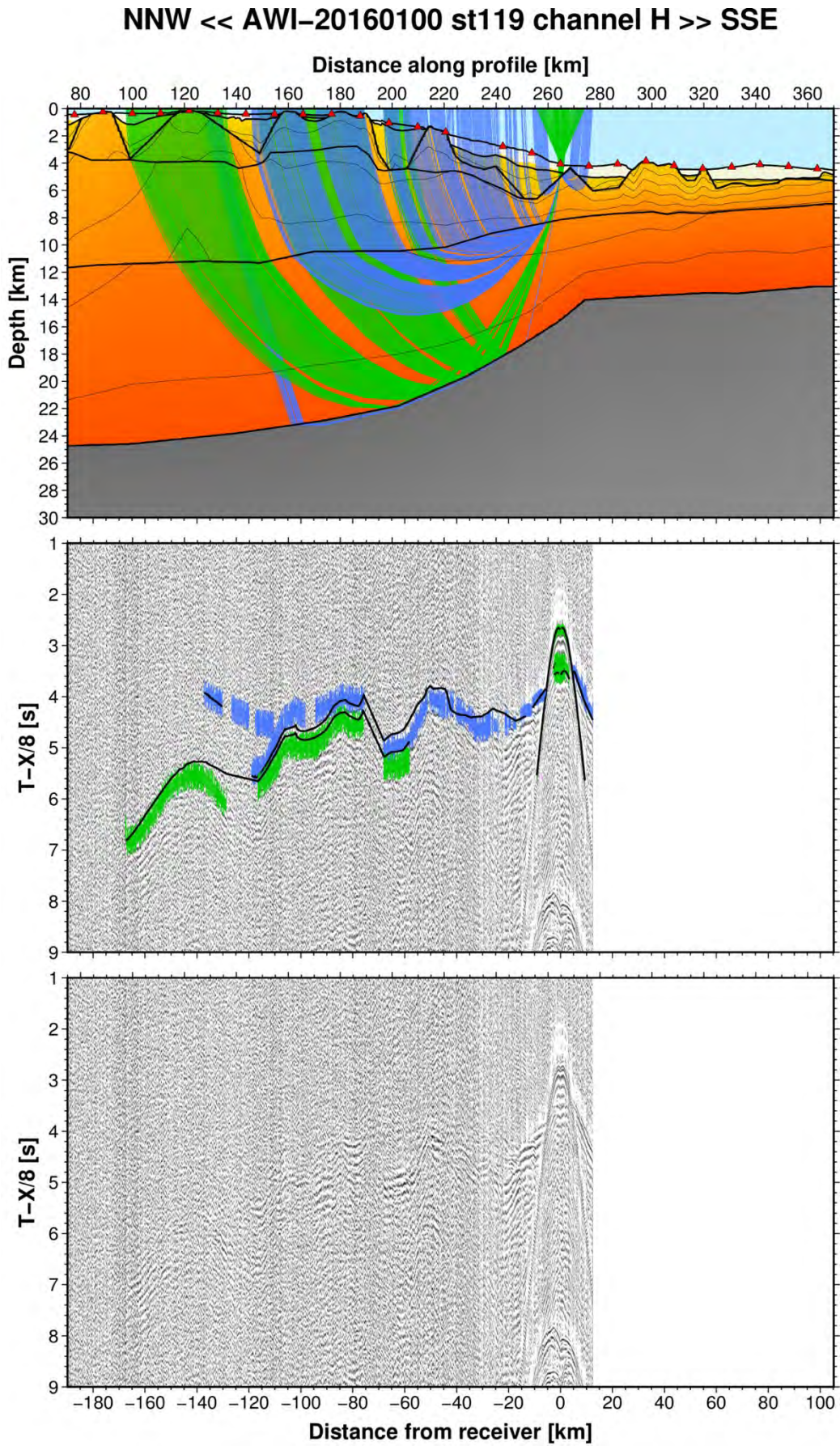


Fig. A17: Ray tracing results for station st119 along profile AWI-20160100. Lower panel: Seismic record; Middle panel: Picked and modelled arrival times; Upper panel: Section of the resulting P-wave velocity model; Green colours = reflections, blue colours = refractions.

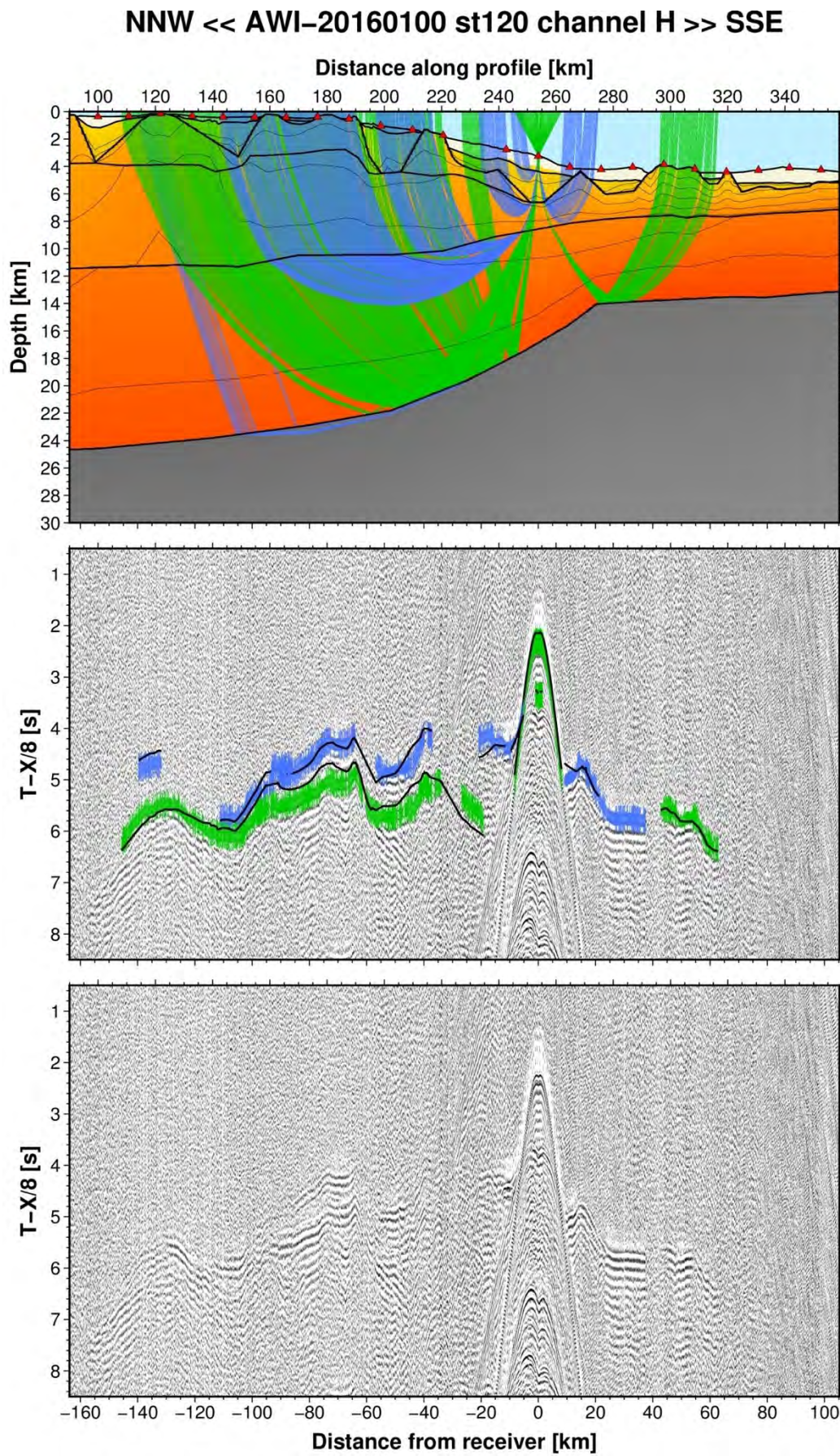


Fig. A18: Ray tracing results for station st120 along profile AWI-20160100. Lower panel: Seismic record; Middle panel: Picked and modelled arrival times; Upper panel: Section of the resulting P-wave velocity model; Green colours = reflections, blue colours = refractions.

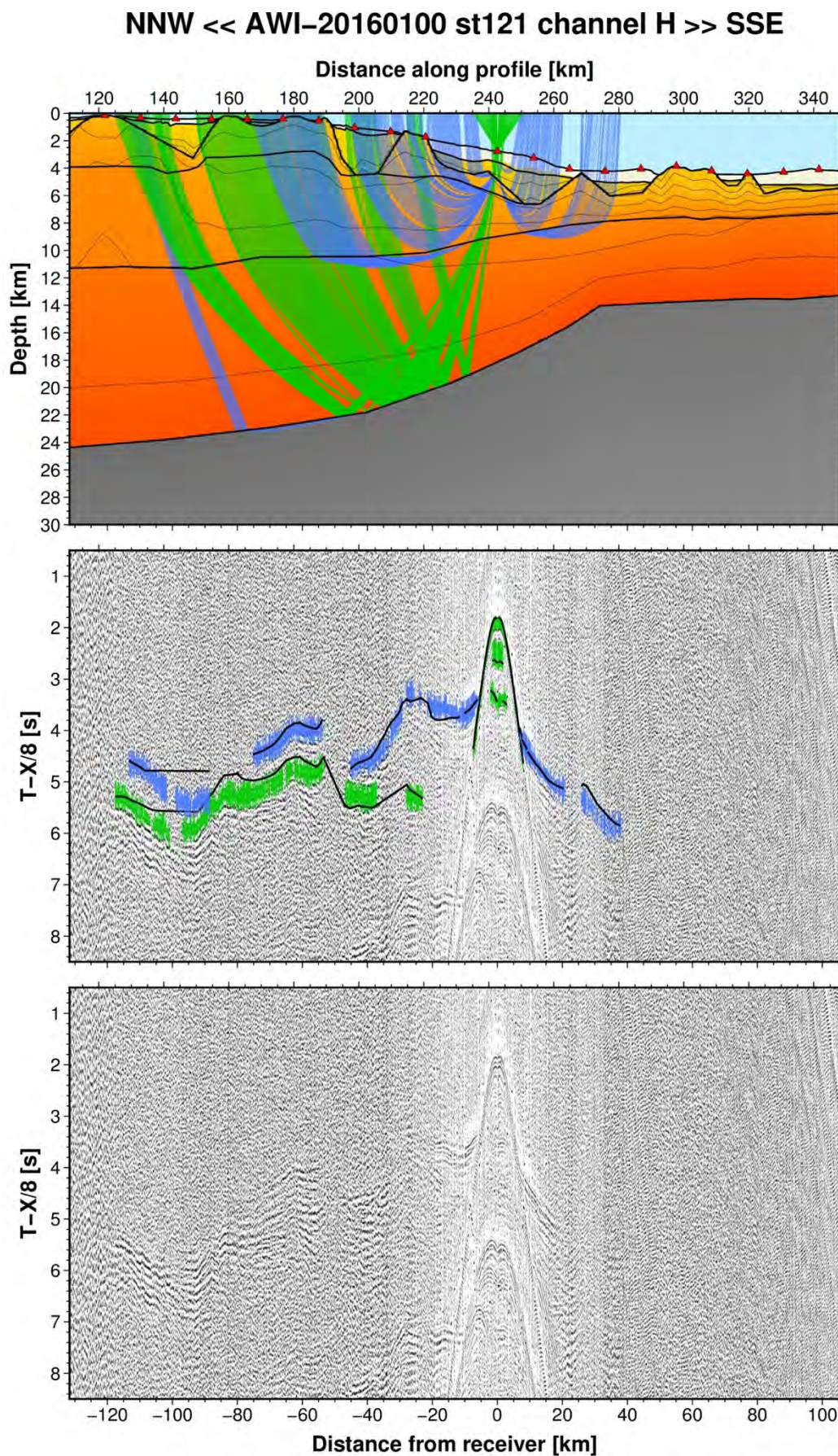


Fig. A19: Ray tracing results for station st121 along profile AWI-20160100. Lower panel: Seismic record; Middle panel: Picked and modelled arrival times; Upper panel: Section of the resulting P-wave velocity model; Green colours = reflections, blue colours = refractions.

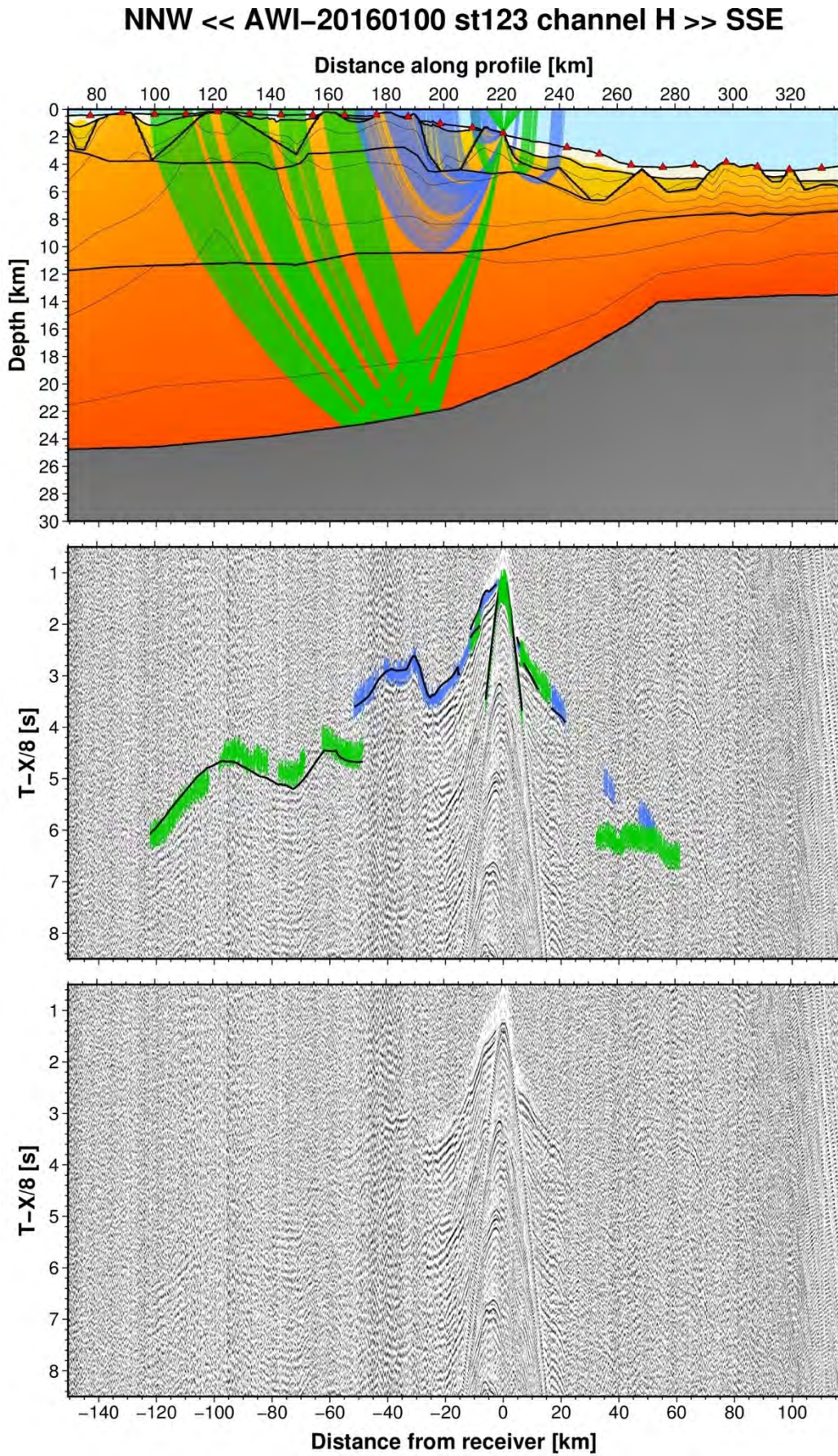


Fig. A20: Ray tracing results for station st123 along profile AWI-20160100. Lower panel: Seismic record; Middle panel: Picked and modelled arrival times; Upper panel: Section of the resulting P-wave velocity model; Green colours = reflections, blue colours = refractions.

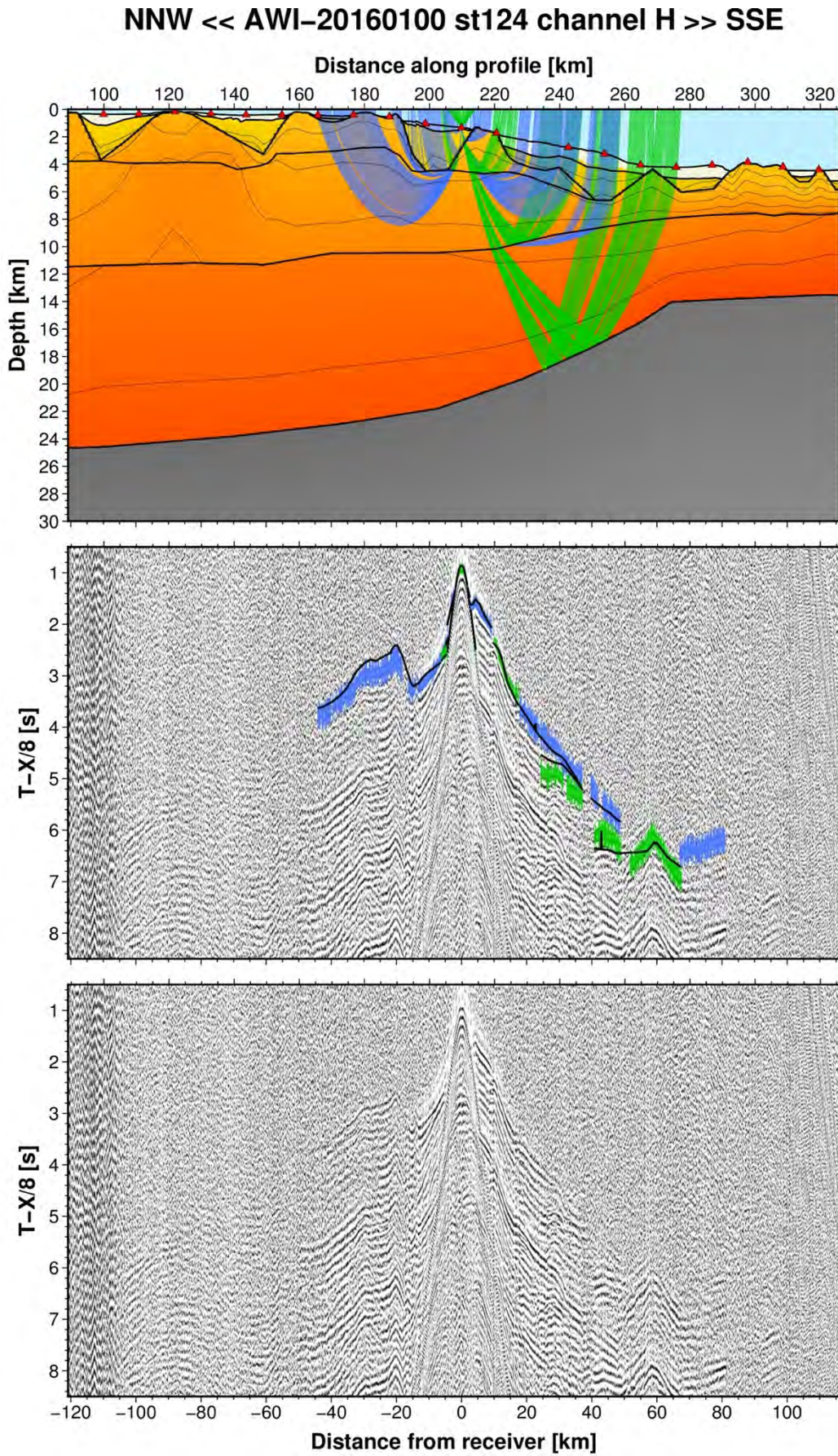


Fig. A21: Ray tracing results for station st124 along profile AWI-20160100. Lower panel: Seismic record; Middle panel: Picked and modelled arrival times; Upper panel: Section of the resulting P-wave velocity model; Green colours = reflections, blue colours = refractions.

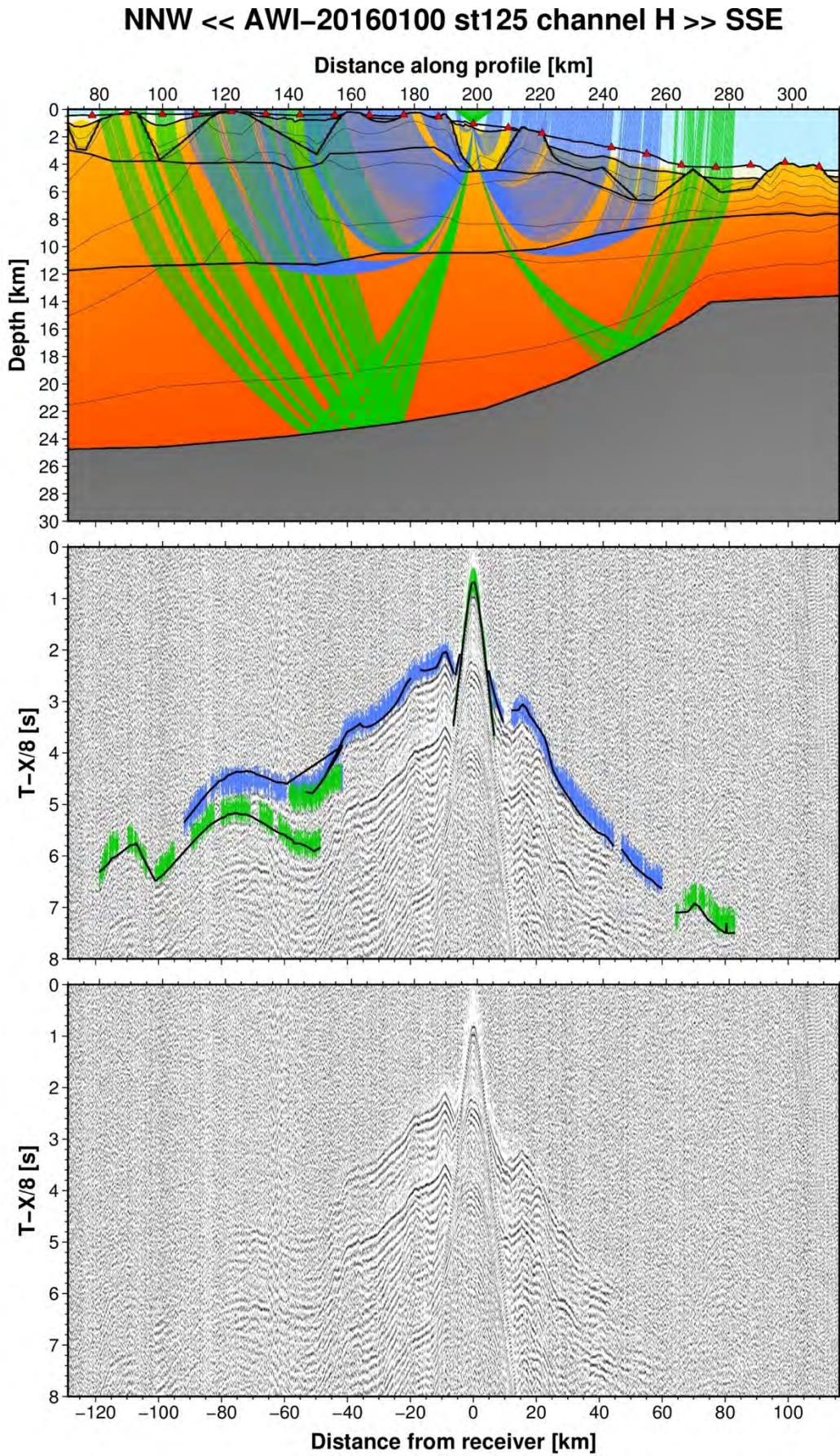


Fig. A22: Ray tracing results for station st125 along profile AWI-20160100. Lower panel: Seismic record; Middle panel: Picked and modelled arrival times; Upper panel: Section of the resulting P-wave velocity model; Green colours = reflections, blue colours = refractions.

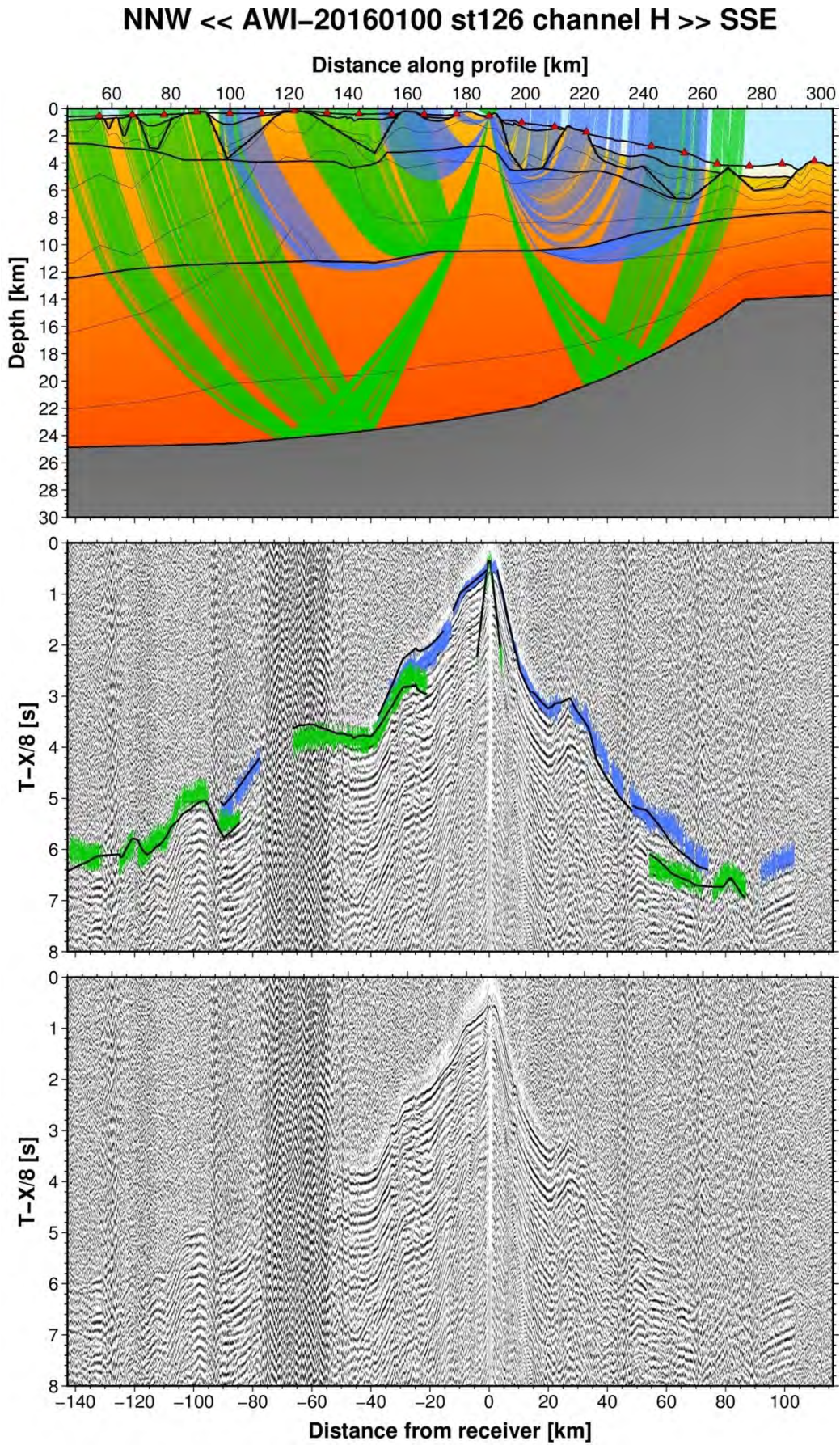


Fig. A23: Ray tracing results for station st126 along profile AWI-20160100. Lower panel: Seismic record; Middle panel: Picked and modelled arrival times; Upper panel: Section of the resulting P-wave velocity model; Green colours = reflections, blue colours = refractions.

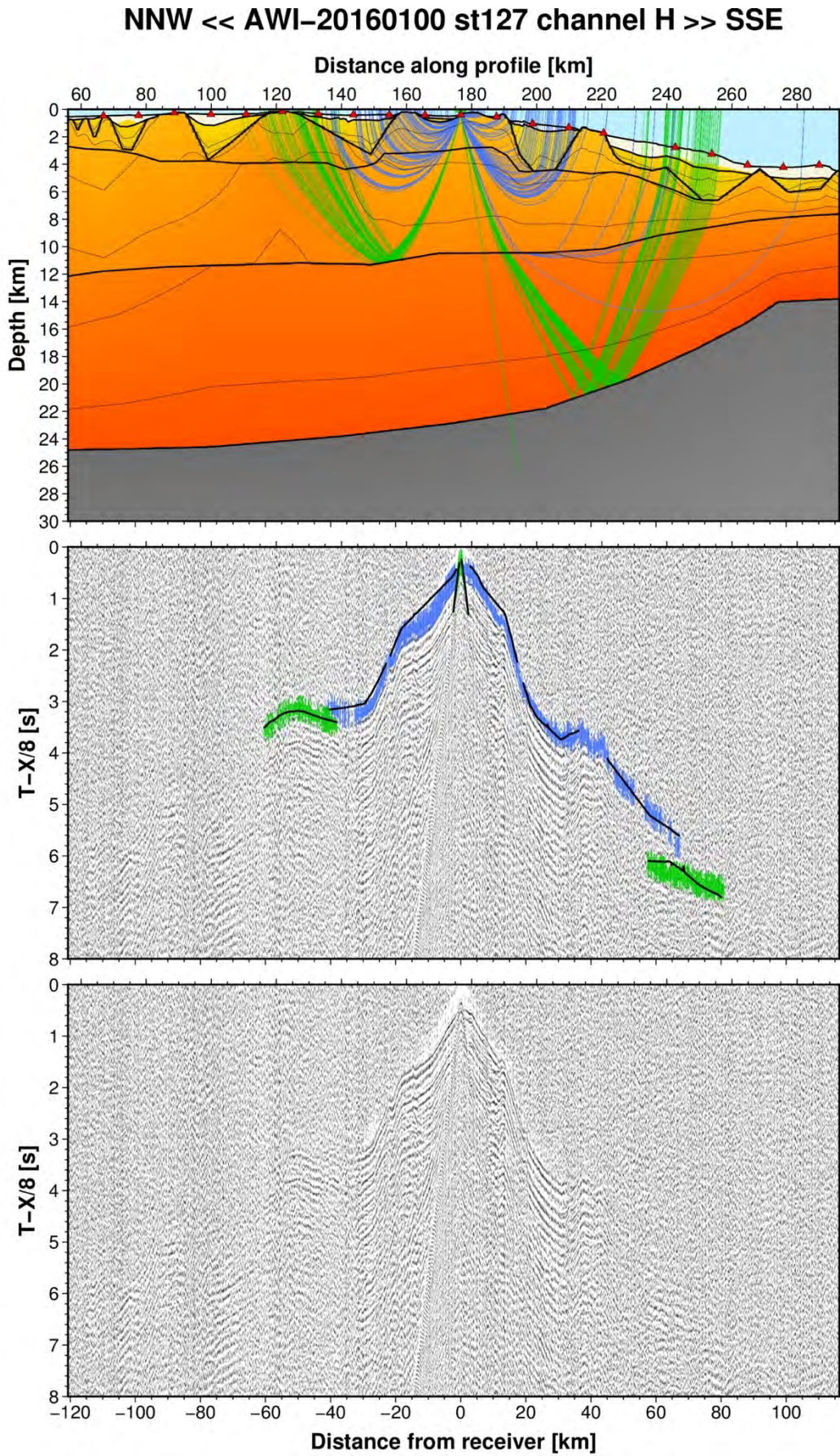


Fig. A24: Ray tracing results for station st127 along profile AWI-20160100. Lower panel: Seismic record; Middle panel: Picked and modelled arrival times; Upper panel: Section of the resulting P-wave velocity model; Green colours = reflections, blue colours = refractions.

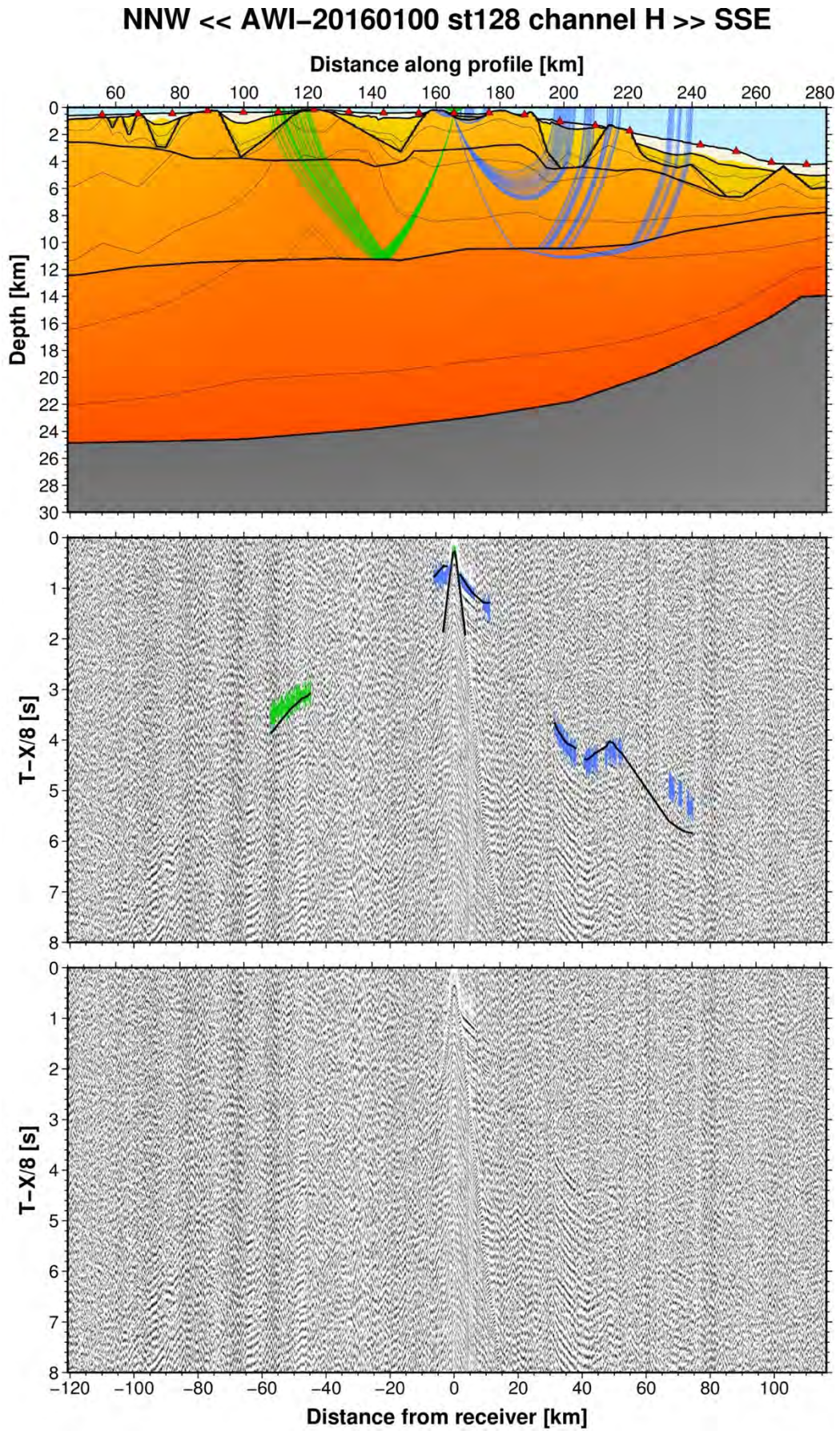


Fig. A25: Ray tracing results for station st128 along profile AWI-20160100. Lower panel: Seismic record; Middle panel: Picked and modelled arrival times; Upper panel: Section of the resulting P-wave velocity model; Green colours = reflections, blue colours = refractions.

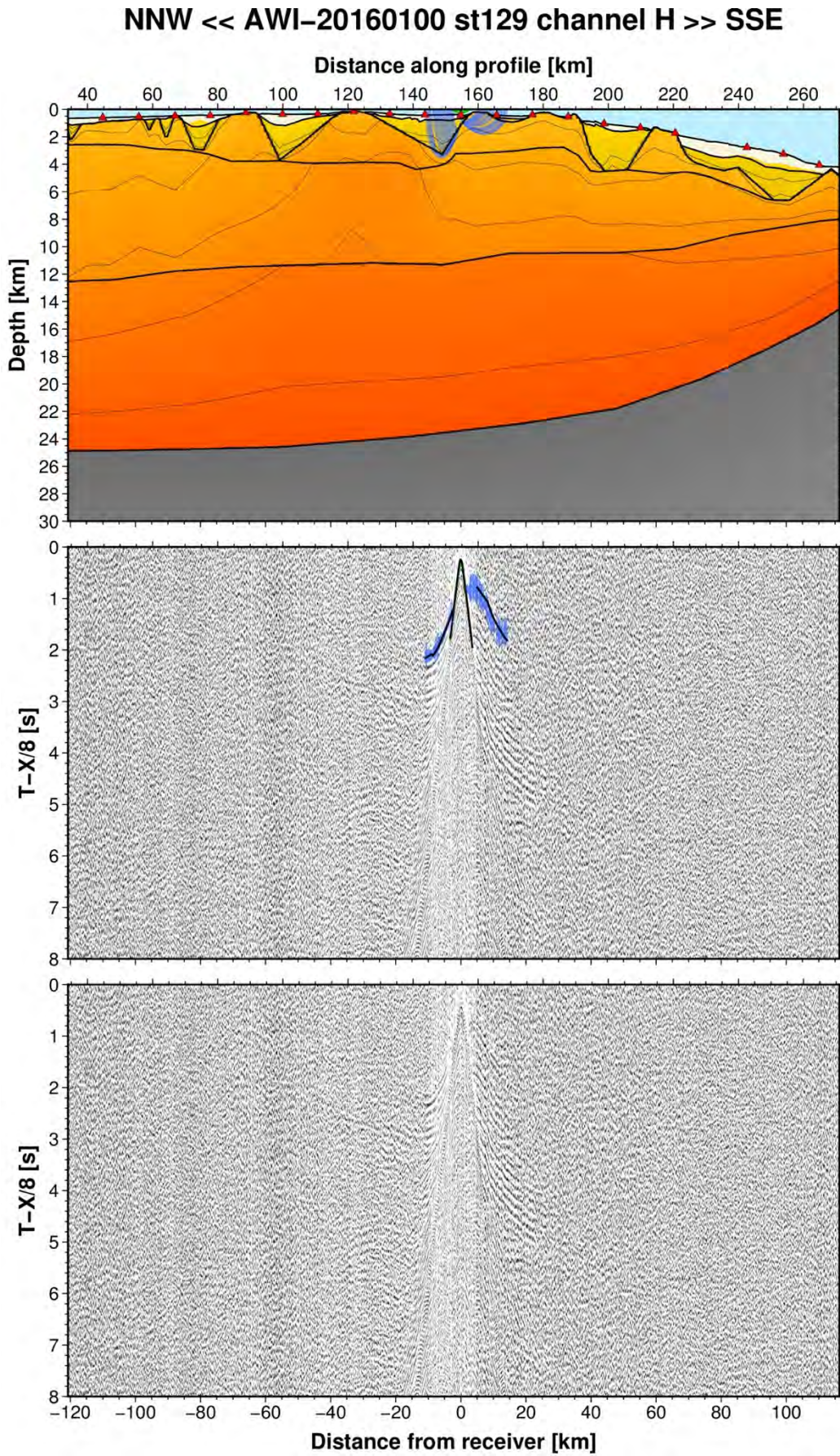


Fig. A26: Ray tracing results for station st129 along profile AWI-20160100. Lower panel: Seismic record; Middle panel: Picked and modelled arrival times; Upper panel: Section of the resulting P-wave velocity model; Green colours = reflections, blue colours = refractions.

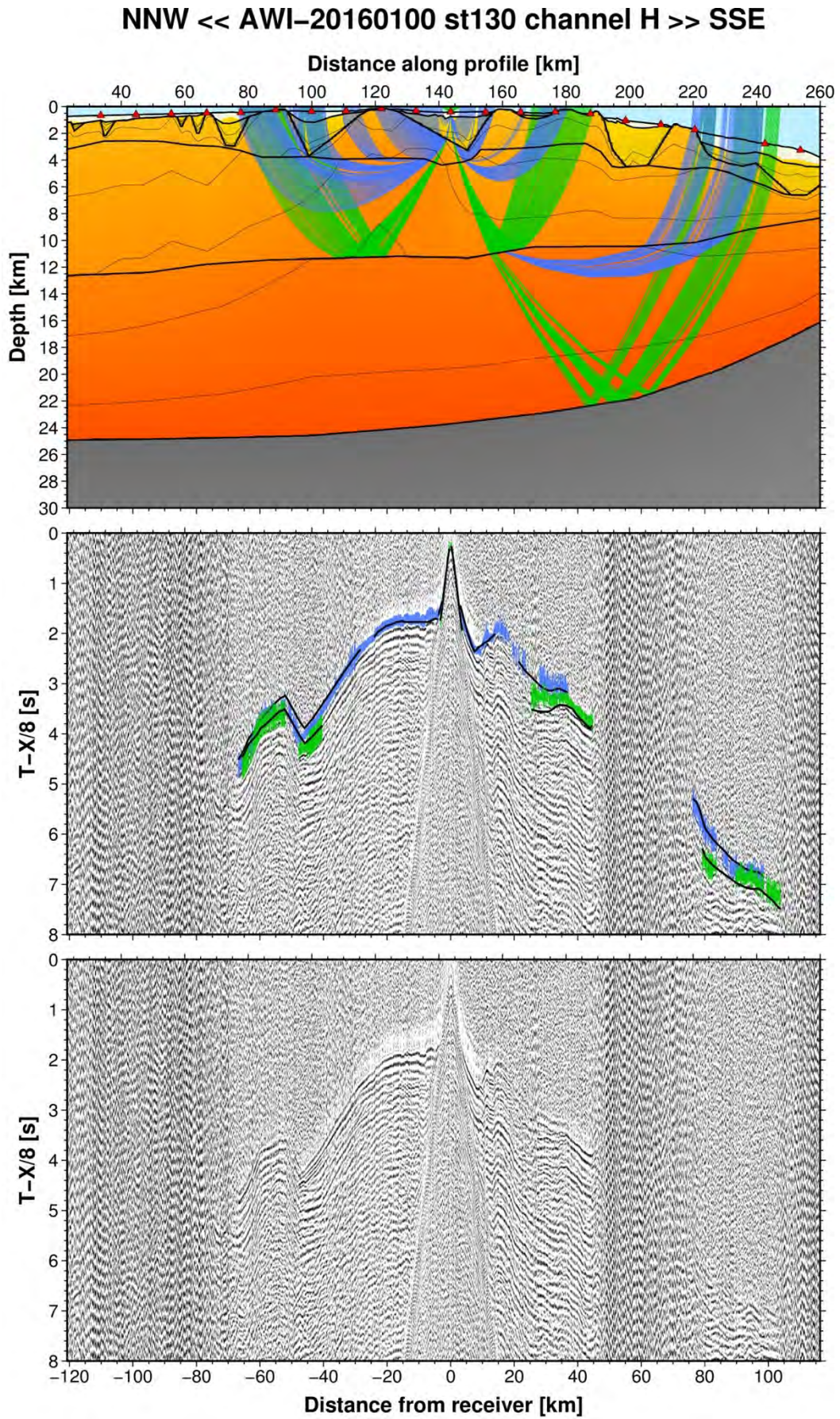


Fig. A27: Ray tracing results for station st130 along profile AWI-20160100. Lower panel: Seismic record; Middle panel: Picked and modelled arrival times; Upper panel: Section of the resulting P-wave velocity model; Green colours = reflections, blue colours = refractions.

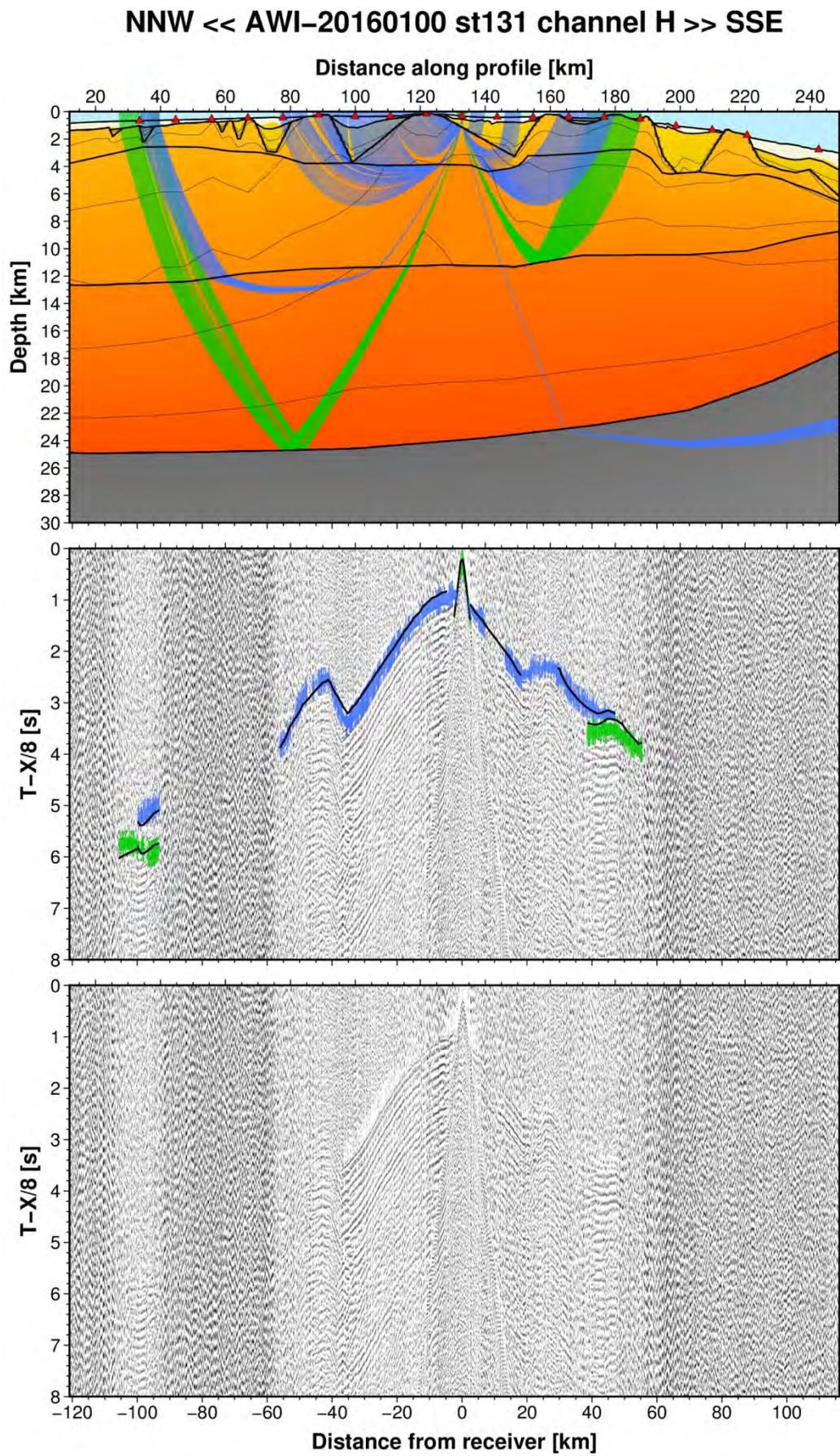


Fig. A28: Ray tracing results for station st131 along profile AWI-20160100. Lower panel: Seismic record; Middle panel: Picked and modelled arrival times; Upper panel: Section of the resulting P-wave velocity model; Green colours = reflections, blue colours = refractions.

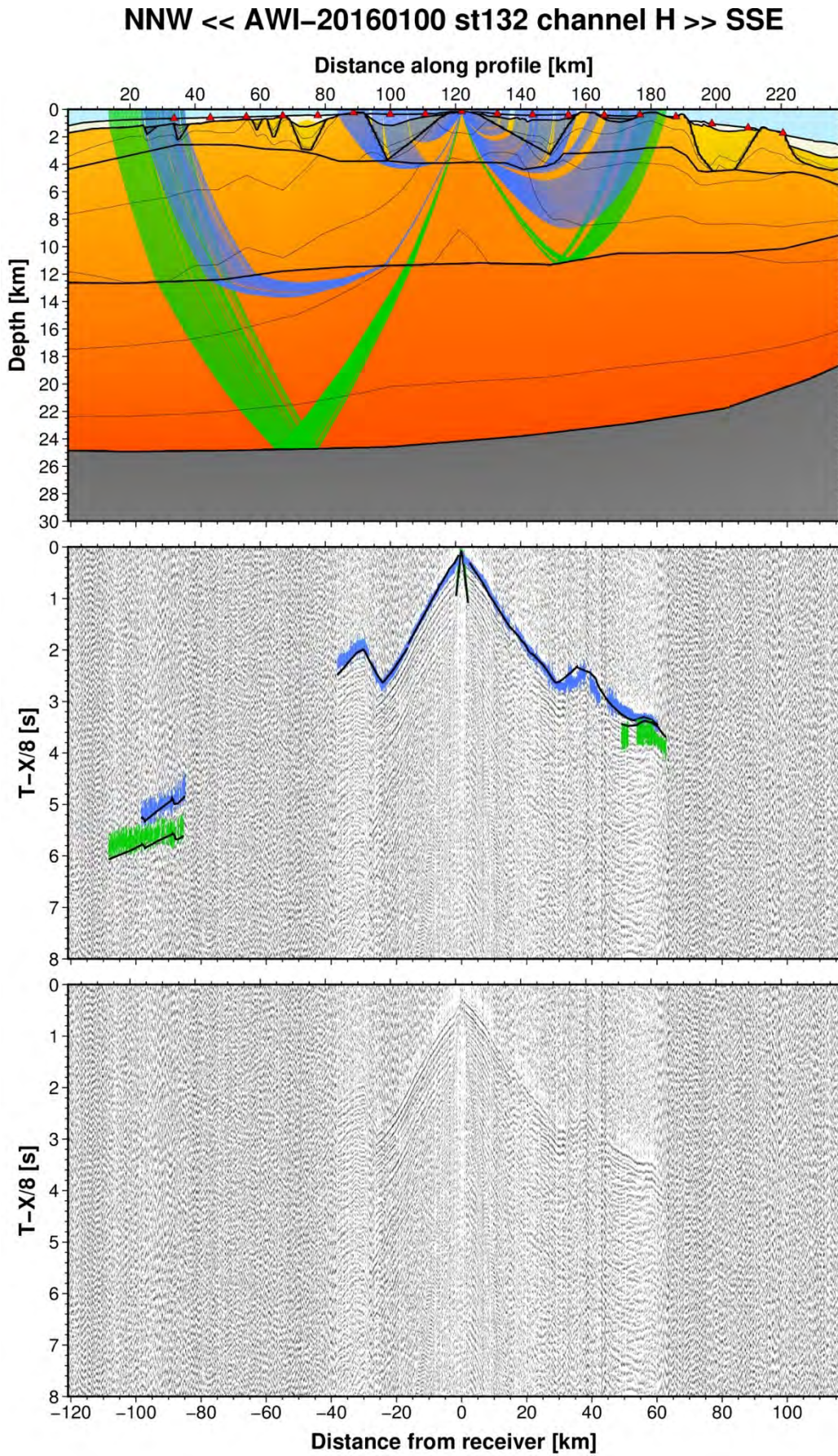


Fig. A29: Ray tracing results for station st132 along profile AWI-20160100. Lower panel: Seismic record; Middle panel: Picked and modelled arrival times; Upper panel: Section of the resulting P-wave velocity model; Green colours = reflections, blue colours = refractions.

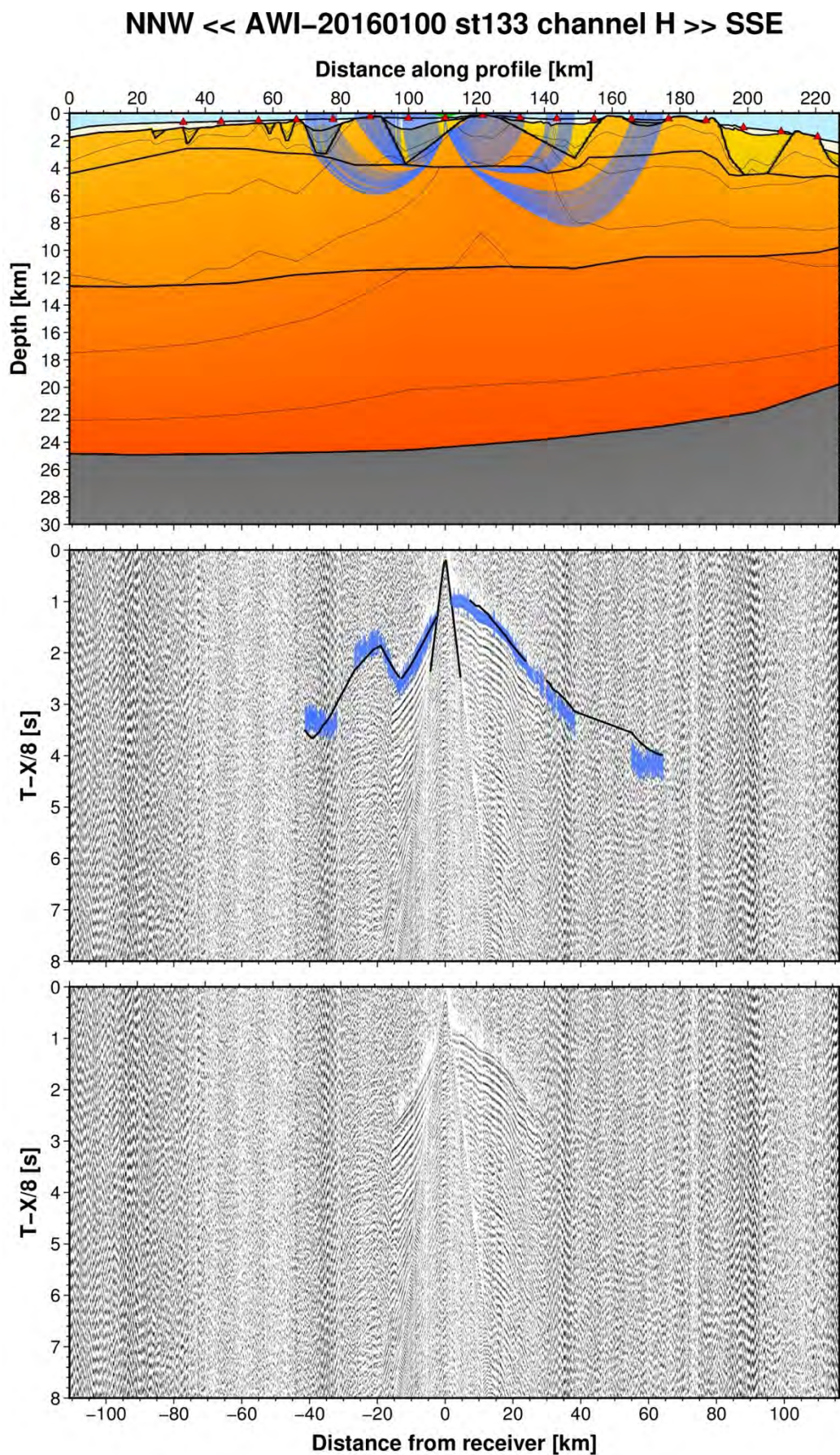


Fig. A30: Ray tracing results for station st133 along profile AWI-20160100. Lower panel: Seismic record; Middle panel: Picked and modelled arrival times; Upper panel: Section of the resulting P-wave velocity model; Green colours = reflections, blue colours = refractions.

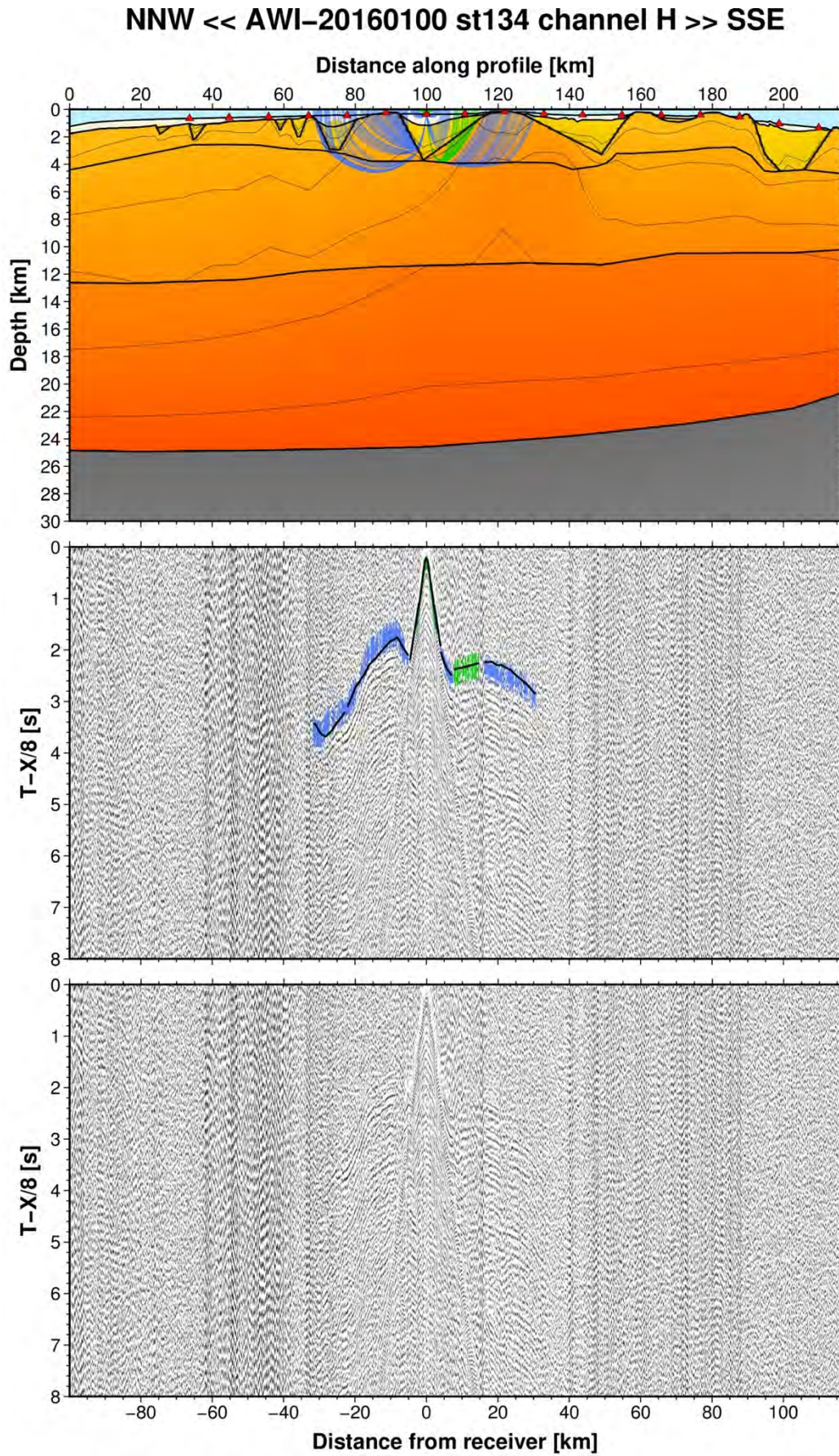


Fig. A31: Ray tracing results for station st134 along profile AWI-20160100. Lower panel: Seismic record; Middle panel: Picked and modelled arrival times; Upper panel: Section of the resulting P-wave velocity model; Green colours = reflections, blue colours = refractions.

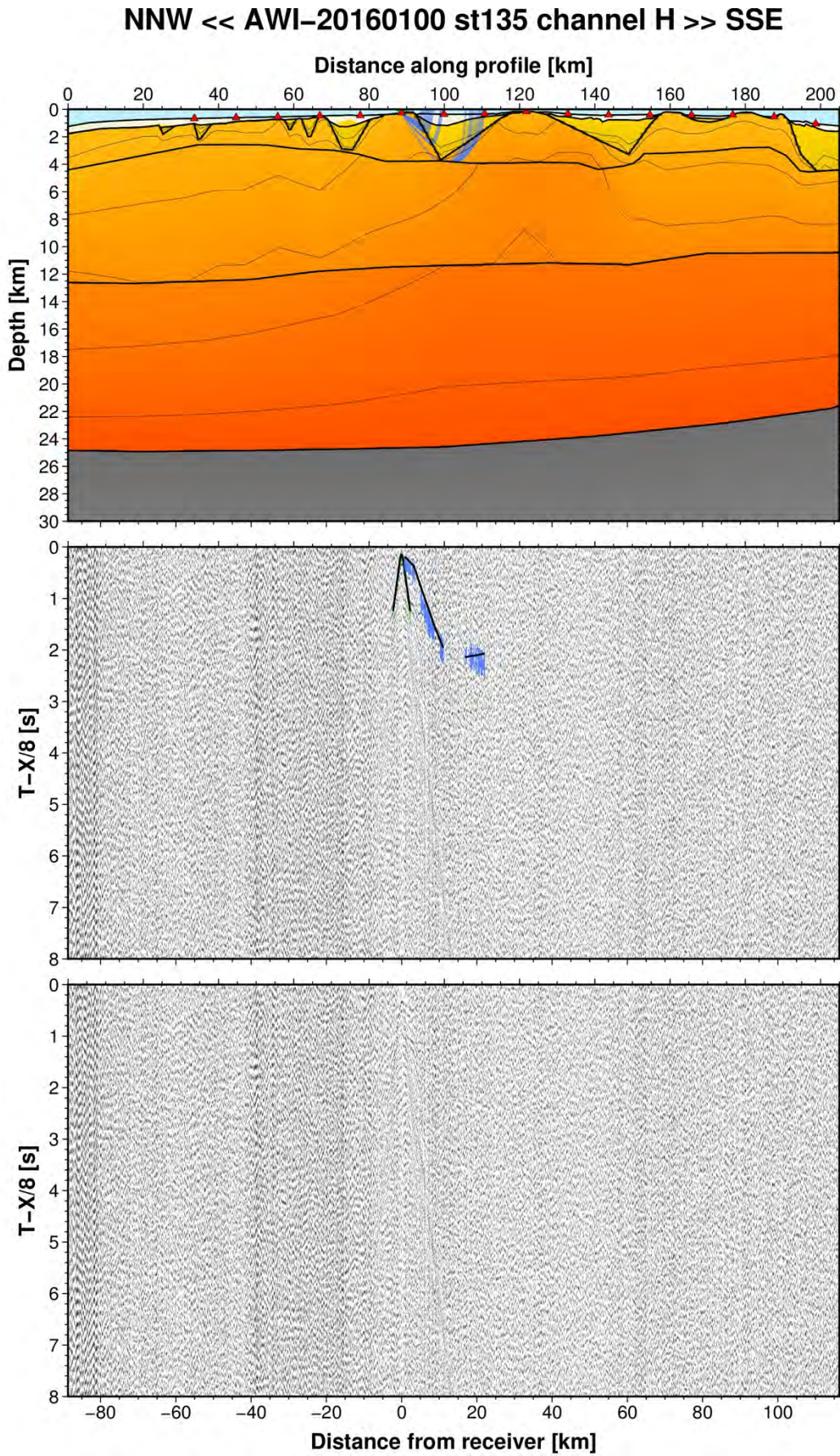


Fig. A32: Ray tracing results for station st135 along profile AWI-20160100. Lower panel: Seismic record; Middle panel: Picked and modelled arrival times; Upper panel: Section of the resulting P-wave velocity model; Green colours = reflections, blue colours = refractions.

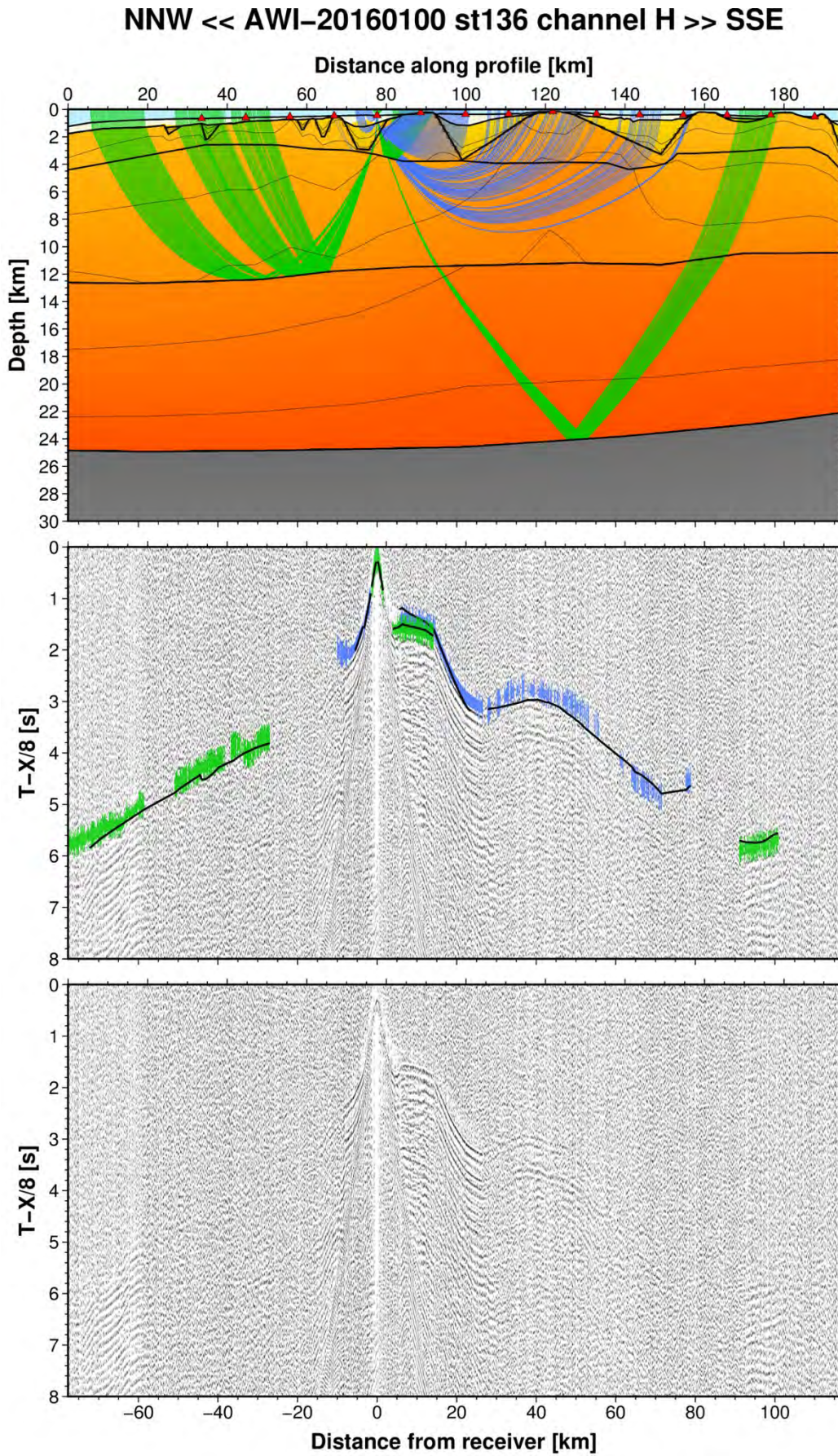


Fig. A33: Ray tracing results for station st136 along profile AWI-20160100. Lower panel: Seismic record; Middle panel: Picked and modelled arrival times; Upper panel: Section of the resulting P-wave velocity model; Green colours = reflections, blue colours = refractions.

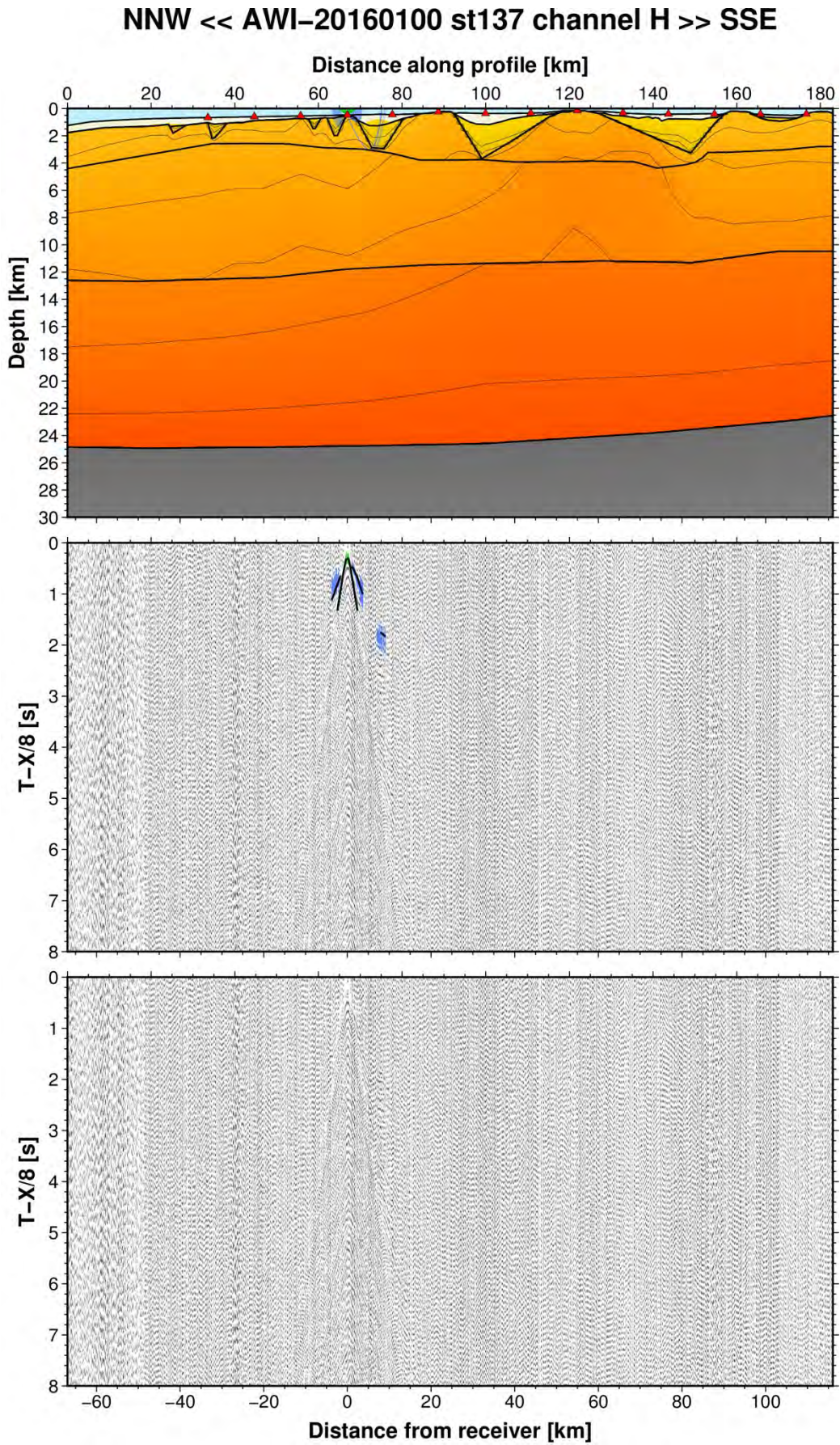


Fig. A34: Ray tracing results for station st137 along profile AWI-20160100. Lower panel: Seismic record; Middle panel: Picked and modelled arrival times; Upper panel: Section of the resulting P-wave velocity model; Green colours = reflections, blue colours = refractions.

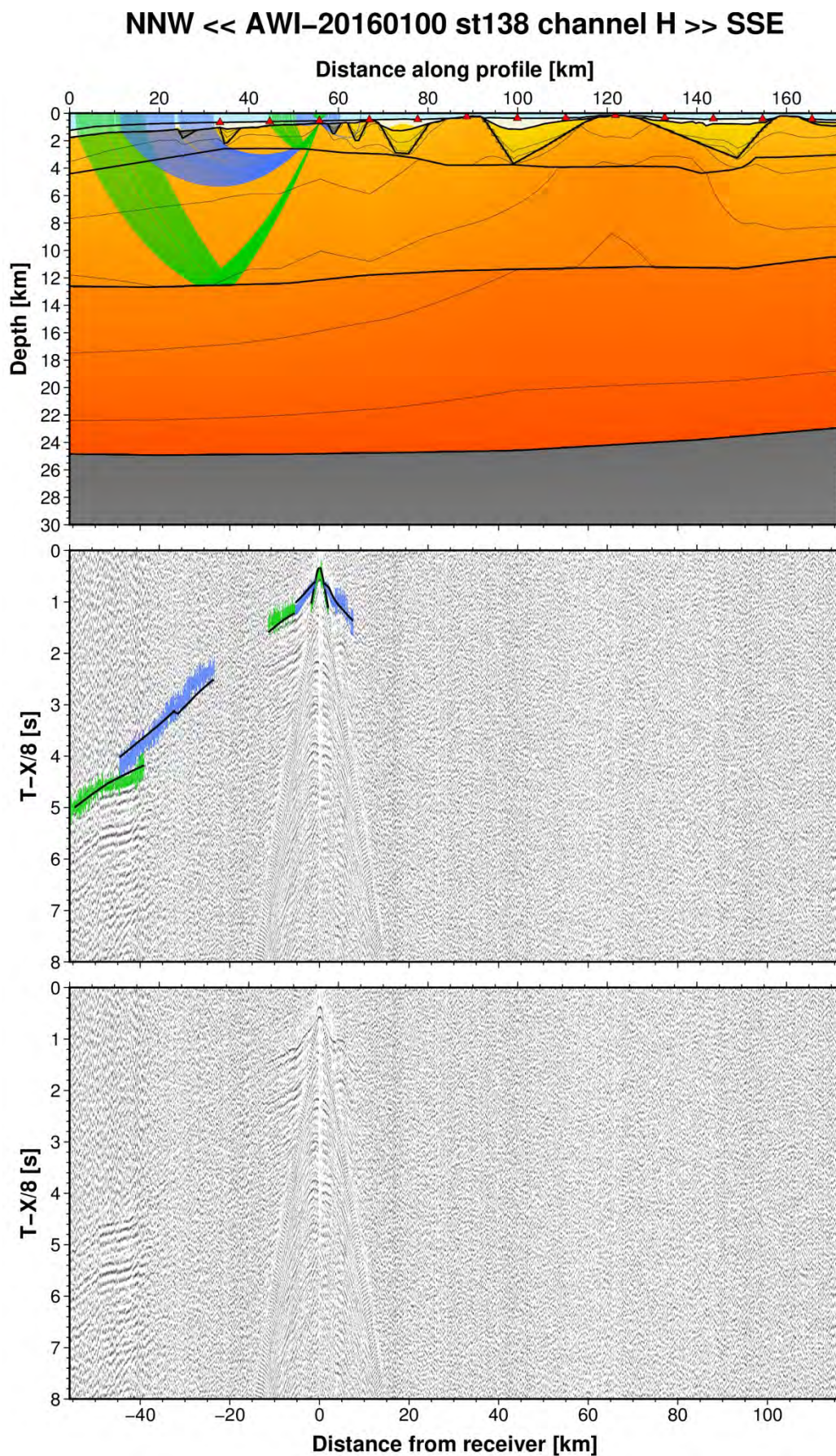


Fig. A35: Ray tracing results for station st138 along profile AWI-20160100. Lower panel: Seismic record; Middle panel: Picked and modelled arrival times; Upper panel: Section of the resulting P-wave velocity model; Green colours = reflections, blue colours = refractions.

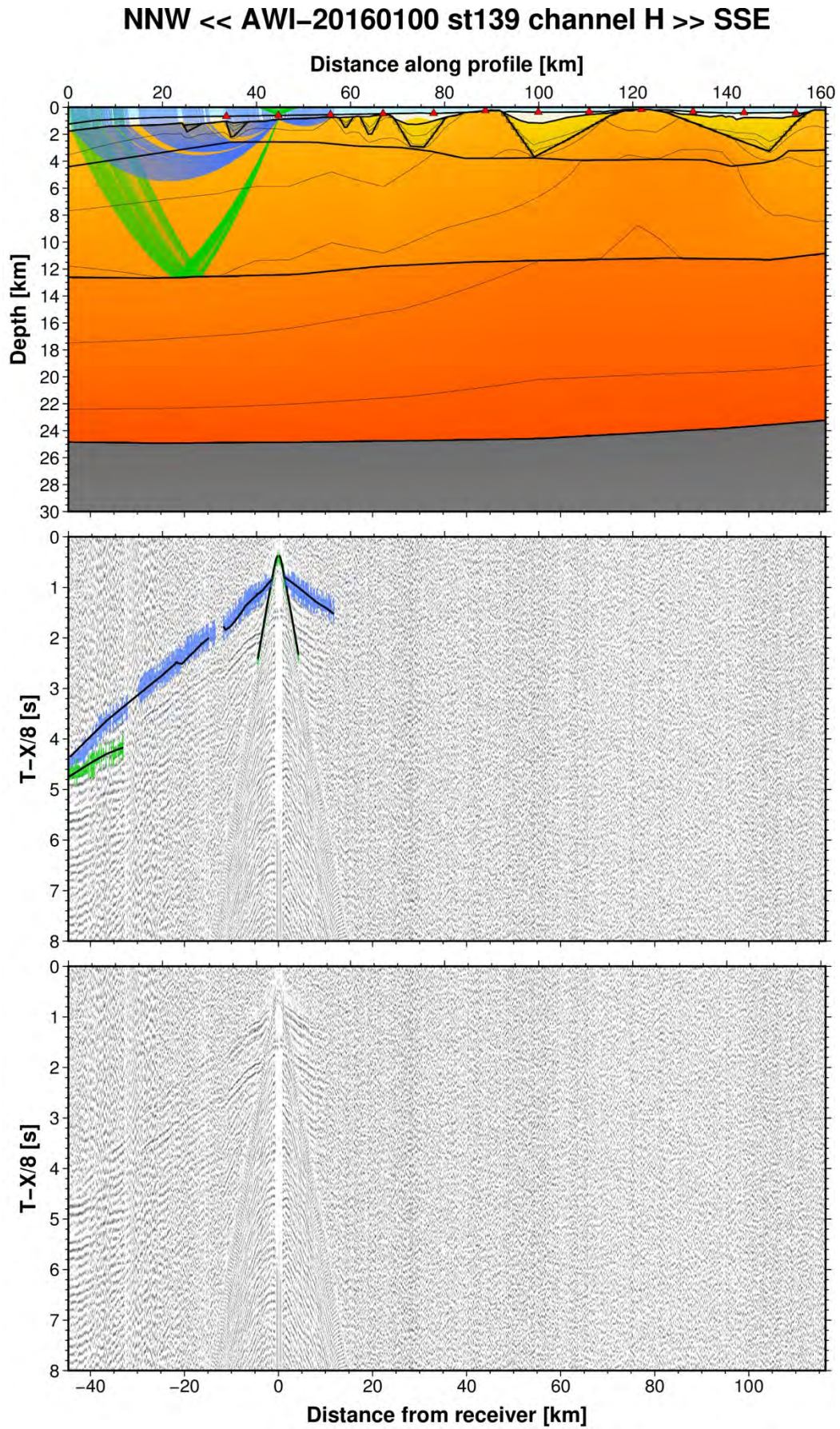


Fig. A36: Ray tracing results for station st139 along profile AWI-20160100. Lower panel: Seismic record; Middle panel: Picked and modelled arrival times; Upper panel: Section of the resulting P-wave velocity model; Green colours = reflections, blue colours = refractions.

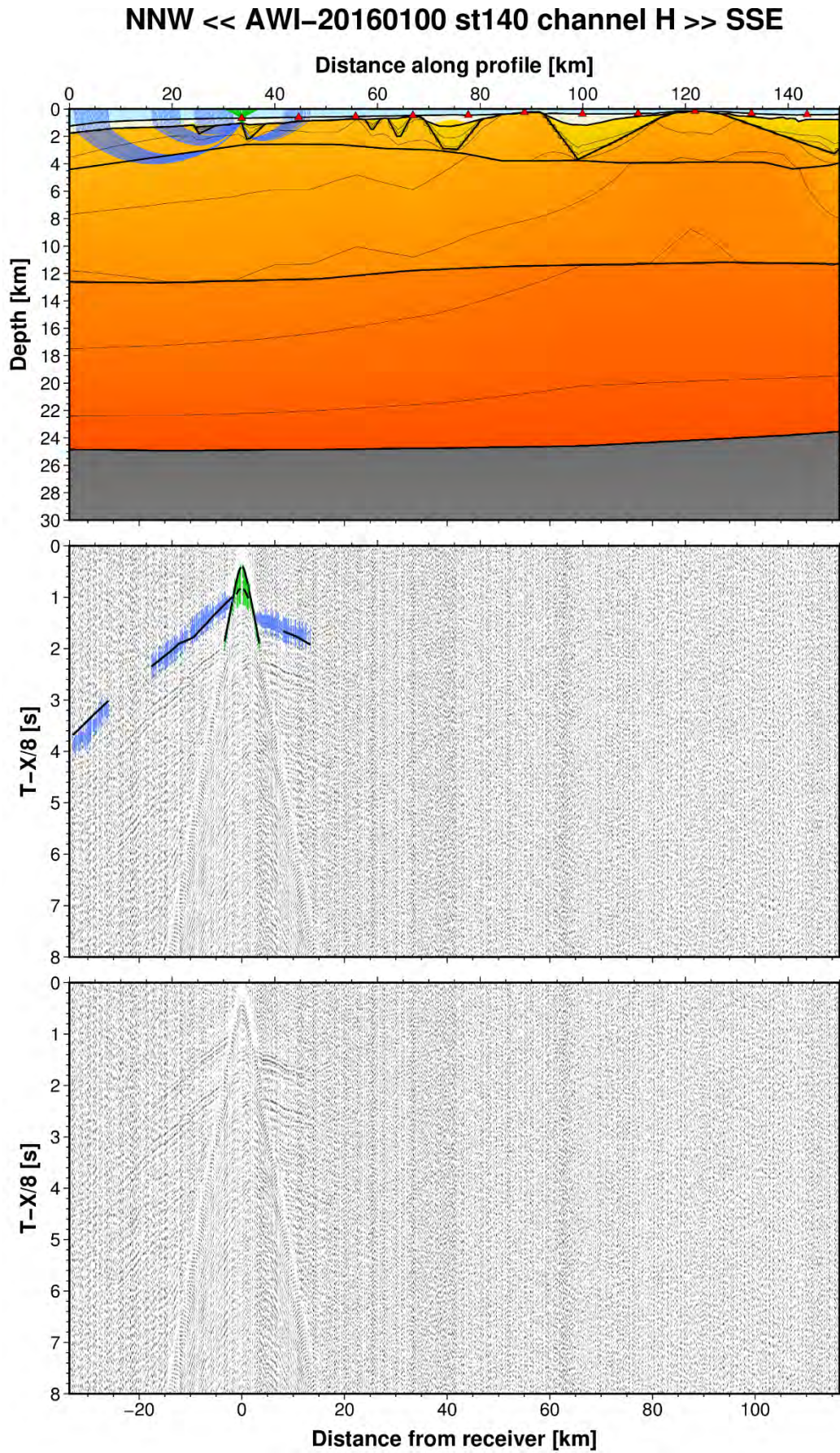


Fig. A37: Ray tracing results for station st140 along profile AWI-20160100. Lower panel: Seismic record; Middle panel: Picked and modelled arrival times; Upper panel: Section of the resulting P-wave velocity model; Green colours = reflections, blue colours = refractions.

A2. AWI-20160200

Tab. A2: Table with information about the configurations and data quality (1 = excellent, 2 = medium, 3 = low, 4 = no data, - = channel not used) of the OBS / OBH stations along profile AWI-20160200. See Gohl & Werner (2016) for more information.

Station	Water Depth [m]	Type	Recorder Type	Sensors	Quality				
					C 1 h	C 2 x	C 3 y	C 4 z	C 5 h
st201	1540	OBS (GEOMAR)	MBS	H,X,Y,Z	1-2	1-2	2	1-2	-
st202	1343	OBS (GEOMAR)	MBS	H,X,Y,Z	1	1-2	1-2	1-2	-
st203	1263	OBS (AWI)	MCS	H	1	-	-	-	-
st204	1166	OBS (GEOMAR)	MBS	H,X,Y,Z	2	2	2	2	-
st205	1104	OBS (GEOMAR)	Geolog	H,X,Y,Z,H	1-2	2	2	2	1
st206	1057	OBS (AWI)	6D6	H,X,Y,Z	2	2	2	2	-
st207	1078	OBS (GEOMAR)	MBS	H,X,Y,Z	1-2	2	2	2-3	-
st208	1113	OBS (AWI)	MCS	H	2	-	-	-	-
st209	1293	OBH (GEOMAR)	MBS	H	1	-	-	-	-
st210	1414	OBS (GEOMAR)	MBS	H,X,Y,Z	1	1	1-2	1-2	-
st211	1519	OBS (GEOMAR)	MBS	H,X,Y,Z	2	2	2	2	-
st212	1613	OBS (AWI)	MCS	H,X,Y,Z	1	1-2	1-2	2	-
st213	1711	OBS (GEOMAR)	MBS	H,X,Y,Z	4	1-2	1-2	1-2	-
st214	1794	OBS (AWI)	MCS	H	1-2	-	-	-	-
st215	1878	OBS (GEOMAR)	MBS	H,X,Y,Z	1	1-2	1-2	1-2	-
st216	1961	OBH (GEOMAR)	MBS	H	1-2	-	-	-	-
st217	2049	OBS (NAMMU)	6D6	H,X,Y,Z	1	1	1	1	-
st218	2184	OBS (GEOMAR)	Geolog	H,X,Y,Z,H	1	1	1	1	1
st219	2430	OBS (AWI)	MCS	H	2	-	-	-	-
st220	2957	OBS (GEOMAR)	MBS	H,X,Y,Z	2	3	3	3	-
st221	3709	OBS (AWI)	MCS	H	1	-	-	-	-
st222	3961	OBS (GEOMAR)	MBS	H,X,Y,Z	1	2	2	2	-
st223	4257	OBS (GEOMAR)	MBS	H,X,Y,Z	1	2-3	2-3	2	-
st224	4493	OBS (AWI)	MCS	H	1-2	-	-	-	-
st225	4562	OBS (GEOMAR)	MBS	H,X,Y,Z	1-2	3	2-3	2-3	-
st226	4593	OBS (AWI)	MCS	H	2	-	-	-	-
st227	4550	OBH (GEOMAR)	MBS	H	1-2	-	-	-	-
st228	4610	OBS (GEOMAR)	MBS	H,X,Y,Z	1-2	1-2	1-2	1-2	-
st229	4636	OBS (GEOMAR)	Geolog	H,X,Y,Z,H	1	2	2	2	1
st230	4678	OBS (AWI)	MCS	H,X,Y,Z	1	2	2	1	-
st231	4706	OBS (GEOMAR)	MBS	H,X,Y,Z	2	3	3	2	-
st232	4760	OBS (GEOMAR)	MBS	H,X,Y,Z	1	2-3	2-3	2-3	-
st233	4801	OBS (AWI)	MCS	H	3	-	-	-	-
st234	4711	OBS (GEOMAR)	MBS	H,X,Y,Z	4	2-3	3	3	-
st235	4888	OBS (GEOMAR)	MBS	H,X,Y,Z	2	2-3	2-3	2	-

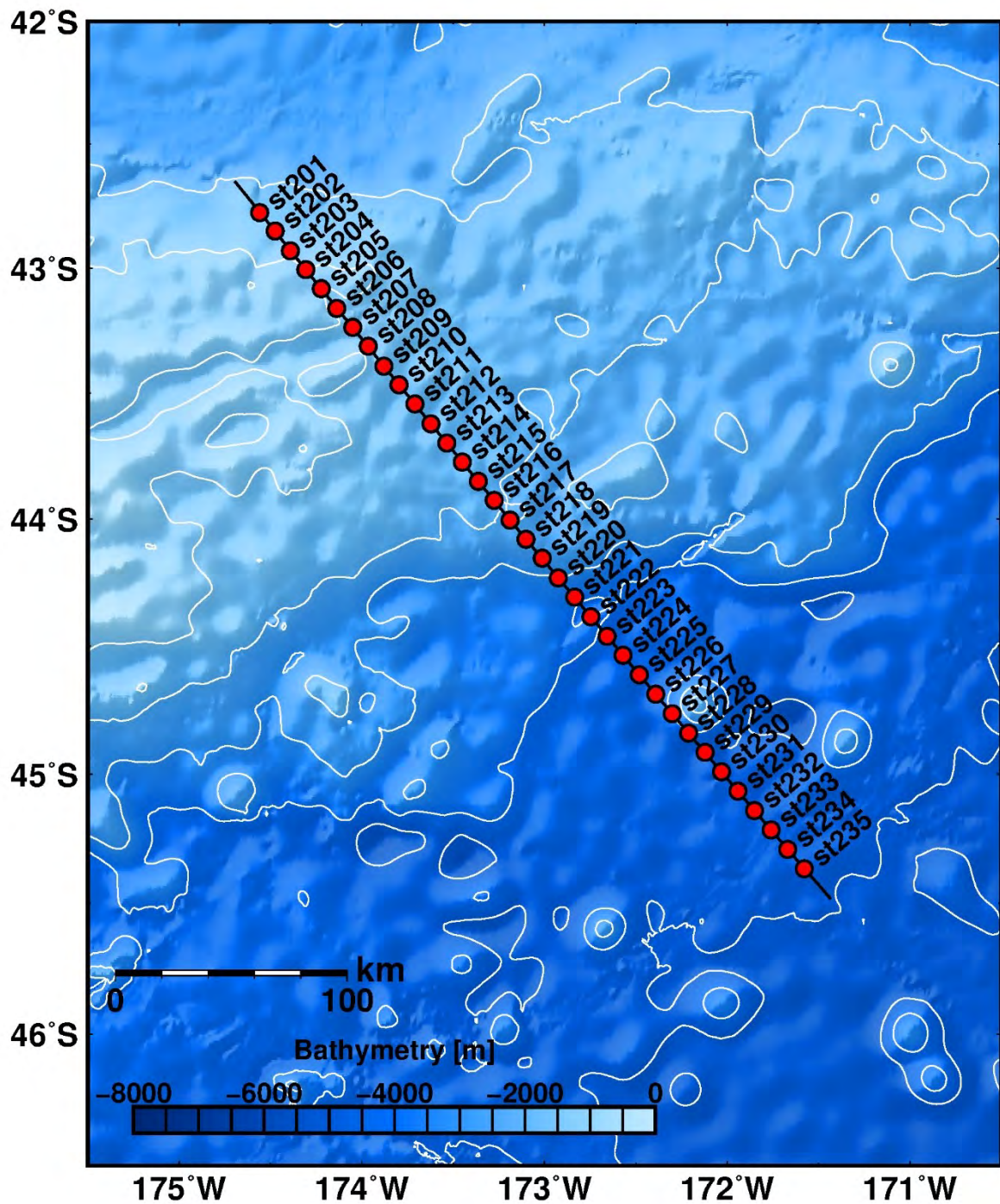


Fig. A38: Bathymetric map of the southern Chatham Rise margin and deployed OBS / OBH stations (red circles) along profile AWI-20160200.

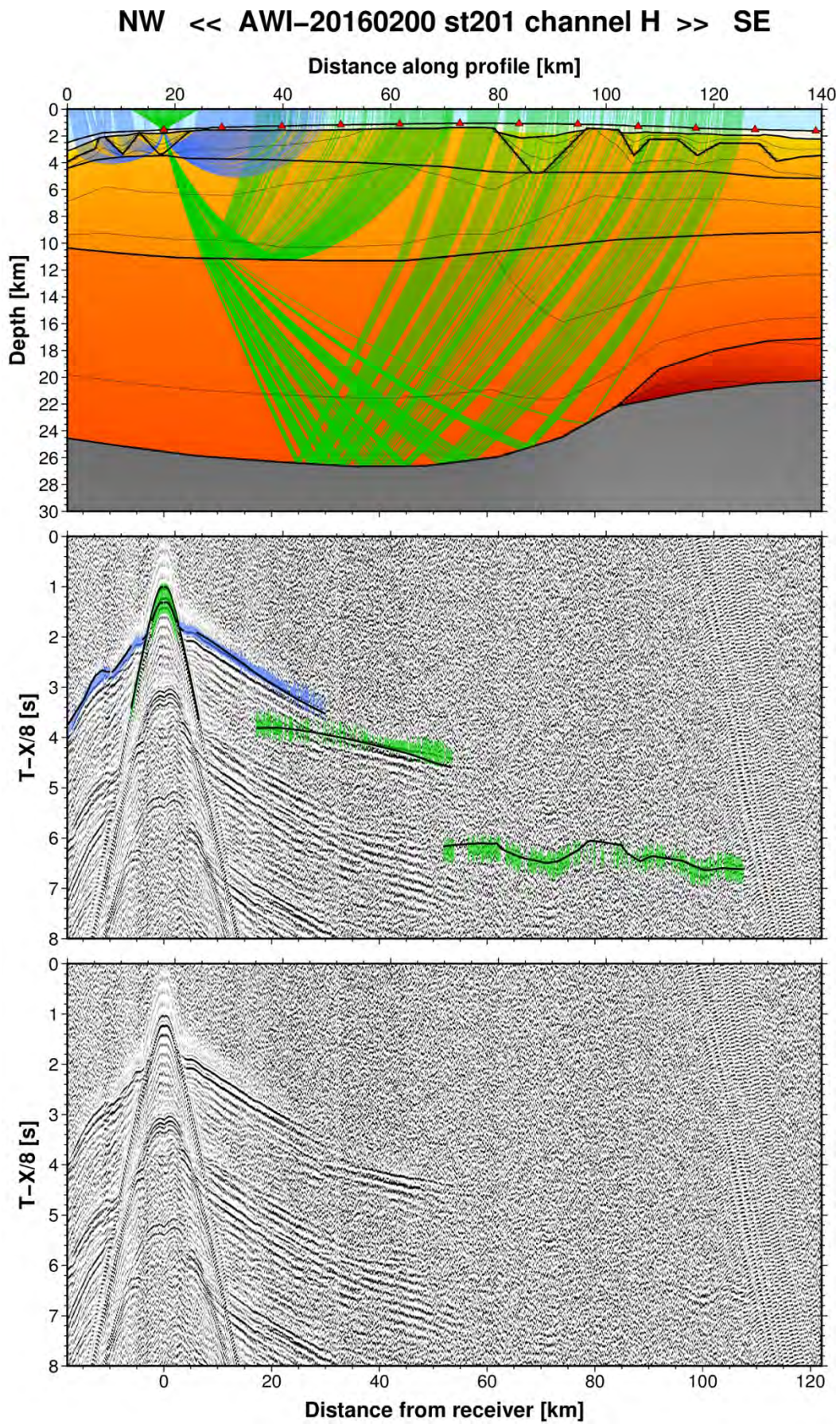


Fig. A39: Ray tracing results for station st201 along profile AWI-20160200. Lower panel: Seismic record; Middle panel: Picked and modelled arrival times; Upper panel: Section of the resulting P-wave velocity model; Green colours = reflections, blue colours = refractions.

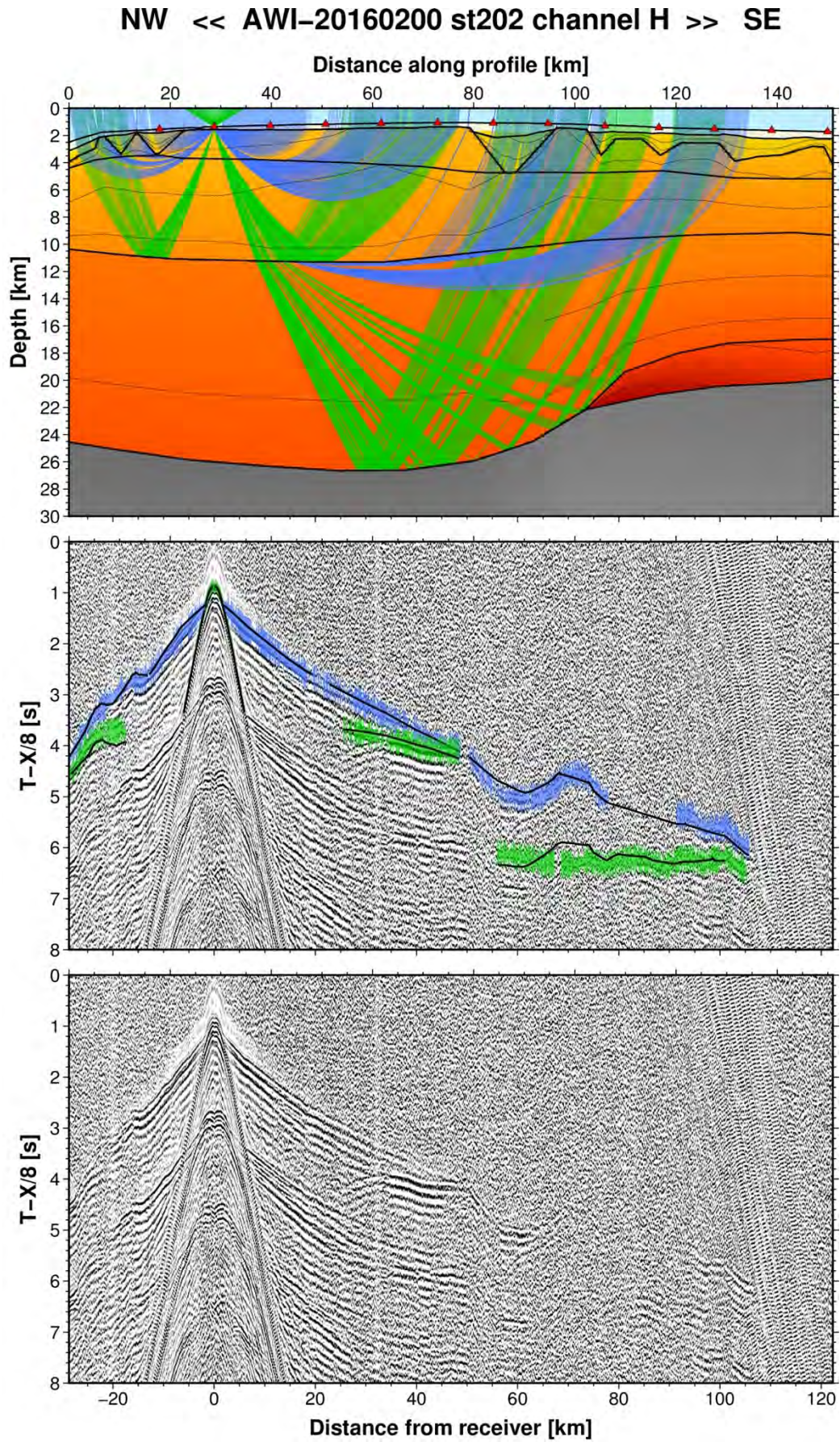


Fig. A40: Ray tracing results for station st202 along profile AWI-20160200. Lower panel: Seismic record; Middle panel: Picked and modelled arrival times; Upper panel: Section of the resulting P-wave velocity model; Green colours = reflections, blue colours = refractions.

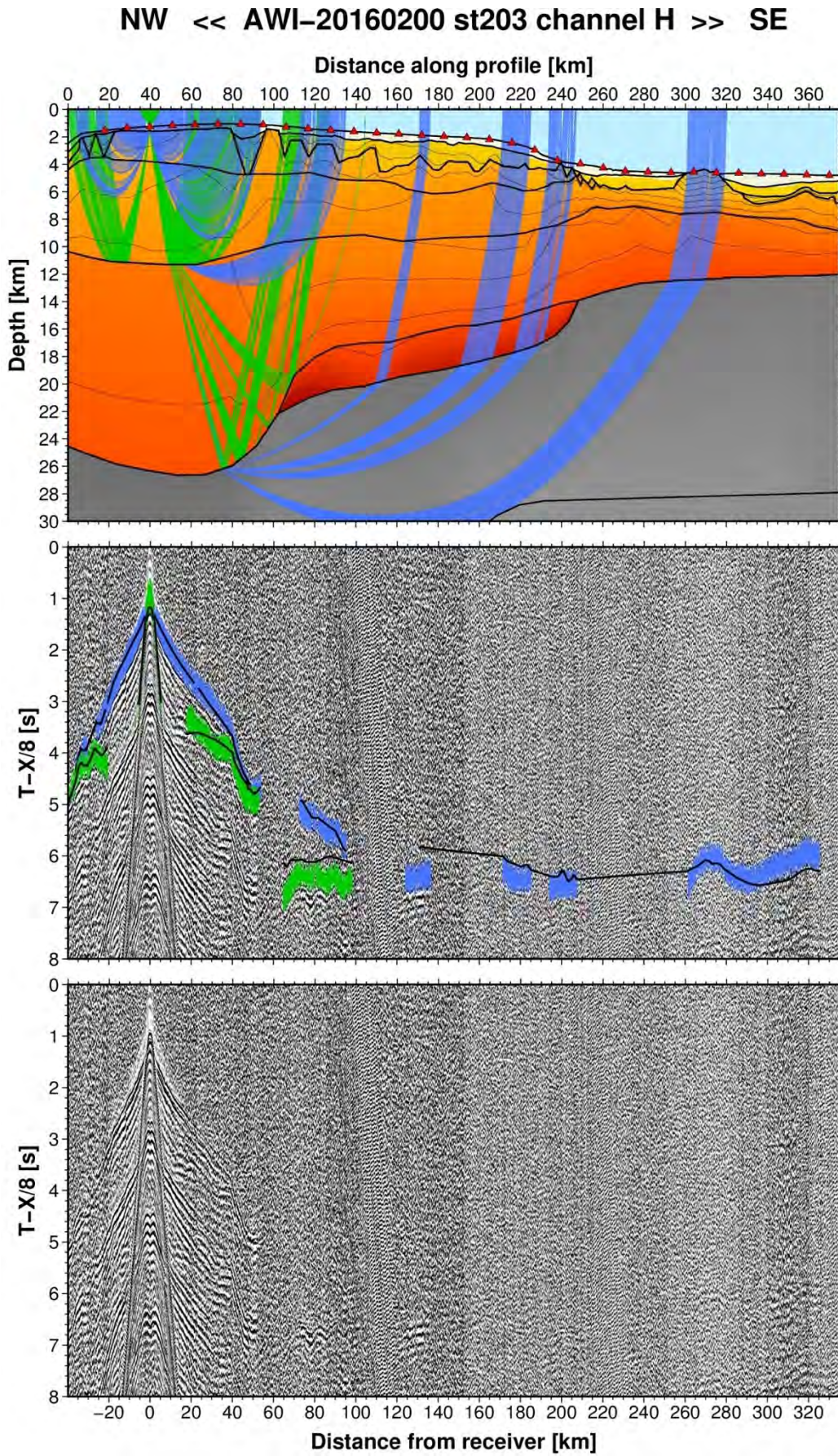


Fig. A41: Ray tracing results for station st203 along profile AWI-20160200. Lower panel: Seismic record; Middle panel: Picked and modelled arrival times; Upper panel: Section of the resulting P-wave velocity model; Green colours = reflections, blue colours = refractions.

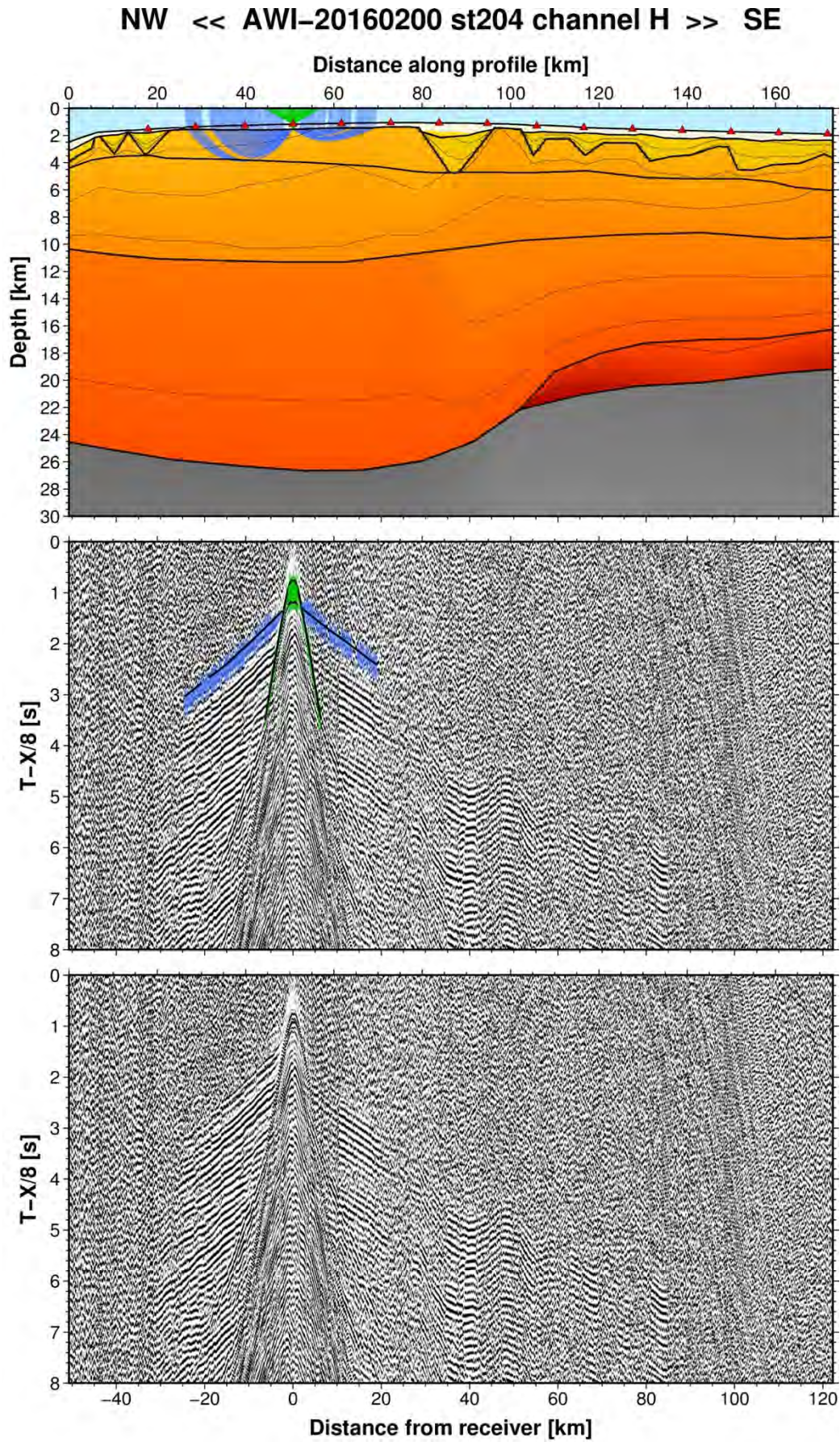


Fig. A42: Ray tracing results for station st204 along profile AWI-20160200. Lower panel: Seismic record; Middle panel: Picked and modelled arrival times; Upper panel: Section of the resulting P-wave velocity model; Green colours = reflections, blue colours = refractions.

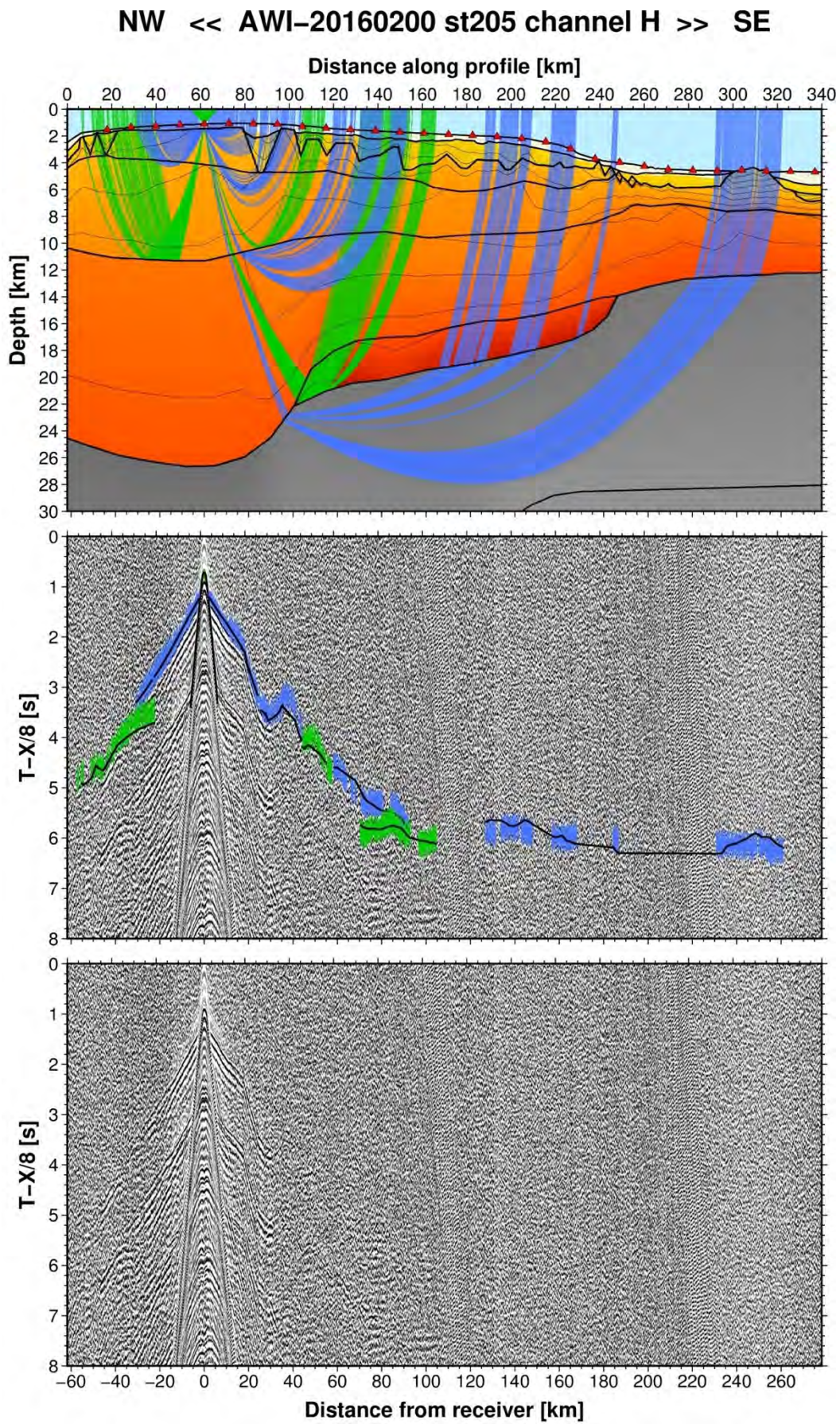


Fig. A43: Ray tracing results for station st205 along profile AWI-20160200. Lower panel: Seismic record; Middle panel: Picked and modelled arrival times; Upper panel: Section of the resulting P-wave velocity model; Green colours = reflections, blue colours = refractions.

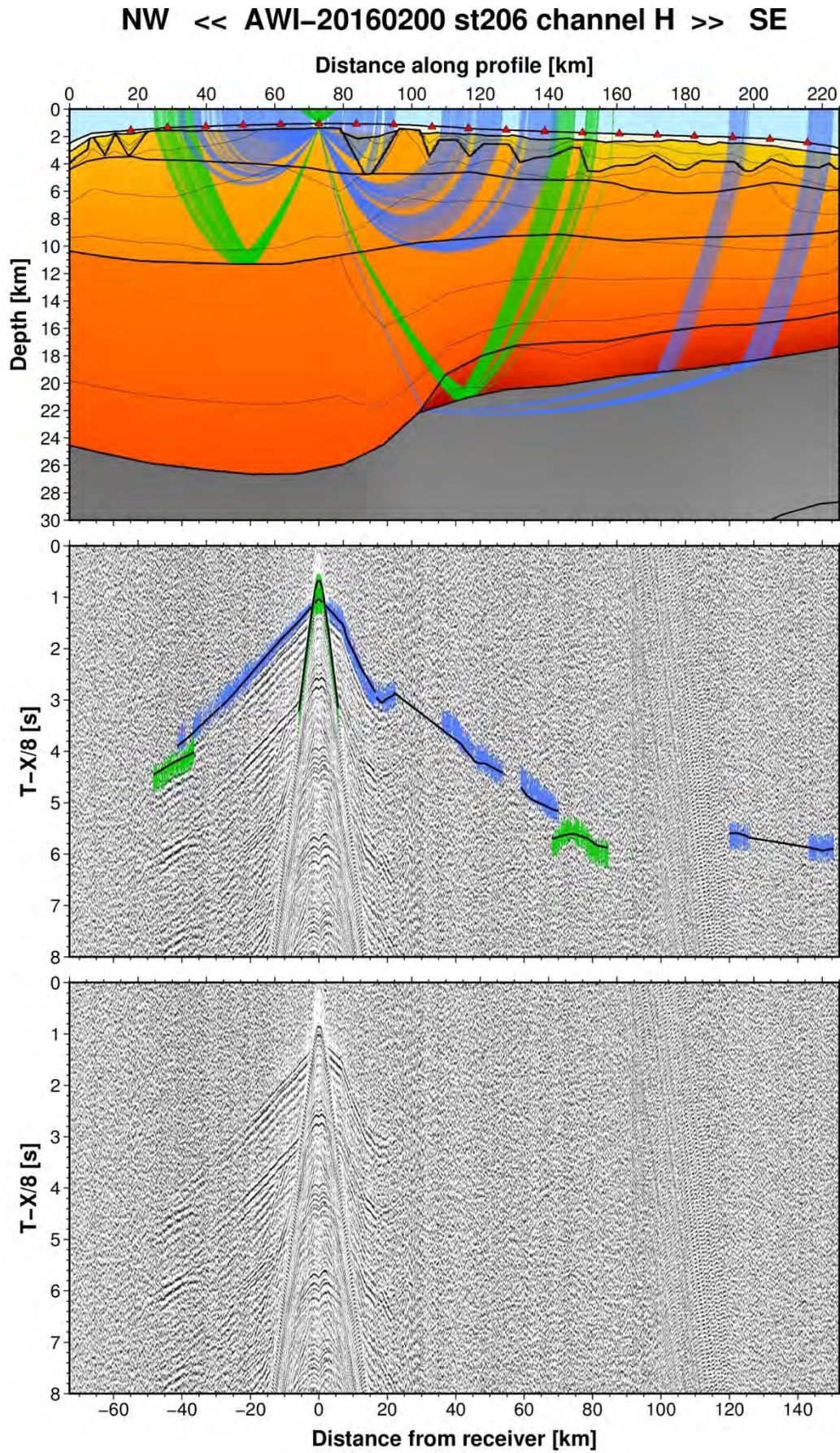


Fig. A44: Ray tracing results for station st206 along profile AWI-20160200. Lower panel: Seismic record; Middle panel: Picked and modelled arrival times; Upper panel: Section of the resulting P-wave velocity model; Green colours = reflections, blue colours = refractions.

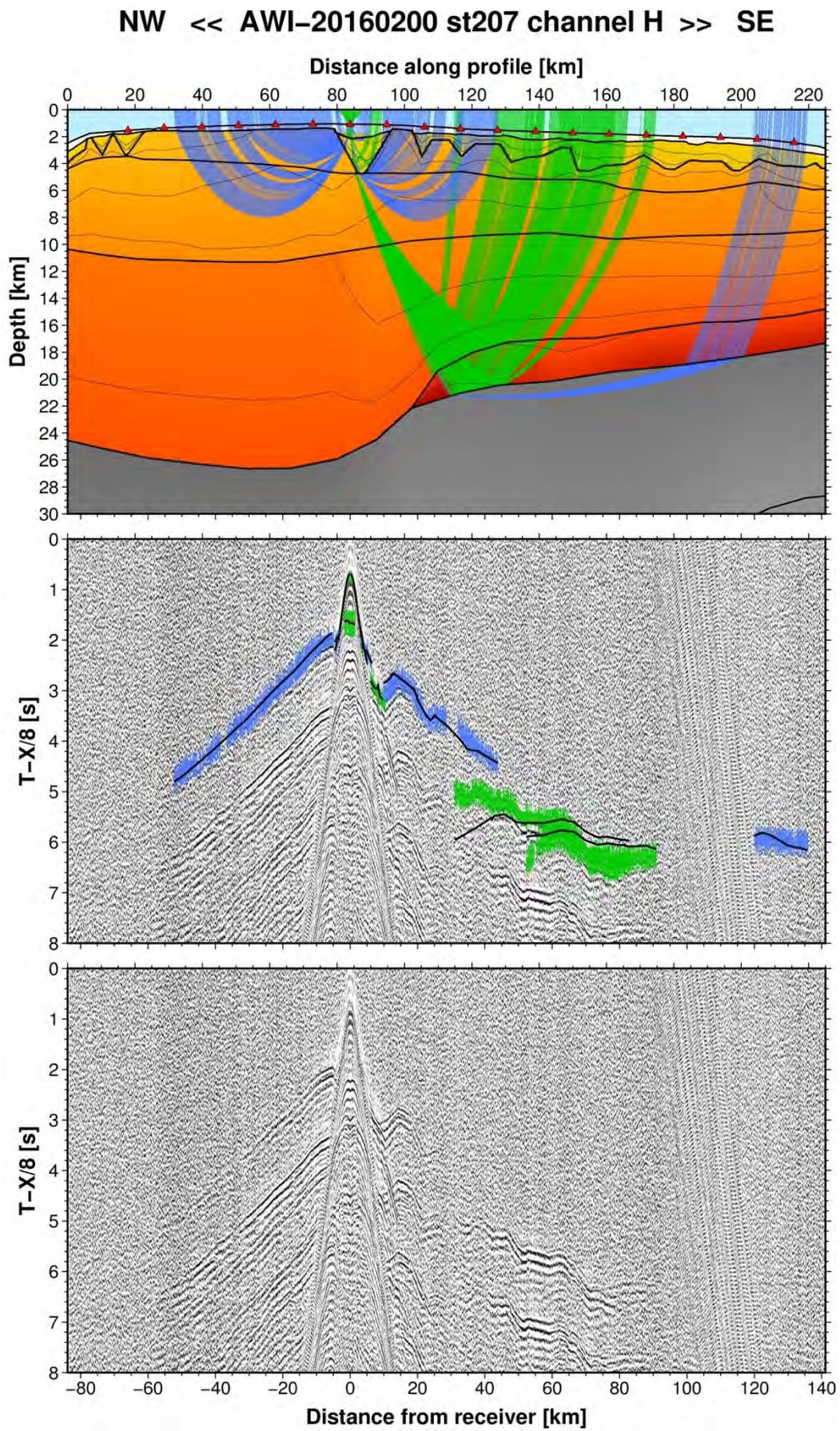


Fig. A45: Ray tracing results for station st207 along profile AWI-20160200. Lower panel: Seismic record; Middle panel: Picked and modelled arrival times; Upper panel: Section of the resulting P-wave velocity model; Green colours = reflections, blue colours = refractions.

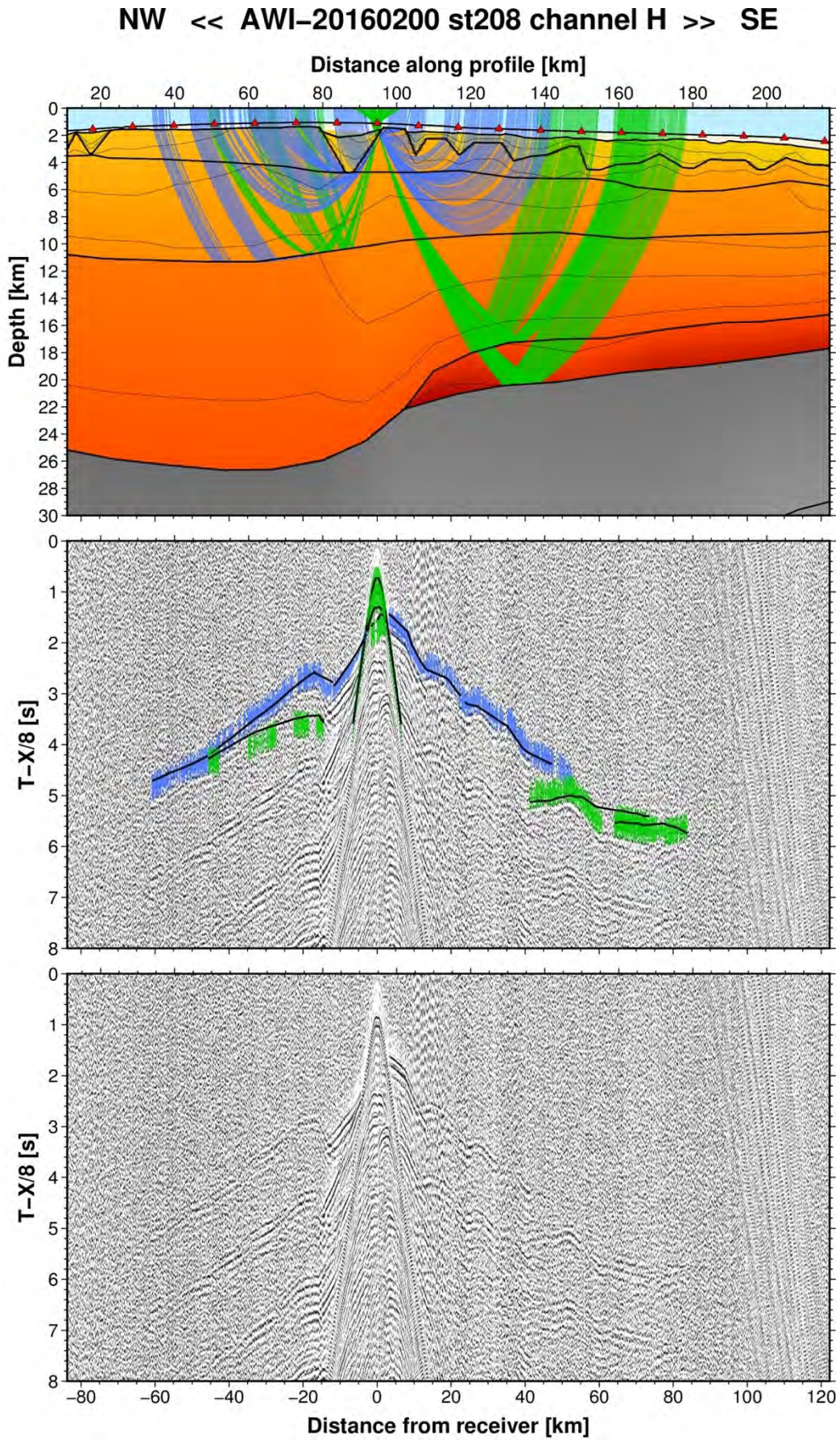


Fig. A46: Ray tracing results for station st208 along profile AWI-20160200. Lower panel: Seismic record; Middle panel: Picked and modelled arrival times; Upper panel: Section of the resulting P-wave velocity model; Green colours = reflections, blue colours = refractions.

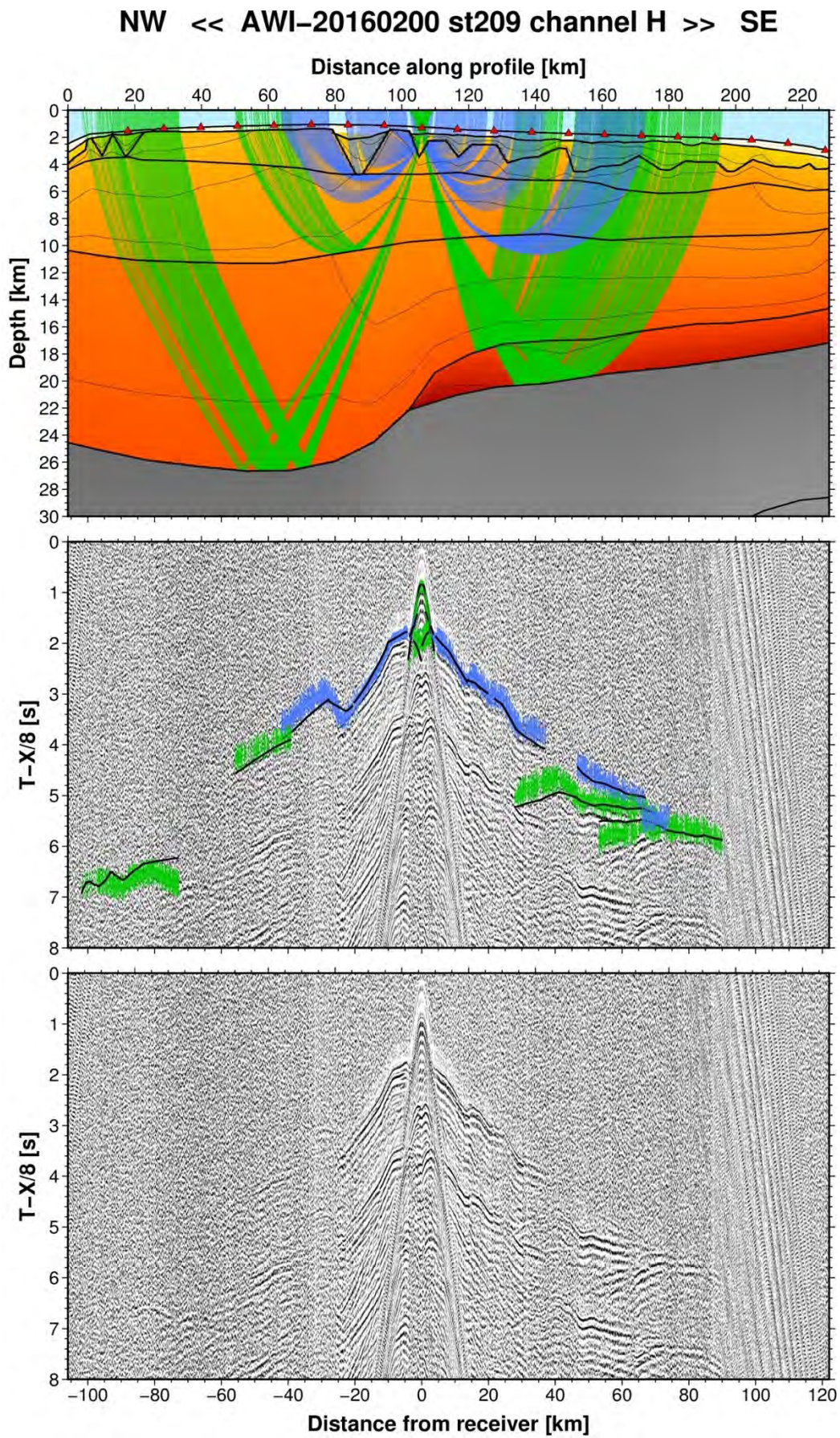


Fig. A47: Ray tracing results for station st209 along profile AWI-20160200. Lower panel: Seismic record; Middle panel: Picked and modelled arrival times; Upper panel: Section of the resulting P-wave velocity model; Green colours = reflections, blue colours = refractions.

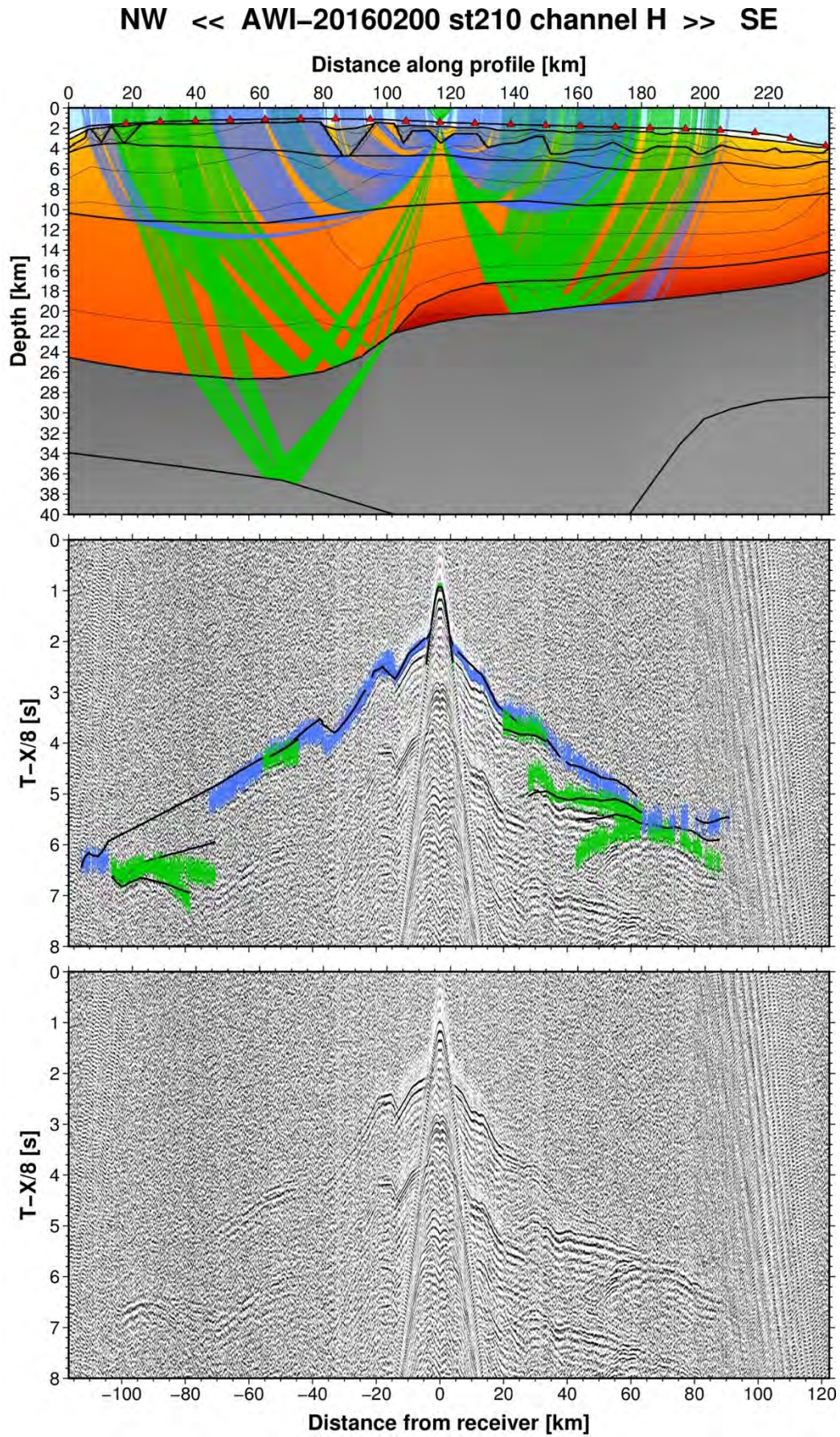


Fig. A48: Ray tracing results for station st210 along profile AWI-20160200. Lower panel: Seismic record; Middle panel: Picked and modelled arrival times; Upper panel: Section of the resulting P-wave velocity model; Green colours = reflections, blue colours = refractions.

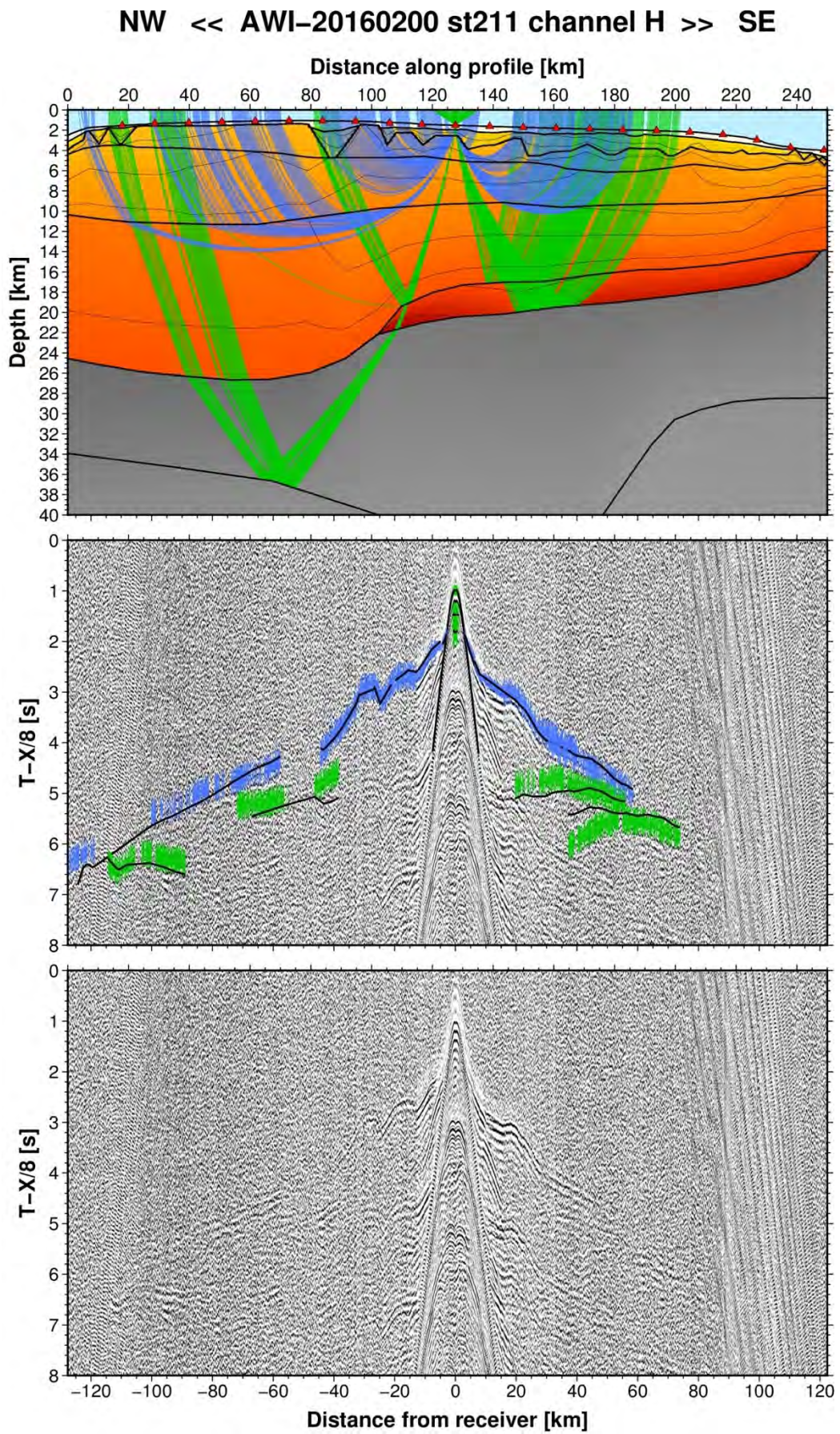


Fig. A49: Ray tracing results for station st211 along profile AWI-20160200. Lower panel: Seismic record; Middle panel: Picked and modelled arrival times; Upper panel: Section of the resulting P-wave velocity model; Green colours = reflections, blue colours = refractions.

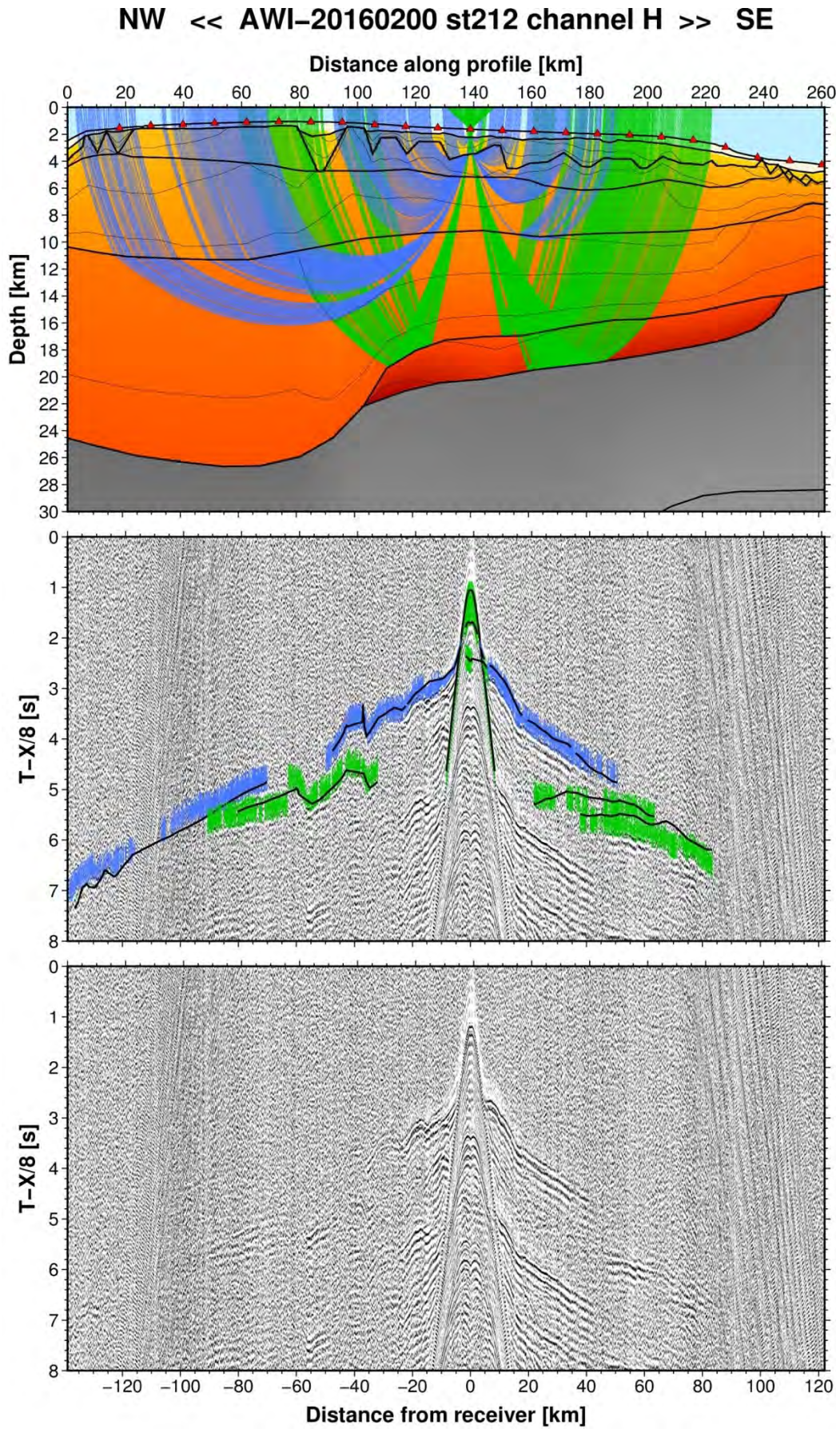


Fig. A50: Ray tracing results for station st212 along profile AWI-20160200. Lower panel: Seismic record; Middle panel: Picked and modelled arrival times; Upper panel: Section of the resulting P-wave velocity model; Green colours = reflections, blue colours = refractions.

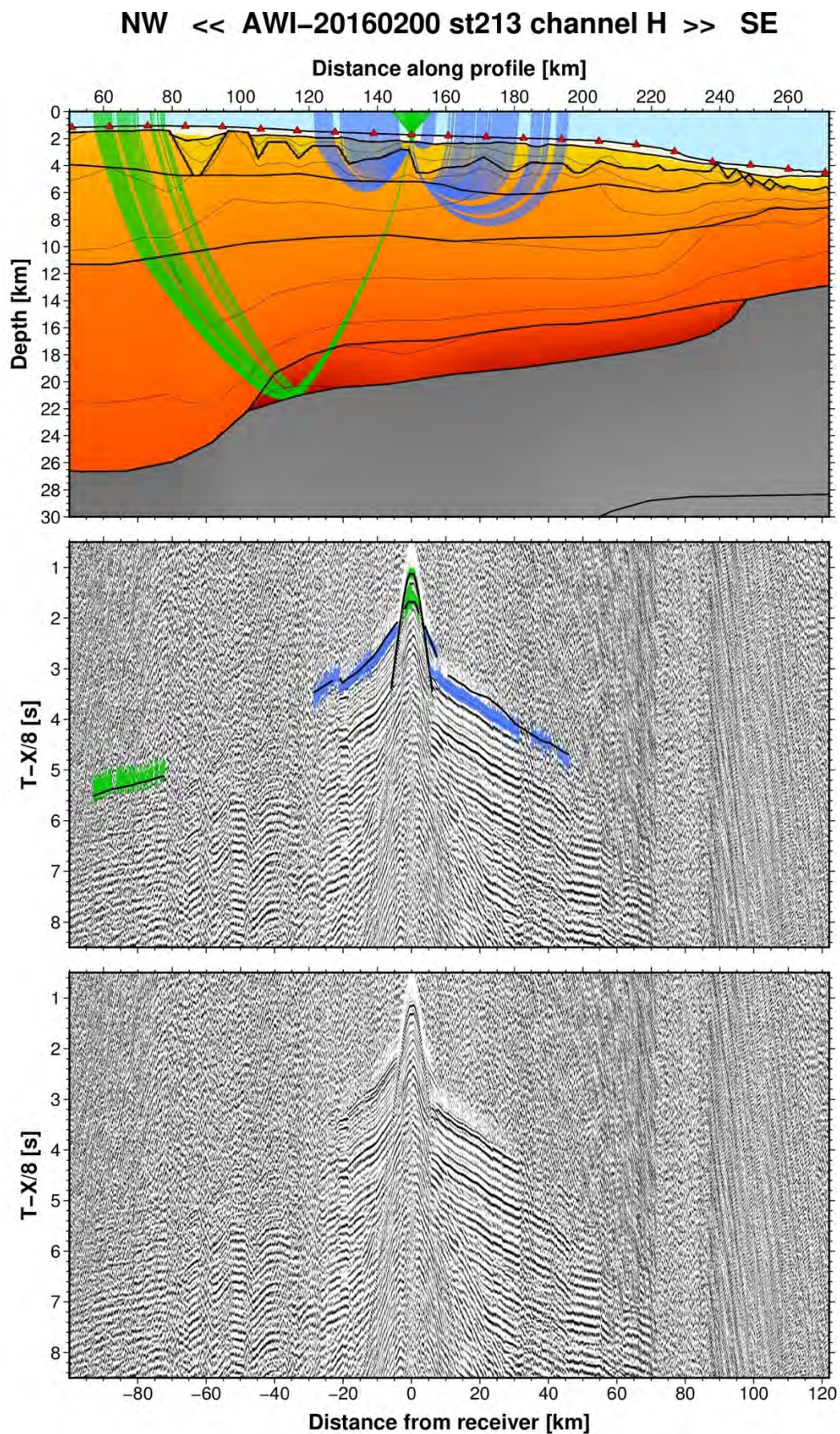


Fig. A51: Ray tracing results for station st213 along profile AWI-20160200. Lower panel: Seismic record; Middle panel: Picked and modelled arrival times; Upper panel: Section of the resulting P-wave velocity model; Green colours = reflections, blue colours = refractions.

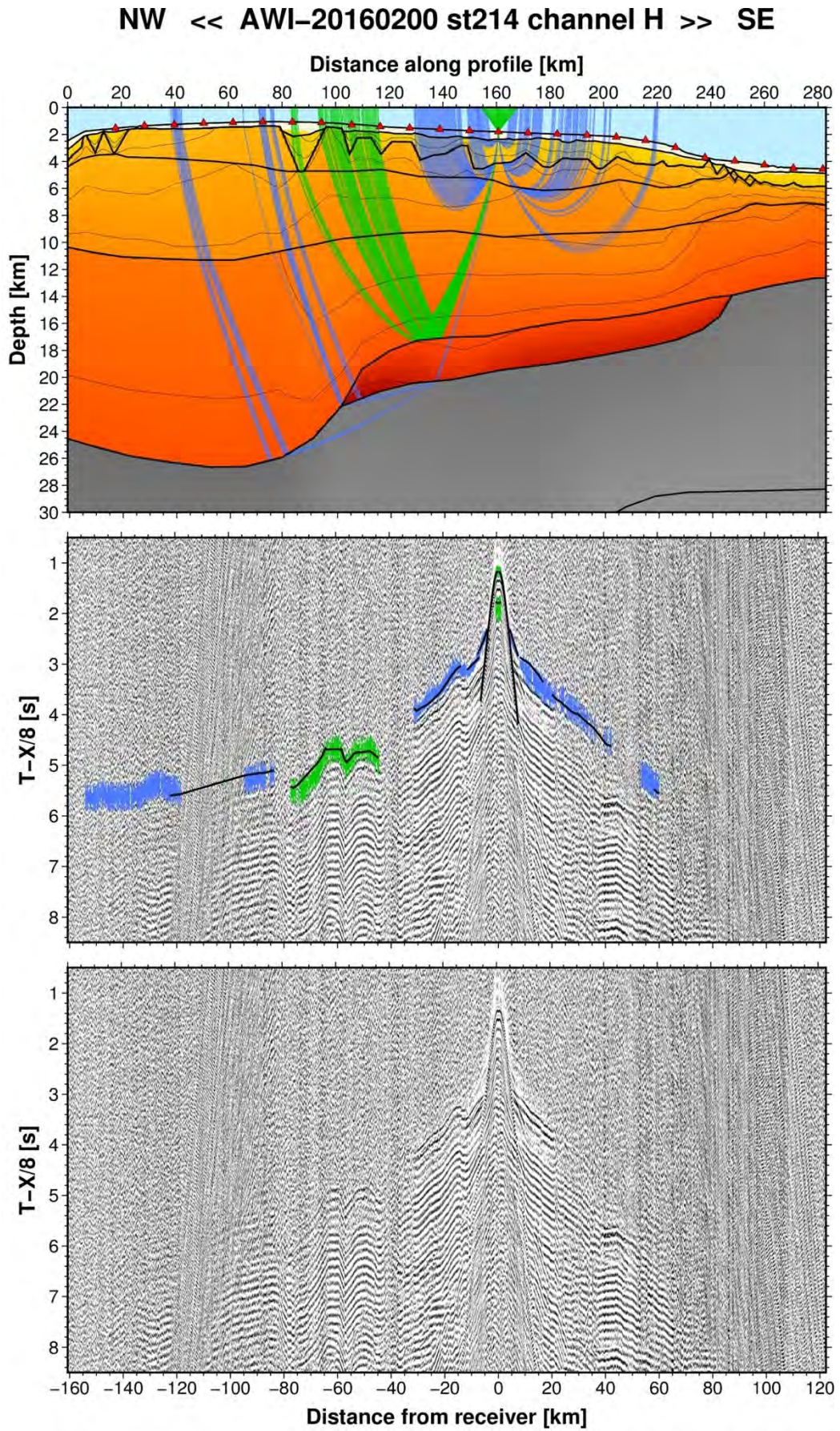


Fig. A52: Ray tracing results for station st214 along profile AWI-20160200. Lower panel: Seismic record; Middle panel: Picked and modelled arrival times; Upper panel: Section of the resulting P-wave velocity model; Green colours = reflections, blue colours = refractions.

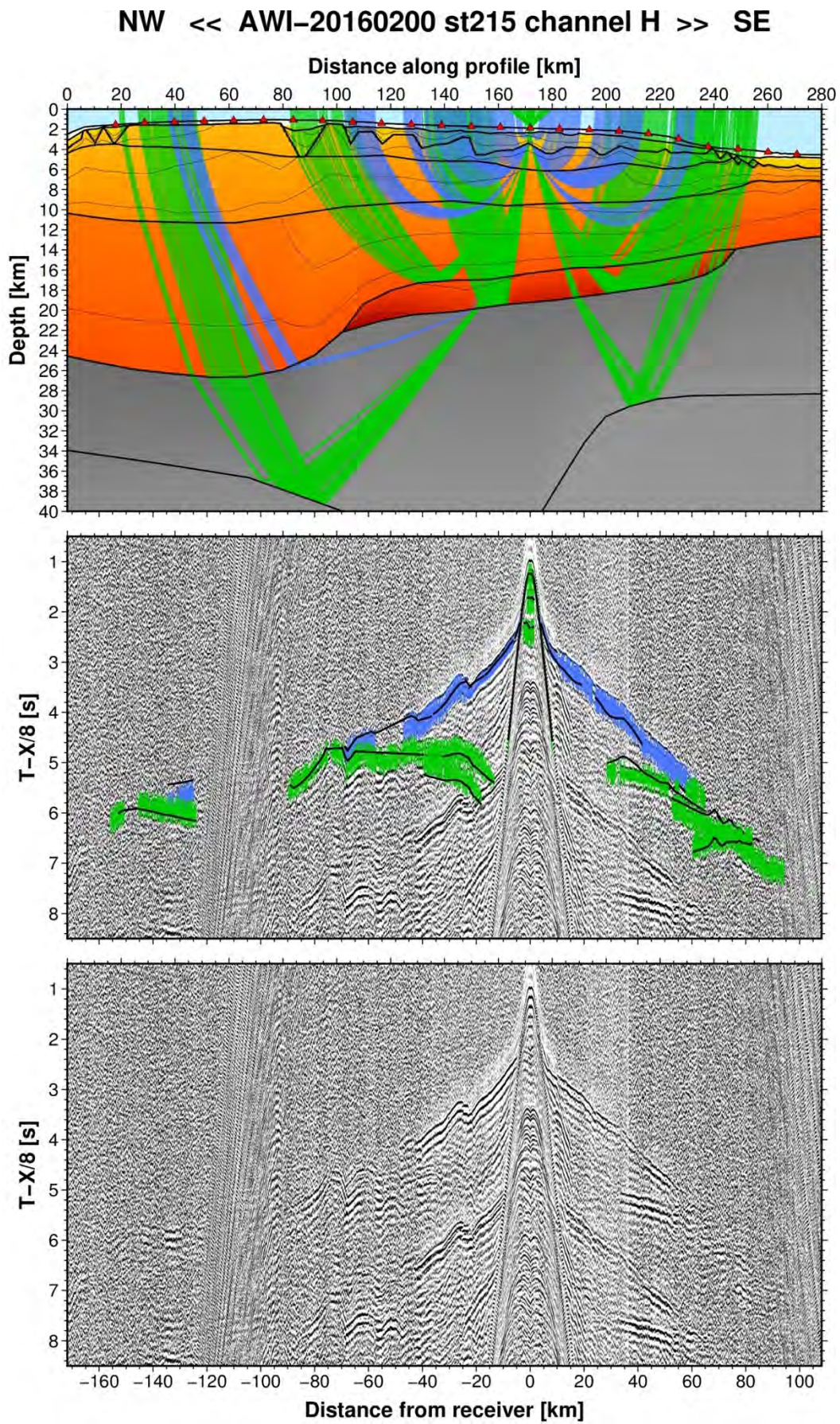


Fig. A53: Ray tracing results for station st215 along profile AWI-20160200. Lower panel: Seismic record; Middle panel: Picked and modelled arrival times; Upper panel: Section of the resulting P-wave velocity model; Green colours = reflections, blue colours = refractions.

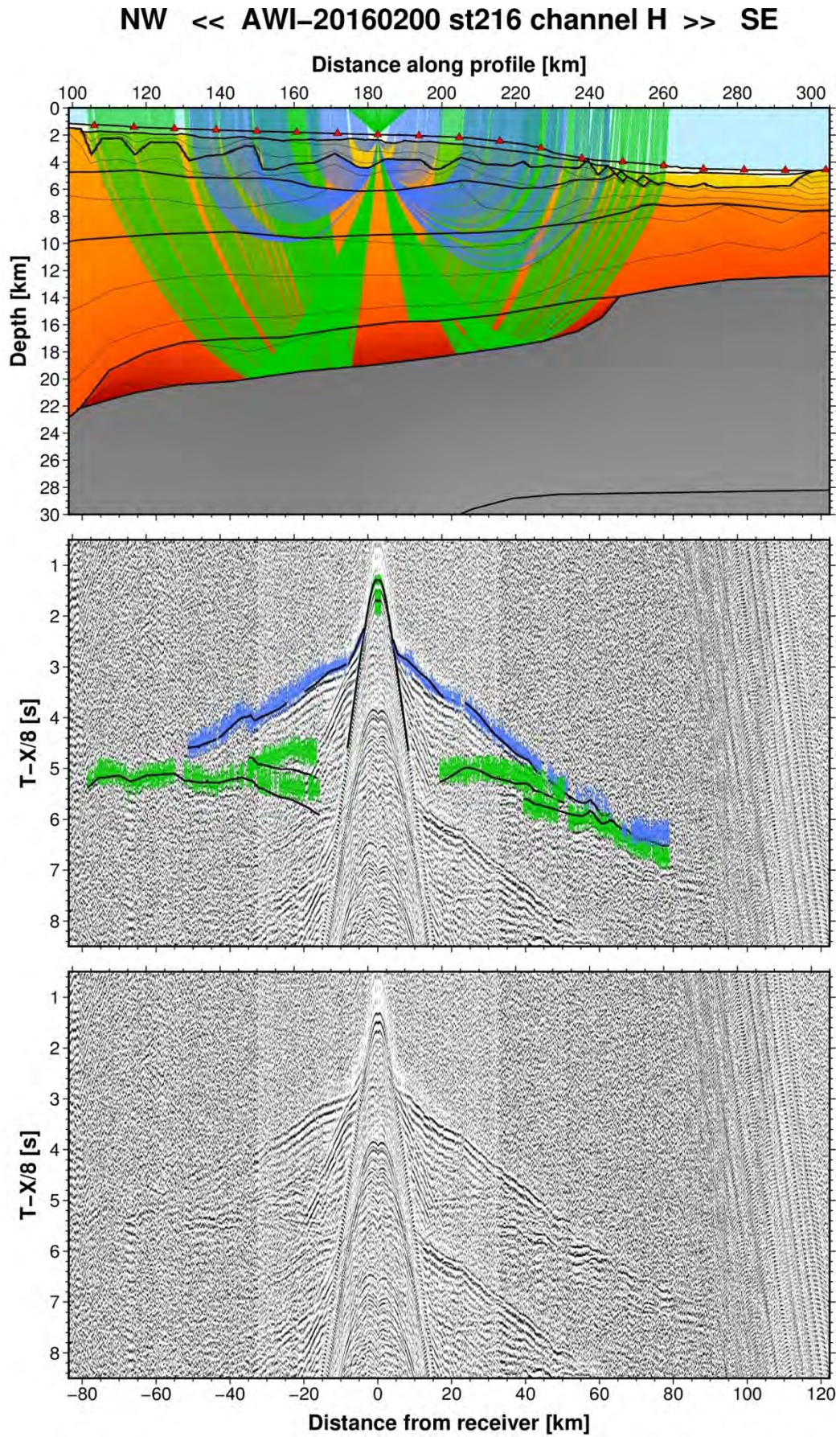


Fig. A54: Ray tracing results for station st216 along profile AWI-20160200. Lower panel: Seismic record; Middle panel: Picked and modelled arrival times; Upper panel: Section of the resulting P-wave velocity model; Green colours = reflections, blue colours = refractions.

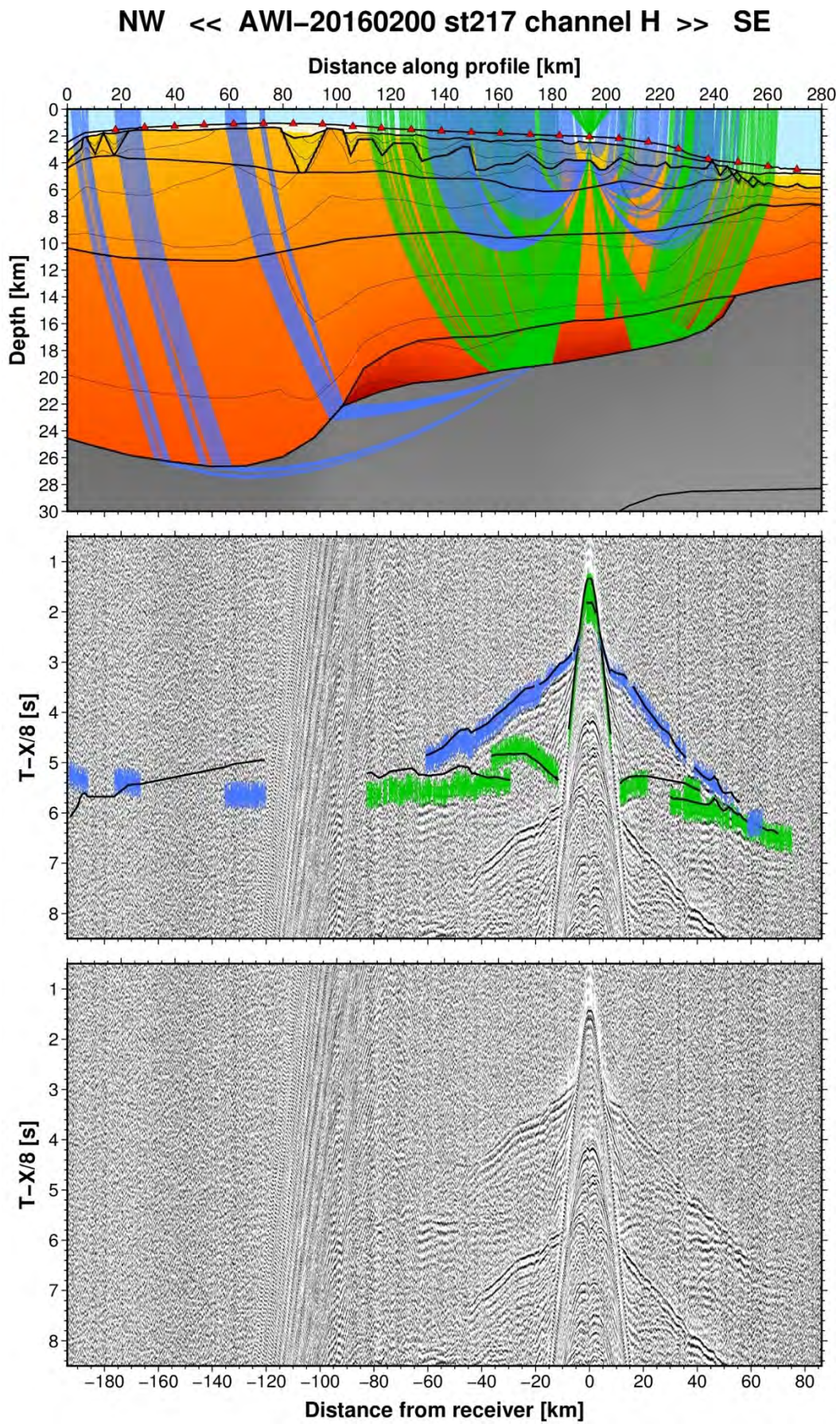


Fig. A55: Ray tracing results for station st217 along profile AWI-20160200. Lower panel: Seismic record; Middle panel: Picked and modelled arrival times; Upper panel: Section of the resulting P-wave velocity model; Green colours = reflections, blue colours = refractions.

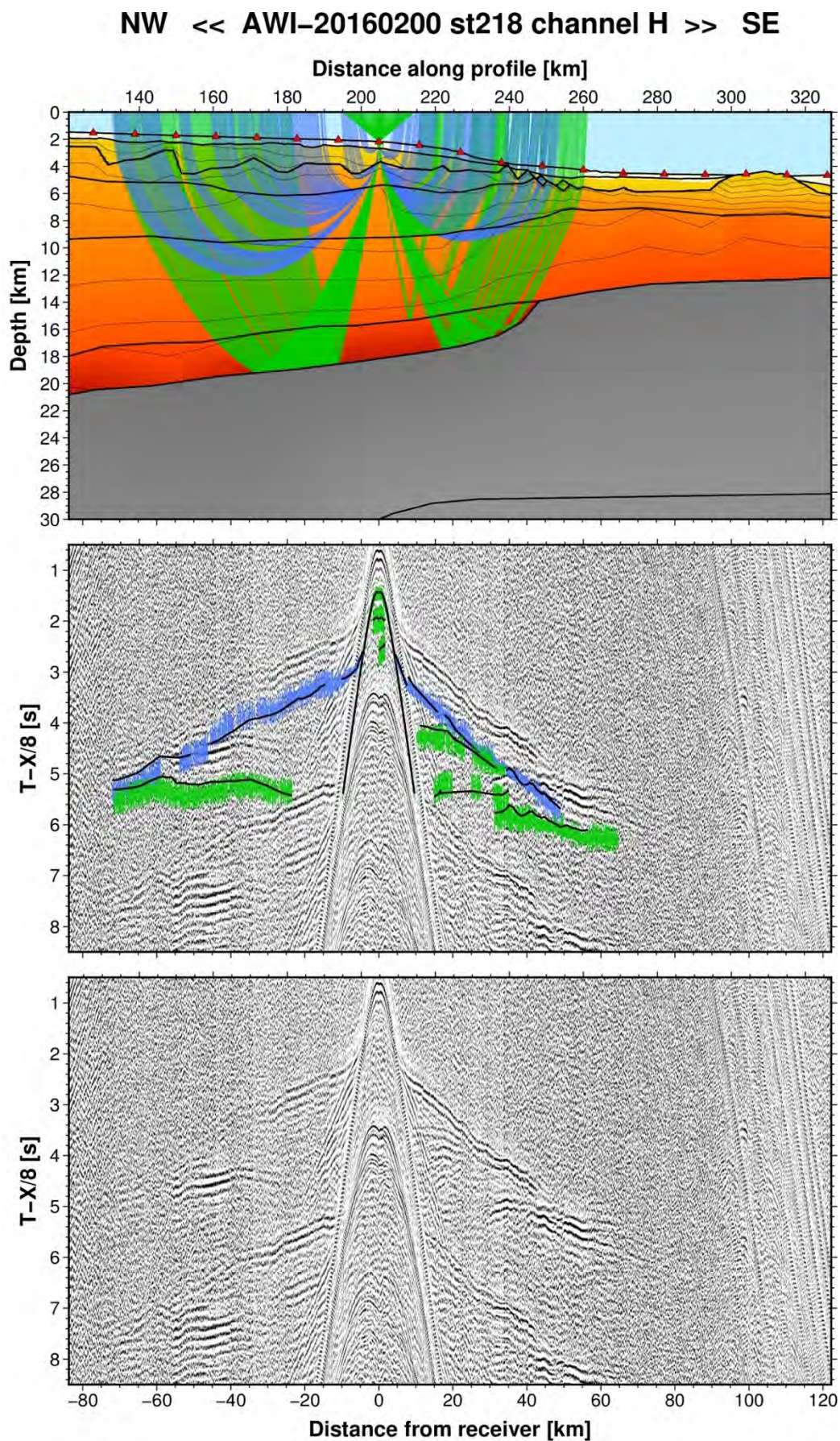


Fig. A56: Ray tracing results for station st218 along profile AWI-20160200. Lower panel: Seismic record; Middle panel: Picked and modelled arrival times; Upper panel: Section of the resulting P-wave velocity model; Green colours = reflections, blue colours = refractions.

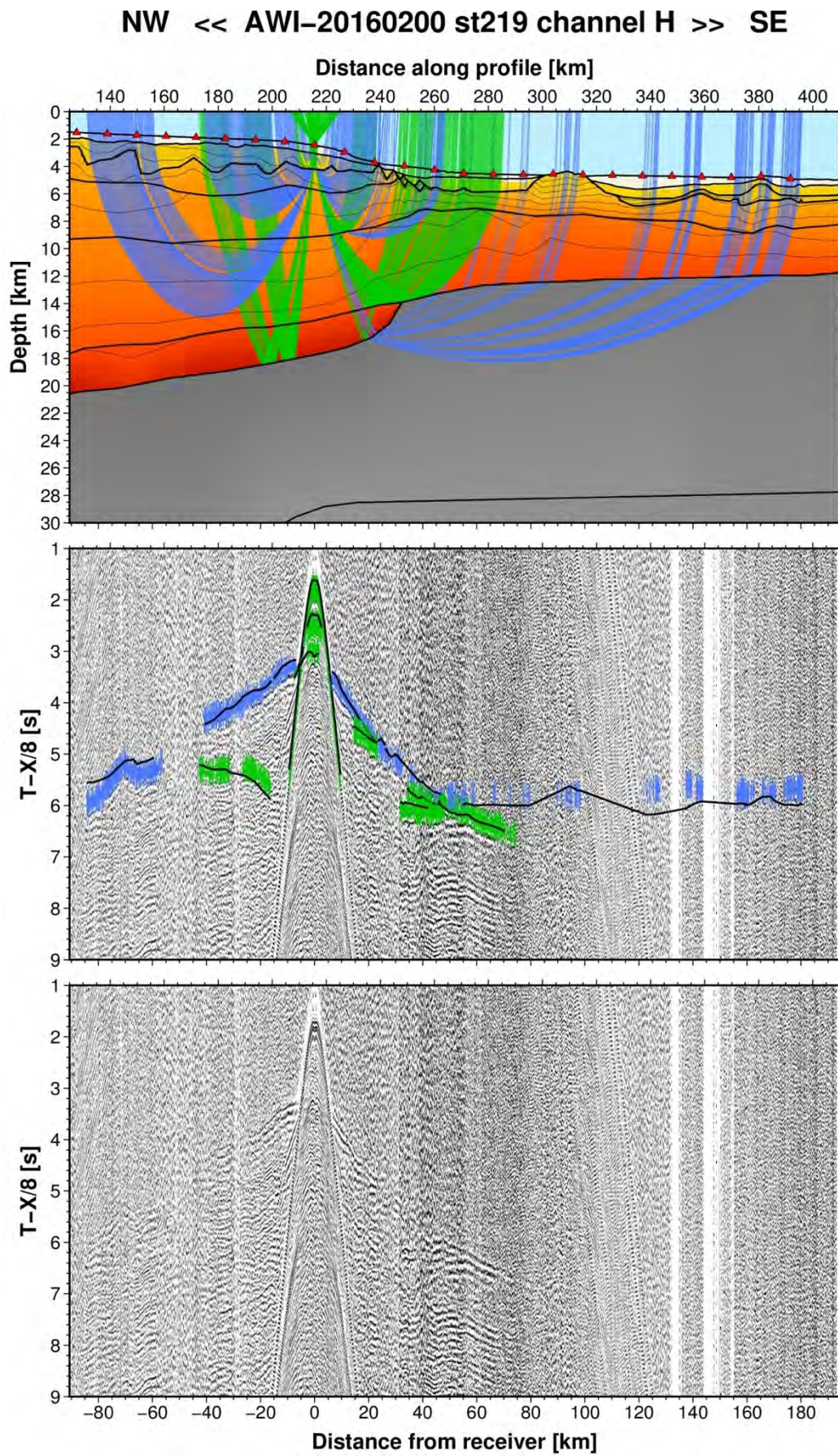


Fig. A57: Ray tracing results for station st219 along profile AWI-20160200. Lower panel: Seismic record; Middle panel: Picked and modelled arrival times; Upper panel: Section of the resulting P-wave velocity model; Green colours = reflections, blue colours = refractions.

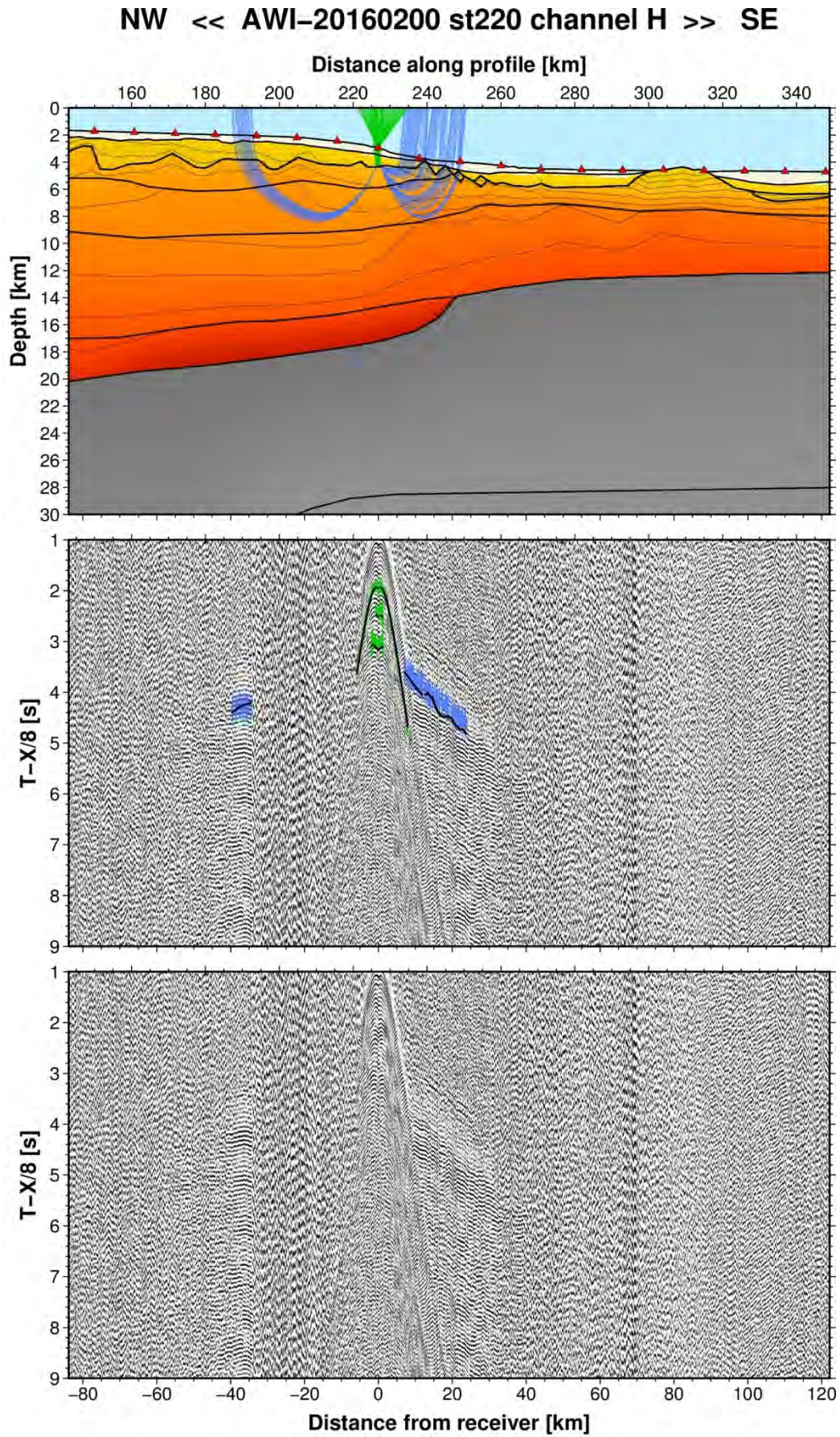


Fig. A58: Ray tracing results for station st220 along profile AWI-20160200. Lower panel: Seismic record; Middle panel: Picked and modelled arrival times; Upper panel: Section of the resulting P-wave velocity model; Green colours = reflections, blue colours = refractions.

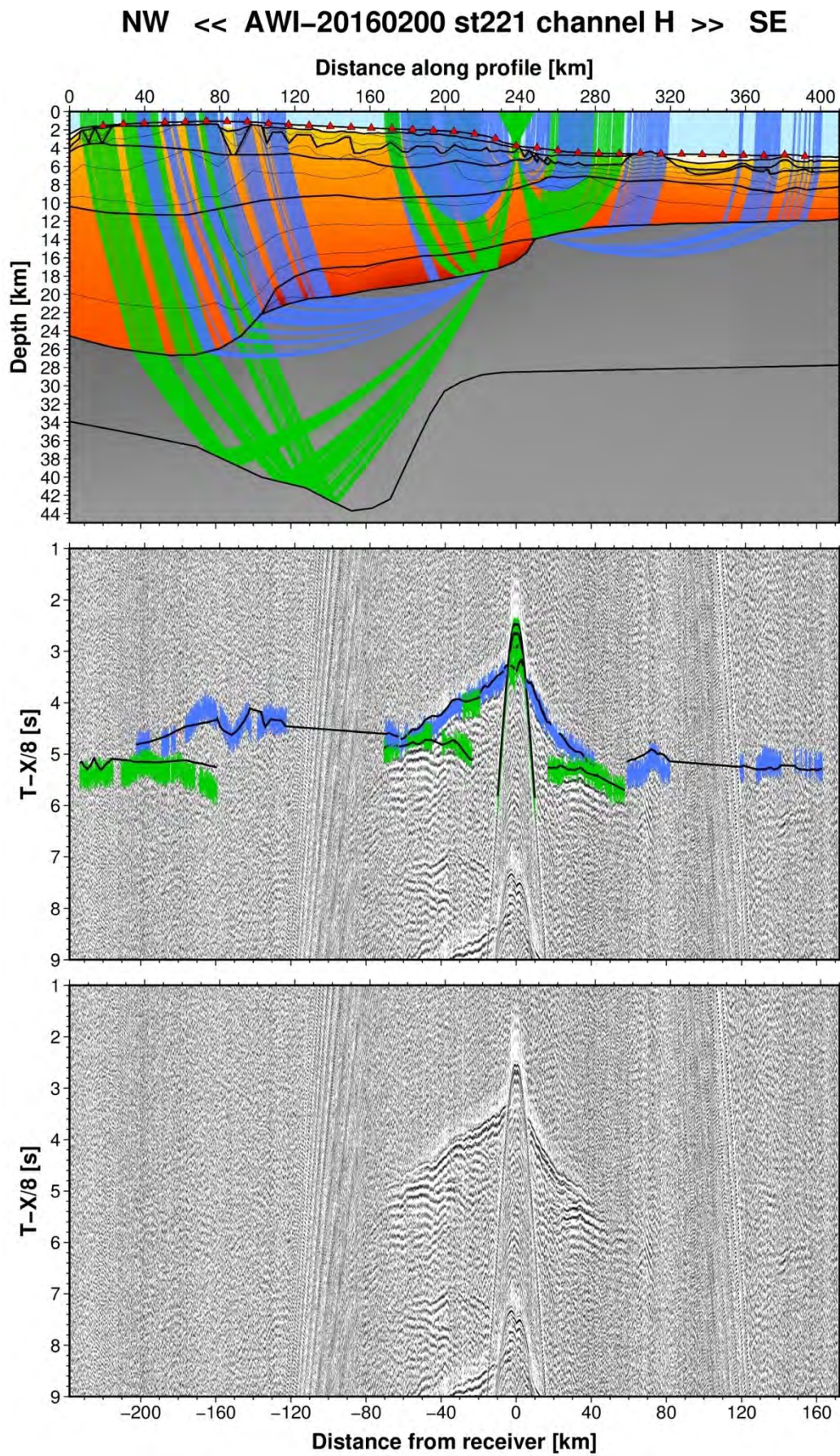


Fig. A59: Ray tracing results for station st221 along profile AWI-20160200. Lower panel: Seismic record; Middle panel: Picked and modelled arrival times; Upper panel: Section of the resulting P-wave velocity model; Green colours = reflections, blue colours = refractions.

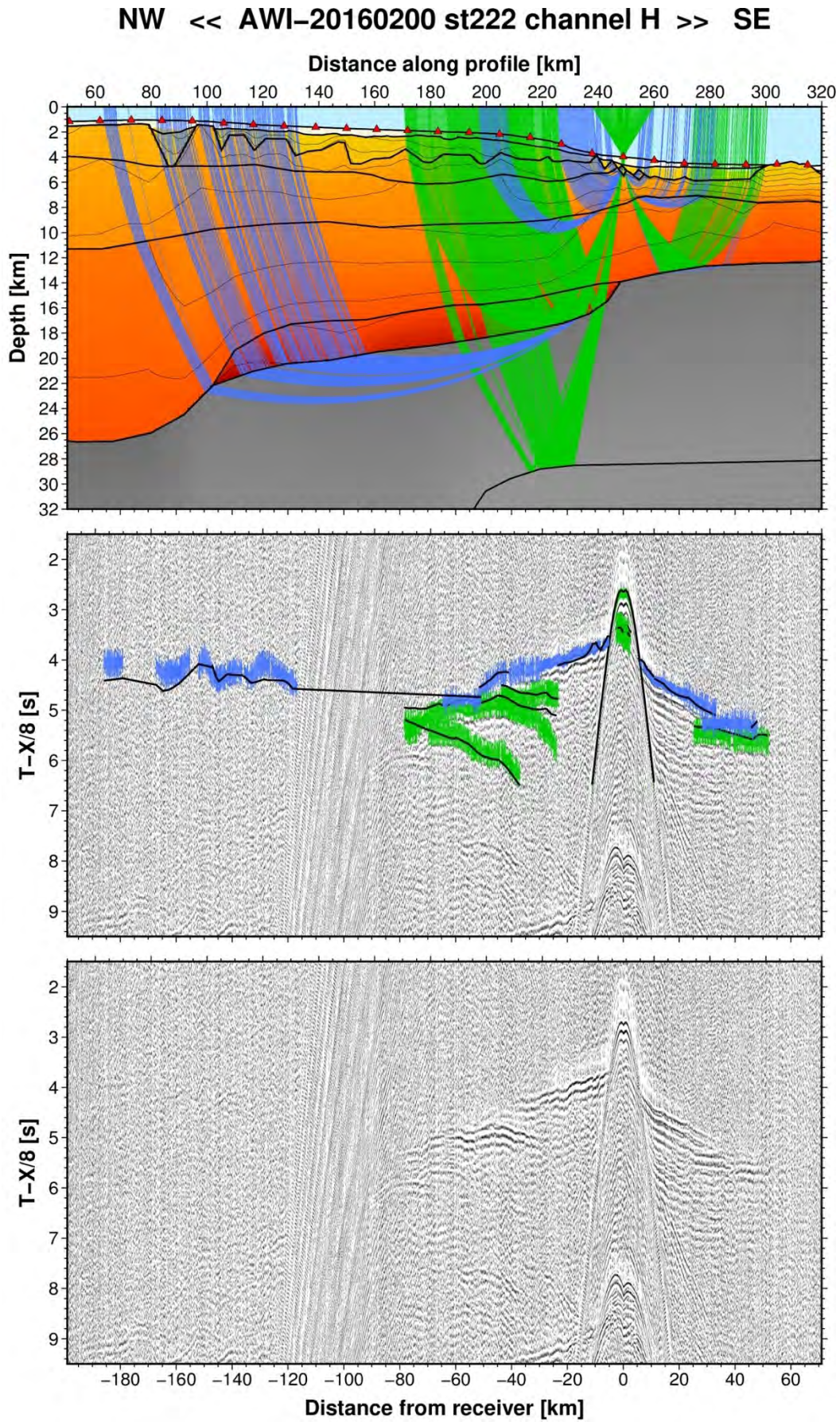


Fig. A60: Ray tracing results for station st222 along profile AWI-20160200. Lower panel: Seismic record; Middle panel: Picked and modelled arrival times; Upper panel: Section of the resulting P-wave velocity model; Green colours = reflections, blue colours = refractions.

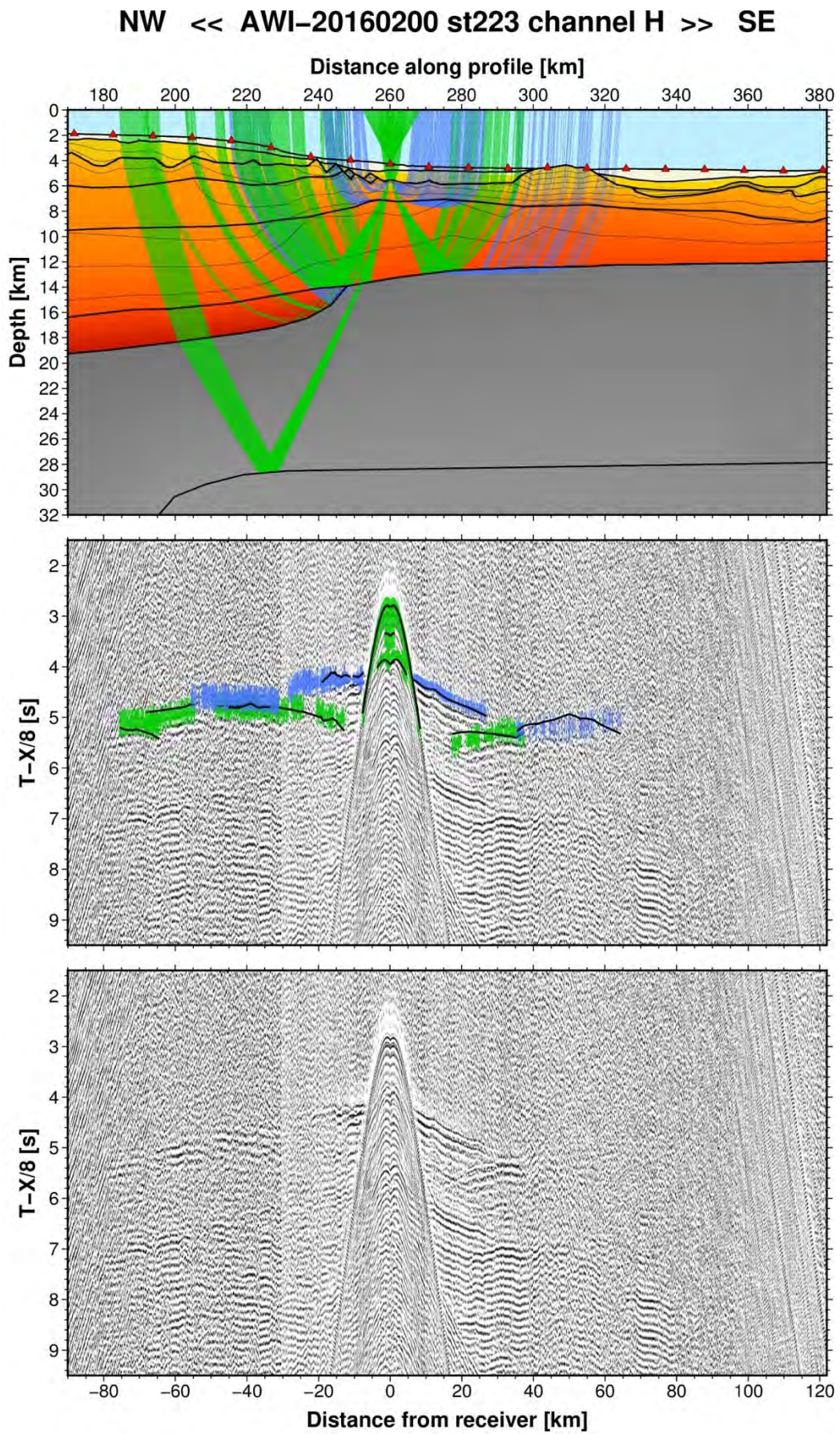


Fig. A61: Ray tracing results for station st223 along profile AWI-20160200. Lower panel: Seismic record; Middle panel: Picked and modelled arrival times; Upper panel: Section of the resulting P-wave velocity model; Green colours = reflections, blue colours = refractions.

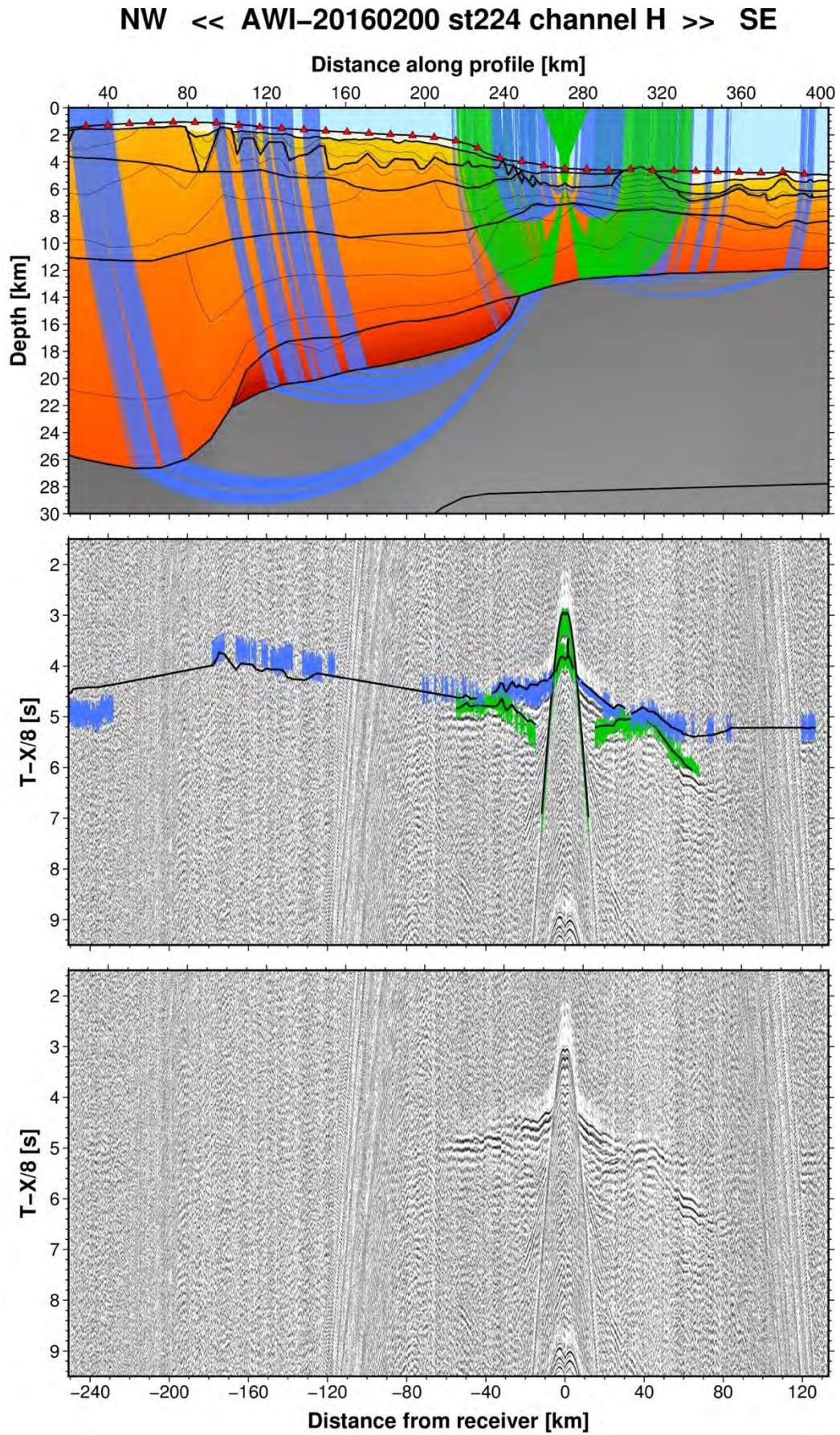


Fig. A62: Ray tracing results for station st224 along profile AWI-20160200. Lower panel: Seismic record; Middle panel: Picked and modelled arrival times; Upper panel: Section of the resulting P-wave velocity model; Green colours = reflections, blue colours = refractions.

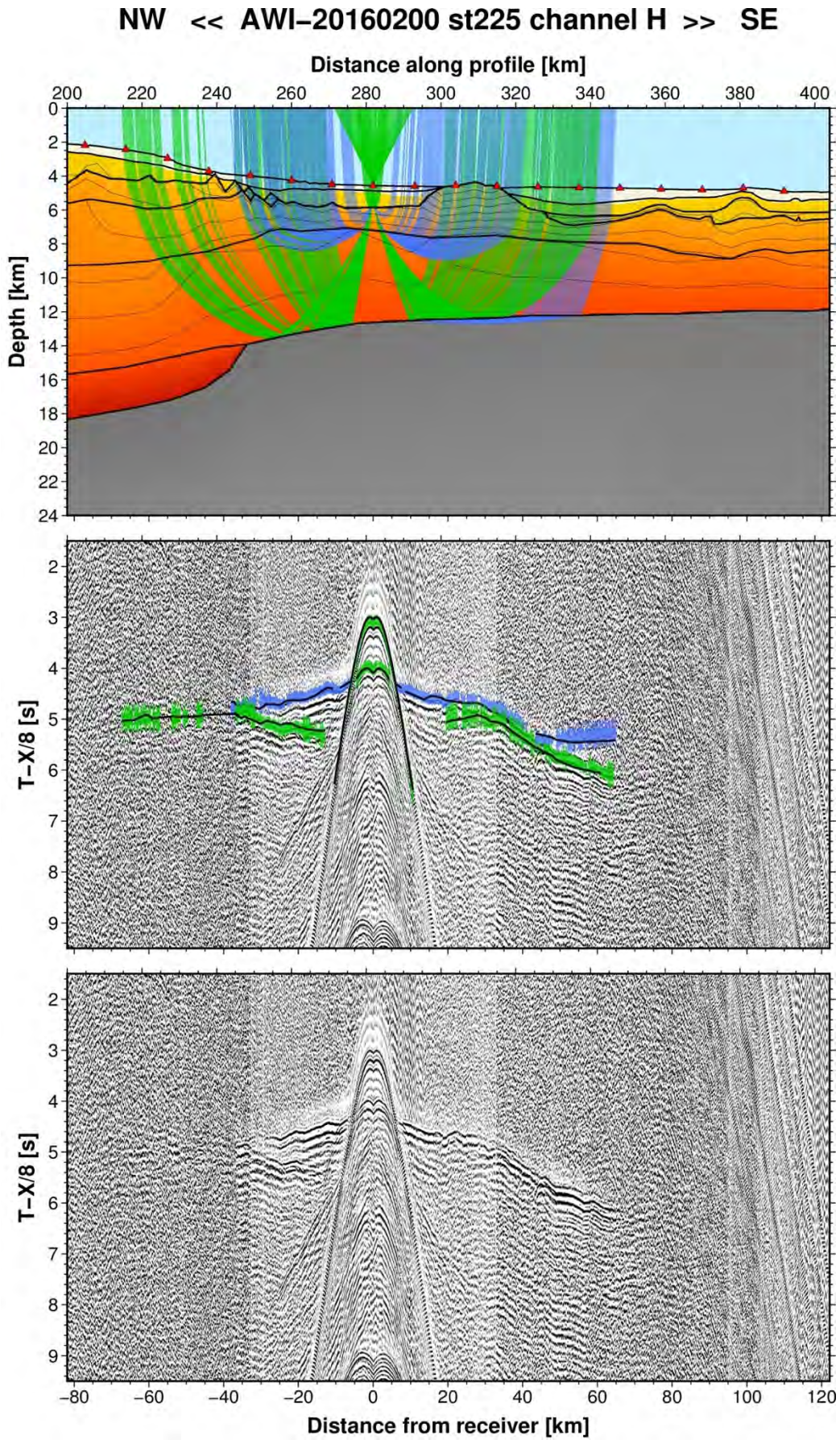


Fig. A63: Ray tracing results for station st225 along profile AWI-20160200. Lower panel: Seismic record; Middle panel: Picked and modelled arrival times; Upper panel: Section of the resulting P-wave velocity model; Green colours = reflections, blue colours = refractions.

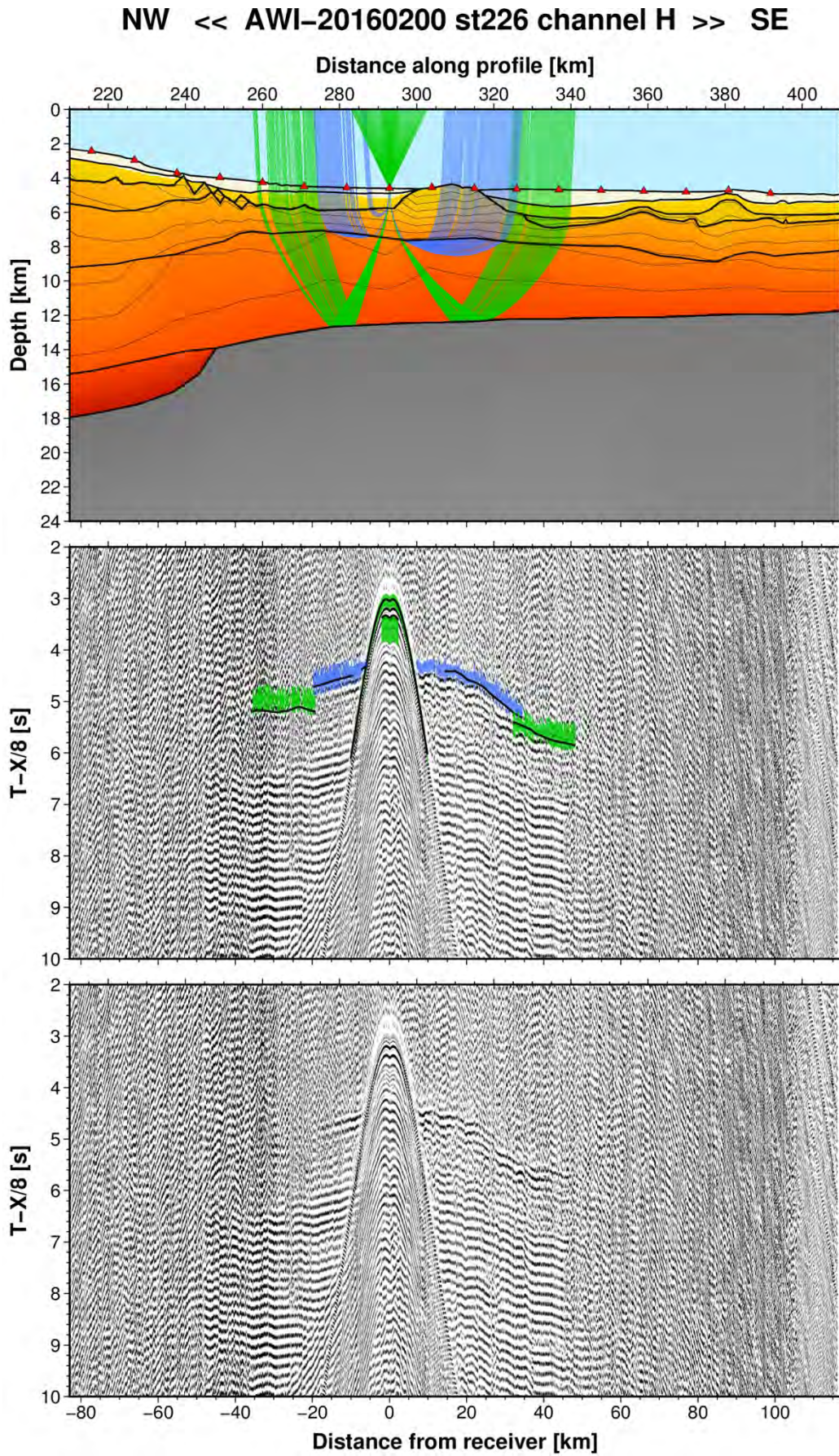


Fig. A64: Ray tracing results for station st226 along profile AWI-20160200. Lower panel: Seismic record; Middle panel: Picked and modelled arrival times; Upper panel: Section of the resulting P-wave velocity model; Green colours = reflections, blue colours = refractions.

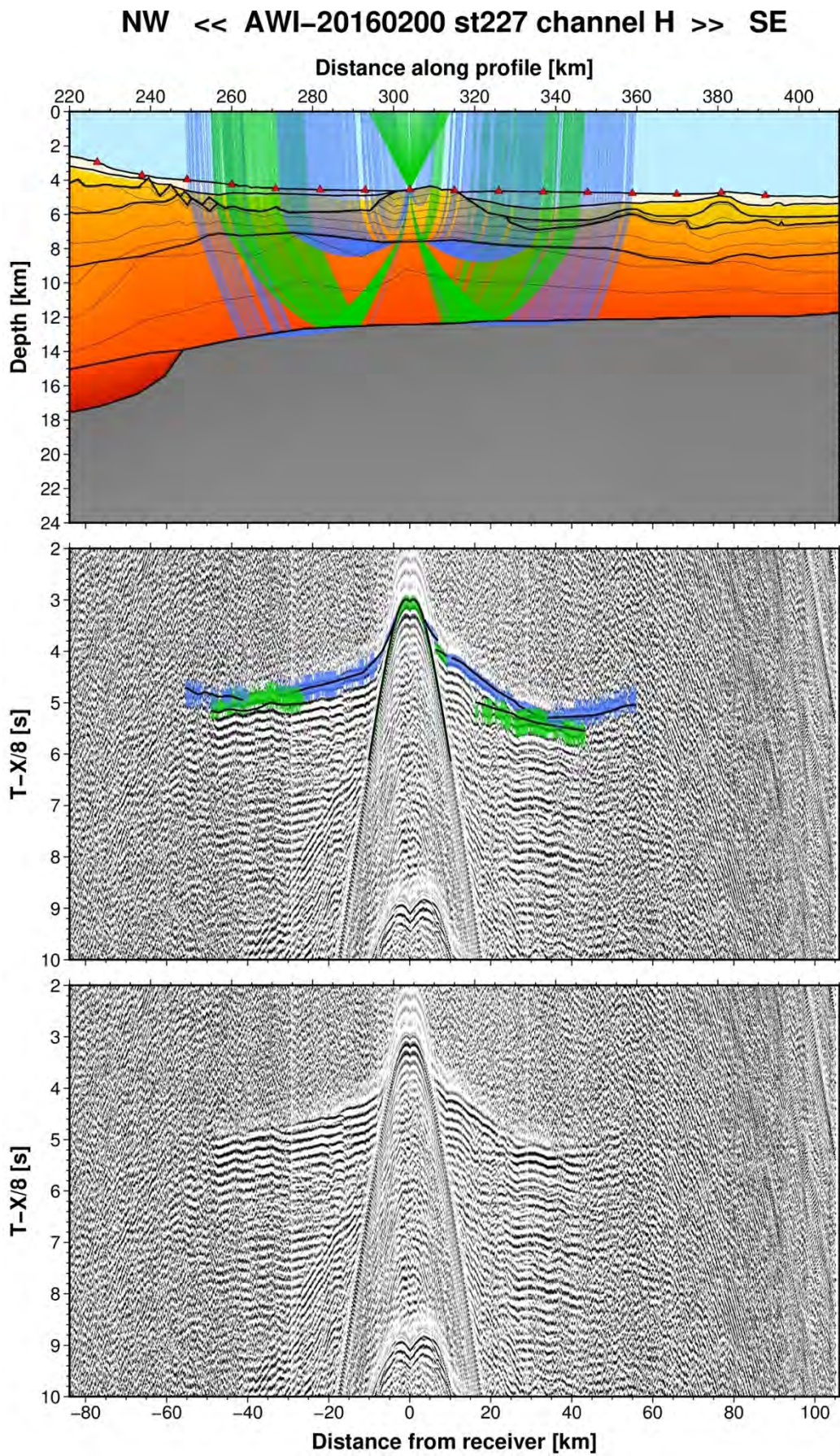


Fig. A65: Ray tracing results for station st227 along profile AWI-20160200. Lower panel: Seismic record; Middle panel: Picked and modelled arrival times; Upper panel: Section of the resulting P-wave velocity model; Green colours = reflections, blue colours = refractions.

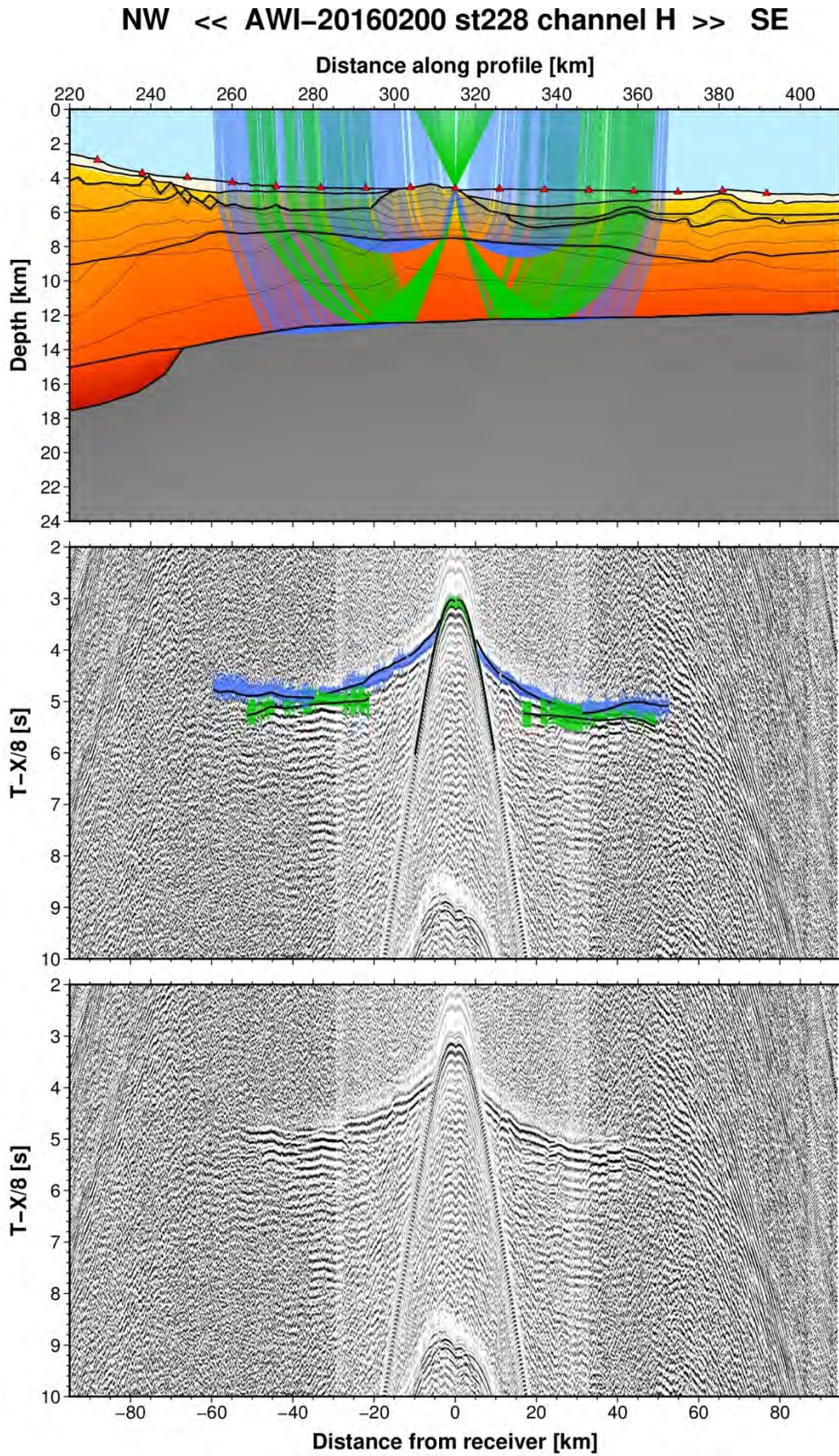


Fig. A66: Ray tracing results for station st228 along profile AWI-20160200. Lower panel: Seismic record; Middle panel: Picked and modelled arrival times; Upper panel: Section of the resulting P-wave velocity model; Green colours = reflections, blue colours = refractions.

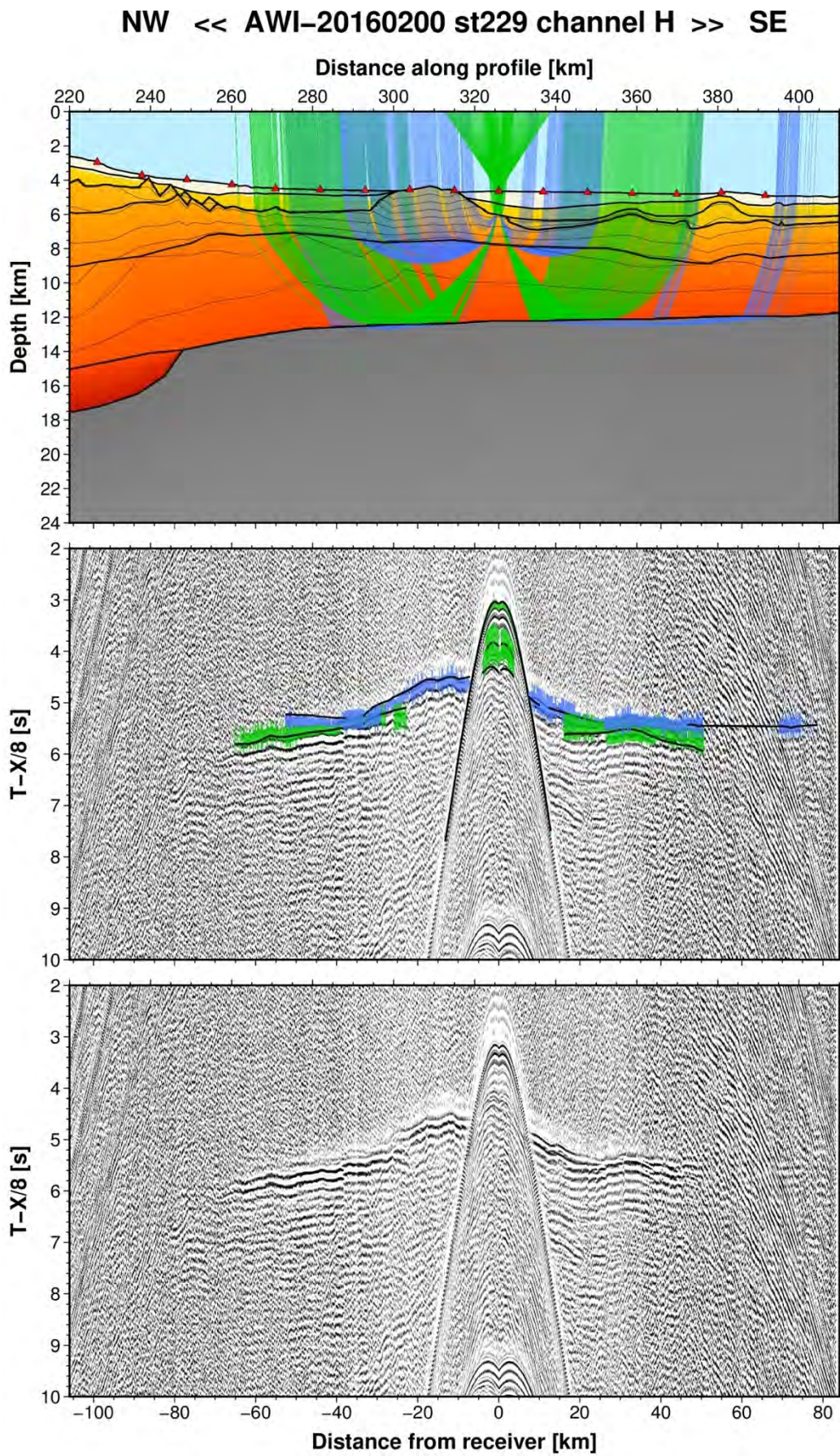


Fig. A67: Ray tracing results for station st229 along profile AWI-20160200. Lower panel: Seismic record; Middle panel: Picked and modelled arrival times; Upper panel: Section of the resulting P-wave velocity model; Green colours = reflections, blue colours = refractions.

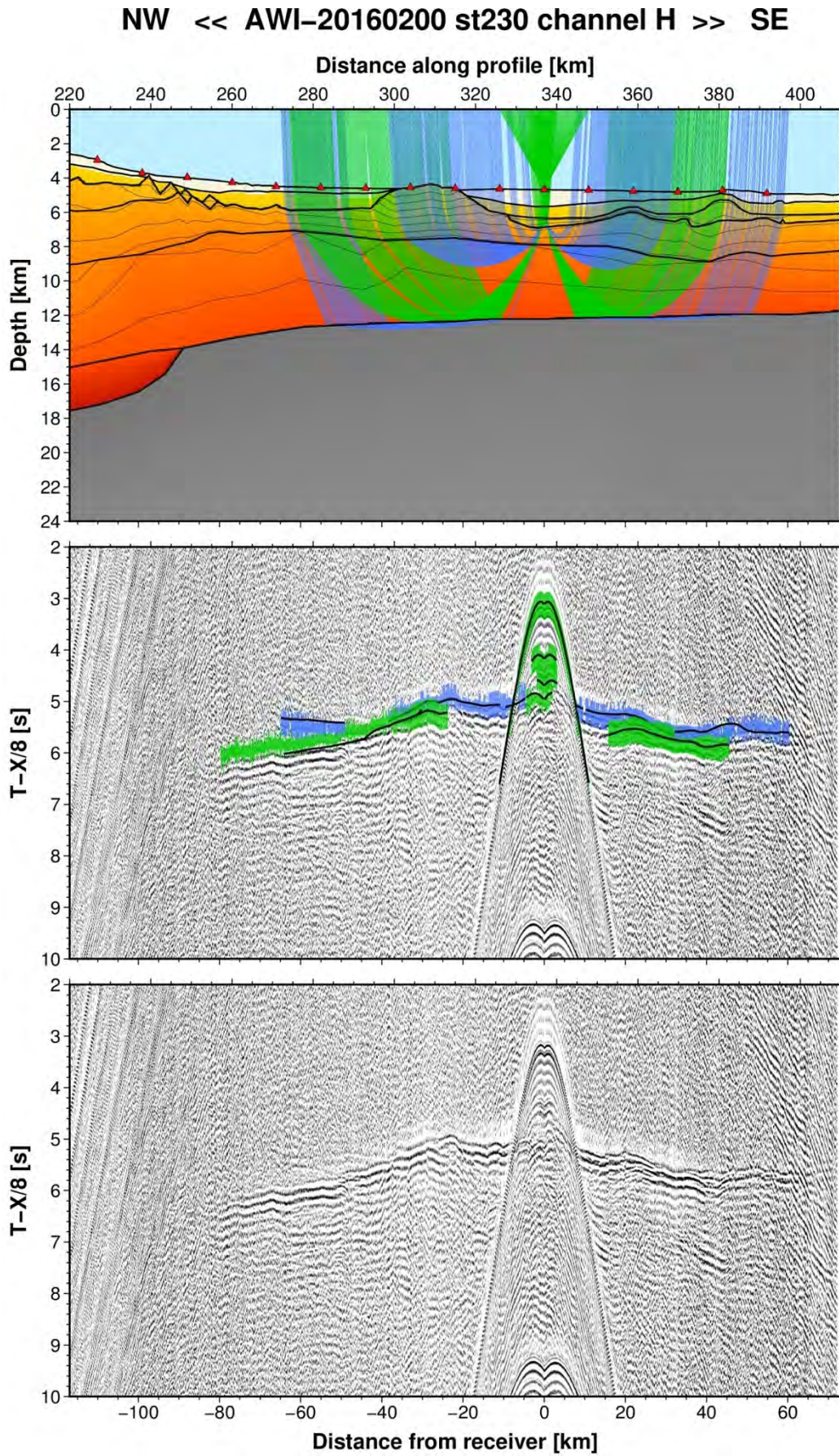


Fig. A68: Ray tracing results for station st230 along profile AWI-20160200. Lower panel: Seismic record; Middle panel: Picked and modelled arrival times; Upper panel: Section of the resulting P-wave velocity model; Green colours = reflections, blue colours = refractions.

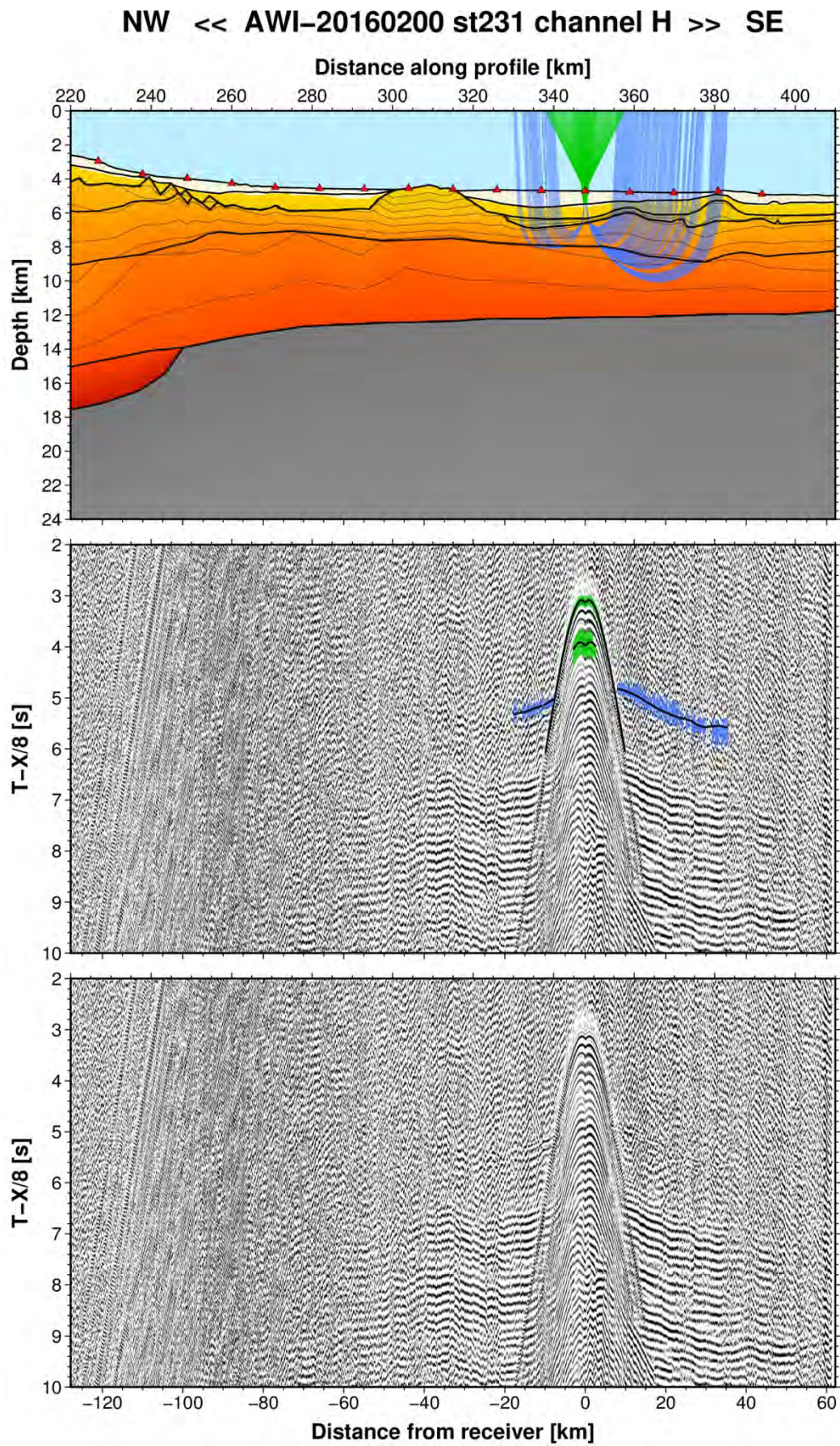


Fig. A69: Ray tracing results for station st231 along profile AWI-20160200. Lower panel: Seismic record; Middle panel: Picked and modelled arrival times; Upper panel: Section of the resulting P-wave velocity model; Green colours = reflections, blue colours = refractions.

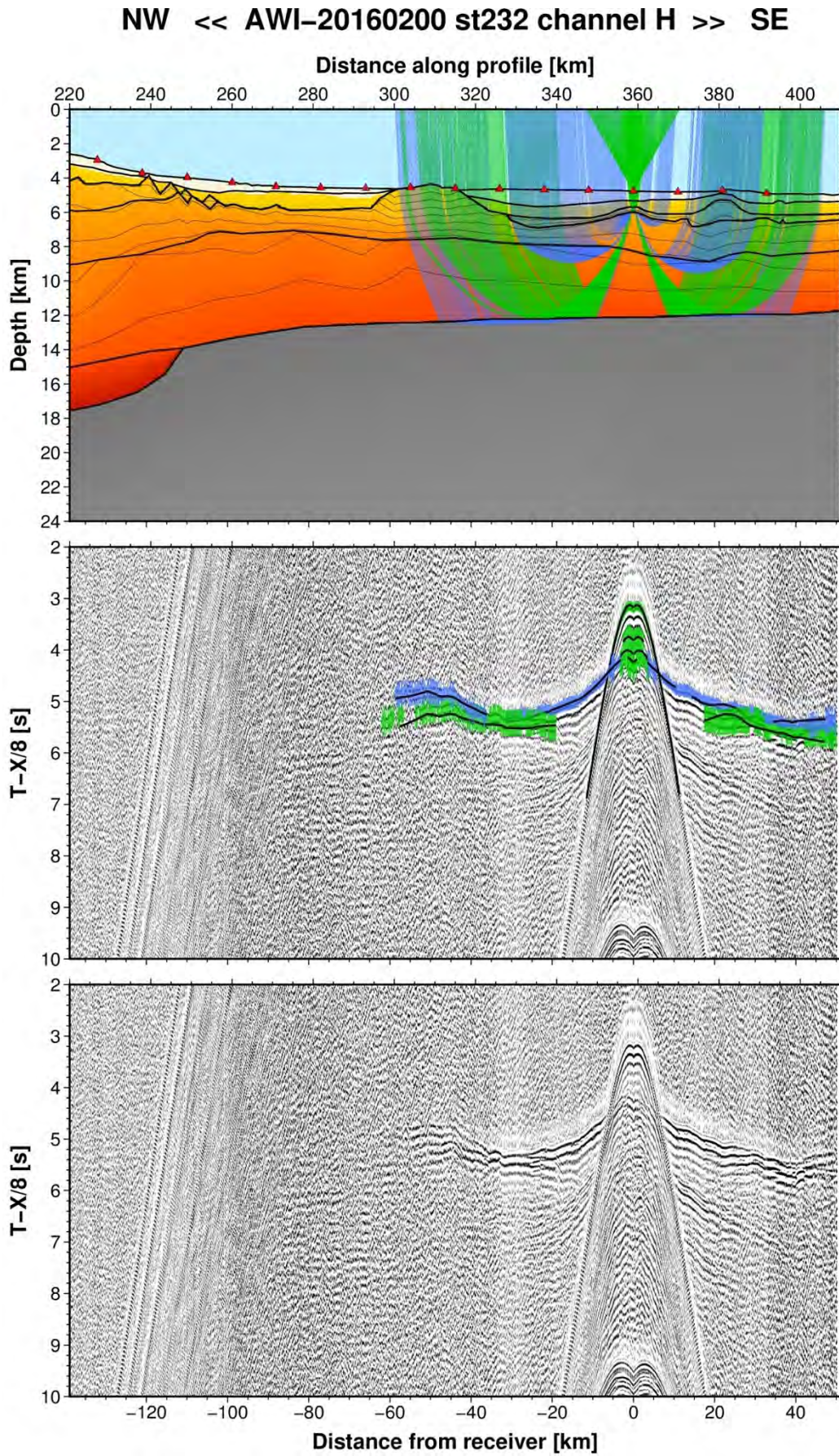


Fig. A70: Ray tracing results for station st232 along profile AWI-20160200. Lower panel: Seismic record; Middle panel: Picked and modelled arrival times; Upper panel: Section of the resulting P-wave velocity model; Green colours = reflections, blue colours = refractions.

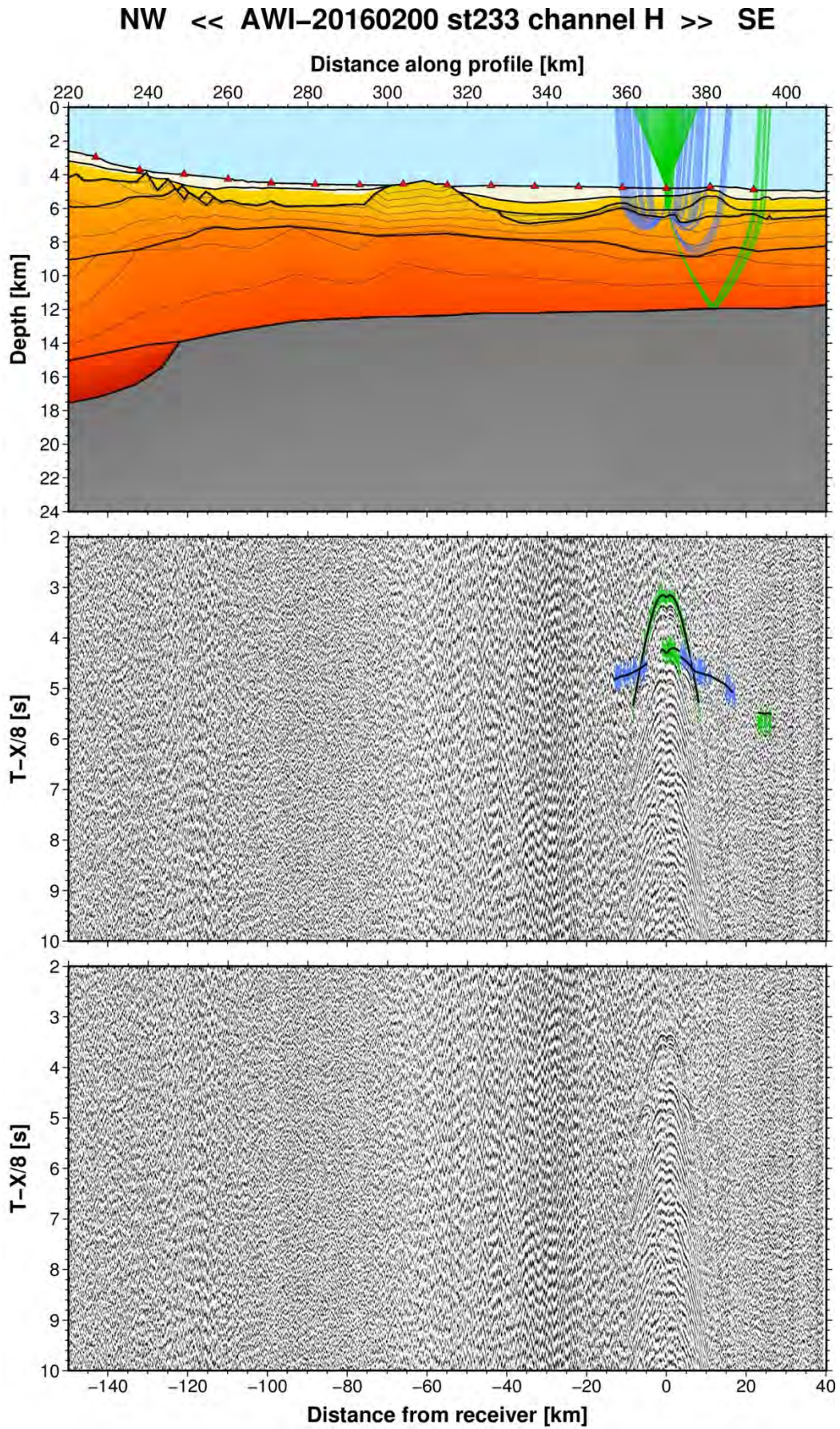


Fig. A71: Ray tracing results for station st233 along profile AWI-20160200. Lower panel: Seismic record; Middle panel: Picked and modelled arrival times; Upper panel: Section of the resulting P-wave velocity model; Green colours = reflections, blue colours = refractions.

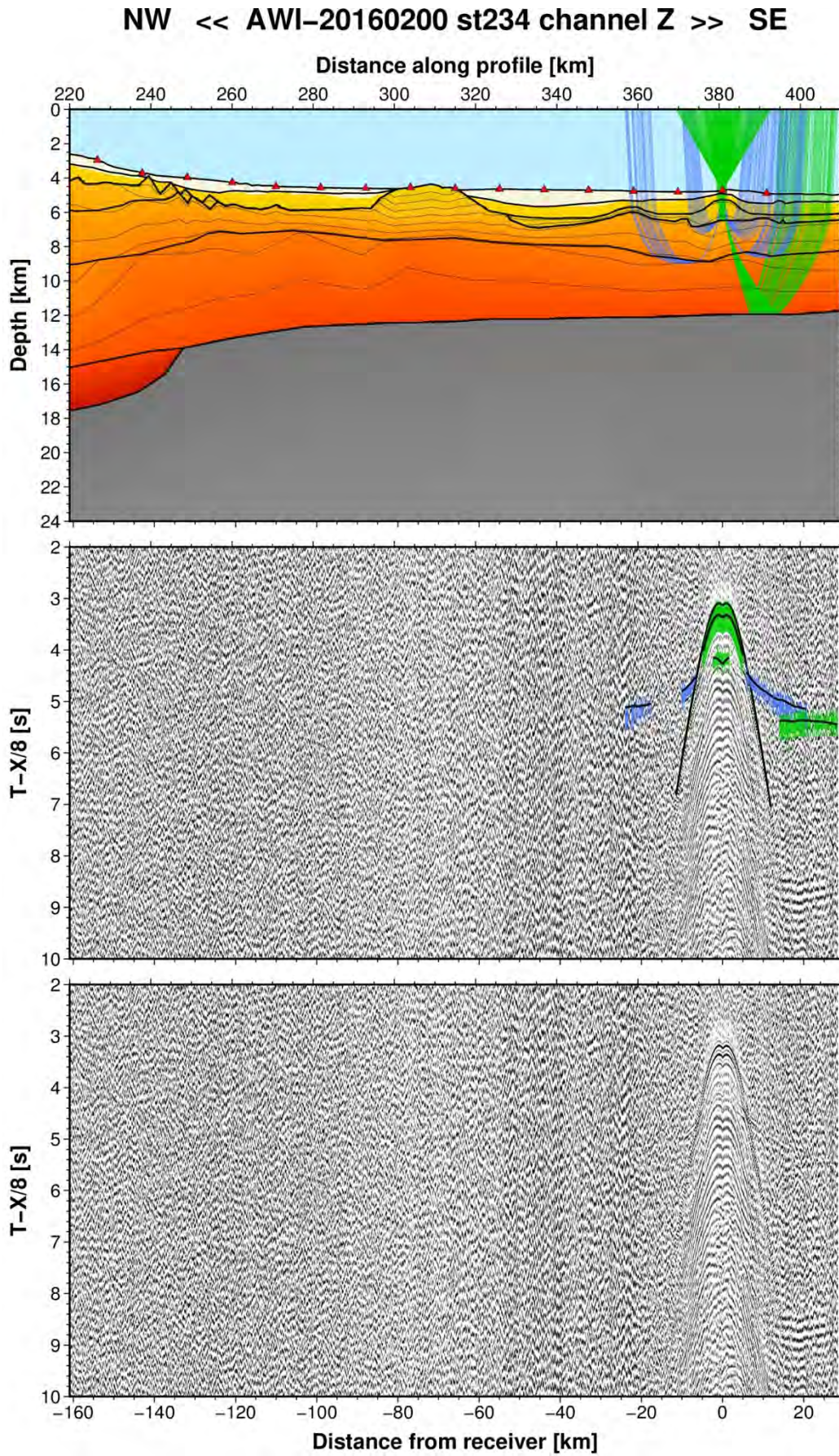


Fig. A72: Ray tracing results for station st234 along profile AWI-20160200. Lower panel: Seismic record; Middle panel: Picked and modelled arrival times; Upper panel: Section of the resulting P-wave velocity model; Green colours = reflections, blue colours = refractions.

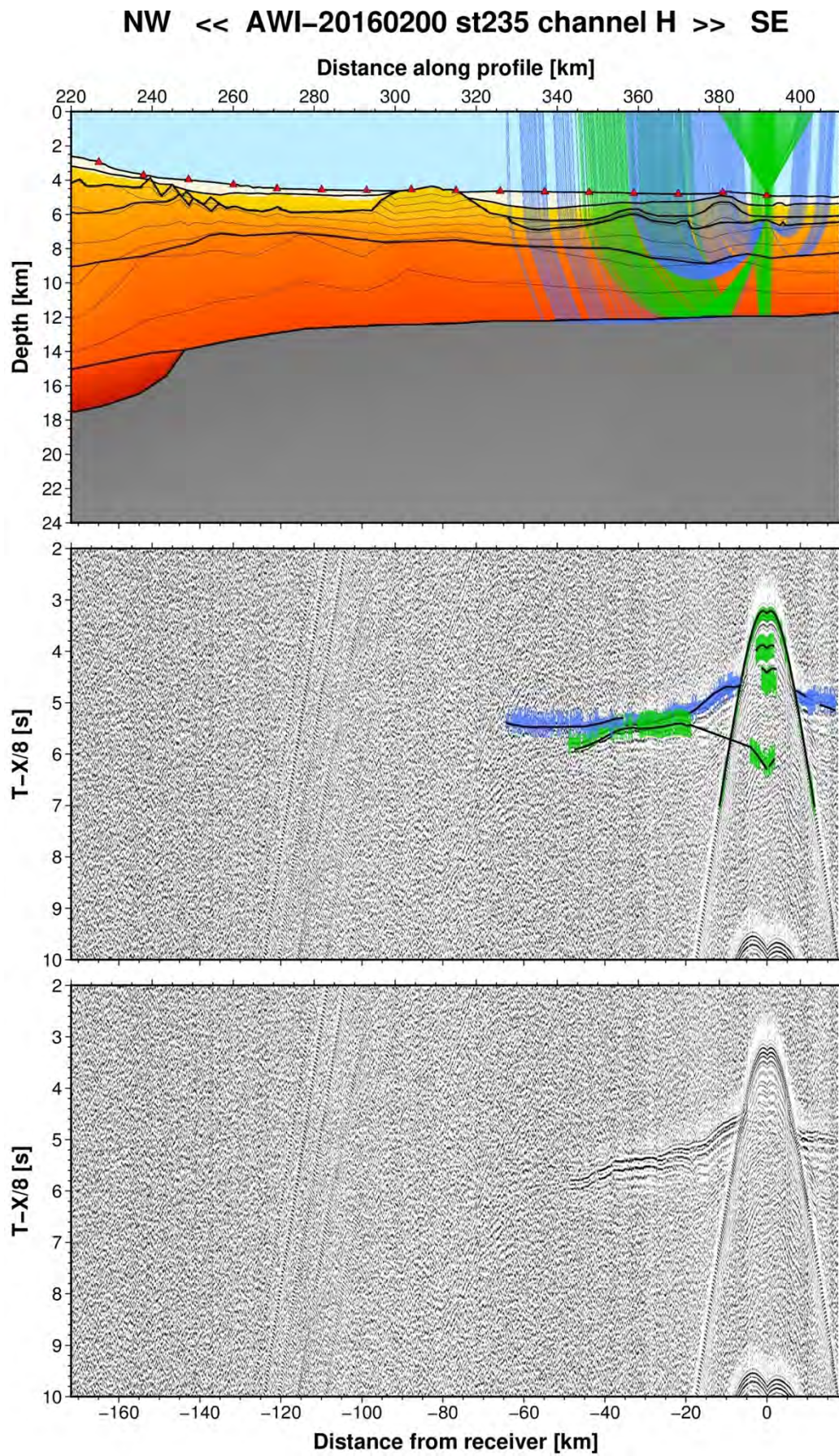


Fig. A73: Ray tracing results for station st235 along profile AWI-20160200. Lower panel: Seismic record; Middle panel: Picked and modelled arrival times; Upper panel: Section of the resulting P-wave velocity model; Green colours = reflections, blue colours = refractions.

A3. AWI-20160300

Tab. A3: Table with information about the configurations and data quality (1 = excellent, 2 = medium, 3 = low, 4 = no data, - = channel not used) of the OBS / OBH stations along profile AWI-20160300. See Gohl & Werner (2016) for more information.

Station	Water Depth [m]	Type	Recorder Type	Sensors	Quality				
					C 1	C 2	C 3	C 4	C 5
					h	x	y	z	h
st301	2616	OBS (GEOMAR)	MBS	H,X,Y,Z	1	2	2-3	2	-
st302	2818	OBS (AWI)	MCS	H	2	-	-	-	-
st303	2937	OBS (GEOMAR)	Geolog	H,X,Y,Z,H	1	1	1	1	1
st304	3291	OBS (AWI)	MCS	H	1-2	-	-	-	-
st305	4303	OBS (GEOMAR)	MBS	H,X,Y,Z	1-2	3	3	2-3	-
st306	4478	OBS (AWI)	6D6	H,X,Y,Z	2	3	3	2	-
st307	4840	OBS (GEOMAR)	MBS	H,X,Y,Z	1-2	3	3	3	-
st308	4874	OBS (AWI)	MCS	H	2-3	-	-	-	-
st309	5006	OBS (GEOMAR)	MBS	H,X,Y,Z	1-2	3	3	3	-
st310	5035	OBS (GEOMAR)	Geolog	H,X,Y,Z,H	1	2	2	2	1
st311	5040	OBS (AWI)	MCS	H,X,Y,Z	1	3	2-3	1-2	-
st312	4970	OBS (GEOMAR)	MBS	H,X,Y,Z	2-3	3	3	2-3	-
st313	5086	OBS (GEOMAR)	MBS	H,X,Y,Z	1	3	3	3	-
st314	5173	OBS (AWI)	MCS	H	1	-	-	-	-
st315	5226	OBS (GEOMAR)	MBS	H,X,Y,Z	1	2-3	2-3	2	-
st316	5233	OBS (AWI)	MCS	H,X,Y,Z	1	2-3	2	1-2	-
st317	5233	OBS (GEOMAR)	Geolog	H,X,Y,Z,H	1	2	2	2	1
st318	5258	OBS (AWI)	MCS	H	1	-	-	-	-
st319	5256	OBS (GEOMAR)	MBS	H,X,Y,Z	1	2-3	2-3	2-3	-
st320	5288	OBS (NAMMU)	6D6	H,X,Y,Z	1	2-3	2-3	2	-
st321	5302	OBS (GEOMAR)	MCS	H,X,Y,Z	1	2-3	3	2-3	-

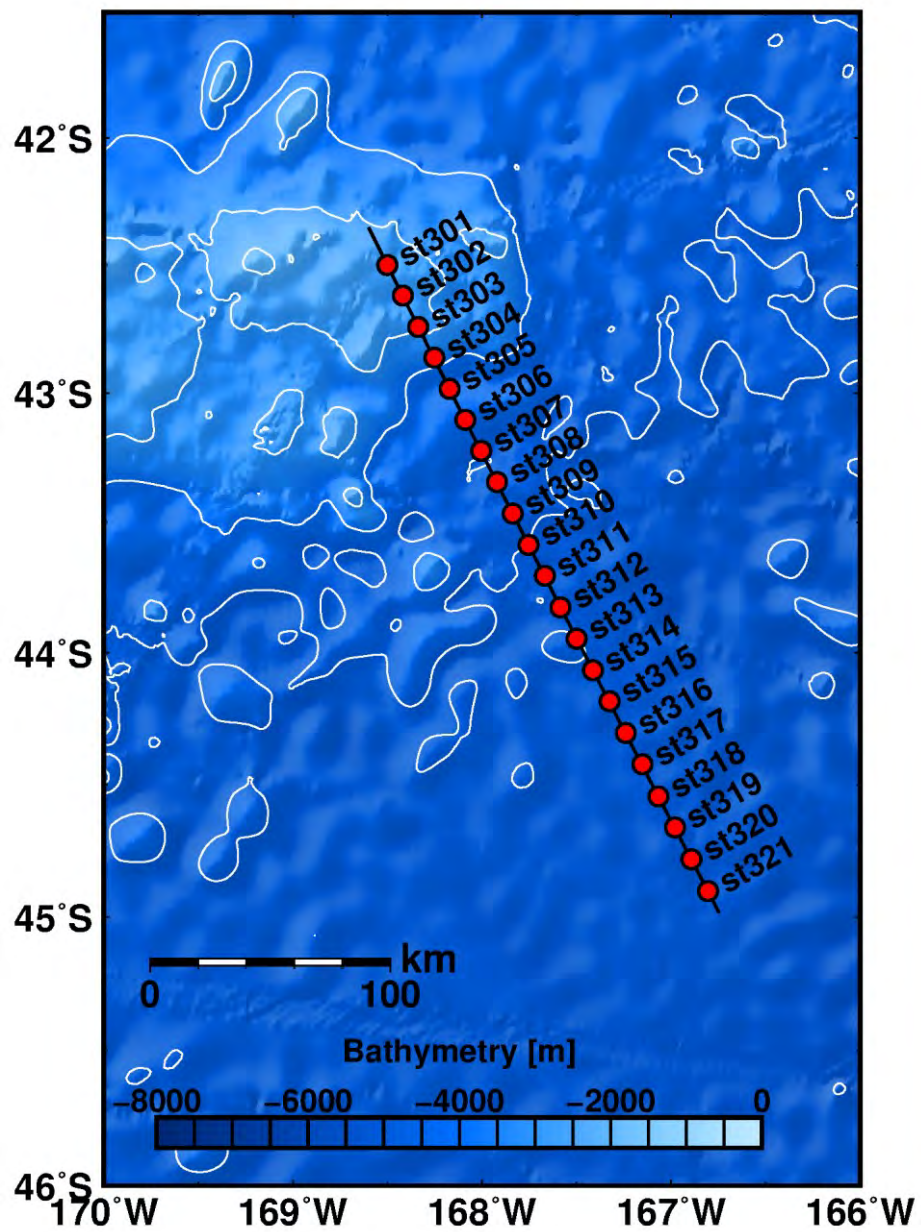


Fig. A74: Bathymetric map of the southern Chatham Rise margin and deployed OBS / OBH stations (red circles) along profile AWI-20160300.

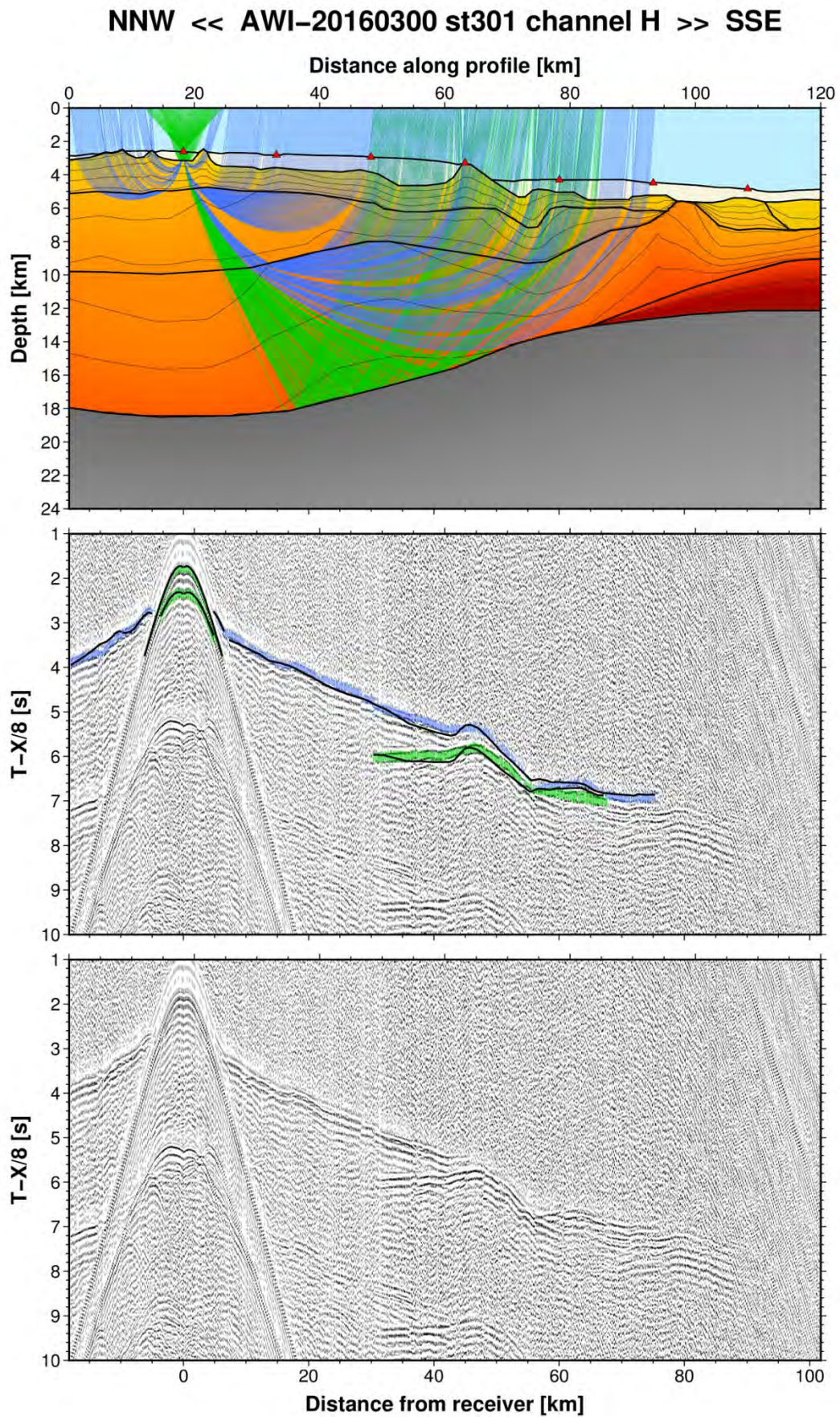


Fig. A75: Ray tracing results for station st301 along profile AWI-20160300. Lower panel: Seismic record; Middle panel: Picked and modelled arrival times; Upper panel: Section of the resulting P-wave velocity model; Green colours = reflections, blue colours = refractions.

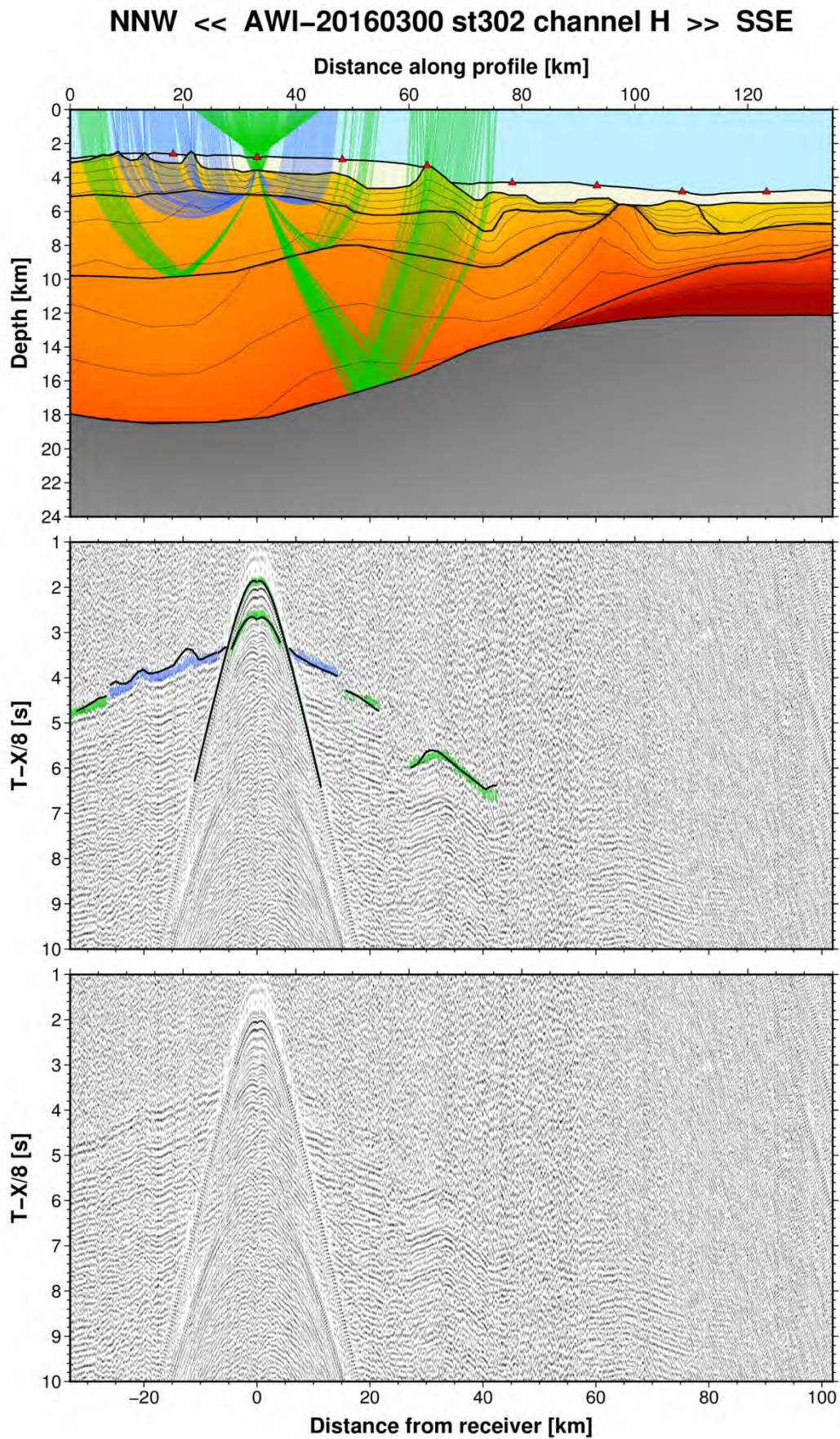


Fig. A76: Ray tracing results for station st302 along profile AWI-20160300. Lower panel: Seismic record; Middle panel: Picked and modelled arrival times; Upper panel: Section of the resulting P-wave velocity model; Green colours = reflections, blue colours = refractions.

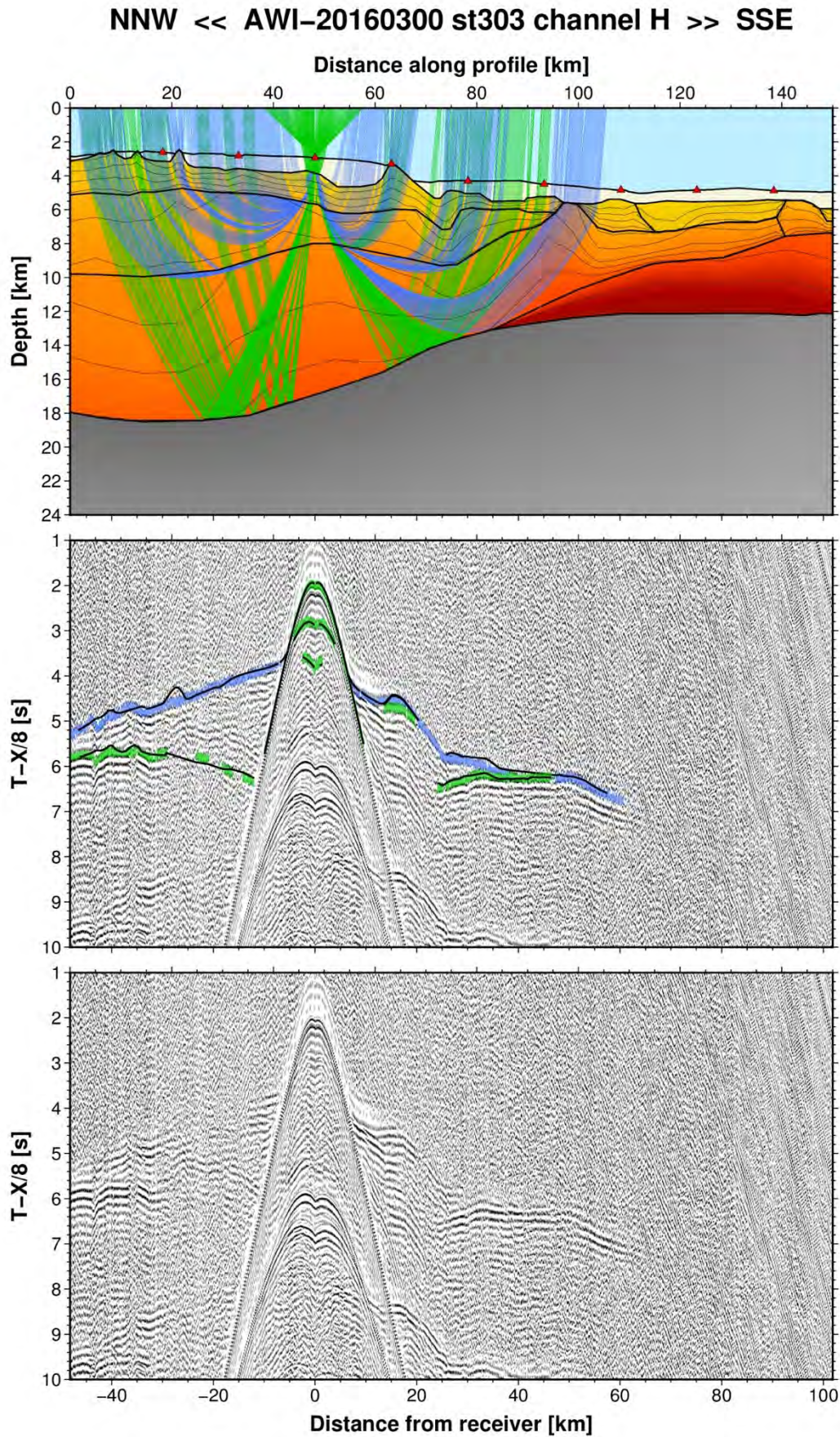


Fig. A77: Ray tracing results for station st303 along profile AWI-20160300. Lower panel: Seismic record; Middle panel: Picked and modelled arrival times; Upper panel: Section of the resulting P-wave velocity model; Green colours = reflections, blue colours = refractions.

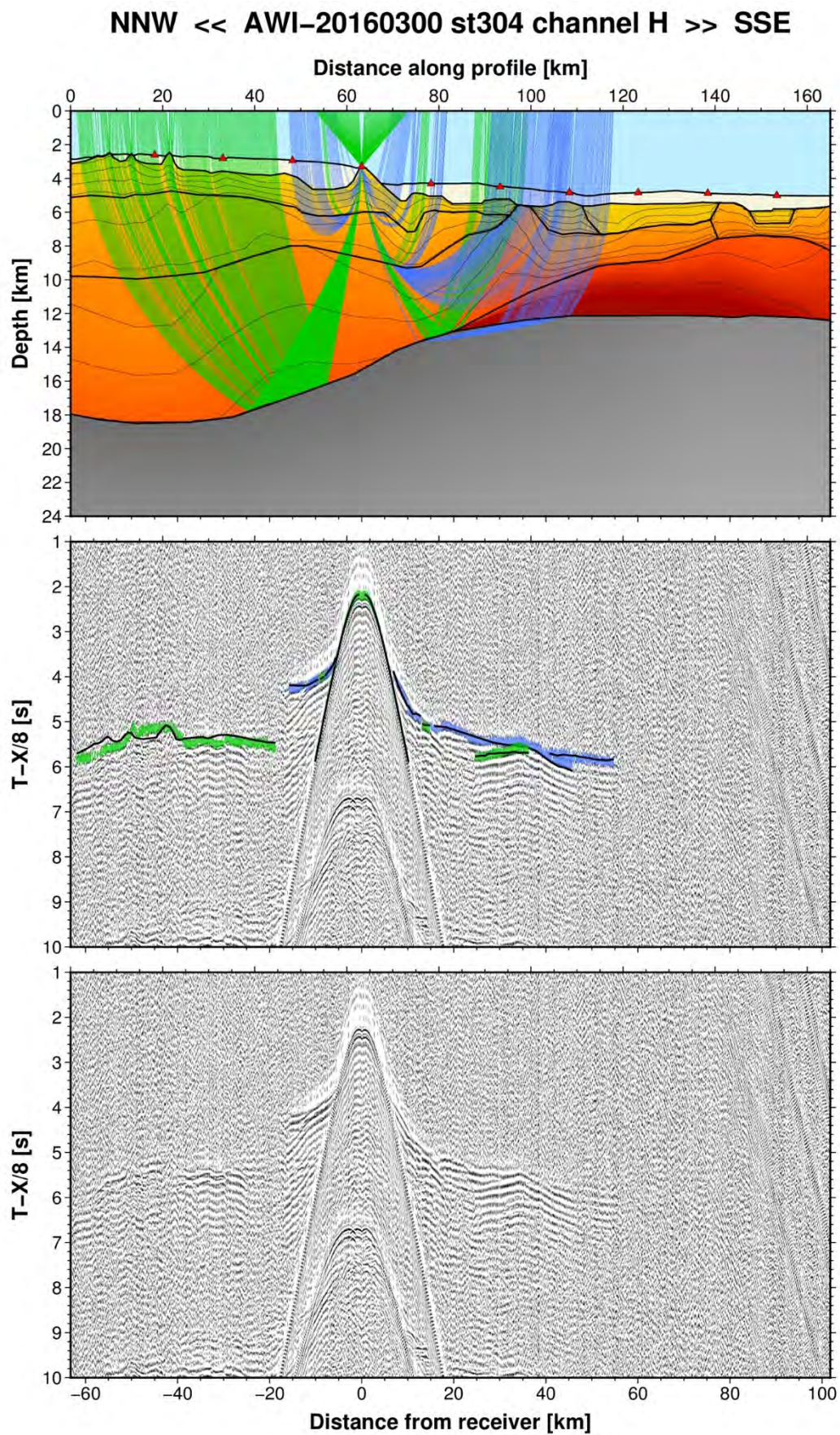


Fig. A78: Ray tracing results for station st304 along profile AWI-20160300. Lower panel: Seismic record; Middle panel: Picked and modelled arrival times; Upper panel: Section of the resulting P-wave velocity model; Green colours = reflections, blue colours = refractions.

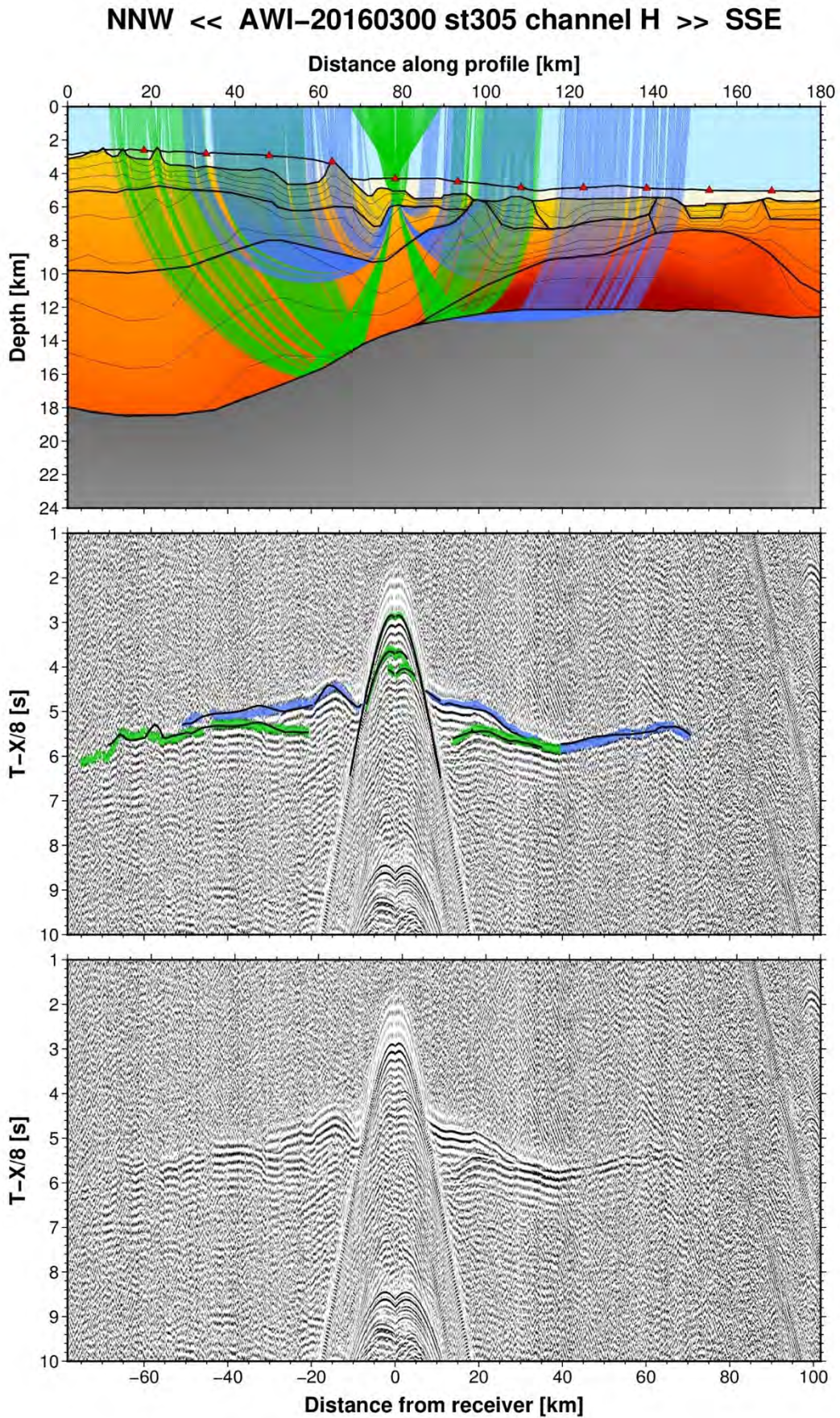


Fig. A79: Ray tracing results for station st305 along profile AWI-20160300. Lower panel: Seismic record; Middle panel: Picked and modelled arrival times; Upper panel: Section of the resulting P-wave velocity model; Green colours = reflections, blue colours = refractions.

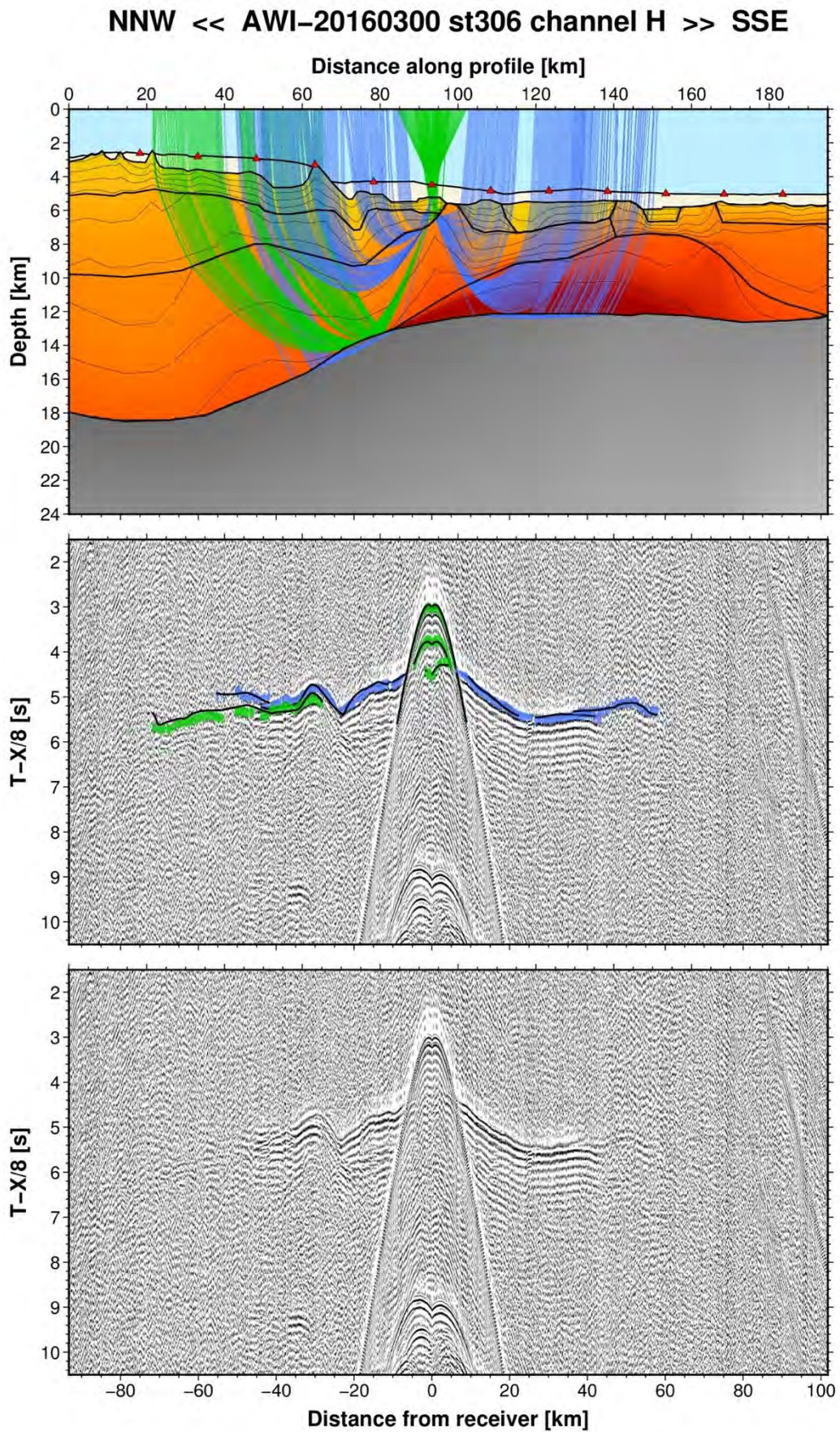


Fig. A80: Ray tracing results for station st306 along profile AWI-20160300. Lower panel: Seismic record; Middle panel: Picked and modelled arrival times; Upper panel: Section of the resulting P-wave velocity model; Green colours = reflections, blue colours = refractions.

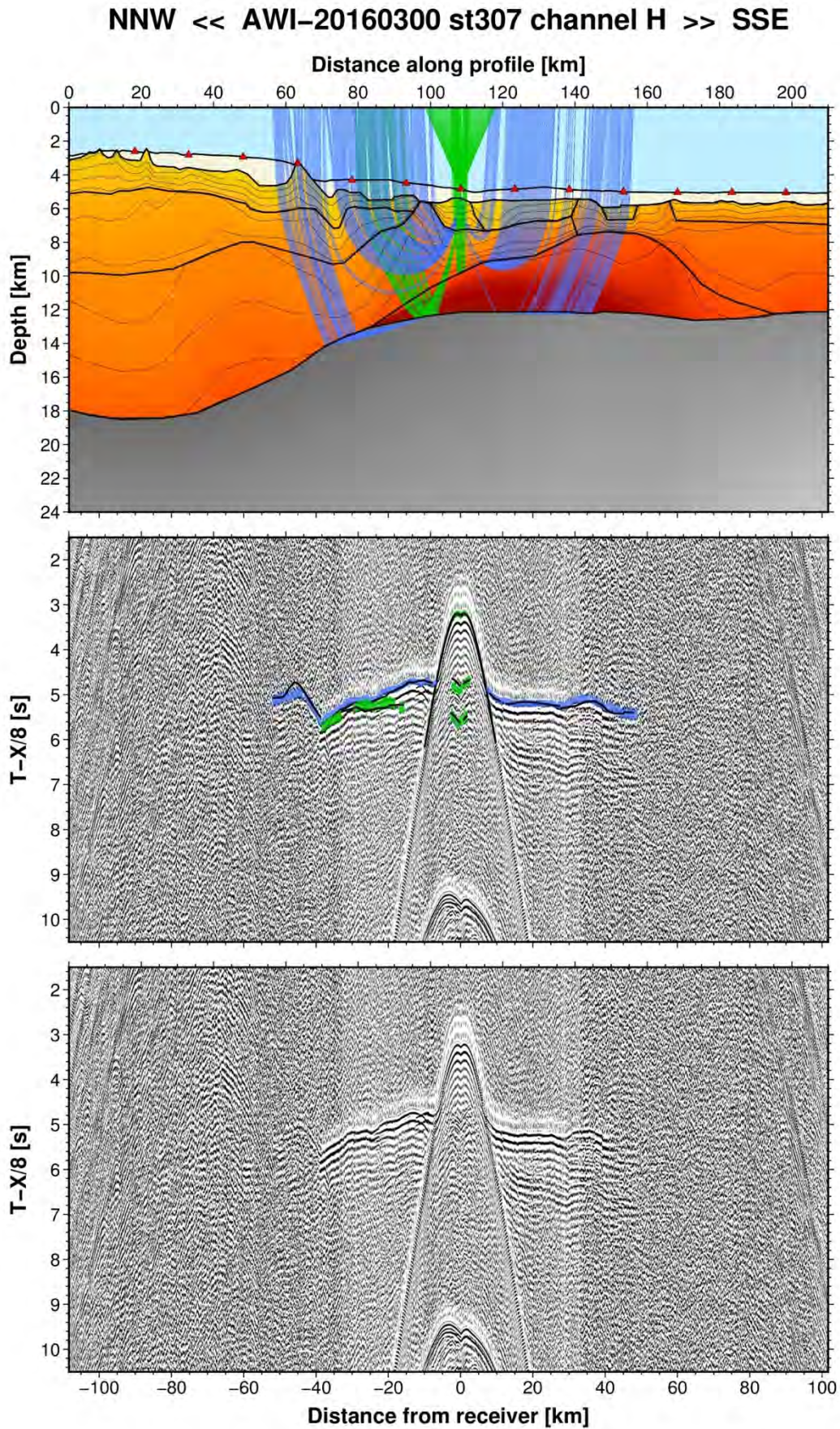


Fig. A81: Ray tracing results for station st307 along profile AWI-20160300. Lower panel: Seismic record; Middle panel: Picked and modelled arrival times; Upper panel: Section of the resulting P-wave velocity model; Green colours = reflections, blue colours = refractions.

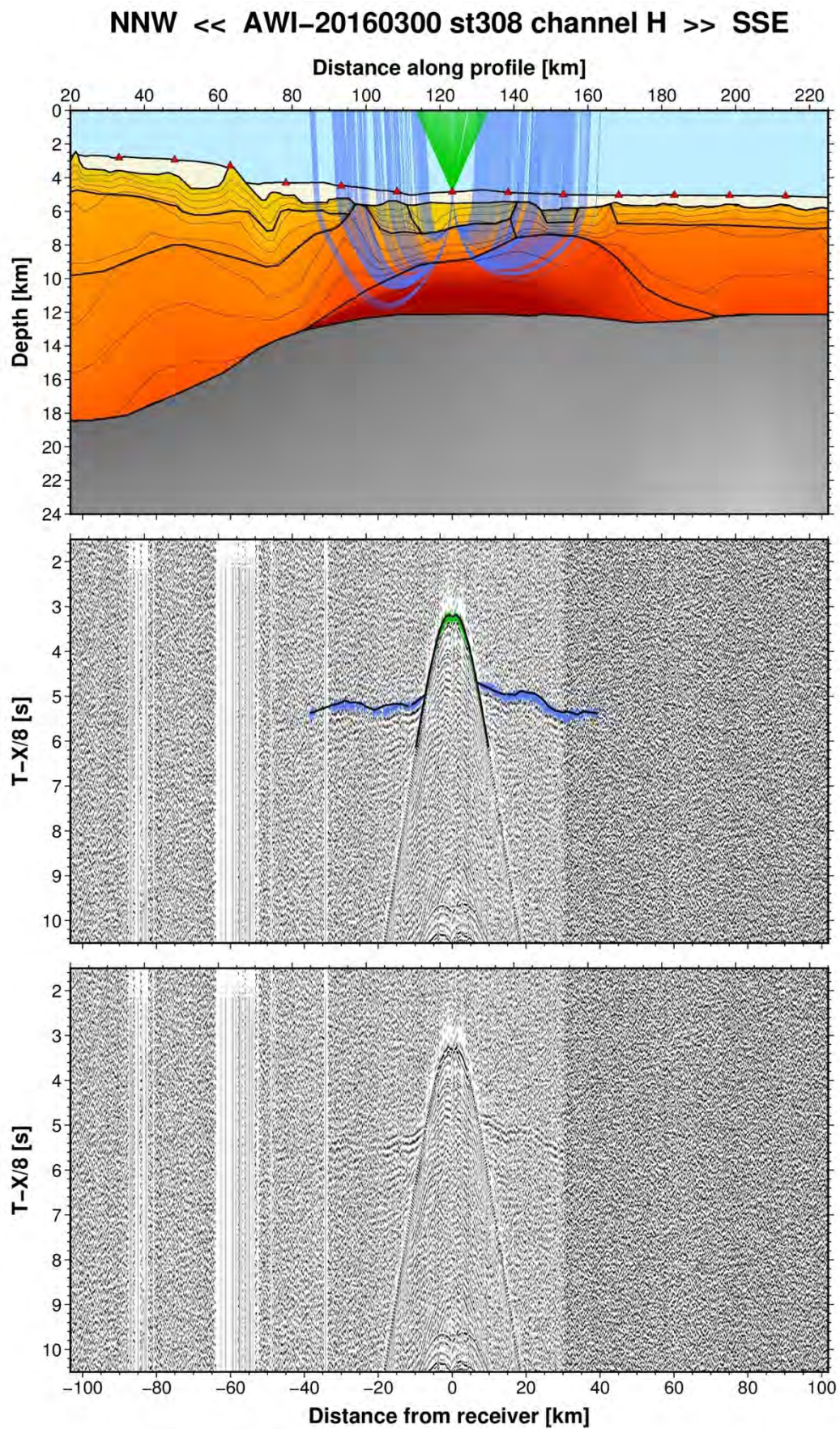


Fig. A82: Ray tracing results for station st308 along profile AWI-20160300. Lower panel: Seismic record; Middle panel: Picked and modelled arrival times; Upper panel: Section of the resulting P-wave velocity model; Green colours = reflections, blue colours = refractions.

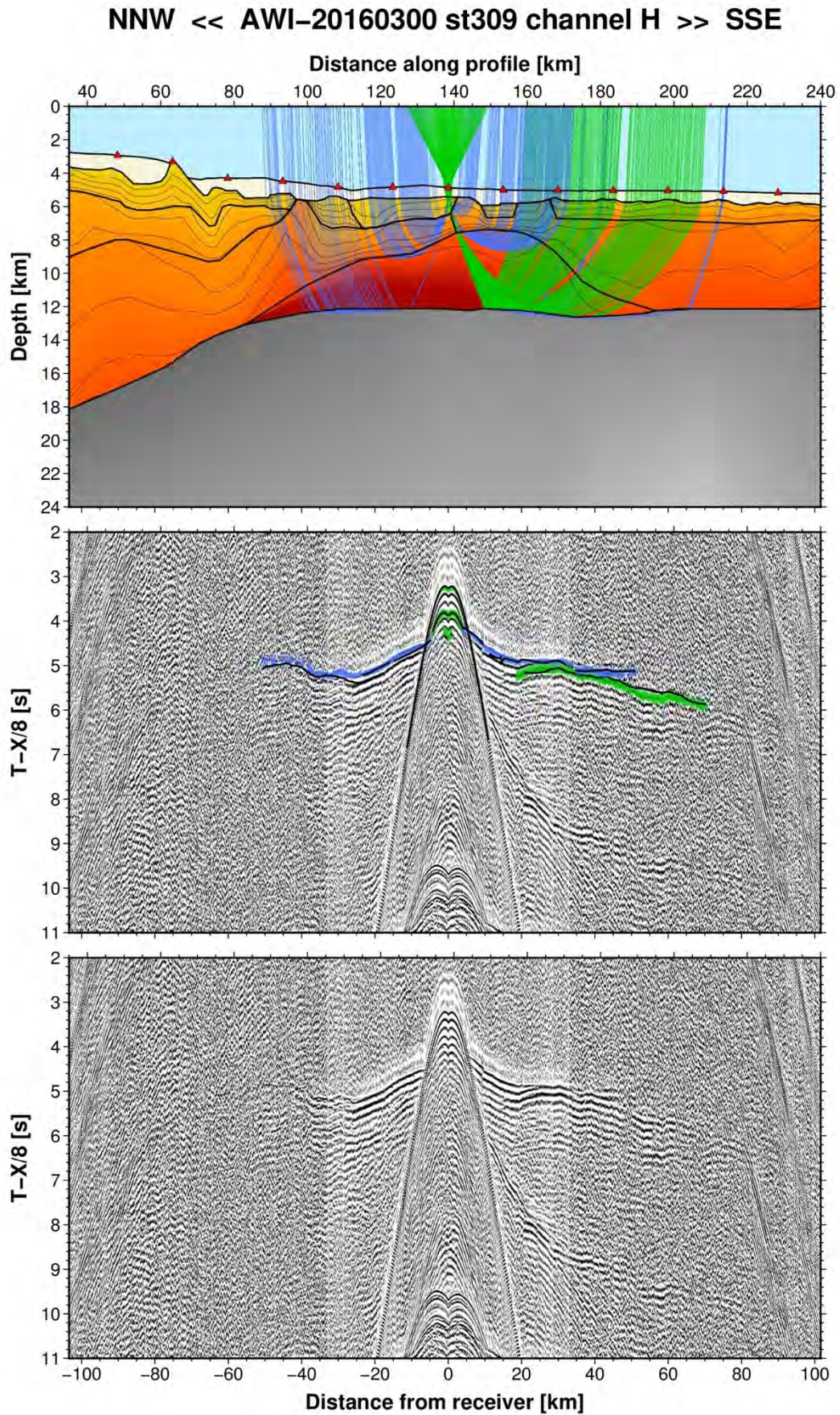


Fig. A83: Ray tracing results for station st309 along profile AWI-20160300. Lower panel: Seismic record; Middle panel: Picked and modelled arrival times; Upper panel: Section of the resulting P-wave velocity model; Green colours = reflections, blue colours = refractions.

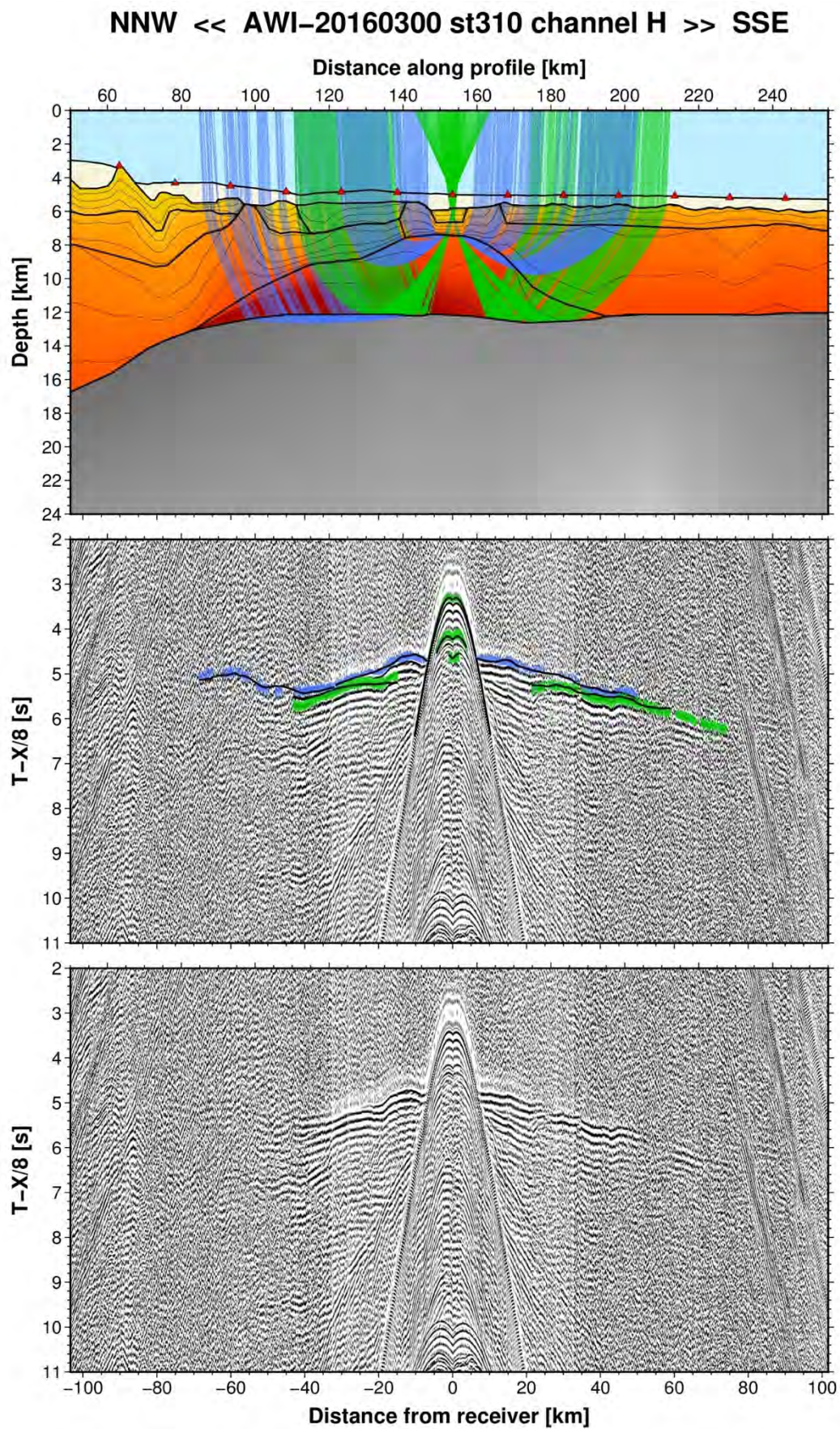


Fig. A84: Ray tracing results for station st310 along profile AWI-20160300. Lower panel: Seismic record; Middle panel: Picked and modelled arrival times; Upper panel: Section of the resulting P-wave velocity model; Green colours = reflections, blue colours = refractions.

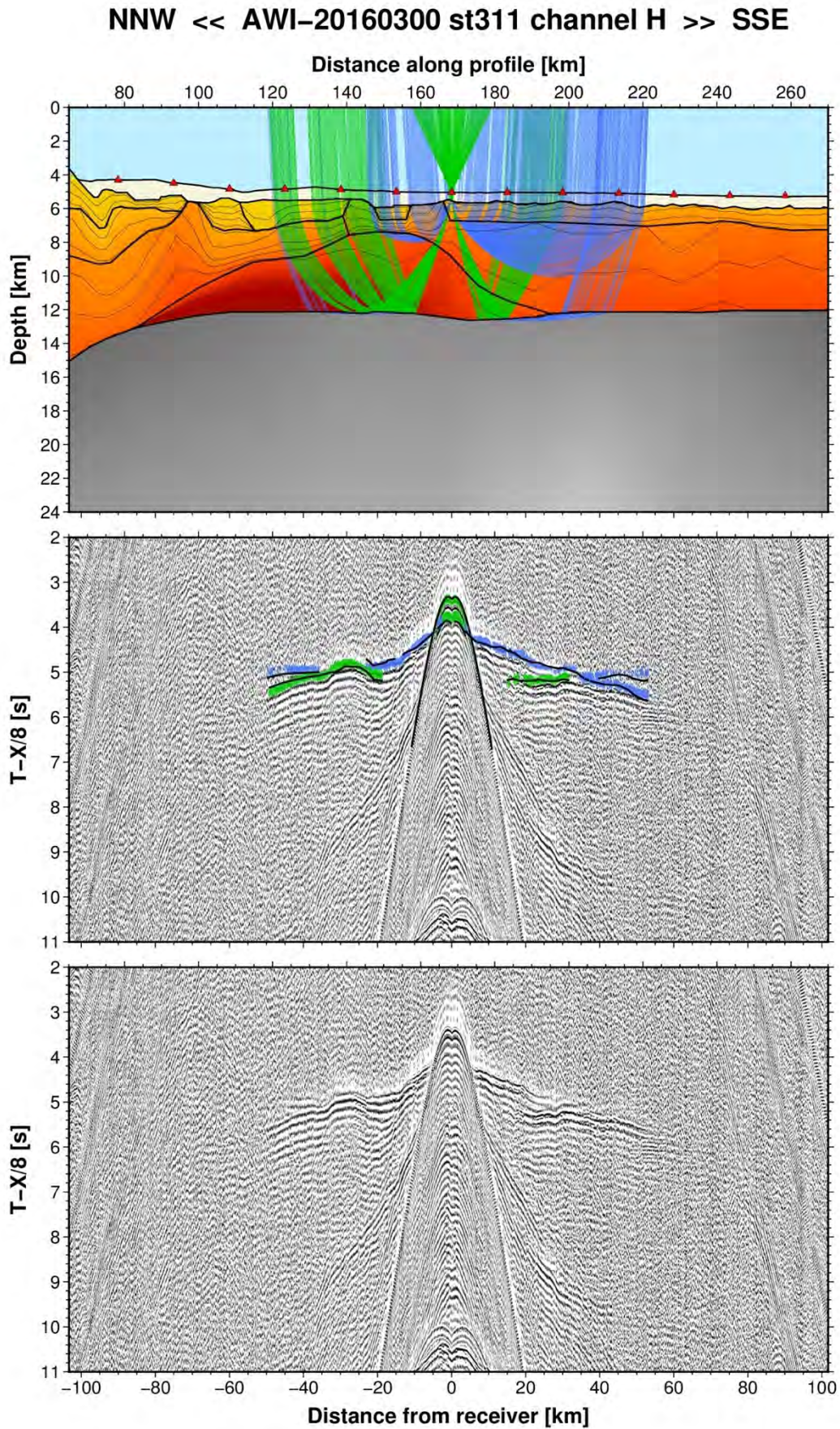


Fig. A85: Ray tracing results for station st311 along profile AWI-20160300. Lower panel: Seismic record; Middle panel: Picked and modelled arrival times; Upper panel: Section of the resulting P-wave velocity model; Green colours = reflections, blue colours = refractions.

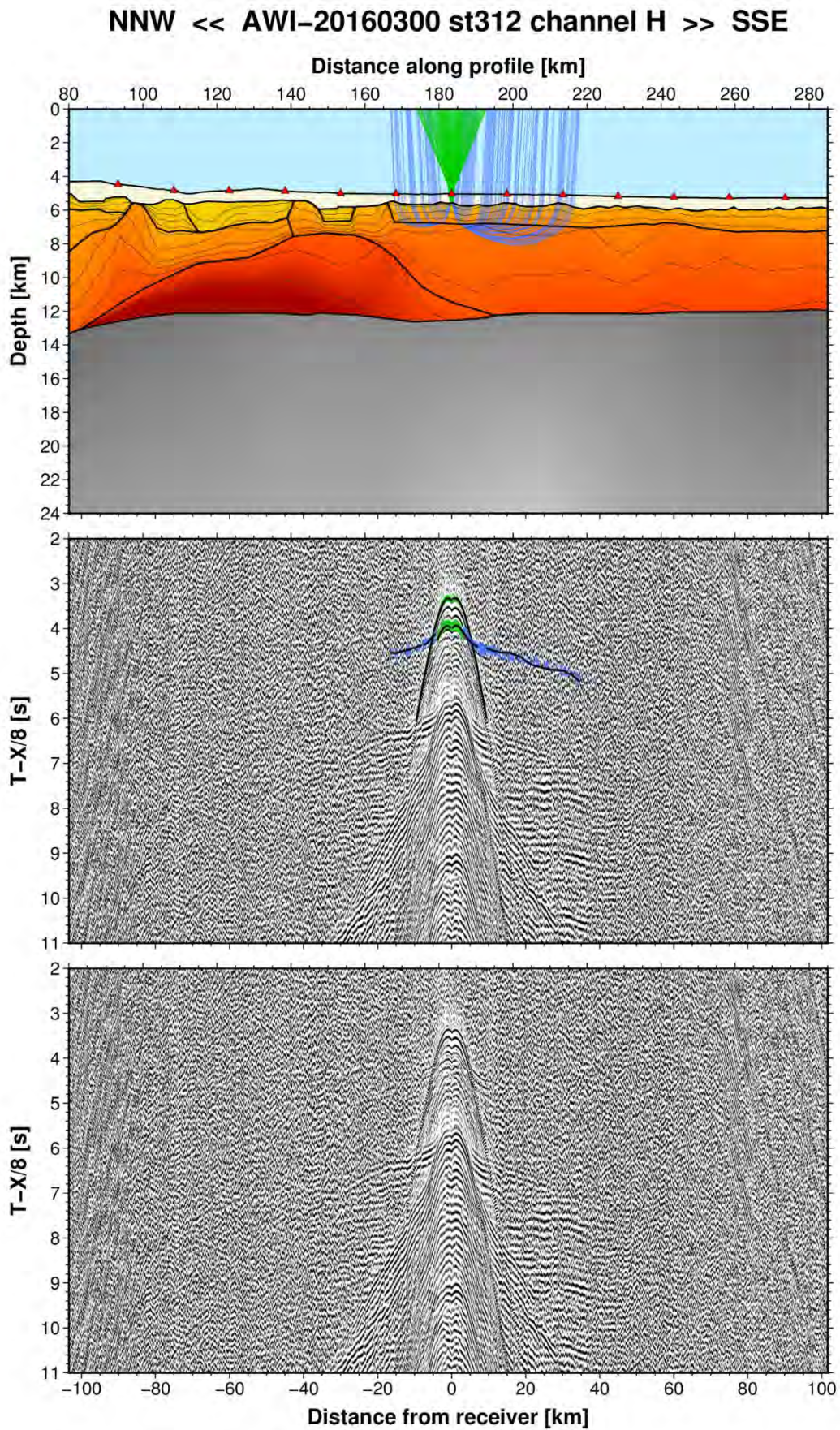


Fig. A86: Ray tracing results for station st312 along profile AWI-20160300. Lower panel: Seismic record; Middle panel: Picked and modelled arrival times; Upper panel: Section of the resulting P-wave velocity model; Green colours = reflections, blue colours = refractions.

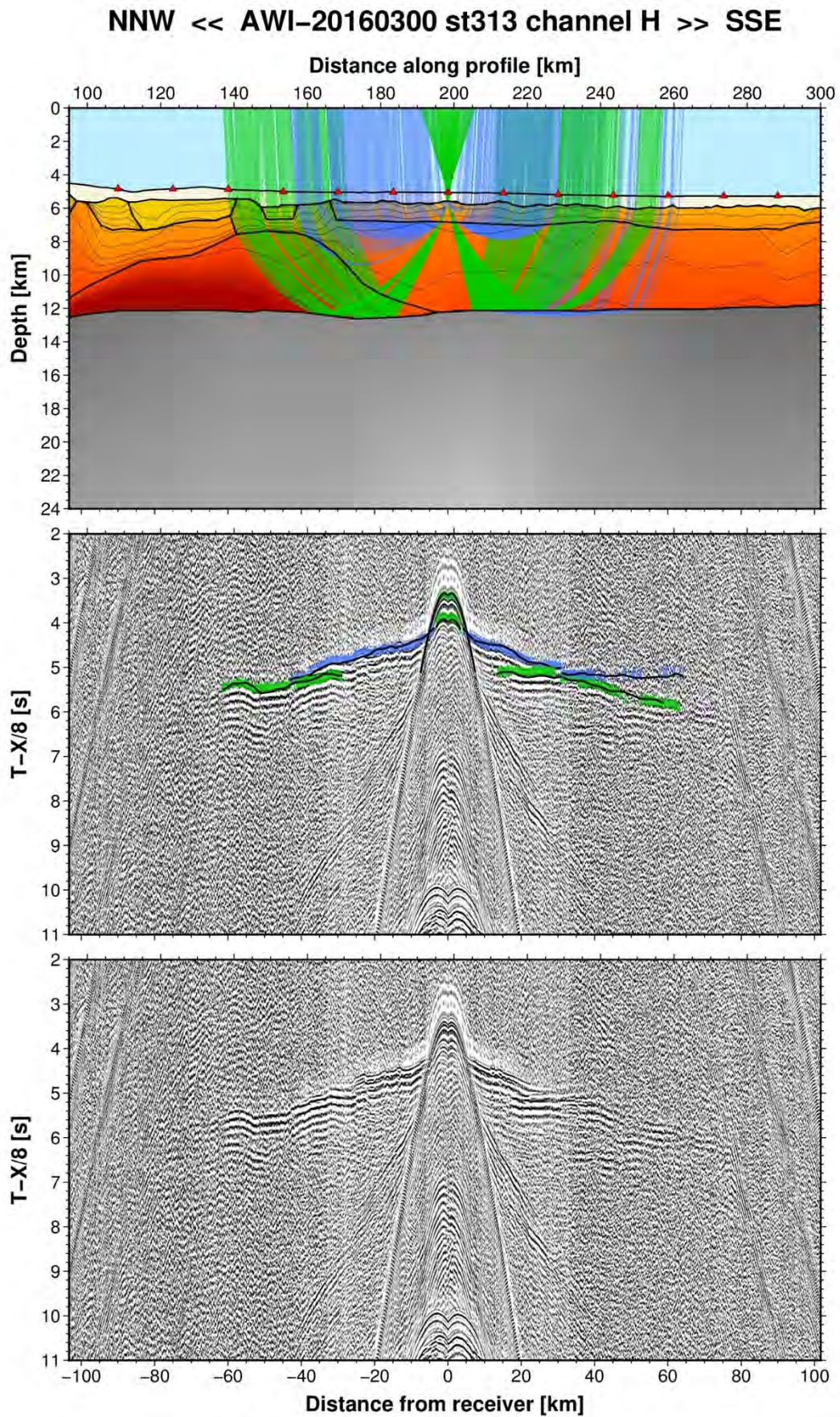


Fig. A87: Ray tracing results for station st313 along profile AWI-20160300. Lower panel: Seismic record; Middle panel: Picked and modelled arrival times; Upper panel: Section of the resulting P-wave velocity model; Green colours = reflections, blue colours = refractions.

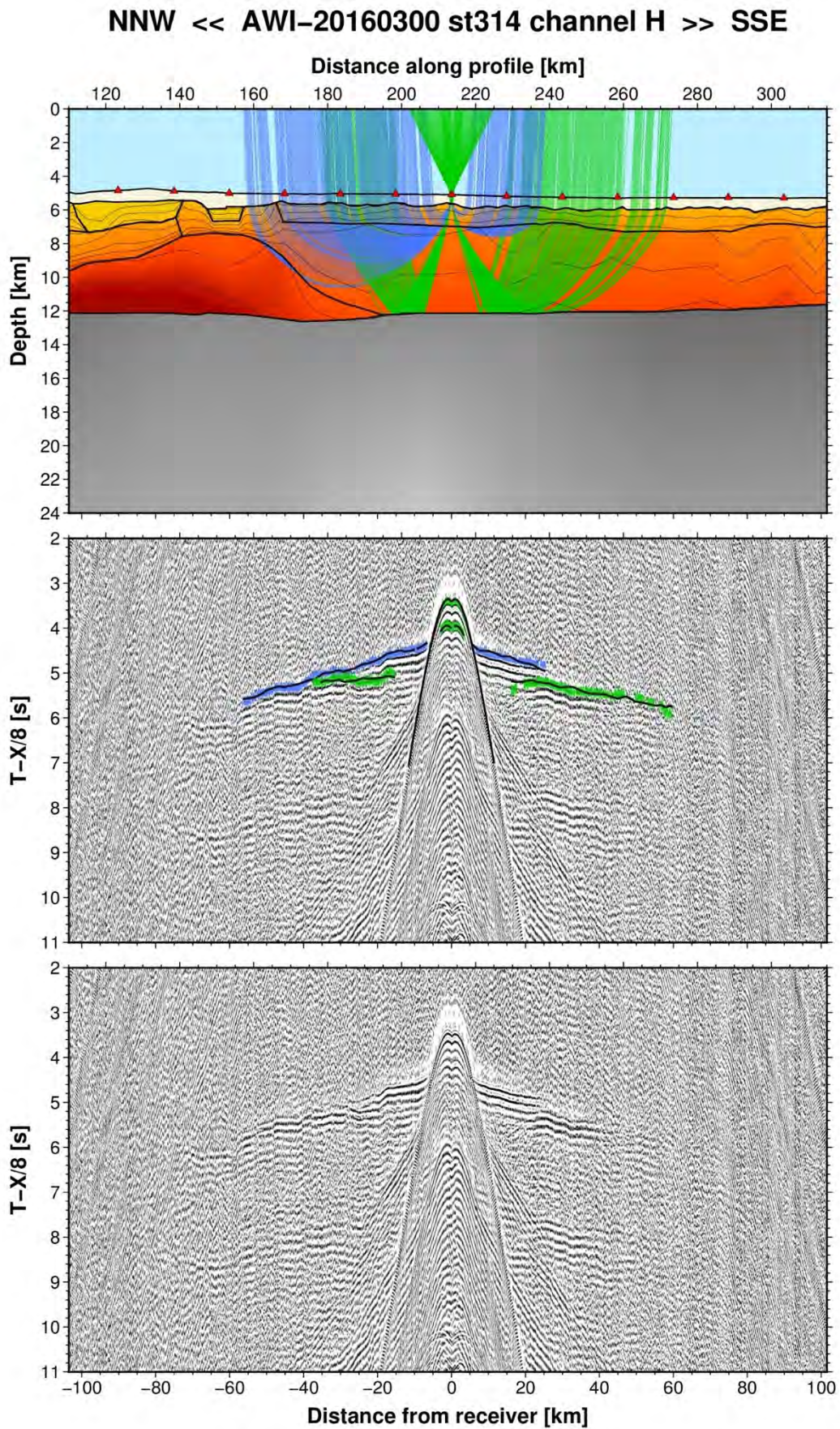


Fig. A88: Ray tracing results for station st314 along profile AWI-20160300. Lower panel: Seismic record; Middle panel: Picked and modelled arrival times; Upper panel: Section of the resulting P-wave velocity model; Green colours = reflections, blue colours = refractions.

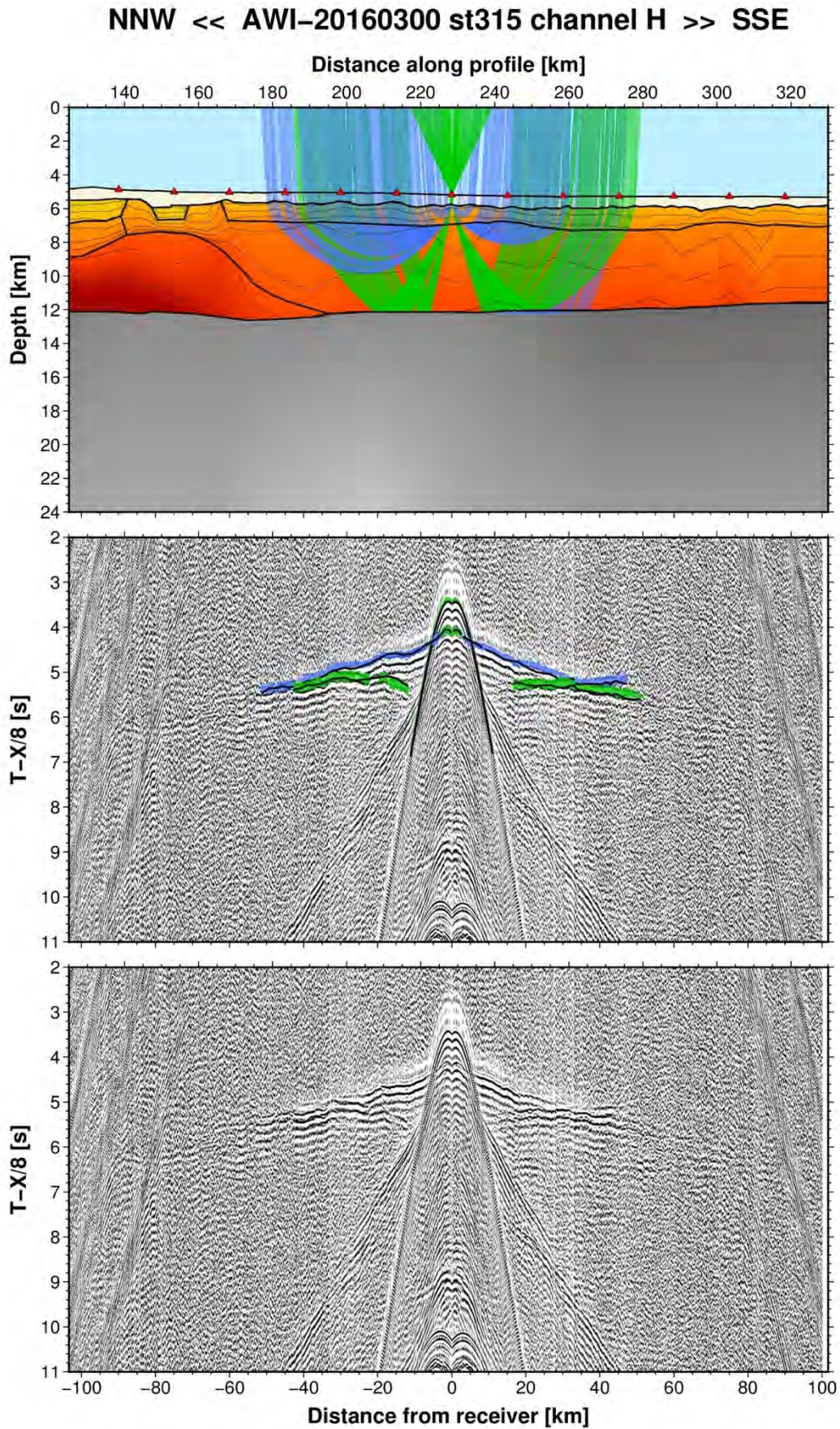


Fig. A89: Ray tracing results for station st315 along profile AWI-20160300. Lower panel: Seismic record; Middle panel: Picked and modelled arrival times; Upper panel: Section of the resulting P-wave velocity model; Green colours = reflections, blue colours = refractions.

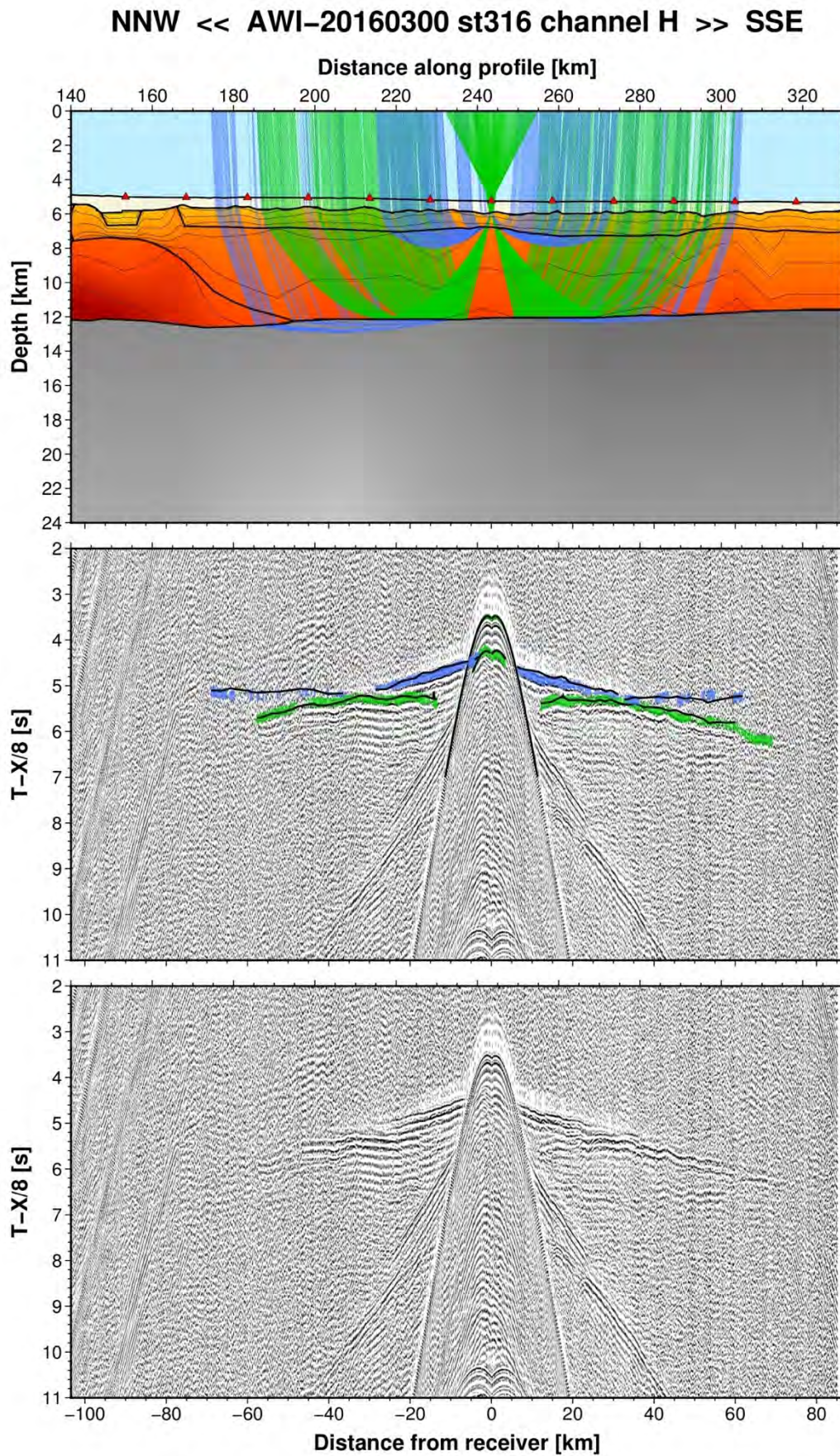


Fig. A90: Ray tracing results for station st316 along profile AWI-20160300. Lower panel: Seismic record; Middle panel: Picked and modelled arrival times; Upper panel: Section of the resulting P-wave velocity model; Green colours = reflections, blue colours = refractions.

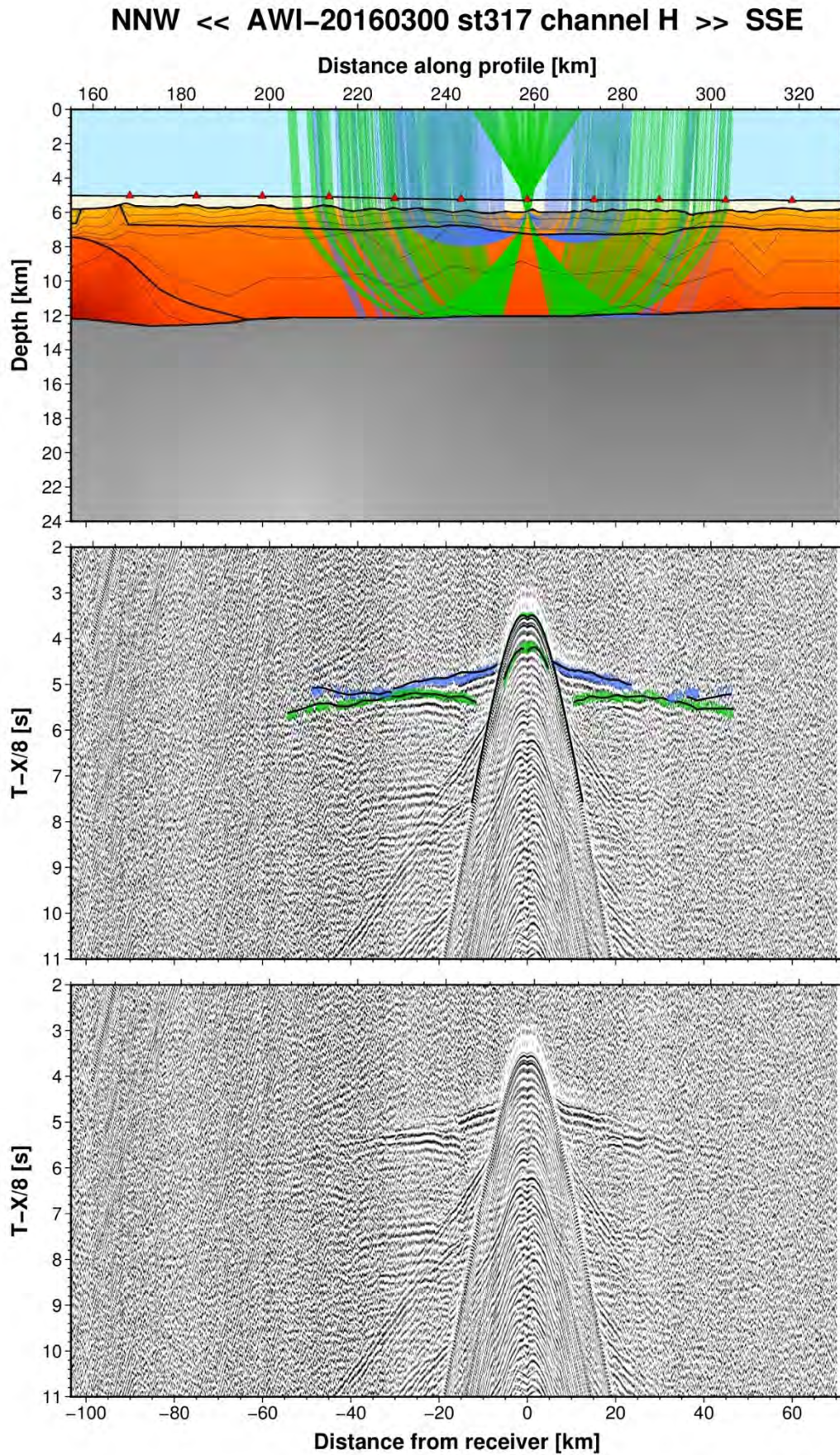


Fig. A91: Ray tracing results for station st317 along profile AWI-20160300. Lower panel: Seismic record; Middle panel: Picked and modelled arrival times; Upper panel: Section of the resulting P-wave velocity model; Green colours = reflections, blue colours = refractions.

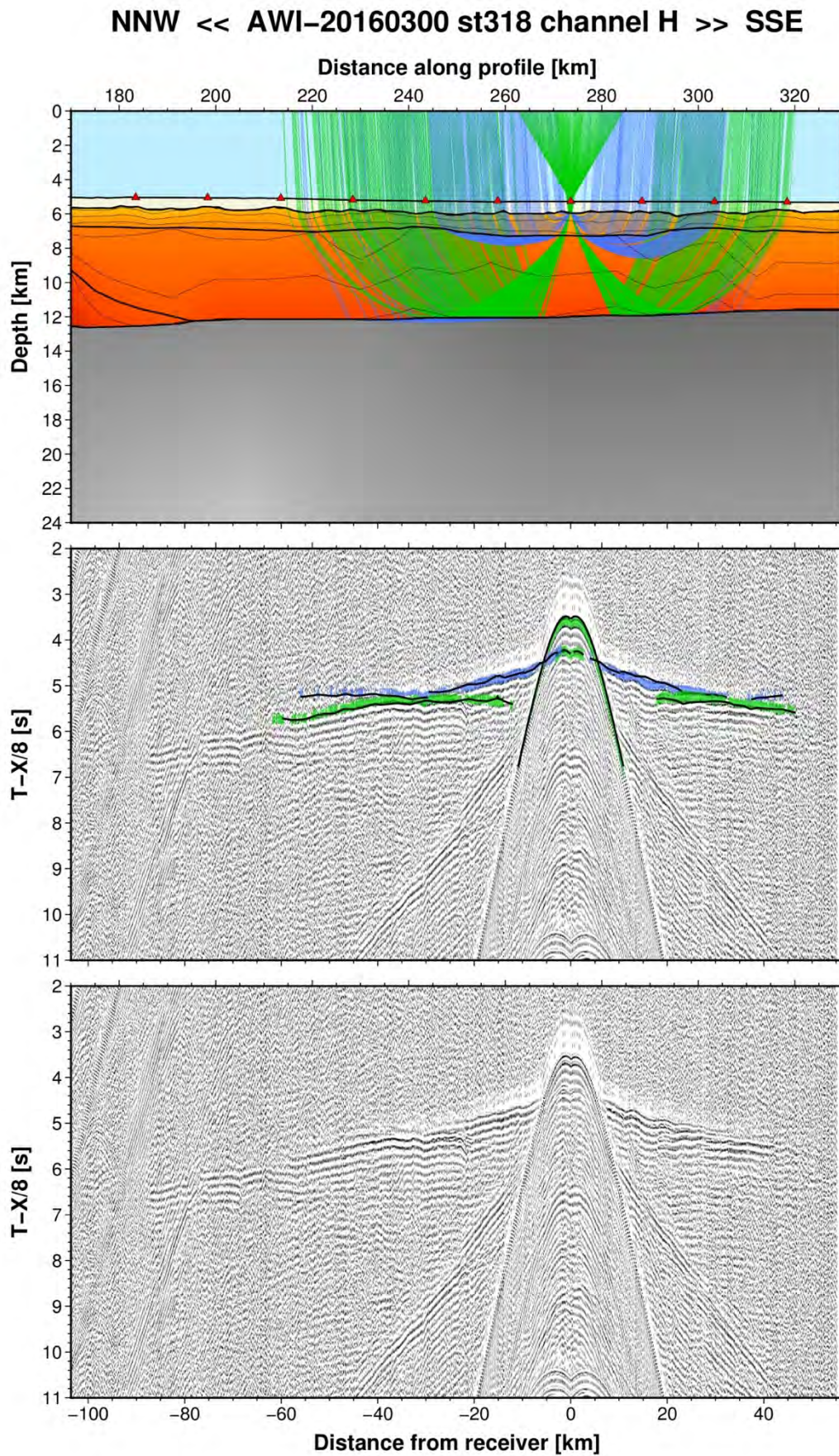


Fig. A92: Ray tracing results for station st318 along profile AWI-20160300. Lower panel: Seismic record; Middle panel: Picked and modelled arrival times; Upper panel: Section of the resulting P-wave velocity model; Green colours = reflections, blue colours = refractions.

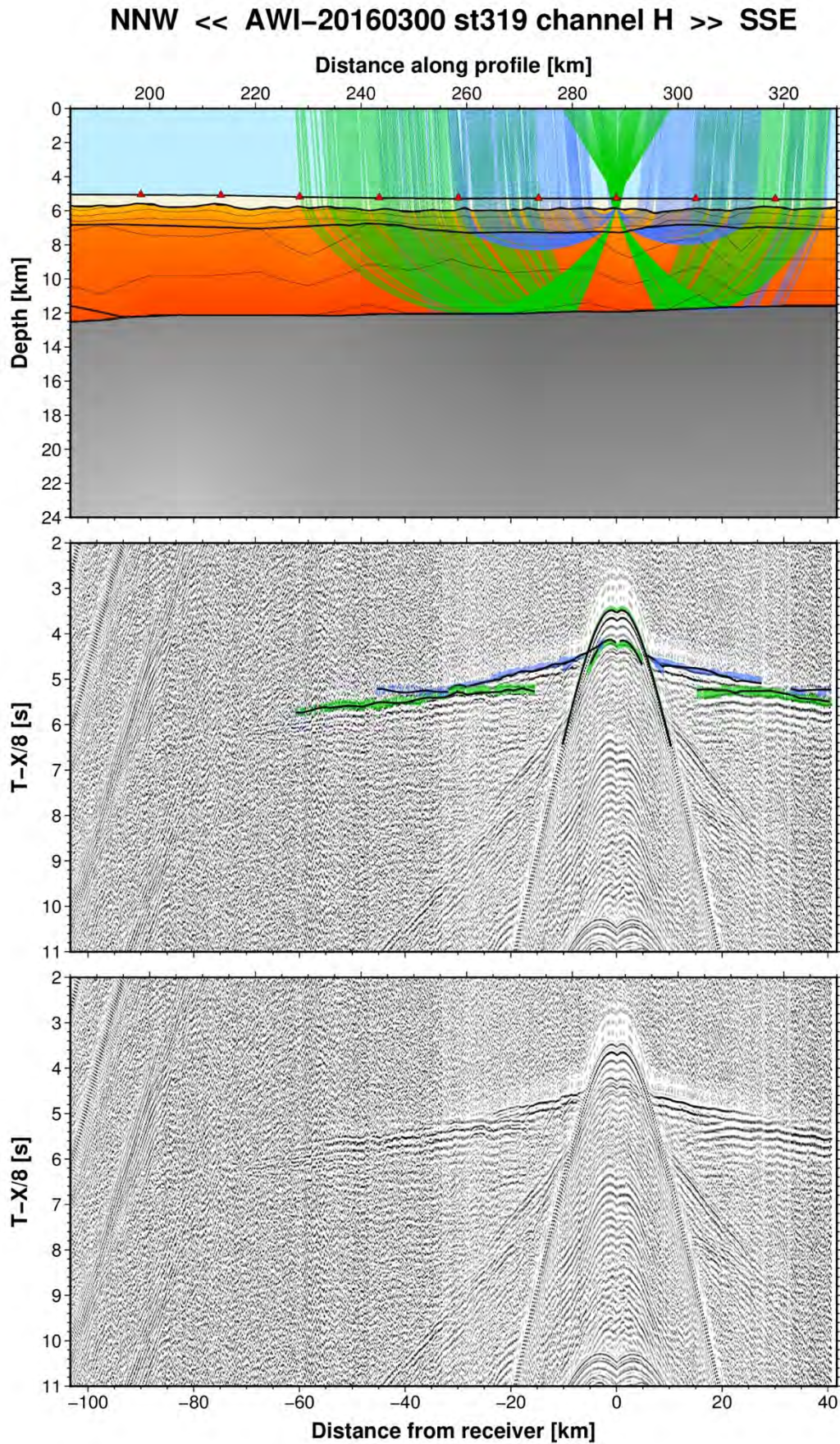


Fig. A93: Ray tracing results for station st319 along profile AWI-20160300. Lower panel: Seismic record; Middle panel: Picked and modelled arrival times; Upper panel: Section of the resulting P-wave velocity model; Green colours = reflections, blue colours = refractions.

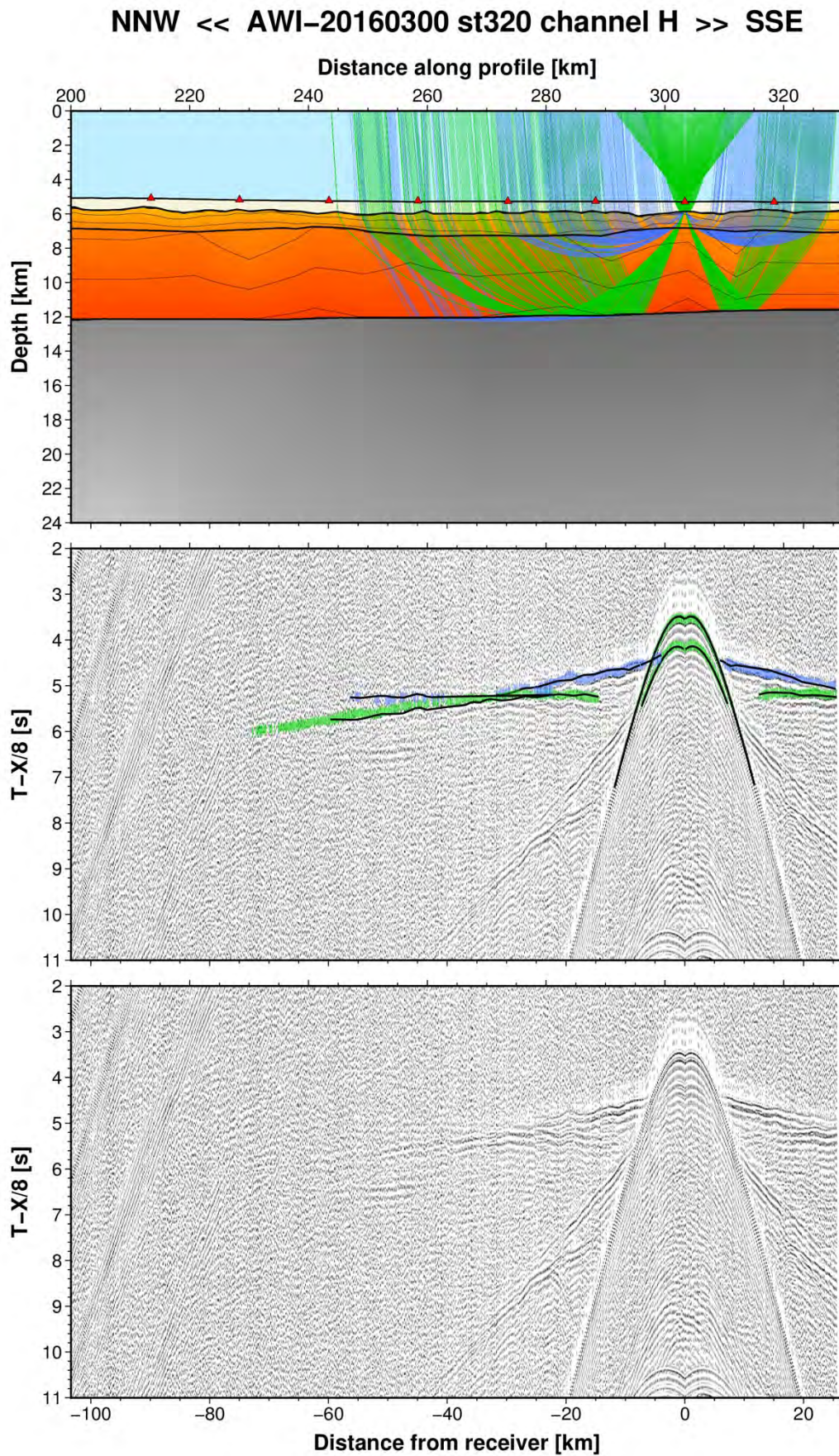


Fig. A94: Ray tracing results for station st320 along profile AWI-20160300. Lower panel: Seismic record; Middle panel: Picked and modelled arrival times; Upper panel: Section of the resulting P-wave velocity model; Green colours = reflections, blue colours = refractions.

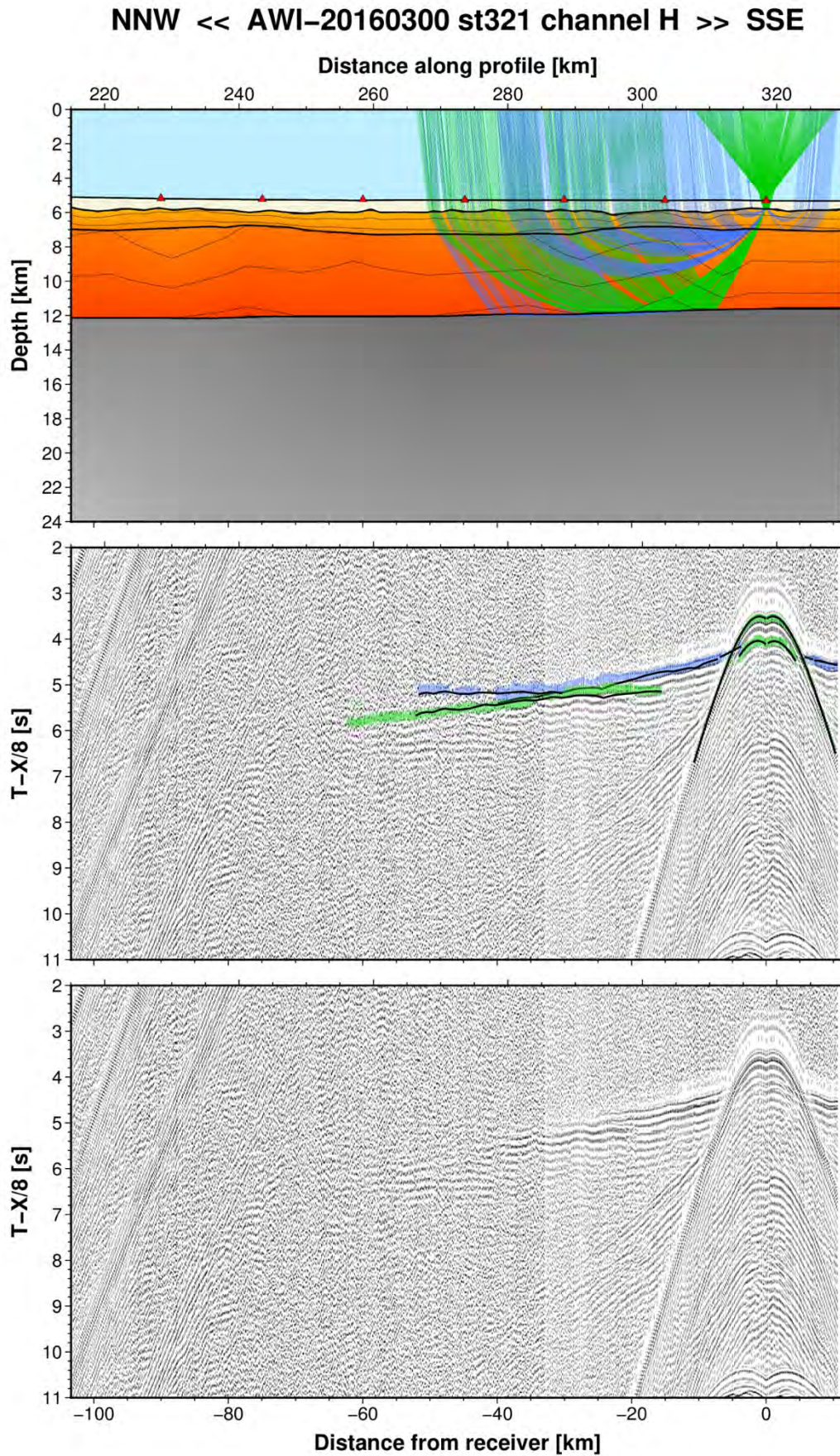


Fig. A95: Ray tracing results for station st321 along profile AWI-20160300. Lower panel: Seismic record; Middle panel: Picked and modelled arrival times; Upper panel: Section of the resulting P-wave velocity model; Green colours = reflections, blue colours = refractions.

A4. AWI-20160400

Tab. A4: Table with information about the configurations and data quality (1 = excellent, 2 = medium, 3 = low, 4 = no data, - = channel not used) of the OBS / OBH stations along profile AWI-20160400. See Gohl & Werner (2016) for more information.

Station	Water Depth [m]	Type	Recorder Type	Sensors	Quality				
					C 1	C 2	C 3	C 4	C 5
					h	x	y	z	h
st401	395	OBS (GEOMAR)	MBS	H,X,Y,Z	2	2-3	3	3	-
st402	437	OBS (AWI)	MCS	H	1	-	-	-	-
st403	417	OBS (GEOMAR)	Geolog	H,X,Y,Z,H	2	2	2	2	2
st404	377	OBS (AWI)	MCS	H	2-3	-	-	-	-
st405	390	OBS (GEOMAR)	MBS	H,X,Y,Z	2-3	2-3	2-3	2-3	-
st406	430	OBS (AWI)	6D6	H,X,Y,Z	1	1-2	1-2	2	-
st407	448	OBS (GEOMAR)	MBS	H,X,Y,Z	2	3	3	3	-
st408	477	OBS (AWI)	MCS	H	1	-	-	-	-
st409	506	OBS (GEOMAR)	MBS	H,X,Y,Z	2	2-3	2-3	2-3	-
st410	650	OBS (GEOMAR)	Geolog	H,X,Y,Z,H	1	2	2	2	2
st411	961	OBS (AWI)	MCS	H,X,Y,Z	1	2	2	1-2	-
st412	1018	OBS (GEOMAR)	MBS	H,X,Y,Z	1	1-2	1-2	2	-
st413	1180	OBS (GEOMAR)	MBS	H,X,Y,Z	1-2	3	3	3	-
st414	1319	OBS (AWI)	MCS	H	3	-	-	-	-
st415	1519	OBS (GEOMAR)	MBS	H,X,Y,Z	1-2	2	2-3	2-3	-
st416	1845	OBS (AWI)	MCS	H,X,Y,Z	1	1-2	1-2	2	-
st417	2244	OBS (GEOMAR)	Geolog	H,X,Y,Z,H	1	2	2	2	1
st418	2443	OBS (AWI)	MCS	H	1	-	-	-	-
st419	2781	OBS (GEOMAR)	MBS	H,X,Y,Z	1-2	3	3	3	-
st420	3223	OBS (GEOMAR)	MBS	H,X,Y,Z	4	4	4	4	-

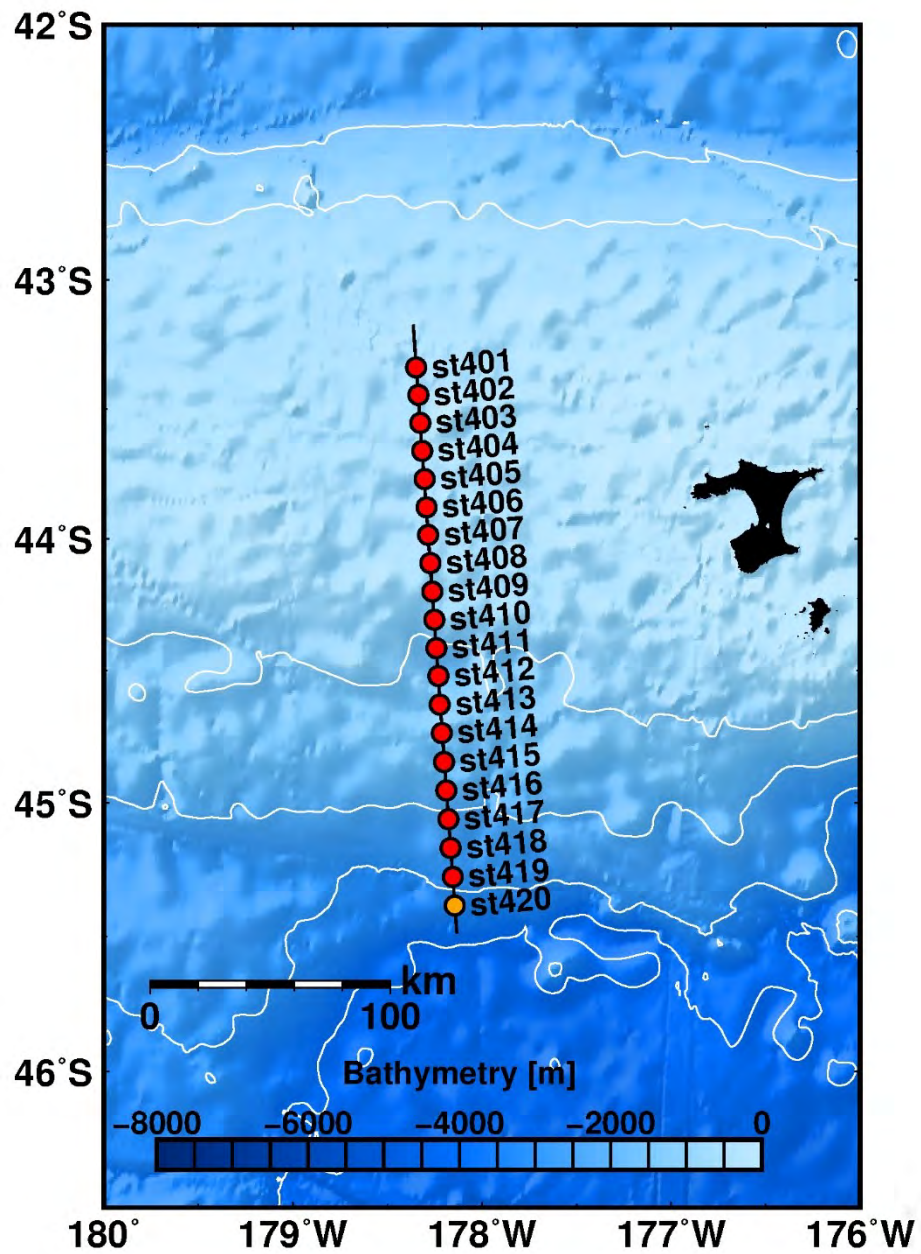


Fig. A96: Bathymetric map of the southern Chatham Rise margin and deployed OBS / OBH stations (red circles) along profile AWI-20160400. OBS / OBH without data are marked as orange circles.

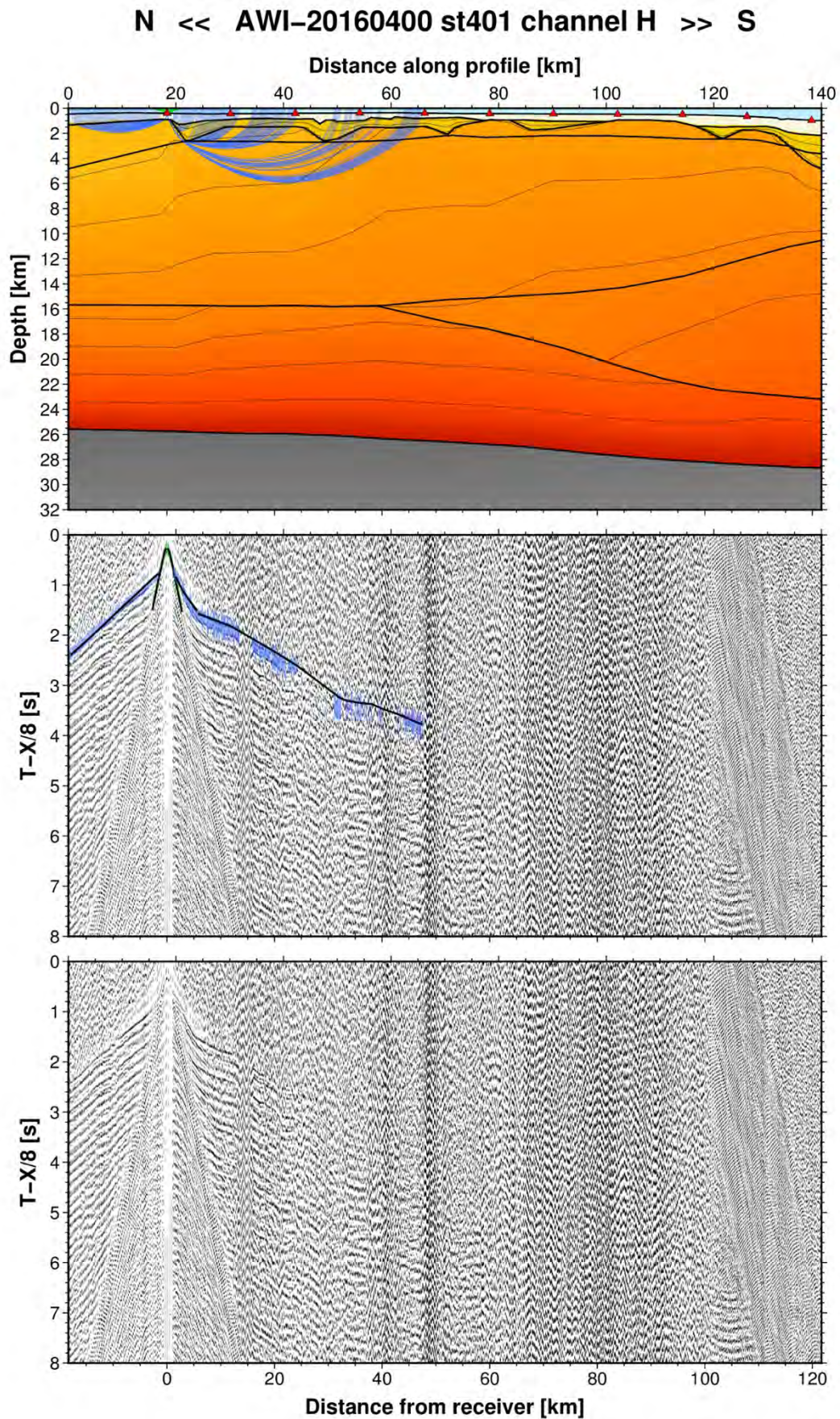


Fig. A97: Ray tracing results for station st401 along profile AWI-20160400. Lower panel: Seismic record; Middle panel: Picked and modelled arrival times; Upper panel: Section of the resulting P-wave velocity model; Green colours = reflections, blue colours = refractions.

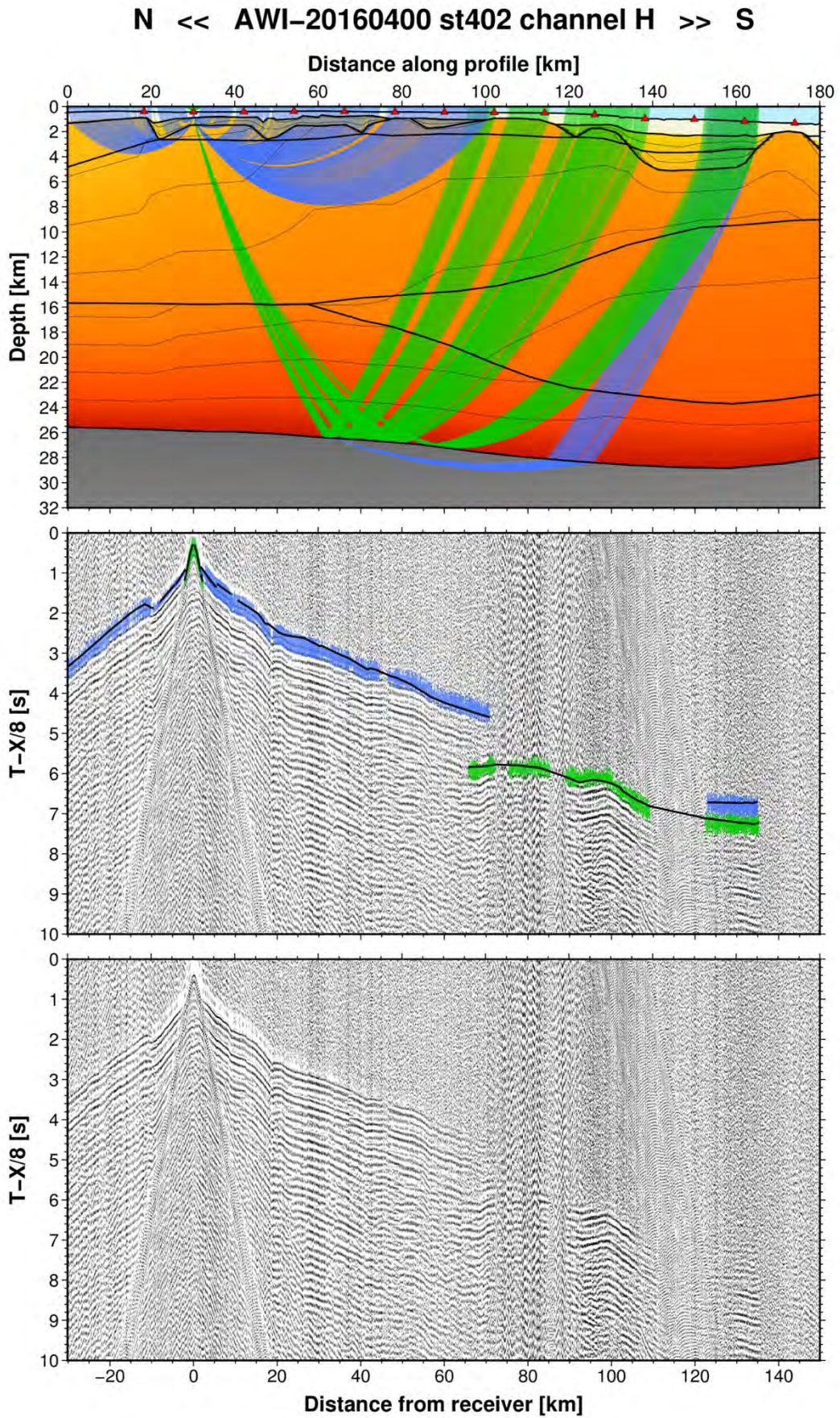


Fig. A98: Ray tracing results for station st402 along profile AWI-20160400. Lower panel: Seismic record; Middle panel: Picked and modelled arrival times; Upper panel: Section of the resulting P-wave velocity model; Green colours = reflections, blue colours = refractions.

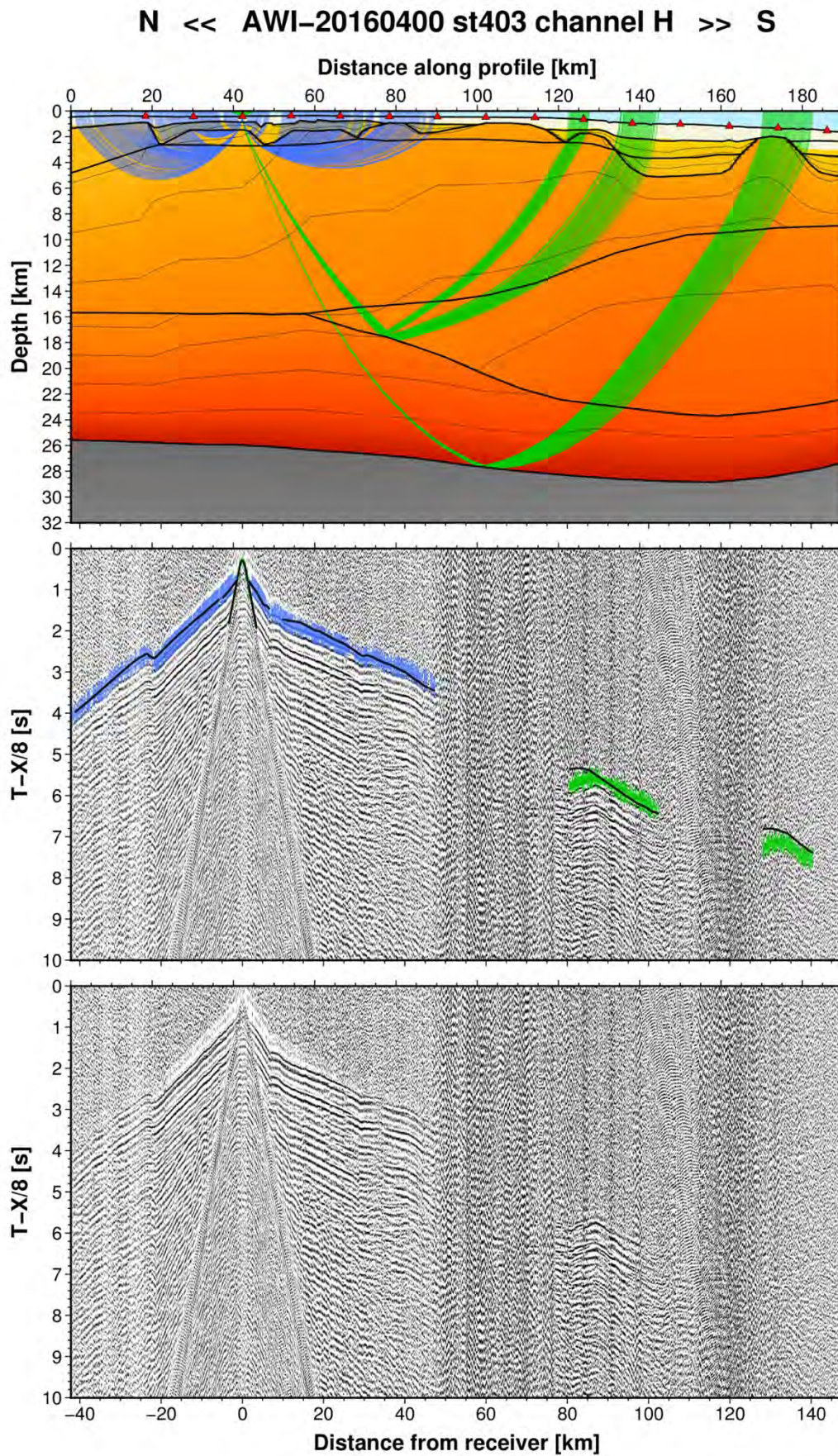


Fig. A99: Ray tracing results for station st403 along profile AWI-20160400. Lower panel: Seismic record; Middle panel: Picked and modelled arrival times; Upper panel: Section of the resulting P-wave velocity model; Green colours = reflections, blue colours = refractions.

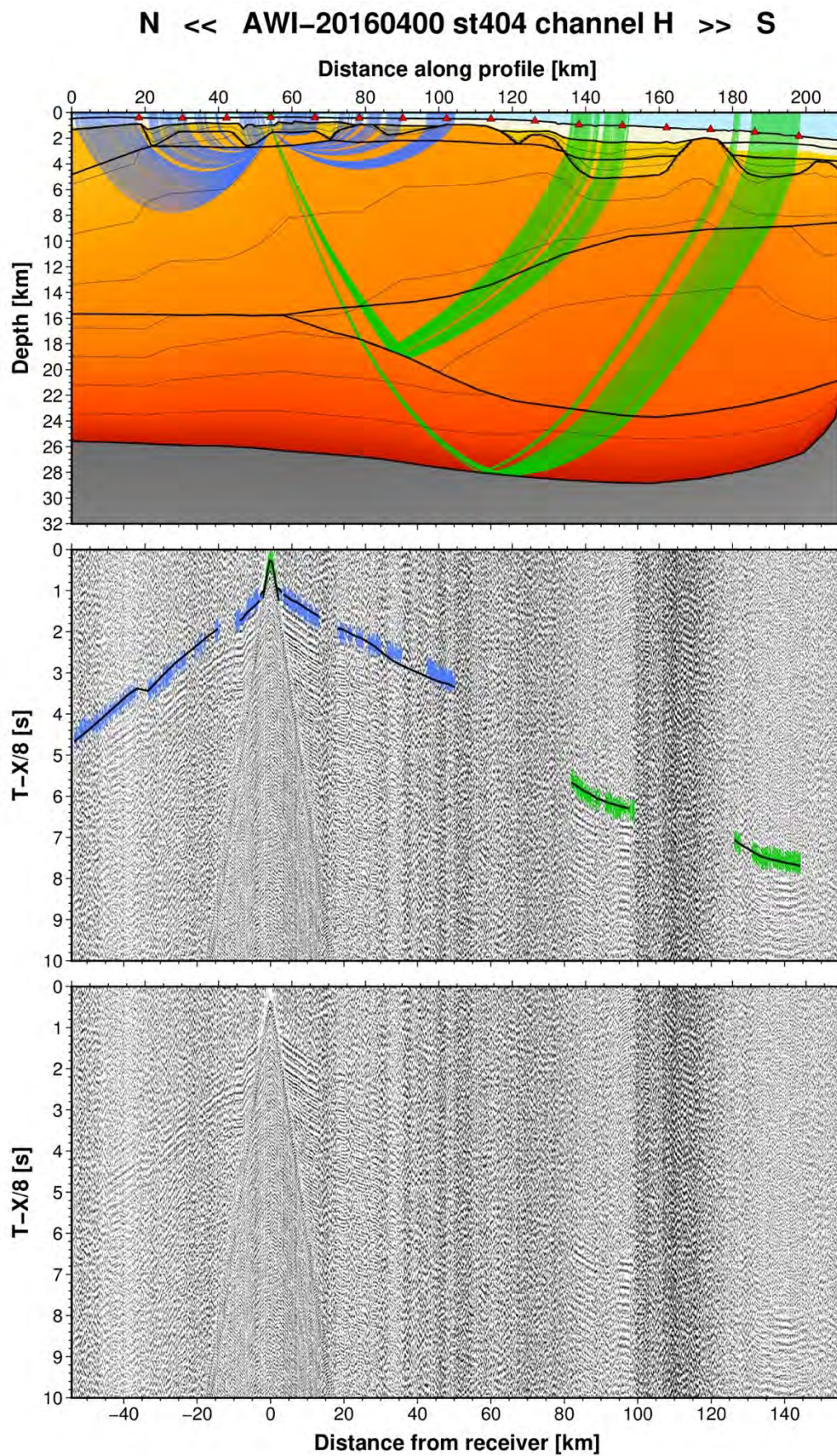


Fig. A100: Ray tracing results for station st404 along profile AWI-20160400. Lower panel: Seismic record; Middle panel: Picked and modelled arrival times; Upper panel: Section of the resulting P-wave velocity model; Green colours = reflections, blue colours = refractions.

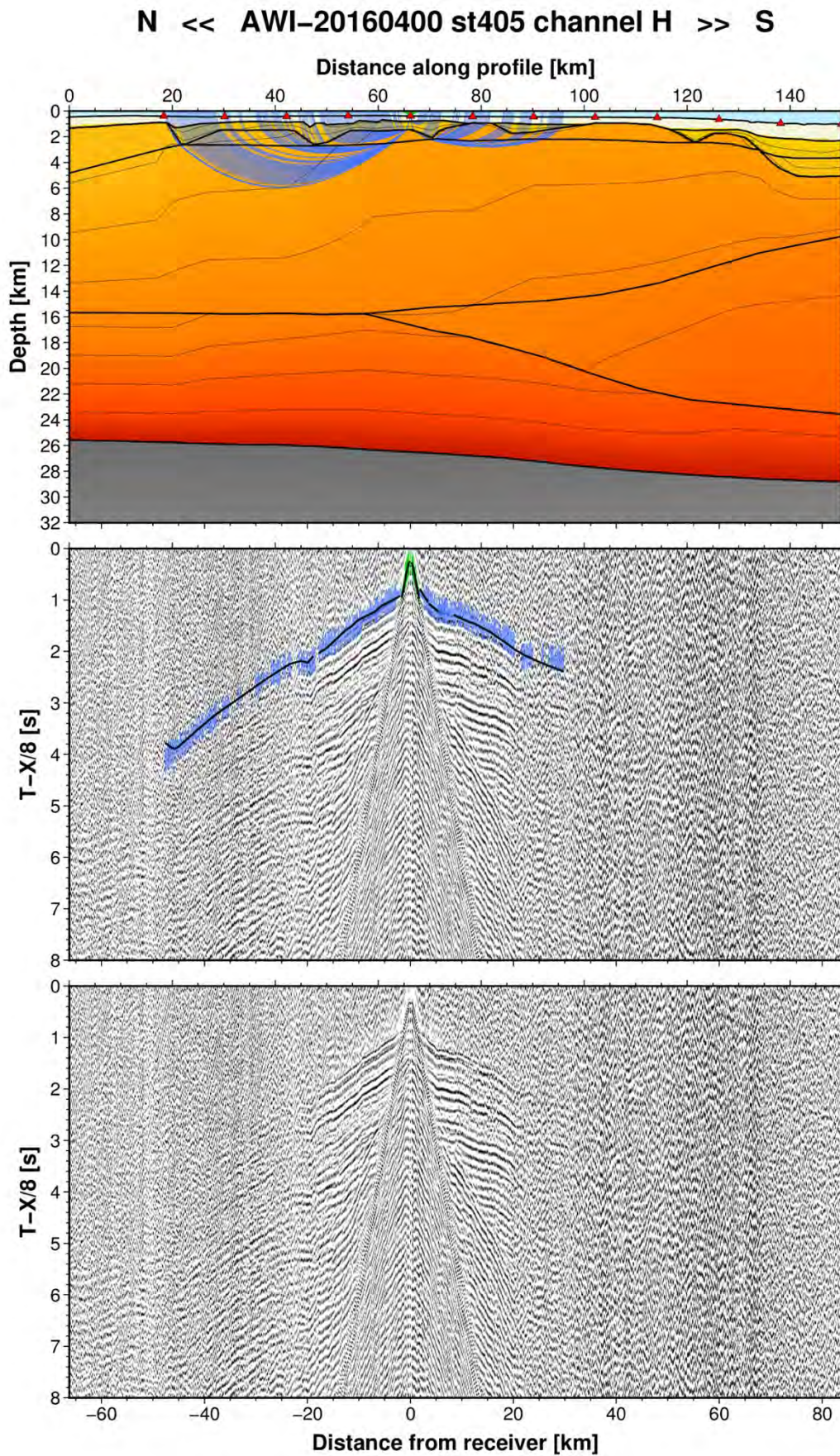


Fig. A101: Ray tracing results for station st405 along profile AWI-20160400. Lower panel: Seismic record; Middle panel: Picked and modelled arrival times; Upper panel: Section of the resulting P-wave velocity model; Green colours = reflections, blue colours = refractions.

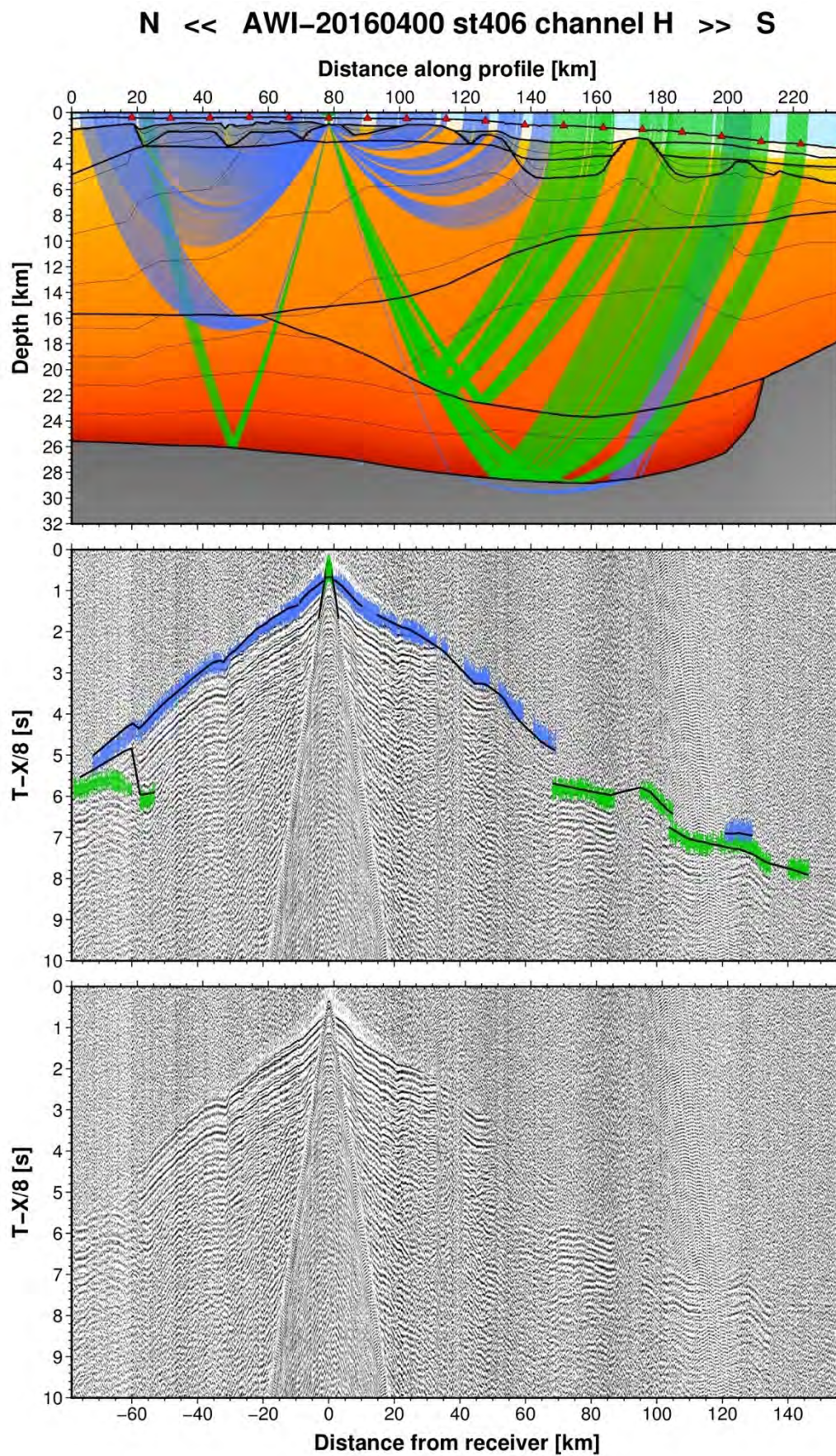


Fig. A102: Ray tracing results for station st406 along profile AWI-20160400. Lower panel: Seismic record; Middle panel: Picked and modelled arrival times; Upper panel: Section of the resulting P-wave velocity model; Green colours = reflections, blue colours = refractions.

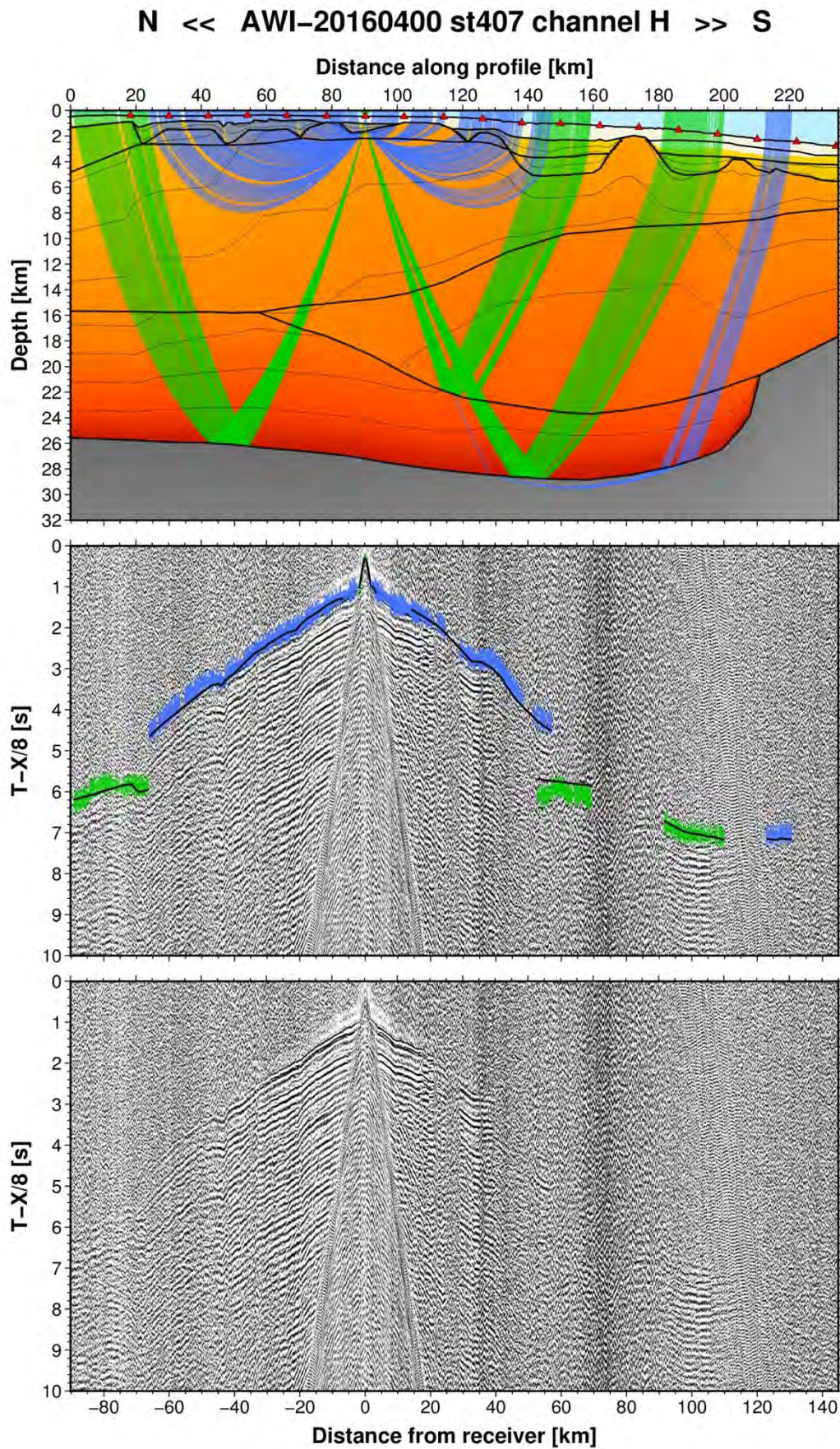


Fig. A103: Ray tracing results for station st407 along profile AWI-20160400. Lower panel: Seismic record; Middle panel: Picked and modelled arrival times; Upper panel: Section of the resulting P-wave velocity model; Green colours = reflections, blue colours = refractions.

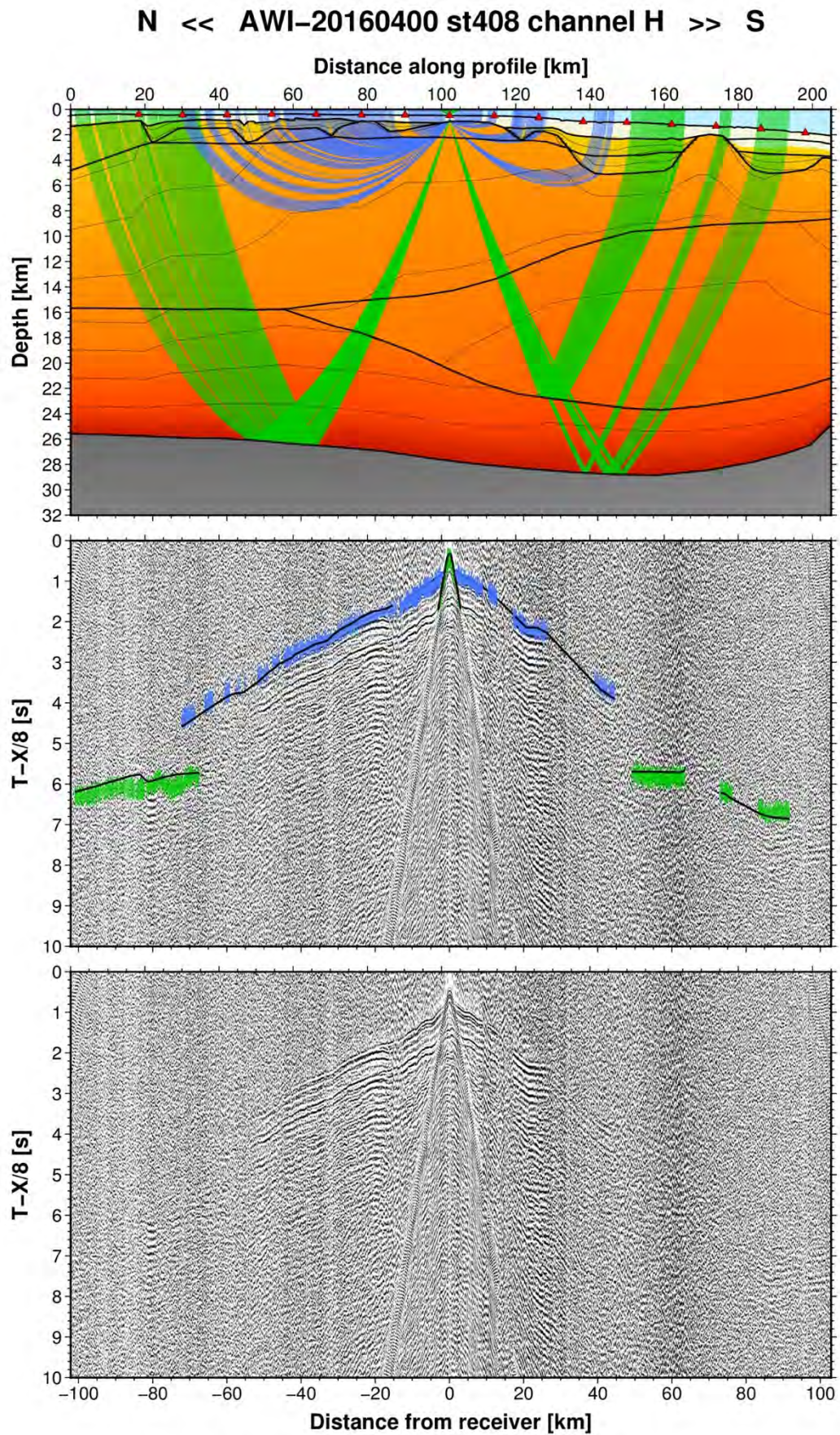


Fig. A104: Ray tracing results for station st408 along profile AWI-20160400. Lower panel: Seismic record; Middle panel: Picked and modelled arrival times; Upper panel: Section of the resulting P-wave velocity model; Green colours = reflections, blue colours = refractions.

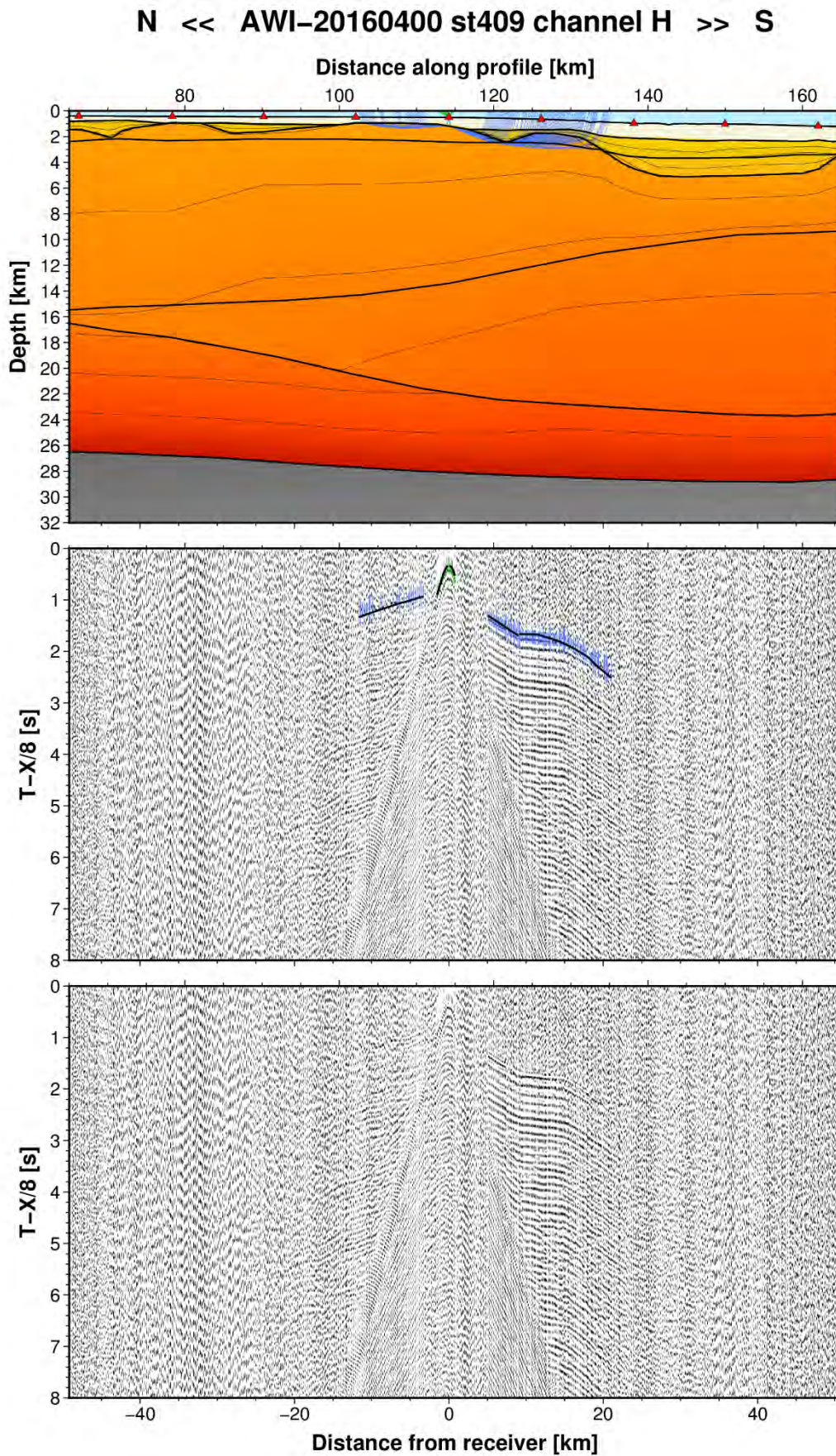


Fig. A105: Ray tracing results for station st409 along profile AWI-20160400. Lower panel: Seismic record; Middle panel: Picked and modelled arrival times; Upper panel: Section of the resulting P-wave velocity model; Green colours = reflections, blue colours = refractions.

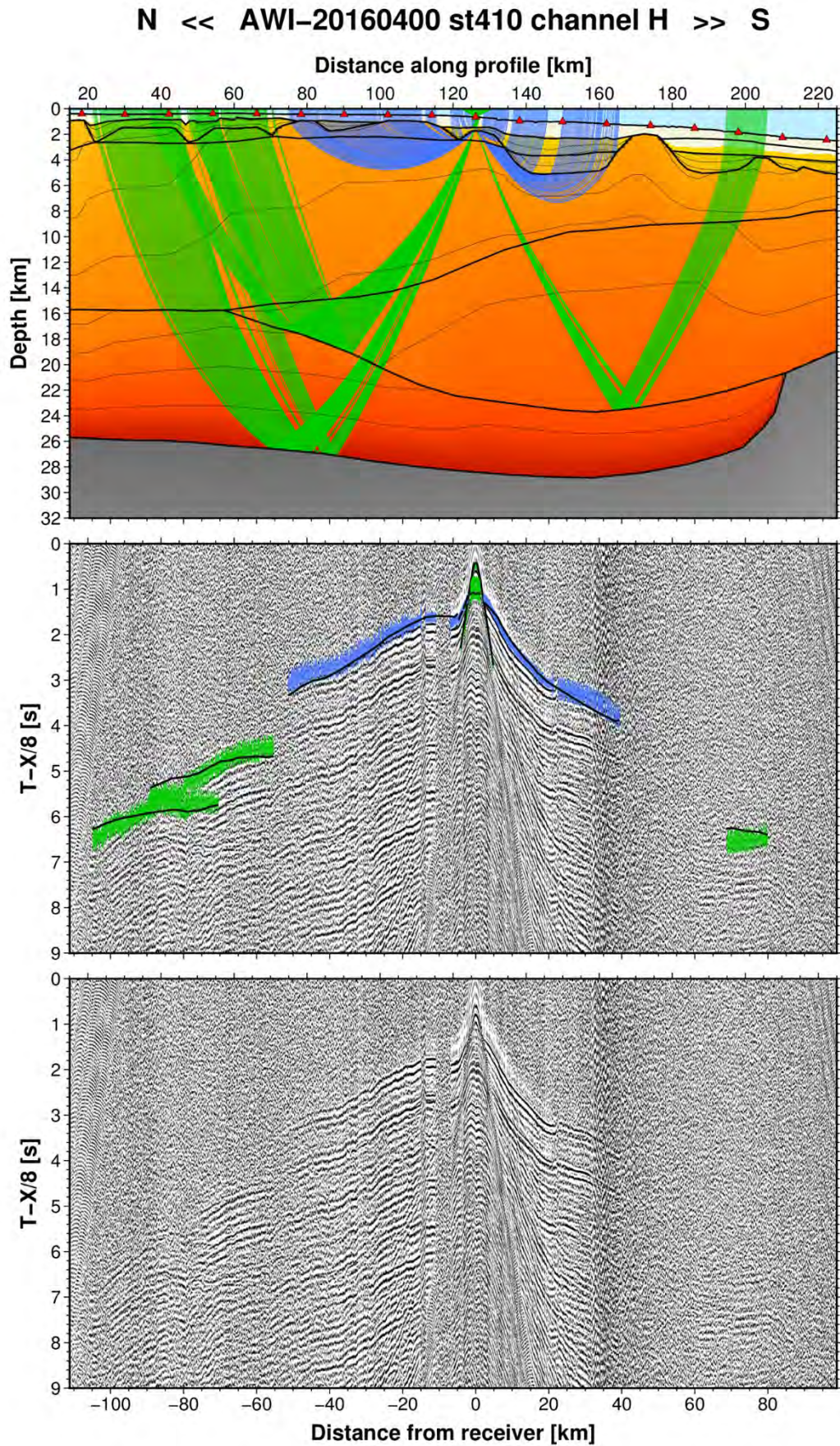


Fig. A106: Ray tracing results for station st410 along profile AWI-20160400. Lower panel: Seismic record; Middle panel: Picked and modelled arrival times; Upper panel: Section of the resulting P-wave velocity model; Green colours = reflections, blue colours = refractions.

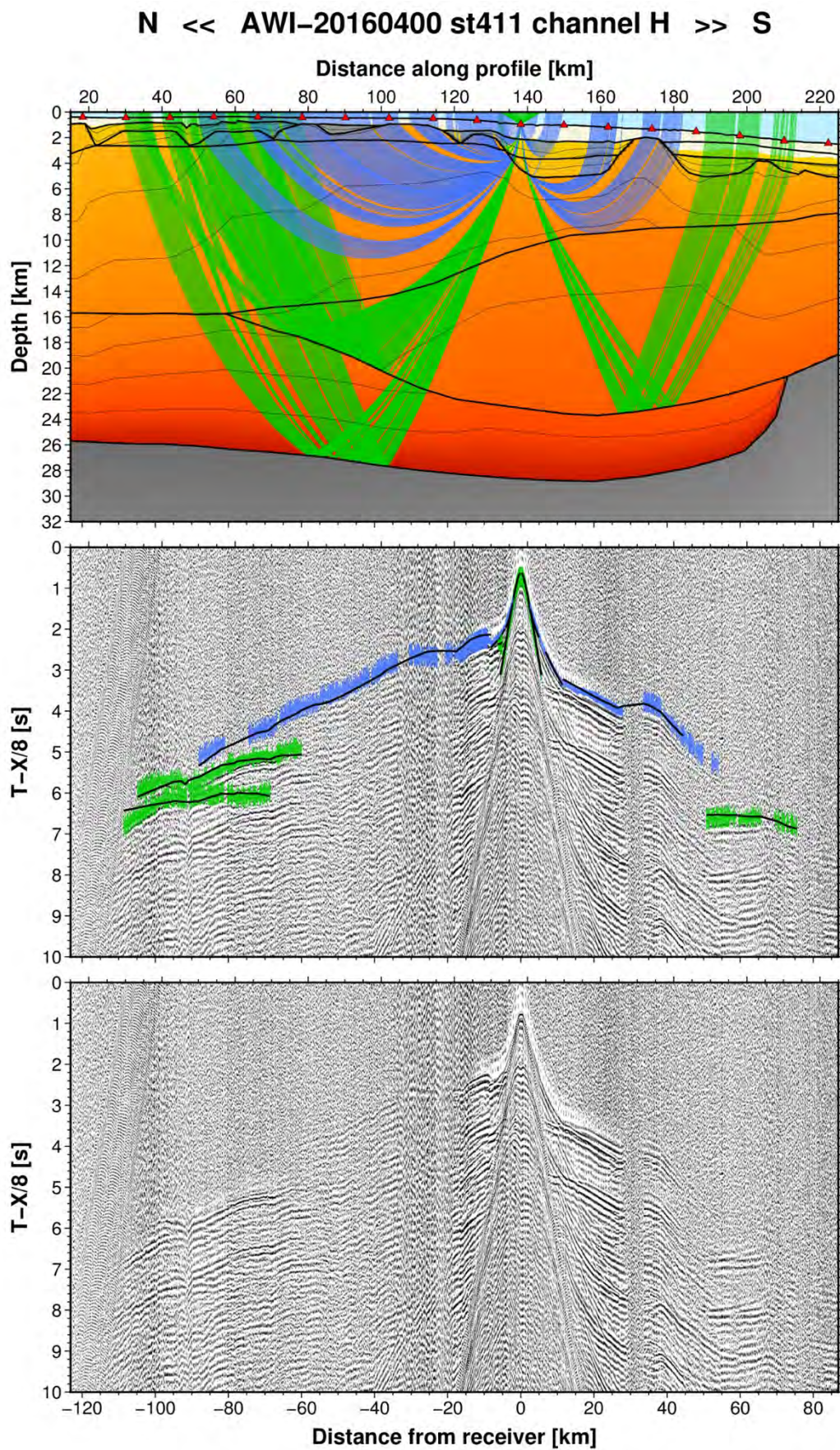


Fig. A107: Ray tracing results for station st411 along profile AWI-20160400. Lower panel: Seismic record; Middle panel: Picked and modelled arrival times; Upper panel: Section of the resulting P-wave velocity model; Green colours = reflections, blue colours = refractions.

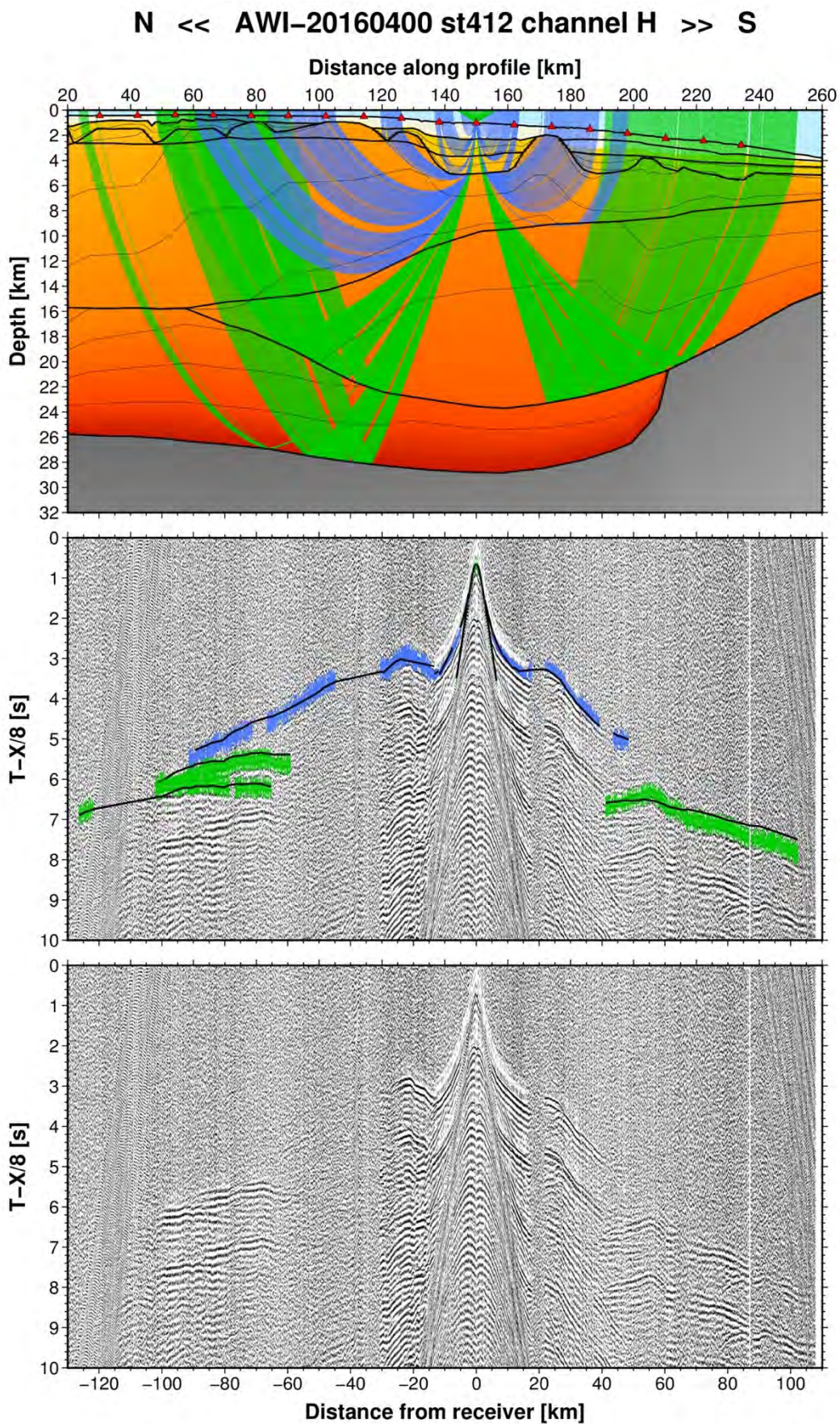


Fig. A108: Ray tracing results for station st412 along profile AWI-20160400. Lower panel: Seismic record; Middle panel: Picked and modelled arrival times; Upper panel: Section of the resulting P-wave velocity model; Green colours = reflections, blue colours = refractions.

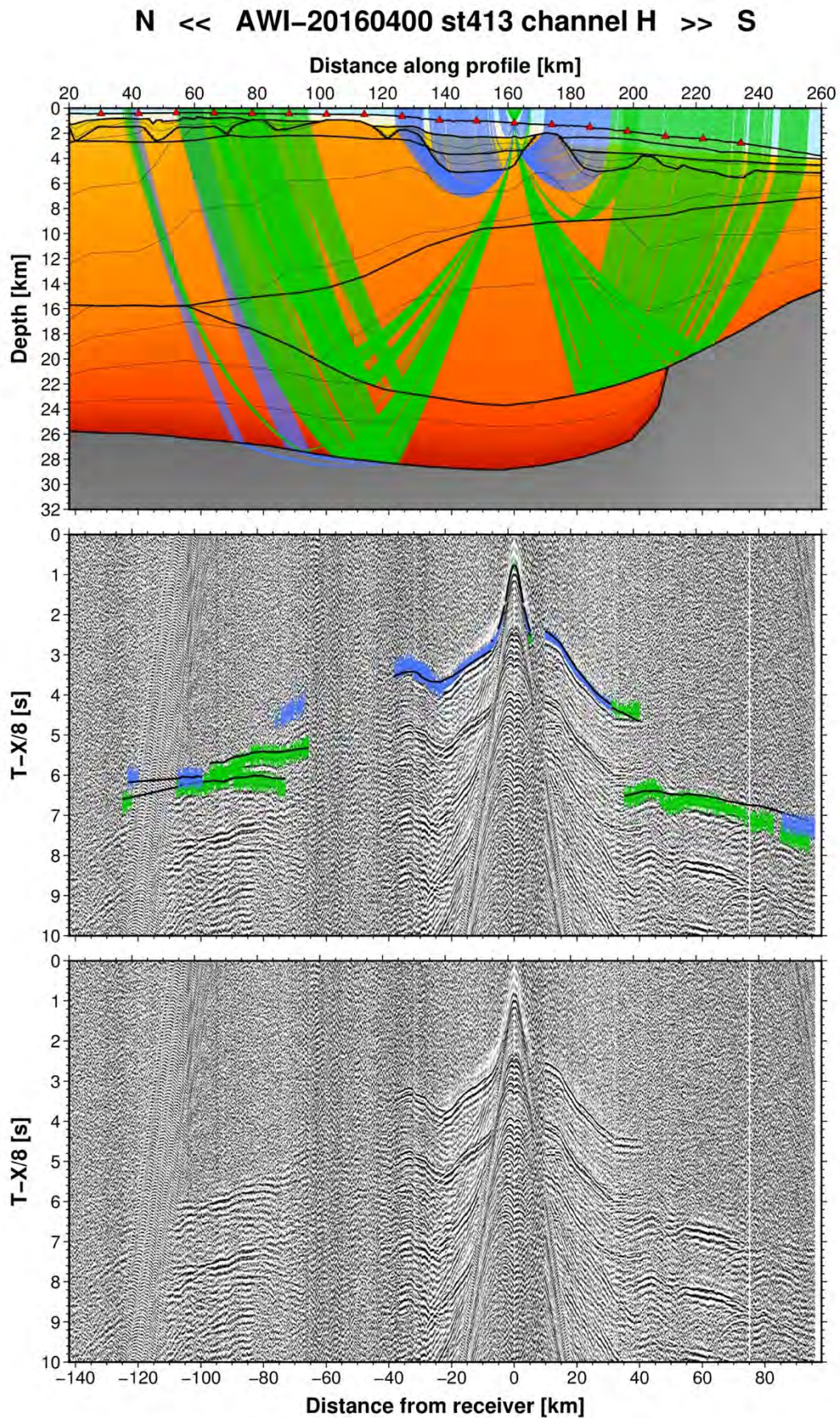


Fig. A109: Ray tracing results for station st413 along profile AWI-20160400. Lower panel: Seismic record; Middle panel: Picked and modelled arrival times; Upper panel: Section of the resulting P-wave velocity model; Green colours = reflections, blue colours = refractions.

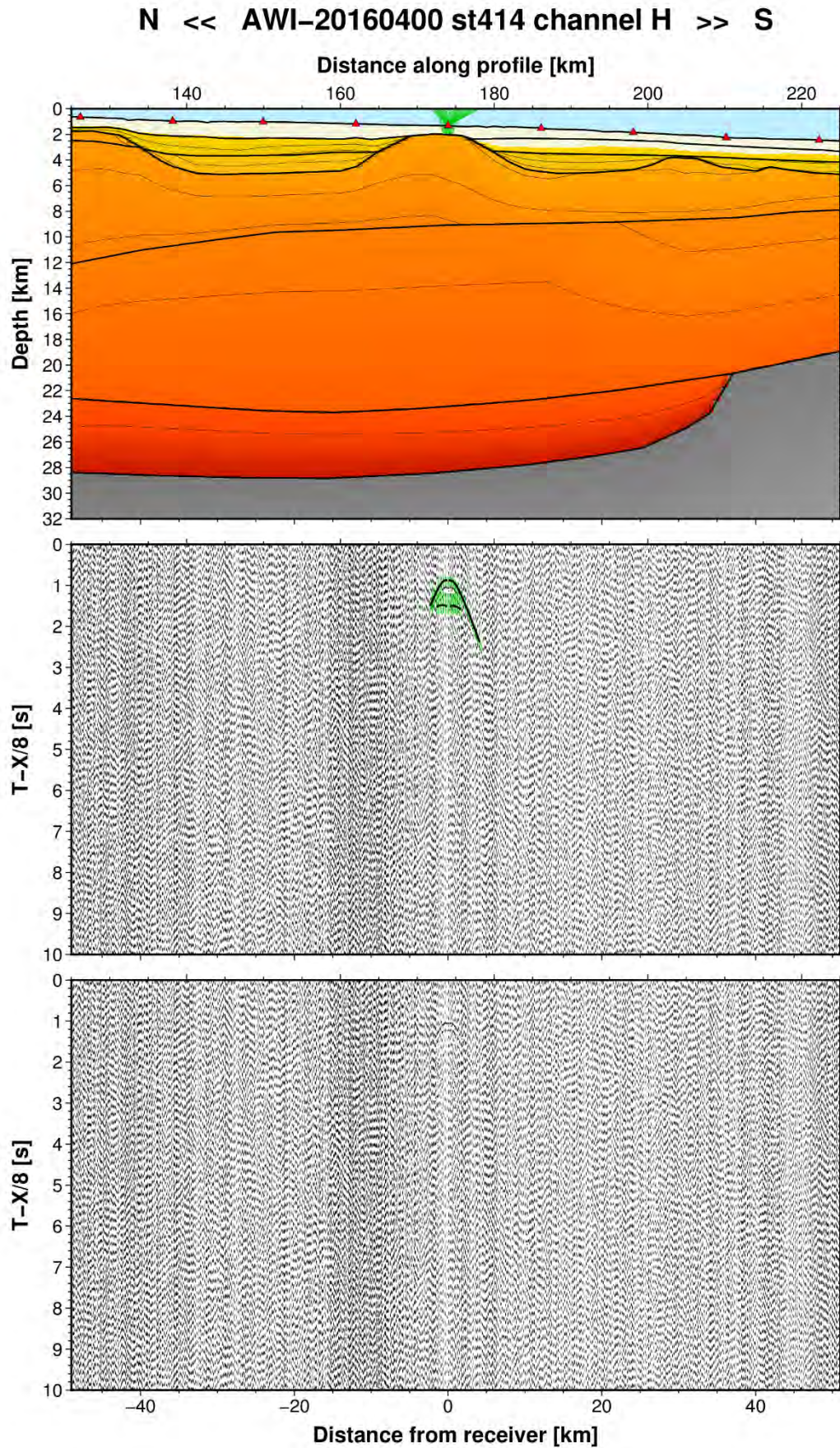


Fig. A110: Ray tracing results for station st414 along profile AWI-20160400. Lower panel: Seismic record; Middle panel: Picked and modelled arrival times; Upper panel: Section of the resulting P-wave velocity model; Green colours = reflections, blue colours = refractions.

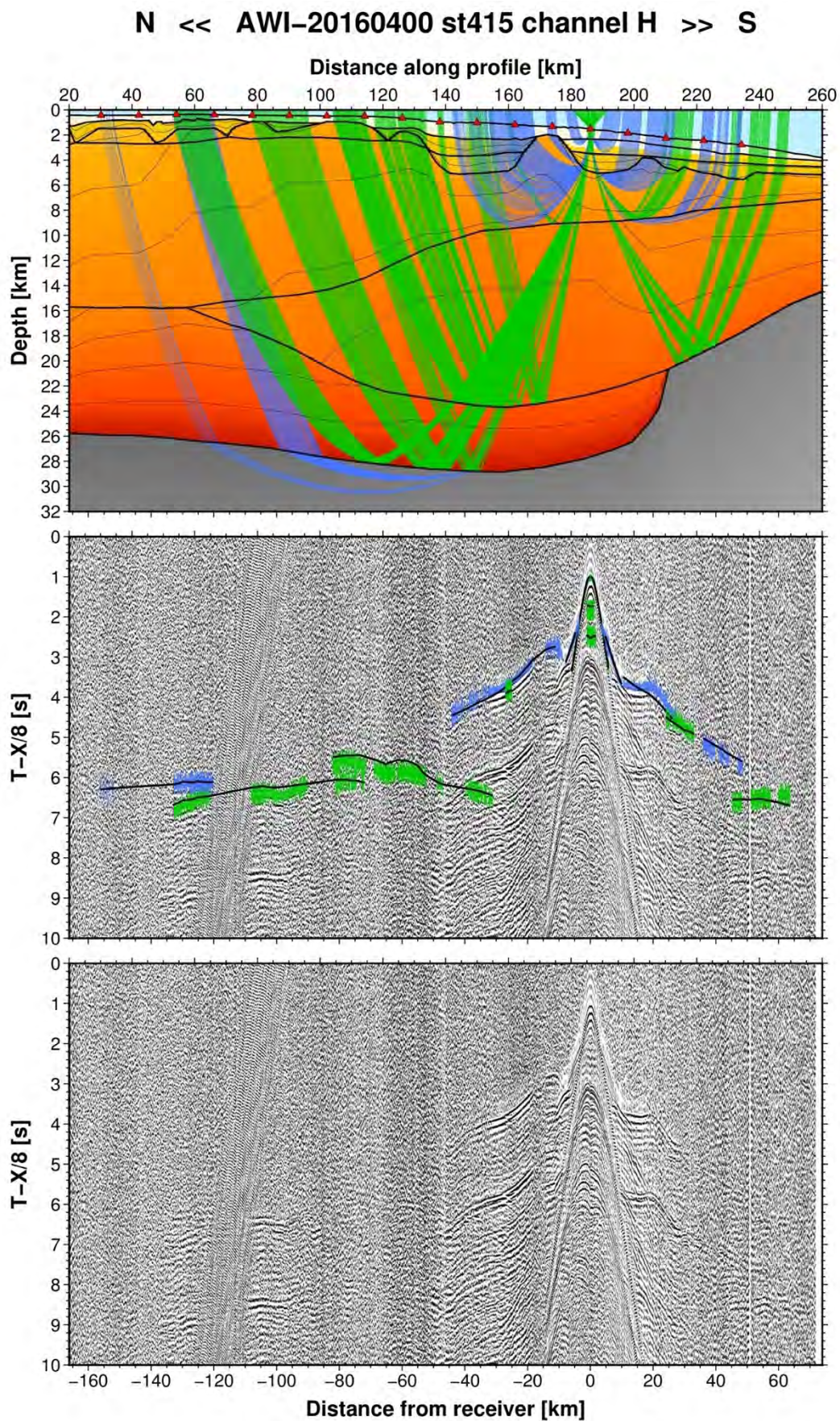


Fig. A111: Ray tracing results for station st415 along profile AWI-20160400. Lower panel: Seismic record; Middle panel: Picked and modelled arrival times; Upper panel: Section of the resulting P-wave velocity model; Green colours = reflections, blue colours = refractions.

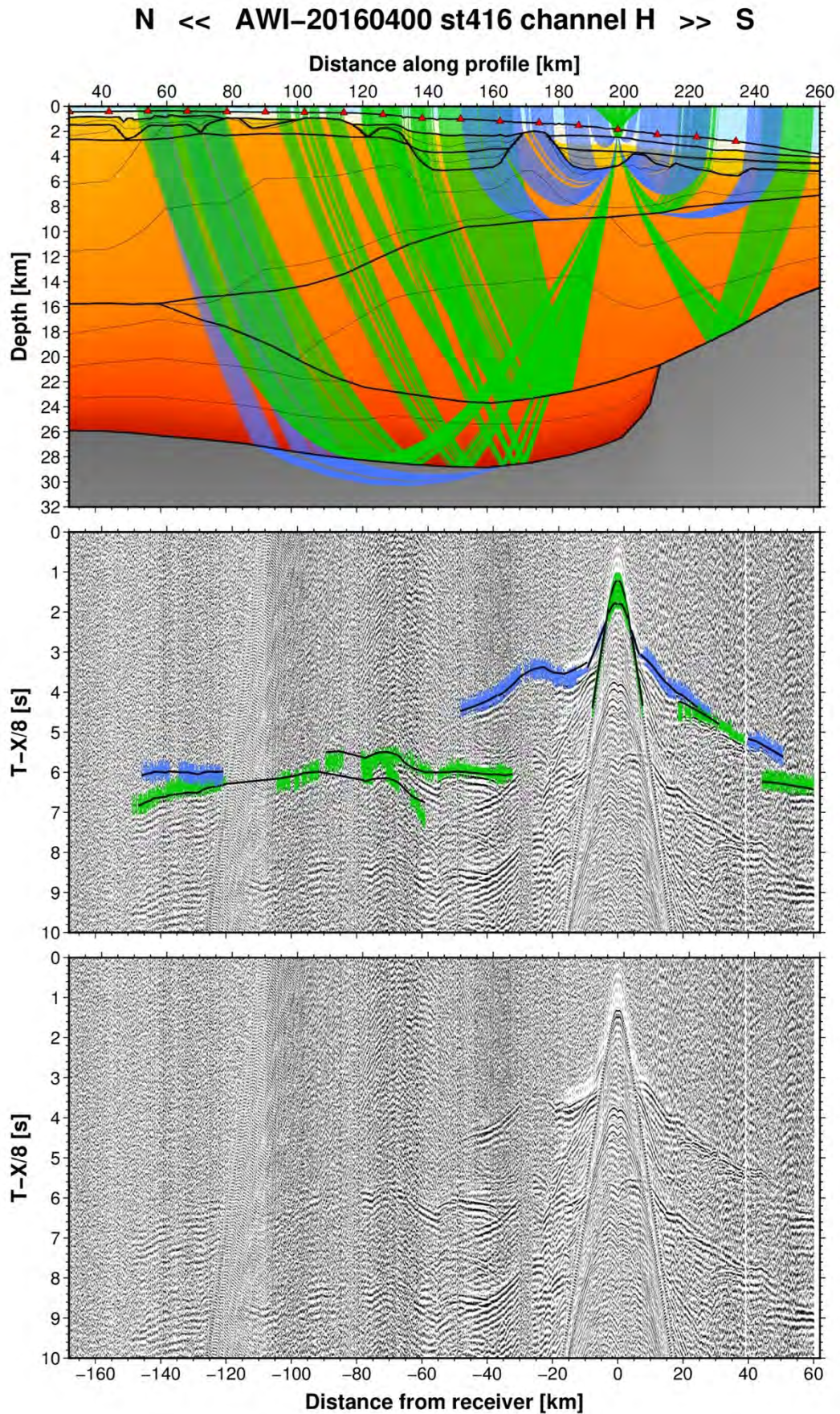


Fig. A112: Ray tracing results for station st416 along profile AWI-20160400. Lower panel: Seismic record; Middle panel: Picked and modelled arrival times; Upper panel: Section of the resulting P-wave velocity model; Green colours = reflections, blue colours = refractions.

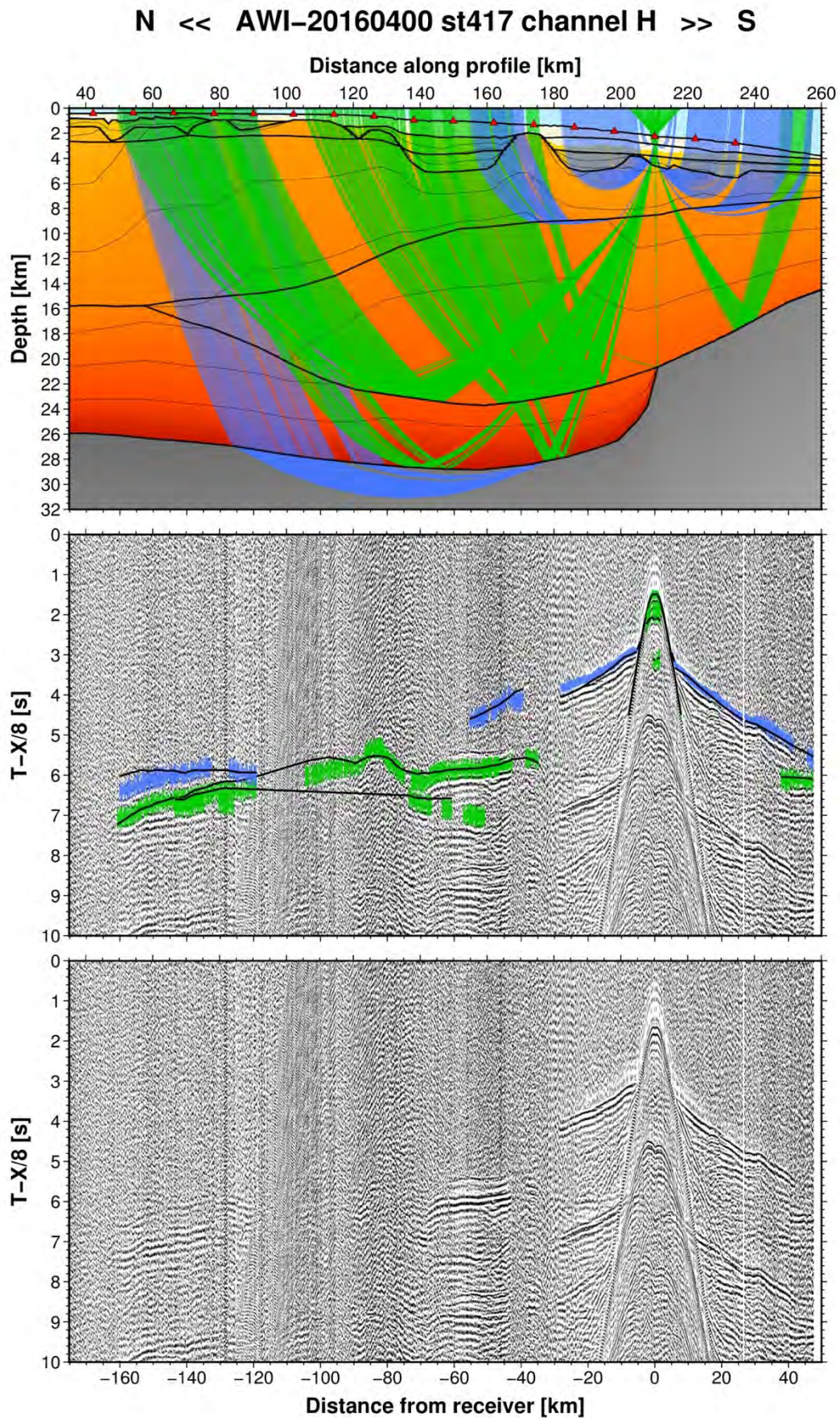


Fig. A113: Ray tracing results for station st417 along profile AWI-20160400. Lower panel: Seismic record; Middle panel: Picked and modelled arrival times; Upper panel: Section of the resulting P-wave velocity model; Green colours = reflections, blue colours = refractions.

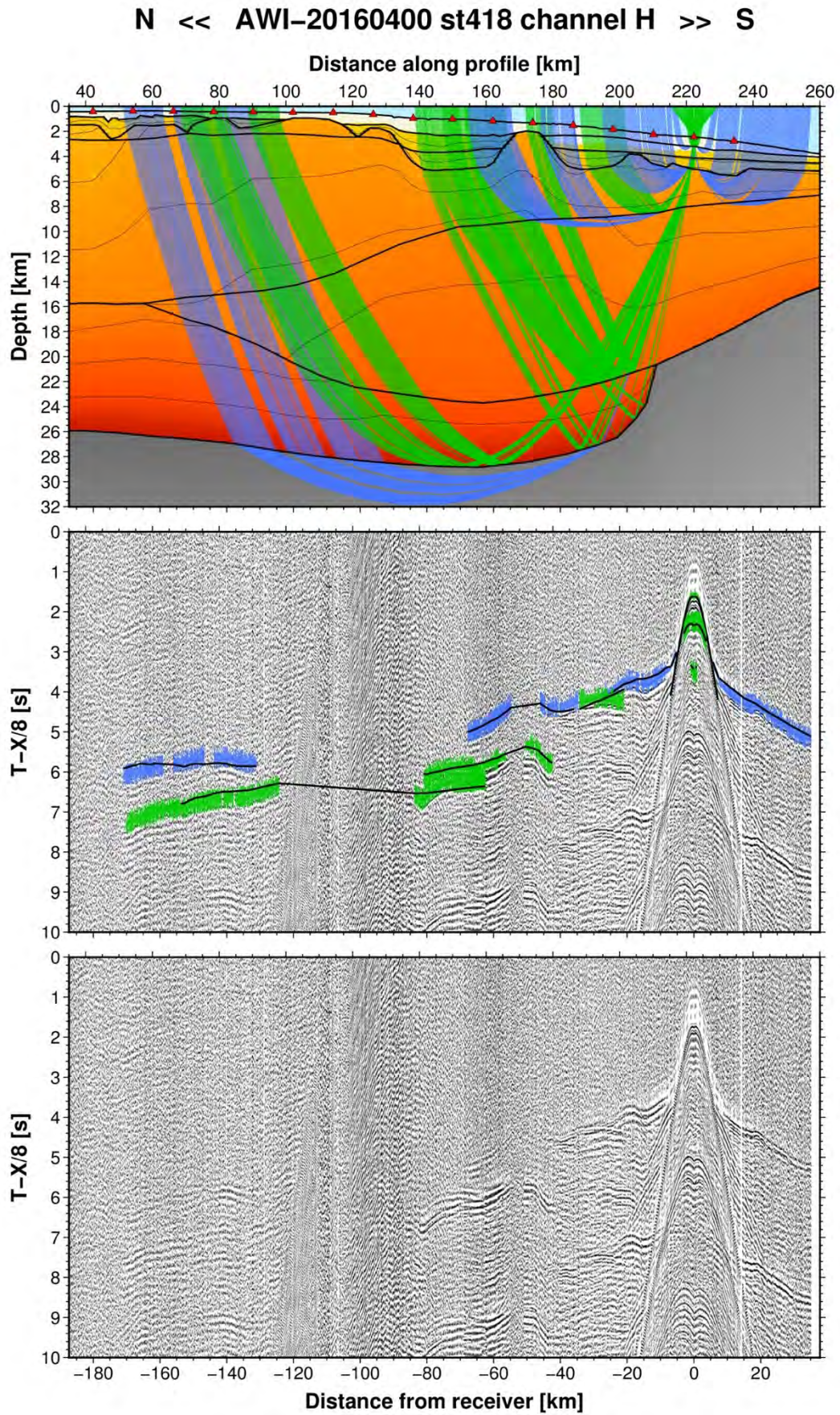


Fig. A114: Ray tracing results for station st418 along profile AWI-20160400. Lower panel: Seismic record; Middle panel: Picked and modelled arrival times; Upper panel: Section of the resulting P-wave velocity model; Green colours = reflections, blue colours = refractions.

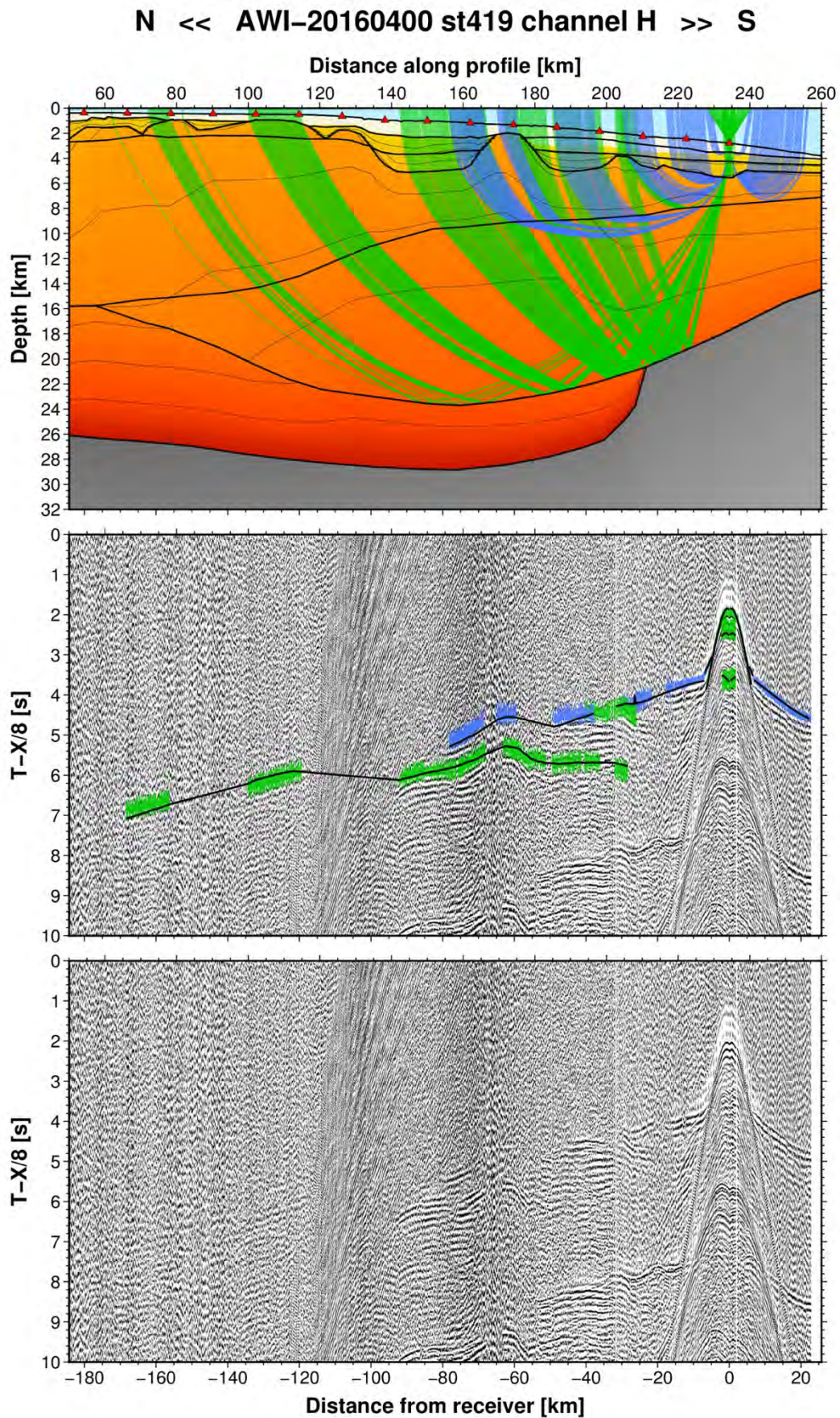


Fig. A115: Ray tracing results for station st419 along profile AWI-20160400. Lower panel: Seismic record; Middle panel: Picked and modelled arrival times; Upper panel: Section of the resulting P-wave velocity model; Green colours = reflections, blue colours = refractions.